FORSCHUNGSZENTRUM JÜLICH GmbH

KFA

Institut für Kernphysik

ANNUAL REPORT 1995

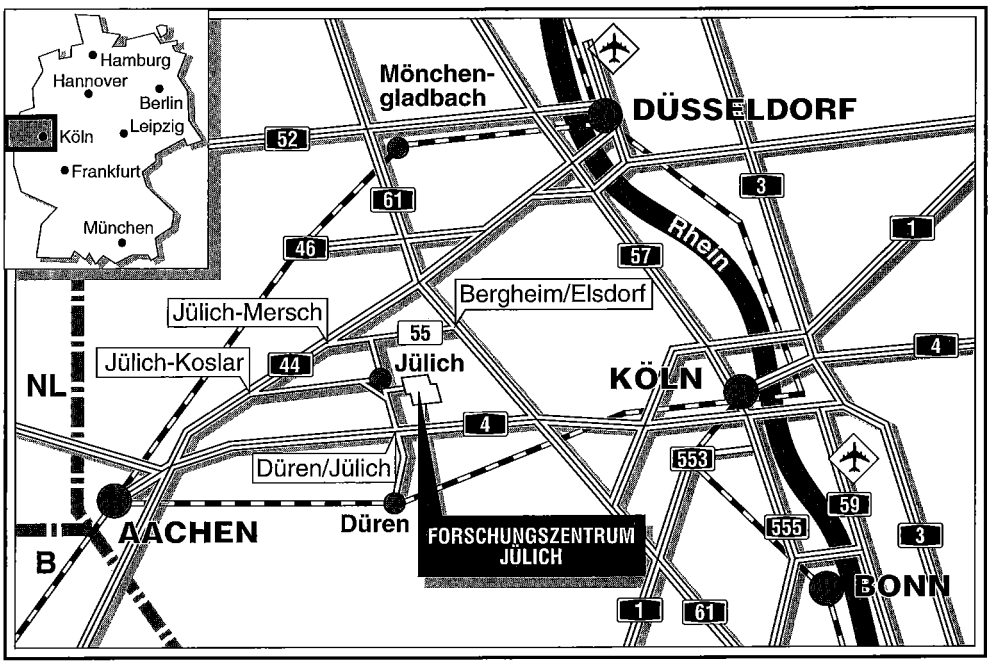

Berichte des Forschungszentrums Jülich ; 3200
ISSN 0944-2952
Institut für Kernphysik Jül-3200

Zu beziehen durch: Forschungszentrum Jülich GmbH · Zentralbibliothek
D-52425 Jülich · Bundesrepublik Deutschland
Telefon: 02461/61-6102 · Telefax: 02461/61-6103 · Telex: 833556-70 kfa d

Annual Report 1995

EDITORIAL BOARD:

Prof. Dr. G. Baur
Priv. Doz. Dr. D. Filges
Prof. Dr. K. Kilian
Priv. Doz. Dr. R. Maier
Dr. P. von Rossen
Prof. Dr. O. Schult
Dr. H. Seyfarth
Prof. Dr. K. Sistemich
Prof. Dr. J. Speth

The internal COSY-11 installation

The photograph shows the main part of the internal (COSY-11 installation at the target station TP3. COSY-11 is designed for meson production studies close to threshold in the pp interaction. Between the two orange dipoles the cluster target is located with the forepumps on the left side visible. Positively charged reaction products leave the dipole gap between the coils and enter the detection system. The tracks of the particles are measured with two drift chamber stacks. The first stack is seen in the middle part to the left of the yellow quadrupole and the second is positioned in the foreground followed by two scintillator hodoscopes. The larger hodoscope consists of bars with 10 cm, the smaller one is movable and has strips with 1.3 cm width to increase the resolution for two close proton tracks. For further details and first experimental results at this facility see the contributions in this report (pages 37 – 44).

Preface

Our most prominent experimental result has been announced at the end of the past year: In an international collaboration under the leadership of the IKP production of antihydrogen atoms has been observed at LEAR/CERN for the first time.

In Jülich the development of the COSY-accelerator has been continued although at a somewhat slower pace after significant milestones had been passed thus making more beam time available for experiments. The most outstanding achievements were: beam extraction over the full energy range, acceleration of a cooled beam and a tenfold increase of the external beam intensity while simultaneously dramatically reducing the amount of beam halo. The latter development was especially crucial for the data taking of the MOMO collaboration which succeeded in getting the first exclusive data for the $pd \rightarrow {}^3He\ \pi^+\pi^-$ reaction. The GEM collaboration continued measurements and analysis of pion production in pp reactions.

The COSY-TOF collaboration obtained the first measurements of the associated strangeness production $pp \rightarrow pK^+\Lambda$ at 2.75 GeV/c. It has more than doubled world's total of such events to date. It could also be shown that multi-particle events in the TOF detector can be measured by high acceptance and completely reconstructed. The first internal target experiment EDDA continued its precision measurements of the elastic pp scattering cross-sections. In the meantime this collaboration collected more than 35 million events over the entire COSY energy range. The improved reconstruction tools of EDDA for the vertices confirmed the high stability of the internal beam in size and position during the acceleration process.

The internal cluster target facility COSY-11 has been installed during last spring. The collaboration, studying the near threshold meson production, observed surprisingly high production probability for η'-mesons in their first experimental runs. Especially for this experiment a new ion optic of the machine has been developed that strongly raised the luminosity for their measurements. The construction of the 0^0-facility ANKE has been started

thanks to financial support of the state government. The dipole magnets are under fabrication and the construction of the vacuum system and the telescopes for kaon detection have began.

With the commissioning of a polarized atomic beam source development of a polarized COSY beam has started brodening significantly the physics capability of COSY.

The nuclear spectroscopy activities were centered around the use and the development of EUROBALL.

The theoretical work gives strong support to the experimental program and connects the physics at COSY with research at other laboratories. A highlight was the consistent description of nucleon-nucleon, pion-nucleon und pion-pion scattering within the Bonn-Jülich meson-exchange model.

Also this year's successes were made possible to a large extent by the accomplishments of our engineers, technicians, the infrastructure of the IKP and the KFA and last but not least by our students.

Josef Speth

INSTITUTE FOR NUCLEAR PHYSICS

Managing director:	Prof. Dr. J. Speth
Experimental Nuclear Physics I, director:	Prof. Dr. K. Kilian
Accelerator division, head of the:	Dr. R.A. Maier
Experimental Nuclear Physics II, director:	Prof. Dr. O. Schult
Theoretical Physics, director:	Prof. Dr. J. Speth

Forschungszentrum Juelich GmbH

D-52425 Juelich, Germany

CONTENTS

I. EXPERIMENTAL NUCLEAR PHYSICS

1. MEDIUM ENERGY PHYSICS

1.1 EXPERIMENTS AT COSY

Status of the Time of Flight Spectrometer at COSY 5

First Measurements of Associated Strangeness Production in pp-Reactions at the COSY Time-of-Flight Spectrometer 6

First Attempts at ppγ Bremsstrahlung 8

Event Identification at TOF 10

An Application of Kinematic Fitting 11

Development in Connection with the Hydrogen/Deuterium Target 12

Development and First Tests of a Hadron Calorimeter for TOF 14

Measurement of the Timing Properties of the TOF Barrel Scintillators by Means of Cosmic Radiation 16

Monte Carlo Simulations of the Three Layer TOF Barrel Hodoscope 18

Measurement on a Prototype Scintillator Module to be used in the COSY-TOF Barrel Hodoscope 21

Apparatus for an Investigation of Long Scintillator Strips through Use of Cosmic Rays 22

Test of Scintillating-Fiber Calorimeter for Photons with Energies below 1 GeV 24

Neutron Time-of-Flight Measurements at the COSY-TOF 25

Pion Production Studies with the GEM Detector System 26

Two-Pion Production at MOMO 31

The EDDA Experiment: Proton-Proton Elastic Scattering Excitation Functions at Intermediate Energies 33

First Measurements of the $p+p \rightarrow p+p+\eta'$ Reaction near Threshold 37

First Measurements on $pp \rightarrow ppK^+K$ at Threshold 38

Production of η Mesons at the COSY-11 Installation 39

$\pi^+\pi^-$ Meson Production at the COSY-11 Installation 40

The COSY-11 Beam Optics 41

Development and Construction of a Luminosity Monitor for COSY-11 42

The Internal Cluster Target of COSY 43

Drift Chambers with Double Sense Wires for the COSY-11 Facility 44

Test Measurements for the Experiment COSY-13 45

The „GEANT" Simulation of the „COSY-13" Experiment of the Production of Heavy Λ-Hypernuclei in Proton-^{238}U Collisions 47

Properties of Heavy Λ-Hypernuclei Produced in p-U Collisions 49

The Preparation of the ANKE Spektrometer 51

The Vacuum Chambers at ANKE 55

Expected Beam Parameters at the Internal Target Positions for Experiments in the COSY Ring 58

TP2 as an Alternative Place for Installing ANKE 60

Reconstruction of Particle Coordinates with the Wire Chambers at the ANKE-Facility 61

MWPC-Test for ANKE at COSY 62

Status of the 2nd Multiwire Proportional Chamber MWPC2 for the ANKE-Facility 63

A LED-Based Monitoring System for Scintillation and Cerenkov Counters at ANKE 64

Development of a Constant Fraction Discriminator and Meantimer 65

First Module of the Forward Detector Proportional Chambers of the ANKE Spectrometer. 67

Feasibility of the Use of Cerenkov Counters in pd Interaction Studies at the COSY 0° Facility (ANKE) 69

A Polarized Deuterium and Hydrogen Gas-Cell Target for the ANKE Project 71

Kinematical Characteristics of the pd Interaction and the Feasibility of Deuteron Break-up Studies at ANKE (unpolarized case) 74

Kinematical Identification of pd→ppn Reaction Events at ANKE 77

Subthreshold K^+-Production in the pd→K^+Λpn Reaction 79

K-Meson Production in Nucleon-Nucleon Interaction 82

Folding Model Calculations for Differential Cross Section of K^+ Prodution in p+Pb Collisions 84

Two-Step Mechanism of Meson Production in pd→^{3}HeX and pd→$^3H_\Lambda K^+$ Reactions 86

Ratio of Kaon- to Pion-Pair Production as a Signature of Enhanced Strangeness Production 88

Study of the $\vec{p}+\vec{p} \rightarrow pp\phi$ Reaction at the ANKE Spectrometer 90

Reconstruction of the ϕ Meson Mass at the 0° Facility ANKE 92

Biophysics for Proton Therapy, Overview and Experimental Results 93

Comparison of Different Monte Carlo Programs for Use in Proton Dosimetry 96

Tests for Pretherapeutic Physical Experiments at COSY using High Resolution Detector Arrays 98

TLD 300 Dosimetry at the COSY Pretherapeutic Proton Beam 100

A Monte Carlo Module for Use in Proton Therapy Planning - First Results 102

Influence of the Proton Beam Modulation on Dose and RBE 104

Threshold Experiments of the COSY Type at Higher Energies 106

1.2 EXPERIMENTS AT EXTERNAL FACILITIES

Production of Antihydrogen 109

Meson Spectroscopy with the JETSET Experiment 112

Hyperon Production at a Antiproton-Proton Mini-Collider 113

$\overline{\Lambda}\,\Sigma^0$- and $\overline{\Sigma^0}\,\Lambda$-Production at high LEAR-Energies 115

Measurement of Strangeness Production in the Reaction $\overline{p}p \rightarrow \overline{Y}Y$ 116

Measurement of Spintransfer and Depolarization in the Reaction $\overline{p}p \rightarrow \overline{\Lambda}\Lambda$ 118

K^+-Meson Production in pBe Interactions at $T_p = 2.9$ GeV 120

Spectroscopy of X-rays from Antiprotonic Hydrogen and Helium Isotopes 122

Feasibility Study to Determine the Pion to Myon Mass Ratio 124

Eta-Production Experiment PROMICE/WASA 126

Exclusive Study of the Roper Resonance Excitation 127

A Combined HETC FLUKA Intranuclear Cascade Event Generator 128

2. NUCLEAR SPECTROSCOPY

Excited Superdeformed Band in the Double Magic Nucleus ^{144}Gd 133

Lifetime Measurements in ^{144}Gd 135

Double Band Crossing in the Superdeformed Nucleus ^{145}Gd 137

Complete Valence Particle Yrast Lines in N=84 Nuclei above Gadolinium 140

Investigation of the Decay of High-K Isomers in ^{180}Os with the CLUSTER Cube 142

Study of Incomplete Fusion Reactions using Charged Particle - Gamma Ray Coincidence Techniques 143

Application Specific Digital Signal Processor 144

II. THEORETICAL NUCLEAR PHYSICS

3. MEDIUM AND HIGH ENERGY PHYSICS

Photon-Photon Physics in Ultrarelativistic Hadron-Hadron Collisions 147

Pion Threshold Production 148

Short-Range Part of the NN Interaction: ω Exchange Versus Quark-Gluon Exchange 150

Structure of Nonlocalities in Meson Exchange *N N* Interactions and their Role in the *N N* and *3N* System 152

A Fully Relativistic Phenomenological Model of πN Scattering 154

The Nucleon Form Factors and the Transition from Meson to Quark Dynamics 155

Testing the Meson Cloud in the Nucleon in Drell-Yan Processes 157

Correlated πρ Exchange in the NN Interaction 158

Investigation of the Pion Production in Pion-Nucleon Scattering 160

Quadrupole Deformation of Deuterons and Final State Interaction in $^2\vec{H}$ (*e, e'p*) Scattering on Tensor Polarized Deuterons at CEBAF Energies 162

Do Final State Interactions Obscure Short Range Correlation Effects in Quasielastic *A* (*e, e'p*) Scattering? 164

Universal Pattern in (*e, e'p*) at Large Missing Momenta: Quasi-Deuteron or Diffractive Final State Interactions? 166

Hypernuclei with Meson-Exchange Hyperon-Nucleon Interactions 168

Pion Absorption on the Deuteron $\pi^+D \rightarrow 2p$ 169

Meson Exchange Currents in (p, n) Reactions on a Deuteron Target 171

Calculation of the NNϕ Vertex in a Hadronic Framework 173

Annihilation of the $\bar{N}N$ System into more than two Pions 175

The Influence of Negative-Energy States on Proton-Proton Bremsstrahlung 176

Pion Photo-Production with a Final State Interaction Based on a Meson-Exchange Model.. 177

Color Dipole Phenomenology of Diffractive Electroproduction of Light Vector Mesons at HERA 179

Breaking of the Ingelman-Schlein-Regge Factorization for Diffractive Deep Inelastic Scattering 181

Chirally Constraining the $\pi\pi$ Interaction in Nuclear Matter 183

Medium Modifications of the Rho Meson at CERN/SpS Energies 185

Correlated $\pi\pi$ and $\bar{K}K$ Exchange in the Baryon-Baryon Interaction 187

Coherent Pion-Electroproduction in the Reaction $^{12}C(e, e'\pi^{+})\ ^{12}B(g.s)$ 189

The Nature of the Δ-Isobar and the Roper Resonance 191

πNN Form Factor Determined from a Microscopic Model for πN Scattering 193

ωNN Vertex Function and the $\gamma\pi\pi\pi$ Anomaly 194

Threshold Effects and Parity Violation for Neutron Resonances 196

The Nucleon-Nucleon Interaction within the Skyrme Model 198

Coherent and Incoherent Pion Photoproduction off ^{12}C in the Δ Resonance Region 200

Short-range Part of the NN Interaction: ω Exchange Versus Quark-Gluon Exchange 203

4. NUCLEAR STRUCTURE AND REACTION MECHANISM

Electromagnetic Excitation in Fast Hadron-Hadron Collisions and its Use for Nuclear Astrophysics 207

Low Energy Charged Particle Interactions Studied with Transfer Reactions 208

Colour van der Waals Effects in Pb-Pb Scattering? 209

A Brueckner-Hartree-Fock-Bogoliubov Model for Proton and Neutron Rich Nuclei 210

Radiative Capture of Neutrons to Bound States of Higher Angular Momentum 211

Properties of Neutron and Proton Rich Nuclei in the Vicinity of ^{100}Sn in Relativistic Mean Field Theory 212

Effects of Strong Interaction on the Electromagnetic Dissociation 213

5. GENERAL PHYSICS

On Thermodynamic Systems in Static External Fields 219

III. ACCELERATOR DIVISION

6. COOLER SYNCHROTRON

Machine Development at COSY in 1995 223

Acceleration of a Cooled Proton Beam in COSY 226

Experimental Investigation of Amplitude Dependent Tune 229

Chromaticity Measurements at COSY 231

First Vertical Beamsize Measurements 233

Improved Ramping-Functions for COSY 235

First Transverse Schottky-Noise Spectra with Resonant Schottky-Pickups 238

Transverse Measurements with Kicker Excitation 239

Development of Beam Extraction 240

Phase Space Boundary Studies at the Electrostatic Septum of COSY 242

Tools for Online Evaluation of Phase Space Measurements 244

Intensity Calibration of Multi Wire Proportional Chambers 246

Real Time Position Signal for the BPM System 248

State of the COSY Stochastic-Cooling System and Interpretation of the First Schottky-Signals 249

Status and Development of RF-Systems at COSY 251

Report of the Power Supply Group 254

New Design and Implementation of the COSY-Control Operator Interface 255

Beam Profile and Phase Space Measurements of the Beam Extracted from COSY 256

Beam Properties and Beam Focussing Near the TOF Target 257

Numerical Models for COSY 258

Closed Orbit Description in COSY 259

Acceleration of Polarized Protons at COSY 261

Tune Jumping System for COSY 263

Beam Quality and Detector Size 265

Magnets for the 0°-Spectrometer ANKE at COSY-Jülich 266

7. ISOCHRONOUS CYCLOTRON AND ION SOURCES

The Polarized Ion-Source for COSY 271

Emittance Measurement of the Extracted Cyclotron Beam 272

8. SPECTROMETER BIG KARL

Magnetic Spectrometer BIG KARL 277

Graphical User Interface and Monitor System for the BIG KARL Spectrometer 278

9. RADIATION PROTECTION

Radiation Protection 281

IV. TECHNICAL DEVELOPMENTS

10. DATA ACQUISITION AND PROCESSING

COSY Experiment Data Processing 285

COSY Experiment Data Acquisition 287

11. ELECTRONICS

Electronics 293

12. DETECTORS

Semiconductor Detectors 297

Silicon Quirl-Detectors 298

13. EUROPEAN SPALLATION SOURCE (ESS)

Nuclear Studies of Different Target Systems for the European Spallation Source (ESS) 301

The Design of FFAG - Fixed Field Alternating Gradient - Synchrotron 305

V. SCIENTIFIC COUNCIL COSY 309

VI. ADVISORY COMMITTEES AT COSY 309

VII. COLLABORATIONS 310

VIII. PERSONNEL 319

IX. PUBLICATIONS 326

X. CONFERENCE CONTRIBUTIONS, TALKS 330

XI. PATENTS 337

XII. INTERNAL REPORTS 337

XIII. INTERNAL TALKS 338

I. Experimental Nuclear Physics

1. MEDIUM ENERGY PHYSICS

1.1 EXPERIMENTS AT COSY

Status of the Time of Flight Spectrometer at COSY

The COSY-TOF-Collaboration
U. Bechstedt, P. Cloth, V. Drüke, D. Filges, R. Geyer, H. Hadamek, A. Hassan, P. Jahn, K. Kilian, R. Klein, H. Machner, H.P. Morsch, Chr. Nake, N. Paul, V. Renken, U. Rindfleisch, E. Roderburg, M. Rogge, O. Schult, T. Sefzick, G. Sterzenbach, P. Turek, D. Wallom:
Institut für Kernphysik, KFA Jülich
H. Nann : *IUCF Bloomington USA*
R. Gehring, P. Hermanowski, H. Koch, J. Krug, H. Matthäy, W. Meyer, G. Reichertz, C. Rohloff, M. Steinke, U. Zielinski :
Institut für Experimentalphysik, Ruhr-Universität Bochum
H. Dutz : *Physikalisches Institut der Universität Bonn*
A. Böhm, K. Brinkmann, H. Freiesleben, B. Hübner, E. Kuhlmann, S. Lange:
TU Dresden Institut für Kern- und Teilchenphysik
M. Müller-Veggian : *Fachhochschule Jülich*
R. Bilger, H. Clement, T. Czarnecki, G. J. Wagner : *Physikalisches Institut Universität Tübingen*
P. Michel, K. Möller, B. Naumann, L. Naumann, A. Schamlott, A. Schülke:
Institut für Subatomare Physik, FZ Rossendorf, Dresden
M. Dellert, H. Dennert, W. Eyrich, M.Fritsch, S. Gabler, J.Hauffe, J. Hays, A. Metzger, M. Moosburger, R. Sperl, F. Stinzing, S. Wirth: *Physikalisches Institut, Universität Erlangen*

In 1995 the Time of Flight Spectrometer (TOF) was used for a total of four weeks with the COSY beam.

One set of measurements was dedicated to detect the associated strangeness production, the following to examine the proton-proton bremsstrahlung (for a more detailed discussion of both measurements see the following contributions in this report). For the measurement of associated strangeness production it was the first time that the Cosy Beam was extracted with a momentum higher than the pKΛ threshold. Up to now more pKΛ events are analysed than have been measured world wide before [Fig. 1]

All scintillators are connected via a quartz fibre to a nitrogen laser for test signals.

For adjusting the beam to the target and the start detectors it could be controlled optically with a rubin and a CCD camera. In the beam exit of the TOF the beam size was measured with a scintillating fibre hodoscope. The beam spot at the target was less than 2 mm in diameter. The remaining halo events were detected with two veto counters. These are disks of plastic scintillators with inner holes of 12 mm and 2 mm.

Due to the better beam, detector adjustment and due to the veto-counters the quality of the data (signal to background) was improved by a factor of 100 compared with the first measurements in 1994.

The software analysis has made a big step forward, with precise time and dE/dx calibration the missing masses of the reactions pp -> d π^+ , pp π^0 and pn π^+ can be deduced from the same measurement and shown in one plot. (see for details the article on missing mass reconstruction in this report). A kinematical fit separates the event types and allows for filling Dalitz plots for the reactions pp π^0 and pnπ^+ (Fig. 2).

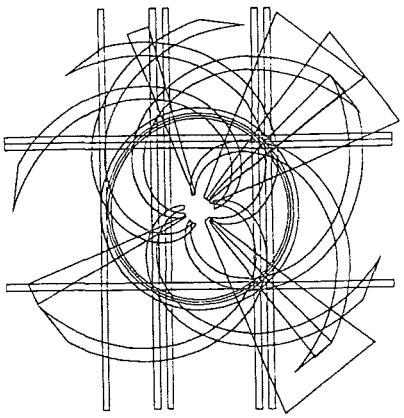

Fig 1. Signature of a pKΛ Event

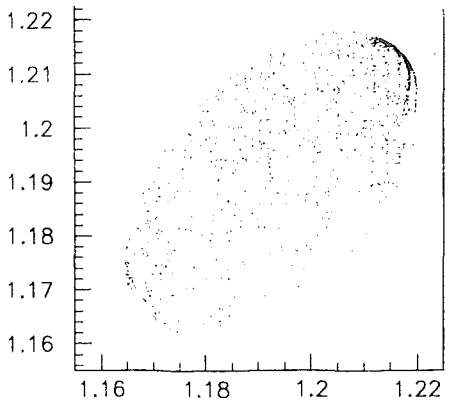

Fig. 2 Dalitz Plot of the reaction pp -> pnπ^+. The beam momentum is 880 MeV/c. The abscissa is the invariant mass of the nπ^+ system [GeV/c^2], the ordinate gives the invariant mass of the pπ^+ system. The enhancement in the right upper corner is due to the reaction pp -> d π^+.

First Measurements of Associated Strangeness Production in pp–reactions at the COSY Time-of-Flight Spectrometer*

The COSY-TOF Collaboration
Experiment E7 (Spokesperson: W. Eyrich)

In the experiment E7, the hyperon production in pp–reactions close to threshold is studied exclusively at the external COSY beam using the time–of–flight spectrometer TOF.

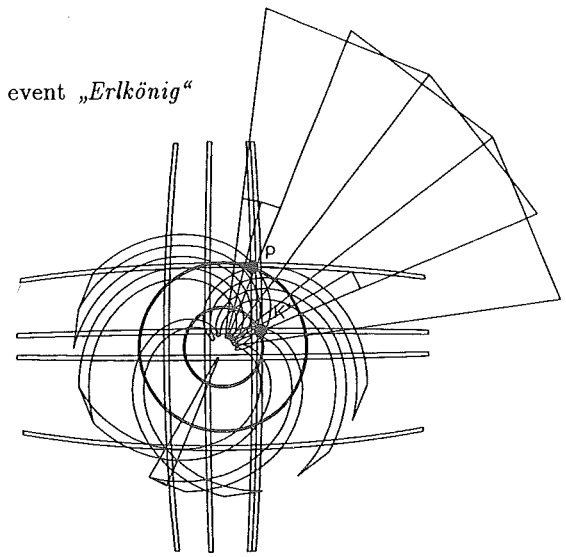

Figure 1: first $pp \rightarrow K^+\Lambda p \rightarrow K^+p\pi^-p$ event seen in θ-φ–projection from the LH_2-target, responding segments of the whole detector arrangement.

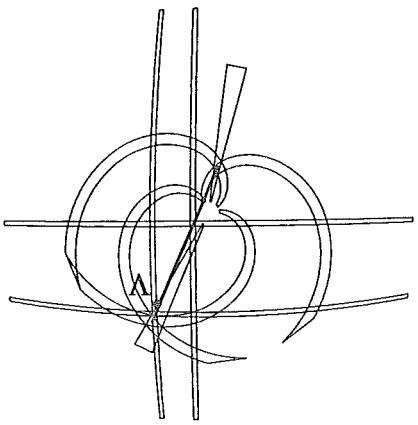

Figure 2: separated secondary tracks of the charged Λ–decay particles.

For the first time, a proton beam of sufficient energy was transported into the TOF area in April 1995. At a beam momentum of p_p=2.75GeV/c, pilot measurements of the associated strangeness production in the channel $pp \rightarrow K^+\Lambda p$ could be performed successfully.

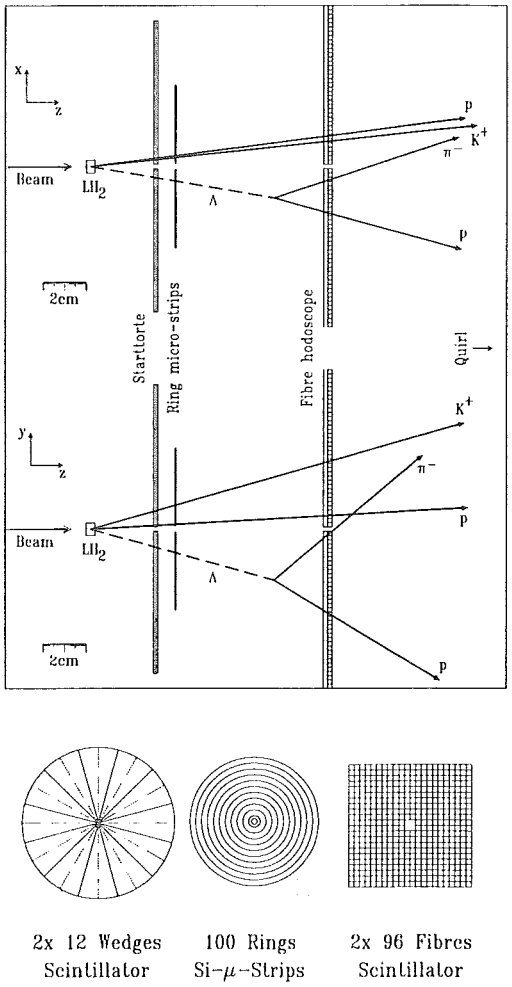

Figure 3: first event in x-z- respectively y-z-projection in the „Erlangen start detector“ setup.

The experimental setup, which was installed in a short version of the TOF vacuum vessel, consisted of a tiny liquid hydrogen target (LH_2) with a length of 4 mm, the „Erlangen start detector“ and in 1 m distance the „Jülich Quirl“ as stop detector. The start detector system, covering the whole phase space of the primary reaction products, consists of two segmented layers of scintillators, a ring microstrip detector and a two layer fibre hodoscope. The Quirl is built up by three segmented scintillator planes, two of them with helic curved elements.

Due to the high granulation of all detector components, the interesting events can already be fully reconstructed with high precision, using only the hit pattern of the various detector components. This includes especially the delayed decay of the Λ–particle, which gives the unique signature of the reaction and which is also

used as the main trigger signal due to the increase of charged particles from 2 to 4.

Figure 1 shows the hit pattern of the first identified event („Erlkönig") of the type $pp \rightarrow K^+\Lambda p$ seen from the target in a θ–φ–projection, in which it was explored „online". The tracks of the kaon and the primary proton starting from the target are identified by common crossing points of fired components in all eight detector layers. The tracks corresponding to the delayed Λ–decay in this projection have to show a unique four hit sequence of two hodoscope crossing points between two quirl pixels, altogether forming a quasi straight line. This can be seen more clearly in fig.2, where the hits of the kaon and the primary proton are removed. This hit pattern also allows to reconstruct the Λ–direction and even its momentum. Transforming the θ–φ–projection into the usually used x-z- and y-z-projections, one gets fig.3, where the same event is shown together with the start detector system.

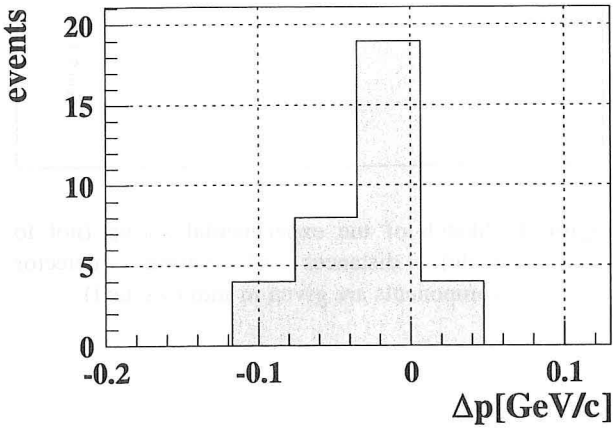

Figure 4: difference spectrum between kinematically reconstructed and actual beam momentum

Scanning through about one half of the taken data using most restrictive cuts, a sample of 35 „golden events" was extracted. Testing these events kinematically using the hypothesis $pp \rightarrow K^+\Lambda p$ and reconstructing the beam momentum, one gets a clear peak, free from any background as can be seen in fig.4. The optained resolution corresponds to a missing–mass resolution of 80 MeV/c^2 (FWHM) and the small shift from zero is equivalent to a 0.3 percent uncertainty in the beam momentum measurement. This sample of „golden events" already exceeds the world data of the $pp \rightarrow K^+\Lambda p$ reaction in the COSY energy range significantly. The phase space distribution of the Λ event sample corresponding to fig.4 is shown together with the kinematical limits in fig.5. Taking the whole '95 data set under less restrictive conditions, which are still sufficient to reconstruct the events of interest in a unique way, it is estimated to get a sample of about 200 events.

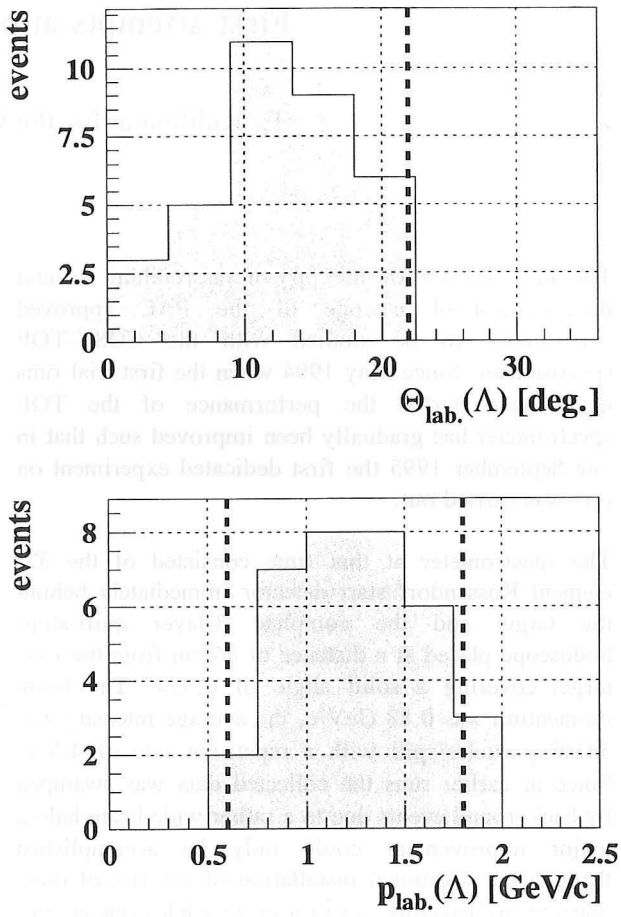

Figure 5: laboratory phase space distribution of the detected Λ–particles (the dashed lines mark the kinematical limits).

In a more precise analysis, including kinematical fitting and the time–of–flight- and dE/dx–information, which is on the way, a much better momentum resolution will be obtained, also allowing to identify and separate the channel $pp \rightarrow K^+\Sigma^o p$ quantitatively.

In summary, the '95 pilot run shows that all parameters of the experiment meet their design values, including the detector performance and the efficiencies of the trigger and the data analysis. Due to the eminent progress in the beam extraction, which could be achieved in the mean time, high statistical measurements of the reaction $pp \rightarrow K^+\Lambda p$ with the identical experimental setup will be possible in 1996.

* supported by BMBF and FZ Jülich

First attempts at ppγ Bremsstrahlung *

E. Kuhlmann for the COSY-TOF collaboration

The investigation of the ppγ-bremsstrahlung around the π-threshold is one of the PAC approved experiments to be studied with the COSY-TOF spectrometer. Since May 1994 when the first trial runs have been started the performance of the TOF spectrometer has gradually been improved such that in late September 1995 the first dedicated experiment on ppγ was carried out.

The spectrometer at that time consisted of the 32-element Rossendorf start detector immediately behind the target and the complete 3-layer quirl-stop-hodoscope placed at a distance of 86 cm from the LH_2 target covering a solid angle of 0.35π. The beam momentum was 0.88 GeV/c, the average intensity was $3*10^6$ particles/spill with a repetition rate of 4.5 s. Since in earlier runs the collected data was swamped by background events due to a rather wide beam halo a major improvement could only be accomplished through the additional installation of a series of three plastic veto detectors, set in form of a telescope at 260, 80 and 1.4 cm in front of the target with central holes of 150, 12 and 2 mm, respectively. A sketch of the setup is shown in fig. 1. By incorporating signals obtained from these detectors as veto signals into the trigger condition (either directly through hardware or in the ensuing analysis as a software cut) much cleaner spectra were obtained than before.

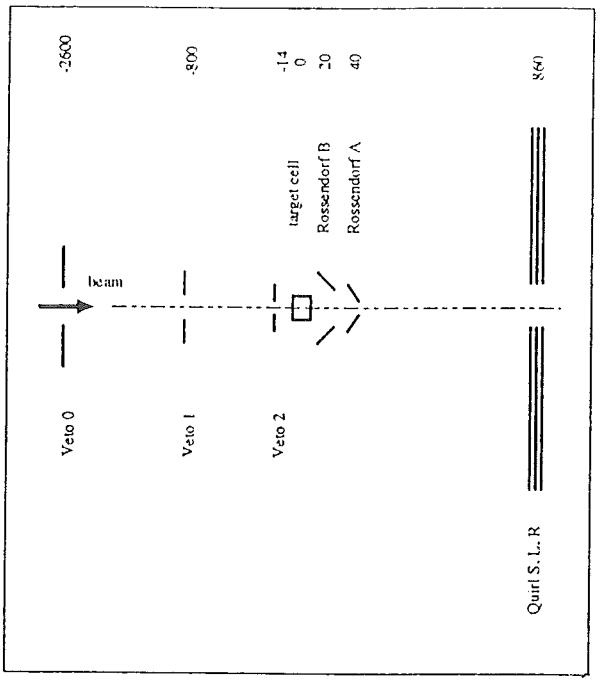

Figure 1: Sketch of the experimental set-up (not to scale); distances of various detector components are given in mm (see text).

It was also found to be absolutely necessary to heat-up the target cell every 10-12 hours in order to remove vapor and gas particles which were collected as a solid surface with slowly but constantly growing thickness onto the cold (14 K) foils separating the main volume of the target cell from the vacuum. The chosen beam momentum of 0.88 GeV/c was a compromise between low enough for not being saturated by π-producing reactions and high enough for also collecting data of the 2-particle reaction $d\pi^+$ which was found to be ideally suited for internal calibration purposes.

The chain of analysis pursued at Bochum, Dresden and Jülich consisted of the following steps: i) determination of QDC pedestals and ii) TDC offsets, iii) walk corrections and finally iv) determination of beta- values via time-of-flight as well as dE/dx data extracted from the TDC and QDC modules, respectively.

An overall time resolution of Δt = 0.6 ns (FWHM) was deduced between any pair of scintillator elements of the (straight) start- and the stop-hodoscopes. The flight direction of each detected particle was deduced from the labels of the hit scintillator elements; it should be mentioned that in the first stage of the analysis only those events were considered where each hit was observed in all three layers. Neglecting for the moment any background reactions due to interactions of beam protons with heavier nuclei in the target windows or other material in the beam path, hence concentrating on the pp-entrance channel alone, only 5 reactions are energetically allowed, and due to the limited acceptance only 4 of these can be detected by the quirl hodoscope. The possible reaction channels to be considered are $d\pi^+$, $pn\pi^+$, $pp\pi^\circ$ and ppγ. Apart from the $d\pi^+$ reaction with its unique signature, which allows an almost unambiguous classification, the events originating from the latter three can only be correctly assigned through more elaborate means like missing mass analysis and/or kinematic fitting, both of which require appropriate mass hypotheses.

As an example fig. 2 shows the result of the missing mass analysis of events collected in runs following right after one of the repeated cleaning procedures of the target cell mentioned above. A strong and rather narrow peak at 0.018 GeV^2/c^4 shows up at the position expected for events due to the $pp\pi^\circ$ reaction which is accompanied to the left by a weak and slowly falling continuous background. To arrive at this rather clean sample only those events have been considered where both charged particles not only were observed in two complete pixels, i.e. ones which are formed by hits in each of the three layers of the quirl, but also where particles passed through the A-elements of the Rossendorf start detector alone ($\vartheta_{max} = 25°$). The total cross section for the $pp\pi^\circ$ reaction at the given beam momentum is 17 μb [1]. When interpreting the slight concentration of events around missing mass 0 as $pp\gamma$ events and making some approximate corrections for acceptance losses one deduces a cross section of a few μb, which is in the expected range. The recent improvements regarding better vacuum and higher duty cylce and lower beam emittance will definitely help to arrive at much cleaner spectra with much higher statistics.

Summarizing, the main results of this first run were the following: i) the TOF spectrometer is indeed capable of detecting and identifying 3-particle reactions with 1 neutral particle, ii) the achieved overall time resolution of 0.6 ns (FWHM) is as required and iii) reactions with cross sections of a few microbarns can actually be investigated. This experiment will be continued.

* supported by BMBF and KFA Jülich

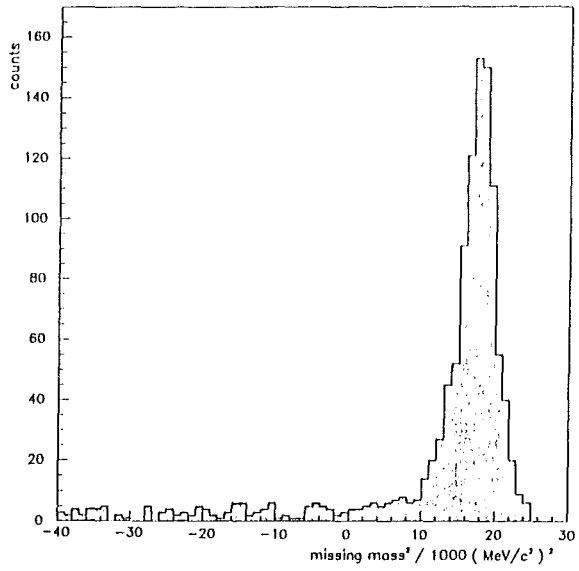

Figure 2: Missing mass (MM) spectrum for the $pp\pi^\circ$ reaction. Events due to the $pp\gamma$ reaction are expected around $MM^2 = 0$.

References:

[1] H.O. Meyer et al., Nucl. Phys. **A539** (1992) 633

Event Identification at TOF

M. Dahmen, R. Geyer, K. Kilian, E. Kuhlmann[1], E. Roderburg
for the COSY-TOF collaboration

Let us consider proton-proton interactions at energies just below the two meson threshold. In this case only seven reactions are possible:

$$pp \rightarrow pp$$
$$pp \rightarrow pp\gamma$$
$$pp \rightarrow pp\pi^{o}$$
$$pp \rightarrow p\pi^{+}n,\ pp \rightarrow \pi^{+}pn$$
$$(pp \rightarrow d\pi^{+},\ \pi^{+}d)$$

The deuteron reactions have been put into brackets, because we can not distinguish them from $pn\pi^{+}$ rections where the relative momentum between the proton and the neutron is close to zero. The difference is due to the 2.2 MeV binding energy of the deuteron which is relativly small.

The time of flight spectrometer TOF measures the velocity vectors $\vec{\beta}$ of all charged particles. Because of the large accpetance of the device, almost always two $\vec{\beta}$ are obtained for any of the possible reactions. To identify the type of an event we have to compare our measured vectors with the kinematics of all possible reaction channels. This can be done by missing mass technique. The two measured particles can only be a pp, $p\pi^{+}$ or $\pi^{+}p$ pair. If we take any of the three possibilities as an hypothesis, we can calculate the four vectors p_1 and p_2 of the charged tracks by the following relation:

$$\vec{p} = (m\gamma, m\vec{\beta}\gamma) \qquad \text{with } \gamma = 1/\sqrt{1-\beta^2}.$$

The assumption can now be tested to be true or false by determing the missing four vector p_x and the missing mass $m_x = \sqrt{p_x \cdot p_x}$ of the neutral particle using energy and momentum conservation:

$$p_{beam} + p_{target} = p_1 + p_2 + p_x .$$

p_{beam} and p_{target} are the four vectors of the beam and target particles which are perfectly known. If the assumption is right that both particles are protons, p_x must either be the zero vector (elastic scattering) or m_x has to correspond to either the γ or the π^{o} mass. If the assumption $p\pi^{+}$ or $\pi^{+}p$ is correct, m_x must be equal to the neutron mass. Figure 1 shows m_x for all three hypothesis in a three dimensional plot simultanously.

Normaly it is found that only one hypothesis holds. Then the solution lies in a disk at the correct mass value in the coordinate of that hypothesis. It happens sometimes that mathematical ambiguities exist between the different reaction channels where under certain phase space conditions the disks intersect. Here additional detector information for example about the kinetic energy of the particles or the range of the particles within the quirl detector help to distinguish beween the possibilities.

[1] University of Bochum, Germany

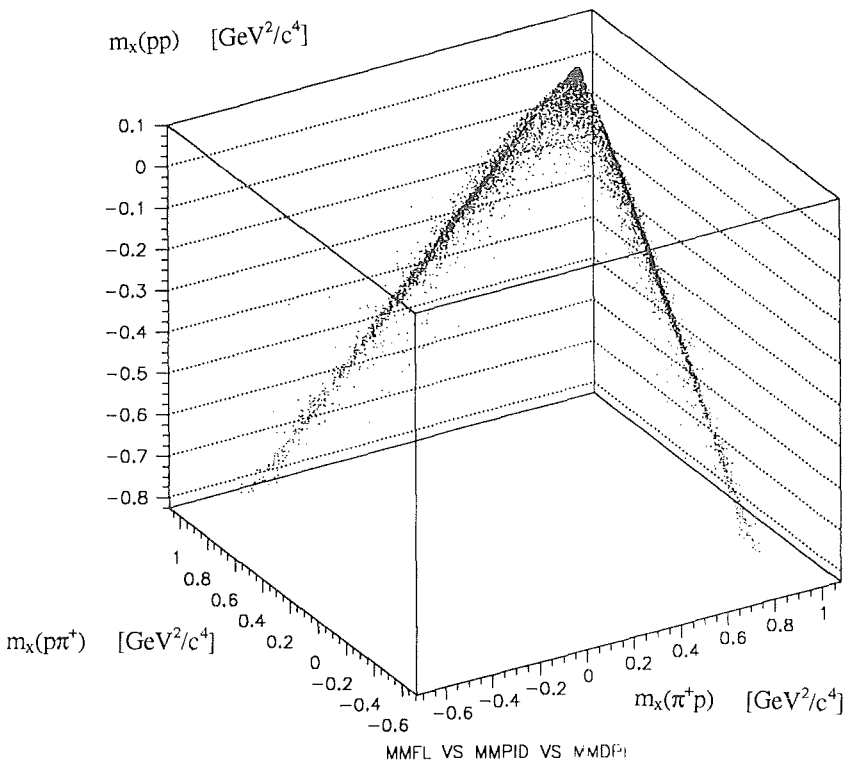

Figure 1: The missing mass m_x^2 for all three hypothesis in units of GeV²/c⁴.

An Application of Kinematic Fitting

A. Schülke[1], H. Freiesleben[2] and K. Möller[3]
for the COSY-TOF collaboration

At the COSY-TOF spectrometer [1] the scattering angles and the time-of-flight of charged particles are measured. In spring 1994 a first TOF-experiment has been carried out [2] using a 455-MeV proton beam impinging on a liquid-hydrogen target.
For the extraction of three-body reactions ($pp\pi^0$, $pn\pi^+$) the complete reconstruction of the velocity vectors and a hypothesis for the particle masses are necessary to uniquely determine the nature of the neutral particle, i.e. the four-momentum-vectors of the measured particles are inferred from a certain particle-hypothesis.

The missing mass analysis has shown that the $pn\pi^+$-reaction can clearly be extracted. In order to separate the reaction channels, $p\pi^+n$ or π^+pn, the method of kinematic fitting [3] is utilized.
The momentum components, the variables to be fitted, are modified according to their error range such that the new values fulfill the reaction hypothesis best. Energy and momentum conservation are the kinematical constraints. The method consists in a least squares fitting procedure which incorporates constraints among the variables by the use of Lagrangian multipliers. In the case where the errors of the measured values are correlated one can construct the quantity

$$S = (\vec{\varrho} - \vec{\varrho}_0)^T \cdot \hat{G}^{-1} \cdot (\vec{\varrho} - \vec{\varrho}_0) + 2 \cdot \vec{\Lambda}^T \cdot \vec{f}(\vec{\varrho}, \vec{\xi}),$$

where $\vec{\varrho}$ is the vector of measured values, $\vec{\xi}$ that of unmeasured ones, $\hat{G}^{-1}$ is the inverse matrix of correlated errors. One has to find S_{min} by varying the components of $\vec{\varrho}$. To solve this problem the constraints $\vec{f}(\vec{\varrho}, \vec{\xi})$, which connect the components of $\vec{\varrho}$ and $\vec{\xi}$, are linearized. The vector $\vec{\Lambda}$ contains the Lagrangian multipliers.
All possible configurations of momentum vectors of the outgoing particles are considered. Then, from this infinite number of possible sets, the one closest to the observed set (in the least square sense) is chosen. A detailed derivation of the fitting procedure and its application for the TOF spectrometer data can be found in [4].

Here χ^2_{norm} is calculated as

$$\chi^2_{norm} = \frac{1}{n-1}(\vec{\varrho} - \vec{\varrho}_0)^T \cdot \hat{G}^{-1} \cdot (\vec{\varrho} - \vec{\varrho}_0),$$

where n is the number of degrees of freedom of the fit and χ^2_{norm} is determined for both hypotheses. In fig. 1 the χ^2_{norm}-distributions versus the reconstructed mass of the unmeasured particle are shown.

In case of a correct hypothesis the value of χ^2_{norm} is in the range $\chi^2_{norm} \leq 1$. This normalized condition is the criterion for the assignment of a certain reaction to a given event.

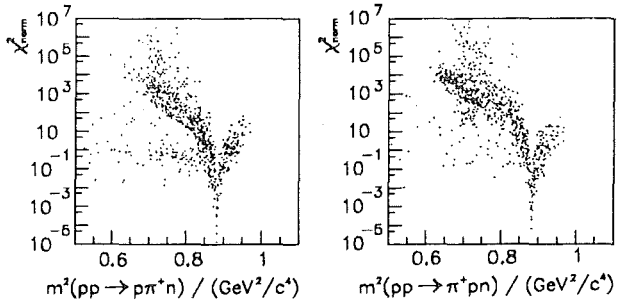

Fig. 1 *χ^2_{norm}-distribution versus missing mass for the hypothesis $pp \to p\pi^+n$ (left) and $pp \to \pi^+pn$ (right)*

Fig. 2 represents the reconstructed missing mass spectra without cut (left) and with a cut on $\chi^2_{norm} \leq 1$(right) in the chosen reaction channel $pp \to p\pi^+n$. The calculation shows that about 95% of events are unambiguously assigned if a cut on $\chi^2_{norm} \leq 0.1$ is applied.

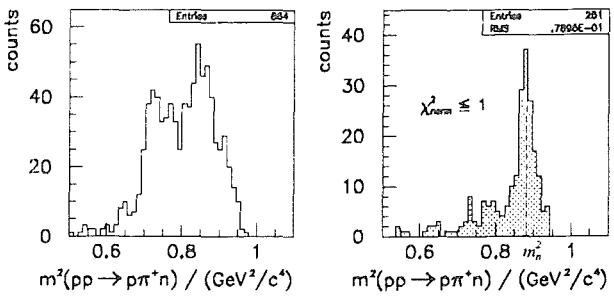

Fig. 2 *Missing mass spectrum for the hypothesis $pp \to p\pi^+n$ without (left) and with cut (right) on $\chi^2_{norm} \leq 1$*

[1]Institut für Kern- und Hadronenphysik, FZ Rossendorf e.V.
[2]Institut für Kern- und Teilchenphysik, TU Dresden
[3]Institut für Kern- und Teilchenphysik, TU Dresden and Institut für Kern- und Hadronenphysik, FZ Rossendorf e.V

References

[1] COSY proposal #9, 1990
[2] A. Schülke et al., Annual Report 1994, Jül-3035, 1995
[3] L. Lyons, *Statistics for nuclear and particle physicists*, Cambridge 1989
[4] A. Schülke, doctoral thesis, 1995

Development in Connection with the Hydrogen/Deuterium Target

A. Hassan*, St. Igel, P. Jahn, K. Kilian, R. Klein, Chr. Nake, E. Roderburg, K. Scho**, D. Wallom

The liquid hydrogen/deuterium target [1] is now routinely used in the external COSY experiments GEM, MOMO, and TOF. The target cell is typically 4 mm long and has windows made of 1.5 microns thick 'Hostaphan' foils. Several improvements have been introduced in 1995:

For the adjustment of the hydrogen target and other parts in the vicinity of the TOF axis two optical telescopes have been installed in front and behind the spectrometer. They were adjusted with respect to the building's coordinate system which is also the basis for the positioning of the beam line elements, e. g. the last quadrupole magnets before the target. These telescopes can be positioned in a reproducible way. The interior of the spectrometer can be observed through windows without breaking the vacuum. The axes of the telescopes normally coincide with the beam/spectrometer axis, but can be shifted up-down and left-right by ± 2 mm.

The arrangement of the target cell and a small veto counter is shown in Fig. 1. The axes of both were adjusted to one another before assembly. For the measurements within the TOF the veto counter was illuminated through its light guide and observed by the upstream telescope. Both lines of the telescope cross-hairs were adjusted to be tangents to the well-defined edge of the 2 mm diameter hole of the veto counter. Results of a position measurement as function of the temperature is given in Fig. 2. The vertical motion amounts to about 1.2 mm over the temperature range 300 - 14 K without any effects in the range 40 - 14 K. The horizontal motion stays within 0.1 mm and is negligible.

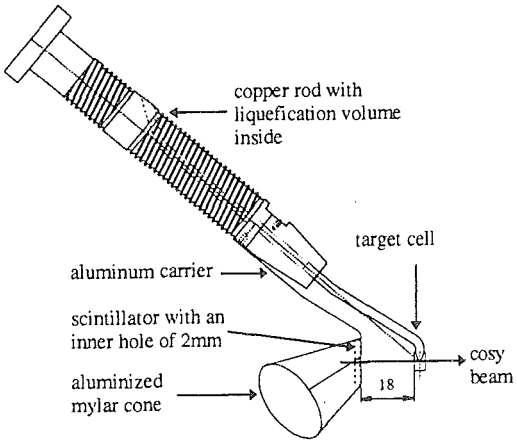

Fig. 1: Arrangement of target cell and 'veto' scintillator counter

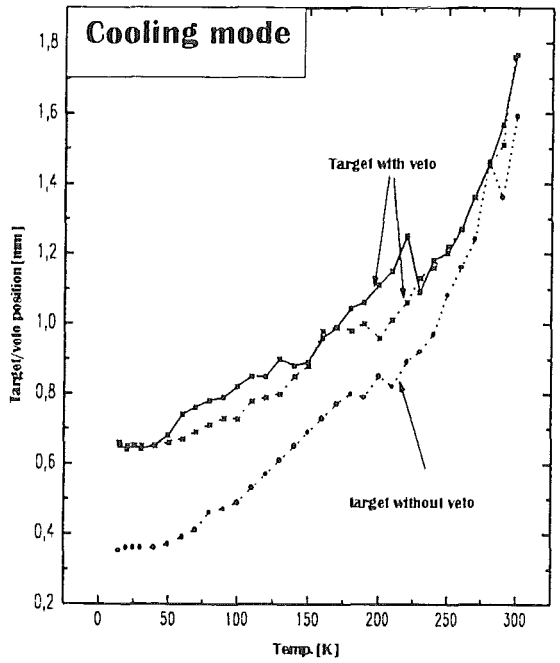

Fig. 2: Relative vertical motion of the veto counter and the target (= without veto)

The downstream telescope (near to the beam-dump, at a distance of roughly 10 m from the target region) offers an additional possibility for the relative adjustment of the veto counter with respect to the 'Rossendorf' start detector. The 2 mm diameter hole of the veto can be observed through the 2.4 mm diameter hole of the start detector (ring 'A') at a distance of 80 mm behind the veto. With these distance and diameter ratios given, a high accuracy can be obtained.

In 1995, the hydrogen target was used in combination with cooled Ge counters for GEM experiments at the BIG KARL spectrometer for the first time. The increased vacuum requirements suggested a test measurement investigating possible leakage of the target. For this purpose the usual test apparatus was equipped with a helium leak detector, and the target filled with helium which has permeability values comparable to those of hydrogen. The results are shown in Fig. 3. It can be seen that the leak rate is correlated linearily with the inner cell pressure, and that the main vacuum is not affected. In actual experiments, a pressure of $2.0 \cdot 10^{-7}$ mbar could be obtained, the limit not being imposed by the target but by the spectrometer vacuum.

For the TOF spectrometer the target has been equipped with the already mentioned small veto counter made of a NE102A scintillator disk (15 mm diameter, with a 2 mm hole, see Fig.1). The purpose of this device is beam halo suppression. As the counter is mounted at or very near to the target, it seemed worthwhile to compare the scintillation performances at room and liquid hydrogen temperatures. A first measurement was done within the BIG KARL

tures. A first measurement was done within the BIG KARL target chamber with an arrangement similar to that in Fig. 1 and including a 90Sr/Y electron source. The comparison of the two electron single spectra at 14 K and at 300 K is shown in Fig. 4 without revealing significant differences. A second measurement was performed using cosmic rays. In this case the ADC was gated by coincidences between the veto counter and a larger scintillator situated above and outside the vacuum chamber. Again, the spectra show no temperature effect (see Fig.5).

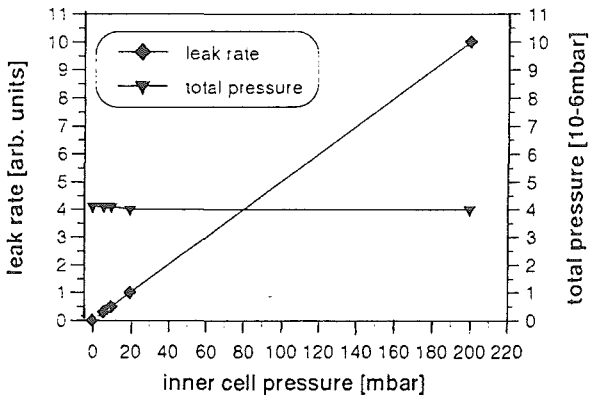

Fig. 3: Leak rate and main vacuum as a function of target cell pressure

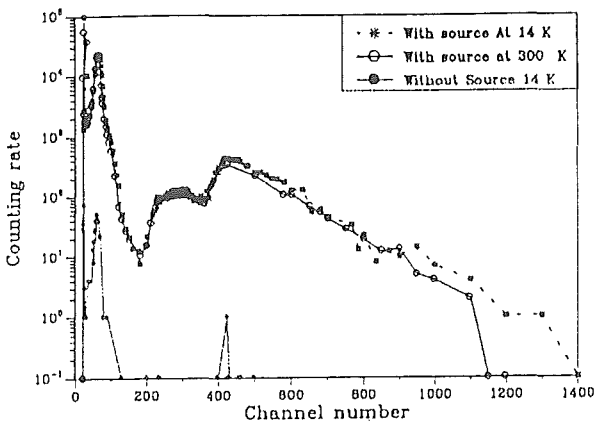

Fig. 4: Electron single spectra of the uncooled and cooled veto counter

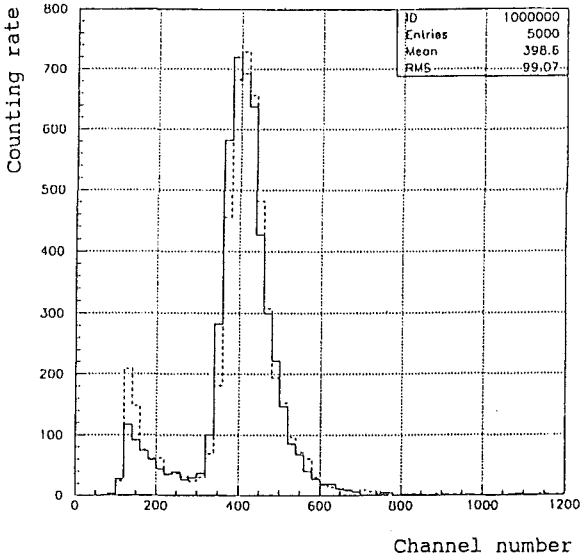

Fig. 5: Cosmic ray spectra of the uncooled and cooled veto counter

Reference:

[1] V. Jaeckle et al., Nucl. Instr. Meth. Phys. Res. A349 (1994) 15

* NRC, AEA, Egypt
**ISKP, University of Bonn, Germany

Development and First Tests of a Hadron Calorimeter for TOF

H. Clement[1], R. Geyer, K. Kilian, E. Roderburg, K. Schmidt, P. Turek, G.J. Wagner[1]
for the COSY-TOF collaboration

To the TOF-spectrometer will be added a scintillator calorimeter. This device will be installed directly behind the central Quirl hodoscope within the vacuum vessel. Changes of existing detector components are not necessary. A large aperture flange was forseen and exists at TOF for that detector. The calorimeter is especially helpful for measurements of reactions where highly ionizing particles are emitted into the forward direction. The information about the particle energies allows to reconstruct the 4-vectors with relativly high precission also for short time of flight distances. Short distances help to improve the reconstruction efficiencies especially for charged π- and K-mesons ($c \cdot \tau$ = 7.804 m, 3.709 m). If particles are stopped inside the calorimeter, particle identification can be done by using the measured kinetic energy and the tof information simultanously. A separation between π^+, K^+ and π^-, K^- is possible because of the delayed decays of the positive mesons compared to the prompt signals of the negative ones. Another option of the calorimeter might be the detection of neutrons.

A front view of the calorimeter is shown in fig. 1. It consists of 84 plastic scintillator blocks. Each of them has a length of 45 cm and a width of 14 cm. Six scintillator blocks are already available for testing. They were read out in first tests with either 12 cm or 22 cm long plexiglass light guides and photo-multiplier tubes (XP4512 B from Phillips). One of the test modules is shown in fig. 2.

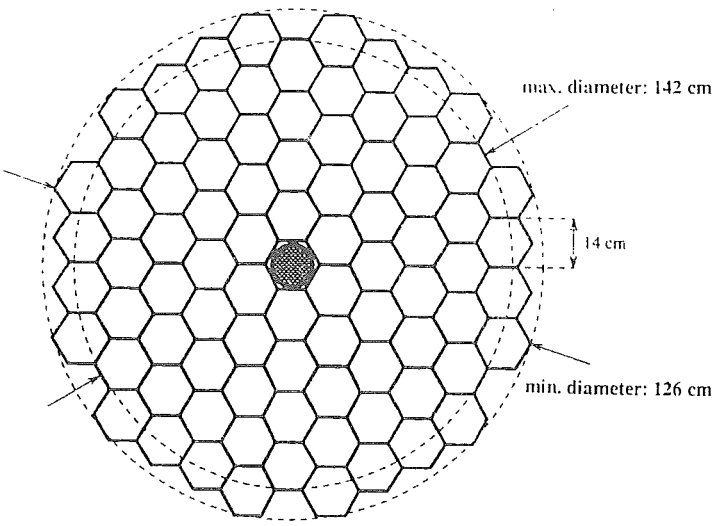

Figure 1: Front view of the scintillator calorimeter. The device consists of 84 hexagonal plastic scintillator elements. It is positioned just behind the central Quirl hodoscope within the vacuum vessel.

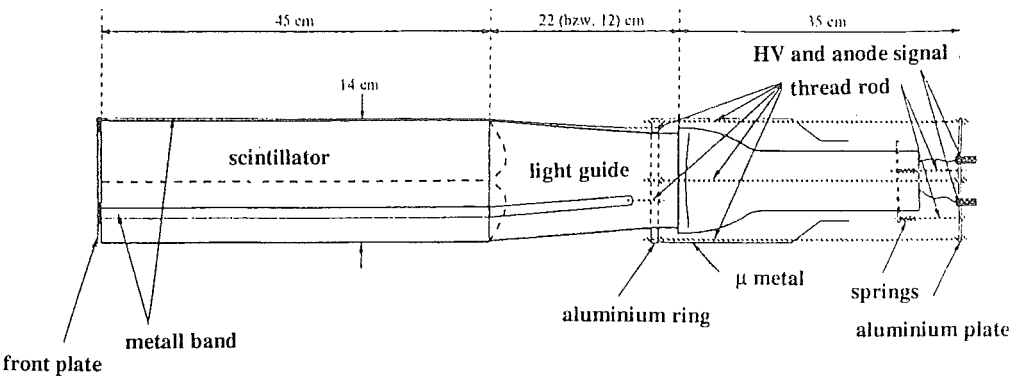

Figure 2: Test module with scintillator block, plexiglass light guide and 4 " photo-multiplier tube.

With cosmic rays and 12 cm long light guides 200 primary electrons per 1 MeV energy loss were found. The light output was compared for data samples, where the particles' trajectories had distances of 7.5 cm, 22.5 cm and 37.5 cm to the light guide. The amplitudes stayed stable within 2%, which indicates a very homogenous light output. For a path length of the cosmic ray particles within the scintillator of 14 cm we obtained about 3600 dynode electrons in the photomultiplier and a resolution of 10 % FWHM.

A test was carried out at the PSI pion facility in order to study the separation ability of the modules for π^+- and π^--mesons. The π^- is captured in atoms and doesn't show the delayed decay. Because of the decay $\pi^+ \rightarrow \mu^+ \bar{\nu}_\mu$, which has a time constant of τ = 26 ns, a delayed second signal can be seen after the meson was stopped within the scintillator. This signature of the delayed π^+ decay was identified by a pulse shape analysis via two ADC's. ADC 1 measured the first part of prompt signals (caused by the incoming particle) while ADC 2 measured the second part of prompt signals plus the delayed signals of any decays. The integration time of ADC 2 was set to about 150 ns. Fig. 3 shows, that π^+- and π^--mesons can be clearly separated by this technique. The efficiency is better than 70 %. An alternative way of separation is the identification of the decay $\mu^+ \rightarrow e^+ \bar{\nu}$, which has a time constant τ = 2.2 µs. This method has been tested as well and worked very efficiently, but it has the disadvantage that it can only be used at moderate counting rates below 50 kHz

The light output of the scintillator with the XP4512B photo multiplier tube and the plexiglass light guide is 200 electrons per MeV energy loss. This corresponds to 60000 electrons being the maximum signal expected for protons being stopped after 45 cm in the scintillator. Since by now we are not limited by the amount of light output we decided to continue the development of the calorimeter with the smaller XP2020 photo multiplier tube and mirror light guides. The smaller diameter of this tube allows us to install the calorimeter within the vacuum vessel and the PM tubes outside. It helps to avoid any unnecessary plexiglass material between it and the central hodoscope. As light guides we use boxes of mirror foils and our standard plexiglass light guides, which act at the same time as vacuum seals. Development and testing is going on.

[1] University of Tübingen

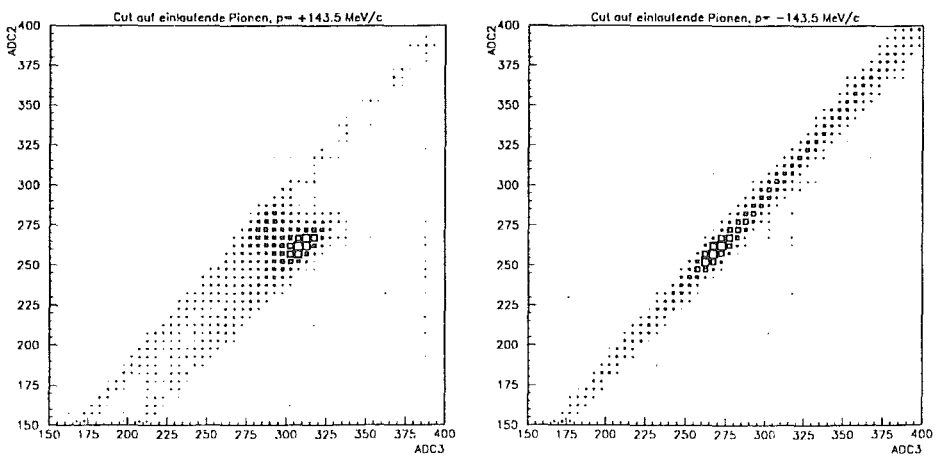

Figure 3: ADC 1 on the prompt signal plotted verus ADC 2 on the slow signal component for π^+ (a) and π^- (b) events. The pion momentum in both cases was 143 MeV/c. π^+ events with their delayed decays are off diagonal.

Measurement of the Timing Properties of the TOF Barrel Scintillators by Means of Cosmic Radiation

J. Patt, P. Cloth, V. Drüke, D. Filges, K. Kilian, N. Paul, E. Roderburg
for the COSY-TOF Collaboration

In Monte Carlo simulation of the TOF scintillator hodoscopes it is necessary to make use of reliable data about the relevant properties of the provided scintillator strips, i.e., to know the light gain and the time resolution of charged particle induced signals. The measurement of those is advantageously done by using cosmic radiation, as it consists of high energetic particles especially myons, which are minimum ionizing at cosmic energies. The only disadvantage of this method is the relatively low intensity of this myons of about 100 $m^{-2}s^{-1}$ in case of vertical impact.

A helically wound scintillator strip of the TOF barrel with original dimensions was available, besides several straight ones. Each had a thickness of 5 mm and a width of 12 cm. The wound strip was 420 cm long, whereas the straight ones had a length of 440 cm. The material was BC408 and NE 110A, respectively, for one of the straight strips.

Theoretical considerations of the light attenuation along the strip lead to the assumption, that the light output of the bent strips should not differ very much from that of straight ones. This was found to be not true in the case of the wound test strip. It was believed that the observed light attenuation was obviously strongly affected by the bending procedure, i.e. by the visible destruction of the surface quality. Thus, an enhenced bending technique, recently developed by BICRON, promises time resolution for the wound strips similar to these of the straight ones.

The strips, packed within a reflecting aluminium foil and light tight black foil, were coupled via a twisted-strips light guide to a XP 2020 photomultiplier. The experimental setup is depicted in Fig. 1.

Two of the straight strips in sandwich arrangement are lying on a special table and are read-out on opposite ends. Above and below the scintillators rails are installed on which additional detectors with multiplier channels 3, 4, 5 and 6 can be moved.

TDC and also ADC signals of all channels are recorded. As trigger signal the four-fold coincidence of the two top and the two bottom channels is used. The signal of channel 2 is delayed by 30 ms with respect to channels 3, 4 and 5 and determines thus always the time of coincidence. In what follows channel 2 is denominated as start channel for the TDC as well as for the ADC with a gate lenght of 200 ns.

The resolution of the start channel in principle limits the time resolution measurement to 400 ps. The resolution decreasing influence can, however, be reduced by some corrections using all of the involved detector channels.

The setup for the measurement of the wound strip is very similar to that of the straight strips with the difference that only one strip is investigated instead of the sandwich pair. Also there is a device to keep the direction of impact of the cosmic rays vertical on any area of measurement on the strip.

In a special measurement the single-electron spectrum of the photomultiplier was determined by using a pulsed light emitting diode. Thus, the ADC signals can be given in units of dynode electrons. The results are given in and Fig. 2.

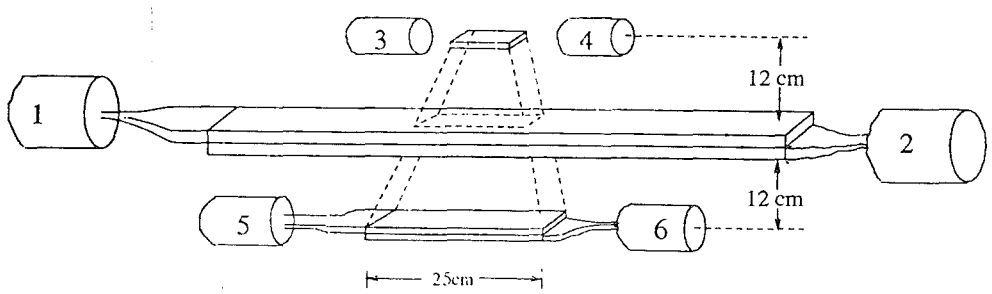

Fig. 1: Experimental setup

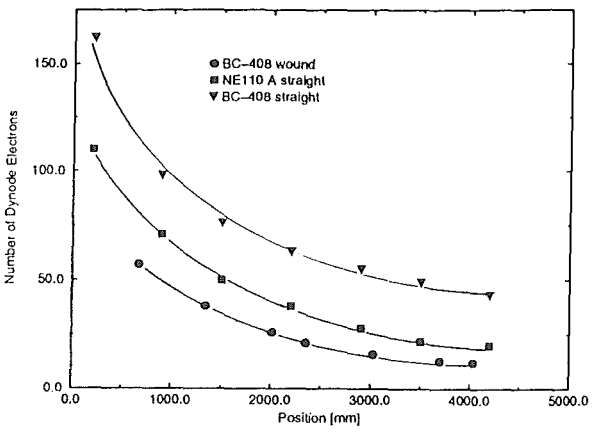

Fig. 2: Number of dynode electrons gained from the TOF barrel scintillator strips

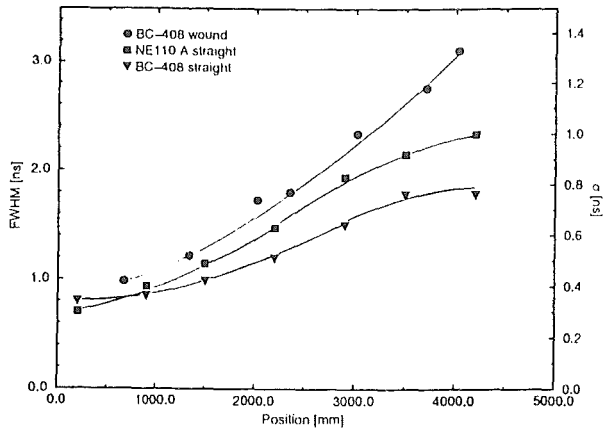

Fig. 3: Measured time resolution of the TOF barrel scintillator strips

The BC 408 strip shows not only a higher light gain as the NE110 strip, its attenuation is also smaller. This is in contrast to the claimed bulk attenuation lengths of 600 cm by Nuclear Enterprises and 380 cm by BICRON. The NE strip, however, had badly polished edges.

As a result of the higher light output the time resolution of the BC408 strip is better than that of the NE110. Near the read-out, at about 100 dynode electrons the 3 time resolution curves run together at about 0.3 ns. Towards the opposite ends of the strips, however, the influence of the light gain on the time fluctuations becomes visible. The round strip gains only 12 dynode electrons giving a resolution of 1.3 ns. 23 NE electrons give 1.0 ns, whereas the 45 BICRON dynode electrons result in 0.75 ns. Time resolution results are given in Fig. 3. Details are given in Ref. [1].

Reference

[1] J. Patt, Diplomarbeit, Universität Bonn, September 1995

Monte Carlo Simulations of the Three Layer TOF Barrel Hodoscope

P. Cloth, V. Drüke, D. Filges, K. Kilian, G. Sterzenbach for the COSY-TOF Collaboration

The TOF detector was designed as a multi-purpose experimental tool covering the requirements of a great variety of reactions as far as possible. We considered different possibilities for the barrel configuration and the 3 layer version was found the best compromise. The TOF detector concept is described in detail in Ref. [1]. The main design goals of the TOF detector are:

- Maximum acceptance in order to obtain good statistics and undistorted phase space occupation for multi-particle reactions
- Good space and time-of-flight resolution of all charged particle tracks with especially good track-pair resolution at small angles
- A virtually massless structure in the sensitive parts of the detector in order to avoid acceptance losses and background
- High rate capability even with high multiplicity reactions in order to guarantee exclusive measurements of multi-particle events.

To demonstrate the capabilities of the 3 layer TOF barrel hodoscope full Monte Carlo simulations were done using the MC4 code system (Refs. 2,3), which was developed by IKP-KFA especially for medium energy detectors. The large number of reaction channels and energies that can be studied together with the great flexibility of the detector setup leads to a tremendous choice of possible cases for simulation studies. By a suitable selection of a few cases we demonstrate properties of the 3 layer barrel system. We concentrate on pp→ppγ bremsstrahlung, and the competing reaction pp→ppπ^0.

- Choice of beam momenta

Proton beam momenta of 0.8 GeV/c, 1.020 GeV/c and 1.2 GeV/c were chosen for the simulations. The target position corresponding to a 1 barrel TOF detector setup is considered.

- Acceptance limits of the TOF detector

In Fig. 1 we have confronted the angular coverage of a "Quirl", "Ring" and barrel setup with momentum distributions of products of the pp→ppγ reaction. The dashed ellipse on the left is the maximum of the possible photon momenta. The dashed ellipse on the right is the momentum distribution of the (p,p) di-proton system for the limiting case of relative pp energy $\varepsilon = 0$. For larger ε there are smaller ellipses for the pp as well as for the photon distribution. The rosette in the center of the picture shows two correlated proton momentum distributions corresponding to a relative energy of ε=10 MeV between the two protons in the exit channel. In addition the low momentum detecting limit for protons in the 3 layer scintillator system is presented. It should be mentioned that the picture shows an example with only one arbitrarily chosen relative energy of 10 MeV. With such diagrams, however, the momentum acceptance of the detector system can be understood. We see that for $0<\varepsilon<10$ MeV we have practically 100% acceptance for ppγ. This is the high photon energy region. For the other extreme of $\varepsilon=\varepsilon_{max}$ where $E_\gamma \to 0$ (elastic scattering) we still have > 80% acceptance.

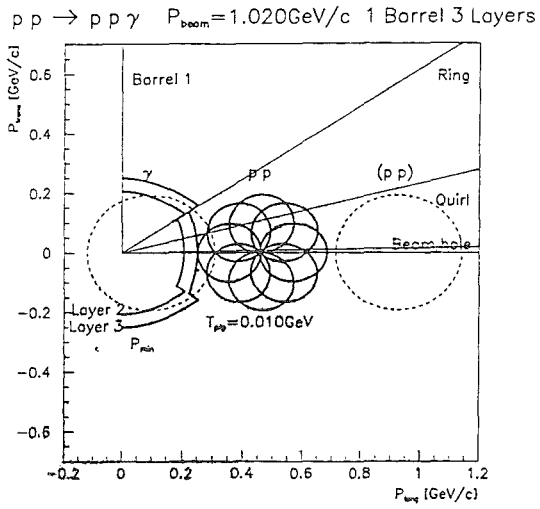

Fig. 1: Acceptance limits of a 1 barrel geometry and laboratory momentum distribution of pp→ppγ (P_{beam} = 1.020 GeV/c, target distance = 2.5 m) layer 2 (layer 3): Protons penetrate at least 1 mm into the second (third) scintillator layer

Figure 2 shows the relative momentum acceptance for proton pairs in the 1 barrel TOF detector setup (ratio of reconstructed events over Monte Carlo events). The figure tells within the kinematical limits and detector cuts (angular range, proton range) that the system has an acceptance for proton pairs near 100%. The reduction of the acceptance at forward angles and high particle momenta reflects the efficiency loss of the correlated low energy protons. The very small - but not zero - relative acceptance below the detector cutoff of about 0.2 GeV/c is due to reconstruction insufficiencies for events where two protons go closely into the same direction.

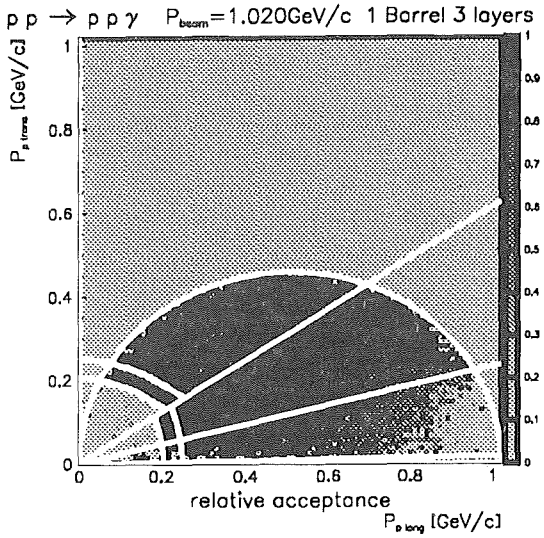

Fig. 2: Relative momentum acceptance for proton pairs (1 barrel setup) LAB system. The elliptic border line is the limit for elastic proton proton scattering ($E\gamma$ = o). The broken line in the lower left part shows momenta where protons reach at least 1 mm into the third layer

- Low energy cut and reconstruction efficiency

As it is necessary for space information to have at least signals in two layers, there exists a low energy cutoff which is still angular dependent. The effect may be judged from the proton range table (Table I) taking into account the scintillator thickness of 5 mm (see Table II and Fig. 2). The reconstruction efficiency is presented in Table III under the condition that tracks hit the third plane with a penetration of at least one mm.

Table I: Proton Range in Plastic Scintillator Material

P MeV/c	T MeV	R mm
100	5.3	0.4
160	13.5	2.0
220	25.5	6.3
280	40.9	19.9
340	59.7	29.8
400	81.7	52.6

Table II: Reconstruction Efficiency of a Monte Carlo Sample of Proton Track Pairs (1 Barrel TOF Setup)

complete TOF setup					
		ppγ		ppπ°	
	beam momentum (Gev/c)	No. of events	efficiency (%)	No. of events	efficiency (%)
Monte Carlo	0.8	10000	100.0	10000	100.0
	1.02	10000	100.0	10000	100.0
	1.2	10000	100.0	10000	100.0
2 and 3 layer recon-struction	0.8	8435	84.4	9765	97.7
	1.02	9128	91.3	9764	97.6
	1.2	9348	93.5	9665	96.7
3 layer recon-struction	0.8	6945	69.5	9552	95.5
	1.02	8254	82.5	9106	91.1
	1.2	8660	86.6	9052	90.5

at least 1 proton hits the barrel					
		ppγ		ppπ°	
	beam momentum (Gev/c)	No of events	efficiency (%)	No. of events	efficiency (%)
Monte Carlo	0.8	6444	100.0	0	-
	1.02	6488	100.0	1150	100.0
	1.2	6473	100.0	3419	100.0
2 and 3 layer recon-struction	0.8	5280	81.9	0	-
	1.02	5816	89.6	1043	90.7
	1.2	5995	92.6	3221	94.2
3 layer recon-struction	0.8	4305	66.8	0	-
	1.02	5175	79.8	890	77.4
	1.2	5477	84.6	2944	86.1

These efficiency losses of slow protons are related mainly to low energy photons (in center of mass). Losses in reconstruction of the more interesting high energy photons can happen when the two proton tracks hit the same pixel in the 3 layer barrel. The high granularity of solid angle elements reduces these losses to a negligible number.

- Missing mass reconstruction

In Table III we show the missing mass resolution for the γ and the π^0, respectively. The simulations were performed for the 1 barrel case. The measured scintillator data (Ref. 4) for the time resolution were used in the Monte Carlo simulations.

The discrimination of reconstructed γ's and π^0's via their rest mass alone is possible upto beam momenta of 1.020 GeV/c. At higher values overlapping slightly becomes visible, but separation remains still possible. One should note, that the kinetic energy of pions and γ's still allows a perfect separation of high energy γ's at $p_p = 1.2$ GeV/c.

Table III: Missing Mass Resolution of the 3 Layer TOF-Detector (2 and 3 Layer Reconstruction)

complete TOF setup			
		ppγ	ppπ°
	beam momentum (GeV/c)	σ(GeV/c^2)	σ(GeV/c^2)
2 and 3 layer recon struction	0.8	$3.49 \cdot 10^{-2}$	$1.25 \cdot 10^{-3}$
	1.02	$5.01 \cdot 10^{-2}$	$5.55 \cdot 10^{-3}$
	1.2	$6.34 \cdot 10^{-2}$	$1.10 \cdot 10^{-2}$

at least 1 proton hits the barrel			
		ppγ	ppπ°
	beam momentum (GeV/c)	σ(GeV/c^2)	σ(GeV/c^2)
2 and 3 layer recon struction	0.8	$3.41 \cdot 10^{-2}$	-
	1.02	$4.86 \cdot 10^{-2}$	$3.70 \cdot 10^{-3}$
	1.2	$6.06 \cdot 10^{-2}$	$9.05 \cdot 10^{-3}$

- Differences of 4 vector components

In Fig. 3 the 4 momentum fluctuations of the outgoing particles p,p,γ are shown. The γ particle is reconstructed from the 4 momentum balance and every event is kinematically fitted with the constraint of $m_\gamma = 0$. The small 4 momentum fluctuations indicate the high resolution of the TOF detector.

References

[1] Annual Report 1991, Jül-2590, March 1992
Annual Report 1992, Jül-2590, February 1993
Annual Report 1993, Jül-2879, February 1994

[2] P. Cloth et al., Monte Carlo Simulations of Medium Energy Detectors at COSY Jülich, MC93, Int. Conf. on Monte Carlo Simulation in High Energy and Nuclear Physics, Tallahassee, Florida, Feb. 22-26, 1993

[3] G. Sterzenbach et al., MC4 - A Program for Particle Detector Simulation, IKP-Annual Report 1992, Jül-2590, Feb. 1993

[4] J. Patt, Diplomarbeit, Universität Bonn, September 1995

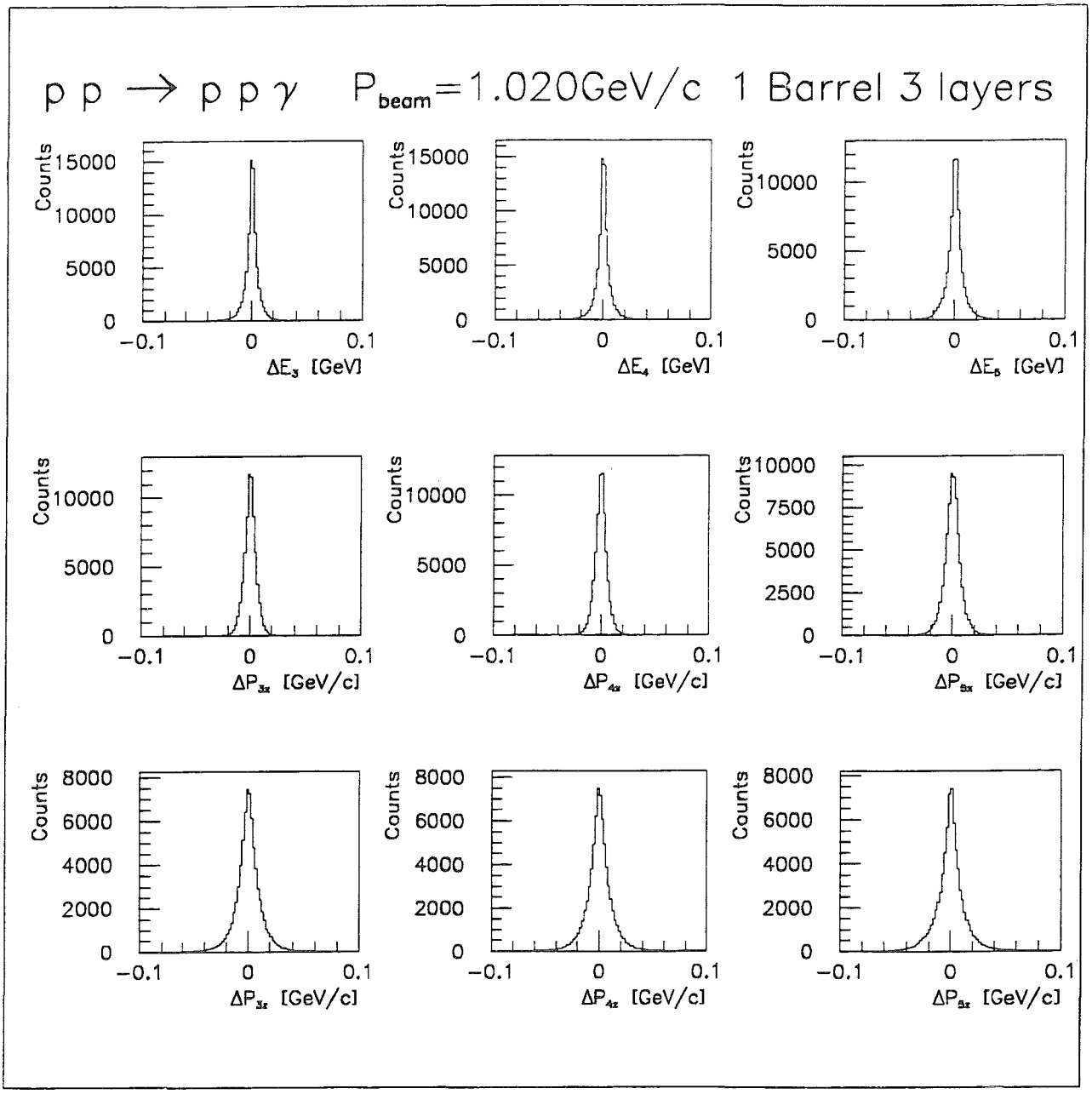

Fig. 3: Difference of 4 vector components between Monte Carlo simulation and reconstruction of the pp→ppγ reaction after kinematic fitting (1 barrel case)

Measurement on a Prototype Scintillator Module to be used in the COSY-TOF Barrel Hodoscope *

P. Michel[1], K. Möller[2], A. Schamlott[1] and A. Schülke[1]
for the COSY-TOF collaboration

Recently a test facility was developed [1,2] to investigate the possibility of building the COSY-TOF barrel hodoscope on the basis of an one-layer scintillator configuration with two-sided PM read-out.
In the present paper a short account is given on results of measurements performed with the help of this test facility. Details on the measuring procedure are described in Ref. [2].
In a first step of the test program the efficiency of scintillator-light guide coupling was investigated for different coupling configurations. Resulting attenuation lengths and light output are shown in Fig.1. Here, as expected, the light output increases with the quality of the coupling being improved. As concerns the attenuation length so it is not a mere intrinsic property of the scintillator bar but is strongly influenced by the coupling to the PM as well.
A remarkable feature of the results shown in Fig.1 is the fact that the attenuation length decreases with the light output increasing. This seemingly contradictory result can be explained by the fact that the different coupling conditions act as different „angular filters" with respect to the angular spectrum of the photons emerging from the scintillator bar. In a next step of the measuring program the time resolution of the prototype scintillator module was determined for the best coupling configuration case (right-most column in Fig.1).

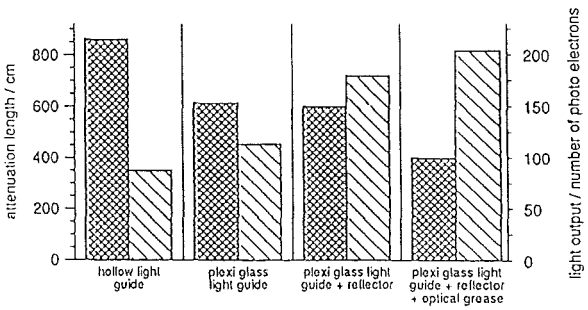

Figure 1: Attenuation lengths and light output for four different light guide systems

In Fig.2 (line a) the resulting time resolution is presented for light read-out at the left end (see Fig.1 in Ref.[2]) of the scintillator bar. By symmetry arguments the same situation is observed at the other end of the scintillator bar (not directly measured in the present case). The relevant time of flight information T for two-sided scintillator read out is obtained by $T=(T_l+T_r)/2-L/2v_D$, where T_l and T_r denote the time of flight values measured at the left and the right side respectively of the scintillator bar with respect to a common time reference unit (start detector or master scintillator in the present case). The quantities L and v_D describe the length of the scintillator bar and the drift velosity respectively.
The time-of-flight resolution σT for two-sided read out is given by $\sigma_T^2 =(1/4)(\sigma_{Tl}^2+ \sigma_{Tr}^2)$. The value σ_T (multiplied by 2.35) is plotted in Fig.2, line b. It should be noticed that $\sigma_T < \sigma_{Tl}, \sigma_{Tr}$ and that the time-of-flight resolution is nearly position independent. Another important property to be measured is the spatial resolution of the prototype scintillator module.

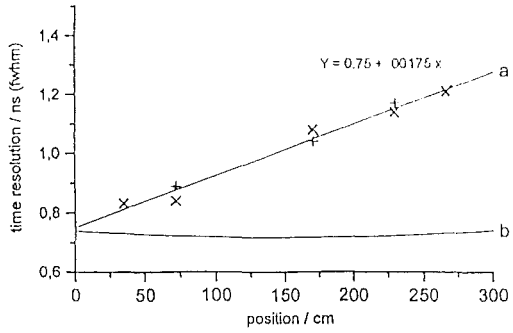

Figure 2: Time resolution of the prototype scintillator module (NE110A).

The point x of particle impact is determined by measuring photon drift time differences at both ends of the scintillator bar. Then the position x is given by $x=L/2-(v_D/2)*(T_r-T_l)$ and the position resolution σ_x by $\sigma_x^2 =(v_D/2)^2 (\sigma_{Tl}^2+\sigma_{Tr}^2)$. The measured spatial resolution is shown in Fig.3.

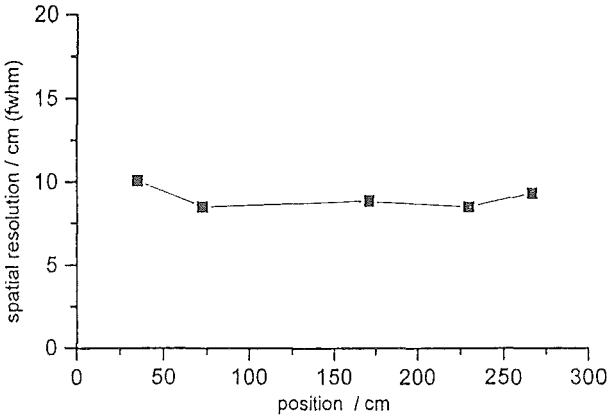

Figure 3: Spatial resolution of the tested scintillator module.

* This work has been supported by the BMBF and the Forschungszentrum Jülich.

[1] Institut für Kern- und Hadronenphysik, Forschungszentrum Rossendorf, Dresden
[2] Institut für Kern- und Teilchenphysik, TU Dresden

References:

[1] P.Michel et al., Annual Report 1994, IKP, Jül-3035, p.11
[2] P.Michel et al., this Annual Report

Apparatus for an Investigation of Long Scintillator Strips through Use of Cosmic Rays*

P. Michel[1], K. Möller[2], A. Schamlott[1] and A. Schülke[1]
for the COSY-TOF collaboration

In the past two years a vacuum chamber has been built which partially resembled those conditions as given by the COSY-TOF spectromer [1,2]. With this set-up various scintillator configurations were to be tested which will be used in the presently discussed barrel detector. It should be recalled that a new version consisting of one-layer scintillator elements with up to 3 m long strips has been developed, since larger problems with the original version were found.

A sketch of the test set-up consisting of scintillator strip, reflector and light guide is shown in Fig. 1. The 90° read out light guide as well as the vacuum-tight seal at the outlet are identical to those as will be used for the TOF-spectrometer. Test measurements with respect to position and time resolution were performed with cosmic rays. To identify the position of impact of the traversing myons three pairs of additional 5 mm thick scintillator sheets (area 30·100 mm^2) were used which could be moved along the long axis of the strip. These scintillator pairs, called „master pairs", were mounted outside of the chamber 30 cm above and below the central axis, thus limiting the angular spread of the traversing myons to 90°±5°. With an observed coincidence rate of approximately 10 events/h reasonable statistics could be obtained within 24 h.

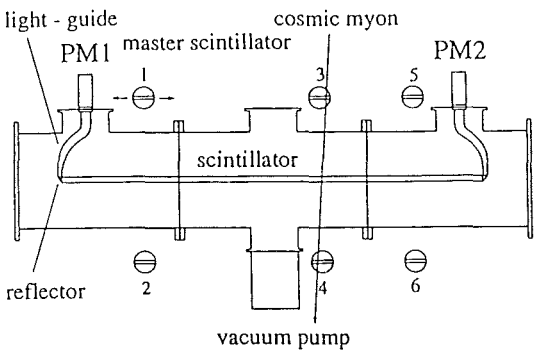

Figure 1: Set-up for the investigation of the prototype scintillator module.

In Fig. 2a is shown an energy spectrum obtained with one such master in coincidence with its upper unit. A strong peak corresponding to about 80 photoelectrons is clearly visible, the low energy continuum is due to Cerenkov light. The latter stems from reactions of the traversing myons with the long light guide made from plexi glass (length 100 mm, Ø 43 mm). A suitably set threshold allows elimination of those events in the off-line analysis. The time spectrum as obtained for such a master pair is shown in Fig. 2b; the resolution was found to be 520 ps (FWHM).

A sketch of the electronics used for these test measurements is shown in Fig. 3. CAMAC units were employed with read-out via a suitably chosen adapter by means of a PC; the CAMDA-software was used for data-acquisition-analysis. As a valid trigger a coincidence between signals of any pair and one observed at either side of the long strip was chosen which in turn started the read out procedure.

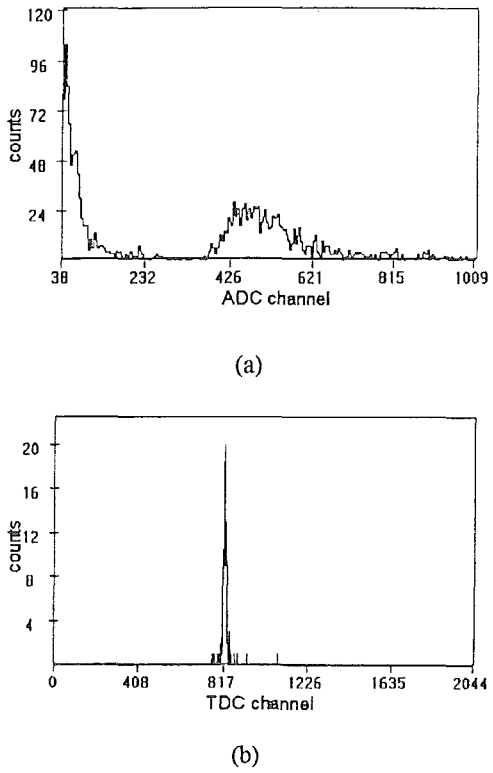

Figure 2: Typical spectra of master pairs; energy spectrum (a), time spectrum (b).

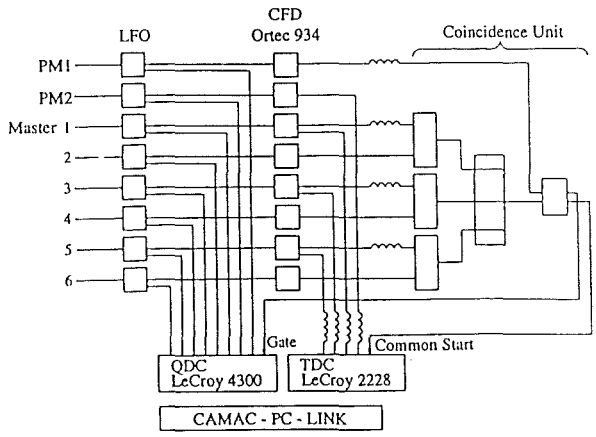

Figure 3: Electronical set-up for the test measurements.

The common start signal is taken from the left side of the long strip, various stop signals are generated from the right end as well as the coincident master pairs. If this coincidence condition is fulfilled the TDC is started by the time signal from the long strip.
The right side of the scintillator strip as well as the upper scintillators of each master pair generate corresponding stop signals leading to peaks at different positions in the TDC-spectra. Thus the position of myon-hits on the scintillator strip can be measured and the spatial resolution be determined (time difference spectrum of signals from COMMON START and the right side of the long strip).

The time resolution of the long strip for read-out at either side can be extracted from the measured time difference between COMMON START and the corresponding master pair. The two-sided read out of the long strips results in an improvement of the time of flight resolution of the TOF spectrometer compared to one-sided read out.

* This work has been supported by the BMBF and the Forschungszentrum Jülich.

[1] Institut für Kern- und Hadronenphysik, Forschungszentrum Rossendorf, Dresden
[2] Institut für Kern- und Teilchenphysik, TU Dresden

References:
[1] P. Michel et al., Annual Report 1994, Jül-3035, p. 11
[2] E. Kuhlmann et al., Physica Scripta 48 (1993) 226
[3] P. Michel et al., this Report

Test of a Scintillating-Fiber Calorimeter for Photons with Energies below 1 GeV +

B. Hübner[1], K.-Th. Brinkmann[1], H. Freiesleben[1], J. S. Lange[1], B. Naumann[2], and L. Naumann[2]
for the COSY-TOF collaboration

In certain cases, such as the pp-bremsstrahlung experiment at the COSY TOF spectrometer, the detection of photons requires the coverage of large solid angles with good angular resolution, i.e. granularity, and high efficiency. The energy resolution may be less important in this special case. Therefore, a calorimeter of the spaghetti type (consisting of scintillating fibers embedded in a lead matrix) may offer an affordable and efficient alternative to high-resolution calorimeters of e.g. CsI type. The performance of such a device at low photon energies (50 MeV $\leq E_\gamma < 1$ GeV) was studied [1] using an early prototype of the SPACAL array [2] which operates at CERN. Its properties were investigated experimentally with real photons from the Mainz microtron MAMI and were verified in extensive Monte-Carlo studies using the computer code GEANT. Experimentally, the detector efficiency was found to equal 100% above the minimum available photon energy of 110 MeV as shown in figure 1. The Monte Carlo studies reveal that the efficiency drops rapidly around $E_\gamma = 40$ MeV. The energy resolution is $(\sigma/E) \approx 10\%/(E_\gamma/\mathrm{GeV})^{-1/2}$ over the full energy range as extracted from a fit to the experimental results presented in figure 2. Typical GEANT results are included in the figure.

The energy resolution obtained with this array is sufficient for a discrimination of ppγ events from π^0 production background. Based on these studies design criteria for future arrays can be matched to experimental requirements. In particular, the average density of the scintillator-lead array is useful in the extrapolation of design parameters for the possible future development of new arrays of this type.

The detector was tested during the TOF beamtime in October 1995. The evaluation of the photon detector data rests on the identification of photon-accompanied events (ppγ or ppπ^0). Because of the small solid angle covered by the array, events of this type have to be pre-selected through a properly prepared missing mass calculated from protons detected with the TOF quirl. This prerequisite is not yet available.

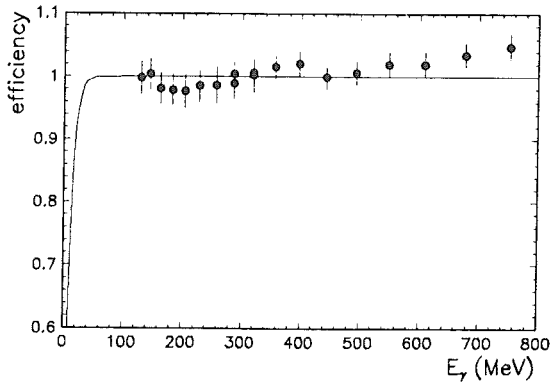

Fig. 1 *Efficiency for photon detection as a function of energy. The full line shows the result of calculations using GEANT.*

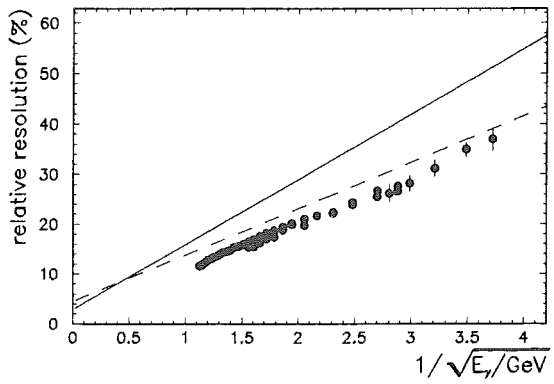

Fig. 2 *Photon energy resolution; the full line is a typical GEANT result using a fiber diameter of 1 mm, the dashed line is for Ø =1.2 mm.*

[1]Institut für Kern- und Teilchenphysik, TU Dresden
[2]Institut für Kern- und Hadronenphysik, FZ Rossendorf e.V.

References

[1] B. Hübner, diploma thesis, Dresden (1995)
[2] D. Acosta et al., Nucl. Instr. Meth. **A294**, 193 (1990), *and* D. Acosta et al., Nucl. Instr. Meth. **A305**, 55 (1991).

+supported by BMBF and KFA

Neutron Time-of-Flight Measurements at the COSY-TOF

A. Böhm [1], K.-T. Brinkmann [1], H. Freiesleben [1], J. S. Lange [1], W. Scobel [2]
for the COSY-TOF collaboration

For the examination of the reaction $pp \rightarrow pn\pi^+$ a large area neutron detector is under construction at the Institut für Kern- und Teilchenphysik of the TU-Dresden as a supplement to the TOF-Spectrometer. This measurement is motivated by the unsatisfactory experimental data of the cross-section near threshold. On the one hand side, the pn subsystem in $pn\pi^+$ may be in either isospin state I=0 or I=1, while on the other hand side the bound pn system (deuteron) in $d\pi^+$ has I=0. Hence, only the measurement of both channels provides a complete picture of the π^+ production mechanism. We expect that the reconstruction and the resolution of the missing mass of the reaction-channel $pn\pi^+$ will be essentially improved by the use of the neutron detector. The Dresden neutron detector COSYNUS (COSY Neutron Spectrometer) has a modular setup (Fig. 1). In each module, three scintillators with 2 m length and a cross-section of 10 cm*10 cm are mounted in a rack. In front of them is a 4mm thin scintillator paddle which covers the whole front area as a veto-detector for charged particles. All scintillators are read out on both sides with XP2020 photomultipliers enabling a resolution of the position of interaction along the scintillator. This detector is presently assembled in Dresden. The two different types of lightguides are in production. In both cases prototypes of excellent optical quality were built. Fig. 2 shows the efficiency of the detector for neutrons calculated with the Monte-Carlo code MODEFF [1]. At the TOF-beamtimes in June and September/October 1995 we could already gain data using a neutron detector from the University of Hamburg. This detector has a similar setup to ours except that the length of the scintillator bars is only 1 m [2]. The position resolution along the bar was found to be 7.5 cm FWHM. A time calibration for the September/October-beamtime was obtained for the neutron detector using the time of flight of photons from hadronic interactions in a lead target. The resolution of the extracted γ-peak is 1.4 ns FWHM.

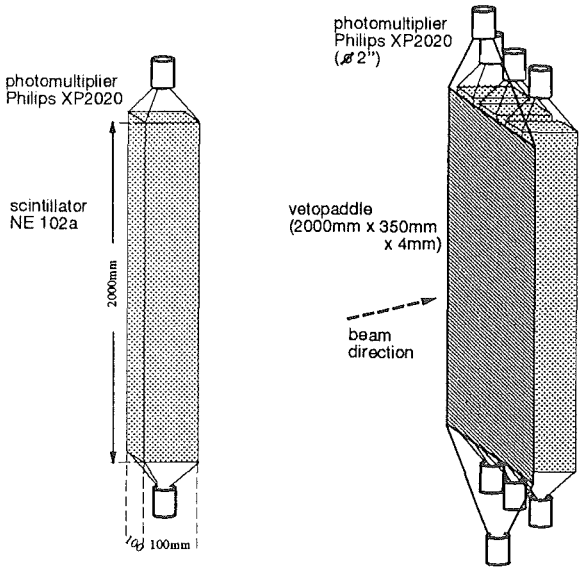

Fig. 1 *Schematic view of one module of the Dresden neutron detector COSYNUS.*

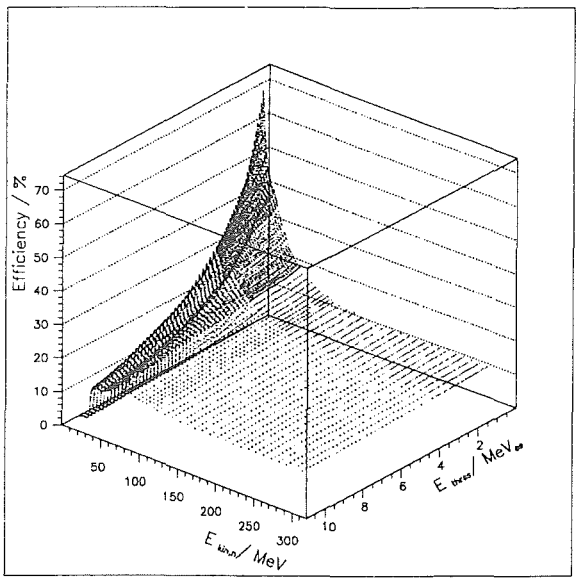

Fig. 2 *Calculated efficiency for one scintillator bar of COSYNUS in dependence of the threshold and the neutron energy. For the calculation we took regard to the expected setup at the next TOF-beamtime (distance target-detector = 10 m, smallest distance of one side of the bar to the beam =10 cm)*

[1] Institut für Kern- und Teilchenphysik, TU Dresden
[2] 1. Institut für Experimentalphysik, Universität Hamburg

References

[1] J. Erxmeyer, Studienarbeit, Technische Universität Berlin (1985)
[2] L. Lüdemann, diploma thesis, Hamburg (1992)

Pion Production Studies with the GEM Detector System

The GEM Collaboration

1. Introduction

This report discribes the progress made at GEM in the last year. In this time we performed three beam times: one with the goal to continue the measurements of the $p+p \rightarrow \pi^+ + d$ reaction [1] further to the threshold. The other two beam times were used as running in of the GErmanium wall. While the first one of these was a pure technical test we tried in the second one to use pion production as test of the combined GEM detector in an operational mode as foreseen to study pionic atoms (COSY proposal 10). The runs were also used to improve the set up and to study the performance of the beam. One such study was the measurement of the time of a reaction to have taken place relativeley to the beginning of the spill. This measurement did not show a variation of the beam momentum with extraction time. Another interesting quantity of the beam is its emittance.

2. Emittance Estimate

The emittance of the extracted beam was measured with the experimental set-up discussed below. First the beam was adjusted to the symmetry axis of the experiment which corresponds to the one of the beam line. Then, the beam was focused with the help of a pair of magnetic quadrupole lenses to the center of the target position. The target was replaced by a synthetic ruby as scintillator which was observed with the help of a TV system. This observation yielded a beam spot with a ratio of the diameters of 1:2 for the horizontal and vertical direction, respectively. Furthermore, the intensity distribution of the beam was measured by a counting ratio measured on an annular scintillator counter with 1.5 mm inner radius to the one measured on another counter covering the inner part. It was found to be between 1:5 to 1:4. The intensity ratio $\nu(a)$ for the axis ratio of 2 as function of the beam spot diameter is shown in Fig. 1. This ratio is calculated under the assumption of a Gaussian in horizontal as well as in vertical direction. The assumption of triangular distributions yields almost the same result.

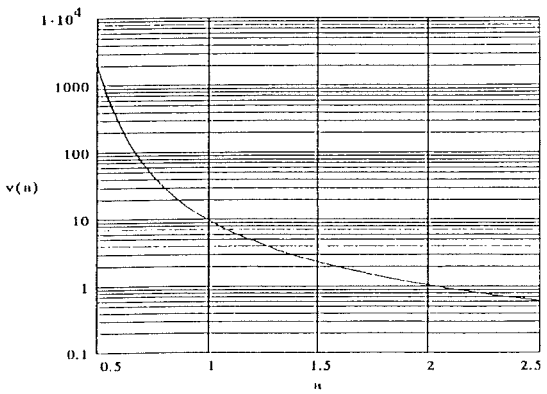

Figure 1: The intensity ratio $\nu(a)$ on the counters as discussed in the text as function of the spot extension (FWHM) a for a ratio of 2 for the horizontal to vertical axis.

From this graph we estimate the beam spot size (FWHM) to be 1.3 mm in the vertical and 2.6 mm in the horizontal direction, corresponding to σ_h = 0.47 mm and σ_v = 0.94 mm, respectively. The beam was then led into the focal plane area of the magnet spectrometer and its momentum analyzed. The spectrometer allows also to measure horizontal and vertical distributions of the beam as shown in Fig. 2. These distributions were fitted again by Gaussians (see Fig. 2), leading to 1.7 mrad in the horizontal and 3.8 mrad in the vertical direction. These measurements yield estimates for the emittance of ε_x = 1.6 π mm mrad for the horizontal and ε_y = 1.8 π mm mrad for the vertical direction. One should stress that these results were obtained with an uncooled beam which was extracted from COSY through a resonance extraction with spill length of 1 s with 50 % duty cycle. However, recently an ultra-slow extraction was performed with a rather constant beam during 20 s within a 30 s cycle. The total momentum was found to be uncertain by $\Delta p/p = 4 \cdot 10^{-4}$ (see Fig. 3). Such a beam is an ideal footing for a sophisticated detector like GEM.

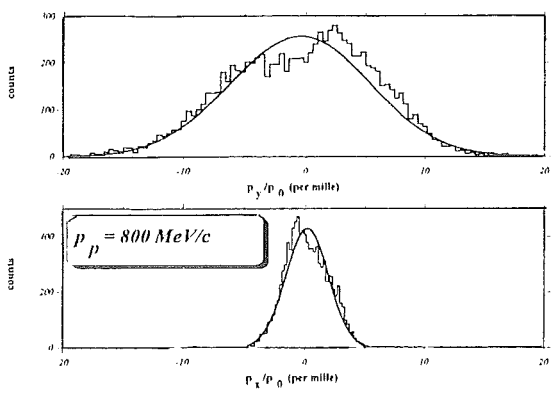

Figure 2: The distribution of the beam in the horizontal (x) and vertical (y) plane with respect to the beam axis. The measured distributions as well as Gaussian fits are shown.

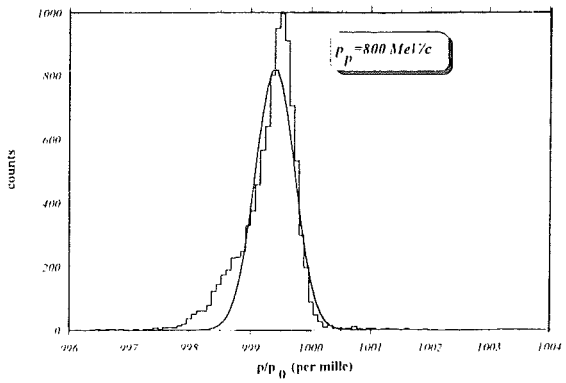

Figure 3: The momentum analyzed COSY beam (histogram). The Gaussian fit is shown as curve.

GEM is a high resolution hybrid detector with a large acceptance for recoiling nuclei when mesons are produced close to threshold. In this energy range all reaction products emerge into small cones close to the beam axis. The idea behind GEM is to cover this spatial area by high resolution detectors: high resolution with respect to momentum or energy measurements and to emission angle measurement as well. GEM consists of two main parts: the GErmanium wall and a Magnet spectrometer. The performance of the GErmanium wall will be discussed below.

3. Further Experiments

As stated in the introduction we performed further measurements of the $p+p \rightarrow \pi^+ + d$ reaction. They were done with the external proton beam of the COSY accelerator at momenta below 800 MeV/c (the threshold momentum is 788.85 MeV/c). The target was a cell containing liquid hydrogen. Its dimensions were 6 mm diameter and 2.2$\pm$0.1 mm thickness, respectively. The windows made of Mylar were of 2 μm thickness each. Further details on the target are given in Ref. [2]. Tracks of recoiling deuterons were measured in the focal plane area of a magnetic spectrometer by two stacks of multi wire drift chambers (MWDC) which allow measurements in the horizontal and vertical direction as well. In addition π's from the reaction were detected in coincidence by another annular scintillator behind the target with a 5 mm diameter hole. This pion detector and the scintillators in the focal plane (multi layer trigger hodoscope) served as start and stop detectors, respectively for a time of flight (TOF) measurement over a flight path of approximately 18 m through the spectrometer. A measured TOF spectrum is shown in Fig. 4. Background protons and reaction deuterons are clearly separated. These background protons are a severe problem in experiments of this type. The magnetic rigidity of the reaction deuterons is close to the one of the beam protons. A first reduction of the protons in the trigger is achieved by an absorber between the last two layers of the trigger hodoscope with thickness sufficient to stop the deuterons. The last layer can then act as veto detector. A threshold in the discriminator on the signals from the first layer is set to level sufficient to suppress most of the protons. From the tracks measured by the two packs of MWDC's we reconstructed the momentum vectors of the deuterons at the target yielding count rate distributions shown earlier [1]. These distributions were transformed into centre of mass system angular distributions, and the count rates were transformed to cross sections. Applying the known quantities and energy conservation and linear momentum conservation the mass of the unobserved π^+ can be deduced. Its distribution is an indication of the quality of such an experiment. In Fig. 5 such a distribution for the measurement at 793 MeV/c beam momentum is shown.

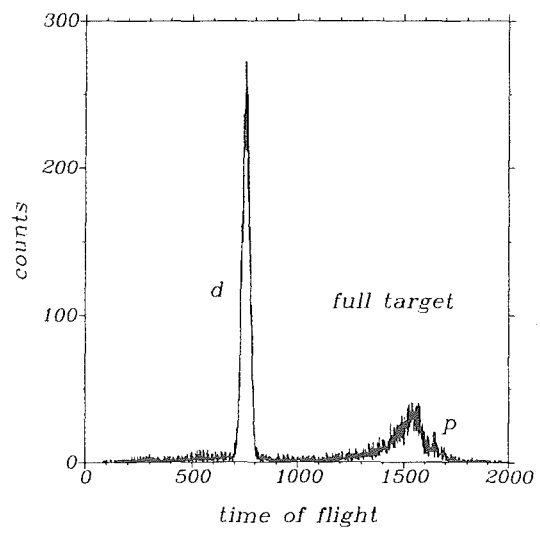

Figure 4: The time of flight spectrum. Shown is the time difference between the deuteron measured in the focal plane area and a pion detected in the target area.

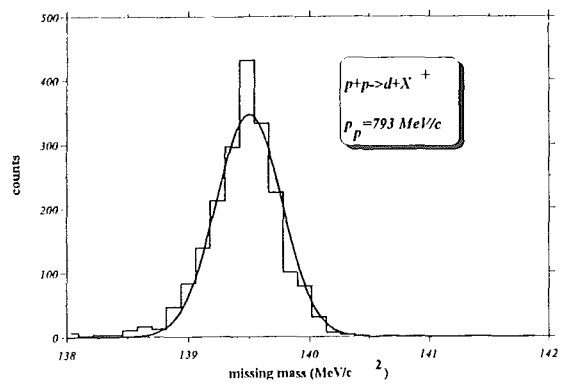

Figure 5: The deduced missing mass distribution for the unobserved π^+.

In the following we will concentrate on only two out of five momenta, namely 793 MeV/c and 800 MeV/c where the data have been analyzed in part. While for the lower beam momentum the magnet spectrometer has full acceptance both with respect to momenta of the deuterons as well as to the geometry, it is somewhat truncated in the case of the higher momentum. However, the effective acceptance can be extracted from the data itself. The acceptance-corrected differential cross sections are almost flat indicating the dominance of the s-wave. In order to be quantitative we have fitted a Legendre polynomial expansion to the differential cross sections. For the present case only two partial waves contribute. Such a fit to the data taken at 793 MeV/c is shown in Fig. 6.

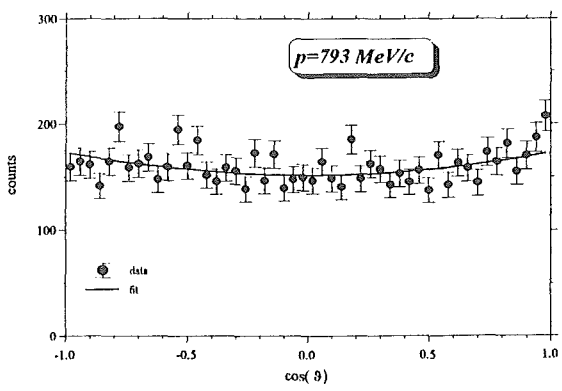

Figure 6: Angular distribution in the centre of mass system of the deuterons from the indicated reaction. Also shown is a fit with Legendre polynomials to the data (solid curve).

In the following we will discuss the results obtained for the total cross section. The two values are indicated in Fig. 7 as full dots. In the figure these results are compared with other data taken from the literature. Here we have restricted ourselves to only recent data compiled in Table 1.

Table 1: The pp and πd reactions used for the analysis. Included in this table are only data taken after 1967 and in the range $\eta < 2$.

reaction	η	measured	comments	Ref.
pp	0.884, 1.12	$d\sigma/d\Omega$	non-magnetic, LH_2-target	[3]
pp	1.	$d\sigma/d\Omega$	-	[4]
pp	1.338,...,1.57	$d\sigma/d\Omega$	non-magnetic, CH_2-target	[5]
pp	0.49,1.03,1.34,1.61,1.88	σ_t	bubble chamber	[6]
π+d	0.15,...,0.484	σ_t	bubble chamber	[7]
π+d	1.51, 1.78	$d\sigma/d\Omega$	non-magnetic, LD_2-target	[8]
π+d	0.5,...,0.971	$d\sigma/d\Omega$	non-magnetic, LD_2-target	[10]
π+d	0.214,...,0.518	$d\sigma/d\Omega$	non-magnetic,active target	[9]
π+d	1.53, 1.68, 1.818	$d\sigma/d\Omega$	non-magnetic, LD_2-target	[11]
π+d	0.59,...,0.73	σ_t	non-magnetic, gas-target	[12]

It is interesting to note that up till now no measurements were perfomed with a magnetic spectrometer. One reason may lay in the difficulties when measuring deuterons with momenta close to the beam and in the geometrical vicinity of the beam as discussed above. Low energy pions decay to a large extent in such a long flight path. The present data seem to be a smooth extension of the earlier data closer to threshold. There is no visible difference between the $p+p \rightarrow \pi^+ + d$ and the time reversed reaction.

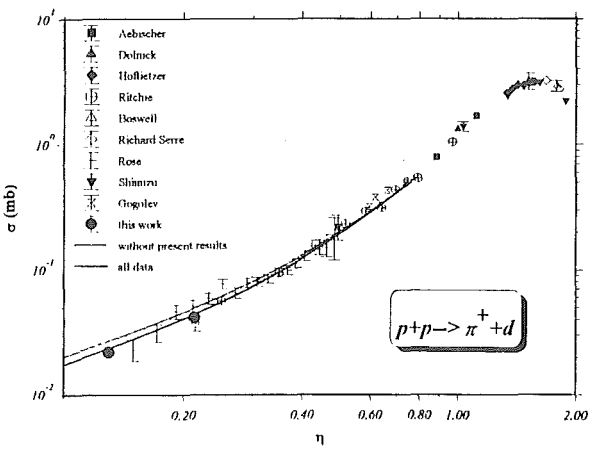

Figure 7: The total cross section for pion production for the indicated reaction as function of the relarive pion momentum. Shown are data compiled in Table 2 (different symbols) and the present results (full dots). All data from $p+p \rightarrow \pi^+ + d$ reactions are shown as full symbols while those from $\pi^+ + d \rightarrow 2p$ reactions are indicated as open symbols. The data from the reversed reaction have been transformed employing the principle of detailed balance. Also shown are fits as discussed in the text.

The excitation function can be parametrized in terms of the centrifugal model given by Watson and Brueckner [13]

$$\sigma(\eta) = \sum_{L_{\pi d}=0}^{L_{max}} \alpha_L \eta^{2L+1} \qquad (1)$$

with $\eta = p_\pi/m_\pi$ and α_L constants which give the strength of the different partial waves between the π and deuteron, respectively. We have fitted Eq. 1 to all data up to $\eta \leq 0.8$. Up to this value only s-wave and p-wave are found to contribute. This is in accord to earlier findings [3,11]. The resulting values are α_o = 0.194±0.005 mb and α_1 = 0.816±0.011 mb. When the two present points are added, the results are changed to α_o = 0.166±0.003 mb and α_1 = 0.877±0.007 mb. The two corresponding curves are also shown in Fig 7.

We have here neglected any comparison with theories since these usually have performed calculations without Coulomb corrections. Therefore, the theoretical values are slightly larger than the present ones. With this caveat in mind we cite the results obtained by Horowitz [14] which are α_o = 0.102±0.009 mb for only pion exchange and α_o = 0.203±0.021 mb when also heavy meson exchange is taken into account. However, this approach was recently critisized by Niskanen [15], claiming that already inclusion of the Δ initial state interaction followed by rescattering of the pion accounts for such yields without heavy meson exchange. With more data and also differential cross sections presently in the analysis we hope to contribute to this puzzle.

3.1 The GE-wall

In order to increase the acceptance of the magnet spectrometer, which is 50 mrad in the horizontal and 150 mrad in the vertical direction, a solid state detector system was developed. It consists of 4 position sensitive diodes made of HPGe. A hole in the middle is equivalent to the acceptance of horizontal acceptance range of the magnet spectrometer. It allows also the primary beam to pass through. A value of 3.5 mm for the diameter in the first diode next to the target sheds light on the quality demanded for the beam. This diode with thickness of 1.7 mm has 200 Archimedes' spirals („quirls") on both sides with opposite bending direction thus defining 400000 pixels. It acts as a tracker for the emission direction and energy loss measurement. The following three diodes -1.7 cm thick each- have 32 wedges on one side. These allow for further energy measurements and because of the 32 fold use of electronic circuits rather high counting rates. This feature is also supported by the radial symmetry of the set up with respect to the beam axis. At present the quirl and the last diode with 10.8 cm diameter are operational and have been used in first runs.

The August beamtime was used to test the Germanium Wall only and gave the opportunity to learn how the whole setup - the detector, the electronics, as well as the online-analysis - behaved under real beam conditions. This new knowledge lead to a variety of improvements, mainly with respect to the analog and digital electronic circuits.

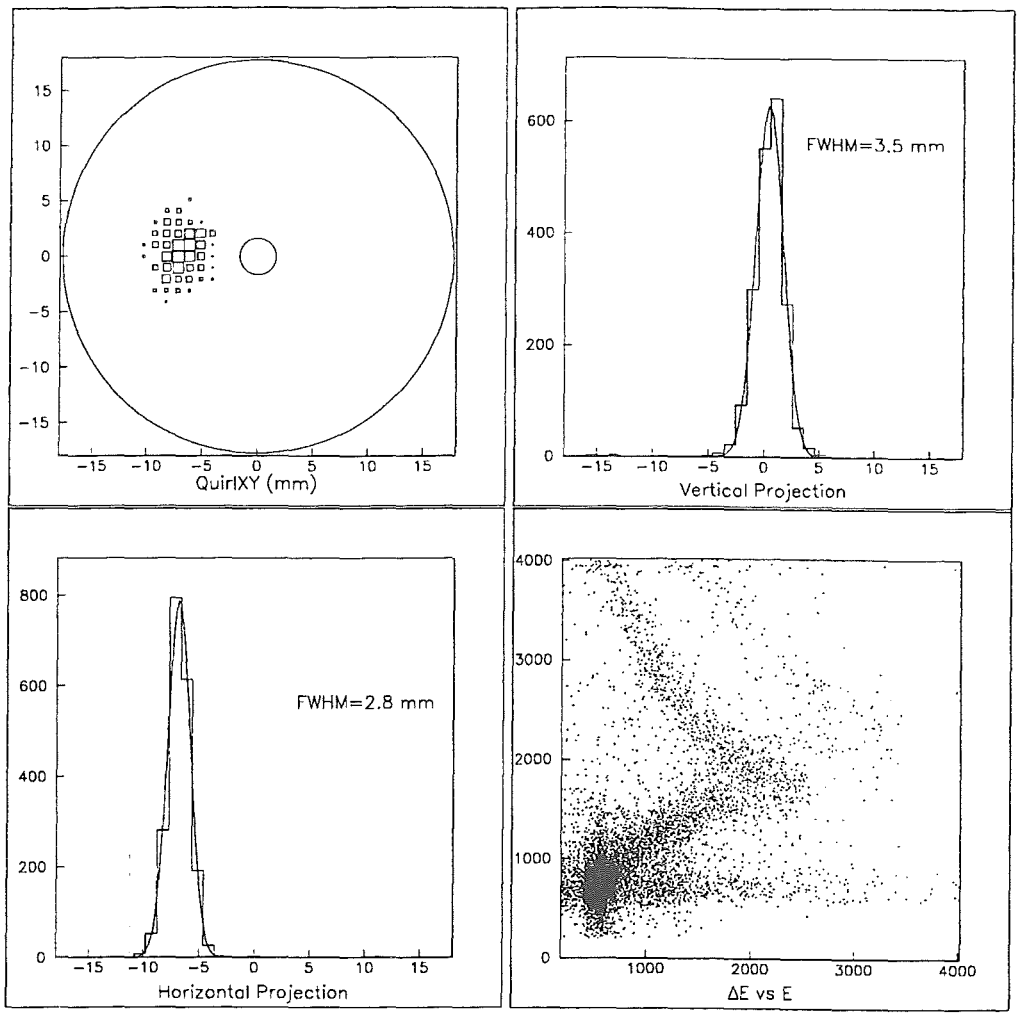

Figure 8: Upper left: the geometry of the GE-quirl and the primary beam hitting it (squares with sizes indicating the intensity. Upper right: the projection of the beam distribution to the vertical (histogram) and a Gaussian fit (solid curve). Lover left: Same as upper right but for horizontal axis. Lower right: Distribution of the energy losses in the quirl (y-axis) and the pizza (x-axis).

Already 3 month later more than 400 analog and digital channels were modified and tested.

The beamtime in November 1995 was a further step in combining the magnetic spectrometer and the Germanium Wall to one common detector. While measuring $p+p \rightarrow \pi^+ + d$ with the spectrometer BIG KARL, for the Germanium-Wall it was choosen to investigate the reaction $p+p \rightarrow p+p+\pi^0$. Due to the kinematics of this reaction, one should observe the two coincident protons in the Germanium Wall and a trigger condition similar to that which is required for measuring pionic atoms (proposal COSY 10) could be tested. For that purpose, every logic combination of the OR'ed signals from the quirl's frontside, it's rearside and the E-detector could be set as a trigger condition. Furthermore, a user defineable multiplicity with respect to the number of hits in the Ge-Wall, could be added as an additionally condition.

For beam monitoring on online-display of the hit-pattern of the Quirl was sent to the COSY control. Figure 8 shows the beam spot and it's profile, as the beam was shifted directly onto the Quirl. The diameter of the beam was found to be 2.8 mm in the horizontal direction and 3.5 mm in the vertical direction (FWHM). As can be seen from these distributions, the tail of the beam has approximately a diameter of more than 5 mm and was therefore larger than the quirl's hole (4.3 mm). To prevent the germanium detector from suffering too much radiation damage, the beam intensity was limited to a maximum counting rate of less than 10000 counts/s.

Already the preliminary analysis of the data show clearly the typical ΔE against E signature of detected protons in the Germanium Wall (see again Figure 8). In the lower left corner of this figure the primary proton beam can be seen as a large spot. After switching the trigger condition to demand at least two hits in the Germanium Wall, this spot was heavily suppressed and the trigger rate dropped down by an order of magnitude, yielding a maximum of $\approx$ 70 triggers per second. At the same time the maximum focal plane trigger rate from the reaction $p+p \rightarrow \pi^+ + d$ was $\approx$ 15 per second and the data aquisition was able to accept more than 96 % of all the triggers. The future analysis of the data will clearify, whether the two proton events from the reaction $p+p \rightarrow p+p+\pi^0$ can be seperated from the strong beam proton background. Furthermore, a comparison with the focal plane data will shed some light on the capabilities

of detecting coincident particles in the focal plane and the Germanium Wall, respectively.

References:

[1] A. Budzanowski et al., Annual Report 1994, ISSN 0944-2952, p. 36
[2] V. Jaeckle et al., Nucl. Instruments and Methods A349 (1994) 15
[3] D. Aebischer et al., Nucl. Phys. B 108 (1976) 214
[4] C. L. Dolnick et al., Nucl. Phys. B 22 (1979) 461
[5] J. Hoftiezer et al., Phys. Lett 100 B (1981) 462
[6] F. Shimizu et al., Nucl. Phys. A 386 (1982) 571
[7] C. M. Rose, Phys. Rev. 154 (1967) 1305
[8] J. Boswell et al., , Phys. Rev. C 25 (1982) 2540
[9] B. G. Ritchie et al., Phys. Rev. Lett. 66(1991) 568 and Phys. Rev. C 47 (1993) 21
[10] B. G. Ritchie et al., Phys. Rev. C 24 (1981) 552
[11] C. Richard-Serre et al., Nucl. Phys. B20 (1979) 413
[12] S. I. Gogolev et al., Phys. Lett. B 300 (1993) 24
[13] K. Watson and K. Brueckner, Phys. Rev. 83 (1951) 1
[14] C. J. Horowitz, Phys. Rev. C 48 (1993) 2920
[15] J. A. Niskanen, Helsinki University preprint (1995) and private communication

Two - Pion Production at MOMO

F. Bellemann[1], A. Berg[1], J. Bisplinghoff[1], G .Bohlscheid[1], J. Ernst[1], R. Frascaria[5], C. Henrich[1], F. Hinterberger[1], R. Ibald[1], R. Jahn[1], L. Jarczyk[2], R. Joosten[1], A. Kozela[2], U. Kuhn[1], H. Machner, A Magiera[2], R. Maschuw[1], T. Mayer-Kuckuk[1], G. Mertler[1], B. Metsch[3], P.v. Neumann-Cosel[4], T.v. Oepen [1], H. R. Petry[3], D. Rosendaal[1], P. v. Rossen, K. Scho[1], F. Schwandt[1], R. Siebert[5], J. Smyrski[2], A. Strzalkowski[2], R.. Tölle, R. Wurzinger[5], R. Ziegler[1]

The MOMO experiment focusses on near threshold meson production via the reactions pd → ^{3}He $\pi^+\pi^-$ and pd → ^{3}He $K^+ K^-$. It takes advantage of the high quality of the cooled external COSY beam and the existing spectrometer BIG KARL. The setup consists of a high granularity scintillating fibers meson detector near the target with a ± 45 deg. opening angle, and the spectrometer, which is used for ^{3}He-identification. The large solid angle and high resolution of this detection method will yield precision data on the low energy (T<50MeV) meson-meson interaction and probe into questions like meson-nucleon resonances and KK-molecule.

The MOMO vertex dector consists of 672 scintillating fibers (round, 2.5mm diameter) arranged in three planes tilted 60 deg. versus each other. Each plane is subdivided into two identical modules. The fibers are read out by 16-fold photomultipliers (Hamamatsu R4760) followed by individually adjustable level adapters for each channel, which match the signals for the utilized PCOS III data aquisition system. All six modules are installed on location and the detector is fully operational. The efficiency was measured to be better than 99% for minimal ionising particles.

The MOMO scattering chamber houses the 4mm LD2 target as well as a remotely steerable ladder for beam viewers and solid targets. The 5 mm thin Al front end of the chamber faces the vertex detector on the outside and keeps straggeling of the mesons at a small level.

The BIG KARL spectrometer is also fully operational. Its status is described in detail elsewhere in this annual report.

In 1995 the MOMO - collaboration obtained two COSY - beam times, each two weeks long. In the January run some 350 events from the reaction pd → ^{3}He $\pi^+\pi^-$ at 1150 MeV/c beam momentum could be unambigiously identified. The maximal available beam intensity was about 10^8 protons per burst. By then, the 2mm sharp beam spot was surrounded by a massive (about 10% of the beam intensity) 10 cm diameter halo. However, the excellent high rate capability of the vertex wall enabled almost background free data taking at that beam intensity.

The second beam time in the summer was a major breakthrough for MOMO, since the COSY team managed to improve the beam parameters substantially just at the beginning of our run. New beam line optics completely removed the halo and the beam intensity could be increased to some 2×10^9 protons per burst (1s beam on target every 6s).

This high quality beam yielded more than 6000 two-pion events on our data tapes. Fig. 1 shows the mesonic hits on the scintillating fibers vertex detector. The absense of a beam halo is evident.

The BIG KARL spectrometer was calibrated via the two-body reaction p+d → t + π^+. In addition, this reaction was

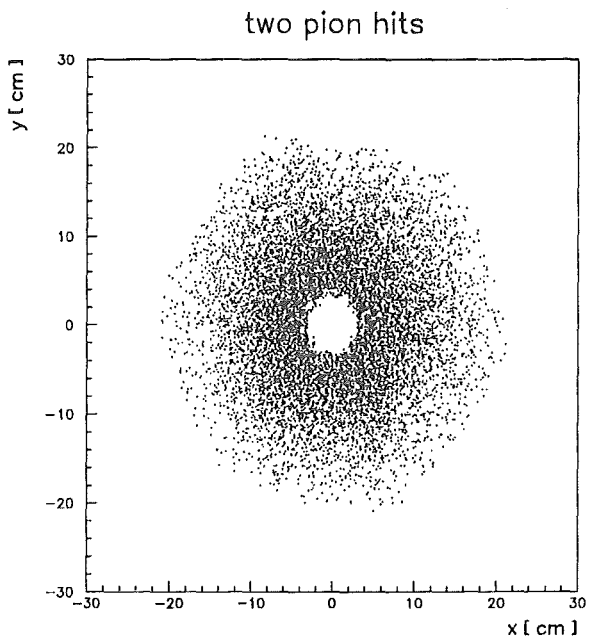

Fig. 1: Two - pion hits on the vertex wall

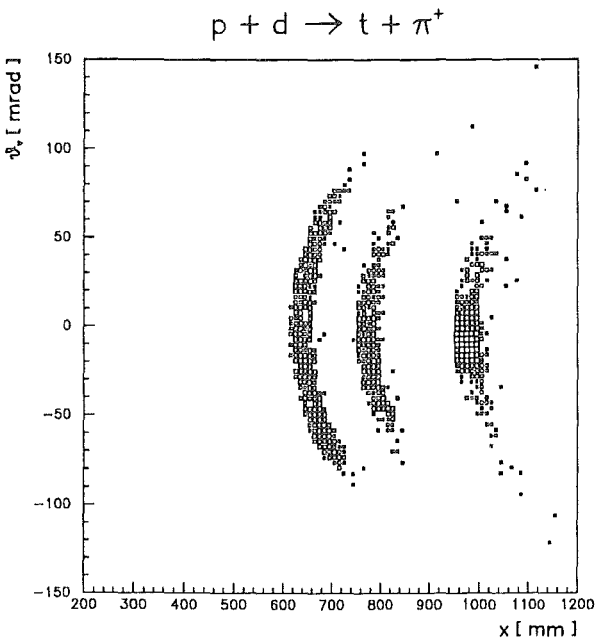

Fig. 2: Focal plane tritium spectra of the reaction pd → tπ^+ at three different field settings

used to check the acceptance of the spectrometer. Fig. 2 depicts focal plane spectra of the $p+d \rightarrow t+\pi^+$ reaction at three different magnetic field settings. The dependence of the acceptance on the focal plane position is evident. However, all three settings yielded within statistical errors the same absolute differential cross section of 19 ± 1 μbarn/sr. This adds confidence to the acceptance calculations utilized in our data analysis.

The $pd \rightarrow {}^3He\ \pi^+\pi^-$ reaction was measured at two different but overlapping BIG KARL settings. The ^3He particles could be unambigiously identified by time of flight and energy loss measurements. Fig. 3 demonstrates the coplanarity of the observed ^3He - coincident double hits in the vertex wall. 'Good' events must be coplanar in respect to the total meson momentum axis, which is defined by the beam and the ^3He momenta.

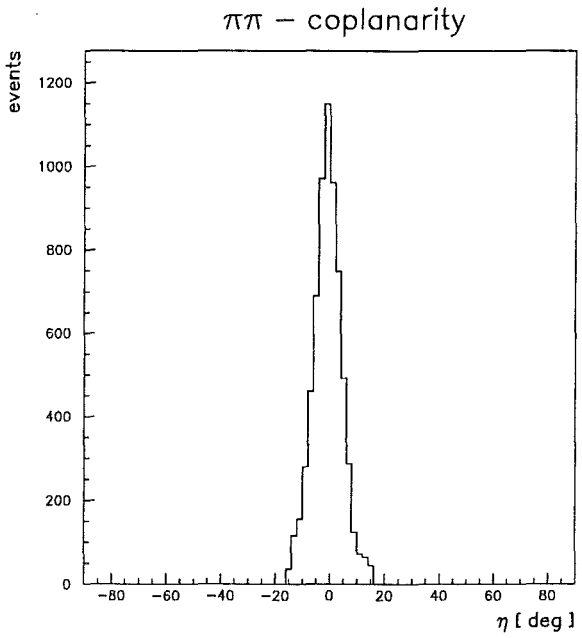

Fig. 3: Coplanarity of the $\pi^+\pi^-$ - events

Fig. 4 shows results of a preliminary analysis of the 1995 data.

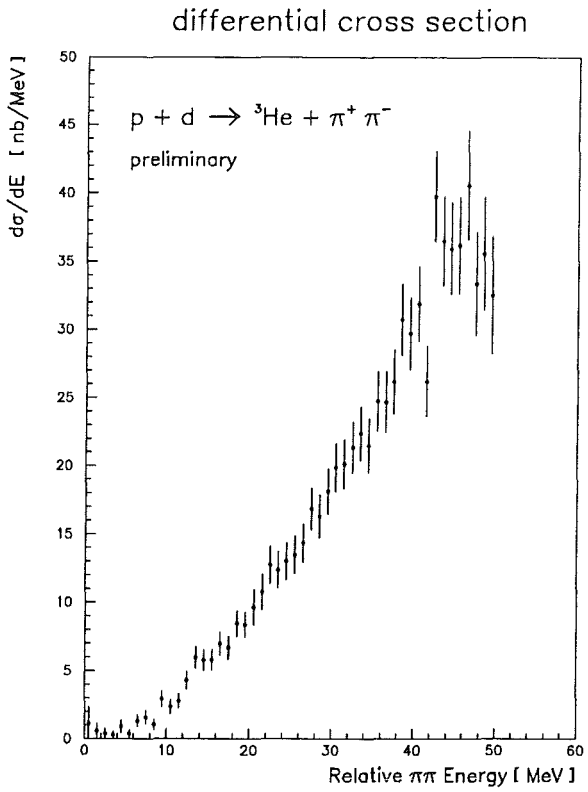

Fig. 4: Relative energy spectrum of two - pion events from the reaction $pd \rightarrow {}^3He\ \pi^+\pi^-$ at 1150 MeV/c incident proton beam momentum

[1] Institut für Strahlen- und Kernphysik, Universität Bonn
[2] Institute for Physics, Jagellonian University, Crakow, Poland
[3] Institut für theoretische Kernphysik, Universität Bonn
[4] Institut für Kernphysik, Technische Hochschule Darmstadt
[5] IPN Orsay, France

The EDDA Experiment: Proton-Proton Elastic Scattering Excitation Functions at Intermediate Energies [1]

J. Bisplinghoff[a], F. Hinterberger[a] and W. Scobel[b] for the EDDA collaboration [2]
[a] Inst. f. Strahlen- und Kernphysik, Universität Bonn
[b] I. Institut f. Experimentalphysik, Universität Hamburg

The EDDA experiment is designed to provide a high precision measurement of proton-proton elastic scattering excitation functions ranging from 0.5 to 2.5 GeV of (lab) incident kinetic energy. It utilizes the proton beam of the cooler synchroton COSY operated by KFA Jülich.

EDDA is meant to make a significant contribution to the global proton-proton phase shift analysis, particularly in the energy domain above 1.2 GeV, where existing data is sparse. It will also test the energy range in which meson exchange models are a valid approximation for the nucleon-nucleon interaction. Furthermore, EDDA is highly sensitive to the existence - or non-existence - of dibaryonic resonances with any appreciable coupling to the elastic channel. Hence the acronym: Elastic Dibaryons Dead or Alive.

Both for phase shift analysis as such, and its use in identifying dibaryonic resonances, it is mandatory to measure not only spin-averaged cross sections, but also spin observables such as analyzing powers, spin correlation coefficients etc.. This requires a polarized COSY beam as well as a polarized EDDA target. A polarized ion source has been built and fitted [3] to the COSY injector cyclotron, and the developement of the-polarized COSY beam may commence. The polarized EDDA target is a polarized atomic beam device now under construction [4]. With reasonably achievable atomic beam densities in mind, EDDA was conceived as an experiment using the **internal (recirculating) COSY beam** to obtain sufficient luminosities. Spin-averaged cross sections are measured with a CH_2 fiber target [5]. Data collection proceeds **during synchroton acceleration** in a multi-pass technique, so that a full excitation function is measured in each accelerator cycle. Statistical accuracy is obtained by averaging over many cycles. Elastic pp events are identified by kinematic coincidence. The luminosity is monitored as a function of the COSY beam energy by means of the electrons knocked out of the target. An integral measurement of the secondary electron current is performed as well as detection of high energy δ-electrons emerging at 40° using PIN-diodes.

The EDDA detector [6] consists of two cylindrical double layers covering 30° to 150° in $\theta_{c.m.}$ for the elastic pp channel and some 85% of the full solid angle. The inner layers are composed of scintillating fibers which are helically wound in opposing directions. The outer layers consist of scintillator bars which are running parallel to the beam axis and are surrounded by scintillator semi-rings. The scintillator cross sections are designed so that each particle traversing the outer layer produces a signal in two neighbouring bars and rings. Analysis of the fractional light output may then be used to determine the angle, at which the particle traverses the outer layers, much more accurately (by a factor of 5) than would be possible on the basis of detector granularity alone. Combined with the spatial resolution of the 2.5 mm diameter scintillating fibers, this provides for vertex reconstruction to a precision of some very few millimeters.

Vertex reconstruction is essential, when a polarized atomic beam target is used. Unpolarized data can be taken with the outer detector layers alone, however, and measurements have begun in 1994. Fig. 1 illustrates the identification of elastic proton-proton events by kinematic coincidence. The events in the conspicuous peak (upper part of Fig. 1) show the kinematics of elastic proton-proton scattering, coplanarity with the beam and the characteristic combination of polar angles. Quasielastic background due to the carbon content of the CH_2 fiber target, on the other hand, results in a wide and rather structureless distribution (lower part of Fig. 2) that can be measured separately using a carbon fiber target and subtracted out.

In 1995, EDDA had two production runs and recorded some 35 million elastic pp events covering the entire COSY energy range. This constitutes the bulk of the unpolarized data to be taken. Detailed data analysis is now under way and expected to yield publishable results in the near future.

The analysis focusses on identifying the nature of events with more than two hits in the detector, and on determining beam position, beam width and direction during synchroton acceleration in order to apply proper angle corrections. For the latter purpose, the pp elastic events recorded were grouped into several bins in polar

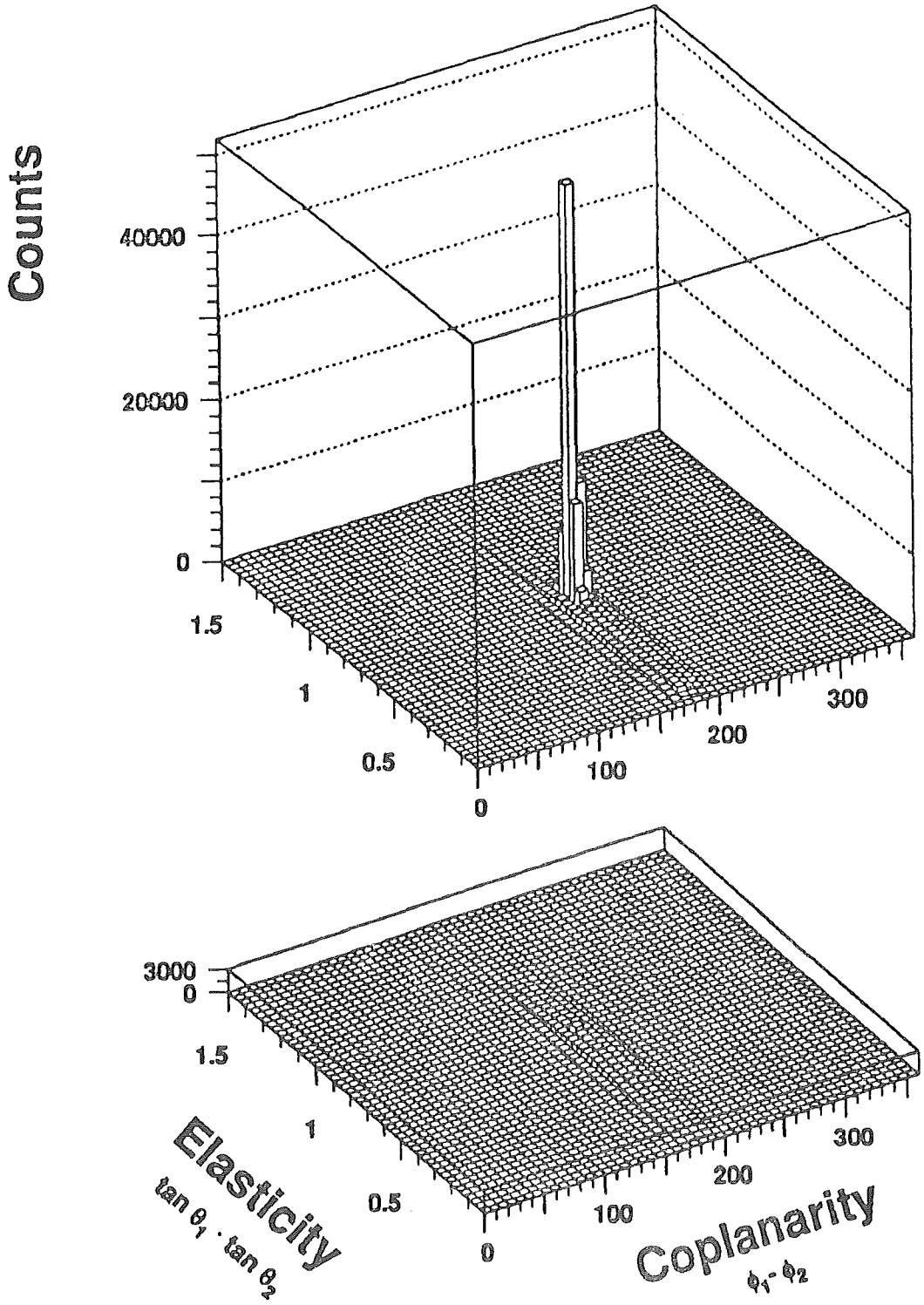

Fig. 1 Kinematic distribution of EDDA events as obtained with a CH_2 (upper part) and with a carbon (lower part) fiber target (T_p = 793 MeV)

and azimutal angle and their spacial distributions determined. These can be converted into beam position, beam width and beam direction as a function of beam energy (i.e. time within acceleration cycle), as displayed in Fig. 2. For calibration purposes, the beam was swept back and forth horizontally in the flat top, using steering magnets ("calibration bump").

The results shown in Fig. 2 are solely based on detector response, exploiting nothing but the coplanarity of two body events with the

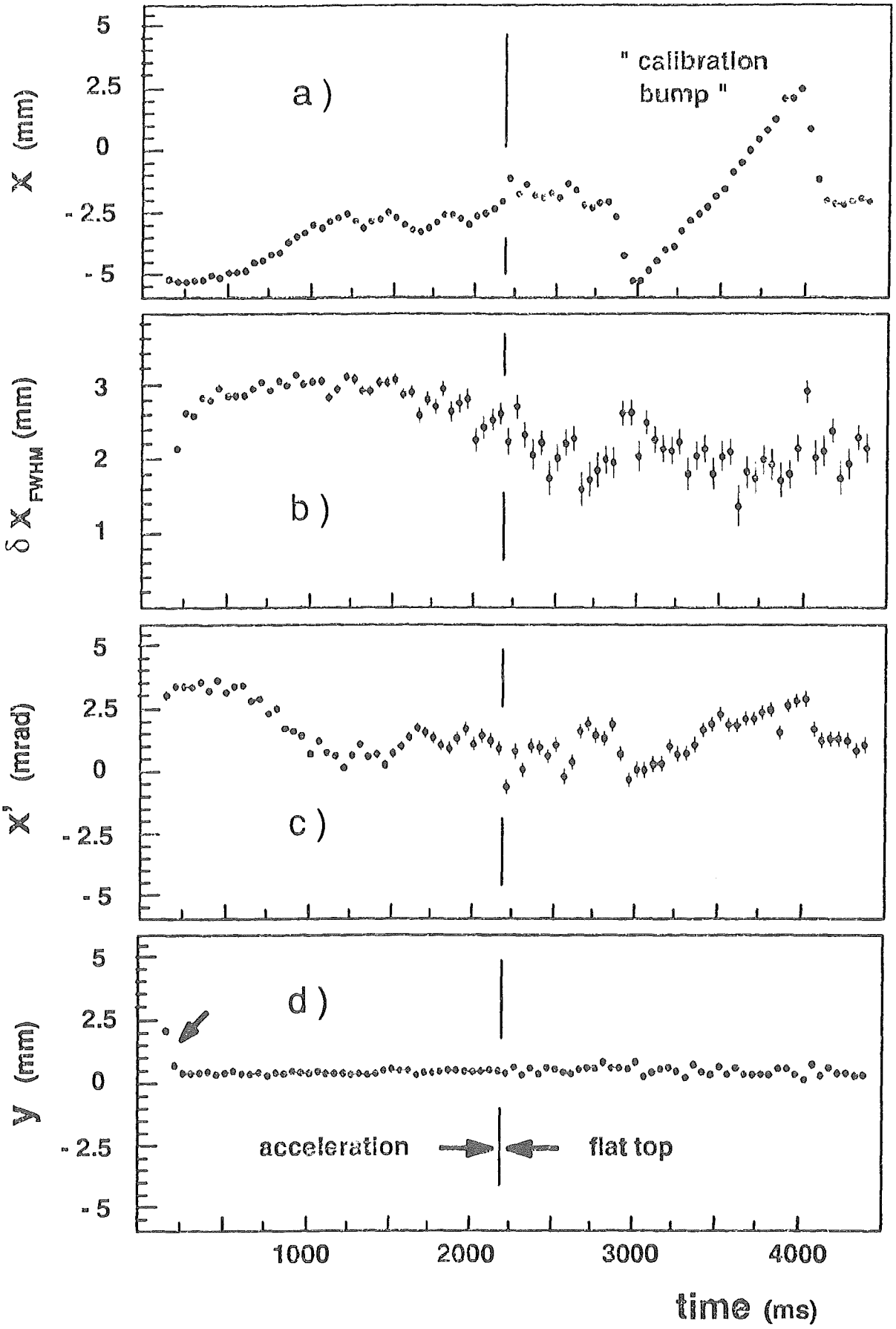

Fig. 2 Horizontal beam position (a), width (b) and direction (c) and vertical beam position (d) during acceleration and flat top as seen by the EDDA detector. The "calibration bump" was induced by steering magnets for calibration purposes.

beam. As seen in Fig. 2a, the COSY beam was slightly off axis (ca. 2 mm in this particular run) horizontally, and it moved no more than about 3 mm during acceleration. The "calibration bump" induced by steering magnets in the flat top is clearly visible. The beam direction changes by about 3 mrad during acceleration (Fig. 2c), correlated with the change in position, and the "calibration bump shows up as expected. This attests to a remarkable stability of the beam, which forms the basis for taking data during acceleration. In this context, the EDDA collaboration wishes to acknowledge the extraordinary support it has been receiving from the COSY team. The width of the (uncooled) beam starts out at ca. 2 mm, increases to about 3 mm upon insertion of the fiber target and remains constant (or decreases) thereafter. This shows that adiabatic cooling roughly compensates (even overcompensates) small angle scattering off the target, resulting in a much smaller loss of luminosity than would otherwise be expected. The vertical position of the interaction zone (Fig. 2d) is determined by the horizontally strung fiber target and should remain constant except for a short overshoot as the target is moved into the beam (see arrow). Its determination from detector data serves as a demonstration of the reliability of the method employed, rather than providing any new information.

EDDA has taken the bulk of the unpolarized data required. In 1996, the center of effort will be in preparing to measure spin observables, namely

- commissioning the inner detector layer,
- contruction of the polarized atomic beam target, and
- helping to develop the polarized beam for COSY.

[1] Supported by BMFT under contract 06 BN 664 I(6)

[2] The **EDDA** collaboration:
D. Albers[b], J. Bisplinghoff[a], R. Bollmann[b], K. Büsser[b], P. Cloth[c], R. Daniel[a], O. Diehl[a], F. Dohrmann[b], V. Drüke[c], H.P. Engelhardt[a], J. Ernst[a], P.D. Eversheim[a], D. Filges[c], M. Gasthuber[b], R. Gebel[a], J. Greiff[b], A. Groß[b], R. Gross-Hardt[a], S. Heider[a], A. Heine[a], F. Hinterberger[a], M. Igelbrink[b], R. Jahn[a], M. Jeske[a], R. Langkau[b], J. Lindlein[b], R. Maier[c], R. Maschuw[a], T. Mayer-Kuckuk[a], G. Mertler[a], B. Metsch[e], F. Mosel[a], M. Müller[b], M. Münstermann[b], H. Petry[e] D. Prasuhn[c], H. Rohdjeß[a], D. Rosendaal[a], U. Roß[a], P. von Rossen[c], H. Scheid[a], H. Paetz gen. Schieck[d], N. Schirm[b], M. Schulz-Rojahn[a], F. Schwandt[a], V. Schwarz[a], W. Scobel[b], G. Sterzenbach[c], B. Steeg[b], H.J. Trelle[a], A. Wellinghausen[b], W. Wiedmann[a], K. Woller[b], R. Ziegler[a]

[a] Institut f. Strahlen- und Kernphysik, Universität **Bonn**
[b] I. Institut für Experimentalphysik, Universität **Hamburg**
[c] Institut für Kernphysik, Forschungszentrum **Jülich**
[d] Institut für Kernphysik, Universität **Köln**
[e] Institut f. Theoretische Kernphysik, Universität **Bonn**

[3] D. Eversheim, AIP Conf. Proc. **293**, Am. Inst. of Phys., 1993, p. 92

[4] D. Eversheim, this report

[5] F. Mosel, PhD thesis, Universität Bonn, December 1994
F. Mosel et al., Research Report 1993, ISKP, Universität Bonn, p. 107

[6] AIP Conf. Proc. **221**, Am. Inst. of Phys, 1990, p. 312
Physica Scripta **48** (1993) 92
Nucl. Instr. Meth **A329** (1993) 151
Nucl. Instr. Meth. **A335** (1993) 113

[7] F. Schwandt, PhD thesis, Universität Bonn, submitted January 1995
F. Schwandt et al., Research Report 1993, ISKP Universität Bonn, p. 108

[8] A.J. Simon et al., Phys. Rev. **C48** (1993) 662
D.T. Williams et al., Nuovo Cimento **8A** (1972) 447

First Measurements of the p+p→p+p+η' Reaction near Threshold

COSY-11 Collaboration

The η and η' mesons are composed of the $u\bar{u}$, $d\bar{d}$ and $s\bar{s}$ quarks. They differ only in the content of the $s\bar{s}$ quark pair. A few MeV above the threshold the cross section for the p+p→p+p+η reaction, is in the order of 1 μb see [1]. Till now there are no data concerning the production of the η' meson in proton-proton collision. There exists only estimation [2] according to which the cross section for the p+p→p+p+η' reaction is about two or three orders of magnitude smaller than the one for η production.

In October this year we performed two measurements with beam energy of 4 MeV/c above and 3 MeV/c below the reaction threshold. In both cases the experiment last about 40 hours. The estimated luminosity was about $5 \cdot 10^{29} cm^{-2} s^{-1}$.

Our detection system [3] allow us to measure the velocity and momentum of each positively charged particle. Having momentum and velocity we can calculate the registered particle mass. Thus we can choose all events with two protons in the exit channel. As η is a neutral particle and is not registered by the COSY-11 system we identify it by means of the missing mass method. In the preliminary analysis we obtained missing mass spectra for above and below threshold measurement which are shown in figure 1 and figure 2 respectively. These spectra are still not normalized to the elastic scattering. However taking into account that the time of the measurements were equal in both cases and assuming that the changes in flux were not larger than a factor of 2, we can conclude that during this first trial at least fifty events were observed which are due to the production of η' meson.

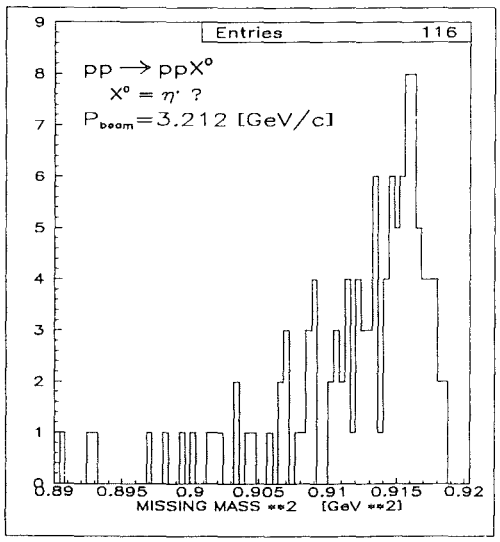

Figure 1: Missing mass of the unobserved particle in the p+p→p+p+X° reaction at a beam momentum of 3.212 GeV/c, 4 MeV/c above threshold.

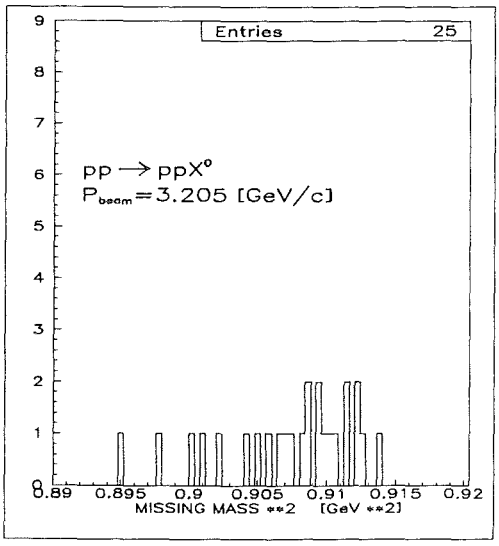

Figure 2: Missing mass of the unobserved particle in the p+p→p+p+X° reaction at a beam momentum of 3.205 GeV/c, 3 MeV/c below threshold.

References:

[1] U. Schuberth, The Reaction pp→ppη Close to Threshold, Ph.D. Thesis, Uppsala 1995

[2] Y. Le Bornec, The interactions of heavy mesons with nuclei, IPNO-DRE 90.07

[3] A. Budzanowski et al., COSY-11 Detector Arrangement Report KFA-IKP(I)-1991

First Measurements on $pp \to ppK^+K^-$ at Threshold

COSY-11 Collaboration

A study of the reaction $pp \to ppK^+K^-$ is especially motivated by the discussion on the nature of the scalar mesons $f_o(975)$ and $a_o(980)$. Existing data lead to differing interpretations: A two-quark two-antiquark state, a simple $s\bar{s}$ structure, and a $K\bar{K}$ molecule structure as well are suggested in case of the f_o [1-6].

With no data being available up to few GeV excess energy, data of high precision and sufficiently large statistics are needed especially in the threshold region.

In addition, threshold experiments generally result in vanishing relative momenta of the reaction products. Thus, final state interaction should be observable for the two-proton, proton-kaon and two-kaon systems in near threshold K^+K^- production.

In October 1995 first data on the reaction $pp \to ppK^+K^-$ have been taken at the COSY-11 installation with beam momenta of 3.305 GeV/c and 3.308 GeV/c (threshold beam momentum p_{beam}^{thresh} = 3.3016 GeV/c), corresponding to excess energies of 1 MeV and 2 MeV, respectively. Using new beam optics (see separate contribution "The COSY-11 Optics" to this report) an estimated luminosity of $\approx 8 \cdot 10^{29} cm^{-2} s^{-1}$ has been reached during these measurements.

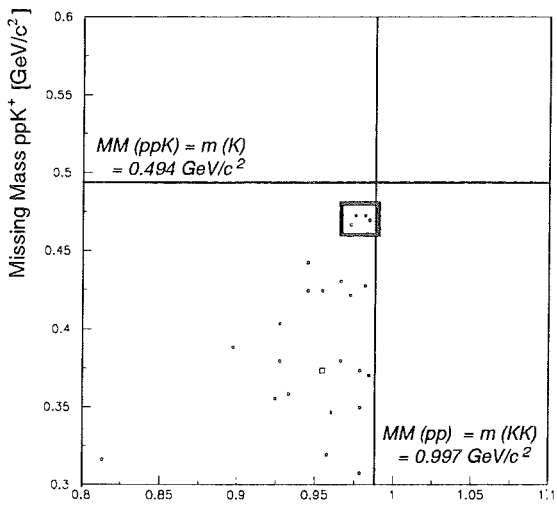

Figure 1: Reconstructed missing mass in the (ppK)-system as a function of the missing mass in the (pp)-system obtained from three track events.

Although the analysis of these data is being continued, first encouraging signals can already be presented.

Besides the reconstruction of the four-momenta of both protons in the exit channel of the $pp \to ppK^+K^-$ reaction, the COSY-11 detection system allows for a detection of both charged kaons, with reduced acceptance due to the limiting gap of the analyzing COSY dipole (for a general description of the detection system and the experimental technique in more detail see [7,8]).

Figure 1 shows a preliminary result of a four hour run at 3.308 GeV/c beam momentum out of a total of about 150 hours beam time: Only events with three reconstructed tracks crossing the start and stop scintillators S1 and S3 within wide areas limited by Monte Carlo simulations and corresponding to invariant masses of two protons and one kaon, respectively, are accepted. A group of four events close to the expected missing masses in the two subsystems are chosen to be candidates for a ppK^+K^- final state. The reconstructed tracks from one of those four candidates are shown in fig. 2, indicating the corresponding hits in the drift chamber systems D1 and D2 as well as in the scintillation counters S1, S2 and S3.

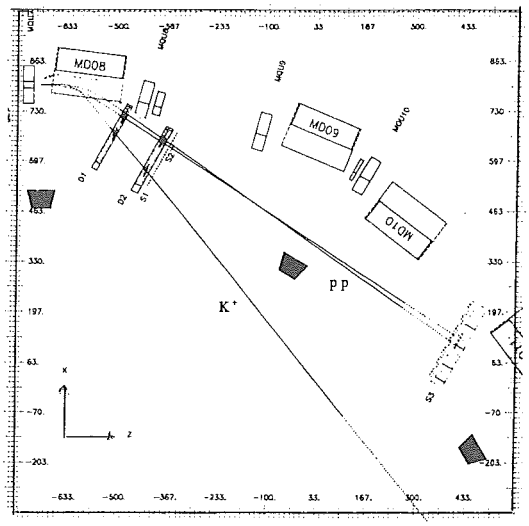

Figure 2: Schematic view of the COSY-11 detection system with reconstructed tracks of two protons and a positively charged kaon.

Further analysis of these data, including the determination of absolute cross section values, will go on in preparation for a second beam time on $pp \to ppK^+K^-$ planned in early 1996.

References:

[1] R. Jaffe, Phys. Rev. D15 (1977) 267
[2] K. Au et al., Phys. Lett. 167B (1986) 229
[3] D. Lohse, J.W. Durso, K. Holinde, J. Speth, Phys. Lett. 234B (1990) 2236
[4] J. Weinstein, N. Isgur, Phys. Rev. D41 (1990) 2236
[5] D. Morgan, M.R. Pennington, Phys. Lett. 258B (1991) 444
[6] R.J. Apsimon et al., OMEGA Photon Collaboration, CERN-PPED/92-135
[7] J. Balewski et al., Annual Report IKP-KFA 1994 (1995) 40
[8] J. Balewski et al., Report KFA-IKP(I)-1995-1

Production of η Mesons at the COSY-11 Installation

COSY-11 Collaboration

Measurements of the pp→ppη reactions were performed at beam momenta of 1.993 GeV/c and 1.981 GeV/cc (i.e.: 11 MeV/c above and 2 MeV/c below the threshold). The details of the COSY-11 experimental setup are described in [1]. Events with two reconstructed tracks were analyzed. The following conditions were required for each of the tracks:

- it has to cross the start and stop scintillators in the area determined by means of the Monte-Carlo simulation (plus a reserve of 50 %).
- the invariant mass of detected particles $m^2 = p^2(1/\beta^2-1)$ has to be the proton mass, where the momentum P was determined from deflection in the magnetic field, while ist velocity β was extracted from time of flight.

Spectra of the square of the missing mass are shown in Fig. 1a,b for both beam momenta. The mean value mass of the η peak is 548 MeV compared to the η mass of 547.45 MeV and the experimental width is about 2 MeV FWHM.

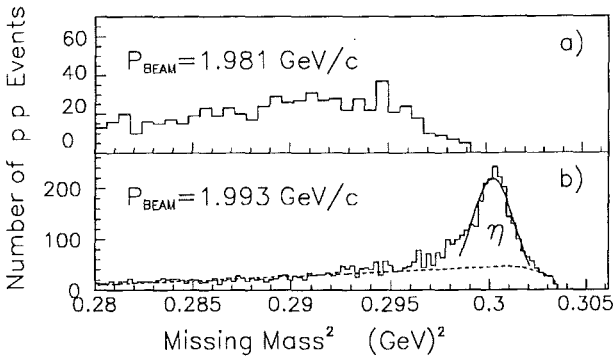

Figure 1: Spectra of the square of the missing mass for beam momentum of 1.993 (a) and 1.981 GeV/c (b).

In order to evaluate an absolute value of the cross section the acceptance and the luminosity have to be calculated. The acceptance was determined by means of Monte-Carlo simulations. The integrated luminosity was calculated from normalization of simultaneously measured p-p elastic scattering to existing data [2].

The obtained value for the cross section of the pp→ppη reaction (Fig. 2) is equal to 0.77 μb with following errors: statistical: 3 %, luminosity: 6 %, background subtraction: 17 % and acceptance determination: 10 %. The results agree well with existing measurements from other groups.

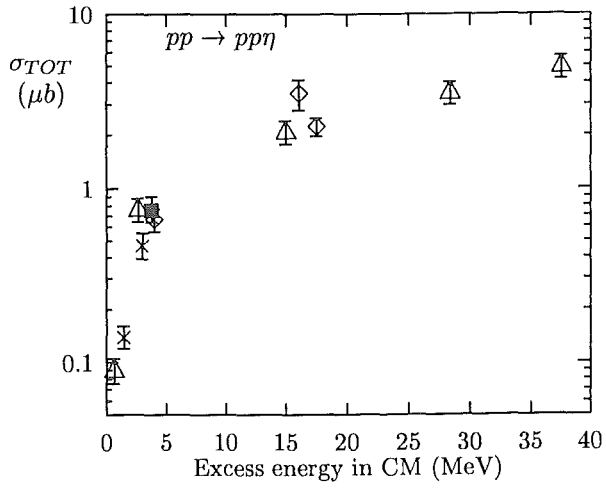

Figure 2: Cross section for pp→ppη reaction. The COSY-11 point (■), is consistent with results of Calén (Δ) [3], Chiavassa (x) [4] and Bergdolt (<>) [5].

References:

[1] S. Brauksiepe et al., KFA-IKP(I)-1995-1, and to be published in NIM.

[2] Williams et al., Nuovo Cimiento A8 (1972) 447; B.B. Brabson et al., Phys. Rev. Lett. 23 (1969) 1306; Kammerund et al., Phys. Rev. D4 (1971) 1309.

[3] H. Calén et al., ISV/TSL-9-0121, Uppsala University 1995.

[4] E. Chiavassa et al., Phys. Lett. B322 (1994) 270.

[5] A.M. Bergdolt et al., Phys. Rev. D48 (1993) R2969.

$\pi^+\pi^-$ Meson Production at the COSY-11 Installation

A. Khoukaz[1] for the COSY-11 Collaboration

The COSY-11 installation is an internal experiment, which has been designed for full geometrical acceptance for meson production studies close to threshold, especially in the 1 GeV/c^2 mass range. The main goal of this experiment is to study effects of final state interactions in meson-meson and meson-baryon systems.

The Münster cluster target [1,2] has been installed in front of a normal C-type COSY bending magnet at the internal target location TP3. Due to their lower momenta, positively charged reaction products are separated from the circulating beam by the magnetic field. Passing through a specially developed large thin exit foil of the vacuum chamber the ejectiles reach the detection system operated at normal atmosphere.

Two stacks of six and eight drift chamber planes, respectively (DC1 and DC2), are used to measure the direction of the protons. With the known strength of the dipol field, a reconstruction of their particles's momentum vector is possible.

An arrangement of two scintillation hodoscopes (S1,S2) is used to detect two separate protons in the exit channel. In combination with the scintillation wall S3 (Amadeus), separated by a distance of 9.1 m, this detector system works as a time-of-flight system for the protons. In addition, the π^+ mesons can be detected by scintillator modules and the drift chamber system.

The π^- mesons, with their tracks being bent towards the inside of the dipole gap, are detected by an array of silicon pad detectors and an additional scintillation counter.

From previous experiments data of cross sections for the reaction $pp \rightarrow pp\pi^+\pi^-$ (threshold: p_{beam} = 1218.7 MeV/c) are available down to beam momenta of about 1.379 GeV/c [3-5], thus experimental data for the first 160 MeV/c above threshold are still missing. Therefore this reaction was examined close to threshold at beam momenta of 1.222 GeV/c and 1.224 GeV/c, i.e. 3.3 MeV/c and 5.3 MeV/c above threshold. The reaction is identified by the following conditions:

- only events with two reconstructed tracks are accepted
- each track must pass an area of the S1- and S3-detector (plus reserve of 50 %) determined the by means of Monte-Carlo simulation
- an additional hit of either the π^+ or the π^- must be detected
- the time difference between the two hits in the S1/S2-detector must be in a kinematically permitted range.

By this selection less than 50 events survived from a number of more than 14 million taken at p_{beam} = 1.224 GeV/c.
First very preliminary estimation of the total cross section lead to a value of less than 100nb at a beam momentum of 1.224 GeV/c. The analysis of the data is still in progress.

[1] University of Münster

References:

[1] Annual Report 1992/93, Institut für Kernphysik, Universität Münster
[2] see this annual report
[3 L. Dakhno et al., Sov.J.Nucl.Phys. 37(4), April 1983
[4] D. Cochran et al., Phys.Rev.D, Vol.6, Number 11, 1972
[5] F. Shimizu et al., Nucl.Phys., A386, 1982

The COSY-11 Beam Optics

COSY-11 Collaboration

The special feature of COSY is high flexibility in adjusting the tune and choosing optimized beam conditions for each experiment [1].

The specific requirement of COSY-11 with its target point in one of the arcs is amongst a high luminosity a small diameter of the interaction zone, because in particular an uncertainty of the point of interaction in the horizontal plane leads to an increase of the width of the reconstructed mass spectrum [2].

The beam dimensions horizontaly and verticaly are given by the standard deviations:

$\sigma_x(s) = \sqrt{\varepsilon \cdot \beta_x(s) + D_s^2 \cdot (\Delta p/p_o)^2}$ and $\sigma_y(s) = \sqrt{\varepsilon \cdot \beta_y(s)}$.

Notice that at present (without any cooling) at 3.3 GeV/c beam momentum $\varepsilon \approx 1.7$ mm mrad and the momentum $\delta = (\Delta p/p_o) = 0.7 \cdot 10^{-3}$. Thus with standard values at the target point in the arc of $\beta_x \approx 10$ m and $D_x \geq 10$ m the enlargement of the beam diameter in the horizontal plane is mainly caused by the dispersion.

In the calculated „COSY-11 optics" it was attained to constrain the horizontal beam dimension to the width of the cluster target (actual 9 mm) by minimizing the dispersion at the target point (fig. 1, tab. 1).

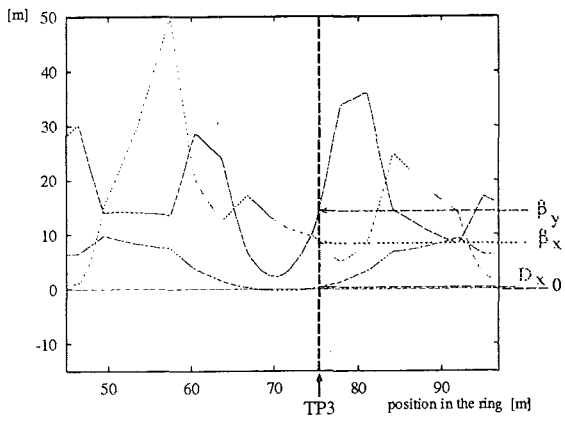

Figure 1: The optical functions of the COSY-11 optics at the target point TP3.

Table 1: The values for the COSY-optics representing the required optics. The finally installed optics has got a horizontal tune of $Q_z = 3.65$ staying underneath the 2/3-resonance.

optics	beam parameters at flat top							
	β_x[m]	β_y[m]	D_x[m]	σ_x[mm]	σ_y[mm]	Q_x	Q_y	γ_{trans}
standard	11.0	10.8	16.9	12.6	4.3	3.57	3.58	-13.9
COSY-11	8.5	14.4	0.2	3.8	4.9	3.68	3.53	2.4

For the calculations the program MAD (Methodical Accelerator Design) was used [3].

Due to the symmetry of COSY the three families of focusing quadrupoles in the arcs are varied to different values, the three defocusing families are varied in the same manner (tab. 2).

Table 2: Quadrupole currents at flat top [A] (at 3.205 GeV) representing the focussing strength.

optics	quadrupole currents [A]			
	Qu1/Qu5	Qu2/Qu6	Qu3	Q4
standard	-183.8	216.4	-214.8	344.2
COSY-11	-199.9	308.5	-199.9	179.1

The tune of the calculated COSY-11 optics is only slightly shifted with respect to the „standard optics".
As the measurements of COSY-11 are performed only during the flat top, it is possible to get to the new optic by varying the quadrupole strength in the flat top. Hence injection and acceleration take place with the well known standard optics always moving $\gamma_{trans.}$ forward. Since the COSY-11 optics has a $\gamma_{trans.}$, which is too low for the required beam momentum of 3.3 GeV/c, the beam has to be debunched before changing the optics (fig. 2).

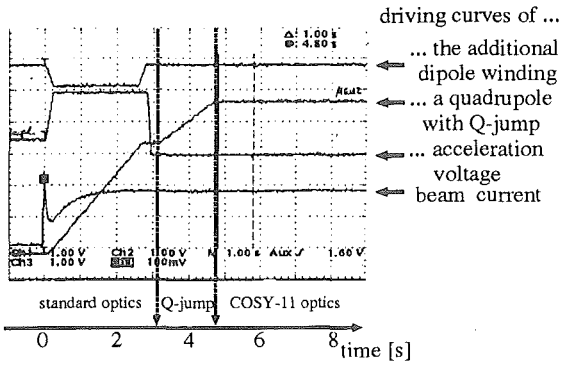

Figure 2: COSY cyclus. The change of the optics takes place after switching off the acceleration voltage.

In the threshold production of the η'(3208 GeV/c) and the K^+K^- (3302 GeV/c) as well the COSY-11 optics has been successfully used already.

References:

[1] R. Maier et al., EPAC 94, Proc. of the Conf. (1994) 165
[2] M. Sokolowski and J. Zejma, Inst. of Physics, Jagellonian Univ., Report 3, Jan. 22, 1991, Crakow
[3] H. Grote and F. Chr. Iselin, The MAD Program Version 8.10, User's References Manual, Geneva, Switzerland, Jan. 19, 1993

Development and Construction of a Luminosity Monitor for COSY-11

H. Dombrowski[1], A. Khoukaz[1], T. Lister[1], C. Quentmeier[1], R. Santo[1]

The internal COSY-11 experiment at COSY is devoted to the study of meson production in pp reactions near threshold. Since absolute cross sections have to be measured, a precise knowledge of the overall luminosity is indispensible; for this reason a specially suited monitor shall be used. The method used will be the measurement of the number and direction of the elastic scattered protons as close to the interaction point as possible. Thus, two detectors will be installed directly above and below the beampipe with their closest sensitive volume 6cm in horizontal and 7cm in vertical direction apart from the interaction point. The available space is limited to a 3cm high gap between the beampipe and the dipole coil. The detectors have to provide a good spatial resolution and high counting rate capability. It turned out that the simplest detectors to fulfill these conditions are multi wire chambers (MWCs). Therefore two of such chambers have been developed and constructed in Münster, following a design from previous studies [1,2]. The chambers are of single stage type and use delay line readout. The sensitive planes have a size of 11cm x 11cm and a position resolution which is better than 1.5mm in each direction. Scintillators on top and on bottom of each chamber will serve as trigger detectors. Due to the high position resolution the MWCs they can also be used for the reconstruction of the interaction zone. This is important to optimize overlap of the beam and the cluster target.

The construction of the chambers is nearly finished and first tests have been made. Installation on the COSY-11 experimental site and efficiency and position resolution tests are foreseen in late spring 1996.

[1] University of Münster, Germany

References:

[1] Petra Nettebrock, Diplomarbeit, Münster, April 1991

[2] Frauke Deusch, Staatsexamensarbeit, Münster, August 1992

The Internal Cluster Target of COSY

H. Dombrowski[1], D. Grzonka, W. Hamsink[1], A. Khoukaz[1], T. Lister[1], R. Santo[1]

In spring of 1995 the Münster cluster target [1] was installed at the COSY ring at the target position TP3, where the COSY 11 experiment is located. The construction of the vacuum chambers of the target device is designed to meet the ultra high vacuum condititions of the scattering chamber and is adapted to the present spacial requirements - i.e. the apparatus had to be fit into a 30 cm wide gap between two magnets. As consisting of hydrogen clusters the target combines the advantages of both a high target density (currently $5 \cdot 10^{13}$ atoms/cm^2) and a low pressure in the scattering chamber (the design value of ~ 10^{-8} mbar is expected to be reached). The target is extremly pure and its geometrical extensions and areal density can be varied in a certain range.

In high vacuum chambers cluster beams are able to pass through meters with a high density, whose distribution is homogeneous within the beam boundaries. Cluster beams consist of molecular formations growing in a supersonic nozzle beam as a consequence of the adiabatic cooling of the gas. To pre-cool the gas below 50 K the nozzle is mounted on a cold head. The cluster beam is peeled off the atomic beam by a skimmer and travels through the vacuum system as a jet with a small angular divergence (< 1°): It traverses two collimators, crosses the scattering chamber and reaches the three-stage beam catcher. Since the highest gas loads are present at the origin and at the final point of impact of the cluser beam, the vacuum system is differentially pumped parallel to the beam from both sides towards the scattering chamber to reach the lowest possible pressure at that very place.

In fig. 1 the setup with the especially constructed cryopumps are shown. They combine vacuum chamber and pump in a very compact arrangement. A hole in the middle of each cone shaped cold surface allowes the cluster beam to pass through. A VME system is used to control pumps, shutters and other components of the device by means of an IEEE-bus system. The software is implemented on the crate utilizing the operating system OS9. Alternatively, manual operation by a switchboard is possible.

Since April 1995 the cluster target has been successfully used during four beamtime periods with a total operation time of about 40 days with continuous operation periods of 14 days.

[1] University of Münster

Reference:
[1] D. Grzonka, W. Oelert, KFA-IKP(I)-1993-1

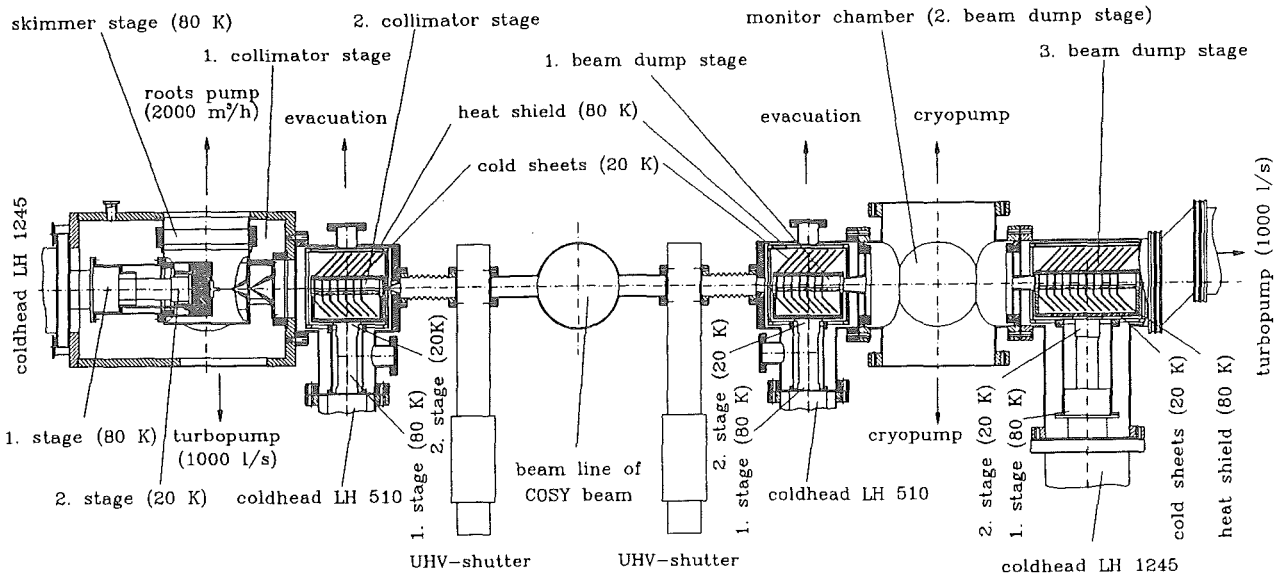

Figure 1: Central vacuum chambers of the cluster target device.

Drift Chambers with Double Sense Wires for the COSY-11 Facility

COSY-11-Collaboration

In view of planned investigation of the dibaryon resonance d' it is necessary to extend the Cosy-11 [1] detection system with additional position sensitive detector, which would allow to measure trajectories of positively charged pions from the applied reaction pp→d' π^+.

For this purpose two drift chambers have been built at the Institute of Physics of the Jagellonian University. The chambers are of graded field type with a cell structure shown in fig.1. The cell geometry is the same as in the existing chambers installed at the Cosy-11 facility [2]. The only difference is connected with the application of two closely spaced sense wires instead of one.

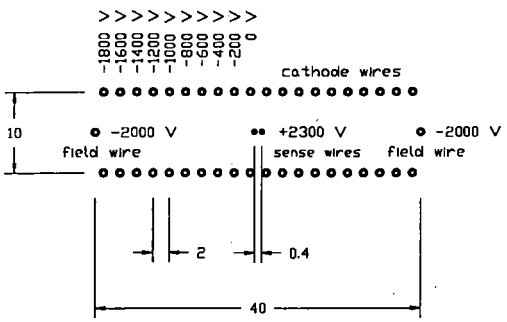

Figure 1: Structure of a drift cell

This feature allows to resolve the left--right ambiguity without using additional detection planes and thus allows to reduce the detector thickness. The spacing of sense wires in each pair is 0.4 mm. They are bound together every 12 cm length with small droplets of Araldite in order to compensate for the electric repulsion between them. Each of two chambers consists of two detection planes with horizontal wires and two planes with vertical ones. The sense area of the chambers is 32x32 cm^2

The chambers were tested during the October 95 run at the Cosy-11 facility using scattered protons and pions with momenta of about 1 GeV/c. For the chambers we used Argon-Ethane 50:50 mixture with a small addition of ethanol as a quencher. The voltages were as those indicated in fig.1. Tests have confirmed usefulness of sense wire pairs for resolving the left-right ambiguity. In 99 % of events only one sense wire in a detection plane was responding allowing for a unique determination of a particle track coordinate. A drift time spectrum for these events is shown in fig.2a.

The width of the drift time distribution is 400 ns what corresponds to the half width of the drift cell being equal to 20 mm. Only in 1 % of events two sense wires in a detection plane were responding.The drift time spectrum for such events is shown in fig.2b.

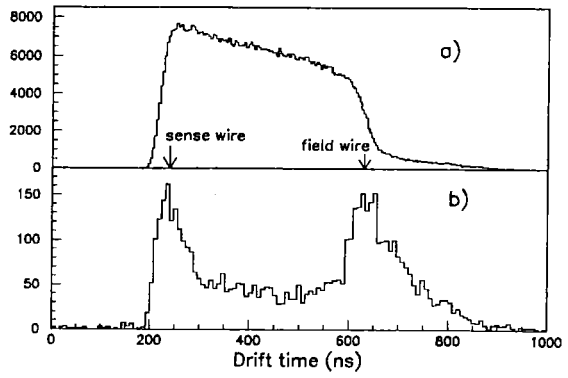

Figure 2: Drift time spectra for events when one sense wire in a detection plane fired (a), and two wires fired (b).

Counts in the spectrum are grouped in two peaks with positions corresponding to the vicinity of the sense wires and the field wires. In the first case two sense wires in the same cell, whereas, in the second case two sense wires in two adjacent cells fired.

References:

[1] S.Brauksiepe et al., KFA-IKP(I)-1995-1, and to be published in NIM.

[2] B. Gugulski et al., KFA-Internal Report, KFA-IKP(I)-1992-3.

Test measurements for the experiment COSY-13

T. Hermes, K. Pysz, Y. Uozumi, H. Ohm and the COSY-13 collaboration

The experiment COSY-13 which is aiming at production and measurement of the decay of heavy Λ hypernuclei has been completed and was run for the first time.

The beam pipe belonging to the experiment, the vacuum vessel with the low-pressure MWPCs for the detection of fragments from the Λ-induced fission, the target manipulator and the target magazine were installed. The computer control of the vacuum system was incorporated into the COSY control system. The software for on-line data acquisition and off-line analysis has been completed.

Fission fragments from a Cf-252 source were used to test track reconstruction, see Fig. 1a). With a strong Sr-90 source the sensitivity of the detectors for the expected high background rate of minimal ionizing particles was measured. In a total counting time of 10 hours 12 events were recorded out of which only 2 could be traced back to a ± 15 mm wide region around the source, see Fig. 1b). With the cut in the direction perpendicular to Fig. 1 no event remains in the background. Correspondingly, the sensitivity for ß-particles is $< 2\times10^{-11}$.

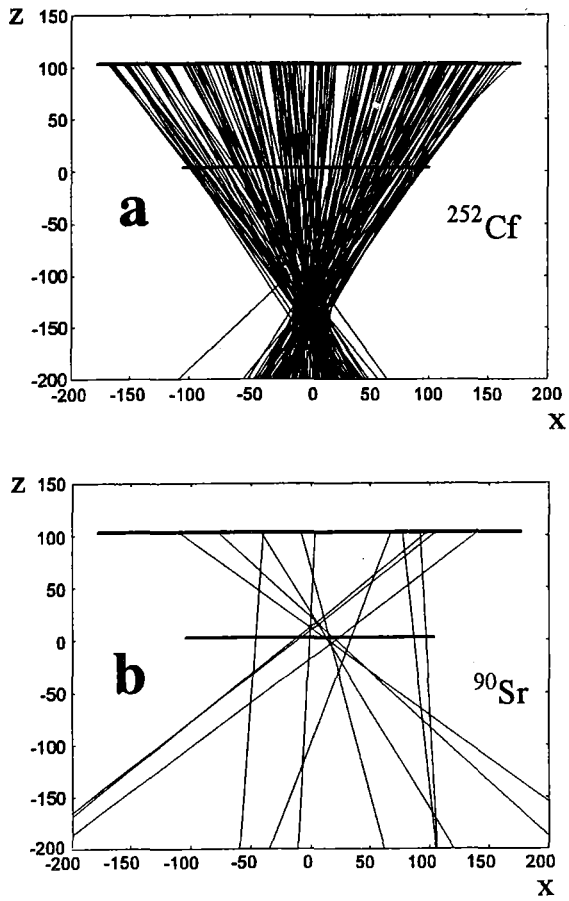

Fig. 1: a) Reconstructed tracks of fission events from Cf-252. Almost all of the events can be traced back to the source area. The counting time was 10 minutes.
b) Tracks measured in the presence of a strong Sr-90 source in the absence of Cf-252. In a counting time of 10 hours only few events were recorded which can be rejected with track reconstruction and appropriate cuts.

The size of the beam at injection energy was measured by scanning it with the COSY-13 target which consisted of a strip of 20 μg/cm² carbon covered at the lower end with a spot of 3 x 3 mm² with 10 μg/cm² U-238. The standard COSY setting resulted in a total vertical beam size of $2y_0$ = 34 mm which is unfavourable for the recoil shadow technique to be applied in the experiment. It was found out that a different working point of COSY gave a considerable improvement with y_0 = 3 mm, see Fig. 2.

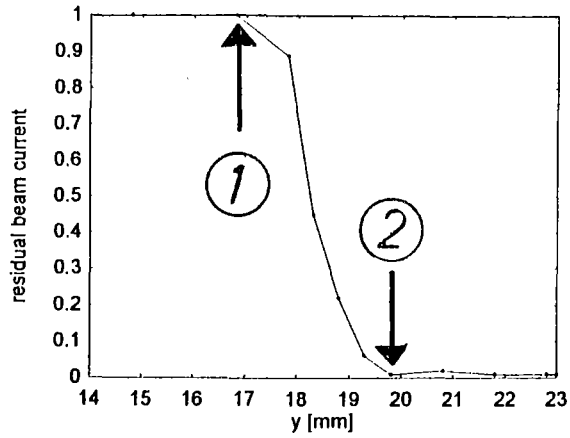

Fig. 2: The residual beam current as a function of the vertical target position. Arrows indicate the outer limit (1) and the center (2) of the beam.

In a first beam time aiming at a test of all functions of the equipment measurements were performed at 1.5 GeV where already a reasonable cross section for the production of hypernuclei is expected. In addition, background measurements were done at 1.0 GeV since here the cross section for strangeness production is expected to be low. The target was positioned above the beam so that during injection it was not hit by beam particles. After acceleration the beam was bumped onto to target using steerer magnets of COSY, see Fig. 3. At first a fast ramp was applied until the beam reached the lower end of the target. Then a slow ramp shifted the beam across the target so as to avoid high instantaneous rates.

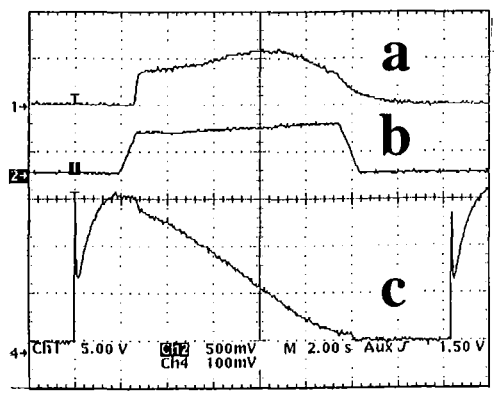

Fig. 3: Bumping of the beam onto the target: a) fission-fragment counting rate; b) current applied to steerer magnets; c) beam current in COSY as measured with a beam-current transformer.

It is crucial for the intended kind of recoil shadow measurement to have a target which is sufficiently planar and does not change its shape upon irradiation. We paid attention to this point by monitoring the target with a TV camera. Furthermore, the target shape is reflected in the two-dimensional position spectra of fission fragments detected in the recoil shadow counters.

The target was placed horizontally slightly upstream of a position where it is coplanar with the edge of the diaphragm shielding the MWPC in the forward direction completely. In this way it is made sure that the shadow edge including part of the prompt fission fragment distribution is measured for normalization. Fig. 4 shows a position sprectrum of fission fragments along the coordinate parallel to the beam measured with a beam energy of 1.0 GeV. There is almost no background in the shadow region which would interfere with events from the fission of hypernuclei. Furthermore, it can be seen that the shadow edge is fairly sharp. Its width is equivalent to an uncertainty of the target position and target planarity of about 0.2 mm which is sufficient for the applied shadow technique.

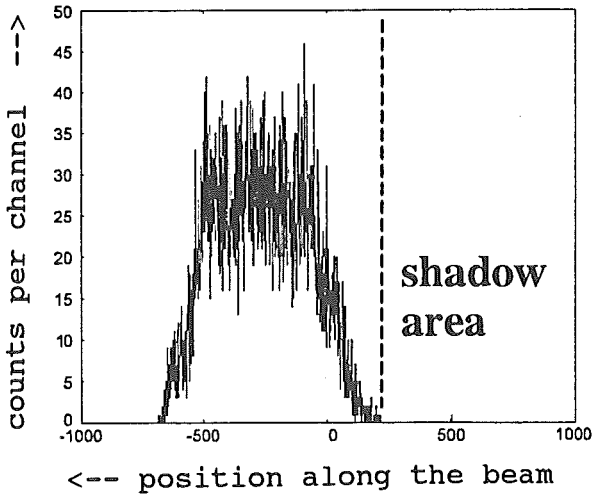

Fig. 4: Position spectrum of prompt fission fragments along the beam direction. The boundaries of the distribution are the edge of the diaphragm below the detector (left) and the shadow edge right above the target.

References:

1. T. Hermes et al., Annual Report 1993, KFA-IKP, 1994, p.65

The „GEANT" Simulation of the „COSY-13" Experiment of the Production of Heavy Λ-Hypernuclei in Proton-^{238}U Collisions

P. Kulessa[a], Z. Rudy[a], T. Hermes, L. Jarczyk[a], B. Kamys[a], H. Ohm, K. Pysz[a], O.W.B. Schult, A. Strzalkowski[a]

The COSY-13 experiment is devoted for measurements of cross sections for the production of heavy-hypernuclei in proton-nucleus collisions and for determination of the time of life of the Λ-hyperon in very heavy nuclei. The idea of the experiment is based on the „recoil-shadow method" which was applied by Polikanov and collaborators[1)] for measurements of the time of life of heavy hypernuclei produced in the annihilation of antiprotons on Bi and U targets.

Heavy hypernuclei which orginate from proton-nucleus reactions may undergo prompt fission, which takes place in very short time (10^{-19} - 10^{-15} s), or delayed fission, which is induced by the decay of the hyperon in the hypernucleus. The latter process occurs after much longer time which is expected to be of order of the free hyperon time of life i.e. 10^{-10} s. Prompt fission happens inside the target since the average velocity of heavy hypernuclei produced by proton-nucleus collisions is rather small (v/c for a proton energy of 1.5 GeV is typically of the order of 0.004[2)]). The delayed fission, on the contrary, occurs mainly outside of the target, at distances which depend on the time of life of the hyperon in the hypernucleus and on the velocity of the hypernucleus. The typical distance from the target where fission of heavy hypernuclei emerging from proton-nucleus collisions at 1.5 GeV takes place is ~ 0.3 mm[2)]. It is thus possible to determine the time of life of the hyperon by measuring the distance from the target at which delayed fission occurs.

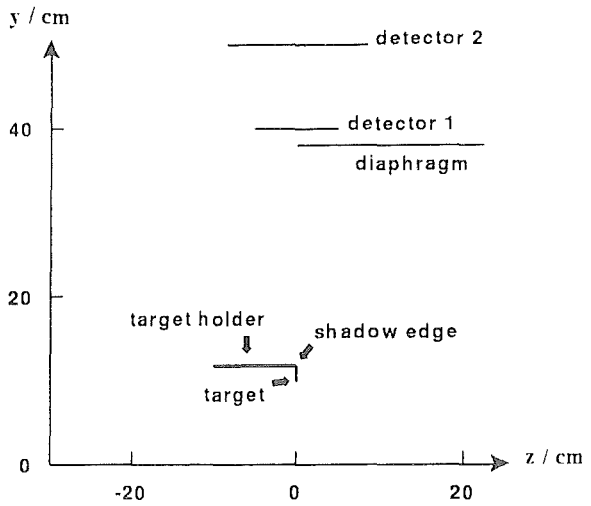

Fig. 1: Projection of the schematic experimental setup on y-z plane. z - axis of the beam, y - vertical axis. The geometrical dimensions of the target are: in x direction - 3 mm, in y direction - 3 mm. The distance between shadow edge and the target is 14 mm. Active surface of detector 1 has length 100 mm in z direction and length 200 mm in x direction.

This may be realized by putting position sensitive detectors (sensitive to fission fragments but not to light particles) in a plane parallel to the beam axis, at a suitable distance from the target, and by locating a diaphragm near these detectors and another one defining the shadow edge closely to the target. The distance of the shadow-edge from the target is crucial for the accuracy of the measurement. The shadow-edge and diaphragm properly adjusted does not allow prompt fission fragments to fly directly from the target to the shadowed part of the detector. Thus only those fragments which originate from the fission downstream of the target, i.e. delayed fission fragments, are able to hit the shadowed area of the detector.

The scheme of the apparatus used in the COSY-13 experiment is shown in the Fig. 1 in projection: The figure presents the plane perpendicular to the target and perpendicular to the planes of two position sensitive detectors. Target holder simultaneously plays a role of the shadow-edge-diaphragm.

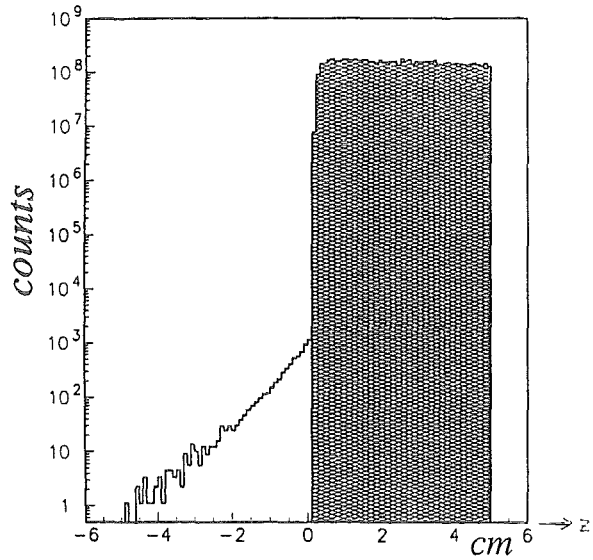

Fig. 2: GEANT simulation - the joint distribution of hits in the detector system of fission fragments from prompt fission of nuclei as well as from delayed fission of hypernuclei along the z direction. The time of life for hypernuclei is assumed to be $t = 2.6 \times 10^{-10}$ s.

The distribution of hits of fission fragments along the z-direction of the detector obtained in the simulation by means of the GEANT program[3)] is shown in the Fig. 2. Physical input for the simulation was taken from the theoretical analysis of the production of hypernuclei in proton-uranium collisions[2)]. It was assumed that the time of life of the hyperon in the hypernucleus is equal to the free hyperon time of life (2.6×10^{-10} s). The shaded histogram in the figure corresponds to the „bright part" of prompt fission fragments which fly into a region covered by the diaphragm below the detector while the other part, with $z<0$ represents the event distribution reaching the „shadow part" of the detector. The $z>0$ histogram contains prompt as well as delayed fission fragments which fly in the forward directions. The latter one holds events from delayed fission of heavy hypernuclei only. While the hits of

prompt fission fragments are distributed randomly along the „bright part" of the detector plane, the delayed fission fragments show a nearly exponential fall off which reflects the distribution of time of life for the hyperon in the hypernucleus. As can be seen in this figure, it should be possible to distinguish well between the delayed fission events and those of the prompt fission, even at such a large ratio of the delayed and prompt fission events.

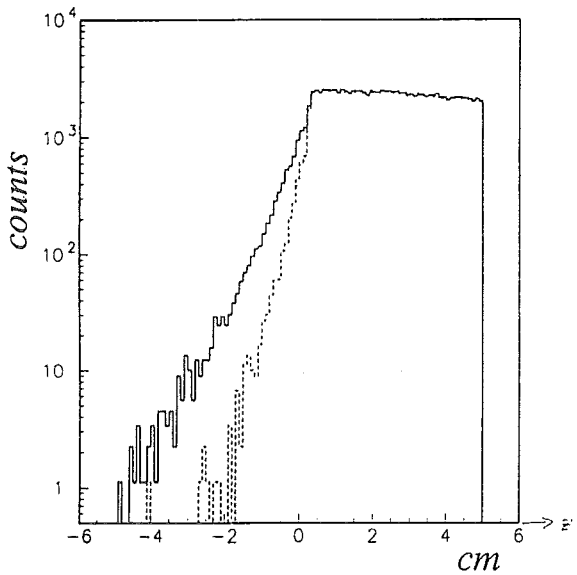

Fig. 3: GEANT simulation of the distributions of hits of fission fragments from delayed fission of hypernuclei along the z axis of the detector system. These results were obtained assuming two different times of life of hyperon in the hypernucleus:
a) $t = 2.6 \times 10^{-10}$ s - solid line,
b) $t = 1.3 \times 10^{-10}$ s - dashed line

In the simulation it was studied how the exponential distribution of hits in the shadow region is sensitive to the time of life of the Lambda hyperon in the hypernucleus. The simulation was done also for a time of life of the hyperon in the hypernucleus half as long as the time of life of the free lambda. The results of this simulation are presented in Fig. 3. The histograms shown in the figure represents only fragments originating from delayed fission. The full-line shows the fission fragment distribution from hypernuclei in which the hypernucleon lives as long as the free $\Lambda(\tau(\Lambda)_{free})$ and the dashed-line histogram contains fragments from hypernuclei where the Λ was a life time of $0.5 \cdot \tau(\Lambda)_{free}$. It is evident that the slope of the latter histogram is much steeper than that of the former one. In the presence of the very abundant prompt fission fragments the isolation of delayed events then becomes more difficult.

The simulation of other effects, important for the interpretation of the COSY-13 experiment is in progress.

The necessity of performing simulation calculations of the COSY-13 experiment is illustrated below by the example concerning the determination of the cross section for hypernucleus formation σ_{Hy}. This cross section can be calibrated with the use of the known prompt fission cross section for p+U collisions - σ_F by measuring the number of fission fragments in the „bright" part of the detector - „L", and the number of delayed fission fragments in the „shadow" part of the detector - „M". The ratio of effective solid angles for „L" fragments and „M" fragments must be determined from the simulation.

It is useful to consider for this purpose the number of delayed fission fragments of hypernuclei which hit the „bright" part of the detector - „N". This number as well as „M" depends on the mean time of life „T" of the hyperon in the hypernucleus: M=M(T), N=N(T). This is also true for the corresponding solid angles: $\Omega_M = \Omega_M(T)$ and $\Omega_N = \Omega_N(T)$. The ratio of solid angle of „L" fragments to that of the „M" fragments $\Omega_M/\Omega_M(T)$ may be written as follows:

$$\Omega_L/\Omega_M(T) = \Omega_L/\Omega_N(T) \times (\Omega_N(T)/\Omega_M(T)).$$

Furthermore the first factor on the right hand side of this formula may be expressed by $\Omega_N(0)/\Omega_N(T)$ i.e. the ratio of solid angles of prompt fission of hypernuclei (in which hyperons decay immediately) to the solid angle of delayed fission of hypernuclei (in which hyperons have mean time of life equal „T").

Then, the cross section for formation of hypernucleus σ_{HY} may be written as:

$$\sigma_{HY} = (M/L) \times (\sigma(F)/[f(1-f)]) \times (N(0)/N(T)) \times (N(T)/M(T).$$

The first factor „(M/L)" is determined from the COSY-13 experiment, the cross section of prompt fission of uranium in p+U reactions - „σ_F" is taken from the literatur to be ~ 1.5 barn at a proton energy ~ 1.0 GeV (1.53 b[4], 1.47 b[5], 1.48 b[6]), the survival probability against prompt fission for hypernuclei formed in p+U collisions -"1-f" was determined from theoretical considerations[2] to be equal to 0.115 at this proton energy, and the ratios of the numbers „N(0)", „N(T)", and „M(T)" were estimated in the present simulations. Values of „N" used in evaluations of the ratios given below correspond to the hits which are located in the „bright" part of the detector - not further than 1 cm from the shadow edge. Thus, the same selection of „L" events has to be done for evaluation of the „M/L" ratio.

T	N(T)/M(T)	N(0)/N(T)
2.6×10^{-10} s	3.60	0.92
1.3×10^{-10} s	10.7	0.95

In these simulations it was assumed that the „shadow" region of the detector can be reached only by delayed fission fragments of hypernuclei. The fragments of the prompt fission which are subsequently sent into the shadow region by a „kick" obtained due to decay of hypernucleon were neglected. They will be considered in simulations planned for the future work.

References:

1. T.A. Armstrong et al., Phys. Rev. C47 (1993) 1957, and references therein
2. Z. Rudy et al., contribution to present Annual Report, p.
3. GEANT - experiment simulation program, CERN Library
4. J. Hudis, S. Katcoff, Phys. Rev. C13 (1976) 1961
5. B.A. Bochagov et al., Sov. J. Nucl. Phys. 28 (1978) 291
6. L.A. Vaishnene et al., Z. Phys. A302 (1981) 143

[a] Jagellonian University, Cracow, Poland

Properties of Heavy Λ-Hypernuclei Produced in p-U Collisions

Z. Rudy[a], W. Cassing[b], L. Jarczyk[a], B. Kamys[a], P. Kulessa[a], O.W.B. Schult, A. Strzalkowski[a]

It was recently estimated theoretically[1)], that Λ-hypernuclei may be efficiently produced in proton-nucleus collisions with cross sections of about 100 μb for heavy targets and $T_p \sim 1.5$ GeV. In the present contribution we report on the properties of the heavy hypernuclei which are produced in $p+^{238}U$ collisions. An accurate knowledge of these properties is indispensable for realistic simulations of experiments that are devoted to measurements of the cross section of hypernucleus production and to measurements of the lifetime of the Λ hyperon in hypernuclei[2)].

The hypernucleus production process consists of two well defined time stages: The first stage, which lasts approximately 10^{-21} s, is the creation phase of highly excited („hot") hypernuclei. This production phase is described in the present work by means of coupled Boltzmann-Uehlig-Uhlenbeck transport equations[3)]. The second stage of the reaction, which persists up to 10^{-15} s, is the deexcitation phase of the „hot" hypernucleus where particle evaporation competes with the fission channels. This stage of reaction is treated by means of the Hauser-Feshbach model applying the CASCADE computer code[4)].

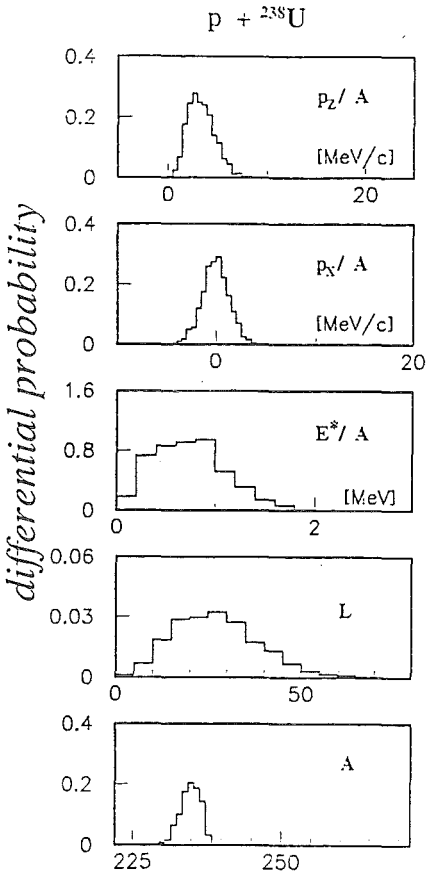

Fig. 1: Longitudinal momentum p_z/A, transverse momentum p_x/A, excitation energy E^*/A, angular momentum L and mass A distributions of the produced Λ-hypernuclei in $p+^{238}U$ at T_{lab}= 1.5 GeV.

The computed momentum distribution of „hot" hypernuclei in the laboratory frame, their distribution in excitation energy per nucleon, angular momentum and mass are presented in Fig. 1 for hypernuclei produced by 1.5 GeV protons impinging on ^{238}U. The average value of the parallel momentum of hypernuclei „p_z" (upper part of the figure) is ~ 3.4 MeV/c per nucleon, with a standard deviation of about 1.4 MeV/c. Thus we expect that in total a momentum of ~ 3.4 MeV/c × 235 ~ 800 MeV/c is transferred to the recoiling Λ hypernucleus prior to fast particle emission. This momentum distribution is essential for application of the recoil shadow detection method for the fragments from „delayed fission", i.e. fission of the Λ-hypernuclei induced by the decay of the Λ-hyperon (experiment COSY13[2)]). The perpendicular momenta of „hot" hypernuclei („p_x") are distributed around zero with a standard deviation of ~ 1.4 MeV/c. This distribution is important for the interpretation of the shape of momentum spectra of fission fragments from delayed fission.

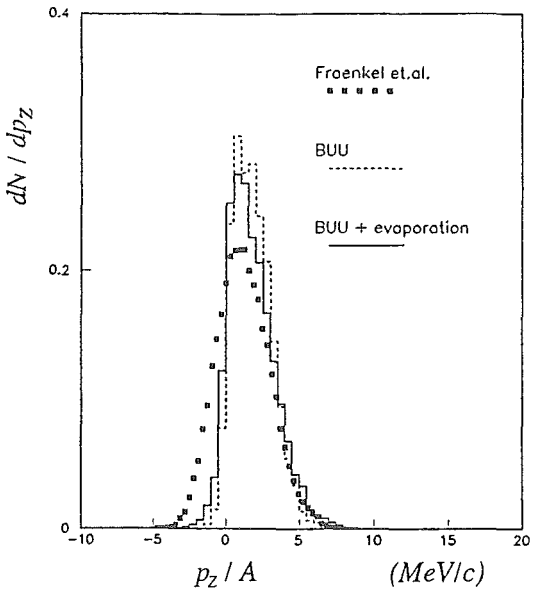

Fig. 2: Comparison of the longitudinal momentum distribution for $p+^{238}U$ at T_{lab} = 475 MeV from the BUU calculation (dashed line) and including evaporation (solid line) with the data from Fraenkel et al.[5)].

The number of nucleons emitted prior to fission depends strongly on the excitation energy and angular momentum of the „hot" hypernucleus. The same is true for the competition between prompt fission and emission of light particles and/or gamma quanta in the next phase of the deexcitation. Therefore, the distributions in excitation energy („E*") and angular momentum („L") of the „hot" hypernuclei, presented in the middle of the Fig. 1, are crucial for the final branching ratio of evaporation to prompt fission processes. The same is relevant for the charge and mass distributions which determine the fissility of nuclei.

All these distributions were used as input for the Hauser-Feshbach model calculations. The influence of the evaporation of light ejectiles on the momentum distribution

of final hypernuclei is illustrated in Fig. 2 in comparison to the experimental data of Fraenkel et al.[5] measured at T_p = 475 MeV. As can be seen, the mean value of the momentum distribution after the first stage of the reaction (dashed histogram denoted by „BUU") remains unchanged during the evaporation process, while the standard deviation of the momentum distribution increases slightly after evaporation (full-line histogram). The agreement between the theoretical and experimental momentum distributions is quite satisfactory, especially for the right-hand-side of the distribution, which is crucial for the „shadow detection method".

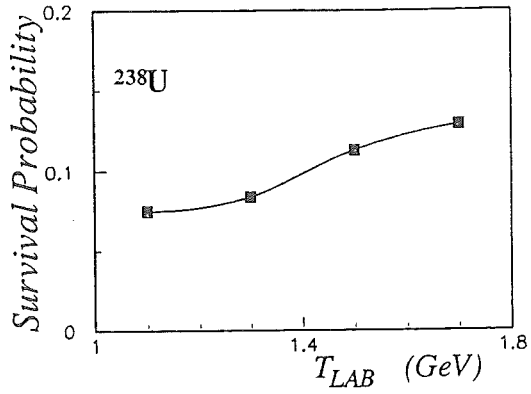

Fig. 3: Survival probability of ^{238}U-like hypernuclei against prompt fission.

The energy dependence of the „survival probability" of heavy hypernuclei against prompt fission, evaluated with the „CASCADE" program is presented in Fig. 3. As can be seen this probability increases slightly with energy from 0.075 at T_p = 1.1 GeV to 0.13 at T_p = 1.7 GeV. This result is caused by the fact that the fissility parameter (Z^2/A), which is decisive for the probability of fission, changes as (2Z/A) (dZ/dE). This quantity is negative, because the ratio (Z/A) is a positive constant (the probability of emission of fast protons and neutrons from „hot" hypernuclei is the same), and the derivative (dZ/dE) is negative, since the number of protons which remain in the hypernucleus decreases with beam energy.

References:

1. Z. Rudy et al., Z. Physik A351 (1995) 217
2. P. Kulessa et al., contribution to this Annual Report, p.
3. Gy. Wolf, W. Cassing, U. Mosel, Nucl. Phys. A552 (1993) 549 and references therein
4. F. Puelhofer, Nucl. Phys. A280 (1977) 267
5. Fraenkel et al., Phys. Rev. C41 (1990) 1050

[a] Jagellonian University, Cracow, Poland
[b] Universität Giessen, Germany

The Preparation of the ANKE Spectrometer

K. Sistemich[a], R. Maier[a], O. Schult[a], S. Abdulazizov[b], S. Barsov[c], U. Bechstedt[a], S. Belostotski[c], W. Borgs[a], W. Bothe[d], W. Bräutigam[a], M. Büscher[a], W. Cassing[e], O.Yu. Denisov[f], S. Dienel[g], J. Dietrich[a], H. Dombrowski[h], J. Ernst[i], R. Eßer[a], A. Franzen[a], A. Gerasimov[k], O.E. Gorchakov[f], D. Gotta[a], O. Grebenyuk[c], D. Grzonka[a], U. Hacker[a], A. Hardt[a], M. Hartmann[a], L. von Horn[a], L. Jarczyk[l], A. Kacharava[f,m], B. Kamys[l], T. Kirchner[7], St. Kistryn[l], F. Klehr[n], W. Klein[o], H.R. Koch[a], M. Köhler[p], V.I. Komarov[f], E.V. Komissarov[f], V. Koptev[c], D. Kopyto[a], R. Krause[a], V. Kruglov[f], P. Kulessa[l], A.V. Kulikov[f], V.S. Kurbatov[f], H. Labus[a], N. Langenhagen[g], K.W. Leege[g], G. Macharashvili[f,m], A. Mamulashvili[m], S. Martin[a], Z. Menteshashvili[m], S. Mikirtichyants[c], G. Müller[p], H. Müller[g], V. Nelyubin[c], M. Nioradze[m], V.P. Nomokonov[f], W. Oehme[g], W. Oelert[a], H. Ohm[a], A.Yu. Petrus[f], S.N. Prakhov[f], D. Prasuhn[a], B. Prietzschk[g], H.J. Probst[a], A.I. Puzynin[f], B. Rimarzig[g], A.M. Roshdestvensky[f], A.I. Rudenko[f], Z. Rudy[h], M. Sauer[a], R. Santo[h], M.G. Sapozhnikov[f], R. Schleichert[a], A. Schneider[a], Chr. Schneider[g], H. Schneider[a], Chr. Schneidereit[g], U. Schwarz[q], H. Seyfarth[a], A.A. Sibirtsev[f], V.V. Sidorkin[f], U. Sieling[p], J. Smyrski[l], H. Stechemesser[n], H.J. Stein[a], A. Strzalkowski[l], V. Tchernyshev[k], W. Tenten[p], V.I. Tretyak[f], S. Trusov[b], A. Vasilyev[c], K.-H. Watzlawik[a], M. Wende[l], V. Yazkov[b], B.Zh. Zalikhanov[f], K. Zwoll[p], I. Zychor[r]

The universal 0° Facility[1)] for studies of reaction products at internal targets at COSY has been given the name ANKE: Apparatus for Studies of Nucleonic and Kaon Ejectiles. The grant of special funds by the government of the state of North Rhine-Westfalia and the final decision by the board of directors of the KFA to build the device laid the basis for the speedy work towards the completion of the apparatus itself and of the appartaining detection systems. This task is shared by the project group for the construction of ANKE and the users collaboration who prepares the experiments.

The layout of the device is shown in Fig. 1. A new target place, TPA, between the quadrupoles MQT28 and MQT29 in the down-stream part of the cooler telescope of COSY is being commissioned for installing the spectrometer. A space of 6.4 m length is there available for the three dipole magnets of ANKE. Targets of different type, beam diagnosis devices and the necessary vacuum equipment can be installed between the dipoles D1 and D2. Detectors are foreseen at the sides of D2 where both positive and negative ejectiles will leave the vacuum system through thin windows and will be focussed horizontally according to their momenta. The detector telescopes for the positive ejectiles are indicated in Fig. 1; the ones for negative ejectiles will be placed in the large window of the yoke of D2. Detectors will also be installed at the far end of D2 for particles with high momenta (forward detectors) and at the side of D1 for those ejectiles which are emitted in backward direction (backward detectors).

The magnet D2 will be assembled on rails and equiped with the vacuum chamber in the central region of the COSY hall outside the accelerator tunnel. After assemblage and tests it will be transferred into the site in the COSY-ring. The necessary mouvements of D2 and the beam tubes in order to create the desired closed orbit bump and momentum dispersion for the individual experiments[2)] will be possible. The detectors are placed on platforms which move together with D2, but which can be disconnected for maintenance.

The layout of the laminated magnets D1, D2 and D3 has been finalized, and they have been ordered. An existing power supply is being adapted for D1 and D3, a new one has been ordered for D2. The magnet supports will be ready by mid-96 when the field measurements will begin. By then also the site preparations including the necessary changes of the concrete in the COSY tunnel will be accomplished.

The system of vacuum chambers of ANKE is in the design phase. In particular the chambers of D1 and D2 are based on non-conventional concepts[3)]. Since eddy currents in these large chambers would be very disturbing during the acceleration process the top and bottom plates will be made out of 2 mm thick stainless steel. This means that they will not be rigid under vacuum conditions. The necessary stability is achieved through their suspension from the magnet pole shoes.

The present design for the target region enables the use of foil targets as well as of a storage cell target[4)] for polarized protons and deuterons.

Calculations[5,6)] and tests have been initiated concerning an optimum tune of COSY for experiments at internal targets. This work is important for the preparation of experiments at ANKE, in particular for those using a storage cell target. Then it is very desirable to have a small beam diameter already at injection energy.

The concept for the side detector system, which will allow to discriminate between K^+ mesons and other ejectiles like pions and protons in the momentum range of ~ 150 to 600 MeV/c is completed. The individual parts are in preparation. The data of the test measurement on a prototype of the scintillator setup for the time-of-flight and ΔE information, which has been performed with the p,π^+ and K^+ beam of the Institute for Theoretical and Experimental Physics (ITEP), Moscow, have been analysed. Information[7)] has been gained on the production cross section for K^+ mesons in p ^{9}Be reactions at T_p = 2.9 GeV. The first of the two multiwire proportional chambers for track reconstruction[8)] has been built at the Forschungszentrum Rossendorf and has been tested both with radioactive sources and the COSY beam[9)]. The concept of the second chamber has been worked out[10)]. LED pulsing is foreseen for monitoring the properties of the scintillators[11)]. The nuclear electronics and the data acquisition devices have, to a large extent, been assembled and the data acquisition system is in preparation.

The most demanding electronical component for the planned identification[12)] of K^+ in the presence of an intense background is the fast trigger system. This system will

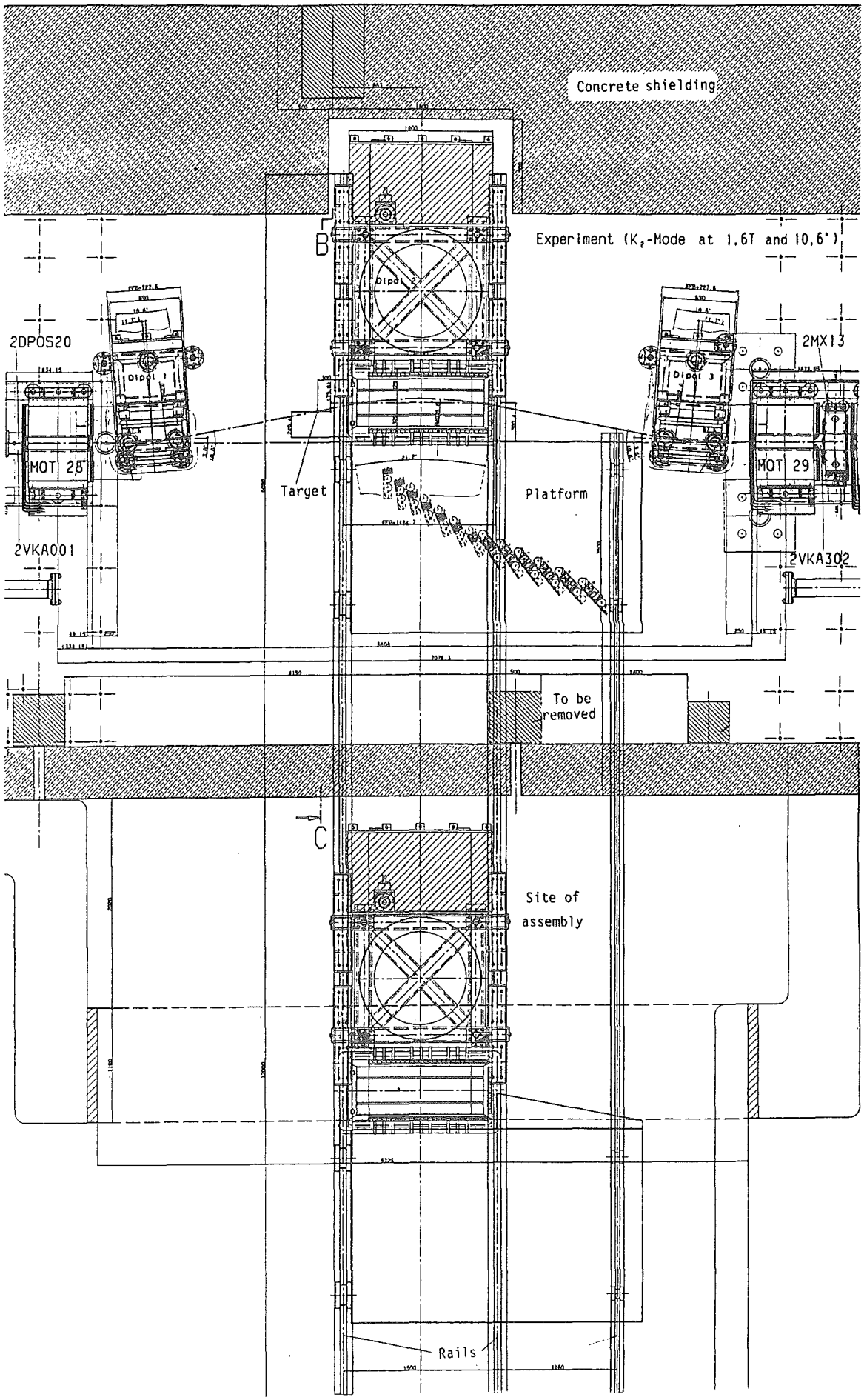

Fig. 1: Layout of ANKE

allow the computer controlled setting of TOF windows for all possible combinations of 23 start scintillation detectors, which are close to the exit window of the D2 chamber, and the 15 stop detector telescopes at the focal surface of D2. The trigger unit and the appartaining electronical devices[13] like discriminators and meantimers have been developed and the production has begun.

The forward and backward detectors are being built at the Joint Institute of Nuclear Reserach, Dubna. These detectors will be needed especially for the deuteron breakup[14] studies where protons in forward and backward directions are emitted. They meet also the requirements to study the variety of other processes accompanied by fast forward and/or backward ejectiles. The multiwire proportional chambers for those detector setups have been developed especially to operate at high particle flux. The first one out of the three detectors needed was produced and tested[15]. Its sensitive area is 320 x 256 mm^2. There are X- and Y-wire planes and two strip planes at ± 18° to the X-wires. The distance of the signal wires is 1 mm, the gap between anode wires and a cathode plane is 1.5 mm. The tests were performed with a ^{90}Sr ß-source in the counting rate conditions close to those anticipated at COSY with a luminosity of $L = 10^{33}\ cm^{-2}\ s^{-1}$. Feasibility studies for the use of Cerencov counters with total reflection in the forward detector system have been performed[16].

Simulations for the forward detector (FD) system have been carried out and verified[17] on the basis of experimental data obtained in a hydrogen bubble chamber at a proton momentum of 1.7 GeV/c. The main background processes for the break-up reaction pd → ppn have been considered[17] and their kinematic characteristics have been studied. The number of particles that will hit the detectors has been estimated for different reactions, and the useful events to background ratio has been determined. In particular, the count rate of the FD detector system has been estimated on the basis of experimental data on pp and pn interactions for projectile momenta of 3.3 GeV/c. It has been shown that the number of background π^+ mesons increases by one order of magnitude compared to that at a projectile momentum of 1.7 GeV/c. Also the distribution of the events over the area of the hodoscope (relative counting rate) and their spectral contents have been obtained. The possibility of studying the elastic scattering of protons under 180° has been investigated. Also the possibilities of track reconstruction with the chambers has been verified by simulation calculations[18].

Theoretical studies concerning the research at ANKE have been continued. The subthreshold K^+ production in pd reactions[19] and the K^+ production in elementary interactions[20] have been investigated. For the latter case, the production cross section could be parameterized in a form valid from threshold up to 400 GeV. Also the K^+ production in $p^{208}Pb$ interactions at 2.1 GeV has been studied[21].

The theoretical work also comprised the reaction pd → ^3HeX and pd → $_\Lambda{}^3HeK^+$[22]. It was shown[23] that the K^+/π^+ production ratio may provide a useful signature for an enhanced strangeness production. The preparation of proposals for the ϕ production[24] in the interaction of polarized protons with polarized deuterium and for the K^- production in pA interactions has been continued both in theoretically and through detector concept studies. It was shown[25] that ϕ mesons can be identified in missing mass spectra of K^+K^- pair even when a 40 cm long storage cell target for hydrogen is used.

In conclusion, the construction of the ANKE spectrometer, the preparations for its installation in the COSY ring and for the experiments at this device are progressing rapidly. According to the present time schedule first measurements should be possible early in 1997. After calibration measurements, the subthreshold K^+ production will be investigated.

References:

1. K. Sistemich et al.: Ann. Report 1994 of the IKP, Berichte des Forschungszentrums Jülich; 3035, ISSN 0944-2952, p. 41
2. O.W.B. Schult et al.: Ann. Report 1992 of the IKP, Berichte des Forschungszentrums Jülich; 2726, ISSN 0366-0885, p. 11
3. F. Klehr et al.: contribution to this report, p. 55
4. V. Nelyubin et al.: contribution to this report, p. 71
5. I. Zychor, R. Maier et al.: contribution to this report, p. 58
6. I. Zychor, S. Martin et al.: contribution to this report, p. 60
7. M. Büscher et al.: contribution to this report, p. 120
8. Th. Kirchner et al.: contribution to this report, p. 61
9. L. von Horn et al.: contribution to this report, p. 62
10. T. Kirchner et al.: contribution to this report, p. 63
11. B. Prietschzk et al.: contribution to this report, p. 64
12. K. Sistemich: Proc. WE-Heraeus-Seminar on Hadronic Processes at Small Angles in Storage Rings, Bad Honnef, Germany, February 1-3, 1993, Konferenzen des Forschungszentrums Jülich, (E. Rössle, O. Schult, eds.), Vol. 12, p. 1
13. R. Schleichert et al.: contribution to this report, p. 65
14. V.I. Komarov: Loc. cit. in Ref. 12, p. 281
15. V.I. Komarov et al.: contribution to this report, p. 67
16. A.K. Kacharava, G.G. Macharashvili et al.: contribution to this report, p. 69
17. A.K. Kacharava, V.I. Komarov et al.: contribution to this report, p. 74
18. V.M. Artimov et al.: contribution to this report, p. 77
19. A. Kacharava, M. Nioradze et al.: contribution to this report, p. 79
20. A.Yu. Petrus and A.A. Sibirtsev: contribution to this report, p. 82
21. B. Kamys et al.: contribution to this report, p. 84
22. L.A. Kondratyuk: contribution to this report, p. 86

23. V.I. Komarov and H. Müller: contribution to this report, p. 88
24. O.E. Gorchakov et al.: contribution to this report, p. 90
25. A. Franzen and M. Büscher et al.: contribution to this report, p. 92

[a] Institut für Kernphysik, KFA Jülich, D-52425 Jülich
[b] Dubna Branch of the Moscow State University, Dubna, Russia
[c] St. Petersburg Institute of Nuclear Physics, Russian Academy of Sciences, Gatchina, Russia
[d] DESY, D-22603 Hamburg
[e] Institut für Theoretische Physik, Universität Gießen, D-35392 Gießen
[f] Joint Institute of Nuclear Research, Dubna, Russia
[g] Zentralinstitut für Kernforschung, Rossendorf, D-01474 Dresden
[h] Institut für Kernphysik, Universität Münster, D-48149 Münster
[i] Institut für Strahlen- und Kernphysik, Universität Bonn, D-53115 Bonn
[k] Institute for Theoretical and Experimental Physics, Moscow, Russia
[l] Institute of Physics, Jagellonian University, Cracow, Poland
[m] High Energy Physics Institute, Tbilisi State University, Tbilisi, Georgia
[n] Zentralabteilung Allgemeine Technologie, KFA Jülich, D-52425 Jülich
[o] Institut für Schicht- und Ionentechnik, KFA Jülich, D-52425 Jülich
[p] Zentrallabor für Elektronik, KFA Jülich, D-52425 Jülich
[q] FH Soest, D-59494 Soest
[r] Soltan Institute for Nuclear Studies, Swierk, Poland

The Vacuum Chambers at ANKE

F. Klehr, W. Borgs, H. Stechemesser, O. Schult

As the 0° facility ANKE will be integrated into the COSY ring the vacuum chambers have to satisfy ultra-high vacuum (UHV) requirements for minimal scattering of COSY beam protons in order to achieve low background and long lifetime of the circulating beam. Furthermore, ramping of the magnetic fields B_A of the ANKE dipole magnets in proportion with the field B_C in the COSY dipole magnets - in order to operate ANKE with a stable closed orbit bump - makes it necessary to keep eddy current effects sufficiently small. It is therefore necessary to realize a concept with as thin as possible walls of the chambers in regions of strong fields. Finally the desire for maximal acceptance of ejectiles to be measured with ANKE suggests a vacuum chamber design which makes maximum use of the gap widths of the spectrometer magnets D2 and D1.

Tube between D2 and D3

As shown in Fig. 1 ANKE consists of the deflection dipole D1, the spectrometer dipole D2 and the inflection dipole D3. D1 and D3 are oriented at a fixed angle of 3.6° relative to the COSY beam for $B_A = 0$. Standard UHV elements can be used to connect the D1 and D3 chambers with the neighbouring quadrupole beam tubes of COSY. A standard vacuum chamber with connections for vacuum pumps will be installed in D3. We will employ[1)] one pair of beam position monitors between D1 and D2 and one between D2 and D3, as shown in Fig. 1. This will permit us to control the closed orbit bump in ANKE. The UHV connection between D2 and D3 contains a bellow located near D2 where the COSY beam axes - expected for the different modes of operation of D2 - come close to each other. Here the diameter of the tube is minimal in order to have sufficient space for the first MWPC of the forward detector which will be placed right outside the vacuum system. A standard COSY beam position monitor for horizontal and vertical position determination is located in the center region of the tube. Near D3 there is another bellow. The two bellows allow the movement of D2 perpendicular to the COSY beam direction for $B_A = 0$ (Orbit) so that the COSY beam can be deflected - by D1 and D3 - through any angle ϑ between 0° (ANKE switch-off position, $B_A = 0$) and 10.6°, and they compensate the elongation of the D2-D3 vacuum tube section which results from the displacements of D2.

D2 chamber

More demanding vacuum components are the D2 chamber, the D1 chamber and the target tube between D1 and D2. The requirements regarding apertures with windows for the *D2 chamber* are: open for ejectiles with positive charge and momenta $\gtrsim$ 140 MeV/c; open for ejectiles with negative charge and momenta as far down as possible; open for ejectiles on both sides and as near as possible to the circulating COSY beam (for angles $\theta \sim 0°$ ejectiles with high momenta and for at $\theta \sim 0°$ outgoing neutrons - as ANKE creates a variable closed orbit bump, it can be used as beam swinger -). This has led us to a design with a

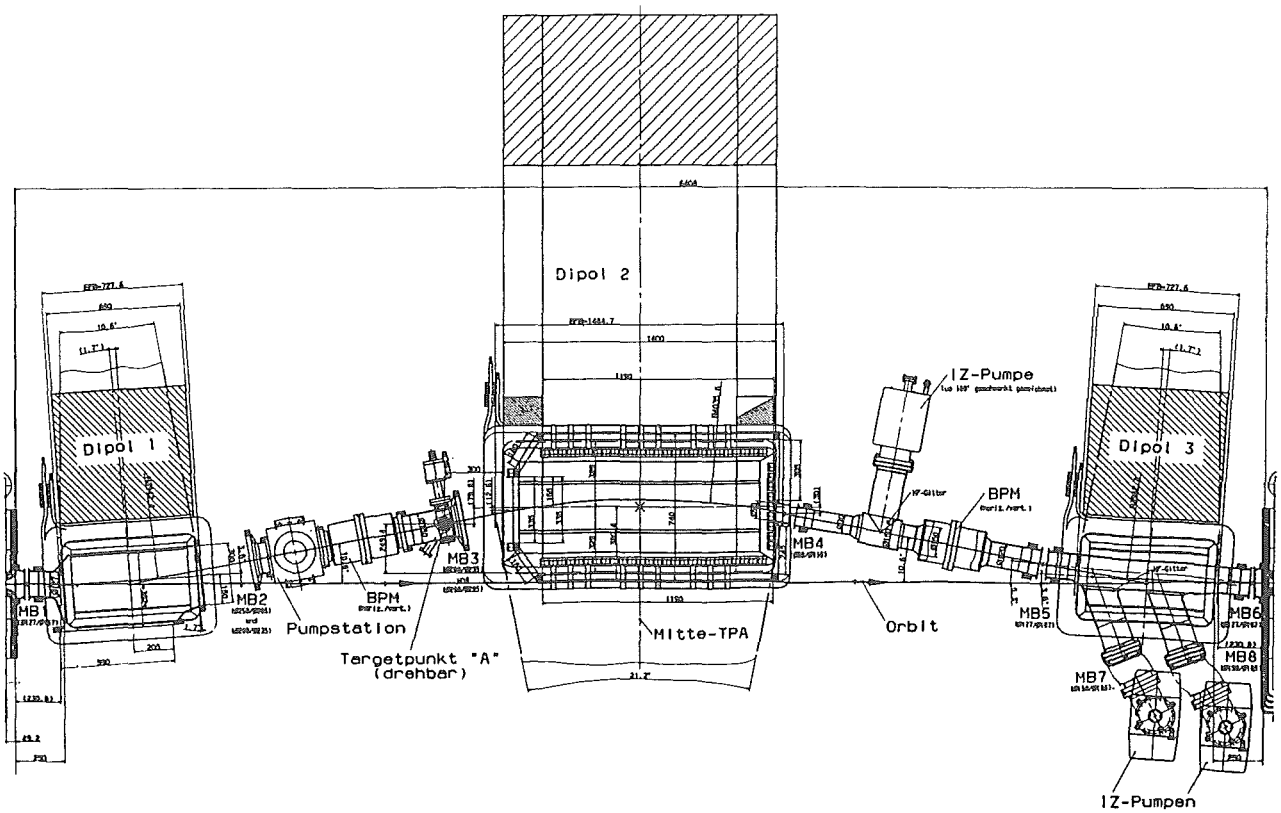

Fig. 1: Zero-degree facility ANKE and its UHV components with exception of the bellows MB1-MB6.

large entrance opening - to minimize background from „slit" scattering -, with two access flanges on both sides of the entrance opening - also for pumping -, with two large windows at the sides for the exit of positively and negatively charged ejectiles with a very large momentum acceptance, and with two windows on both sides of the central D2-exit hole for the circulating COSY beam.

The basic idea of the design of the D2 chamber is the „suspension bridge" technique. Using the massive pole pieces of the D2 magnet in order to pick up the forces it is possible to use plates of stainless steel with a thickness of only 2 mm as top and bottom plate of the D2 vacuum chamber (see Fig. 2). These plates touch under vacuum the outer edges of the pole pieces so that the net gap height is expected to be 198 mm (see left part of the upper figure 2). In the middle of the pole pieces, the net gap height is only ~ 172 mm. But the region which defines the aperture is at the edges of the pole pieces because the ejectiles emerge from a narrow region in the middle plane of ANKE.

The windows will be made of three layers of carbon-fiber-supported epoxy with an Al layer on the inside for RF conductivity and making the epoxy-carbon-fiber compound vacuum tight. The D2-chamber is fixed at D2 after having been moved in between the pole pieces from the downstream side of D2.

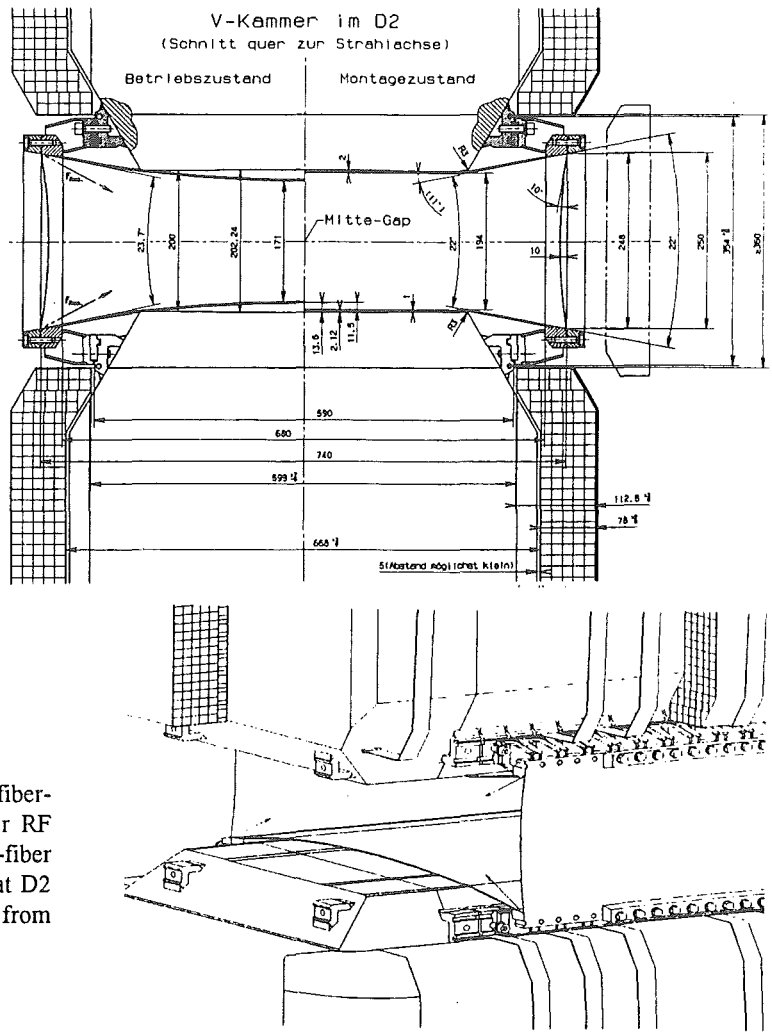

Fig. 2: Cuts through the vacuum chamber of D2. The left part of the upper figure shows the chamber under vacuum, the right part at the stage of mounting.

D1-Chamber

The dipole magnet D1 will be used as $\theta \sim 180°$ backward spectrometer for the deuteron break-up study. The requirements are a wide entrance opening in order to have good acceptance ($\theta \geq 165°$) and a large window at the side of D1 for transmission of the maximum possible momentum bite of ejectiles. As for the D2 chamber we have applied the "suspension bridge" design. As the D1 chamber has to be moved in from the side - looking in COSY beam direction - the left hand side of the chamber consists of a support structure on which clamping blocks will be mounted and tightened after installation of the chamber into D1. This and the pull on the outer flange stretch the bottom and top plates of the chamber so that they bend under vacuum by amounts which will not reduce the net aperture. The window will be made similar to those for the D2 chamber but only of 2 layers.

Target Tube

The target tube must provide space for the targets in addition to pumps and beam position monitors, and its bellows must allow for the necessary degrees of freedom for the various modes of operating ANKE and also for switching ANKE off during other use of COSY, without breaking the vacuum.

Obviously bellows are needed near D1 and near D2 for setting ANKE at any bumping angle ϑ between 0 and 10.6°. As D1 and its chamber are fixed in space while the target tube will be swung around a vertical axis through the middle between the pole pieces of D1 the bellow near D1 has to allow a horizontal displacement of ~ 42 mm in addition to a bending through 5.3° (D1 is oriented at + 3.6° relative to the COSY beam and the exit flange of the D1 chamber is at + 1.7° relative to D1). This covers the $\theta = 0°$ switch-off position as well as the 10.6° extreme setting of ANKE. The bellow near D2 would have to only cover the angle of ± 5.3° if the entrance flange of the D2 chamber is at +5.3°. However, one gains significant freedom in setting D2, if D2 can be shifted by ± 25 mm at a fixed closed orbit bump (see below). This then implies that the bellow near D2 must allow a horizontal displacement of ± 25 mm in addition to the 5.3° bend.

Installation of a ribbon target (carbon, polyethylene or other solids) can be accomplished with a system which moves the target down (-y direction) into the circulating beam in a computer controlled manner so that the luminosity L remains approximately constant (to avoid L peaks with poor peak/background rates). The position of the target in z-direction (direction of COSY beam) is not critical. The alignment in x direction is easily achieved by

adjusting the target tube (possible because of the degree of freedom of moving D2 by ± 25 mm relative to the COSY beam). The ribbon target would be moved into the beam during each cycle. The ribbon target system and standard COSY beam position monitors together with a standard COSY UHV pump system is sketched in Fig. 1. ANKE can easily be moved into the switch off position by moving D2 so that $\vartheta \rightarrow 0$ and by leaving the ribbon target out of the COSY beam.

Operation of ANKE with a polarized storage cell target should be possible. For this purpose e.g. a Madison- or Hermes-type atomic-beam source (ABS) could be installed which feeds in -y direction a storage cell. This preferably would be a closed cell with a length of ~ 400 mm and a height 2 x Sy and width 2 x Sx (see contribution by I. Zychor to this report) so that the full COSY acceptance is within the cell. This allows injection and acceleration without opening the cell. For other use of COSY the cell has to be moved out of the beam. One way of achieving this is to follow the NIKHEF approach[2], where the beam tube with the cell is lifted to let the beam circulate underneath the cell. We can easily incorporate this degree of freedom by requiring that the bellows allow, in addition to the horizontal displacement of the beam tube between D1 and D2, a vertical displacement by ± 20 mm. Then the total lateral displacement of the bellows is only slightly increased and we can switch from „storage cell operation with ANKE" to „other use of COSY" without breaking vacuum by lifting the target assembly (ABS together with the storage cell and target tube) by 40 mm and moving D2 with the target assembly to $\vartheta = 0°$. This then yields (with a tube diameter of 140 mm and the storage cell 20 mm above the tube axis) for other COSY beam use $\sqrt{a_x \beta_x}$ = 50 mm and $\sqrt{a_y \beta_y}$ = 30 mm at the ANKE target.

We have developed a first design of such a storage cell target consisting of thin Al sheets, teflon coated, with a feed tube: ~ 130 mm long, 10 mm diameter. We would cool the cell by conduction through the thin sheets and radiation from a thin closed-loop He-gas cooled Al tube which would also serve for supporting the cell. We intend to install an additional tube for filling the cell with normal gas. This additional tube has turned out to be most useful at the Madison - IUCF target[3].

The considered concept of a storage cell located 20 mm above the axis of a thin wall target tube with 140 mm diameter and the ~ 130 mm feed tube length leave enough space around the target tube for a barrel detector which permits vertex detection and an efficient polarization measurement. There is also space in forward direction for a tracker or vertex detector. With a tracker and a barrel vertex detector it is possible to cover together with D2 effectively nearly 4π in the CM at ANKE. These detectors could be built of scintillating fibers similar to the EDDA[4] and MOMO detectors[5]. A much more advanced detector of the size needed for the barrel has been built as micro vertex detector of DELPHI[6].

The modular structure of the target telescope between the bellows near D1 and D2 leaves space for the storage cell, a pair of beam position monitors with reduced lengths, and additional pumps needed in view of the ABS gas load. The location of the storage cell relative to D1 and D2 can be optimized also in order to position it in a region of sufficiently small stray fields. It is also possible to install a storage cell with a different design (see contribution by Nelyubin et al.).

References:

1. D. Möhl and J. Dietrich, priv. communication
2. K. de Jager, priv. communication
3. M.A. Ross, A.D. Roberts, T. Wise et al., Nucl. Instr. & Meth. A344 (1994) 307
4. J. Bisplinghoff et al., AIP Conf. Proc. 221, Am. Inst. of Phys. (1993) 312, Physica Scripta 48 (1993) 92
5. R. Maschuw, Few Body Systems, Suppl. 99 (1995) 1
6. P. Aarnio et al., Nucl. Inst. & Meth. A303 (1991) 233

Expected Beam Parameters at the Internal Target Positions for Experiments in the COSY Ring

I. Zychor[1], R. Maier, S. Martin, D. Prasuhn, O.W.B. Schult

At the internal target positions in COSY both foil and gas targets can be installed. With internal foil targets very high luminosity can be achieved but also sufficiently high luminosity can be obtained with polarized storage cell targets or atomic beam targets because of the high intensity of the circulating beam.

The horizontal aperture of the COSY ring is 75 mm both in straight and arc sections. So the COSY geometrical acceptance in the horizontal direction is equal to $a_x=75*75/\beta_x^{max}$, β_x^{max} is the maximum of the horizontal β function in the ring.

The vertical aperture is equal to 75 mm in the straight sections and 30 mm in the arc sections. So when calculating the geometrical vertical COSY acceptance we have taken as the vertical acceptance $a_y= \min(30*30/\beta_{y,a}^{max}, 75*75/\beta_{y,t}^{max})$, where $\beta_{y,a}^{max}$ and $\beta_{y,t}^{max}$ are the maximum vertical β functions in the arc and telescope sections, respectively.

The acceptance radii are:

$$S_x = \sqrt{a_x \cdot \beta_x^T}$$

$$S_y = \sqrt{a_y \cdot \beta_y^T}$$

where: πa_x, πa_y - are the horizontal and vertical acceptances of COSY, respectively; β_x^T, β_y^T - the beta functions at the target position.

For optimal experimental conditions the ring acceptances should be large and the beta functions at the target position should be small. We define the following figure of merit:

$$M = \frac{1}{\frac{\beta_x}{a_x} + \frac{\beta_y}{a_y}}$$

Good experimental conditions are achieved for large values of M.

For solid targets we require to have good filling of the ring, low Coulomb scattering to minimize particle loss and reasonably small S_y (for COSY#13 the rate is $\propto S_y^{-1}$). For the foil target we introduce the following parameter which includes both figures of merit:

$$F = M_i \cdot M_F$$

where M_i is the figure of merit at the injection point and M_F is the figure of merit at the foil target position. As long as the number N of protons is far below the space charge limit, N is $\propto M_i$. To have good filling of the ring, M_i should then be as large as possible. To have as small as possible particle loss in the ring, M_F should be as large as possible. So we look for a maximum value of the F parameter to find the best experimental conditions for foil targets. At the space charge limit $F \propto M_F$.

In case of a polarized storage cell target it is important to have a high density and good filling of the ring. For a rigid cell, the target dimensions must be $\geq 2S_x$ and $\geq 2S_y$, respectively. The density in a storage cell target is roughly proportional to l^2/d^3, where l is the length of the storage cell and d is its diameter. For a fixed value of l the density in a target is roughly proportional to $(\sqrt{S_x \cdot S_y})^{-3}$. As in case of the foil target we look for the figure of merit and include the properties of the injection point. We can then define a parameter:

$$G_S = \frac{M_i}{\left(\sqrt{S_x \cdot S_y}\right)^3}$$

which should become maximal for maximal luminosity.

The maximum current in the quadrupole coils is 550 A. The length L of arc quadrupoles is 0.372 m and of telescope quadrupoles 0.62 m. The quadrupole coefficient is calculated as $K_1=0.29979 \cdot S/L/p$, where S is a quadrupole strength and p is the proton momentum. For the maximal proton momentum p=3.3 GeV/c, available in the COSY ring, the maximum quadrupole coefficient is equal to $K_1=0.816\ m^{-2}$ for arc quadrupoles and $K_1=0.856\ m^{-2}$ for telescope quadrupoles.

For the purpose of ANKE experiments we propose to add two new power supplies in the straight section around the target place TPA to have higher optical flexibility of the COSY quadrupole setting. We would connect quadrupoles QT21 and QT24 to one power supply, QT22 and QT23 to one power supply, quadrupoles QT25 and QT28 to one power supply, and QT26 and QT27 to one power supply.

As reference values we use data for the standard COSY working point (POINT_A) of the tunes $Q_x=3.63$ and $Q_y=3.55$. The tunes are set by changing the strength of the 14 quadrupole families.

The MAD code [1] was used to calculate the COSY beam parameters of the actual standard working point and to look for the optimal quadrupole settings necessary for experiments at ANKE and for COSY#13.

The following quantities were calculated and analyzed:
- the horizontal acceptance a_x,
- the vertical acceptance a_y,
- the horizontal tune Q_x,
- the vertical tune Q_y,
- the gamma transition γ_{tr},
- the β functions for both planes,
- the phase functions μ for both planes,
- the dispersion function in the horizontal plane (the dispersion in the vertical plane is 0).

From the values calculated by the MAD code the following parameters were obtained:
- the figure of merit M_i at the injection point,
- the figure of merit M_T at the target position (both for foil and gas target),
- the acceptance radii S_x and S_y,
- the parameter F and G_S for foil and gas targets, respectively.

The targets will be installed between dipole magnet D1 and D2 of ANKE. In case of gas targets, calculations were made for three planned target positions: close to D1 (s = 125.29 m), between D1 and D2 (s = 125.76 m), close to D2 (s = 126.24 m). The foil target is placed at s = 126.24 m. We fixed that the injection point to the COSY ring is at s = 0 along the circumference of the ring.

Table 1. Beam parameters for standard actual COSY quadrupole set-up (POINT_A)

a_x = 128.3 π mm mrad a_y = 15.7 π mm mrad
Q_x = 3.630 Q_y = 3.550
γ_{tr} = - 2.03 +) M_i = 1.1
maximal dispersion = 27.6 m

QUANTITY	foil at TP1 s=24.87 m	TPA			
		gas at s=125.29 m	gas at s=125.76 m	gas at s=126.24 m	foil at s=126.24 m
M_T	0.7	2.6	2.8	3.1	3.1
S_x (mm)	50.5	26.2	23.5	21.1	21.1
S_y (mm)	17.2	9.2	8.9	8.6	8.6
F G_S	0.80	0.29	0.36	0.44	3.29
dispersion at target (m)	19.1	8.0	6.5	5.1	5.1

+) the sign of the γ_{tr} is sign of the average over the dispersion function in the bending magnets

For the TPA position and the foil target, the MAD calculations were stopped when the parameter F reached the value 24 times higher than for the standard COSY quadrupole set-up (for the POINT_A working point), but still it is possible to continue calculations. For the gas targets at this position the maximal value of the parameter G_S was reached for almost circular shape of the target cell with S_x~S_y~5 mm.

For the foil target placed at TP1 for COSY#13 the calculations were stopped when F was 102 times higher than for the standard COSY quadrupole set-up. A still higher value seems achievable.

The maximal dispersion in the horizontal plane in the ring is lower than 15 m for all calculated cases.

In Fig. 1 the horizontal and vertical β functions are shown as a function of the distance along the ring circumference for the actual COSY working point (POINT_A) and for the best calculated COSY quadrupole set-up for the polarized gas target placed at s = 125.76 m.

* supported by the TEMPUS project
[1] Soltan Institute for Nuclear Studies, Świerk, Poland

References

[1] H. Grote, F.Ch.Iselin, "The MAD Program", CERN/SL/90-13

Table 2. Beam parameters for the best calculated COSY quadrupole set-up

QUANTITY	foil at TP1	TPA			
		gas at s=125.29 m	gas at s=125.76 m	gas at s=126.24 m	foil at s=126.24 m
a_x (π mm mrad)	278.0	31.6	34.6	37.0	174.1
a_y (π mm mrad)	44.8	9.8	10.0	12.4	38.2
Q_x	3.689	3.520	3.526	3.535	3.547
Q_y	3.234	4.368	4.401	4.300	4.137
γ_{tr}	2.11	1.84	1.84	1.93	1.82
M_i	4.5	0.6	0.7	0.9	4.3
M_T	18.3	4.1	6.1	8.3	18.7
S_x (mm)	44.0	5.1	5.9	4.8	21.3
S_y (mm)	7.7	4.6	3.6	4.0	7.5
F G_S	81.66	5.53	6.85	10.98	80.58

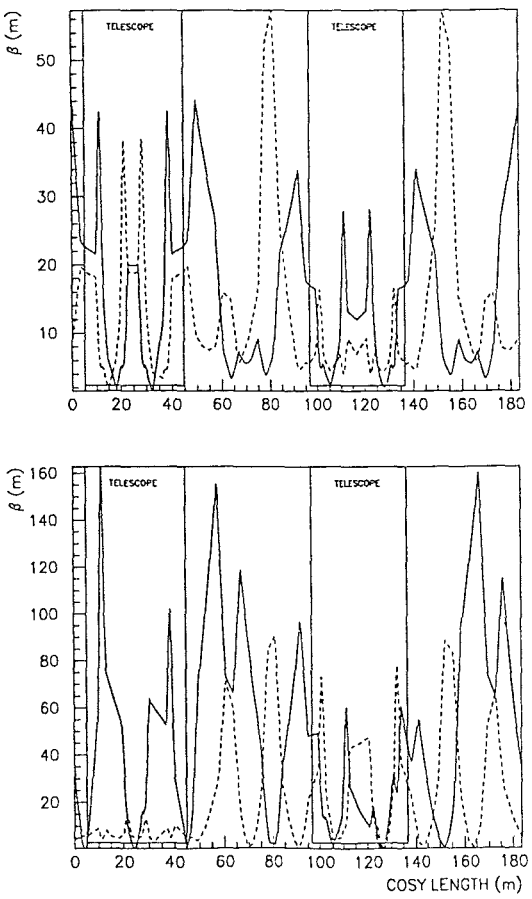

Figure 1. The β functions (solid - horizontal, dashed - vertical) for the standard COSY working point POINT_A (upper) and for the best calculated quadrupole set-up for the polarized storage cell at TPA at s = 125.76 m (lower)

TP2 as an alternative place for installing ANKE *

I. Zychor[1], S. Martin, R. Maier, D. Prasuhn, O.W.B. Schult

The TP2 target place is in the straight section between the quadrupoles QT12 and QT13 in the COSY ring. We have considered this site as an alternative place to TPA for the installation of ANKE.

As in case of the TPA target place for ANKE, we used the MAD code for beam parameter calculations. The following quantities were calculated:
- the horizontal acceptance a_x,
- the vertical acceptance a_y,
- the horizontal tune Q_x,
- the vertical tune Q_y,
- the gamma transition γ_{tr},
- the β functions for both planes,
- the phase functions μ for both planes,
- the dispersion function in the horizontal plane (the dispersion in the vertical plane is 0).

From the values calculated by the MAD code the following parameters were obtained, defined as in the TPA case (see the previous contribution) :
- the figure of merit M_i at the injection point,
- the figure of merit M_T at the target position (both for foil and for gas targets),
- the acceptance radii S_x and S_y,
- the parameter F and G_S for foil and gas targets, respectively.

We look for maximum values of the F and G_S parameters to find the best experimental conditions for foil and polarized storage cell targets, respectively.

To have higher optical flexibility of the COSY setting we added in calculations two new power supplies in the telescope section around ANKE: quadrupoles QT5 and QT8 are connected to one power supply, QT6 and QT7 to one power supply, QT9 and QT12 to one power supply, and QT10 and QT11 to one power supply.

As reference values we use data for the standard COSY working point (POINT_A) of the tunes Q_x=3.63 and Q_y=3.55.

Two different internal target types are considered: a polarized storage cell target and a foil target. The gas target is put at s=32.021 m and the foil target at s=32.508 m along the COSY ring. The injection point to the COSY ring is at s=0 along the circumference of the ring.

For the foil target, the MAD calculations were stopped when the parameter F reached the value 18 times higher than for the standard COSY quadrupole set-up (for the POINT_A working point) but the limit in calculations has not been reached. For the gas targets at the TP2 position the maximal value of the parameter G_S was reached for the almost circular shape of the target cell with S_x~S_y~4 mm. These are similar values to those obtained for the TPA place.

In Table 1 the beam parameters for the standard actual COSY working point are compared with the best calculated parameters.

Table 1. Beam parameters for standard COSY working point and for the best calculated COSY quadrupole set-up

QUANTITY	GAS AT TP2		FOIL AT TP2	
	POINT_A	OPTIMAL	POINT_A	OPTIMAL
a_x (π mm mrad)	128.3	30.3	128.3	221.7
a_y (π mm mrad)	15.7	9.3	15.7	33.3
Q_x	3.630	3.627	3.630	3.320
Q_y	3.550	3.871	3.550	4.120
γ_{tr}	-2.03 +)	-1.97 +)	-2.03 +)	1.45
M_i	1.1	0.4	1.1	4.1
M_T	2.8	5.4	3.6	17.6
S_x (mm)	14.5	4.0	14.0	22.5
S_y (mm)	9.3	3.8	8.1	7.2
F			3.88	71.44
G_S	0.69	7.17		
dispersion at target (m)	1.6	2.4	-0.1	-0.3
maximal dispersion (m)	27.6	51.9	27.6	27.1

+) the sign of the γ_{tr} is sign of the average over the dispersion function in the bending magnets

* supported by the TEMPUS project

[1] Soltan Institute for Nuclear Studies, Świerk, Poland

Reconstruction of Particle Coordinates with the Wire Chambers at the ANKE-Facility

T. Kirchner[a], H. Müller[a], Ch. Schneider[a] and Chr. Schneidereit[a]

At the ANKE-Facility particle trajectories will be reconstructed with the help of two multi-wire chambers MWPC1 and MWPC2[1)] by determining the position and angle of the particle tracks in the detection system. Each chamber has three sensitive anode wire planes. In one plane the wires are inclined by 0° in the two others by ± 30° with respect to the vertical direction. During experiment the chamber read-out electronics will furnish for each detected event the wire-numbers of the fired wires in each anode plane. In most cases this will not be only one wire per plane, but a cluster of several wires. In order to obtain the position information for the detected particles, the wire-numbers have to be transformed in spatial and angular chamber coordinates. A first procedure for that has been worked out and tested in GEANT simulation calculations. The basic idea will be summarized briefly in the following.

We consider the case where the ejectile has been detected in all six anode planes. This restriction is not necessary, but simplifies the description of the procedure. Later in real data analyzing programs other cases have to be included (e.g. only signals available from two planes in the first and second chamber) in order to increase the overall particle detection efficiency. It is a reasonable assumption to use for each cluster of wires the center of gravity for further calculations. In each plane this center of gravity corresponds to a virtual line parallel to the wires of the corresponding plane. In the following this virtual line will be called X_1, U_1 and V_1 for the three anode planes in the chamber MWPC1 and X_2, U_2 and V_2 in the planes of the second chamber MWPC2.

The x-coordinate of the scattered particle in both chambers is automatically determined by the positions of line X_1 and X_2. Both x-coordinates fix the angle θ of the particle trajectory in the median plane at the exit of the spectrometer. The vertical y-coordinate can be determined separately in both chambers using the other virtual lines. In the MWPC1 V_1 and U_1 are translated along the particle track (along the θ-direction) into the anode plane containing the line X_1. As a result of this projection there are now three lines in one plane, one vertical and two inclined lines. The point of intersection between two of them gives the y-coordinate. The best accuracy is obtained by crossing the two inclined lines. The y-coordinate in the chamber MWPC2 is determined in the same way. The z-coordinate is equal to the position of the plane to which the virtual lines have been projected (the plane from which x and Y coordinates were extracted). The x, y and z information of MWPC1 and MWPC2 allow to determine the vertical angle ϕ of particle track with respect to the median plane.

To calculate particle coordinates different geometrical parameters must be known. A complete measurement of the chamber and its position in the detection system before the beginning of the experiment could be one possibility to obtain them.

The accuracy of the position reconstruction can be tested by comparing the calculated coordinates with the coordinates given by the GEANT simulation. For this test particle tracks have been simulated in the whole momentum and angular acceptance of the spectrometer. In addition physical processes like multiple scattering were included. The difference of the two coordinate values (in mm) is shown in Fig. 1 for the x and y coordinates in the chamber MWPC1 and MWPC2.

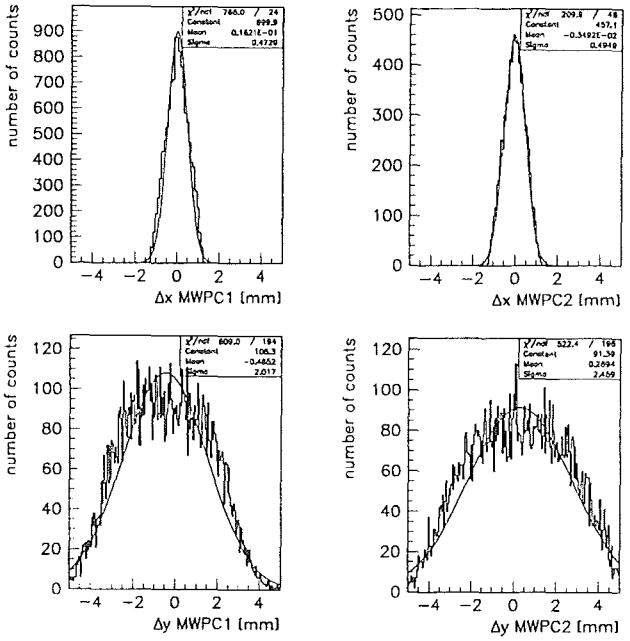

Fig. 1: Difference in mm between simulated and reconstructed x and y coordinates for the chambers MWPC1 and MWPC2.

The x-position resolution is about 1.1 mm FWHM, better than half a wire distance. For the y-coordinate the resolution is lower due to a larger wire distance of about 5.1 mm in the vertical direction. More detailed studies have shown that the obtained position resolutions are independent of the particle momentum and the angle of its trajectory. The discussed procedure for the reconstruction of local track coordinates does not take into account the fringe field of the D2 spectrometer. Tracks are assumed to be straight after the spectrometer exit. Additional investigations have to be performed to include events with more than one detected particle and events without complete chamber informations as already mentioned. Further improvements of the program will give more accurate particle track positions and better resolutions, especially for the y-coordinates.

References:

1. Schult, O.W.B. et al., Nucl. Phys. A583 (1995) 629

[a] Institut für Kern- und Hadronenphysik, Forschungszentrum Rossendorf, Dresden

MWPC–Test for ANKE at COSY

L. v. Horn, Th. Kirchner[a], Ch. Schneider[a], V. Kruglov[b],

The first Multiwire Proportional Chamber for the spectrometer ANKE which will be installed at COSY in early 1997 was tested under beam conditions at the spectrometer BIG KARL.

The proportional chamber which was built at FZ Rossendorf consists of three anode planes (wire spaceing 2.54 mm) sandwiched between four cathode foil planes[1]. Its active surface has dimensions of 130 · 35 cm^2. During the experiment a gas mixture of 70% Ar and 30% CO_2 was used. Since the readout system which will be used at ANKE is still under developement, the wire chamber signals were read out by two different systems. Analog signals could be obtained from 160 channels connected to LeCroy amplifiers while 256 logical signals were provided by amplifier–discriminator cards which were manufacted at the JINR, Dubna.

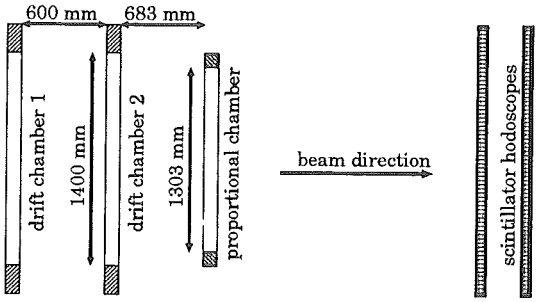

Fig. 1: Setup at the focal plane of BIG KARL. Drift chambers and the scintillator hodoscopes where provided by the GEM collaboration.

After first successful tests with radioactive sources in Rossendorf, the measurements at COSY concentrated on efficiency and spatial resolution of the wire chamber for minimum ionizing protons. In further experimental runs, data for inclined particle tracks were taken. At ANKE it is expected that investigated particles will impinge upon the chamber with angles up to 30°. With the help of the GEM collaboration[2] it was possible to use the position information of the Cracow drift chambers as a reference. The experimental setup is shown in figure 1.

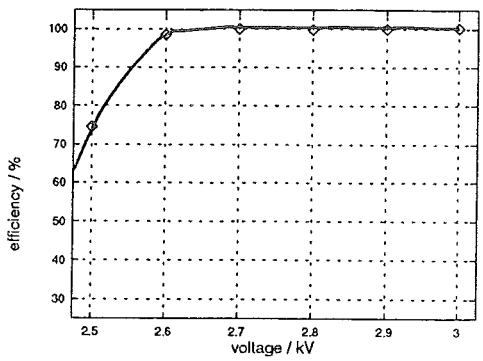

Fig. 2: Efficiency of one plane of the wire chamber for 1 GeV/c protons.

During the experiment the wire chamber operated well which is indicated by the efficiency curve shown in figure 2.

Figure 3 shows the measured resolution for the proportional chamber obtained with the Dubna amplifiers. An analysis of the data taken by the LeCroy readout gives similar results. Considering small–angle scattering and the drift chamber resolution, it can be shown that the position resolution of the proportional chamber is about 1.7 mm (FWHM) as expected for the wire spaceing of 2.54 mm.

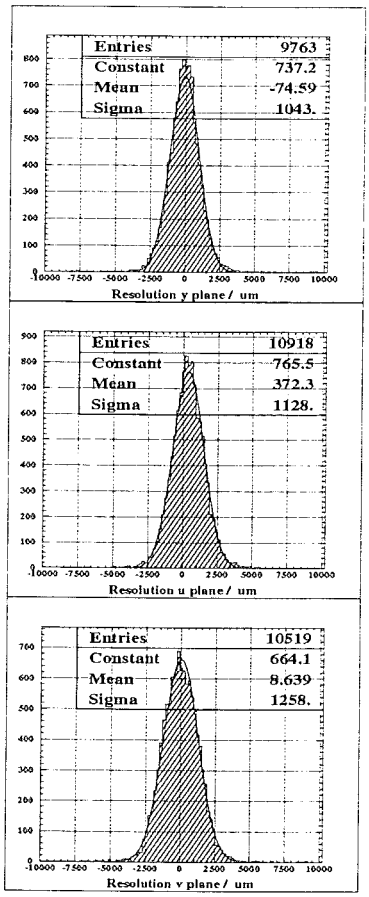

Fig. 3: Difference of drift- and proportional chamber positions. Taking into account small-angle scattering (σ = 460 μm) effects in the air between drift and proportional chambers and drift chamber resolution (about 1.6 mm FWHM) in the plane of the proportional chamber a position resolution of about 1.6 mm (FWHM) chamber has been calculated for the proportional chamber.

References:

1. L. von Horn et al., Ann. Rep. 1994, Institut für Kernphysik, Forschungszentrum Jülich
2. A. Budzanowski et al., Ann. Rep. 1993, Institut für Kernphysik, Forschungszentrum Jülich

[a] Institut für Kern- und Hadronenphysik, Forschungszentrum Rossendorf, Dresden

[b] Laboratory of Nuclear Problems, Joint Institute for Nuclear Research, dubna, Moscow Region, Russia*

* Supported by grant 93-02-3745 of the Russian Foundation for Fundamental Research.

Status of the 2nd Multiwire Proportional Chamber MWPC2 for the ANKE-Facility

T. Kirchner[a], H. Müller[a], Ch. Schneider[a], L. v. Horn, H. Ohm and V. Kruglov[b]

The reconstruction of particle tracks at the ANKE-Facility will be assured by two multiwire chambers running in proportional mode. The first chamber MWPC1[1)] has been constructed and tested with success. The construction of the second chamber MWPC2 will be based on the experience acquired for the first. Although the principle geometrical layout of the 2nd wire chamber is basically unchanged compared to the first chamber, its much larger size demands additional detailed investigations concerning the mechanical tension and diameter of the anode wires, thickness and type of cathode-foils. The following will resume the outcome of these investigations.

The MWPC2 is located closer to the focal surface of the spectrometer magnet D2. Using GEANT calculations the position distribution of ejectiles can be simulated at this location. From this distribution (see Fig. 1) the sensitive area of the chamber can be deduced. For our purpose it has to be 600 mm × 1961 mm, in order to detect the particles emitted within the spectrometer acceptance.

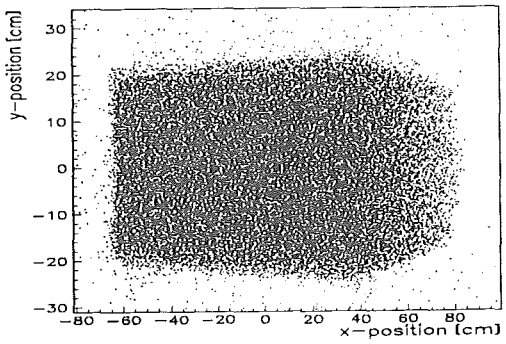

Fig. 1: Position distribution of particles within the momentum range of 150 MeV/c to 600 MeV/c at the location of the 2nd multiwire chamber.

The vertical and inclined (± 30° with respect to the vertical axis) anode wires must be stretched by 70 g each in order to withstand the electrostatic forces during the operation of the chamber. In this case the wire tension is a factor of ≈ 1.6 higher than the critical wire tension T_C = 45 g necessary for the equilibrium between the mechanical and electrostatic forces under operation conditions. The 20 μm wires used in the first chamber are not strong enough to withstand 70 g. Therefore, the wires in the new chamber will have a diameter of 25 μm. A total of 768 wires in each anode plane leads to a total force on the corresponding frame of ≈ 45 kg. The dimensions of the frames must be large enough in order to carry this force. Frames with outer dimensions of 900 mm × 2161 mm will satisfy the needs. Further parameters of the 2nd wire chamber are the gap of 5 mm and a wire distance of 2.53 mm, the same as for the MWPC1. For operation a gas mixture of Argon, CO_2 with a small quantity of Freon (≈ 2%), will be used and the high voltage will be applied, which is estimated to be ≈ 3.4 kV. This value is higher than at the MWPC1 because it takes into account the larger diameter of the anode wires in order to have the same signal (charge) on the wire. This allows to use also the same read-out electronics being developed for the first chamber. The operation parameters have to be verified when the construction of the chamber is finished.

References:

1. Ch. Schneider et al., Ann. Rep. 1994, Institut für Kernphysik, KFA Jülich GmbH

[a] Institut für Kern- und Hadronenphysik, Forschungszentrum Rossendorf, Dresden

[b] Laboratory of Nuclear Problems, Joint Institute for Nuclear Research, Dubna, Moscow Region, Russia*

* Supported by grant 93-02-3745 of the Russian Foundation for Fundamental Research.

A LED-based monitoring system for scintillation and Cerenkov counters at ANKE

B. Prietzschk[a], B. Rimarzig[a], A. Schneider, R. Schleichert, R. Eßer, H. Ohm

The gain and timing stability of scintillation and Cerenkov counters at ANKE will be monitored with pulsed light emitting diodes (LED). The decision in favour of LEDs over laser-based systems has been made since the LED system is more flexible. Delays can easily be changed which is very useful for adjusting the time-of-flight based trigger of ANKE[1].

It is known that LEDs show some systematic variations of the light output which, however, can be kept under control. Therefore, a detailed investigation of the LED performance was carried out.

There is a temperature dependence of the light output with a typical magnitude of -1 % K^{-1}, see fig. 1.This value varies even between different LEDs of the same type. Consequently, the temperature dependence has to be known for each LED separately. The temperature will be measured by several temperature sensors in various places of the detector system. Furthermore there are ageing effects increasing with the LED current. This effect is of minor importance only when the number of pulses applied to the LED is relatively low[2]. A constant DC current was sent through the LED while the light intensity was measured with a PIN photodiode directly coupled to the LED. Even at low currents (5 mA) the drop of intensity is about 40 % within several hours.

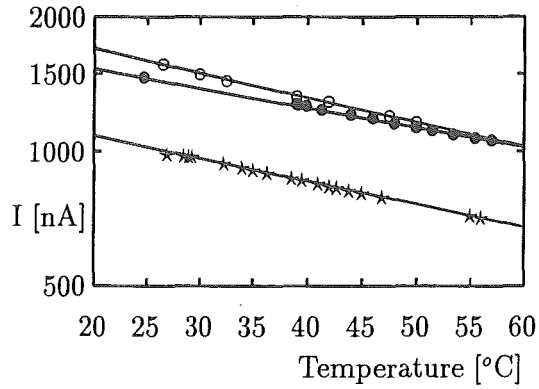

Figure 1: Variation of the light output of three red LEDs of the same type (HP HLMP 3301) with the temperature.

The intensity flattens off until almost constant light output is reached. In addition to this effect the temperature coefficient changes. However, it reaches a constant value after some burn-in. Therefore we have decided to subject all the LEDs to an ageing procedure before they are installed in the counters.

On each scintillator paddle or Cerenkov counter one LED will be mounted in the center of the surface parallel to the particle trajectory. New 'ultrabright' LEDs which became available recently[3] deliver enough light so as to illuminate each photomultiplier tube (PMT) at the ends of the paddle with sufficient intensity. With this position of the LED it is possible to monitor not only the gain of the individual PMTs but also the quality of the optical joints between scintillators, light guides and PMTs.

A pulse generator has been developed which delivers fast pulses with adjustable amplitudes up to 12 V. The timing resolution of a scintillation counter obtained with LED pulses is approximately the same as with minimum ionizing particles traversing the counter. This generator is triggered with logical signals delivered by a commercial device allowing to select a precise delay between a reference signal and the LED pulse. In that way the time of flight of the particles to be considered can be simulated. The pattern of the LEDs which fire will be determined under computer control either directly from a PC or via a CAMAC output register, see fig. 2. The pattern information is sent to a controller which feeds it into the appropriate number of subsequent LED pulser units. For each LED output to be fired a bit is set which opens a gate for the trigger signal. In addition it is possible to select individual LED pulser channels manually for applications of the pulse generators in small laboratory experiments.

[a] Institut für Kern- und Hadronenphysik, Forschungszentrum Rossendorf, Dresden

References:
1. R. Schleichert, contribution to this report, p. 65
2. G. Anton et al., NIM A274 (1989) 222.
3. HEWLETT PACKARD, Optoelectronics Designer's Catalog 1993, p. 3-3

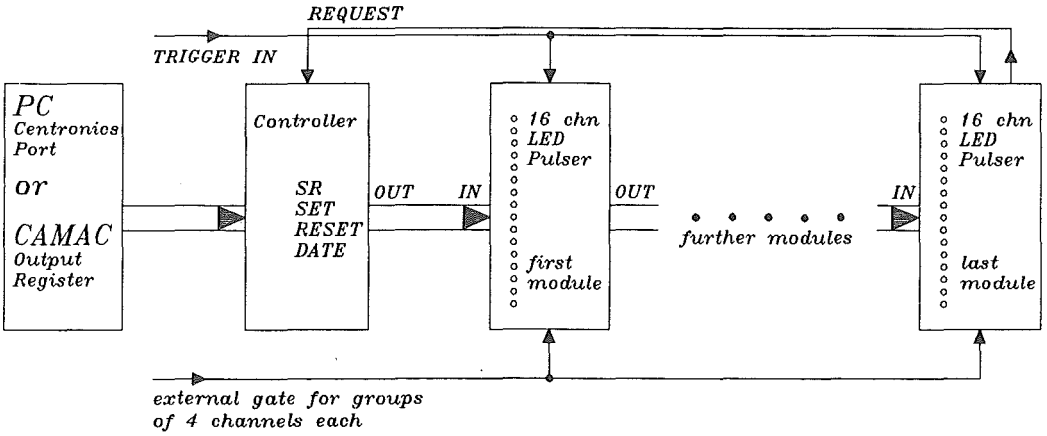

Figure 2: Schematic diagram of the control unit and the LED pulsers.

Development of a Constant Fraction Discriminator and Meantimer

R. Schleichert ,A. Selikov*, H.H.T.S.R. Seyfarth

The side detector of the 0°-Facility at COSY is among other aims designed to study the kaon production mechanism as near as possible to the kinematic threshold. Reasonable kaon detection rates in the order of $1s^{-1}$ at forward emission angles can be obtained with internal targets at high luminosities of up to $L=4*10^{32}cm^{-2}s^{-1}$. For a ^{12}C strip target this corresponds to 10^7 particles per second going through all the start counters and about $5*10^5s^{-1}$ particles going through all the stop counters of the side detector. To discriminate the kaons from direct and scattered protons and pions, it is essential to have a good resolution for the time of flight measurement. The efficiency of the fast trigger system for the side detector is mainly dependent on this time resolution. The time of flight measurement is accomplihed by scintillators with lengths up to 1m. To derive good timing signals, the disturbing effects as position dependence of the signals and the amplitude walk effect have to be compensated. The amplitude walk effect can be compensated by the use of *constant fraction discriminators*. The position dependence of the scintillator signal can be compensated by mounting 2 photomultipliers at both ends of the scintillators. Both discriminated signals will be fed into a meantimer, the output signal of which shows no longer a position dependence.

Here we present the results obtained with our new-developped triple width CAMAC module with 16 Constant Fraction Discriminators and 8 inherent meantimers. It has 16 analog LEMO inputs, 16 activ analog outputs, 16 ECL discriminator outputs, 8 ECL meantimer outputs and (as Fan Out) 8 fast NIM meantimer outputs. First results with a single-channel prototype have already been given [1].

Fig.1 shows the time walk measured for 1 channel with a pulse generator over a range from -4V to -40mV. The input pulses had a leading edge of 2ns and a trailing edge of 13ns which approximately corresponds to the pulses generated by photomultipliers.

Each data point in Fig.1 corresponds to a time distribution measured with a TDC of 25ps bin width. Fig. 2 shows the standard deviations. Only for amplitudes below 100mV they rise but nearly over the whole range they equal to the intrinsic resolution of the test equipment.

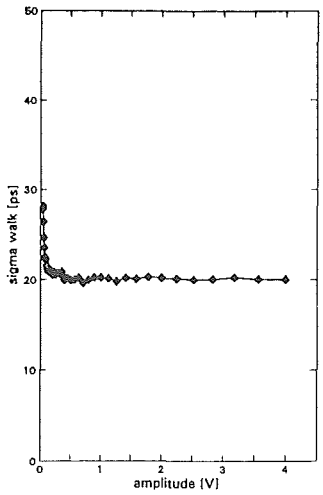

Fig. 2 The standard deviation for every point which is shown in Fig.1

The cross talk between neighbouring channels has been measured by feeding a digital -800mV, 2ns leading and trailing edge signal into a reference channel whereas the neighbour channel had to deal with a digital -2V, 800ps (nominal) leading and trailing edge signal. Fig.3 gives the distortion by cross talk for the reference channel as function of the delay between the signals. Over the full range it is within ±60ps but we hope to improve the behaviour by introducing special filters into the power supply lines.

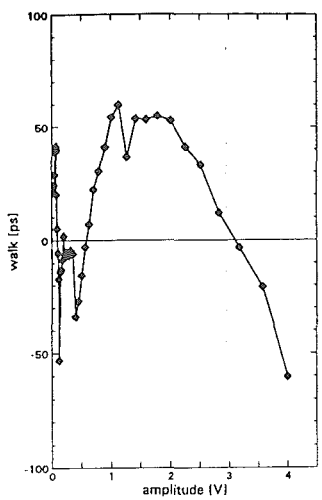

Fig. 1: Time walk for the Constant Fraction Discriminator measured with a pulse generator and attenuator. Over the full range the time walk is within ±60ps.

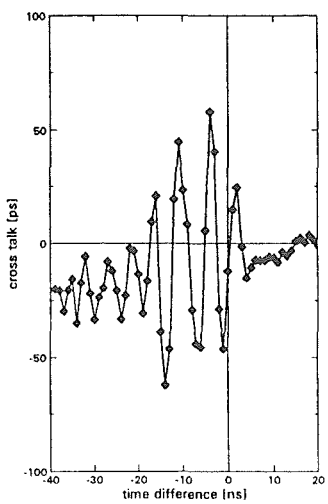

Fig. 3 The distortion by cross talk. Over the full range it is below 60ps. In can be reduced by a better blocking against distortions transmitted through the power supply lines.

The pulse generator measurements have been checked by measurements with photomultipliers. A 4mm thick plastic scintillator has been equipped with 2 photomultipliers. Signals were generated by irradiating the scintillator with a Na^{22} source. Naturally the amplitude spectrum is wide but event by event the pulse amplitudes from both photomultipliers are approximately equal. Both signals were fed into constant fraction discriminators but one signal can be attenuated by an attenuator. With a threshold of -30mV and zero attenuation the mean value of both spectra has been adjusted to 1V by adjusting the high voltage. The start signal for the TDC is always given by the non-attenuated output signal of one photomultiplier. The stop signal is defined by the other one. Fig.4 shows the walk against the mean time difference. Every data point represents the mean value of 1000 events.

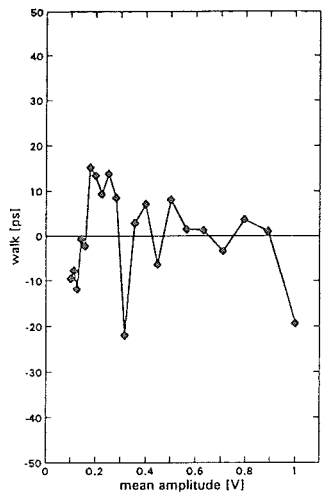

Fig. 4: The walk curve for the measurement with 2 photomultipliers.

The walk is below ±20ps. The sigma of each distribution is about 150ps and almost independent of the attenuation.

The meantimers have been checked by feeding standard NIM signals into the discrimnator channels. The time of the leading edge of the output signal of each meantimer should be given by the mean value of the times when the input signals occur. The deviation from this behaviour is shown in Fig.5.
The deviation from the ideal behaviour is within ±50ps which means that it will not significantly affect the time resolution in the ANKE experiment

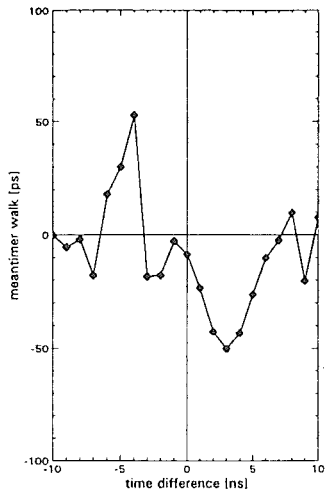

Fig. 5: The meantimer walk. Each point represents the mean value of 10000 events.

References:
[1] R. Schleichert et al., Annual Report IKP 1994, report Jül-3035 (1995), p.66

* JINR Dubna and Moscow State University, supported by RFFR grant 93-02-3745.

First Module of the Forward Detector Proportional Chambers of the ANKE Spectrometer

V. Komarov[a], A. Kulikov[a], A. Puzynin[a], A. Rudenko[a], H. Seyfarth, B. Zalikhanov[a]

Proportional chambers of the forward detector are intended for detection of high energy particles ejected from a target in the forward direction. These chambers must fit the following requirements:

- capability to operate at high particle flux. Monte-Carlo simulations yield counting rates as large as $5 \cdot 10^7$ s^{-1} per plane and up to $3 \cdot 10^5$ s^{-1} per wire at the luminosity L = 10^{33} $cm^{-2}s^{-1}$;
- to reach high momentum resolution, the signal-wire distance has to be 1 mm at a maximum wire length of 550 mm;
- space limitations by the COSY-beam pipe and the side detectors on one hand and the aim to cover a maximum momentum range on the other hand necessitate a lean frame construction.

All these features can be realized with a special type of chambers described here. There will be three modules each containing (vertical) X and (horizontal) Y wire planes and two strip planes.

The first module has been produced. Its sensitive area is 320 x 256 mm^2. The geometry of one half of the chamber is shown in Fig. 1. Signal wires made of 30 μ diameter Au-plated W lie on a dielectric foil with resistivity ρ = 10^9 Ohm · cm. From the opposite side the foil is in contact with strips made by covering mylar foil with conductive Ag paint and inclined by 18° to the X wires. The cathode plane, made of carbon plated mylar, is at 1.5 mm distance from the anode wires.

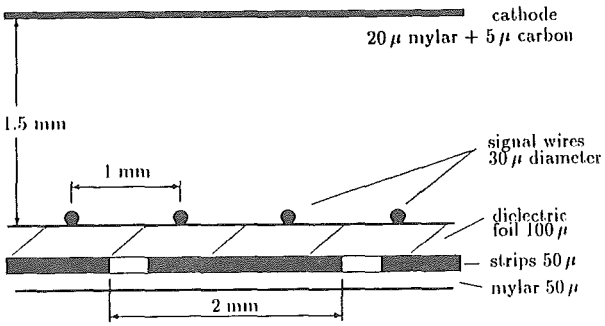

Fig. 1: Geometry of one half of the chamber.

The main role of the dielectric foil is to fix the positions of the signal wires without applying a dangerously high tension. With the chambers of conventional type it is very difficult to realize stable operation at 1 mm signal-wire distance and 550 mm length. In the chambers described here this problem is resolved: the signal wires are pressed (and thus fixed in their position) to the dielectric foil by forces created by the strong electric field to the strips. Another advantage of this scheme is the low multiplicity of hit strips. For most events only one strip gives a signal due to the small distance between wires and strips. The small anode-cathode gap provides low multiplicity of hit wires, too. The small gap combined with a fast gas mixture (80% CF_4 + 20% isobutan) results in very short (~ 10 ns) signals and low jitter that is essential at high rate conditions.

There are not bulky frames in the chamber. This helps to save space outside the sensitive area. The frame of the whole chamber is made of Al profile, stretching of the foils and subjecting the wires to tension is ensured by a special technology using rods of stainless steel[1]. The beam-up view of the chamber is shown in Fig. 2. The connectors for front-end electronics are placed at the upper and lower edge of the frame and, looking beam-up, to the left of its beam-down front side. The right side (close to the beam-pipe) is free of any connectors. The total number of signal channels in this module is 960 including 320 X wires, 192 U strips (X + 18°), 256 Y wires, and 192 V strips (X - 18°).

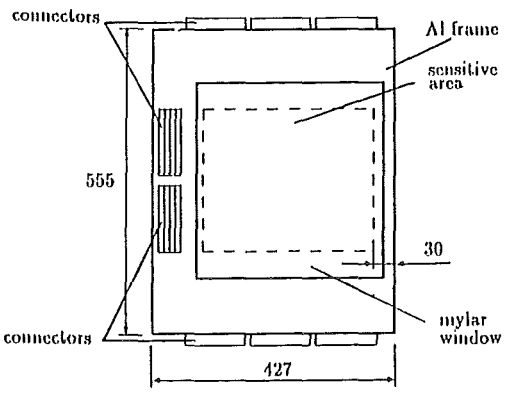

Fig. 2: Beam-up view of the chamber (the beam pipe will be close to the right edge of the chamber).

The chamber was tested with a ^{90}Sr ß-source using front-end electronics developed in JINR. They included 32-channel preamplifier boards placed on the chamber and 16-channel amplifier-comparator boards in a dedicated mini-crate. The efficiency characteristics, time and amplitude spectra were measured both for wires and strips. Measurements were made at intensities up to (1 - 2)·10^5 minimum ionizing particles per second and wire. The efficiency curves for the Y wires and strips, taken at the highest intensity, are shown in Fig. 3. The

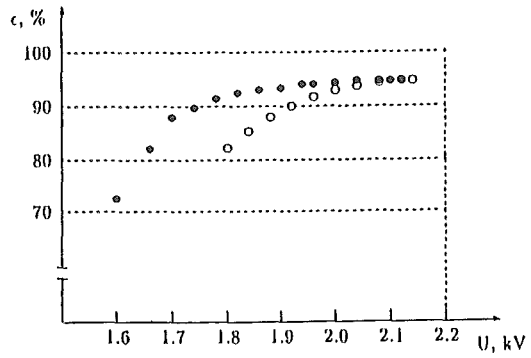

Fig. 3: Measured efficiency of wires (full) and strips (open) as function of voltage on the strip plane (final correction see text).

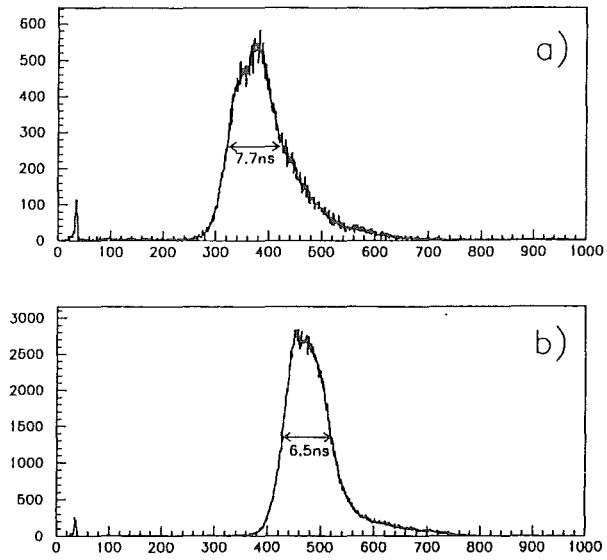

Fig. 4: Time spectra of signals from a single wire (a) and from 32 OR'd strips (b). One channel corresponds to 71 ps.

absolute efficiency lies slightly higher because part of the low energy electrons from the source pass the chamber outside the area of sensitive wires, but hit the trigger counter due to large scattering angles. In Fig. 4 time spectra from the chamber are shown. The threshold of the comparators was 1 μA and the start signal was taken from the trigger scintillation counter. The upper spectrum is for a single wire, the lower one is for 32 OR'd strip signals.

A rough estimate of the cluster distribution shows that for 94% of the events only one wire has fired and no clusters wider than three wires are observed. The parameters of singlas, with an oscilloscope, are as follows: the risetime is 2 ns, the full width (at 10% level) is 10-12 ns for wires and around 15 ns for strips. So the first tests of the forward detector proportional chamber demonstrate its capability to work under the hard conditions of the forward region.

Reference:

1. H. Kalmar et al., Nucl. Instr. and Meth. A307, 279 (1991)

[a] Laboratory of Nuclear Problems, Joint Institute for Nuclear Research, dubna, Moscow Region, Russia*

* Supported by grant 93-02-3745 of the Russian Foundation for Fundamental Research.

Feasibility of the Use of Cerenkov Counters in pd Interaction Studies at the COSY 0° Facility (ANKE)

A.K. Kacharava[a,b], G.G. Macharashvili[a,b], V.I. Komarov[b], A.V. Kulikov[b], M.S. Nioradze[a], V.S. Sopov[c], V.P. Tchernyshev[c]

The possibility of the use of Cerenkov counters of total internal reflection in the pd-interaction studies at COSY is considered. The proposed Cerenkov counters have been described recently[1,2]. In this type of counter the light propagates via total internal reflection in the radiator. Therefore, the detection threshold can be tuned by rotation of the detector relative to the particle direction. Such counters are proposed for particle separation in the FD detector system of ANKE. The results of Monte Carlo simulations of the characteristics of the proposed detectors, as well as of tests carried out at the ITEP accelerator are presented.

The simulation procedure has been described in detail[2]. The PM pulse heights expressed in the number of photoelectrons are obtained for various momenta of protons and π mesons. It has been assumed that $\Delta p/p$ = 10% over the width of the detectors and that the particle entrance angle varies in the range $\delta \in [0°,4°]$. The photoelectron number fluctuations were taken into account assuming the Poisson distribution. The typical simulated pulse height spectra for protons and pions, obtained at perpendicular placement of the radiator, are presented in Fig. 1. These spectra have been simulated for various momenta at optimal radiator inclination angles. On the basis of the simulated data the 'fast particle detection efficiency' (pions) has been plotted in fig. 2 at the fixed 'slow particle loss probability' (protons). The 'slow particle loss probability' (misidentification as fast particles) is fixed to 10% for the lower curve and 20% for the upper one. The test gave a value of 98% for the pion identification efficiency and 15% misidentified protons, cf. in Fig. 2. The corresponding plot of the proton identification efficiency against deuterons is shown in Fig. 3.

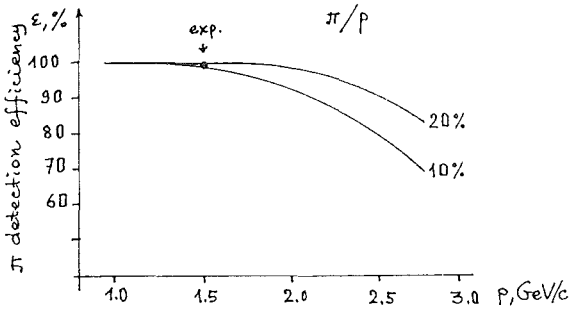

Fig. 2: Pion detection efficiency for 10% and 20% misidentified protons vs momentum. The measured value is shown.

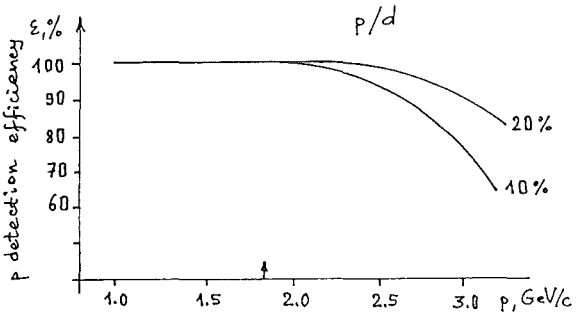

Fig. 3: Proton detection efficiency for 10% and 20% misidentified deuterons vs momentum. The arrow denotes the Cerenkov threshold for deuterons.

The Cerenkov counter prototype was a plane parallel radiator made of lucite (n = 1.49) with a 2" PM FEU-143 glued on one end. The radiator was polished on all sides except the side opposite to the PM and wrapped up into a

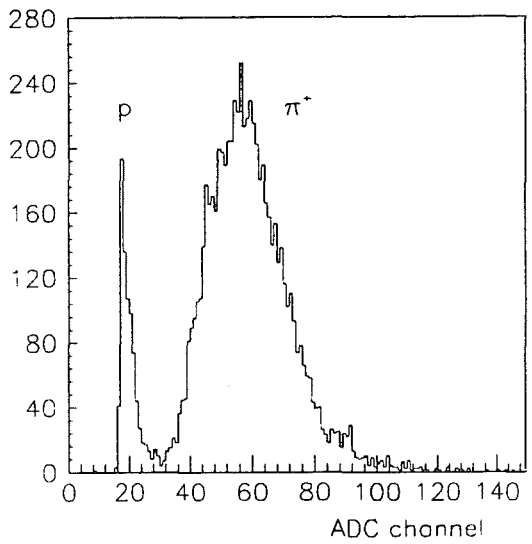

Fig. 1: Typical simulated pulse height spectra for protons and pions, obtained at perpendicular orientation of the radiator.

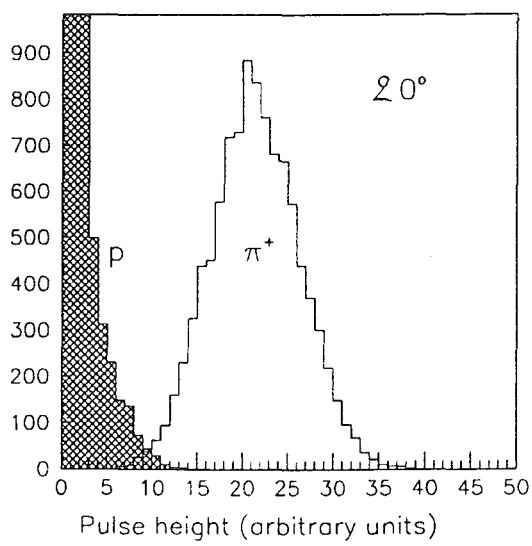

Fig. 4: Result of the test of the Cerenkov counter prototype for optimal inclination angle 20°. The pion beam contained 10% protons.

black paper to suppress diffusion reflection. The dimensions of the radiator were 8 × 5 × 60 cm^3. The counter prototype has been tested in the ITEP-accelerator secondary beam of 1.5 GeV/c containing protons and pions. The test results for the optimal inclination angle 20° are presented in Fig. 4. Using this curve we conclude that the pion beam contained 10% protons.

The tasks that could be resolved using the Cerenkov-counter response at the trigger level are the following: discrimination of fast and slow protons, deuteron identification in pd elastic scattering at 180°, and pion-proton discrimination. The last one needs more detailed consideration. The pulse heights from the Cerenkov counters can be used also in off-line data processing, when the particle momentum and direction are already defined. Using the Cerenkov pulse heights, the particle type can be defined with higher confidence level. An important aspect of the use of this type of Cerenkov counters is that they do not need complicated engineering and manufacturing, and that the threshold tuning is simple.

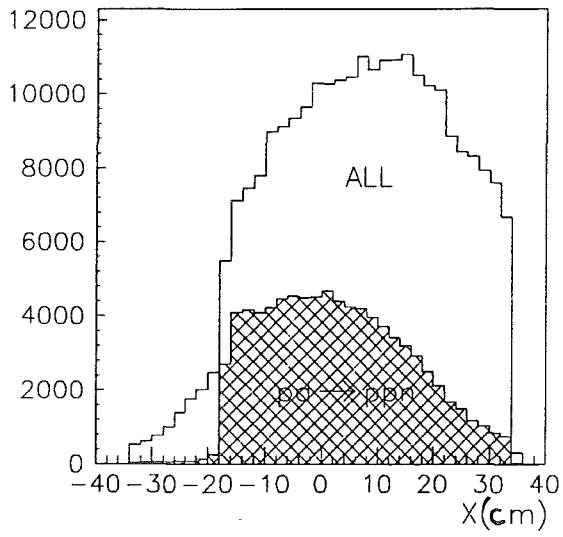

Fig. 5: The relative counting rate for the plane of Cerenkov counters. The shaded area corresponds to protons from the deuteron break-up.

In Ref.[3] (table 1) the estimated counting rates of the FD detector system at a luminosity of L = 10^{30} cm^{-2} s^{-1} have been obtained with the use of experimental data in pd interactions at 1.7 GeV/c. In Fig. 5 the relative counting rate of charged secondaries from the pd interaction is presented for the plane of Cerenkov counters. The shaded area corresponds to protons from deuteron break-up. One can see that the counting rate is approximately uniform in transverse direction. The counting rate in the vicinity of the vacuum chamber of the accelerator is expected to be somewhat higher. Therefore, all Cerenkov counters must have similar transverse dimensions except the ones placed close to vacuum chamber.

Spectra and composition of particles that hit the FD detector system are given[3] for pd interactions at 1.7 GeV/c momentum. The spectrum of π mesons extends up to 0.7 GeV/c at this momentum and the fraction of pions is small. But at 3.3 GeV/c incident momentum π mesons have momenta up to 1.5 GeV/c. At the same time the number of π^+ increases by one order of magnitude due to the increase of the two meson production cross section.

References:

1. A. Kacharava et al., 1994 Annual Report, KFA Jülich (1995) p. 70
2. A. Kacharava et al., JINR preprint, E1-95-380, Dubna (1995)
3. A. Kacharava et al., contribution to this report, p. 74

[a] High Energy Physics Institute, Tbilisi State University, Tbilisi, Georgia

[b] Laboratory of Nuclear Problems, Joint Institute for Nuclear Research, Dubna, Moscow Region, Russia

[c] Institute for Theoretical and Experimental Physics, Moscow, Russia

A Polarised Deuterium and Hydrogen Gas-Cell Target for the ANKE Project

V. Nelyubin[a], H. Seyfarth, A. Vasiliev[a], V. Koptev[a], O.W.B. Schult

The experiments, planned for the spectrometer ANKE with polarised COSY proton beam and/or internal polarised hydrogen or deuterium target[1)] necessitate the development of the polarised atomic source (ABS) and the appropriate gas target set-up. Internal polarised gas targets are used now at storage rings in BNPI (Novosibirsk), NIKHEF (Amsterdam), IUCF (Bloomington), and by the HERMES-collaboration at DESY (Hamburg). The decisive parameters of the ABS and target are now well known[2,3)]. The experience from operation of these installations and also of the polarised proton source for COSY[4)] is used in developing the target for ANKE.

The target will be placed between the first beam-bending dipole magnet D1 and the spectrometer dipole magnet D2 (see fig. 1 or ref. 1). The gas-target cell consists of a windowless tube of 40 cm length positioned coaxially around the proton beam. Such a target allows to increase the target thickness or luminosity by about 2 orders of magnitude compared with polarised gas-jet targets[5)].

A magnetic field of variable strength and direction at the target position would be desirable to allow any wanted target-gas polarisation. Therefore the strong magnetic stray field in front of D2 has to be reduced from about 1000 G to a few Gauss by appropriate shielding. In addition to the target-cell region also for other components of the ABS critical upper limits for the magnetic field strength have to be regarded.

1. In the radio-frequence transition units the values of the magnetic holding fields have to range from a few Gauss up to about hundred Gauss. Thus there the final shielding has to yield rest fields in the order of Gauss.

2. The turbomolecular pumps are allowed to work in magnetic fields not exceeding 130 Gauss[6)].

The integral value of the stray field, calculated with the 2-dimensional computer code POISSON, and the assumption that the magnetic flux density in an additional field clamp should not exceed 1 T, as first approximation yield 8 cm as minimum thickness of a field clamp. With use of the computer code MAFIA, 3-dimensional field calculations have been performed to obtain the distribution of the magnetic rest field between D1 and D2 with the field clamp of fig. 1 in front of D2 (fig. 2). In the coordinate system defined in fig. 2, the iron sheet of the field clamp ranges from z = -92 cm to z = -100 cm. The ABS will be installed in front of the field clamp vertically in the +y direction. In fig. 3 we show the calculated distributions

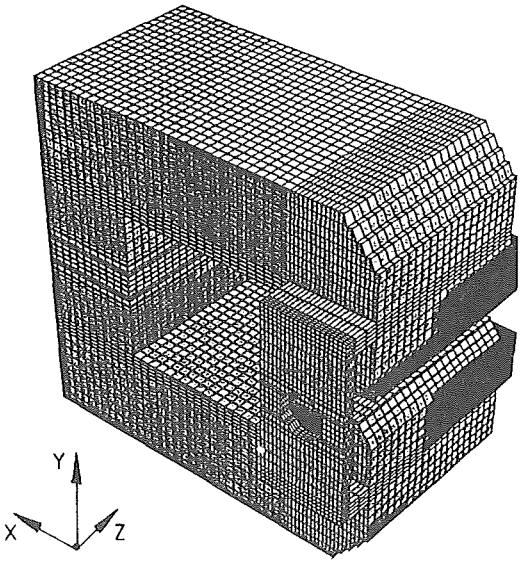

Fig. 2: The dipole magnet D2 with the field clamp and the mesh grade used in the calculation. The origin of the used coordinate system, also shown, lies in the center of the gap. Thus the front edge of the iron yoke is at z = -70 cm.

of the magnetic field component B_y from the region in front of D2 to the center of the dipole magnet D2 along the center line of the gap (z axis). Due to the up-down symmetry of the magnet the x and z components

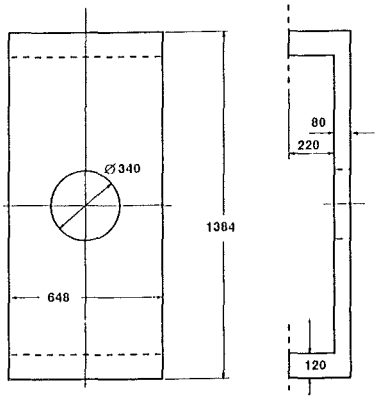

Fig. 1: Dimensions (mm) of the field clamp used in the first 3-dimensional magnetic rest-field calculations. Its magnetic properties have been assumed to be those of the dipole magnet D2.

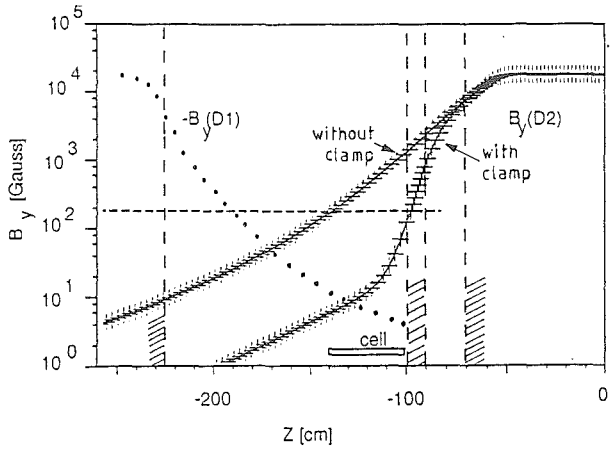

Fig. 3: Calculated distributions B_y along the z axis (x = 0 cm, y = 0 cm). From left to right the dashed vertical lines indicate the iron-yoke edge of D1, the edges of the field clamp, and the iron-yoke edge of D2.

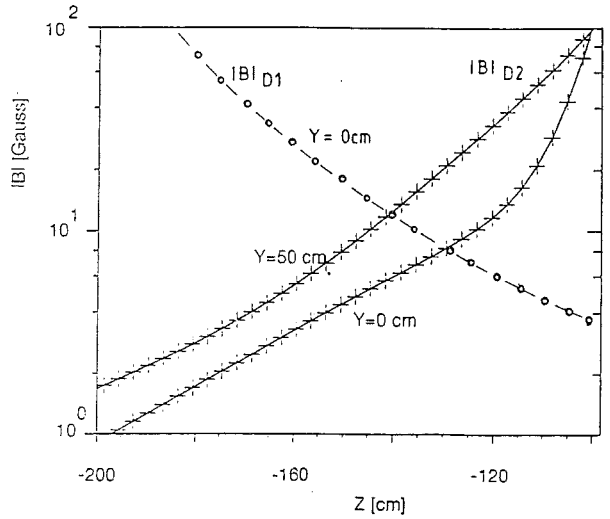

Fig. 4: Distributions of |B| in front of the dipole magnet D2 calculated with the field clamp of fig. 1. In the medium plane (y=0) the direction of the field from D1 is opposite to that from D2 ($B_x = B_z = 0$).

have to be zero. The figure also shows the stray field from D1 calculated with the POISSON code. A possible position of the target-cell tube is indicated. Without the field clamp, the strength of the stray field from D2 is > 200 Gauss over the whole tube length. Being used as holding field it allows, e.g. tensor polarisation P_{zz} = -2 and +1 for deuterium with use of the medium and strong field rf-transition units in the ABS (states 2+5 and 3+6, respectively, following the numbering of ref. 7).

In an enlarged scale, fig. 4 shows calculated distributions of the absolute stray-field strength from D2 in front of the clamp in the medium plane (target-cell region) and 50 cm above (region of the weak and strong field rf-transition units). In addition the figure contains the (unshielded) absolute value of the stray field from D1, the direction of which is opposite to those from D2. Obviously the resulting total field even changes the sign at z = -130 cm. Thus, with the present fields it is impossible to obtain an appropriate weak homogeneous holding field of about 5 Gauss by simple Helmholtz coils around the target cell. Further studies have to investigate the possibilities to create a sufficiently homogeneous weak holding field around the cell tube.

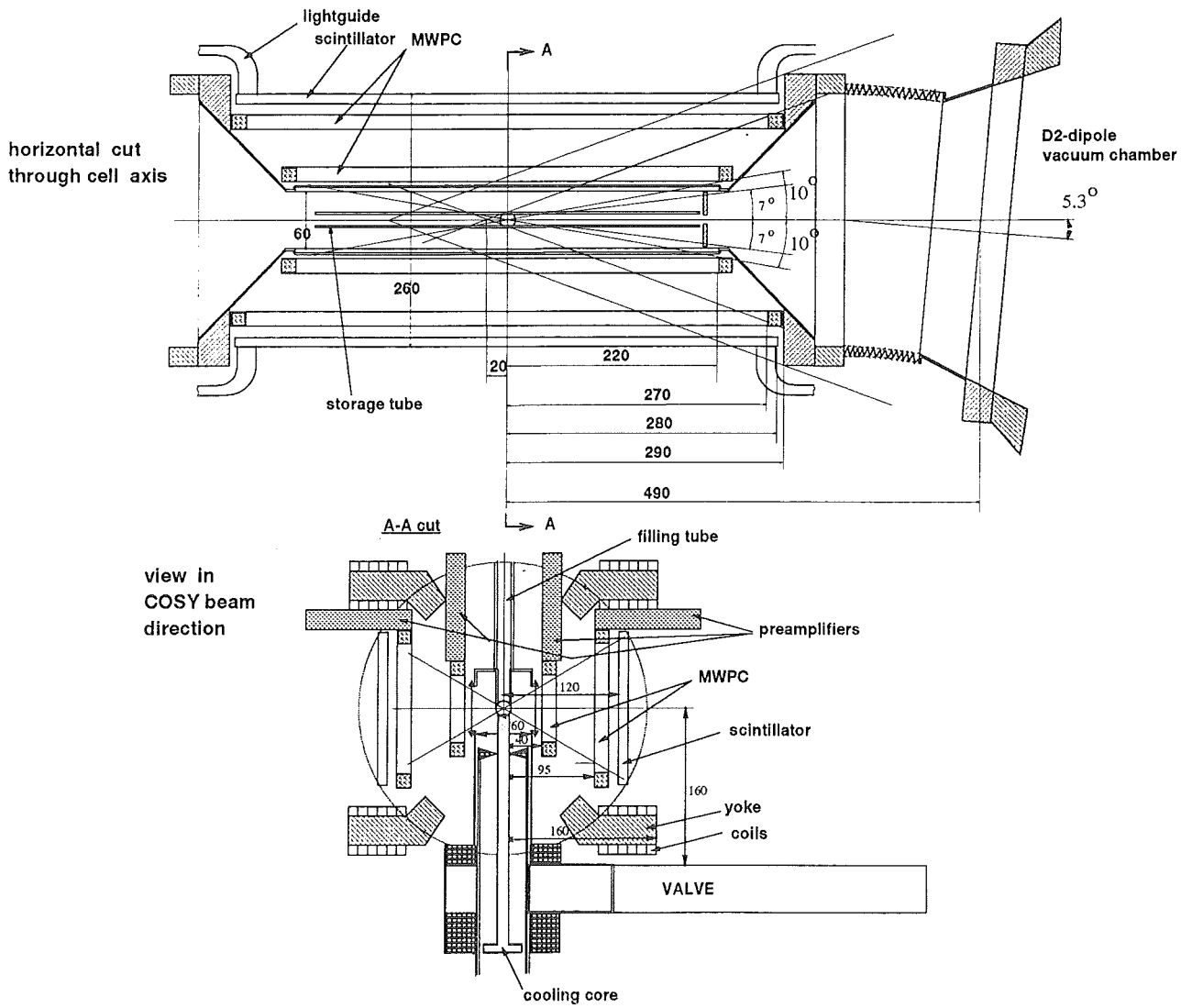

Fig. 5: A possible set-up with target cell, cooling finger, vacuum chamber, polarimeter detectors, and holding-field coils (description in the text, dimensions in mm).

Application of a strong external holding field at the target tube would allow to overcome these problems. Its strength has to be $\gtrsim B_{crit}$, where the critical field strength is 117 and 507 Gauss for deuterium and hydrogen, respectively.

The coil system to produce these fields has to provide space for the detectors of a polarimeter set-up or future detectors surrounding the target to measure, e.g. decay products from short-lived reaction products.

The fig. 5 shows one of various possible solutions for the cell tube with the cooling finger, the surrounding vacuum chamber, the polarimeter detectors, and the coil system. The fixed gas-filling tube ends at the upper wall of the vacuum chamber. The cell tube, mounted on a cooling finger and connected with the lower end of the filling tube, can be removed through the rectangular valve window (open area about 5 cm x 45 cm) without further disassembling. This solution would allow easy use of the COSY beam for other experiments and work on the cell (and possible future detectors around it) in the laboratory. The multiwire proportional chambers (MWPC) and scintillation counters of the polarimeter set-up can be placed near the side windows of the vacuum chamber.

The magnetic holding field is produced by four separate rectangular coils with iron cores extending parallel to the target tube. With 1 kA in the 4 coils, each consisting of 6 water-cooled windings, a 2-dimensional calculation using the code POISSON yields the field distribution shown in the fig. 6. The resulting holding field B_y is 214.53 Gauss in the cell axis, its variation over the cell cross section remains within $\pm$ 0.04 Gauss. There the B_x component is < 0.05 Gauss, too. The field is strong enough to keep the polarisation of deuterium. Additional calculations shows that closing pairs of coils by additional iron yokes yields a B_y of about 600 Gauss sufficient for hydrogen, too. The present design of the coils allows easy assembling and polarisation along the y and x axis by changing the coil connections. However, the effect of the additional external vertical or horizontal field on the COSY beam has to be studied. It may necessitate installation of a compensating coil set-up. This effect is negligible, if the coil system around the cell is used to produce a weak homogeneous field of about 10 Gauss only. This should be achievable by sets of coils on the iron yokes along the z axis or by sets of iron-free coils. Their currents could be adjusted in a way compensating the field gradients shown in fig. 4. Field calculations for such a solution have been started.

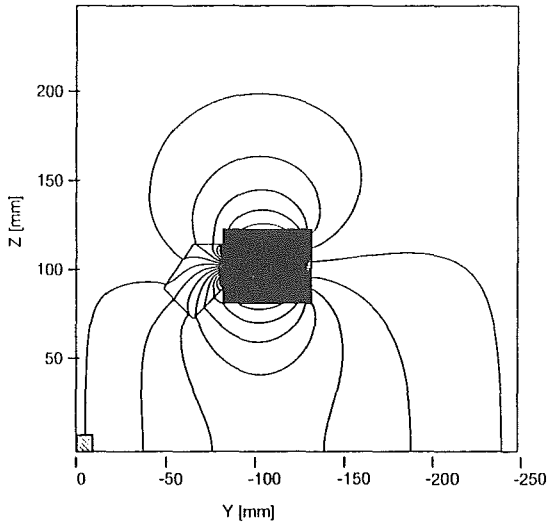

Fig. 6: One quadrant of the calculated magnetic field distribution for 6000 Ampere windings in each of the 4 coils of fig. 4. The cell tube is indicated in the lower left corner of the figure.

References:

1. K. Sistemich et al., contribution to this report, p. 51
2. Proc. Workshop on Polarized Gas Targets for Storage Rings, Heidelberg, September 1991. Edt. H.G. Gaul, E. Steffens and K. Zapfe (Max-Planck-Institut für Kernphysik Heidelberg
3. Proc. Int. Workshop on Polarized Beams and Polarized Targets, Köln 1995. Edt. H. Paetz gen. Schieck (in print)
4. R. Gebel, PhD thesis, Universität Bonn (1994) and contribution to Annual Reports IKP/KFA 1993, p. 206 and 1994, p. 244
5. W. Haeberli, AIP Conf. Proc. 128, 251 (1985)
6. BALZERS, Das Arbeiten mit Turbomolekularpumpen
7. W. Haeberli, Ann. Rev. Nucl. Sci. 17, 373 (1967)

[a] St. Petersburg Nuclear Physics Institute, Gatchina, Russia

Kinematical Characteristics of the pd Interaction and the Feasibility of Deuteron Break-up Studies at ANKE (unpolarized case)

A.K. Kacharava[a,b], V.I. Komarov[b], A.V. Kulikov[b], M.S. Nioradze[a], G.G. Macharashvili[a,b], Z.R. Menteshashvili[a], A.Yu. Petrus[b]

The system of forward detectors (FD) at ANKE which is under construction at COSY, is foreseen for studies of different facettes of the pd interaction[1]. In the present paper some specific topics of the deuteron break-up through the proton beam are considered for the unpolarized case. The importance of such investigations is discussed in Refs. 1 and 2. Here, the efficiency of the FD system for the registration of different channels of the proton-deuteron interaction is estimated as well as the possibility of identifying the events of the deuteron break-up pd → ppn and the amount of background.

Our calculations are based on experimental data obtained with the 1 meter hydrogen bubble chamber of the Laboratory of High Energies at JINR[3] bombarded with a deuteron beam at a momentum of P_d = 3.3 GeV/c, which corresponds to 1.7 GeV/c proton momentum in the deuteron rest frame (T_p = 1.0 GeV). Using the observed events of pd interactions we can estimate the physical background processes accompanying the break-up process and study the possibility of the separation of the latter. In this way the available experimental data can be used for optimization of the experimental setup for the planned studies.

The experimental setup at ANKE is shown in Ref. 4. The central part of the setup is the separator magnet D2. For the detection of particles in the forward and backward directions the systems of forward detectors (FD) and backward detectors (BD) will be used. The system of FD consists of three thin proportional chambers for the measurement of momenta and emission angles of charged particles, two one-plane scintillation hodoscopes and of Cerenkov counters of total internal reflection. The BD consists of drift chambers, two one-plane scintillation hodoscopes and anticoincidence (veto) counters. In our simulations a beam momentum of 1.7 GeV/c has been assumed and the field of D2 has been approximated by a homogeneous box field with a field strength of B = 1.05 T, which fully corresponds to the proton momentum of the used data as a basis for the calculations. For the description of the setup geometry, the determination of its characteristics, the particle tracing and the development of unified methods of data processing the program GEANT[5] has been used. The events have been generated on a point-like target placed in the circulating beam of the accelerator, at a distance of 35 cm in front of the effective homogeneous field boundary of D2. The above-mentioned experimental data obtained under 4π geometry in the hydrogen bubble chamber have been used as input events of the program (only a small part of the events of the elastic scattering at small angles has been lost). This experimental material contains all reactions with cross sections of more than 1 mb. Each input event is a set of 4-momenta of all reaction products. The total number of pd events was equal to 165,000. In order to increase the statistics during tracing through the experimental setup each event has been used 36 times with rotation in 10° steps around the beam axis. This can be justified by the non-symmetry of the setup with respect to the beam axis. By this method the statistics has been increased up to 6 million events. A particle has been considered as detected if it was passing through all detectors in the FD arm and reached the second scintillation hodoscope. On this stage of the simulation, interactions of secondary particles (electromagnetic as well as nuclear) with components of the apparatus and the air have been neglected.

It is known[6] that the dominant type of reaction in pd interactions is the mesonless break-up of the deuteron pd → ppn, with a cross section of 37.2 ± 1.4 mb. It amounts to 45% of the total cross section of the pd interaction, σ_{tot}(pd) = 82.89 ± 0.06 mb. The deuteron break-up can be considered as 'direct' break-up or 'charge exchange', depending on the type of the fastest particle. The cross sections of all reactions with $\sigma_i > 1$ mb are given in the second column of Table 1. The number of real events used in the simulation, the detection efficiency (for the individual detected particles) and the expected counting rates are also presented there.

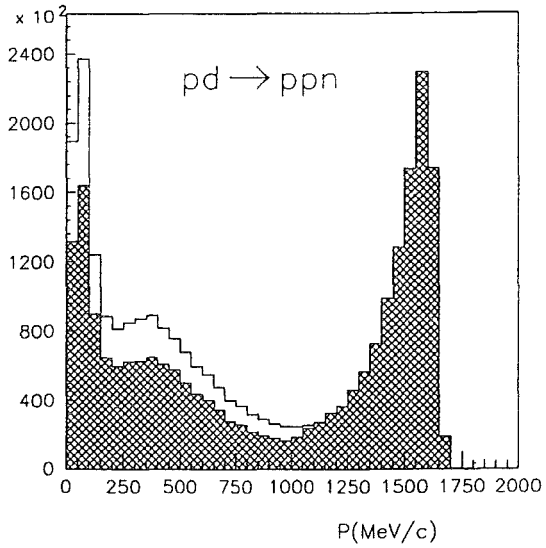

Fig. 1: Momentum distribution of protons from the reaction pd → ppn. The shaded part of the histogram corresponds to the direct channel.

In Fig. 1 the momentum distribution of both protons from the deuteron break-up events is presented with a separation into the direct (shaded) and charge-exchange channels. One can see that for the charge-exchange reaction, the momenta of protons do not exceed 1.0 GeV/c. Taking into account that the FD system is designed for the detection of fast particles, we can assume that we will mainly be sensitive to direct break-up of the deuteron.

One can also see from Table 1 the main background

processes to mesonless deuteron break-up are the following ones:

$$pd \rightarrow pd \quad (1)$$
$$pd \rightarrow p\pi^{+}(2n) \quad (2)$$
$$pd \rightarrow pp(n\pi^{o}) \quad (3)$$

The particles in parenthesis will not be detected in FD and have not been considered. Other reactions are excluded from the simulation because the sum of their cross sections at 1.7 GeV/c does not exceed 4 mb.

Table 1: Cross sections of different channels of the pd interaction[6,11-13] and corresponding counting rates p_p = 1..7 GeV/c obtained with $L=10^{30}$ $cm^{-2}s^{-1}$; $R_i = N_i\varepsilon_i\, 0.46\, L \cdot 10^{-30}/s$. Rough estimates of unpublished cross sections are denoted by (*).

$pd \rightarrow ...$	σ_i, mb	σ_i/σ_{tot}, %	N_i	ε_i, %	R_i, s^{-1}
ppn(dir)	30.1±1.2	36.3	$63 \cdot 10^3$	3.2 (p)	$0.93 \cdot 10^3$ (p)
ppn(cex)	6.4±0.2	7.7	$13 \cdot 10^3$	0 (p)	0
pd	12.2±0.4	14.5	$24 \cdot 10^3$	13 (p) $\ll$1 (d)	$2 \cdot 0.85 \cdot 10^3$ (p) 2 (d)
$pd\pi^{o}$	$\leq 1.0^{*}$	—	—	—	—
$nd\pi^{+}$	1.32±0.22	1.6	$2.8 \cdot 10^3$	not used	—
$pp n\pi^{o}$	11.2±0.4	13.5	$22 \cdot 10^3$	6 (p)	$0.61 \cdot 10^3$ (p)
$pnn\pi^{+}$	17.0±0.6	20.5	$36 \cdot 10^3$	4 (p) 0.6 (π)	$0.66 \cdot 10^3$ (p) $0.10 \cdot 10^3$ (π)
$ppp\pi^{-}$	2.2±0.2	2.7	$4 \cdot 10^3$	not used	—
$pd\pi^{+}\pi^{-}$	0.276±0.024	0.3	$0.5 \cdot 10^3$	not used	—
$ppn\pi^{+}\pi^{-}$	$< 1.0^{*}$		—	—	—
$pnn\pi^{+}\pi^{o}$	$< 0.5^{*}$		—	—	—
$\pi^{+}\pi^{+}X$	$< 0.5^{*}$		$0.2 \cdot 10^3$	not used	—

Elastic scattering pd → pd is the main background channel, because the main part of protons from this reaction is scattered at small angles and therefore will hit the forward detector. It should be noted that due to methodical reasons half of the elastic events (mainly at small angles) has not been detected in the bubble chamber[7]. These lost events correspond to small momentum transfer or small angles. The correction factor (≈ 2) will be included in all calculations related to background protons from this reaction.

The amount of deuterons from elastic scattering, which hit the forward detector is small, ≪ 1%, but these events are interesting for the following reason. The differential cross section $d\sigma/d\Omega$ for elastic pd scattering at $\vartheta_p = 180°$ in the „plane wave approximation" depends on the 4-th power of the deuteron wave function, while for the break-up process it depends on the second power. Therefore, this process, dominated by the one nucleon exchange mechanism („pick-up" mechanism), is sensitive to the high momentum part of deuteron wave function.

The reaction channel (2) has the largest cross section among the background processes (17.0 ± 0.6 mb). It will also be the main background channel with respect to the mesonless deuteron break-up. The fraction of the protons that hit the detector has been found to amount to 4%, the one of pions is 0.6%. The fraction of protons from the reaction (3) hitting the detector is equal to 6%.

In order to estimate the ratio of break-up and background events in the FD we calculated the number of charged particles from all reactions that hit the hodoscope. The ratio of background events from reactions (1,2,3) (under consideration of the losses in the elastic channel) to deuteron break-up events amounted to 3:1. The π/p ratio is equal to 1:10, the d/p ratio is 1:500. One can judge the importance of the separation of different types of particles without inclusion of the information from the backward detector BD by the momentum spectra given in Fig. 2. Here the spectrum of protons from the reaction pd → ppn detected (solid line) is given along with the spectra of protons from elastic scattering (shaded) (1) and inclusive protons from background processes (2) and (3) (shaded with wide gap). The spectrum of the π mesons (black area) from reaction (2) is also shown. One can see that the overlap occurs mainly for spectra of protons from the mesonless break-up of the deuteron and the elastic scattering.

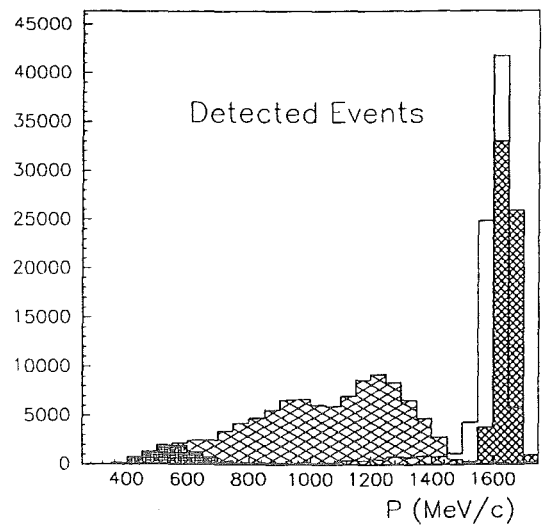

Fig. 2: Momentum distribution of particles from reaction pd → ppn and background processes (1), (2) and (3) that reached the detector.

For an estimation of the counting rates of the different detectors of the FD system we used a luminosity of $L = 1 \cdot 10^{30}\, cm^{-2}s^{-1}$. The available experimental data after normalization to the number of interactions in the bubble chamber have the following weight: one event, independently of the reaction type, corresponds to 0.46 μb (with ≤ 10% precision). The counting rate R_i was estimated using the detection efficiency ε_i: $R_i = N_i\varepsilon_i\, 0.46\, L \cdot 10^{-30}\, s^{-1}$. The estimated rates for background reactions are presented in Table. 1.

The study of the pd interaction is also proposed[1,2] at p_p = 3.3 GeV/c, where the total cross section of the pd interaction is 82.7 ± 0.1 mb and the elastic cross section is 12 mb. No information exists on exclusive cross sections. This region differs significantly from the one considered above from the point of composition and momentum spectra of secondary particles (the contribution of inelastic channels with π meson production increases, while σ_{tot} and σ_{el} remain the same). Using the data on pp and pn interactions[8,9,10] one can estimate exclusive cross sections of the pd interactions. The reasons for the validity of such an approach are the following. As was stated above, at ener-

gies under consideration here the mechanism of quasi-two particle scattering dominates in pd interactions. The detector system FD is designed for the detection of positively charged particles. Therefore, below we consider cross sections of processes with the production of positively charged particles.

The main contribution to the cross section for the deuteron break-up is given by quasi-two particle processes pp → pp and pn → pn. At higher momentum, the cross sections of these reactions decrease. This allows to assume that the cross section of mesonless break-up of the deuteron pd → ppn will correspondingly decrease. $\sigma_{pnn\pi^+}$ (pd) is equivalent to $\sigma_{pn\pi^+}$ (pp) and expected to be equal to 11 mb. $\sigma_{ppn\pi^\circ}$ (pd), which is equivalent to $\sigma_{pp\pi^\circ}$ (pp) and $\sigma_{pn\pi^\circ}$ (pn), remains equal to 10 mb. Adding the cross sections of all above-mentioned channels one can conclude that the cross section of the pd interaction with the production of two π mesons increases approximately by one order of magnitude and equals the remaining ~ 20 mb. This cross section is mainly shared between the channel pd → $pd\pi^+\pi^-$, (due to weak binding of the deuteron the channel pd → $pd\pi^+\pi^-$ is suppressed in comparison with pd → $ppn\pi^+\pi^-$) and the channel pd → $pnn\pi^+\pi^\circ$. The number of π^+ mesons increases approximately by one order of magnitude compared to the situation at p_p = 1.7 GeV/c leading to an integral ratio of protons from deuteron break-up to π^+ mesons equal to 1:1.

The main conclusions are the following:

- Simulation calculations of the FD-system have been performed on the basis of experimental data obtained in a hydrogen bubble chamber at 1.7 GeV/c proton momentum. The method of determination of measurement conditions has been worked out.

- The main background processes accompanying the break-up reaction pd → ppn have been considered and their kinematic characteristics have been studied.

- The fractions of particles that hit the detector have been estimated for different reactions. The ratio of particles from useful events to the background has been determined for the forward detector system.

- The distribution of the events over the area of the hodoscope (relative counting rate) and their spectral contents have been obtained.

- The study of the elastic scattering of protons at 180° is possible.

- An estimation of the expected counting rate of the FD system at 3.3 GeV/c momentum has been obtained on the basis of experimental data on pp and pn interactions. It has been shown that the number of background π^+ mesons increases by an order of magnitude.

The authors are grateful to the 100 cm-Hydrogen-Bubble-Chamber Collaboration for the possibility to use their experimental data on dp interactions at p_p = 3.3 GeV/c. The authors are also grateful to Prof. Yu.A. Trojan for the access to unpublished data and useful discussions.

[a] High Energy Physics Institute, Tbilisi State University, Tbilisi, Georgia
[b] Laboratory of Nuclear Problems, Joint Institute for Nuclear Research, dubna, Moscow Region, Russia*
* Supported by grant 93-02-3745 of the Russian Foundation for Fundamental Research.

References:

1. S. Dshemuchadze et al., COSY Proposal 20, KFA Jülich (1991)
2. V.I. Komarov, Exclusive deuteron break-up study with polarized protons and deuterons at COSY, Proceedings WE Heraeus-Seminar, Bad Honnef, Febr. 1-3, 1993 (1993) 281
3. B.S. Aladashvili et al., NIM 129 (1975) 109
4. K. Sistemich et al., contribution to this report, p. 51
5. R. Brun et al., GEANT, Detector description and Simulation Tool, CERN (1993)
6. B.S. Aladashvili et al., Nucl. Phys. B86 (1975) 461-478
7. B.S. Aladashvili et al., JINR preprint 1-7645, Dubna (1973)
8. A. Abdivaliev et al., Nucl. Phys. B99 (1975) 445
   K. Beshliu et al., Yad. Fiz. 43 (1986) 888
9. J. Bystricky et al., DPhPE 87-03, Saclay (1987)
10. F. Shimizu et al., Nucl. Phys. A386 (1982) 571
11. Compilation of cross-sections, CERN-HERA 84-01 (1984)
12. V.V. Glagolev et al., Yad. Fiz. 27 (1978) 704
13. V.V. Glagolev et al., Acta Phys. Pol. 25 (1994) 1199

Kinematical Identification of pd → ppn Reaction Events at ANKE

V.M. Artemov[a], S.N. Dymov[a], A.G. Ketikian[a], V.I. Komarov[a], A.V. Kulikov[a], V.S. Kurbatov[a], E.I. Smogailov[a], S.V. Yaschenko[a]

We describe a scheme of a kinematical identification of pd → ppn reaction events. This step in the data analysis for exclusive processes is usually the final one in event selection. This technique was introduced into data processing more than thirty years ago[1,2]. The purpose of this procedure is twofold: to check that a given event is of the type of interest and if this is true, to find more accurate estimates of the events kinematical parameters. The idea of this technique is as follows: for the ANKE setup the observables are the coordinates of straight tracks in the backward and forward detectors and the time-of-flight difference between protons. In addition the missing mass is equal to the neutron mass. Thus, the best estimates for the kinematical parameters (vertex coordinates and particle-momentum vectors) are obtained by a least square fit under the assumption that the missing mass equals the neutron mass.

The authors of Refs. 1 and 2 proposed to search for the minimum of such a constrained functional using the so called Lagrange multipliers minimizing the function consisting of a least square quadratic form plus constraints. We are using a technique which we developed[3-6]. The main idea of this method - on each step of the iteration procedure we linearize constraints and express increments of some variables through others - is a substitution algorithm. The minimization includes the free parameters left. The advantage of this method in comparison to the Lagrange-multiplier method is that it can be applied to a much wider range of problems especially when the constraints have the form of inequalities. This method was extensively tested on model and real data and is presently used in our data processing system for the Serpukhov setup[7].

In Fig. 1 the setup is sketched. It consists of the target, the backward magnet D1 with a system of drift chambers and the forward magnet D2 with a system of proportional chambers.

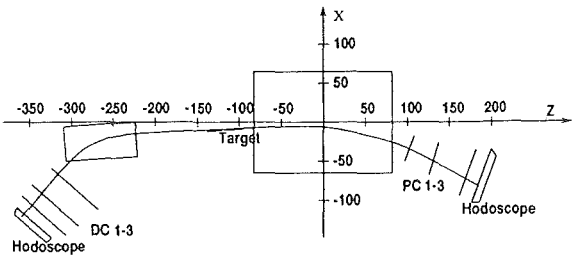

Fig. 1: Layout of the setup of ANKE which was used for our calculations.

The pd → ppn process is described by the following variables: the coordinates of the interaction point and the momentum vectors of the forward and backward protons. In the model used for testing we have made the following simplifications: taking into account the fact that the beam diameter is small (~ 2 mm), the only essential parameter is the interaction-point coordinates along the beam line. The second simplification is that the kinematics of the reaction was calculated according to phase space. Finally we assumed that the measurement accuracy of all track detectors is 500 μm and the accuracy in time-of-flight is 1 ns.

The field map was calculated using the program PROFI[8] in form of three field components on nodes of a 3d space lattice. In Ref. 9 a polynomial model of an analytic representation of the magnetic field, which satisfies Maxwell equations, was described. To calculate the values of the field components we used a third order interpolation. In this case 24 coefficients for any elementary volume were defined by a preliminary fitting using the known values at the 8 corner points of the volume.

We generated about 3000 deuteron break-up events in which one proton goes through all backward- and another one through forward-detector chambers and hit the corresponding scintillation hodoscopes. Their tracking was done according to the method described in Ref. 10.

These events were used as an input for the fitting program. For the fitting we have to express the „measured" coordinates as a function of the parameters. The equation of motion of a particle in a magnetic field is the Lorentz equation which, in coordinate representation, is equivalent to differential equations of the second order. When the magnetic field is inhomogeneous these equations are usually solved using the Runge-Kutta method if five initial parameters are known: two coordinates, their derivatives and the momentum at some point. However, in our case we have only four initial parameters: the vertex longitudinal coordinate, two derivatives and the momentum. Then the hit coordinates are some regulary functions of these four coordinates and the problem is how to find such functions. There is some history behind the answer to this question. A lot of people used approximations by orthoghonal polynomials, for example by Tchebycheff polynomials[11]. Our method[12] was compared with the method described in Ref.11. Our method is faster and gives the same accuracy at least for the magnet and the energies in Serpukhov. The idea of our method is: instead of using a five dimensional lattice in the orthogonal polynomial method we propose to use a simple Taylor series expansion. The maximum power of the series is defined by the condition that the approximation inaccuracy is less than other unavoidable inaccuracies. In our case the major source of unavoidable inaccuracy is the Coulomb scattering. We used Taylor series with four variables and have obtained the approximation accuracies better than the Coulomb scattering errors.

In Table 1 we show the Coulomb-scattering errors for backward and forward protons. The errors were calculated for average proton momenta of 0.5 GeV/c for the backward and 1.5 GeV/c for the forward detectors. The method of taking into account Coulomb scattering is described in Ref.

13. In Table 1 we also show the inaccuracies due to approximations expressed as mean square deviations.

Table 1: Inaccuracies of approximation functions and Coulomb scattering (cm).

	Backward spectrometer			Forward spectrometer		
	σ_1	σ_2	σ_3	σ_1	σ_2	σ_3
Function inaccuracy	0.080	0.120	0.150	0.055	0.084	0.125
Coulomb inaccuracy	0.380	0.540	0.620	0.160	0.190	0.230

In the first column of Table 2 we show accuracies obtained with our model. It is seen that the accuracies are ~ 1.0% in the momenta, ~ 4.5 cm in vertex longitudinal coordinate and ~ 3.5 mrad in the angle.

In the second column the same accuracies are shown in the so called „ideal" model - when we assume that the functions for observables are known correctly. One can see that the accuracies are ~ 10% better than those received with our model. Runge-Kutta tracking would also result in „ideal" accuracies.

In the third column we show the results of a fit without taking into account Coulomb scattering. It can be seen that in case of the matrix being written correctly the errors are at least ~ 40% smaller (column „ideal"). This means that Coulomb scattering must be taken into account during the fit. In the fourth column the accuracies are shown for the case when only the diagonoal elements in the Coulomb matrix are taken into account during the fit.

Table 2: Parameter accuracies for the different models.

	Model	„Ideal"	Measured	Diagonal
$\sigma(\Delta L)$, cm	4.39	4.20	5.86	4.84
$\sigma(\Delta p_1/p_1)$, %	1.15	1.11	1.48	1.20
$\sigma(\Delta p_2/p_2)$, %	0.96	0.88	1.31	1.01
$\sigma(\Delta x'_1)$, mrad	3.38	3.28	4.32	4.30
$\sigma(\Delta y'_1)$, mrad	2.14	2.05	3.11	3.30
$\sigma(\Delta x'_2)$, mrad	3.13	2.97	4.55	3.50
$\sigma(\Delta y'_2)$, mrad	0.89	0.80	0.99	0.94

Summarizing, the results of our calculations show that

- The proposed scheme gives good estimates of the parameters and, to our opinion, may be considered as a candidate for future data processing with some refinements.
- The method of expressing observables as polynomials of the third order decreases the accuracy by ~ 10%.
- Coulomb scattering should be taken into account for the kinematical analysis. Without Coulomb scattering we lose ~ 40% in accuracy.
- The proposed scheme can be applied to any exclusive process. Like for inclusive processes we recommend the minimization of quadratic forms with the correct covariation matrix and use of the Runge-Kutta method simultaneously. Such an approach is resource-consuming but we think the performance of modern computers is high enough to permit it.

[a] Laboratory of Nuclear Problems, Joint Institute for Nuclear Research, Dubna, Moscow Region, Russia*

* Supported by grant 93-02-3745 of the Russian Foundation for Fundamental Research.

References:

1. J.P. Berge, F.T. Solmitz and H.D. Taft, Rev. Sci. Instr. 32 (1961) 539
2. R. Bock, CERN 60-30 (1960)
3. A.J. Ketikian, E.V. Komissarov, V.S. Kurbatov, I.N. Silin, NIM A314 (1992) 572
4. A.J. Ketikian, E.V. Komissarov, V.S. Kurbatov, I.N. Silin, NIM A314 (1992) 578
5. A.J. Ketikian, V.S. Kurbatov, I.N. Silin, CHEP-92, p. 833, CERN 92-07, 1992
6. V.S. Kurbatov, I.N. Silin, NIM A345 (1994) 346
7. V.M. Artemov et al., Communication of JINR, P10-95-334, 1995 (in Russian)
8. M. Büscher et al., Ann. Rep. 92, KFA-IKP, 14 (1993)
9. H. Wind, DH/67-8, Journal of Computational Physics
10. J. Myrheim, L. Bugge, NIM 160 (1979) 43
11. C. Lechanoine, M. Martin, H. Wind, NIM 69 (1969) 122
12. A.D. Volkov et al., NIM A306 (1991) 278
13. V.M. Artemov et al., Communication of JINR, P10-93-521, Dubna, 1994 (in Russian)

Subthreshold K^+-Production in the pd → $K^+\Lambda pn$ Reaction

A.K. Kacharava[a,b], M.S. Nioradze[a], V.I. Komarov[b], G.G. Macharashvili[a,b], A. Mamulashvili[a], Z. Menteshashvili[a]

The study of the subthreshold K^+-production in proton-deuteron collisions pd → $K^+\Lambda X$ is of special interest, as this reaction can provide most direct information about the mechanisms involved in the K^+-production at subthreshold energies. This is especially the case, when in the final state the proton or the deuteron is detected in coincidence with the K^+-meson. This process has not yet been studied.

At kinetic energies of incident protons below the nucleon-nucleon threshold, the energy necessary for production of K^+-meson can only be gained from internal motion of nucleons inside the nucleus. It is obvious, that the momenta of nucleons involved in the production process must be much higher than the average momenta of the intrinsic motion. But at these momenta the description of the nucleus in terms of nonrelativistic wave function is not valid and one has to use the relativistic approach for the description of internal motion of nucleons in nuclei. Here we use the light front formalism for composite systems[1)] to describe the process of subthreshold K^+-production in the reaction
pd → $K^+\Lambda pn$.

In the light front formalism the deuteron is described in terms of the relativistic wave function $\Phi(x_N, \vec{p}_{\perp N})$, where $\vec{p}_{\perp N}$ is the transverse momentum of the nucleon and the „longitudinal motion" of nucleons is parametrized by means of the scale-invariant variable $x_N = (E_N + p_{N,z})/(E_d + P_d)$, where E_N, $p_{N,z}$ and E_d, P_d are the energies and z-components of momenta of the constituent nucleon and deuteron, respectively. In terms of this variable the relativistic wave function of the deuteron reflects the dependence of the internal motion of nucleons on the total momentum of the deuteron, which is a specific feature of relativistic bound states. The dependence of the intrinsic motion of the total momentum of the composite system (deuteron) results in a non-symmetry of the relativistic wave function in comparison with the nonrelativistic wave function, which is symmetric. For momenta directed against the momentum of the incident proton the relativistic wave function gives higher values than the nonrelativistic one. Note that this is the area of momenta which plays the dominant role in subthreshold-K^+ production, therefore one can expect that the cross section of K^+ production calculated with a relativistic wave function will be higher than the one calculated with a nonrelativistic wave function.

The calculation of the differential cross section for the K^+-production in proton-deuteron collisions in the framework of the Spectator Model gives the following result:

$$E_K \frac{d^3\sigma_{pd}(s)}{d\vec{p}_K} = \frac{1}{8(2\pi)^5\sqrt{\lambda(s, m_d^2, m_N^2)}} \times \int \frac{d\vec{p}_N}{E_N} \frac{|\Phi(x_N, \vec{p}_{\perp N})|^2}{(1-x_N)^2} \sqrt{\lambda(s_{NN}, m_N^2, m_N^2)} E_K \frac{d^3\sigma_{NN}(s_{NN})}{d\vec{p}_K}$$

where s is the usual Mandelstam variable for the proton-deuteron system, sNN is the similar variable for the subsystem consisting of the incident proton and the interacting nucleon of the deuteron. The relation between these variables looks as follows:

$$s_{NN} = s + m_N^2 - 2E_N(m_d + E_p) + 2p_N p_d \cos\theta_N$$

$E_K d^3\sigma_{NN}(s_{NN})/d\vec{p}_K$ is the differential cross section for the K^+-production in the NN-collision, for which we took the expression determined by energy-momentum conservation[2)] and λ is the kinematical function $\lambda(x,y,z) = (x-y-z)^2 - 4y^2z^2$.

A similar expression is valid for the total cross section with replacement of the differential cross sections by the total cross sections of the K^+-meson production in pd and NN-collisions.

To construct a relativistic wave function of the deuteron, we used the fact that in the framework of the light front formalism the Lorentz-invariant combination $(\vec{p}_{\perp N}^2 + m_N^2)/x_N(1-x_N)$ plays the role analogous to that of p^2 - the square of the three-dimensional relative momentum in nonrelativistic theory. We obtained the relativistic wave function from the corresponding nonrelativistic expression[3)] by the substitution

$$\vec{p}^2 \to \frac{\vec{p}_{\perp N}^2 + m_N^2}{4x_N(1-x_N)} - m_N^2 .$$

Results of the calculations of the total cross section for the subthreshold K^+-production with the use of relativistic and nonrelativistic wave functions are shown in Fig. 1, where the dependence of the cross section on the kinetic energy of the incident proton is plotted. As expected, the calculation with relativistic wave function gives higher values of cross section in the whole energy range.

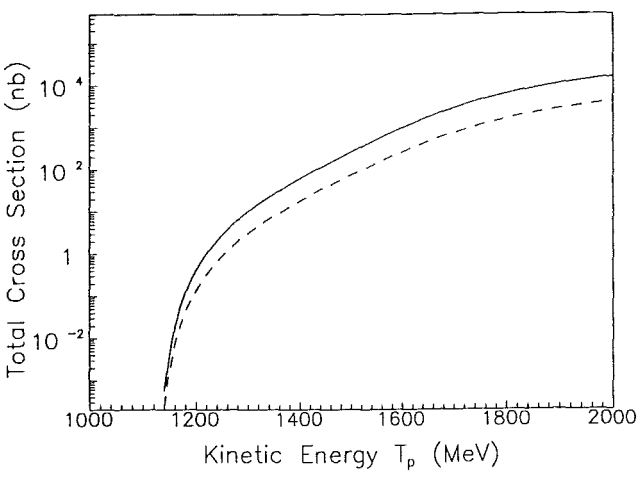

Fig. 1: Total cross section of the K^+-production in the reaction pd → $K^+\Lambda pn$ vs. the incident proton kinetic energy T_p, calculated with relativistic (solid line) and nonrelativistic (dashed line) wave functions.

In Fig. 2 the momentum distribution of K^+-mesons produced in the reaction pd $\rightarrow$ $K^+\Lambda pn$ at kinetic energies in the vicinity of the absolute proton-deuteron and the nucleon-nucleon thresholds are presented. For the K^+-production the absolute thresholds in proton-deuteron and proton-proton collisions are 1130 and 1580 MeV, respectively. These plots are calculated in the framework of the Spectator Model with a relativistic wave function of the deuteron at different emission angles of the K^+-mesons.

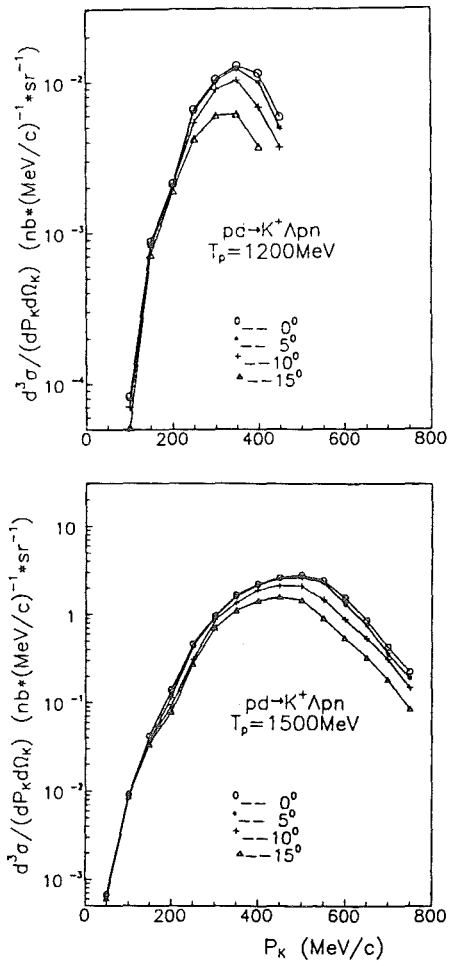

Fig. 2: Momentum spectra of the K^+-mesons for different emission angles at T_p = 1200 MeV and T_p = 1500 MeV.

The angular distributions of the K^+-mesons produced with different momenta are shown in Fig. 3. As one can see close to the absolute proton-deuteron threshold (1200 MeV) K^+-mesons with momenta of 550 MeV/c do not appear due to the limited phase space for the particle production. It should be noted that the momentum and angular distributions are similar to the ones calculated for the K^+-production in the $p^{12}C$-collision[4].

The double differential cross sections $d^2\sigma/dp_K dp_{sp}$ for the K^+-meson production in coincidence with a proton-spectator in the forward direction at kinetic energies of the incident proton T_p = 1200 MeV and T_p = 1500 MeV are presented in Fig. 4. These momentum spectra clearly show

that the production of K^+-mesons in the process pd $\rightarrow$ $K^+\Lambda p_{sp}n$ occurs in coincidence with protons which

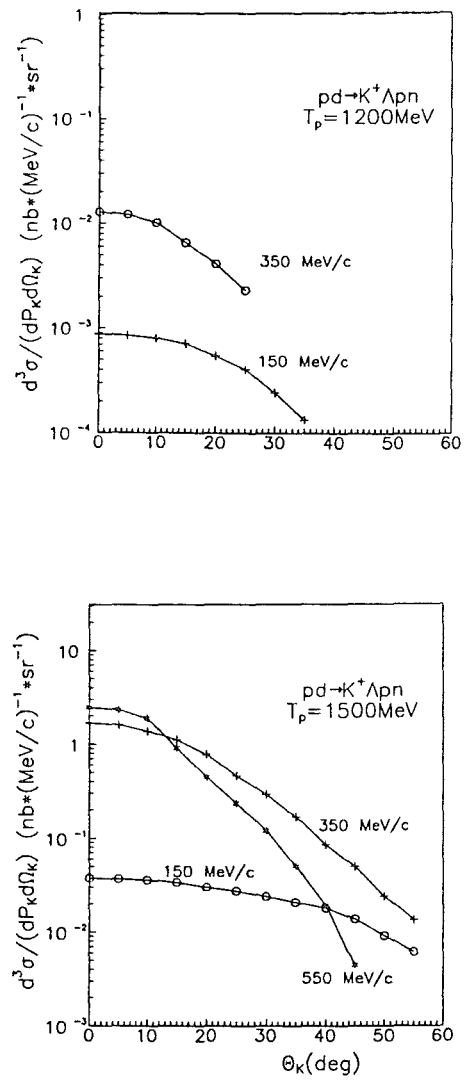

Fig. 3: Angular spectra of K^+-mesons for different momenta at T_p = 1200 MeVand T_p = 1500 MeV.

have momenta in the range of 300 - 400 MeV/c, that is significantly higher than the average momentum (80 - 100 MeV/c) of nucleons inside the deuteron. This indicates that the production of K^+-mesons is dominated by the collision of the incident proton with nucleons of the deuteron having momenta which correspond to the high momentum component of the wave function.

For the investigation of the subthreshold K^+-production we are planning to study the correlation between K^+ and d in the process pd $\rightarrow$ $K^+\Lambda d$. The experimental investigation of these processes can be extremely useful in studies of high momentum components of the wave function of the deuteron as well as for the determination of the subthreshold K^+-production mechanism in proton-deuteron collisions.

The authors are indebted to Dr. A Sibirtsev for helpful discussions. The Tbilisi team was supported in part by the grant MXQ000 from the International Science Foundation.

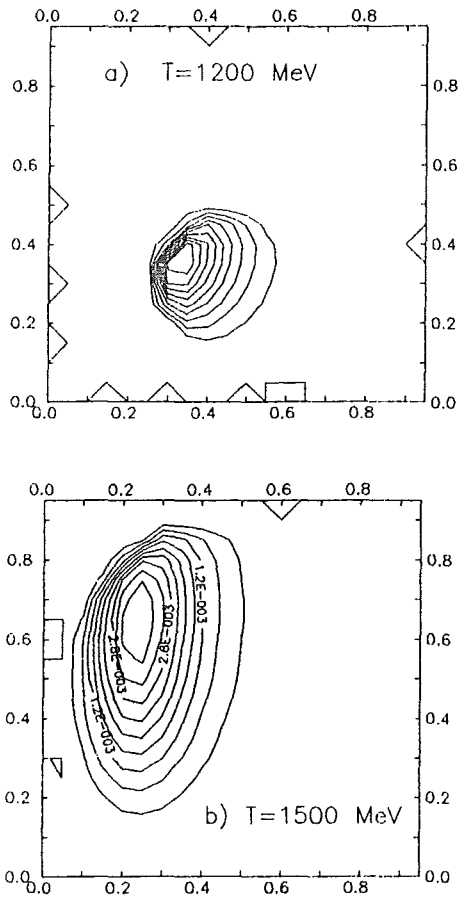

Fig. 4: Double differential cross section $d^2\sigma/dp_K dp_{sp}$ of the K^+-meson production in coincidence with the spectator nucleon at T_p = 1200 MeV (a) and T_p = 1500 MeV (b).

[a] High Energy Physics Institute, Tbilisi State University, Tbilisi, Georgia

[b] Laboratory of Nuclear Problems, Joint Institute for Nuclear Research, dubna, Moscow Region, Russia

References:

1. V.R. Garsevanishvili et al., Sov. J. Theor. Math. Phys., 23 (1975) 310
2. S.V. Efremov et al., Sov. J. Nucl. Phys. 55 (1992) 521
3. G. Alberi et al., Phys. Rev. Lett. 34 (1975) 503
4. B. Kamys et al., IKP-Annual Report 1991, KFA, Jülich (1992) 30

K-meson Production in Nucleon-Nucleon Interaction

A.Yu. Petrus[a], A.A. Sibirtsev[a]

One of the most important ingredients in the analysis of the experimental data for K-meson production in pA and AA collisions is the cross section of K-meson production in the elementary process pp → K^+X. The difficulty of such an analysis lies in the fact that, first, the experimental data are extremely limited and fragmentary especially close to the K-meson production threshold. Second, the few available theoretical calculations are at variance with each other in terms of the consideration of the different diagrams and the employment of the coupling constants, but nevertheless describe the experimental data similarly well.

In our calculation we take into account the one-pion exchange diagram shown in Fig. 1a.

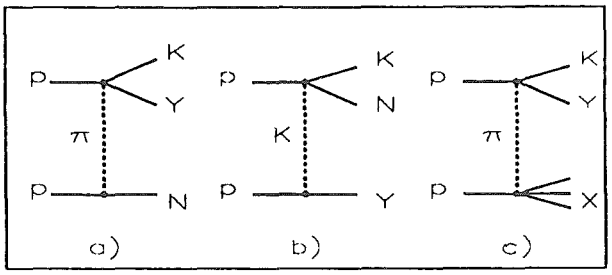

Fig. 1: The diagrams for the boson exchange model and for the reggeized pion exchange model.

The cross section of the reactions pp→pΛK^+ and pp→NΣK is given as[1].

$$\sigma(pp \to NYK, \sqrt{s}) = \frac{m_N^2}{2\pi^2 p_i^2 s} \int_{W_{min}}^{W_{max}} kW^2 dW \times \int_{t_-}^{t_+} \frac{g_{\pi NN}^2}{\mu^2} F^2(t) D^2(t) \sigma(\pi N \to KY, W) t dt, \quad (1)$$

where $\sqrt{s}$ and W are the invariant masses of the colliding protons and the produced kaon-hyperon pair, respectively. Obviously $W_{min} = m_Y + m_K$ and $W_{max} = \sqrt{s} - m_N$ with m_N, m_Y, m_K being the masses of the nucleon, Λ or Σ hyperon and K-meson, respectively. The parameter t stands for the squared four-momentum transferred from the initial to the final nucleon and $t_\pm = 2\ m_N^2 - 2E_iE_f \pm 2p_ip_f$ where E_i, p_i are the energy and the momentum of the initial nucleon in the center-of-mass frame and E_f, p_f are those for the final nucleon. μ and k denote the mass and the momentum of the exchanged pion.

The pion propagator was taken in the form

$$D(t) = \frac{1}{t - \mu^2} \quad (2)$$

The coupling constant $g_{\pi NN}^2 = 1.0$ was used[2]. To take into account the off-shell modification of the vertex we use the pion form factor as

$$F(t) = \frac{\Lambda_\pi - \mu^2}{\Lambda_\pi - t}, \ \Lambda_\pi = 0.9\ \mathrm{GeV}^2 \quad (3)$$

σ(πN→KY,W,t) is the cross section of the corresponding πp→KY channel. We use the total cross section of the reaction πN→KY from Ref.3, which was obtained with the resonance model calculations and parametrized for different reaction channels as

$$\sigma(\pi N \to KY) = \sum_j \frac{A_j(\sqrt{s} - \sqrt{s_{th}})^{f_j}}{(\sqrt{s} - M_j)^2 + B_j^2} \quad (4)$$

where $\sqrt{s}$ is the invariant mass of the πN system, $\sqrt{s_{th}} = m_K + m_Y$. The parameters A_j, f_j, M_j and B_j are shown in Table1.

Table 1: Parameters of approximation (4) used in our calculations.

Reaction	j	A[μb]	f	M[GeV]	B[MeV]
$\pi^+p \to \Sigma^+K^+$	1	35.91	0.9541	1.89	124.418
$\pi^+p \to \Sigma^+K^+$	2	159.4	0.01056	3.0	970.155
$\pi^0p \to \Sigma^0K^+$	1	3.978	0.5848	1.74	81.67
$\pi^0p \to \Sigma^0K^+$	2	47.09	2.165	1.905	79.737
$\pi^-p \to \Sigma^-K^+$	1	9.803	0.6021	1.742	81.1357
$\pi^-p \to \Sigma^-K^+$	2	6.521	1.4728	1.94	79.044

Fig. 2 shows the results of the calculation of the cross section within the framework of the one-pion exchange model. As we can see, the calculation yields an essentially underestimated value for the total cross section with respect to the experimental data[4], which is to say that we must take into account the contribution from the kaon exchange.

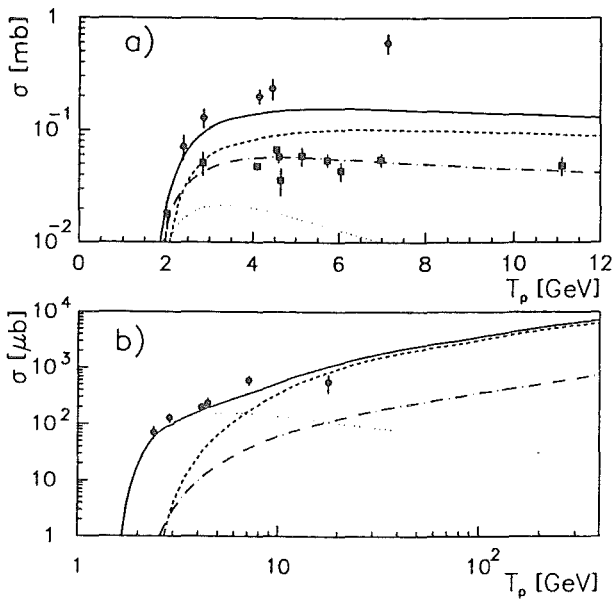

Fig. 2: a) Experimental cross section of the inclusive K^+ production (dots) and the reaction pp→pΛK^+ (squares). The lines show contributions from the Λ channel (dotted for the pion exchange, dash-dotted for the sum of the pion and kaon exchange), Σ (dashed) and the sum (solid) calculated with the boson-exchange model for pp→NYK^+. b) Total cross section of inclusive K^+ production. The dots show experimental data from[4]. The lines show the contribution from associated Σ (dashed), Λ production (dashed-dotted) and reaction pp→NYK^+ (dotted) and their sum (solid).

contribution from associated Σ (dashed), Λ production (dashed-dotted) and reaction pp→NYK$^+$ (dotted) and their sum (solid).

The kaon exchange diagram is similar to the one for the pion (see Fig. 1b). The cross section connected with a graph like this is described by a formula similar to (1) with the difference that now the final nucleon and hyperon are exchanged with each other and that instead of the exchanged pion we have a K-meson. The kaon propagator and the form factor are taken in the same form as in (2,3). Here Λ_K appearing in the form factor instead of Λ_π was determined from a comparison with the experimental data. In the same way we defined the coupling constants $g^2_{KN\Lambda}$ and $g^2_{KN\Sigma}$. With the fitting procedure we get the following parameters for the kaon exchange model

$$\Lambda_K = 0.67 \pm 0.14 \text{ GeV}^2 \qquad g^2_{KN\Lambda} = 14.6 \pm 3.1$$

$$g^2_{KN\Sigma} = 0.88 \pm 0.26 \tag{5}$$

Let us note that the accuracy of the experimental data is very bad which caused large uncertainties of the adjusted parameters.

The calculated cross sections of the reaction pp→NYK were parametrized as

$$\sigma(pp \to NYK, \sqrt{s}) = a\left(1 - \frac{s_{th}}{s}\right)^b \left(\frac{s_{th}}{s}\right)^c \tag{6}$$

with s_{th}=6.487 GeV^2 for Λ and 6.864 GeV^2 for Σ production. The parameters a, b and c are shown in Table 2.

Table 2: Parameters of approximation (6).

Reaction	a [μb]	b	c
pp→pΛK$^+$	732.16	1.8	1.5
pp→pΣ$^+$K°	338.46	2.25	1.35
pp→pΣ°K$^+$	275.27	1.98	1.0
pp→nΣ$^+$K$^+$	381.61	1.87	0.98

As we can see from Fig. 2, taking into account only three-body final states does not allow a description of the inclusive K$^+$ production data at energies higher than 3.5 GeV and, therefore, we must consider channels with additional mesons in the final state. To describe the process pp→NYKX, where X = $\ell\pi$ + ..., $\ell \geq 1$, we use the reggeized pion exchange model. The corresponding graph is shown in Fig. 1c. The cross section is[5)]

$$d\sigma(pp \to K^+X) = \frac{64\pi s_1 \lambda^2(s_1, m_N^2, \mu^2)}{\lambda(s, m_N^2, m_N^2)} \frac{d\sigma}{dt_1}(\pi N \to YK^+, s_1, t_1)$$
$$\times \lambda(s_2, m_N^2, \mu^2)\sqrt{s_2}\sigma_{tot}(\pi N, s_2) F^2(t, s, s_1, s_2) \frac{d^3P_Y}{(2\pi)^3 2E_Y} \frac{d^3P_K}{(2\pi)^3 2E_K} \tag{7}$$

where

$$\begin{aligned} s_1 &= (P_Y + P_K)^2 \\ s_2 &= (P_1 + P_2 - P_Y - P_K)^2 \\ t &= (P_1 - P_Y - P_K)^2 \\ t_1 &= (P_1 - P_Y)^2. \end{aligned} \tag{8}$$

The function F(t,s,s$_1$,s$_2$) accounts for the pion propagator and an off-shell modification of the vertices and was taken as suggested by Boreskov et al[6)]

$$\begin{aligned} F(t, s, s_1, s_2) &= \exp\left(\left[R^2 + \alpha'_\pi \ln \frac{s(p_t^2 + m_K^2)}{s_1 s_2}\right](t - \mu^2)\right) \times \gamma \\ \text{with } \gamma &= \frac{\pi\alpha'_\pi}{2} \frac{1}{\sin(\pi\alpha_\pi(t)/2)}, \quad |t| < |T_0| \\ \gamma &= \frac{\pi\alpha'_\pi}{2} \frac{1}{\sin(\pi\alpha_\pi(T_0)/2)} \exp[R_1^2(t - T_0)], \quad |t| > |T_0| \end{aligned} \tag{9}$$

where p_t and m_K denote the transverse momentum and the mass of the K$^+$ meson, respectively. The pion trajectory was parametrized as $\alpha_\pi(t) = \alpha'_\pi(t-\mu^2)$ with $\alpha'_\pi = 1$. T_0 = -0.5 GeV^{-2}, R^2 = -0.55 GeV^{-2} and R_1^2 = 2.25 GeV^{-2}. Fig. 2 shows the results of the calculation of the pp→NYK$^+$X cross section.

We parametrize the total cross section of the inclusive K$^+$ production in pp collisions as

$$\sigma(pp \to K^+X) = a(1 - 6.48/s)^b (s/6.48)^c \tag{10}$$

with a = 2.021 mb, b = 1.829, c = 0.6 at s < 15 GeV^2 and a = 0.494 mb, b = 2.03, c = -1.294 at s > 15 GeV^2, where s is the invariant mass squared of the initial protons in GeV^2. The parametrization is valid from the reaction threshold to the beam energy of 400 GeV.

References:

1. Yao, T., Phys. Rev. 125 (1962) 1048
2. Laget, J.M., Phys. Lett. B259 (1991) 24
3. Tsushima, K., Huang, S.W., Faessler, A., Phys. Lett. B337 (1994) 245
4. Flaminio, V. et al., CERN preprint CERN-HERA 01/84 (1984)
5. Turbiner, A.V., Sov. J. Nucl. Phys. 22 (1976) 551.
6. Boreskov, K.G. et al., Sov. J. Nucl. Phys. 15 (1972) 203

[a] Laboratory of Nuclear Problems, Joint Institute for Nuclear Research, Dubna, Moscow Region, Russia*

* Supported by grant 93-02-3745 of the Russian Foundation for Fundamental Research.

Folding Model Calculations for Differential Cross Sections of K^+ Production in p+Pb Collisions

B. Kamys[a], W. Cassing[b], L. Jarczyk[a], Z. Rudy[a], O.W.B. Schult[c], K. Sistemich[c]

It was shown[1)] that the K^+ production in relativistic heavy ion collisions is more sensitive to the baryonic density in the reaction zone than the pion production and, moreover, this sensitivity is most pronounced for subthreshold energies (in the NN system). Thus, the subthreshold kaon production may be used for testing the nuclear matter equation of state in relativistic collisions of heavy ions. In such collisions the interaction process may be imagined as resulting from binary nucleon-nucleon collisions. It is, therefore, obvious that before achieving a proper understanding of K^+ production in heavy ion reactions, where two „clouds" of nucleons collide, one has first to understand this process in simpler reactions i.e. in proton-nucleus collisions. It is astonishing enough that up to recently[2,3)] there were almost no experiments devoted to measurements of differential cross sections for K^+ production in proton-nucleus collisions.

One of the main purposes of the new spectrometer „ANKE", which will be installed in the COSY ring to become operational in 1997, is the measurement of kaon ejectiles (Apparatus for measurements of Nucleonic and Kaon Ejectiles). Therefore, one of the first experiments will be the measurement of K^+ subthreshold production cross sections using proton beams impinging on various targets. For planning this experiment it is important to have realistic estimates for the data to be expected, performed in the frame of a theoretical model. It was shown some years ago[4)] that realistic predictions for the total cross sections may be achieved within the folding model. The folding model extrapolates information known from elementary reactions, i.e. the one-step process: $p+N \rightarrow K^+ + N + \Lambda$ (or Σ), and two-step processes: $p+N \rightarrow \pi + N + N$ followed by $\pi + N \rightarrow K^+ + \Lambda$ (or Σ), to proton-nucleus reactions by the evaluation of the folding integral over the (Fermi motion) momentum distribution and the corresponding elementary cross sections. In spite of its simplicity the model was able to reproduce quite well the total cross sections of K^+ subthreshold production from Koptev et al.[5)], i.e. the only existing data at subthreshold energies at that time.

In the present report we discuss the application of the folding model to differential cross sections and compare our results with the experimental differential cross sections for K^+ production in p+Pb collisions at $T_p = 2.1$ GeV[2)]. The parametrization of Zwermann and Schürmann[6)] was used for the elementary $p+N \rightarrow N+\Lambda+K^+$ cross sections in the one-step mechanism. The total cross sections for pion production in p+N collisions were described by the Ver West and Arndt[7)] parametrization while the total cross sections of the second step process, i.e. $\pi+N \rightarrow K^+ + \Lambda/\Sigma$, were taken from the work of Cugnon and Lombard[8)] (for kaons associated with Λ-hyperons) and that of Tsushima et al.[9)] (for kaons associated with Σ-hyperons). Isotropic angular distributions of elementary processes were assumed, but rescattering of pions in the intermediate stage of the reaction was not taken into account.

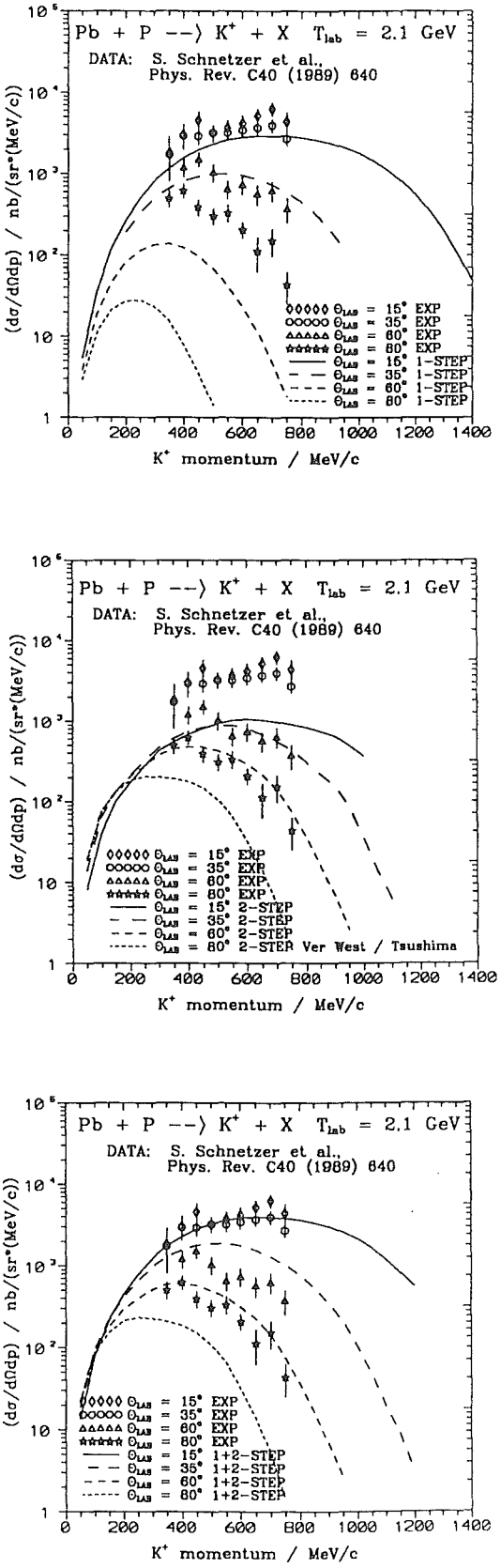

Fig. 1: The sum of one-step and two-step cross sections seems to reproduce the data quite reasonably due to the fact that cross sections for both mechanisms demonstrate complementary features.

The results of the calculations are presented in Fig. 1 together with the experimental data of Schnetzer et al.[2] measured at a proton beam energy of T_p = 2.1 GeV impinging on the Pb target. The data consist of the K^+ spectra measured at four angles and are represented by different symbols in the figure: 15 deg. - diamonds, 35 deg. - circles, 60 deg. - triangles, and 80 deg. - stars (all in the laboratory system). The curves correspond to theoretical calculations: full line for 15 deg., and long dashes, medium length and short dashes for 35, 60 and 80 deg., respectively. The results of the one-step mechanism of K^+ production are shown in the upper part of the figure, those of the two-step mechanism are in the middle part and the sum of the contributions from both mechanisms is presented in the lower part of the figure. As can be seen, the differential cross sections of the one-step production at 15 deg. agree quite well with the data. The experimental data at larger angles are, however, not reproduced by the one-step reaction for which the theoretical cross sections decrease too fast with the scattering angle, in contrast to the experimental data. Two-step production cross sections, on the other hand, vary with the angle in the manner similar to that of the experimental data being, however, still smaller than the experimental cross sections.

The two-step cross-sections presented here depend strongly on the pion production cross sections in the first-stage of the reaction as well as on the rescattering of the pions during their propagation through the nuclear medium before the collisions in which they produce kaons. Our results for two-step cross sections can be treated as an estimation only since we use the parametrization of Ver West and Arndt for the pion production cross section, which is valid for lower protons energies than those considered here. We think that the rescattering of pions will be necessary for a more detailed comparison with the measured data.

References:

1. M. Cieslak, Ph.D. thesis, 1995, Jagellonian University, Cracow, and to be published,
   D. Miskowiec et al., Phys. Rev. Lett. 72 (1994) 3650
2. S. Schnetzer et al., Phys. Rev. C40 (1989) 640
3. M. Debowski, Ph.D. thesis, 1995, Jagellonian University, Cracow,
   M. Debowski, E. Grosse, P. Senger, Nachrichten GSI 10-95, (unpublished data of GSI-IPN-Cracow-LNS-TH Darmstadt collaboration)
4. W. Cassing et al., Phys. Lett. B238 (1990) 25
5. V. Koptev et al., Sov. J. JETP 67(11), 2177 (1988)
6. W. Zwermann and B. Schürmann, Nucl. Phys. A423 (1984) 525
7. B.J. Ver West, R.A. Arndt, Phys. Rev. C25 (1982) 1979
8. J. Cugnon, R.M. Lombard, Nucl. Phys. A422 (1984) 635
9. K. Tsushima, S.W. Huang, Amand Fäßler, Phys. Lett. B337 (1994) 245

[a] Jagellonian University, Cracow
[b] University of Giessen
[c] IKP, Forschungszentrum Jülich

Two-Step Mechanism of Meson Production in pd → ^{3}HeX and pd → $^3H_\Lambda K^+$ Reactions

L.A. Kondratyuk[a], V.I. Komarov[b] and Yu.N. Uzikov[b]

The reactions pd → $^3H_\Lambda K^+$ and pd → ^{3}HeX, where X stands for a meson heavier than the pion, are of great interest for several reasons. First, these processes are accompanied by high momentum transfer (~ 1 GeV/c) to the nucleons. Second, an unexpectedly strong energy dependence of the η-meson production was observed near threshold[1]. In this respect the possible existence of quasi-bound states in the η-^{3}He system is discussed in the literature[2,3]. Third, production of η,η',ϕ mesons, whose wave functions contain valence strange quarks, raises questions concerning intrinsic strangeness of the nucleon and the mechanism of the possible Okubo-Zweig-Iizuka rule violation[4]. As a result of this discussion the experimental investigation of the reaction $\vec{d}\bar{p}$ → ^{3}Heϕ is proposed[5] to be studied in Dubna.

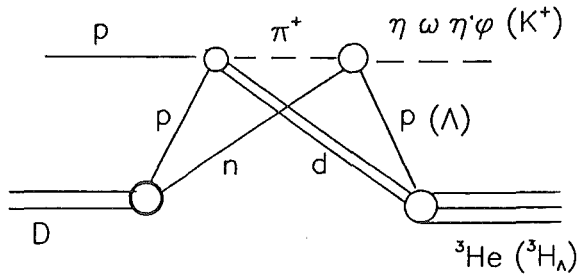

Fig. 1: Two-step mechanism of the reactions pd → ^{3}HeX and pd → $^3H_\Lambda K^+$.

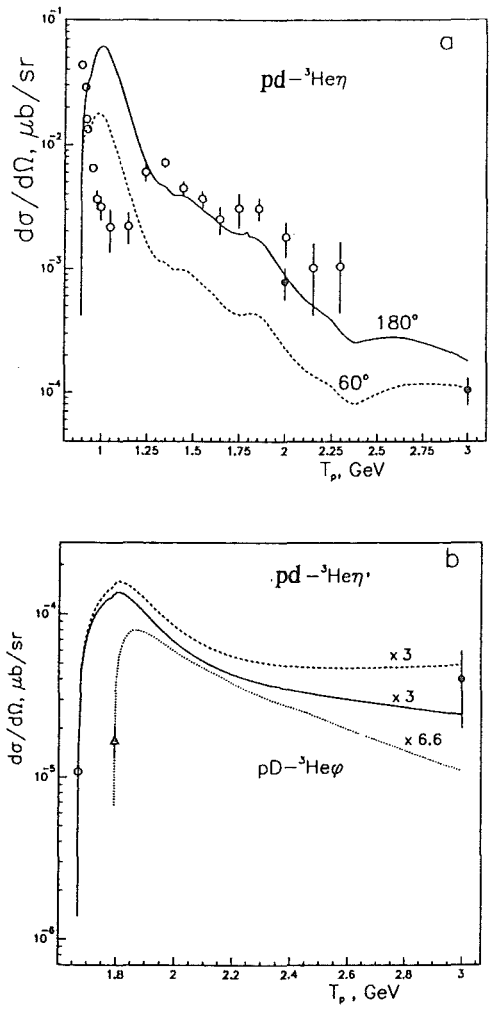

Fig. 2: Differential cross sections of the pd→^{3}Heη(ω,η',ϕ) reactions as a function of the proton lab. kinetic energy T_p. The curves show the results of calculations in the two-step model at different angles $\theta_{c.m.}$ multiplied by an appropriate normalization factor N.
a) pd → ^{3}Heη: 180° (full line, N=3), 60° (dashed curve, N=3); the circles are experimental data: ∘ - $\theta_{c.m.}$ = 180°, Ref. 1; • - $\theta_{c.m.}$ = 60°, Ref. 10.
b) pd → ^{3}Heη' at $\theta_{c.m.}$ = 180° (full, N=3) and $\theta_{c.m.}$ = 60° (dashed, N=3); the circles are experimental data for η' production: ∘ - $\theta_{c.m.}$ = 180°, Ref. 11; • - $\theta_{c.m.}$ = 60°, Ref. 10; the dotted line shows the results of calculations for the pd → ^{3}Heϕ reaction at $\theta_{c.m.}$ = 180° normalized by a factor N = 6.6 to the experimental point (Δ) from[11].

Both reactions, pd → ^{3}Heη and pd → $^3H_\Lambda K^+$, have a remarkable kinematical feature called in literature „velocity matching"[6]. It means that in the framework of two-step mechanisms (Fig. 1) which include the subprocesses pp → dπ$^+$ and pN → ηN (for η production) or π$^+$n → K$^+$Λ (for K$^+$ production) all intermediate particles are practically on mass-shell. This peculiarity occurs at any scattering angle near the corresponding threshold and at $\theta_{c.m.}$ ~ 90° above threshold. Therefore, the probability of these mechanisms is supposed to be high in the above mentioned kinematical regions.

The two-step model of the pd → ^{3}Heη reaction was developed in Refs.[3,7]. Recently Fäldt and Wilkin[8] found that the two-step model can describe the shape of the threshold cross section of the pd → ^{3}HeX° reaction as a function of the mass of the produced meson X° = η,ω,η',ϕ. In this work we (i) extend the two-step model[3] to the production of η,ω,η' and ϕ mesons above the thresholds[9], (ii) predict the pd spin-spin correlation for the reaction $\vec{d}\bar{p}$ → ^{3}HeX[9] in the energy region of Dubna[5] and COSY and (iii) predict the cross section of the pd → $^3H_\Lambda K^+$ reaction[13]. Numerical results presented in Figs. 2-4 are obtained under the assumption that the spin-flip amplitude dominates in the subprocess pp → dπ$^+$ in the forward-backward approximation. As follows from Fig. 2a, the pd → ^{3}Heη differential cross section at an initial proton energy above 1.5 GeV can be explained by the two-step mechanism. Near threshold there is a strong disagreement between model and experimental data. The reason for it is the strong final state interaction (FSI) in the η-^{3}He system at low energies caused by excitation of the N*(1535)

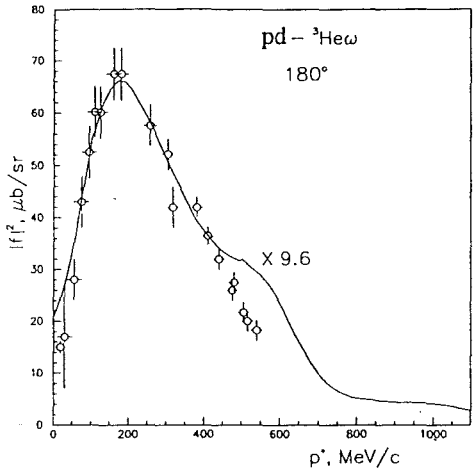

Fig. 3: The modulus squared to the amplitude of the pd → ^{3}Heω reaction as a function of the c.m.s. momentum of the ω meson, p*. The curve is the result of calculations multiplied by a normalization factor N=9.6, the circles (∘) are experimental data[12].

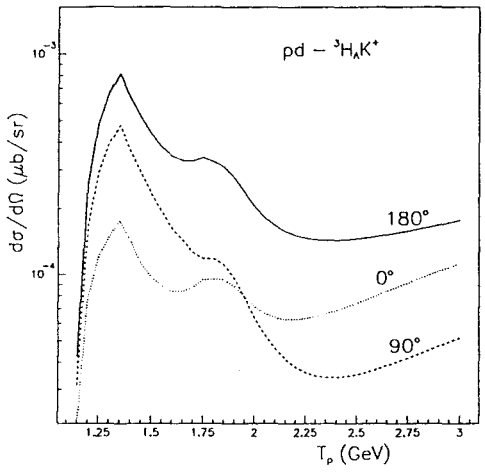

Fig. 4: The differential cross section of the pd → $^3H_\Lambda K^+$ reaction calculated for the two-step mechanism as a function of the incident proton kinetic energy at different angles of the K^+ meson $\theta_{c.m.}$ = 0°, 90°, 180°.

resonance. The parameters of possible quasibound states of the η-^{3}He-system are found by fitting of the experimental data to the prediction of the two-step model with FSI[3]. It can be seen from Figs. 2 and 3 that the two-step model describes well the shape of the energy dependence of available experimental cross sections at a final c.m.s. momentum p* = 0.4 - 1 GeV/c for η and p* = 0 - 0.5 GeV/c for ω mesons as well as the ratios R(η'/η) and R(ϕ/ω). The absolute values of the cross sections are underestimated by an overall factor of about 3 for η and η'. However, for the vector mesons the normalization factor is essentially larger: 6.6 for ϕ and 9.6 for ω. For the spin-spin correlation which is defined as

$$\Sigma_X = [d\sigma(\uparrow\uparrow) - d\sigma(\uparrow\downarrow)] / [d\sigma(\uparrow\uparrow) + d\sigma(\uparrow\downarrow)] \qquad (1)$$

we have found[9] that, near the threshold of the pd → ^{3}Heϕ reaction, Σ_ϕ = -0.95 and that Σ_ϕ becomes -1 above the threshold very rapidly. A very similar result is obtained for the ω meson: Σ_ω = -0.92. Neglecting the D component of the deuteron wave function we obtain the same result for vector and pseudoscalar mesons: $\Sigma_{\phi,\omega} = \Sigma_{\eta,\eta'}$ = -1. According to the hypothesis[4] concerning a $s\bar{s}$ contents of the nucleon this value is expected to be $\Sigma_1 \sim +1$.

The maximal value of the differential cross section of the reaction pd → $^3H_\Lambda K^+$, Ref. 13 predicted by the two-step model (fig. 3), $d\sigma/d\Omega_{c.m.} \sim 0.5$ nb/sr, is 20 - 30 times smaller than that one for the η-meson production. The contribution of the one-step mechanism involving the subprocess pp → $K^+\Lambda$p is by 2 - 3 orders of magnitude smaller than that of the two-step mechanism[13].

This work was supported in part by grant N° 93-02-3745 of the Russian Foundation For Fundamental Researchers.

References:

1. J. Berger et al., Phys. Rev. Letter. 61 (1988) 919; P. Berthet et al., Nucl. Phys. A443 (1985) 589
2. C. Wilkin, Phys. Rev. C47 (1993) R938
3. L.A. Kondratyuk, A.V. Lado and Yu.N. Uzikov, Yad. Fiz. 58 (1995) 524
4. J. Ellis, M. Karliner, D.E. Kharzeev, M.G. Sapozhnikov, Phys. Lett. B353 (1995) 319
5. B. Khachaturov et al., Talk in Int. Symp. DEUTERON-95, Dubna (4-7 July, 1995)
6. K. Kilian and H. Nann, Preprint KFA, Jülich (1989)
7. G. Fäldt and C. Wilkin, Nucl. Phys. A587 (1995) 769
8. G. Fäldt and C. Wilkin, Phys. Lett. B354 (1995) 20
9. L.A. Kondratyuk, Yu.N. Uzikov, Preprint JINR E4-95-389; nucl-th/9510010
10. H. Brody, E. Groves, R. Van Berg et al., Phys. Rev. D9 (1974) 1917
11. R. Bertini et al., Preprint LNS/Ph/94-16
12. R. Wurzinger, R. Siebert, J. Bisplinghoff et al., Phys. Rev. C51 (1995) R443
13. V.I. Komarov, A.V. Lado and Yu.N. Uzikov, J. Phys. G: Part. Nucl. 21 (1995) L69

[a] Institute of Theoretical and Experimental Physics, Moscow, Russia
[b] Laboratory of Nuclear Problems, Joint Institute for Nuclear Research, dubna, Moscow Region, Russia*
* Supported by grant 93-02-3745 of the Russian Foundation for Fundamental Research.

Ratio of Kaon- to Pion-Pair Production as a Signature of Enhanced Strangeness Production

V.I. Komarov[a], H. Müller[b]

The study of strange-particle production in proton-nucleus (pA) and nucleus-nucleus (AA) collisions has become an important research area since Rafelski and Müller[1] and Greiner et al.[2] predicted strangeness enhancement for heated and compressed nuclear matter. In this picture nuclear matter, which consists primarily of u and d quarks at normal density, melts into a „soup" of quarks and gluons at high density and temperature. Under such conditions $s\bar{s}$ creation is no longer suppressed and nearly equal amounts of $s\bar{s}$ as well as $u\bar{u}$ and $d\bar{d}$ pairs are produced.

In the experimental studies on strangeness production in heavy-ion collisions at high energies performed by E802[3], NA34[4] and NA35[5] $s\bar{s}$ creation has been indeed observed to be about three times larger then in free pp collisions. For pBe, pAu and SiAu[3] collisions at 14.6 GeV/u the K^+/π^+ ratio becomes larger if the size of the system increases. Such results support the quark-gluon hypothesis, which, nevertheless, needs further confirmation. In particular, there is no clear definition how to determine the meaning of enhanced production of strangeness. To minimize the influence of trivial kinematical factors we propose to measure the ratio $R_{K\pi} = \sigma_{K^+K^-}/\sigma_{\pi^+\pi^-}$ of the cross sections for the production of $K^\pm$ and $\pi^\pm$ pairs having the same invariant mass. This is a way to compare the creation of $s\bar{s}$ pairs with that of $u\bar{u}$ ($d\bar{d}$) pairs at comparable conditions. Although quark-gluon plasma is expected to be created in AA collisions at high energies we consider here the subthreshold region for kaon production. Under the assumption that particle production in pA interactions arises from locally heated and compressed pieces of nuclear matter[6] one can imagine the following scenario: For relatively low invariant masses the reaction proceeds above the threshold of a free NN-interaction and the ratio $R_{K\pi}$ should be similar to that observed in NN collisions. If, however, the invariant mass becomes larger then the energy necessary for the pair production increases until the subthreshold regime is reached. While the production of a low-mass pair proceeds predominantly at a single nucleon inside the target nucleus the creation of a high-mass pair requires the interaction with several target nucleons, in order to gain the necessary energy. Since the energy-momentum transfer to the participating few-nucleon subsystem is rather high, it can be considered as a locally heated and compressed piece of nuclear matter where enhanced strangeness production might be possible. Therefore, for large invariant masses of the observed pairs the value of the considered ratio will exceed the „normal" one if density and temperature become, at least locally, sufficiently high.

The proposed approach makes the search of the phenomenon more definite, because the ratio $R_{K\pi}$ is considered as a function of an observable, the invariant mass, which allows a tuning of the conditions between creation from „normal NN-interactions" and „locally heated few-nucleon groups". The same kind of effect can be expected if not the invariant mass but the incident energy is changed. In case of production at heated pieces of nuclear matter with enhanced strangeness production the ratio $R_{K\pi}$ should decrease more slowly if the energy is decreased below the NN threshold than in the case of „normal" strangeness production.

The ANKE spectrometer[7] being installed at COSY is well suited to carry out the proposed investigations. Kaons emitted at angles $\theta \leq 10°$ will be measured by two similar detection systems at both sides of the deflecting magnet. Due to the smaller mass of the pions a larger relative momentum of the two pions is needed for a pair having the same invariant mass as the kaon pair. This can be accomplished by measuring the π^- at forward angles with the same detector as the K^- mesons and the π^+ at angles $\theta \geq 165°$ using the backward detector of ANKE.

In Figs. 1 and 2 predictions for $p^{12}C$ interactions at 2.0 and 2.5 GeV from the Rossendorf collision model[8] and references therein for the invariant mass spectra of kaons and pions as well as the ratio $R_{K\pi}$ are plotted. The peak around 1.02 GeV in the invariant mass spectra of kaons originates from the production of ϕ mesons with subsequent decay into kaon pairs. In the peak region the creation of a single $s\bar{s}$ pair forming the $\phi(s\bar{s})$ meson dominates. Outside the peak region the associated production of a $s\bar{s}$ with a $u\bar{u}$ pair, which form the $K^+(u\bar{s})$ and the $K^-(s\bar{u})$ mesons directly, is more important. It is of interest whether these different production mechanisms influence the energy dependence of the ratio $R_{K\pi}$ in the discussed mass regions. The calculated cross sections for the production of the kaon and the pion pair are of comparable magnitude under the selected kinematical conditions. They may serve for an

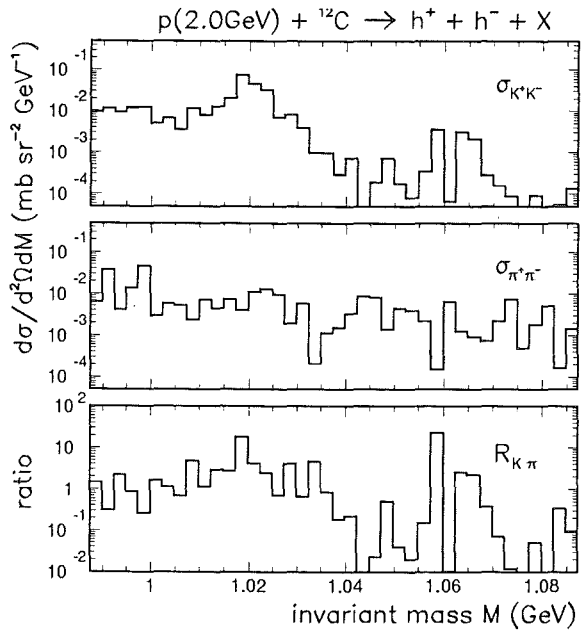

Fig. 1: Calculated invariant mass spectra of kaon ($\sigma_{K^+K^-}$) and pion pairs ($\sigma_{\pi^+\pi^-}$) and the ratio $R_{K\pi} = \sigma_{K^+K^-}/\sigma_{\pi^+\pi^-}$ for $p^{12}C$ interactions at 2.0 GeV.

estimate of the expected counting rates. The cross sections increase by more than one order of magnitude if the energy is changed from 2.0 to 2.5 GeV, the ratio $R_{K\pi}$, however, is much less affected.

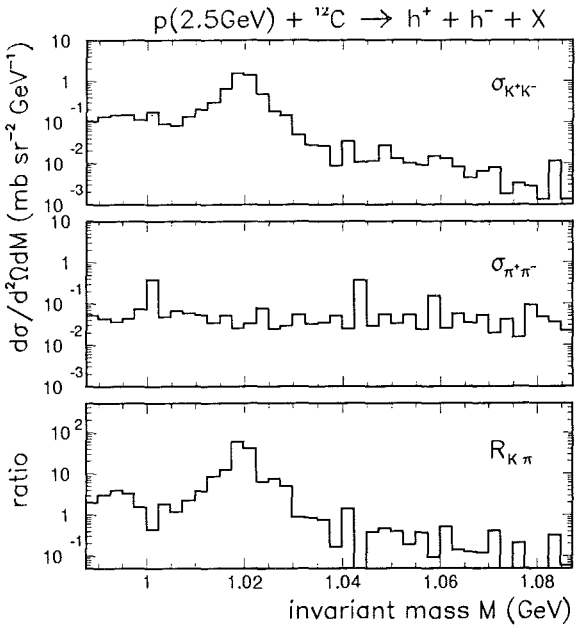

Fig. 2: The same as Fig. 1 for 2.5 GeV.

In the calculations a constant ratio u : d : s = 1 : 1 : 0.15 for the production of up, down and strange quark pairs is used. No peculiarities concerning the dependence of this ratio on density and temperature are taken into account. Therefore, these calculations may serve as a measure of „normal" $s\bar{s}$ creation. Enhanced strangeness production should then manifest itself in a larger measured ratio at high invariant masses in comparison to the calculated one.

References:

1. J. Refelski, B. Müller, Phys. Rev. Lett. 48 (1982) 1066
2. C. Greiner, P. Koch, H. Stöcker, Phys. Rev. Lett. 58 (1987) 1825
3. T. Abott et al., Phys. Rev. Lett. 66 (1991) 1567
4. Helios Collaboration: Nucl. Phys. A525 (1991) 227c
5. J. Bartke et al., Z. Phys. C48 (1990) 191
6. T. Maruyama et al., Nucl. Phys. A573 (1994) 653
7. O.W.B. Schult et al., Nucl. Phys. A583 (1995) 629
8. H. Müller, Z. Phys. A353 (1995) 237

[a] Laboratory of Nuclear Problems, Joint Institute for Nuclear Research, Dubna, Moscow Region, Russia*

[b] Institut für Kern- und Hadronenphysik, Forschungszentrum Rossendorf, Dresden

* Supported by grant 93-02-3745 of the Russian Foundation for Fundamental Research

Study of the $\vec{p}+\vec{p}\to pp\phi$ Reaction at the ANKE Spectrometer

O.E. Gorchakov[a], F.M. Lev[a], M.G. Sapozhnikov[a]

The study of the ϕ-meson production in the interaction of a polarized proton beam with a polarized proton target

$$\vec{p}+\vec{p}\to p+p+\phi \qquad (1)$$

was proposed to be performed at the ANKE spectrometer[1]. It is predicted[2] that the ϕ production should be enhanced for parallel spins of both nucleons in the initial state and suppressed for the antiparallel configuration.

This prediction was based on the assumption that there exists a substantial (at a level of a few percent) admixture of strange quarks in the nucleon wave function even at small momentum transfer. Remarkably, the strange quarks should be polarized. The possible presence of strange quarks in the nucleon wave function and the degree of their polarization is a very hot experimental topic in view of recent results from LEAR, SATURNE, the SMC and SLAC. Thus, recent results of the experiments with stopped antiprotons at LEAR (CERN) (for a review see [3]) show a strong dependence of the ϕ production on the quantum numbers of the initial state. This effect was interpreted[2] as a manifestation of the polarized intrinsic nucleon strangeness.

The conditions for the detection of the ϕ mesons from (1) in the ANKE spectrometer have been investigated. Our main goal was to calculate the acceptance of the spectrometer within different hypotheses on the ϕ production. We would like to demonstrate that the ANKE spectrometer does not artifically enhance or suppress ϕ mesons arising from the initial spin-triplet or spin-singlet states.

Three possibilities for the amplitude of reaction (1) are considered:

- the orbital angular momentum in the final pp system is $l_1 = 0$, the orbital angular momentum of the pp system relative to the ϕ meson is $l_2 = 0$. This corresponds to the spin-triplet $^3P_1$ initial state.
- $l_1 = 1$ and $l_2 = 0$
- $l_1 = 0$ and $l_2 = 1$. These two states are formed from spin-singlet initial states of the pp system.

The differential cross-section of reaction (1) is

$$d\sigma = d\Gamma\ \{2|f_1|^2+(1-\mathbf{P}_1\mathbf{P}_2)k^2[\sin^2\theta(|\tilde{f}_2+2f_3|^2+|\tilde{f}_2-2f_4|^2) + 2\cos^2\theta|\tilde{f}_2+2f_4|^2]+(1-\mathbf{P}_1\mathbf{P}_2)Q^2(\sin^2\alpha|\tilde{f}_5|^2+\cos^2\alpha|\tilde{f}_5+2f_6|^2) + 2\mathrm{Re}(f_1\tilde{f}_5^*)(\mathbf{n}\times\mathbf{Q})(\mathbf{P}_1-\mathbf{P}_2)\} \qquad (2)$$

Here P_1 and P_2 are the polarization vectors of the protons of the beam and target, f_l ($l = 1,...6$) are corresponding amplitudes, $\cos\theta = \mathbf{kn}/k$, $\cos\alpha = \mathbf{Qn}/Q$, $\tilde{f}_2 = f_2 - 2/3f_3$ and $\tilde{f}_5 = f_5 - 2/3f_6$, $\mathbf{k}$ is the relative momentum in the c.m. frame of the final pp system, $\mathbf{Q}$ is the momentum of the final pp system in the c.m. frame of the final ppϕ system, $\mathbf{n}$ is the unit vector along the momentum of the first proton in the c.m. frame of the initial system.

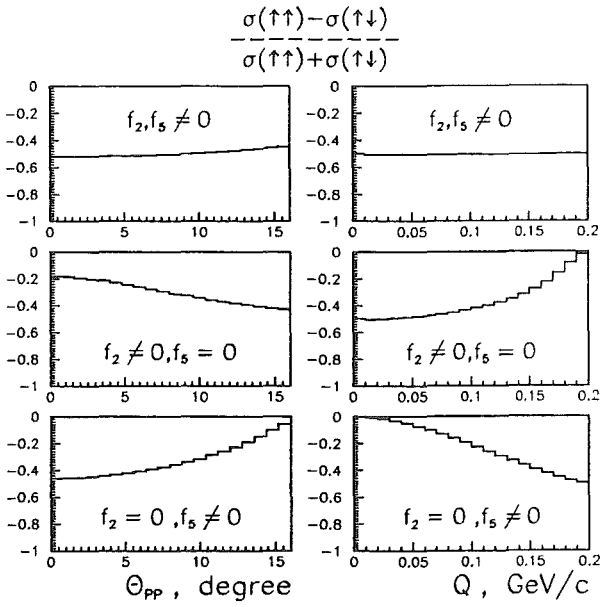

Fig. 1: The asymmetry for reaction (1) calculated under different assumptions about amplitudes f_i. Assuming equal contributions from the initial $^3P_1$, $^1S_0$ ($l_1 = 1$, $l_2 = 0$) and $^1S_0$ ($l_1 = 0$, $l_2 = 1$) states (upper part), from $^3P_1$ and $^1S_0$ ($l_1 = 1$, $l_2 = 0$) states only (center part), or $^3P_1$ and $^1S_0$ ($l_1 = 0$, $l_2 = 1$) states (bottom).

The phase space element of the three-body final state is

$$d\Gamma = \frac{Qk\cdot dM\cdot do_1\cdot do_2}{32\cdot p\cdot s\ (2\pi)^5} \qquad (3)$$

We use do_1 and do_2 to denote the element of the solid angle corresponding to the unit vectors $\mathbf{k}/k$ and $\mathbf{Q}/Q$, respectively. M is the invariant mass of the final pp system, s is the invariant mass of the initial pp system squared an dp is the momentum in the c.m. frame of the initial pp system.

It is assumed that the $\phi\to K^++K^-$ decay mode will be used for the detection of reaction (1). We consider that both final protons have to be registered by all three wire chambers and by the scintillator hodoscope of the Forward Detector, see Ref. 5. The K^+-meson has to be registered by the K^+-hodoscopes (the efficiency of the hodoscope is supposed to be 50%).

GEANT simulations of the acceptances $\varepsilon(l_1,l_2)$ calculated at T=2.68 GeV for the three different amplitudes mentioned above gives the following:

1. $\varepsilon(l_1 = 0, l_2 = 0) = (1.0 \pm 0.02)\%$
2. $\varepsilon(l_1 = 1, l_2 = 0) = (0.8 \pm 0.01)\%$
3. $\varepsilon(l_1 = 0, l_2 = 1) = (1.2 \pm 0.02)\%$

This approximate equality of the acceptances for different amplitudes means that the ANKE spectrometer does not

produce (too large) artificial asymmetry in the registration of the ϕ resulting from the spin-triplet initial state (that corresponds $\varepsilon(l_1 = 0, l_2 = 0)$) or from spin-singlet initial states ($\varepsilon(l_1 = 1, l_2 = 0, \varepsilon(l_1 = 0, l_2 = 1)$).

Assuming that the cross-section of the reaction (1) at T_{kin} = 2.68 GeV is 120 nb[4)], the intensity of the polarized proton beam is $N_{beam} = 3 \cdot 10^{10} s^{-1}$ and the polarized gas target with the storage cell provides a density $N_{target} = 5 \cdot 10^{13}$ atoms·cm^{-2}, the rate of reaction (1) will be 109 Φ's/day.

In Fig. 1 the examples of the possible asymmetry $A = (\sigma_{\uparrow\uparrow} - \sigma_{\uparrow\downarrow})/(\sigma_{\uparrow\uparrow} + \sigma_{\uparrow\downarrow})$ are shown. We calculated the dependence of the asymmetry A on the momentum Q and on the angle between two final protons Θ_{PP}.

References:

1. U. Bechstedt et al.: COSY LOI N.35 (1995)
2. J. Ellis et al.: Phys. Lett. B353 (1995) 319
3. M.G. Sapozhnikov: Proc. LEAP'94 Conference Proceedings, Bled, Slovenia, Sept. 1994, p. 355
4. A.A. Sibirtsev: private communication
5. V.M. Artimov et al.: contribution to this report, p. 77

[a] Laboratory of Nuclear Problems, Joint Institute for Nuclear Research, dubna, Moscow Region, Russia*

* Supported by grant 93-02-3745 of the Russian Foundation for Fundamental Research.

Reconstruction of the ϕ meson mass at the 0° Facility ANKE

A. Franzen, M. Büscher

It is planned to study the ϕ production in the reaction $\vec{p}\vec{p} \rightarrow pp\phi$ with a polarized beam and a polarized storage-cell target at ANKE[1]. As the ϕ meson has a mean life time of $\tau_\phi = 1.5 \cdot 10^{-22}$ s it will be identified by its decay products K^+ and K^- (branching ratio: 49.1%), which will be detected in the side-detector system[2] and detectors inside the return yoke of the spectrometer magnet[3] of ANKE. The mass of the ϕ can then be calculated from the invariant mass of the two kaons $s = m_\phi^2 = p_\mu p^\mu = (E_{K+} + E_{K-})^2 - (\vec{p}_{K+} + \vec{p}_{K-})^2$ where the momenta of the kaons (and thus their energy) have to be reconstructed using the information of wire chambers. Because of the small width of the ϕ meson (Γ = 4.43 MeV) and a target length of 40 cm one expects that the reconstructed mass spectrum will be smeared out, since the extended target will deteriorate the momentum resolution of the spectrometer. Therefore, a simulation with GEANT3.21 has been carried out to determine the mass resolution of the apparatus in this particular case.

The events of the mentioned reaction have been created for a beam energy of 2.6 GeV using a phase-space approach. To determine only the effects of the apparatus on the resolution of the mass reconstruction, the width of the ϕ meson was assumed to be Γ = 0 MeV. Multiple scattering and energy losses have been taken into account during the simulation. The geometry of the detection systems is described e.g. in [2] and [3]; the magnetic field was taken as 1.6 T. The events have been started at the target, where the position along the beam axis was smeared out with a triangular distribution with a length of 40 cm, and are traced through the magnetic field into the detectors. K^+K^- events have only been considered when they were coming directly from the target (if a particle hits the magnet it is rejected). The reconstruction of the momenta has been done via a fit with a polynomial using the 4 coordinates of the two wire chambers which the particles cross on each side of the spectrometer magnet.

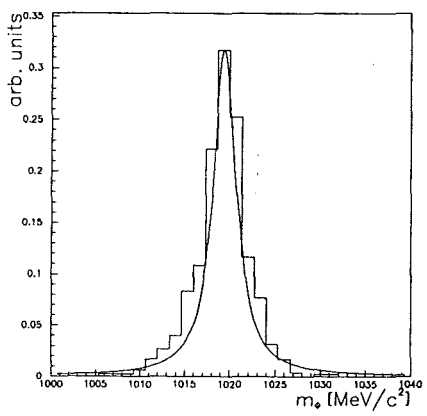

Fig. 1: Reconstructed ϕ-mass spectrum using the invariant mass of the two kaons from the ϕ decay for the reaction $\vec{p}$ (2.6 GeV) $\vec{p} \rightarrow pp\phi$. In the simulation the width of the ϕ mass was taken as Γ=0 MeV. For comparison, the ϕ mass is drawn with a Breit-Wigner form with E_0= 1019,41 MeV and Γ=4.43 MeV.

Fig. 1 shows the reconstructed mass spectrum of the ϕ mesons in comparison to the mass spectrum following a Breit-Winger form with the natural ϕ width. The reconstructed mass spectrum is slightly wider than the Breit-Wigner curve. Thus, the smearing of the reconstructed mass spectrum due to energy loss, multiple scattering is comparible to the natural width of the ϕ meson in spite of the long storage cell target.

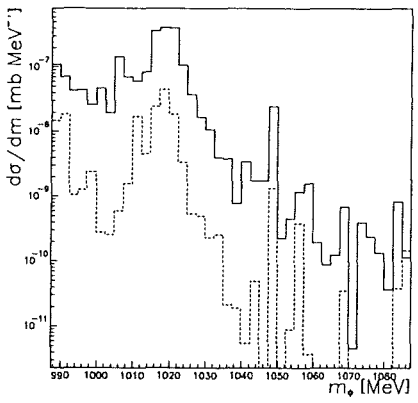

Fig. 2: ϕ-mass spectrum for the reaction p(2.0GeV) $+^{12}C \rightarrow \phi + X$ at the target (solid line) and reconstructed spectrum (dashed line) using the invariant mass of the two kaons. In the simulations all physical effects (e.g. hadronic interactions) have been taken into account; the efficiency of the detectors are assumed to be 100%.

A proposal will be submitted to investigate also the ϕ production in pA reactions at ANKE. In order to see whether, in such a study, it will be possible to identify the ϕ mesons in spite of the expected background in the invariant mass spectrum in $p+^{12}C$ reactions, the mass of the ϕ coming from those reactions has been calculated according to the procedure described above. A file with events coming from the reaction $p+^{12}C$ at 2.5 GeV has been created with the Rossendorf Collision Model[4] ($\Gamma_\phi \neq 0$ MeV). The geometry is the same as mentioned before, but in this simulation the target was assumed to be a point-like foil target. Fig. 2 shows the invariant mass distribution at the target and the reconstructed one: It can be seen that the smearing of the reconstructed spectrum.

References:

1. M.G. Sapozhnikov et al., COSY letter of intent Nr. 35
2. K. Sistemich et al., contribution to this report, p. 51
3. M. Büscher, H. Müller, Ann. Rep. 1994, KFA Jülich (1995), p. 72
4. H. Müller et al., Ann. Rep. 1994, KFA Jülich (1995), p. 47

Biophysics for Proton Therapy, Overview and Experimental Results

D. Barthmann*, R. Becker*, J. Bienen***, P. Cloth, M. Dellert**, V. Drüke, W. Eyrich**, D. Filges, M. Fritsch**, J. Hauffe**, W. Hoffmann***, H. Kobus, R. Maier, M. Moosburger**, H. Paganetti*, N. Paul, H.P. Peterson*, Th. Schmitz*, K. Schwenke*, R. Sperl**
COSY-Med Collaboration

*Institut für Medizin, KFA-Jülich, D-52425 Jülich, Germany, **Physikalisches Institut, Universität Erlangen, Germany
***Fachbereich Physik, Universität Wuppertal, Germany

One goal in radiation therapy has always been to conform the therapeutic dose as close as possible to the target volume and at the same time to minimise the volume of and the dose to normal tissues, which necessarily have to be irradiated during a treatment. In contrast to photons and also electrons, protons have a finite range in tissue, deposit most of their energy at the end of their range in the Bragg-Peak and are far less strongly scattered laterally. Consequently, protons are very well suited for high precision conformal tumor therapy.

Conformal tumor therapy places higher requirements on the planning of treatments than conventional irradiations. This is in particular true, when protons or other light ions are used, due to the sharp edges in the dose profiles that can be produced. Wrong calculations of the maximum depth of penetration may lead to either underdosage of parts of the target area or to unwanted overdosage of adjacent healthy tissues. Likewise, tissue inhomogeneities influence the depth dose distribution of protons stronger then for photons or electrons (1).

In addition, the biological effectiveness of protons changes as they are slowed down in tissue, i.e. the physical dose is not a good parameter for accessing the therapeutical potential. This effect is not as pronounced as for heavier ions, but should be observed in particular at the distal part (in and behind the Bragg Peak) of the dose profiles (2). To date, the biophysical basis for proton therapy is not satisfactory (3).

Therefore, the COSY-Med. Collaboration decided to perform biophysical investigations, which follow two aims: To establish a systematic biophysical basis for proton therapy and to develop realistic proton dose calculation routines for treatment planning based on Monte Carlo methods.

COSY is very well suited for these studies, since it delivers well defined proton beams in the whole range of energies of interest for the therapy of deep ,seated tumors.

The intention of the program is, to contribute to the optimisation of the treatment modality. The results may be used by proton therapy centers already in operation or by organisations, which intend to establish clinical proton therapy. It should be noted that the KFA is the only center at least in Germany, where biophysical investigations for proton therapy in the whole energy range of interest can be carried out. It is not the intention of the COSY-Med. Collaboration to establish clinical proton therapy at COSY.

The COSY-Med. Program

It is the aim of the program to gather the necessary dosimetric and biophysical information for the development of optimal dose calculation routines for treatment planning (4).The program has an experimental and a calculational part, which complement each other.

Experiments are performed to determine the incident beam characteristics for data normalisation and to provide input data for the calculations. Experiments in a water or a plastic phantom determine, as a function of depth, absolute dose, microdosimetric energy deposition distributions, energy loss spectra and high resolution dose profiles. For these purposes different kinds of detectors are applied.

The initial biological experiments concentrate on the determination of cell killing as a function of depth in the water phantom. The selected cells are V79 hamster cells. For the determination of the relative biological effectiveness, ^{60}Co is used as reference radiation.

The experiments are and will be performed in proton pencil beams of about 0.5 cm to 1 cm diameter and for initial energies between 100 MeV and 250 MeV.

Depth dose profiles, secondary particle spectra and energy deposition spectra are calculated as a function of incident beam parameters and depth in matter using Monte Carlo programs. The biophysical simulations use the results of these calculations and apply two different approaches to predict the RBE of protons. One is the microdosimetric method, using so called response functions, which represent the cumulative probability that a given energy deposition event in a biological target will have a given effect (5, 6, 7, 9). The other one is the track structure model of Katz and coworkers (10, 11). More details are given in a separate contribution to this annual report.

Central part of the program is the comparison of experiment and simulation. On the one hand, inconsistencies in the measurements can be detected. On the other hand, the precision of the calculation can be assessed. The intercomparison should in the end help to identify, which physical processes necessarily have to be included into simulations to achieve sufficient accuracy in the predictions of dose profiles. First results regarding the simulations and the comparison to experiments are given in a separate contribution to this annual report.

Very important is the comparison between measured and simulated microdosimetric distributions. They depend on

the total radiation field (protons and any secondary radiation) and therefore clearly reveal how realistic the radiation transport calculations describe the radiation field at depth in the phantom. This is important for judging the quality of the biophysical simulations.

First Experimental Results

Experiments have been performed in the water and in the plastic phantom. The water phantom is a Plexiglas vessel with a volume of 50 cm x 50 cm x 40 cm (width x depth x height). The wall thickness is 1 cm. A 3-axis scanner unit is used to position the detectors within the phantom with an accuracy of better than 1 mm. The plastic phantom is fabricated from Plexiglas and its thickness can be varied between 4 cm and 30 cm. The Si-microstrip detectors and the fiber hodoscopes are either placed in front or behind the phantom. COSY delivered protons of 175.5 MeV (±1%) kinetic energy (600 MeV/c momentum). The momentum spread was about 5.10^{-3} and the beam diameters on the surfaces of the phantoms had been adjusted to about 1 cm FWHM and 0.5 cm FWHM respectively in case of the water and the plastic phantom. The extraction pulse duration was about 200 ms. About 50% percent of the protons were delivered within the first 50 ms, which caused serious dead time problems in the electronics of the scintillators used as beam monitors in case of the water phantom experiments. Therefore, these measurements cannot be normalised to the number of incident protons, which would be desirable.
Below results of a depth dose measurement with an ionisation chamber and TLDs and of microdosimetric measurements, using a proportional counter are shown. Other Experimental results are discussed in separate contributions of the COSY Med. collaboration.

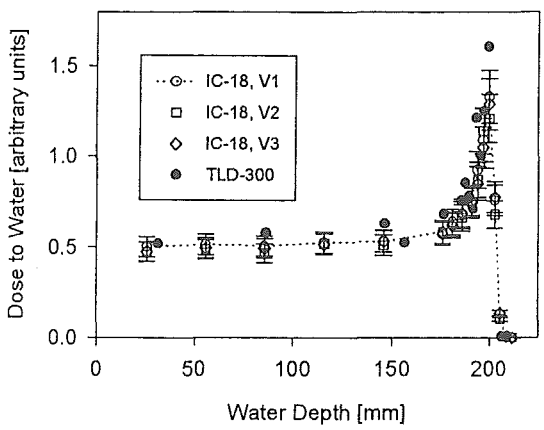

Fig. 1: Measured depth dose profiles

Figure 1 displays a depth dose profile measured with the small-volume (0.1 cm^3) ionisation chamber and with TLDs. The data are normalised to the monitor counts, even though this number is as mentioned distorted by dead time effects. It is assumed, since the extraction was very stable that on average all monitor counts are equally affected. Nevertheless, only arbitrary units are given on the ordinate. The error bars reflect the standard deviation of the mean of five repetitive measurements taken at each point during one scan, again assuming a constant effect of the electronic dead time on the monitor counts. The precision of the measurements cannot be assessed from these experiments and have to be studied during the next beam time. This information is important, since the ionisation chamber must serve for the dose estimation in the biological measurements.

Presented below (Fig. 2) are microdosimetric dose distributions measured at different depth along the beam axis (8). The spectra are plotted against the logarithmic increment of lineal energy and are normalised to unit dose. In this presentation, equal areas of the distribution represent equal fractions to absorbed dose. The shift of the spectra to higher lineal energies reflects the increase in proton stopping as they are slowed down. The distributions measured near the entrance of the phantom at 19.2 mm and 24.2 mm are surprisingly broad. The reason is not clearly understood, but might be due to either misalignment of beam axis and counter centre or due to pile up effects because of the unfavourable extraction intensity of the accelerator. No significant contribution of high energy neutrons can be detected from the spectra. They would contribute at lineal energies above the proton edge at about 120 keV.μm^{-1}. This can be expected, since the neutron production at 175 MeV incident proton energy is very low.

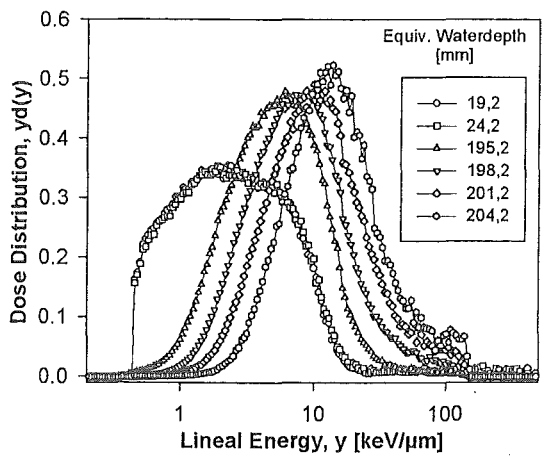

Fig. 2: Microdosimetry dose distributions

Acknowledgement

We are in debt to Mr. Heinz Rongen (Central Electronics Department, KFA-Jülich) for his help with respect to various electronic problems that had to be solved. Finally, we thank the colleagues from the University of Saarland, Department of Biophysics and Fundamental Physics, Homburg, for giving us their 1/2" proportional counter.

References

(1) Urie, M., Treatment Planning for Proton Beams. IN: Ion Beams in Tumor Therapy, Linz, U (Ed.), Chapman&Hall, London, pp. 279-289 (1995).

(2) Paganetti, H.; Olko, P.; Kobus, H.; Becker, R.; Schmitz, Th.; Waligorski, M.P.R.; Filges, D.; Müller-Gärtner, H.W., Calculation of RBE for proton beams using biological weighting functions. Submitted to Int. J. Rad. Oncol. Biol. Phys.

(3) Blakely, E.A., Biological Beam Characterisation. IN: Ion Beams in Tumor Therapy, Linz, U (Ed.), Chapman&Hall, London, pp. 63-72 (1995).

(4) Bartmann, D., Drüke, V., Wyrich, W., Filges, D., Hoffmann, W., Klasen, C., Linz, U., Maier, R., Neef, R.D., Paul, N., Schmitz, Th., Pre-Therapeutic Physical Experiments on Phantoms with Proton Beams at Energies between 50 MeV and 250 MeV. COSY Proposal No. 26, Forschungszentrum Jülich, 1993.

(5) Menzel, H.G.; Pihet, P.; Wambersie, A., Microdosimetric specification of radiation quality in neutron radiation therapy. Int. J. Radiat. Biol. 57 865-883 (1990)

(6) Morstin, K.; Bond, V.P.; Baum, J.W., Probabilistic approach to obtain hit-size effectiveness functions which relate microdosimetry and radiobiology. Radiat. Res. 120 383-402 (1989)

(7) Pihet, P.; Menzel, H.G.; Schmidt, R.; Beauduin, M.; Wambersie, A., Biological weighting function for RBE specification of neutron therapy beams. Intercomparison of 9 European centres. Radiat. Prot. Dos. 31 437-442 (1990)

(8) ICRU Report 36, Microdosimetry. ICRU Publications, Bethesda, Maryland (1983).

(9) Wambersie, A., Contribution of microdosimetry to the specification of neutron beam quality for the choice of the 'clinical RBE' in fast neutron therapy. Radiat. Prot. Dos. 52 453-460 (1994)

(10) Zaider, M.; Brenner, D.J., On the microdosimetric definition of quality factors. Radiat. Res. 103 302-316 (1985)

(11) Katz, R.; Sharma, S.C., Response of cells to fast neutrons, stopped pions, and heavy ion beams. Nucl. Inst. Methds. 111 93-116 (1973)

Comparison of Different Monte Carlo Programs for Use in Proton Dosimetry

D. Barthmann[2], R. Becker[2], J. Bienen[4], P. Cloth[1], M. Dellert[3], V. Drüke[1], W. Eyrich[3], D. Filges[1], M. Fritsch[3], J. Hauffe[3], W. Hoffmann[4], H. Kobus[1], R. Maier[1], M. Moosburger[3], H. Paganetti[2], N. Paul[1], H. P. Peterson[2], Th. Schmitz[2], K. Schwenke[2], R. Sperl[3]
COSY-Med Collaboration

[1]IKP, Forschungszentrum Jülich GmbH (KFA), [2]IME, Forschungszentrum Jülich GmbH (KFA), 52425 Jülich, Germany
[3]Institute for Physics, Erlangen University, Germany, [4]Department of Physics, Wuppertal University, Germany

Introduction

It is predicted that the use of protons with kinetic energies between about 50 MeV and 250 MeV in cancer radiotherapy offers significant advantages, when compared to radiations conventionally employed. The reason is the characteristic depth dose distribution of protons, which allows an improved conformation of the treatment dose to a target and at the same time a better sparing of healthy tissue. This has been shown for several tumor sites on the basis of comparative treatment planning calculations [1]. However, the dose calculation routines for protons in treatment planning programs are quite simplistic and the results have to be interpreted with great care [2]. Monte Carlo calculation techniques could help to improve this situation and would enable to further exploit the possible advantages of protons in high precision conformal radiation therapy [3].

When developing or applying a Monte Carlo code for dose calculation in treatment planning the main question is, how precise or how realistic are the achieved results. They are dependent on the nuclear data library used, the physical laws applied and the types of particle interactions considered. The best way to test the precision of dose calculations is the comparison to experiments, which have been performed under known conditions and which are modelled by the calculations.
We compared measured depth-dose profiles to calculations performed with two different Monte Carlo codes. Our measurements took place at the Low Energy Measurement Area of COSY.

Used Monte Carlo Codes

HETC (High Energy Transport Code), which is part of the HERMES package [4], was written for transport calculations in High Energy Physics. It is a 3-D transport program. In a three-dimensional combinatorical geometry input, regions with different size and material compositions can be defined. With a variety of different detector modules, parameters like energy deposition, particle flux or energy spectra can be simulated. The detector size and the beam parameters like diameter and energy spread are variable and can be adjusted to the experimental set-up. Secondary particles like neutrons, alphas, deuterons, tritons are generated and transported. The energy of the emerging recoil nucleis is deposited locally.
PTRAN [5] is widely used in proton dosimetry. It is a 2-D transport program and calculates the transport of proton pencil beams in water. The proton energy deposition and the proton spectra are always measured over the whole lateral field of the phantom; the detector size is not variable. Secondary particles are not produced, but the program gives an estimation of the number of nuclear collisions which occured on the proton path.
Both programs do not simulate δ-electrons, but deposit their kinetic energy locally.

Experiment and Simulation

Our measurements took place at the Low Energy Experimental Area ("NEMP") of COSY. For our measurements we used protons with a beam momentum of p = 600 MeV/c, which is equal to a proton kinetic energy of 175.48 MeV.
In the water phantom, dose distributions were measured with an IC 18 ionization chamber and with TLD 300.
The measured dose distributions are shown in Fig. 1. The dots are representing the data from the ionisation chamber measurement and the TLD data is printed in squares.

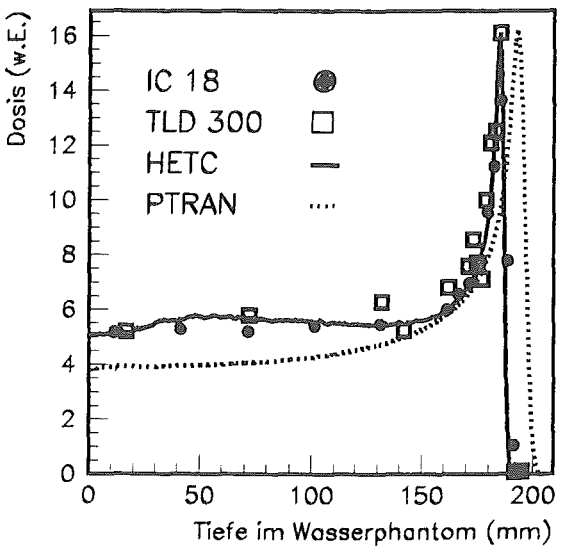

Fig. 1: Measured and simulated depth dose distributions in the water phantom

The beam and detector parameters for HETC (broken line) were close to the real parameters: $\Delta p/p = 0.5$ %, beam radius $\sigma(r) = 2.7$ mm and the size of the cylindrical detector was 1 mm in depth and a diameter d = 3.8 mm. For PTRAN (dotted line), the energy and the momentum spread were chosen accordingly. For both programs, the position of the Bragg peak was at greater depth in the phantom as compared to the experiment. Therefore, an additional HETC-simulation was started with a reduced energy of E = 172.9 MeV in order to match the experimental peak position. All curves were normalized to the peak of the TLD-measurement.

The doses are given in arbitrary units since a normalization to the number of primary protons was impossible due to dead time problems of the szintillator starting counters which led to an underestimation of the number of protons per spill.
The uncertainty of the detector position was in the range of 1 - 2 mm.

Results of the Water Phantom Measurements

The calculated Bragg peak position differs from the measured one; both HETC and PTRAN simulate a deeper beam penetration at the energy used in the experiment. HETC is 5 mm or 2.7 % deeper, PTRAN 7 mm or 3.7 %. The differences between the two programs can be explained by the use of different energy-range tables. In an additional test run of both Monte Carlo codes at an proton kinetic energy of 250 MeV, the positions of the Bragg peaks showed at difference of nearly 2 cm. Because the range tables are an essential part of all therapy planning programs, great store should be set by the development of precise data.
The shift of both programs towards higher ranges compared to the experimental data must be investigated further.
The PTRAN Bragg curve has a too high peak-to-plateau ratio, if compared to the HETC and the experimental Bragg curve. This can be explained due to PTRAN's laterally integrating energy deposition detector. Whereas HETC simulates a detector with a size in the range of the beam diameter, PTRAN also counts protons which were scattered out of the region where the detector in the experiment measured. The slower rise in the plateau region of the curve of the HETC calculation and the experimental data can be explained with this multiple scattering effect.Using a detector with an infinite lateral size also leads to a broader Bragg peak; FWHM(PTRAN) = 16.5 mm, FWHM(HETC) = 10.5 mm. This fact limits the use of PTRAN to the simulation of data acquired with broad detecor systems and excludes the validation of data from small detector measurements.

Outlook

Although the depth dose distribution is an important parameter of interest in proton therapy, it is not suitable for application in biophysical calculations. Here, more detailed measurements like particle spectra, lateral beam distributions and other event-by-event taken data are required (see also [6]). We therefore performed first test measurements with a Silicon microstrip detector developed at the Erlangen University. We measured the energy loss of protons behind a acryl phantom, which is varialble in thickness. A comparison of these data with the simulation is not fully finished, but will give a more detailed look to the precision of Monte Carlo codes.

Summary

The measurements showed that a high precision data acquisition is necessary for Monte Carlo code validation. When using small detector devices, PTRAN is not suitable to reproduce the results. The outcome of the HETC simulation is very promising, although the shift towards higher depths needs to be further investigated at other proton beam energies. We plan more measurements at different energies at COSY in the first half of 1996. The plastic phantom data will be further analyzed. Further calculations will be extended to three dimensions, to simulate the dose distributions in the plastic and the water phantom. The development of a Monte Carlo based treatment planning program will be continued.

References

[1] Tatsuzaki, H., Urie, M., Linggood, R., *Comparative Treatment Planning: Proton Vs. X-Ray Beams Against Glioblastoma Multiforme*, NCI Proton Workshop, Int. J. Radiation Oncology Biol. Phys. Vol. 22, pp. 265 - 273 (1992)

[2] Urie, M., *Treatment Planning for Proton Beams, Ion Beams in Tumor Therapy*, Linz, U. (Ed.), Chapman & Hall, ISBN 3-8261-0063-8, (1995)

[3] White, R.M., Chadwick, M.B., Chandler, W.P., Hartmann-Siantar, C.L., Resler, D.A. and Weaver, Keith A., *High energy data and dose calculation for therapy - the PEREGRINE program*, 8th Symposium on Neutron Dosimetry, Paris (Nov. 1995)

[4] Cloth, P. et al., *HERMES - A Monte Carlo Program System for Beam Materials Interaction Studies*, Report Jülich-2203 (1988)

[5] Berger, M., *Proton Monte Carlo Transport Program PTRAN*, National Institute of Standards and Technology, Publication NISTIR 5113 (1993)

[6] Schmitz, Th., Paganetti, H., *Biophysical Investigations of Therapeutic Proton Beams with Energies between 100 MeV and 250 MeV: Experiments and Calculations*, 8th Symposium on Neutron Dosimetry, Paris (Nov. 1995)

Tests for Pretherapeutic Physical Experiments at COSY using High Resolution Detector Arrays*

M. Dellert, W. Eyrich, M. Fritsch, J. Hauffe, M. Moosburger, R. Sperl, F. Stinzing and S. Wirth
for the COSY-MED Collaboration

At the low energy external COSY beam test measurements for pretherapeutic studies have been performed. In the first stage flux distributions and energy deposit of the primary protons and secondary particles (δ-electrons and neutrons) will be measured for different beam momenta using tissue equivalent phantoms. From this, parameters for the real modelling of optional therapeutic beams can be extracted. To enable measurements with high spatial and sufficient energy resolution which also allow to identify multihit events in order to get information about the energy deposit of secondary particles, detector arrays with high resolution are used. This allows to measure in the order of 10^5 pixels in the beam phantom system simultaneously. Two types of detectors have been prepared for these measurements: Silicon microstrip detectors of various geometrical shapes and areas of scintillating fibres.

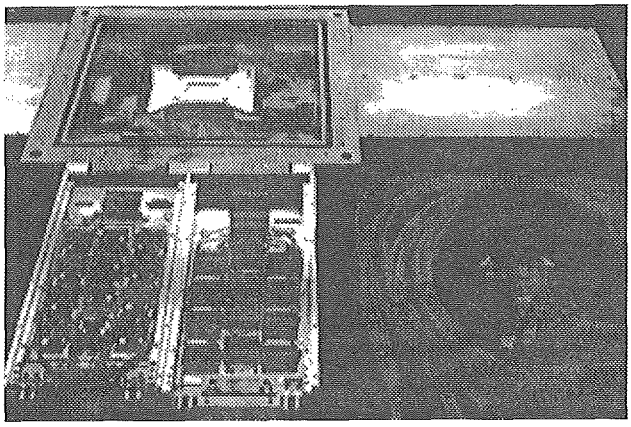

Figure 1: Microstrip detector system

Fig. 1 shows a photo of the microstrip device containing in the actual case two crossed linear detectors with an active area of $2{\cdot}2\,\mathrm{cm}^2$ and pitches of $200\,\mu\mathrm{m}$. Alternatively a ring shaped detector with a central whole for the primary beam can be installed especially suitable to study the outer region of the radiation field. The readout is done by hybrid preamplifiers followed by fastbus electronics. The detector housing is built in a way to minimize non tissue equivalent material close to the detector.

The detector array consisting of scintillating fibres is shown in fig. 2. It has an active area of $3.2{\cdot}3.2\,\mathrm{cm}^2$ built by square fibres of $2{\cdot}2\,\mathrm{mm}^2$. Alternatively fibres of $1{\cdot}1\,\mathrm{mm}^2$ can also be used. The readout is done by 16 fold photomultipliers (Hamamatsu R4760). Fig. 3 shows the setup for the first test measurements in July 1995. To get most exclusive information the coordinates of the incomming beam are measured by a small microstrip array with a resolution of $200\,\mu\mathrm{m}$. The thickness of the plastic phantom built up by wedges can be varied contineously by a step motor.

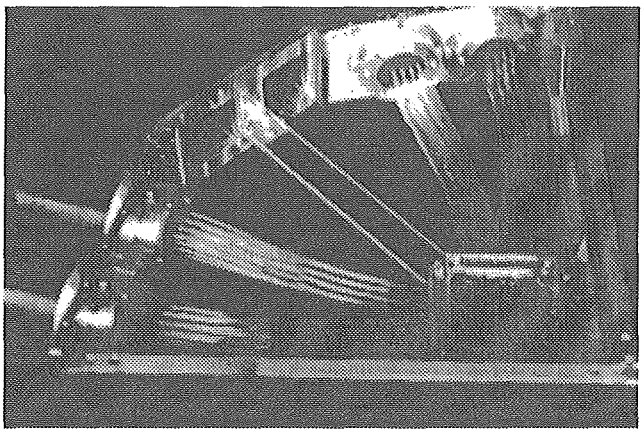

Figure 2: Scintillating fibre detector

In a first test using a beam momentum of 600MeV/c corresponding to a kinetic energy of 175 MeV the two different detector systems were used to get information about their performance and the data aquisition system. Moreover it was the aim to get first information about the energy deposit to test the various simulation programs.

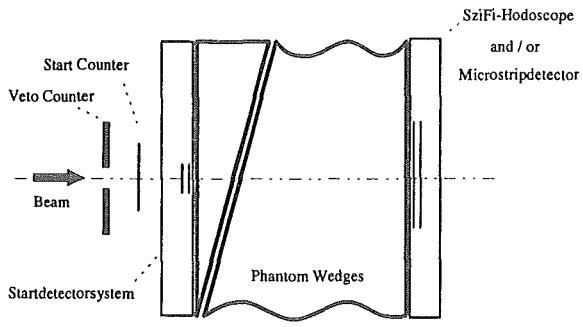

Figure 3: Experimental setup July 1995

Fig. 4 shows energy loss spectra measured by the microstrip device corresponding to the central part of the beam using various phantom thicknesses. From that one gets directly the energy loss curve with the characteristic Bragg Peak at the stop region as can be seen in fig. 5. Taking now the information of all microstrip channels for the different phantom thicknesses the three dimensional energy deposit of the proton beam propagating through the plastic phantom is obtained, which is shown in fig. 6. This directly gives the dose distribution of a point like beam including the influence of its divergency. The nearly total decrease of the energy exposit after stopping of the primary protons is obvious.

Similar test measurements were performed using the scintillating fibre hodoscope.

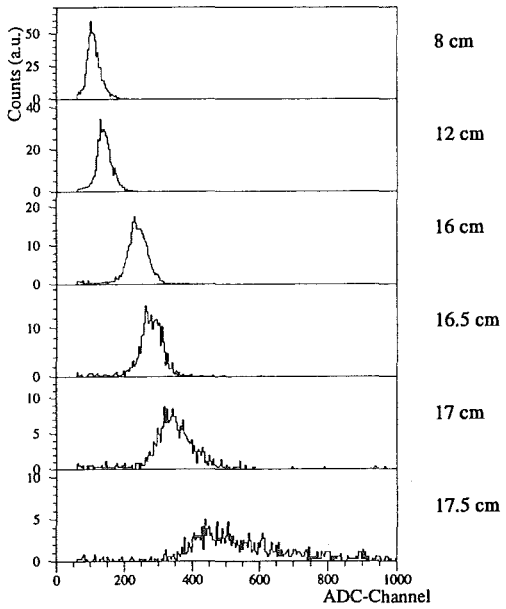

Figure 4: Microstrip spectra

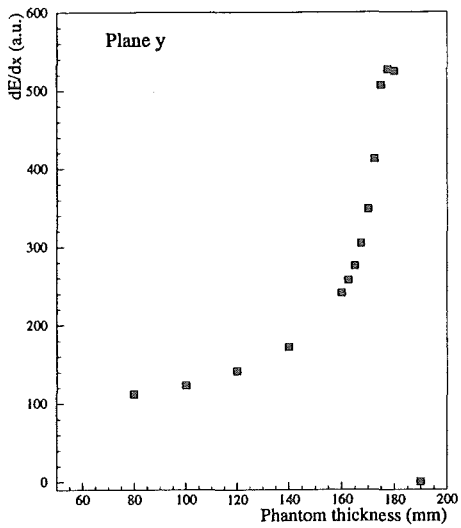

Figure 5: Energy loss

In fig. 7 the energy spectra of the fibre corresponding to the center of the propagating beam is shown. The typical behaviour of the Bragg curve is obvious.

In summary the performance of both detector systems meet the design values and first test measurements show that the used method is suitable to extract the parameters of interest. The next steps should be a systematic measurement at different energies using both detector systems including in addition coincidence measurements of both detectors in or behind the phantom respectively to extract also information about the propagation of secondary particles.

To get most precise information about the energy distribution within the Bragg peak additional measurements had been started at the Erlangen Tandem accelerator including also biological measurements by using cell cultures.

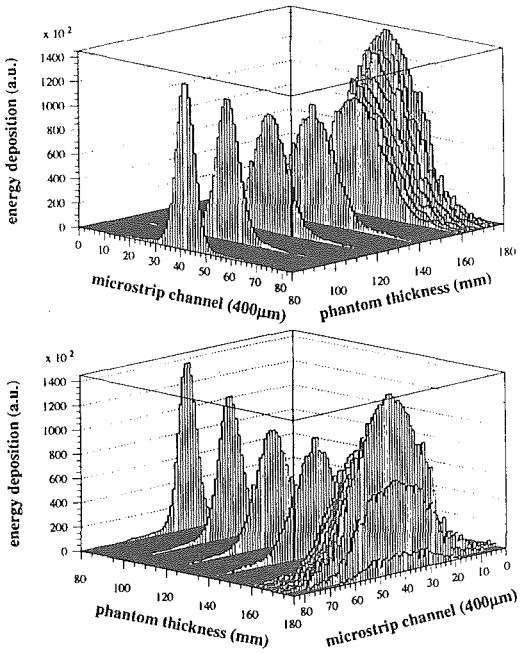

Figure 6: Energy deposit of the proton beam within the plastic phantom

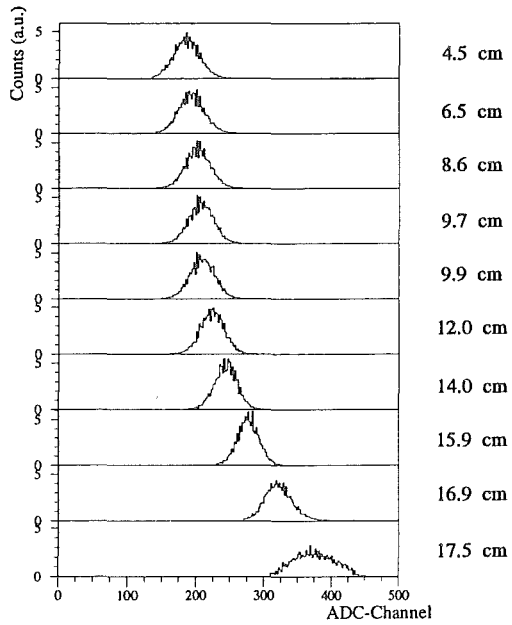

Figure 7: Fibre spectra

* supported by FZ Jülich

TLD 300 Dosimetry at the COSY Pretherapeutic Proton Beam

J. Bienen and W. Hoffmann, Bergische Universität, Physics Dept., 42097 Wuppertal, Germany
for the COSY-Med Collaboration

Thermoluminescent materials are widely used in conventional radiotherapy because of their high sensitivity, small size, self integrating behaviour, fast analysis, linear response in the therapeutic dose range and the possibility to use them as in vivo dosemeters.

In hadron fields the dose response is strongly LET dependent for most materials; it was shown however [1,2], that the sensitivity of the high temperature peak of CaF_2:Tm (TLD 300) is LET independent up to 50 keV/μ, whereas the sensitivity of the low temperature peak decreases rapidly with increasing LET. In some high LET fields like neg. pion or He^{+2} fields it was demonstrated, that it is possible to determine dose an average lineal energy simultaneously from the analysis of a single glow curve [3]. With a proper RBE vs. LET model this allows to determine biological equivalent dose. In therapeutic fast neutron fields it is possible to separate neutron and gamma dose [4].

The aim of this work was to determine the potential of this dosimetry method for therapeutic proton fields. The irradiations were performed at the pretherapeutic 200 MeV proton beam of the COSY accelerator at KFA Jülich/Germany. TLD 300 dosemeters of size 3 mm x 3 mm x 0.9 mm were irradiated inn a water phantom along the depth dose distribution of a 175 MeV proton beam at a dose level of about 0.25 Gy. At the same positions microdosimetric spectra were taken, such that the results could be compared to those spectra. Before irradiation the chips were heated at 400 °C for 1 h. Each dosemeter was calibrated individually with ^{60}Co gammas.

Figure 1 shows three different glow curves taken after irradiation in the plateau (4.5 keV/μ), near the bragg peak at 6.5 keV/μ and in the peak falloff (21.5 keV/μ). As expected the sensitivity of the low temperature peak (peak 1) decreases rapidly with inncreasing y_D, whereas the sensitivity of the high temperature peak (peak 2) remains constant. (The small peak at 100 °C has no significance, since it decays after a few hours.) Therefore the dose can be determined from the peak 2 height independent of LET. Figures 2 gives a depth dose distribution measured with peak 2. For comparison the figure also shows the same dose distribution measured with a 0.1 cc ionization chamber (Far West EC 18) and the corresponding Monte Carlo calculations.

The peak height ratio peak 1/peak 2 (P_1/P_2), which is 3.0 for ^{60}Co irradiations, decreases with increasing LET and therefore can be used to determine y_D. Figure 3 gives the peak height ratio along the depth dose distribution of Fig. 2. The rapid increase of average lineal energy in the bragg peak as determined by the proportional chamber measurements is reflected by the decrease in the P_1/P_2-ratio. For comparison the values $15/y_D$ are plotted as a function of depth; this function shows the same dependance on depth as the peak height ratio.

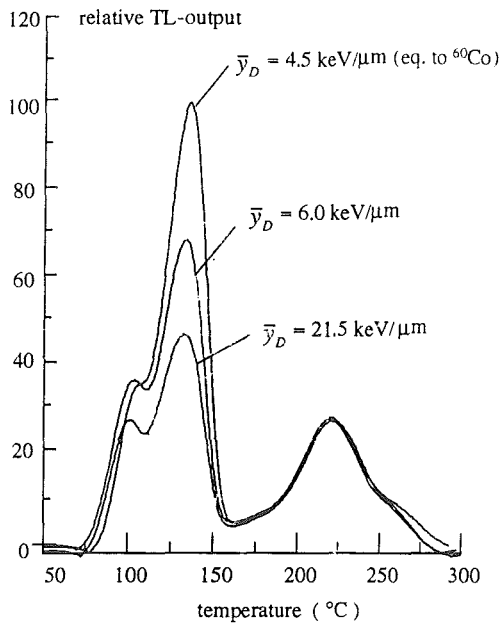

Fig. 1: Glow curves of CaF_2:Tm after proton irradiation at different positions along the depth dose distribution

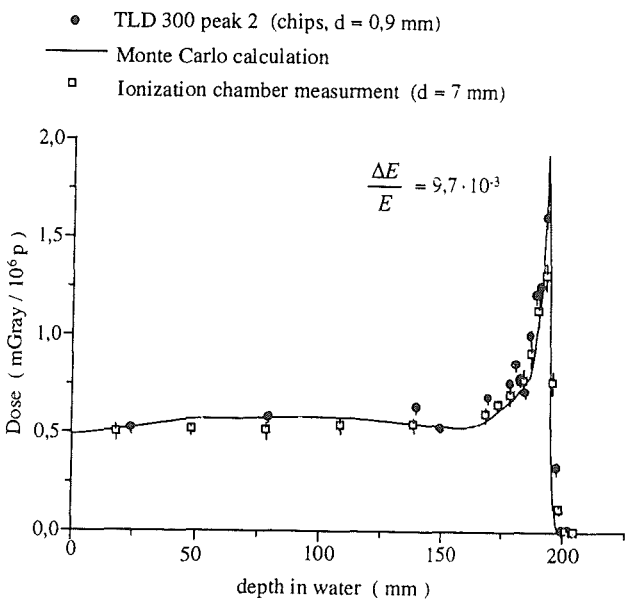

Fig. 2: Depth dose distribution of COSY 175 MeV proton beam

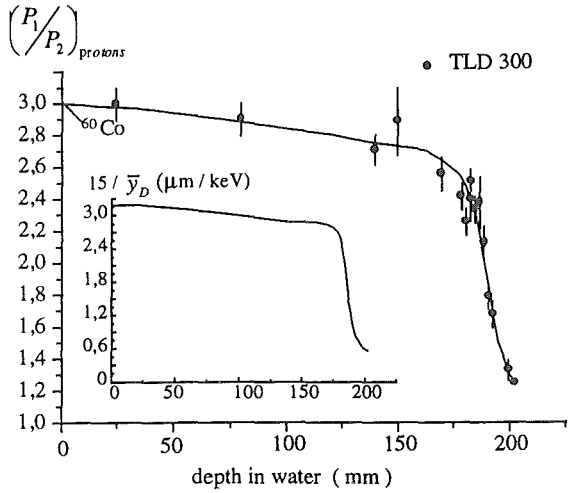

Fig. 3: TLD 300 peak height ratio along the proton depth dose distribution

Those first irradiations clearly demonstrate, that CaF_2:Tm dosimetry can be used in therapeutic proton beams to determine dose and average lineal energy simultaneously. The accuracies achievable will probably be better than ± 5% for the dose and ± 4 keV/µ for y_D. The exact values will be evaluated after further irradiations.

References

[1] W. Hoffmann, G. Möller, H. Blattmann, M. Salzmann, Pion Dosimetry with Thermoluminescent Materials, Phys. Med. Biol.. 25 (1980) 913

[2] W. Hoffmann, G. Möller, Heavy Particle Dosimetry with High Temperature Peaks of Thermoluminescent Materials, Nucl. Instr. Meth. 175 (1980) 205

[3] W. Hoffmann, B. Prediger, Heavy Particle Dosimetry with High Temperature Peaks of CaF_2:Tm and Li^7F Phosphors Radiat. Prot. Dosim. 6 (1984) 149-152

[4] W. Hoffmann, P. Songsiriritthigul, TLD 300 Dosimetry at Chiang Mai 14 MeV Neutron Beam, Radiat. Prot. Dosim. 44 (1992) 301-305

A Monte Carlo Module for Use in Proton Therapy Planning - First Results

H. Kobus for the COSY-Med Collaboration

In proton therapy, the treatment planning has to be done with very high accuracy to take a maximum benefit from the particular dose distribution of light ions. For the calculation of a homogenous dose distribution in the tumor region, two methods are conventionally used: The Broad Beam Algorithm and the Pencil Beam Model [1]. The Broad Beam is a non-divergent beam, composited of parallel-proton pencil beams. The range of the protons and the dose at any given point along the track is determined by the evaluation of the water equivalent pathlength (integral of the water stopping power along the path). Due to the neglect of multiple scattering, a broading of the beam can not be seen in calculations with this algorithm. The Pencil Beam Model takes this effect into account, but still doesn't include nuclear interactions of the protons which lead to a strong deflection of the proton and the generation of secondary particles like neutrons and alpha particles. The Monte Carlo method offers the possibility to get a more realistic impression of the occuring physical interactions which can result in an improved precision of the three-dimensional dose distribution in the patient [2]. We are developing PROVOX, an experimental module based on Monte Carlo calculations to investigate the usefulness of the Monte Carlo method in proton therapy and dosimetry.

Before starting PROVOX, the user has to define the phantom geometry, the location of the target and the direction from where the proton beam should penetrate. The geometrical input mode is based on the Bisectional Geometry developed at KFA [3]. The so defined target region is then divided into a set of cubic voxels of the same size. Then the water equivalent pathlength between the entrance point of the proton beam and every single voxel is determined and - using a predefinded energy-range table - the voxel-dependent energy is calculated. In a next step, the weight of each proton beam is calculated in order to achieve a homogenous dose distribution in all target voxels. The Monte Carlo code is then started with this set of input data for energy, weight and beam entrance points.

PROVOX transports protons and neutrons up to a kinetic energy of 300 MeV. Down to 20 MeV, nuclear interactions are treated according to the Bertini INC model [4]. The maximum particle energy is below the threshold for pion production, so this kind of particles are not included. The energy of the residual nuclei is neglected but may be included in a further version. Below 20 MeV, no nuclear interactions with protons are assumed. Nuclear collisions of neutrons are then calculated using partial cross sections. The cutoff energy for both particles is 1 keV. A correction algorithm is used to compensate deviations of the precalculated homogenous dose distribution due to the nuclear interactions. In order to simulate multiple irradiations from different directions it is possible to add the previously acquired dose distributions to one data set.

The graphical representation of the dose distribution of the whole target region is performed with the visualisation system AVS™ [5]. It has the possibility to visualize three dimensional isodose surfaces, two dimensional slices through the dose distribution and simple dose profiles along the proton path. AVS™ also allows to further process the voxel data, e.g. to show a histogram representation of the frequency of voxels with a given dose in the target volume and to give an estimation of the achieved irradiation quality. In the given example, we used PROVOX to simulate the bi-directional (90°) irradiation of a sphere with a diameter of 4 cm situated inside of a water phantom in a depth of 15 cm. Fig. 1 shows the dose distribution in the central plane of the sphere. In Fig. 2 and Fig. 3 are shown the 10%- respectively 90%-isodose surface. It is obvious that the 90%-isodose matches well the predefined target region.

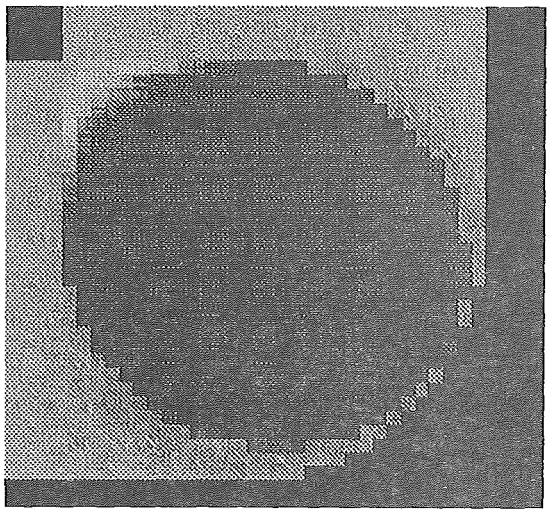

Fig. 1: Dose distribution in the central plane of the sphere

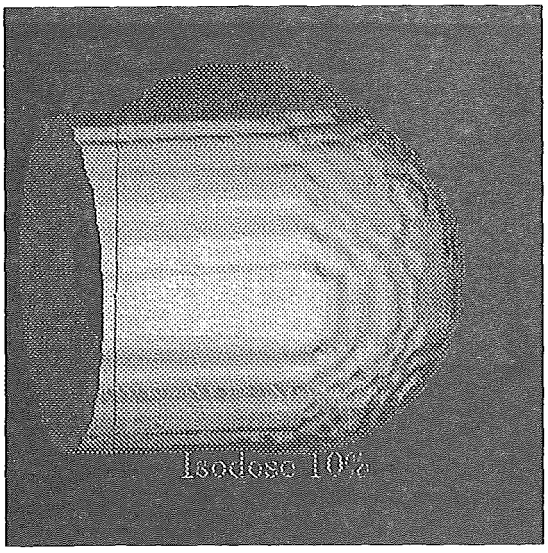

Fig. 2: 10%-isodose surface

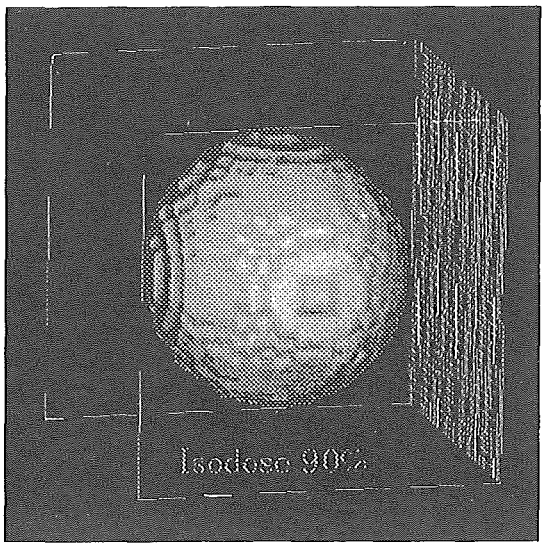

Fig. 3: 90%-isodose surface

In a further development stage it is planned to investigate the transport and the dose deposition of charged light ions emerging from nuclear collisions. An additional calculation of the biological dose is necessary. It is also possible to include PROVOX in an existing therapy planning program to be able to process medical input data from CT images.

References

[1] U. Amaldi and M. Silari (editors), *The Tera Project and the Centre for Oncological Hadrontherapy*, published by INFN - LNF - Divisione Ricerca, SIS, P.O. Box 13, Frascati, Italy, ISBN 88-86409-01-X (1994)

[2] R.M. White, M.B. Chadwick, W.P. Chandler, C.L. Hartmann-Siantar, D.A. Resler and Keith A. Weaver, *High energy data and dose calculation for therapy - the PEREGRINE program*, 8th Symposium on Neutron Dosimetry, Paris (Nov.1995)

[3] P. Cloth, D. Filges and G. Sterzenbach, *The Binary Sectioning Geometry for Monte Carlo Detector Simulation*, Proceedings of the MC93 International Conference on Monte Carlo Simulation in High Energy and Nuclear Physics, Tallahassee, U.S.A. (Feb. 1993)

[4] H.W. Bertini, Phys. Rev. C 6 (1973) 631

[5] *AVS™ User's Guide*, Release 4, AVS Visual Systems Inc., 300 Fifth Avenue, Waltham MA 02154, U.S.A., (May 1992)

Influence of the Proton Beam Modulation on Dose and RBE

P. Olko*, H. Paganetti**, Th. Schmitz**
for the COSY-Med Collaboration

*Institute for Nuclear Physics, Krakau, Polen, **Institut für Medizin, KFA-Jülich, D-52425 Jülich, Germany,

INTRODUCTION

Due to the finite range and the sharpness of the dose gradients, protons offer advantages over radiations conventionally employed in radiation therapy. However, the depth-dose distribution delivered by a monoenergetic proton beam, characterized by the Bragg Peak, is mostly not suited for treating a tumor. As tumors occupy an extended volume, a beam modification has to secure that this volume will be irradiated uniformly. For this dose conformation the energy and the direction of the beam has to be modified during treatment, either by a passive or by an active method. The usual passive beam modulation technique uses a scattering material placed upstream and a collimator placed close to the patient. Using an active method the energy of the beam is changed electronically.

It is, however, not really the dose that has to be uniform over the target volume but the biological effect. A biological dose can be defined as dose times the respective Relative Biological Effectiveness (*RBE*). In the present clinical practice, a single value of a therapeutic *RBE* in the range of 1-1.2 is used for the whole treatment planning. Nevertheless, it is undisputed that the proton *RBE* depends on the type of the biological end-point, on the initial proton energy, on the energy spread of the input proton beam and on the depth of beam penetration (Paganetti et al 1996). Applying a variable proton *RBE*, the biological dose within the SOBP increases in contrast to the dose distribution. This is because the average proton energy is decreasing with depth within the SOBP. Isodose contours are isoeffect contours only if the energy spectra of the accompanying particles remain constant.

In addition, there may be supplementary differences in the distribution of proton energy depending on the beam delivery method. Following the expression that the dose can be described as the product of fluence and *LET* it is evident that similar doses can be achieved with different proton energy distributions.

METHODS

Dose Calculation

Proton transport calculations with the Monte Carlo code PTRAN (Berger 1993) were performed for water. The obtained information includes energy loss curves as well as energy spectra of protons at various depths. To obtain a given SOBP in a water phantom, an initial set of semi-monoenergetic proton beams, characterized by their dose distributions, were superimposed. Here the modulation technique has to be taken into account. For an active modulation device, the doses belong to energetically different proton beams. On the other hand, simulating a passive device, one has to use incident proton beams with constant energy, penetrating different depths in a range filter.

RBE calculation

Two different biophysical models were used:

The microdosimetric model describes the response of cellular systems using a phenomenological weighting function. The main assumption in the model is that a dose-biological effect relationship can be expressed as an integral convolution of two separate functions of lineal energ y. To obtain *RBE* values within this model, microdosimetric distributions were calculated for pencil beam energies. The number of stoppers and crossers traversing a homogeneous spherical target of 1μm diameter were determined by the spectrum of protons at the surface of the cavity. Next, the response function for early intestinal tolerance assessed by crypt regeneration in mice (Loncol et al (1994)), was applied.

The track structure model specifies the biological response of a radiation field by the spatial distribution of radiation damage generated by the passage of a particle and its associated δ-rays (Katz and Sharma 1973, Katz and Sharma 1974). It is based on the assumption that, per average dose, the local response due to δ-rays is identical to that due to secondary electrons following the irradiation of γ-rays. The input data needed are the proton energy distribution at a given depth and the radiosensitivity parameters which are tabulated for certain biological end-point (we used the end-point aerobic survival of Chinese hamster cells, CH2B2; 10% survival level).

RESULTS

Four different initial beam situations were studied. Firstly, an active modulation method considering a beam delivery system which is able to produce semi-monoenergetic beams in 1 MeV steps. Secondly, proton beams modulated using a rotational wheel with energies of 137 MeV, 155 MeV and 250 MeV.

Figure 1 shows one of the results for a SOBP with the condition of a constant maximum dose between the depths of 6 and 13 cm. Within the track structure model the proton doses necessary to reach a flat biological dose distribution for 10% survival within the SOBP were calculated. The effect of an increasing *RBE* with depth within a SOBP has already been observed experimentally and theoretically (see (Paganetti et al 1996) and references therein). Consequently, using a constant *RBE* value will lead to an underestimation of the biological effect at the distal part of the area to be irradiated. As the proton energy spectrum is shifted towards lower energies near the end of a Bragg curve, the *LET* increases and by this the *RBE*. The *RBE* (aerobic survival of Chinese hamster cells, CH2B2; 10% survival) increases within the SOBP from ≈1 to ≈1.12 for the active system and the 137 MeV passive modulation method and to ≈1.10 for the 250 MeV passive modulation method. In the distal part of the SOBP the *RBE* is the higher the lower the maximum proton energy entering the modulator is: Firstly, the beam with the highest range has

the highest weighting for the SOBP. Secondly, at high depths only this beam contributes to the SOBP, whereas in the plateau of the SOBP there is an overlap of various Bragg curves with a high contribution of regions proximal to the Bragg Peak, where the *RBE* is about 1. Differences in the biological effectiveness are caused by differences in the proton energy distribution. The higher the maximum beam energy entering a modulation device, the higher is the average proton energy at a given depth. To obtain the same dose level, the fluence depends on the initial energy of the beam. As the *RBE* is nearly energy independent for energies above 20 MeV, this affects mainly the biological effectiveness in the distal part of the SOBP.

For the active modulation, the rise follows the behavior of the 137 MeV passive beam modulation. With respect to the *RBE*, an active modulation device offers no advantage in comparison with a passive one when the lowest possible beam energy is used.

A manuscript containing the complete results has been submitted to 'Physics in Medicine and Biology': 'The Influence of the Beam Modulation Technique on Dose and RBE in Proton Radiation Therapy'.

Further experiments of the proton *RBE* as a function of different beam modulation techniques are needed for comparison. In addition, biological experiments which determine the parameters for the microdosimetric as well as for the track structure model would offer the possibility to compare the *RBE* predictions from both models.

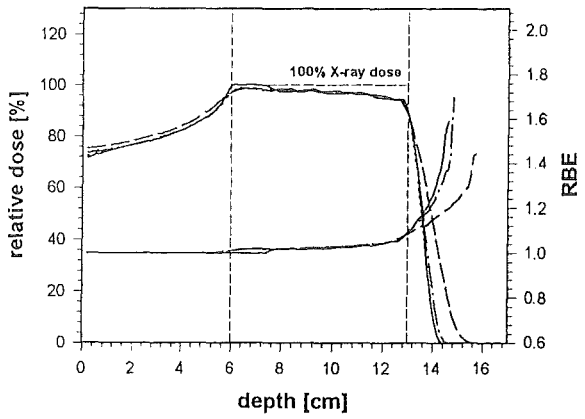

Fig. 1: Depth dependence of the proton doses necessary to reach a flat biological dose distribution for 10% survival (≈6.1 Gy X-ray dose, left scale). Depth dependence of the *RBE* values (10% survival; right scale). Full curve: 88-137 MeV active modulation; dotted curve: 137 MeV passive modulation; chain curve: 155 MeV passive modulation; broken curve: 250 MeV passive modulation (the plots for the active method and the 137 MeV passive method are nearly identical). The 100% X-ray dose value and the target limit is sketched. Biological end-point: aerobic survival of Chinese hamster cells, CH2B2; Biophysical model: track structure.

REFERENCES

(1) Berger M J 1993 Proton Monte Carlo Transport Program PTRAN. National Institute of Standards and Technology Publication NISTIR 5113

(2) Katz R and Sharma S C 1973 Response of cells to fast neutrons, stopped pions, and heavy ion beams. Nucl. Inst. Methds. **111** 93-116

(3) Katz R and Sharma S C 1974 Heavy Particles in Therapy: An Application of Track Theory. Phys. Med. Biol. **19** 413-435

(4) Loncol T, Cosgrove V, Denis J M, Gueulette J, Mazal A, Menzel H G, Pihet P, and Sabattier R 1994 Radiobiological Effectiveness of Radiation Beams with broad LET Spectra: Microdosimetric Analysis using Biological Weighting Functions. Radiat. Prot. Dos. **52** 347-352

(5) Paganetti H, Olko P, Kobus H, Becker R, Schmitz Th, Waligorski M P R, Filges D, and Müller-Gärtner H W 1996 Calculation of RBE for proton beams using biological weighting functions. Submitted to Int. J. Rad. Oncol. Biol. Phys.

Threshold experiments of the COSY type at higher energies

D.Filges, R.Geyer, K.Kilian, W.Oelert, E.Roderburg, T.Sefzick, G.Sterzenbach

Recent results from measurements at IUCF, Bloomington [1, 2] and CELSIUS, Uppsala [3] have revealed that $pp \to pp\pi^0$–production has been described in a too simple framework [4, 5, 6]. Only when taking heavy meson exchange into account the theoretical predictions agree to the experimental situation in the threshold region [7, 8]. Similarly, investigations of threshold $pp \to pp\eta$–production reveal effects not considered before, this time due to strong η–nucleon final state interaction [9]. At COSY–Jülich measurements of the $s\bar{s}$–dissociation in threshold regions have just started, namely the $pp \to pK\Lambda$–reaction at TOF [10] and the $pp \to ppK\bar{K}$ and $pp \to pp\phi$–reactions at COSY-11 [11]. Here, new and unforeseen effects might occur also. Since strange quarks are not existing as valence quarks in the entrance channel, these production experiments isolate the pure $s\bar{s}$–dissociation process. Moreover, hyperon decay in the exit traces back to the polarization of the strange quark directly [12].

A simple analogy of arguments leads to the importance of and interest in charm production. The $c\bar{c}$–dissociation manifests in charm–anticharm meson pair or charmed meson–charmed baryon production. Due to the high mass of the charm quark, model calculations are easier since they can be performed in a non–relativistic approximation. There is no doubt that also hidden charm states can be precisely studied with cooled proton beams, without restrictions to 1^-–states. The two protons allow tagging of the charmonium mass, this together with the characteristic leptonic decay provides a clean sample.

Reaction	Threshold momentum	
$pp \to d\pi^\pm$	0.789	GeV/c
$pp \to pp\,\pi^0$	0.777	GeV/c
$pp \to pp\,\eta$	1.986	GeV/c
$pp \to p\Lambda K^+$	2.339	GeV/c
$pp \to pp\,K^+K^-$	3.302	GeV/c
$pp \to pp\,p\bar{p}$	6.501	GeV/c
$pp \to pp\,\Lambda\bar{\Lambda}$	7.999	GeV/c
$pp \to pp\,\Xi^-\overline{\Xi^-}$	9.901	GeV/c
$pp \to pp\,\Omega^-\overline{\Omega^-}$	13.558	GeV/c
$pp \to pp\,J/\Psi$	12.207	GeV/c
$pp \to p\Sigma_c D^0$	13.750	GeV/c
$pp \to pp\chi_{c2}$	14.760	GeV/c
$pp \to pp\,D^+D^-$	15.837	GeV/c

Table 1: Examples of threshold momenta

Another experimental topic which extends the quark–antiquark production not to higher quark masses but to higher complexity is the baryon–antibaryon production at threshold. The underlying $3q$–$3\bar{q}$–dissociation is a basic process in hadronic physics which opens a wide field of interesting experiments.

For instance, examining the $pp \to pp\,p\bar{p}$–reaction below the threshold of the $pp \to pp\,p\bar{p}\pi^0$–reaction provides an extremely clean sample, firstly because one can identify the antiproton by its annihilation signature, secondly due to the fact that all ejectiles stay at angles which are quite low in the laboratory system ($< 15°$). This allows measurements using an installation like the TOF detector in its longest version or a setup similar to COSY-11.

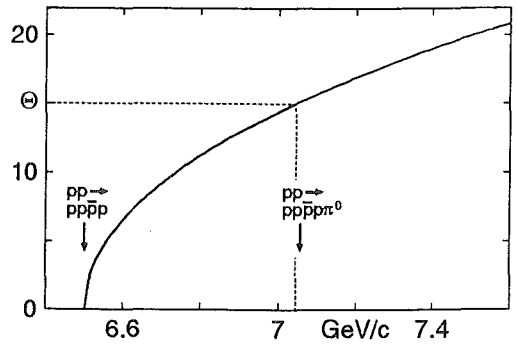

Figure 1: Maximum opening angle of the (anti)protons in $pp \to pp\,p\bar{p}$

At 7.05 GeV/c, i.e. just below the $pp \to pp\,p\bar{p}\pi^0$–threshold, the TOF setup would cover 100 % of the reaction. Monte Carlo calculations show that 99.86 % of the events would contain at least one baryon with $\beta < 0.88$ which would allow time-of-flight reconstruction leading to an overdetermined offline evaluation.

In the baryon–antibaryon production ($pp \to ppB\bar{B}$) it seems interesting to compare dissociation reactions with no ($p\bar{p}$), one ($\Lambda\bar{\Lambda}$), two ($\Xi\bar{\Xi}$), or even three ($\Omega^-\overline{\Omega^-}$) $s\bar{s}$–pairs. Especially the $Y\bar{Y}$–production provides easy access to polarization and spin correlation information like in our PS185 experiment at LEAR [12], where we study the same system in a different hadronic surrounding ($\bar{p}p \to \bar{\Lambda}\Lambda$). Extensions to higher energies were already considered there [13].

References:

[1] H.O.Meyer et al., Phys. Rev. Lett. 65 (1990) 2846
[2] H.O.Meyer et al., Nucl. Phys. A 539 (1992) 633
[3] A.Bondar et al., Phys. Lett. B 356 (1995) 8
[4] D.S.Koltun, A.Reitan, Phys. Rev. 141 (1966) 1413
[5] G.A.Miller, P.U.Sauer, Phys. Rev. C 44 (1991) 1725
[6] J.A.Niskanen, Phys. Lett. B 289 (1992) 227
[7] T.S.Lee, D.O.Riska, Phys. Rev. Lett. 70 (1993) 2237
[8] C.J.Horowitz et al., Phys. Rev. C 49 (1994) 1337
[9] H.Calen et al., Phys. Lett. B 366 (1996) 39
[10] P.Turek, COSY Proposal #15 (1990)
[11] S.Brauksiepe et al., accepted for publication in Nucl. Inst. & Meth.
[12] P.D.Barnes et al., Proposal of the PS185 collaboration CERN/PSCC/81-69/P49 (1981)
[13] W.Oelert, Proceedings of the SuperLEAR Workshop, p. 307, Zürich, 9–12 October 1991, edts. C.Amsler and D.Urner

1.2 EXPERIMENTS AT EXTERNAL FACILITIES

Production of Antihydrogen

W.Oelert, T.Sefzick for the PS210/LEAR/CERN collaboration

The idea of the existence of antimatter goes back to the work of Dirac [1]. For each particle a corresponding antiparticle exists as predicted by the CPT theorem. Furthermore, it follows that particle and antiparticle have the same mass, spin and total life time and the same value but opposite sign of charge and magnetic moment. Since there is no reasonable doubt about the existence of the symmetry between particle and antiparticle, it should be possible to combine antiparticles into antimatter under the same forces as particles bind to form normal matter, in particular, to produce the simplest antiatom out of an antiproton and a positron: $\overline{H}^0$.

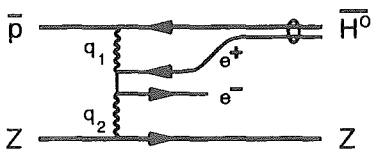

Fig. 1: A schematic view of the two–photon mechanism for e^+e^- and $\overline{H}^0$ production

Though there is hardly any doubt that $\overline{H}^0$ exists, it has never been observed. Once it is produced $\overline{H}^0$ is certainly an ideal laboratory for studying CPT invariance by comparing interactions in matter and antimatter environments.

Two principal solutions for $\overline{H}^0$ production, at rest and in flight, have been suggested and are discussed in References [2]–[7]. The variant of the flight method used here has first been suggested by Munger et al. [5]. An antiproton passing through the Coulomb field of a nucleus with charge Z will create an e^+e^-–pair. Occasionally the antiproton will capture the positron from the produced pair and both will form a fast moving antihydrogen. In lowest order two kinds of mechanisms have been estimated [4],[6]:

1. the space like $\gamma\gamma$–production of e^+e^-–pairs, see Fig.1:

$$\overline{p}Z \rightarrow \overline{p}\gamma\gamma Z \rightarrow \overline{p}e^+e^-Z \rightarrow \overline{H}^0e^-Z$$

2. the e^+e^-–pair production converted from virtual time like Bremsstrahlung photons:

$$\overline{p}Z \rightarrow \overline{p}\gamma^* Z \rightarrow \overline{p}e^+e^-Z \rightarrow \overline{H}^0e^-Z$$

The second mechanism is calculated [7] to be two to three orders of magnitude lower than the $\gamma\gamma$ induced one, which has been evaluated by several authors [5],[7] resulting in a Z^2 and a $ln\,(E_{\overline{p}}/m_{\overline{p}})$ dependence, where $(E_{\overline{p}}/m_{\overline{p}})$ denotes the Lorentz factor. The cross section is expected to be in the order of 2 pb for a $\overline{p}$–momentum around 2 GeV/c, the maximum momentum at LEAR.

The production of $\overline{H}^0$ requires a rather thin target since otherwise the antiatom would break up into its constituents. However, due to the small production cross section a large luminosity is demanded and therefore only the technique of using a cluster target at an internal antiproton beam seems possible. The present results were taken in a dedicated beam time period with effectively 15 hours beam on target, distributed over several days of running in parallel to the Crystal Barrel (PS197) experiment. A Xe–cluster target was used [8]. The beam target interaction intensity was optimized such that a fairly constant luminosity was maintained, i.e. the target density was low (about $1 * 10^{12}$ atoms/cm^2) at the beginning and was increased to about $3 * 10^{13}$ atoms/cm^2 according to the decrease of the 1.94 GeV/c $\overline{p}$–beam intensity. Starting typically with $1.7 * 10^{10}$ $\overline{p}$'s in LEAR beam lifetimes of at least 3 minutes were possible with the optimum settings of the LEAR accelerator and cooling system. A typical run lasted for twelve minutes before a new filling of LEAR was done. The integrated luminosity was estimated from the number of antiprotons and target thickness to be $\mathcal{L} = 5 * 10^{33}$ cm^{-2} $\pm$ 50 % for the total running period in September/October 1995. Since the cross section of the $\overline{H}^0$ production is expected to be $2\text{pb} * Z^2 \simeq 6 * 10^{-33}$ cm^2 a total production rate of 30 $\overline{H}^0$ would be expected. According to both test measurements and Monte Carlo calculations the acceptance of the detection system was determined to be $\epsilon = 0.3$ which would result in the observation of nine $\overline{H}^0$ with a clear signature during the running period.

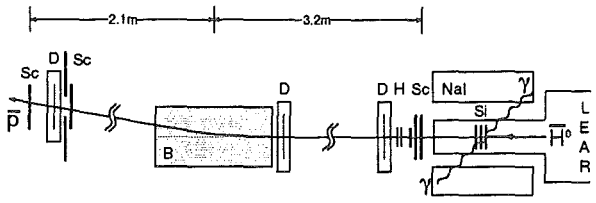

Fig. 2: Lay–out of the experiment PS210: Sc: trigger and time of flight scintillators, Si: three silicon detectors, D: Delay wire chambers, NaI: six–fold segmented NaI detector, H: scintillating fibre hodoscope, B: magnetic dipole field

A clear signature for a good event has to fulfill the following criteria (see Fig.2 for the detector set–up):

i) As a neutral object an $\overline{H}^0$ — produced ten meters upstream in the center of the straight section of LEAR — will exit the accelerator ring tangentially and will be stripped in the first silicon counter still in the LEAR vacuum system. Here both constituents of $\overline{H}^0$ have the same velocity and therefore at a $\overline{p}$ beam momentum of 1.94 GeV/c the kinetic energy is 0.663 MeV for e^+ and 1217 MeV for $\overline{p}$, respectively. These two particles hit simultaneously the first silicon counter (700 μm thick and 1200 mm^2 active area [9]) which, together with

the second one (500 μm thickness and 1200 mm^2) measures the dE/dx of the $\bar{p}$ plus the kinetic energy of the e^+ being stopped in these two detectors. The third silicon counter with dimensions the same as the first one should give a signal proportional to dE/dx of the $\bar{p}$ only.

ii) The two 511 keV photons from the e^+–annihilation will be detected back to back in the cylindrical six–fold segmented NaI counter [10], which forms an inner and outer diameter of 8 cm and 40 cm, respectively, covers a solid angle of 91 %, has an energy resolution of 14 % FWHM, and provides a 511 keV γ–detection efficiency of 82 % which has to be multiplied by 0.71 for the peak–to–total ratio [10]. The silicon counter telescope is located in the center of the NaI crystal arrangement. The NaI detector was temperature controlled during the runs to 17 $\pm$ 0.5 ^{0}C.

iii) The $\bar{p}$'s resulting from the stripped $\overline{H}^0$ will continue with a velocity of $\beta = 0.900$. They penetrate through a set of three start scintillators, each 4 mm thick, a scintillator hodoscope of 16 fibers $2 * 2 * 32$ mm^3 in vertical and horizontal orientation, and a group of four stop scintillators arranged as indicated in the figure. All scintillator ADC and TDC values have to be in specific intervals which were determined by cosmic ray calibrations before and after the installation of the detector system in the experimental set–up at LEAR.

iv) The deflection of the registered charged particles was measured with a spectrometer consisting of three horizontally sensitive delay–line readout drift chambers [11] with a used active area of $8 * 8$ cm^2 and a dipole field varied between 0.05 Tm and 0.15 Tm. The deflection should be within the predicted values for the $\bar{p}$ from $\overline{H}^0$, taking the straggling of $\pm$ 12 mm into account due to matter in the flight path.

Since in the present situation no additional well known reaction could be measured in parallel to the reaction to be studied, the entire detector system had to be calibrated before the start of the experiment. These calibrations were done with cosmic rays for the time–of–flight and energy losses, with a ^{22}Na source for the NaI crystals and with both ^{106}Ru and ^{207}Bi sources for the energy and timing determination for the silicon detectors and the scintillator hodoscope.

The chain of analysis used for the identification of the produced $\overline{H}^0$ employed neither cuts on the time–of–flight nor on the deflection in the magnetic separator. In Fig.3 the time–of–flight via the signal amplitude from one of the time–of–flight start scintillators is shown. In the range from 17 ns to 19 ns the signal amplitude is due to single pion (amplitude $\simeq$ 130), double and multi pion production. The main source of these mesons is most likely the reaction chain: $\bar{p}$Xe $\rightarrow$ $\bar{n}$"anything", where the $\bar{n}$ annihilates in the silicon detector telescope and produces multi–pion events. The band starting at amplitude values

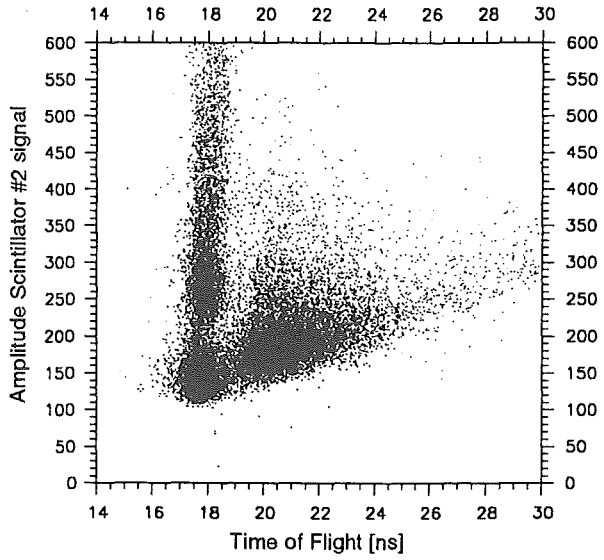

Fig. 3: Two dimensional display of time–of–flight vs. scintillator signal amplitude

of about 160 and ranging from 19.5 ns to 30 ns with decreasing intensity is due to fast and slow protons or antiprotons which probably again are due to secondary reactions from $\bar{n}$'s leaving the LEAR accelerator tangentially. Here we can not distinguish in general whether the slower baryons are due to additional pion production and/or to any kind of excitation of the Xe target nucleus.

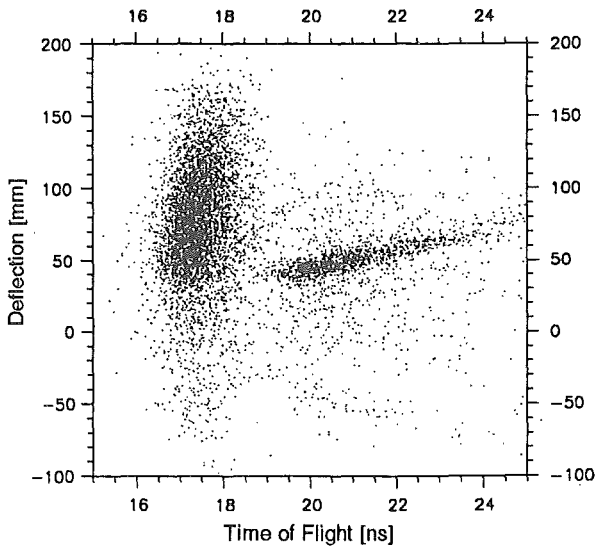

Fig. 4: Two dimensional display of time–of–flight vs. deflection due to the magnetic dipole

Whereas in Fig.3 the sum of all data taken in 1995 with about 300,000 triggers is shown, Fig.4 presents only a single run with a magnetic field setting of 0.136 Tm which results in an expected deflection of the $\bar{p}$'s from $\overline{H}^0$ of 39.5 mm $\pm$ 12 mm and a time–of–flight of 19.7 $\pm$ 0.6 ns where the allowed range corresponds to 2.5 σ around the expected value. In Fig.5 again the integral of all data taken at different magnetic field settings is shown now with the deflection normalized such that the expected position for the $\bar{p}$'s from $\overline{H}^0$ should be zero.

Naturally the upper display in Fig.5 includes and selects only those triggers ($\simeq$ 23,300) where a track through all three wire chambers could be defined, but has no additional cut on the data.

Additional cuts were introduced in order to produce the second part of the figure, with 94 events remaining, where now the essential conditions are that:

i) the sum of the signal from the first two silicon detectors is equivalent to the kinetic energy of the stopped e^+ plus the energy loss of the $\bar{p}$ whereas the third silicon detector gives an energy signal relevant for the $\bar{p}$ energy loss only.

ii) the determined particle trajectory points back into the area of the target region.

iii) the signal amplitude from the time of flight scintillators is in reasonable agreement with the energy loss of the $\bar{p}$'s from $\overline{H}^0$.

With these requirements the pionic events disappear as can be seen from the middle part of Fig.5. Essentially only events due to antiprotons are left. Demanding in addition a back–to–back yy–coincidence from signals in two NaI crystals eleven events remain which follow the clear signature of $\overline{H}^0$. They show an expected deflection and the correct time–of–flight range, as can be seen in Fig.5 bottom. Thus, it can be concluded that **11 $\overline{H}^0$ atoms have been observed**. The $\overline{H}^0$ production rate is in good agreement with the expected value following the theoretical $\gamma\gamma$–production mechanism [5],[7]. No production of $\overline{H}^0$ has ever been reported or observed before.

Based on Poisson statistics the number of background events would be less than three with a confidence level of 95 %. This is in agreement with a background estimate from the present data of 2 ± 1 out of the 11 events.

In the future more $\overline{H}^0$ atoms should be produced and especially under conditions such, that spectroscopy could be done to test the CPT symmetry of matter and antimatter.

Acknowledgements

We appreciate the help of many people. Especially we would like to thank the PS and the LEAR operation teams for delivering excellent $\bar{p}$ beams, the LEAR vacuum group for making it possible to us to use the Xe cluster target in the ultra high vacuum of LEAR, and the transport and handling group for moving the shielding wall of LEAR.

This work could not have been done without the enormous engagement and continuous support from M. Chanel, C. Lacroix, P. Lefevre, D. Möhl, and G. Molinari. We like to thank them as well as W. Niebur for technical support with the set–up, T. Sagefka for preparing and calibrating the magnetic system, and J. Spanggaard for helping us with the wire chambers.

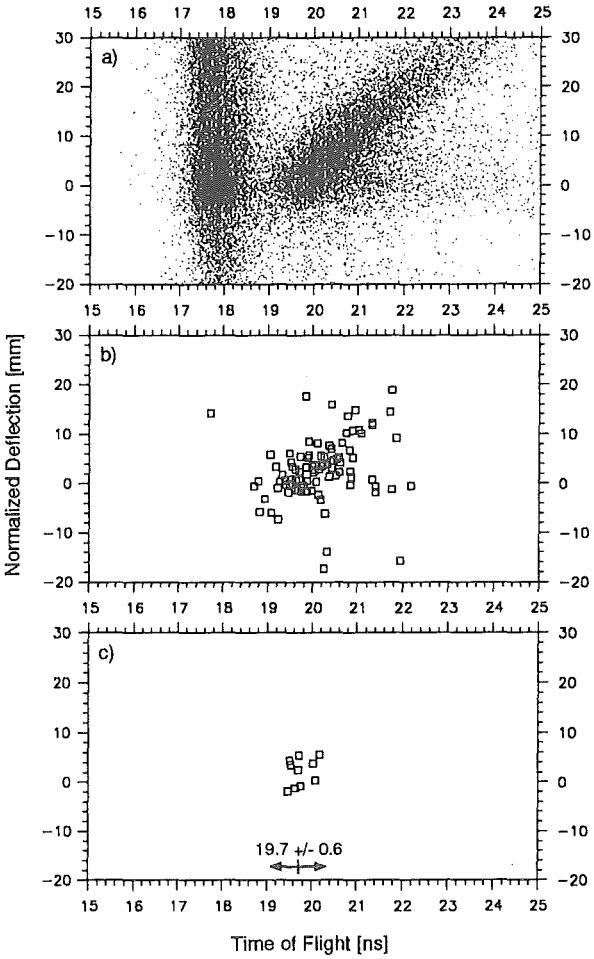

Fig. 5: Time–of–flight vs. deflection spectra, steps of different cuts were applied to the raw data, see text for details

References:

[1] P.A.M. Dirac, Proc. Roy. Soc. A117 (1928) 610, P.A.M. Dirac, Proc. Roy. Soc. A133 (1931) 60

[2] G. Gabrielse et al., Phys. Rev. Lett. 65 (1990) 1317
G. Gabrielse et al., LEAP '94, Bled, Slovenia
G. Gabrielse et al., PS196 experiment at LEAR

[3] A. Wolf, AntiProton '86, Thessaloniki, Greece

[4] H. Poth et al., Hyperfine Interactions 44 (1988) 259
G. Budker and A.N. Skrinsky, Sov. Phys. Usp. 21 (1978) 227
H. Herr et al., Proceedings of the second Workshop Physics at LEAR, Erice (1982) 659

[5] C.T. Munger et al., Hyperfine Interact. 76 (1993) 175
C.T. Munger et al., Phys. Rev. D 49 (1994) 3228

[6] M. Charlton et al., CERN–PPE/94–18, Feb. 1994
M. Charlton et al., Physics Reports 241 (1994) 65

[7] G. Baur, Phys. Lett. B 311 (1993) 343

[8] G. Boero, PS210 note number 1, April 10, 1995

[9] CANBERRA, Fully depleted PIPS Detectors

[10] H. Keller et al., Nucl. Inst. & Meth. A300 (1991) 67

[11] A. Manarin and G. Vismara, 'The delay wire chamber (DWC) description', LEP/BI–TA/Note 85–3, CERN Prevessin

Meson spectroscopy with the JETSET experiment

L.Bertolotto[5]), A.Buzzo[5]), P.T.Debevec[6]), D.Drijard[2]), S.Easo[5]), R.A.Eisenstein[6]), W.Eyrich[3]), T.Fearnley[2]), M.Ferro-Luzzi[2]), H.Fischer[4]), J.Franz[4]), R.Geyer[3]), N.Hamann[2]), P.Harris[6]), D.W.Hertzog[6]), S.A.Hughes[6]), A.Johansson[8]), T.Johansson[8]), R.T.Jones[2]), K.Kilian, K.Kirsebom[5]), A.Klett[4]), H.Korsmo[7]), M.Lo Vetere[5]), M.Macri[5]), M.Marinelli[5]), M.Moosburger[3]), B.Mouëllic[2]), W.Oelert, S.Ohlsson[2]), A.Palano [1]), S.Passaggio[5]), J.-M.Perreau[2]), M.-G.Pia[5]), S.Pomp[3]), M.Price[2]), P.E.Reimer[6]), J.Ritter[6]), E.Robutti[5]), K.Röhrich, M.Rook, E.Rössle[4]), A.Santroni[5]), H.Schmitt[4]), O.Steinkamp, F.Stinzing[3]), B.Stugu[8]), R.Tayloe[6], M.Tscheulin[4]), H.J.Urban[4]), H.Wirth[4]), H.Zipse[4])

The JETSET experiment [1] was designed and set up to investigate strangeness production in antiproton-proton annihilations in flight at LEAR at CERN. The experiment exploits a hydrogen cluster jet target in the LEAR ring. It surrounds this target with detectors with cylinderic geometry. Emphasis was put on a good particle identification. The collaboration has measured the cross sections of $\bar{p}p \rightarrow \phi\phi$ and $\bar{p}p \rightarrow K_sK_s$ in a center of mass energy range from 2.15 to 2.43 GeV. Recent lattice QCD calculations of gluonic states of matter make this mass region of particular interest, as the masses of the tensor and vector glueball are predicted to be in this range [2]. Several states including the $\xi(2230)$ are candidates to be identified with the gluonic matter.

The $\phi\phi$ analysis selects four-track events. It uses the track directions, the beam momentum and a mass hypothesis to solve energy and momentum conservation equations. The results for events with solutions are compared with β and dE/dx measurements from the Cerenkov, RICH and silicon counters in the experiment. The non-four-kaon background is estimated to be approximately 15%. The invariant mass for pairs of tracks can be calculated. Its distribution shows a clear peak at the ϕ mass of 1019.4 MeV/c^2. Assuming $\bar{p}p \rightarrow \phi\phi$, ϕK^+K^- and $K^+K^-K^+K^-$ (phase space) a maximum likelihood method was applied to extract the realtive contributions. The 15% background was subtracted from the $\bar{p}p \rightarrow 4K^\pm$ channel [1]. The resulting cross sections are plotted in Figure 1.

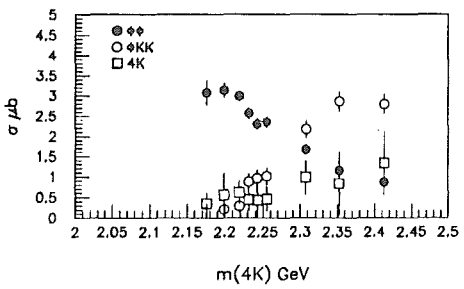

Figure1 Total cross sections for $\bar{p}p$ annihilations into final states containing 2ϕ, ϕK^+K^- and $K^+K^-K^+K^-$.

Using only events in the $\phi\phi$ peak, a partial wave analysis was done. Partial waves up to 4^{++} were taken into account. The incoherent contribution was estimated studying subselections of partial waves and were found within the experiments sensitivity to be non-significant. The only waves which were found to contribute to the cross section were the 2^{++} ($L_{\bar{p}p}S_{\bar{p}p}l_{\phi\phi}s_{\phi\phi}$=3102, 3120, and 3122), the 3^{++} (3122 and 3142) and the 4^{++} (3142)). These contributions are shown in Figure 2. A strong enhancement in the resonant $\phi\phi$ cross section is seen near threshold in the 2^{++} partial wave. The total $\bar{p}p \rightarrow \phi\phi$ cross section is many times larger then would naïvely be predicted by the OZI rule. Additional data in the region of enhancement is currently being analyzed.

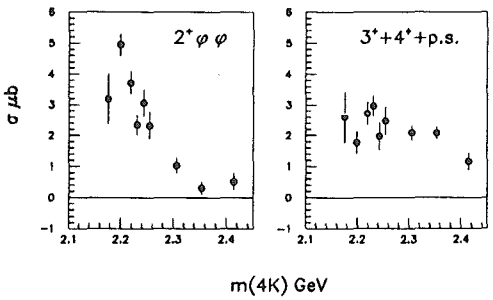

Figure2 Partial cross sections for $\bar{p}p$ annihilations into the 2ϕ final state. The left shows the cross sections for the 2^{++} partial waves. Displayed on the right is the combination of all other significant contributions.

Events of the type $\bar{p}p \rightarrow K_sK_s$ were selected through their delayed decay into $\pi^+\pi^-$. Two vertex events were kinematically reconstructed. Background origines mainly from $\bar{p}p \rightarrow K_sK_s\pi^o$, which could be eliminated using the experiment's calorimeter, and from $\bar{p}p \rightarrow K_sK^\pm\pi^\pm$. The contribution of non-K_sK_s background in the sample was estimated using the distribution of K_s lifetimes, assuming that the vertices of the background events are centered around the origine and do not contribute to the decay distribution at large lifetimes. The $\bar{p}p \rightarrow K_sK_s$ cross sections are in good agreement with other measurements in this energy region.

1) University of Bari and INFN, Bari
2) CERN, Geneva
3) Universität Erlangen-Nürnberg
4) Albert Ludwigs Universität Freiburg
5) University of Genova and INFN, Genova
6) University of Illinois at Urbana Champaign
7) University of Oslo
8) The Svedberg Laboratory, Uppsala

References

[1] L.Bertolotto et al., Phys. Lett. B345(1995)325
L.Evangelista et al., CERN/SPSLC 92-42, SPSLC/M501, 1992

[2] H.Chen et al., preprint
G.S.Bali et al., Liverpool preprint LTH 303

Hyperon production at a antiproton-proton mini-collider

W.Eyrich[1], K. Röhrich and W.Oelert

An experiment has been studied, which explores the physics of $\bar{p}p$ annihilations in the energy range from $\sqrt{s}$ = 2.5 to 4.4 GeV [1], above that of the present LEAR fixed target operation. The main physics objective is to extend hadron spectroscopy, and in particular the search for glueballs and hybrids to the mass range of 2-3 GeV. The experiment requires LEAR to operate as a $\bar{p}p$ collider [2]. The detector is an upgrade of the Crystal Barrel spectrometer [3] with 4π acceptance for photons and charged particles, and good energy and spatial resolution. Here we discuss the physics potential of hyperon production in this mass range.

The maximum center-of-mass energy available at LEAR is 2.43 GeV, which limits investigations to the S=1 hyperon systems. Hyperon production in the reaction channels $\bar{p}p \rightarrow \bar{\Lambda}\Lambda, \bar{\Lambda}\Sigma^o + cc., \overline{\Sigma^+}\Sigma^+$ and $\overline{\Sigma^-}\Sigma^-$ close to their thresholds has been systematically studied at LEAR by the PS185 collaboration. An antiproton-proton collider would be well suited for a continuation of such investigations including the multistrange (S=2,3) sector. Due to a lack of data, especially close to threshold, the Ξ and Ω production mechanism could not be tested yet. In a meson exchange picture $\bar{\Xi}\Xi$ proceeds in lowest order through two-kaon exchange while $\bar{\Omega}\Omega$ needs three kaons. In the quark picture for $\bar{\Omega}\Omega$ this corresponds to a disconnected diagram involving the total annihilation of three $\bar{q}q$ valence pairs into three $\bar{s}s$ pairs in the final state. It was pointed out [7] that the $\bar{\Omega}\Omega$ production should be compared with $\bar{p}p$-annihilation into two or three ϕ-mesons, where the final state particles are identical. The $\phi\phi$ final state is currently being studied by the JETSET collaboration at LEAR. The measurements of cross sections, polarizations and spin-correlations for $\bar{p}p \rightarrow \bar{Y}Y$ will provide insights into the quark dynamics in the non-perturbative region.

$\bar{p}p \rightarrow$	threshold energy (GeV)	cross section (μb)
$\overline{\Sigma^o}\Sigma^o$	2.39	22
$\overline{\Xi^o}\Xi^o$	2.63	3
$\overline{\Xi^-}\Xi^-$	2.64	2
$\overline{\Omega^-}\Omega^-$	3.35	0.3
$\bar{\Lambda}\Sigma(1385)$+cc	2.50	12
$\bar{\Lambda}\Lambda(1405)$+cc	2.52	14
$\bar{\Lambda}\Lambda(1520)$+cc	2.64	7
$\bar{\Sigma}\Lambda(1520)$+cc	2.71	4

Table1 Hyperon and antihyperon production in $\bar{p}p$ annihilations. Threshold center-of-mass energies and cross section values for $\sqrt{s}$ at about 3 GeV [4].

In $\bar{p}p \rightarrow \bar{Y}Y^* + c.c.$ production the ground state particle provides a clear tag for the strangeness in the final state. The recoiling system then carries strangeness with the opposite sign. A study of the missing mass Y^* will reveal the spectrum of excited hyperon states, including resonances like the $\Lambda(1405)$ and the $\Sigma(1385)$. The $\Sigma(1385)$ and $\Xi(1530)$ along with the $\Delta(1232)$ and the $\Omega(1672)$ form a $3/2^+$ decuplet. The $\Lambda(1405)$ and $\Lambda(1520)$, $1/2^-$ and $3/2^-$ respectively, are listed as SU(3) singlets, although this assignment is still debated. These low mass hyperon resonances are all relatively narrow and have dominant two body decay modes. For those states lying below the nucleon-kaon threshold, $\Lambda(1405)$ and $\Sigma(1385)$, also a N-K molecular nature is discussed [5]. Four missing states in the L=1, SU(6) 70-plet are expected and still have to be found.

Near threshold a striking difference compared to the $\bar{\Lambda}\Lambda$ production is expected where the coherent I=1 tensor interaction plays an probably[1] important role. This should not be the case for $\bar{\Lambda}\Sigma(1385)$, $\bar{\Lambda}\Lambda(1405)$ and $\bar{\Lambda}\Lambda(1520)$. The measurements allow the extraction of coupling constants g_{KNY}, and together with a study of decay modes and branching ratios, they shed light on the microscopic structure of these states.

The hyperon decays are of special interest in themselves. Abundantly produced, rare decays can be studied. Semileptonic decays will be accessible. They will allow to study transition matrix elements U_{us} and U_{ud} in different hadronic environments. The search for symmetry (charge, parity or both, for CP violation in $\bar{p}p \rightarrow \bar{\Lambda}\Lambda$ see below) or quantum number violating (like $\Sigma^+ \rightarrow nl^+\nu_l$ or pe^+e^-) decays will extend current limits and perhaps reveal new physics.
Spin observables can be easily obtained through the parity violating weak two-body decay of the hyperons. If there is direct CP violation, it should express itself in a difference of the decay parameters for hyperon and antihyperon. The exclusive reaction chain $\bar{p}p \rightarrow \overline{\Xi^-}\Xi^- \rightarrow \bar{\Lambda}\pi^+\Lambda\pi^- \rightarrow \bar{p}\pi^+\pi^+p\pi^-\pi^-$ is discussed for a search for CP violation. Nothing is known experimentally about the angular distribution and the hyperon polarization in this process, and a search for CP violation must be preceeded by detailed measurements of cross sections and spin variables.
Related to spin observables is the recently discussed strangeness content of the nucleon (see also [6]). The influence of an intrinsic $\bar{s}s$ sea-quark pair should depend on the actual spin and isospin scenario of the different $\bar{Y}Y$ production reactions.

Apart from the exclusive hyperon antihyperon production, reactions with an accompanying meson like $\bar{p}p \rightarrow \bar{Y}Y\pi$ and $\bar{p}p \rightarrow \bar{p}KY$ should provide complementary information about the $\bar{s}s$-creation process. If the $\bar{Y}Y$ are recoiling against the meson, their relative energy can be varied independently of the initial state and the hyperon-antihyperon interaction can be studied. Due to the quantum numbers carried by the meson, new spin parity configurations for the $\bar{Y}Y$-system are allowed, which are not accessible in the exclusive two-body final states. Apart from $\bar{\Lambda}\Lambda\pi^o$ they cannot be

[1] The PS185 collaboration will study spin-transfer and depolarization in $\bar{p}p \rightarrow \bar{\Lambda}\Lambda$ with a polarized proton target. The results will help clarifying the role of the tensor interaction in the process.[6]

reached by the present LEAR.
Hyperon-kaon data receive most attention for their potential to investigate the hadronic production of $\bar{s}s$. The diffractive dissociation of a pre-existing $\bar{s}s$ in the nucleon can be studied. More interest in hyperon-kaon data is partly due to a comparison with data of the type $pp \rightarrow pKY$, which is available from experiments at COSY and SATURNE.

[1]) Universität Erlangen-Nürnberg

References

[1] B.Barnett et al., CERN/SPSLC 95-26, SPSLC/I-203, March 1995
[2] P.Lefèvre, CERN/PS/DI/Note 94-09 March 1994
[3] I.Yu.Brovkin et al., Yad.Fiz. 55(1992)986
[4] R.L.Jaffe, Phys. Rev D15(1977)267 ??????
[5] Rev. of Part. Prop., Phys. Rev. D50(1994)1173
[6] Proposal P287, CERN-SPSLC/95-13, now PS185-3
[7] D.Strottman, Phys. Rev. D20(1979)748
W.Oelert, *Heavy hyperon-antihyperon production.* Paper presented at Workshop on Physics with SuperLEAR; Zürich, October 1991

$\overline{\Lambda}\Sigma^0$- and $\overline{\Sigma^0}\Lambda$-Production at high LEAR-Energies

K. Sachs for PS185 collaboration

The main effort of PS185 is the investigation of the reaction $\bar{p}p \rightarrow \overline{\Lambda}\Lambda$. Though there is a high quality set of data for cross-section, polarization and spin-correlation, it is not possible to distinguish between quark-gluon- and meson-exchange-models. Further quantities or other reactions have to be measured.

The channel $\bar{p}p \rightarrow \overline{\Lambda}\Sigma^0$+cc provides additional information. The constants of $KN\Lambda$ and $KN\Sigma^0$ coupling involved in meson-exchange-calculations are different in value and sign. This should lead to a different distribution of cross-section and spin-correlation for $\overline{\Lambda}\Lambda$ and $\overline{\Lambda}\Sigma^0$-production.

A proper selection is necessary for the investigation of $\bar{p}p \rightarrow \overline{\Lambda}\Sigma^0$+cc with $\Sigma^0 \rightarrow \Lambda\gamma$. Due to the unobserved photon the event-signature is not as clear as for $\overline{\Lambda}\Lambda$. Even with an improved off-line-analysis [1] the kinematical fit with two constraints does not provide sufficient reduction of other channels.

Figure 1 shows the missing-mass-distribution after the fit. Background from reactions at the carbon-atoms within the Polyethylene-target has been subtracted. Besides the reaction of interest a signal of $\bar{p}p \rightarrow \overline{\Lambda}\Lambda$ can clearly be seen. Background of $\bar{p}p \rightarrow \overline{\Lambda}\Lambda\pi^0$ and $\overline{\Sigma^0}\Sigma^0$ can not be excluded, but can be neglected due to the small cross-section. The indicated cut reduces $\overline{\Lambda}\Lambda$ to 2.7% of the data sample. The fraction of carbon-reactions is 29%.

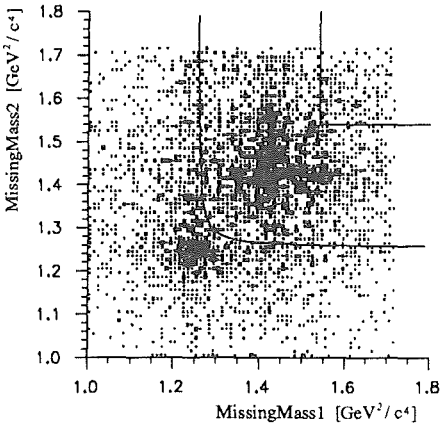

Figure 1: Missing-mass-distribution after the fit. Background from carbon-events has been subtracted. Open squares represents negative values.

Due to a high cross-talk between the channels $\bar{p}p \rightarrow \overline{\Lambda}\Sigma^0$ and $\overline{\Sigma^0}\Lambda$ (13 to 40%) the cross-section has been determined only for the sum of both reactions. Invariance of the strong interaction under C-conjugation requires them to be equal.

The total cross-section for $\bar{p}p \rightarrow \overline{\Lambda}\Sigma^0$+cc amounts to [2]:

primary beam momentum [GeV/c]	effective	cross-section [μb]
1.949	1.9476	41.4±1.1
1.992	1.9906	42.9±1.1

Figure 2 shows the differential cross-section. Background from carbon-reactions has been subtracted properly. The curves indicates the resulting Legendre-fit and the cross-section of the $\bar{p}p \rightarrow \overline{\Lambda}\Lambda$-reaction at the same excess energy respectively. The total cross-section has been adjusted.

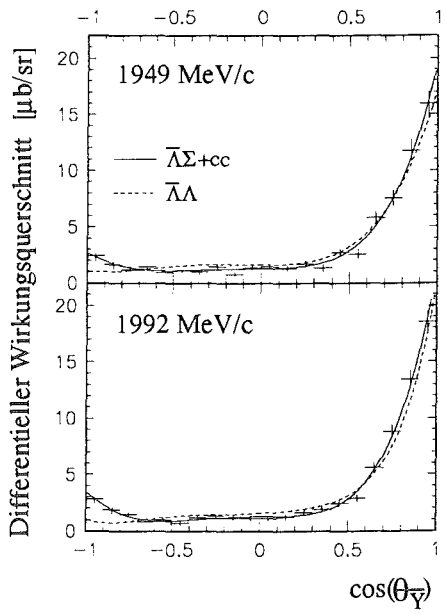

Figure 2: Differential cross-section

Surprisingly there is no significant difference between the distributions for $\bar{p}p \rightarrow \overline{\Lambda}\Lambda$ and $\overline{\Lambda}\Sigma^0$+cc besides the backward region. The data for $\overline{\Lambda}\Sigma^0$+cc show a rise for $\cos\theta \sim -1$. It is not absolutely clear, whether this might be due to background, misidentified reaction-angles or a real effect.

Spin-observables can be determined using the CP-violating decay of the Lambda. This holds also for the Sigma. But in this case the asymmetry is smaller by a factor of 3. The resulting large statistical error and high background-fraction from carbon-reactions hardly allows for a interpretation of polarization and spin-correlation. The singlet fraction yield a nonzero value of 0.31±0.26 (0.54±0.25) for $p_{\bar{p}} = 1949(1992)$, as expected from theory.

References

[1] Annual Report 1994, Jül-3035 (1995) 86
[2] K. Sachs, PhD-Theses, to be published

Measurement of strangeness production in the reaction $\bar{p}p \rightarrow \bar{Y}Y$

D.Afzali[5]), P.D.Barnes[1]), R.Bröders, H.Dennert[4]), R.A.Eisenstein[7]), W.Eyrich[4]), H.Fischer[5]), G.B.Franklin[3]), J.Franz[5]), T.Fuchs[4]), R.Geyer, P.Harris[6]), J.Hauffe[4]), D.Hertzog[7]), T.Johansson[8]), T.Jones[7]), K.Kilian, R.A.Kraft[4]), C.A.Meyer[3]), W.Oelert, S.Pomp[8]), B.Quinn[3]), J.Rauch[5]), K.Röhrich, E.Rössle[5]), M.Ruh[5]), D.Ruschmeier[5]), K.Sachs, H.Schmitt[5]), T.Sefzick, F.Stinzing[4]), R.Tayloe[7]), R.Todenhagen[5]), E.Tranens[8]), T.Walter[5])

The SU(6) wavefunction of the Λ hyperon decomposes into a spin and isospin zero (ud)-diquark cluster and the s-quark, which determines the quantum numbers of the hyperon. The Λ particle can therefore be regarded as a tracer for strangeness and the $\bar{p}p \rightarrow \bar{\Lambda}\Lambda$ reaction should reflect the dynamics of $\bar{q}q$ annihilation and production.

The PS185 collaboration has studied this reaction in great detail [1,2]. Angular distributions of cross sections, polarizations and spin correlations have been measured at LEAR at CERN. The cross section is found to be forward peeking even very close to the reaction threshold at an incident antiproton momentum of 1435 MeV/c, implying the contribution of higher partial waves ($L > 0$). The observation of a relatively strong p-wave at low energies is usually attributed to a supression of the s-wave due to strong annihilation at small distances or due to a p-wave enhancement by baryon-antibaryon resonances. The total cross section rises from the reaction threshold up to 100 μb at the maximum LEAR momentum at 2 GeV/c (figure 1). Polarizations of the final state Λ and $\bar{\Lambda}$ have been determined from their asymmetric, charged two body decay. The polarizations are small and positive at forward production angles $\Theta_{\bar{\Lambda}}$ or small momentum transfer. They change sign at a fixed reduced momentum transfer

$$t' = t - t_{min} = -\tfrac{1}{2}\sqrt{(s-4m_p^2)(s-4m_{\bar{\Lambda}}^2)}(1-\cos\Theta_{\bar{\Lambda}})$$

of about 0.2 (GeV/c)^2 and are negative and up to 50% at larger angles. From the spin correlations the fraction of spin-singlet final state can be extracted. It was found, that the hyperon antihyperon pair is always produced in the spin triplet final state, even at the highest momenta. The spin-singlet fraction is vanishing $S_F = 0.006 \pm 0.008$. New data have been added at 1657, 1662, 1726, 1774, 1835, 1948 and 1991 MeV/c antiproton momentum. The new data mainly confirm the results of the former measurements. They complete the data set for the $\bar{p}p \rightarrow \bar{\Lambda}\Lambda$ reaction in the threshold region. The increased statistics allows for a test of CP-violation with the world largest data sample outside the neutral meson system. The comparison of the decay asymmetry parameters of Λ and $\bar{\Lambda}$ is consistent with no CP-violation $A = 0.006 \pm 0.015$.

Kaon exchange models [3] as well as QCD inspired constituent quark models [4] are employed to describe the $\bar{p}p \rightarrow \bar{\Lambda}\Lambda$ reaction. The elementary production operator acts between initial and final states which are distorted by optical potentials. The currently available data are just enough to fix all the model parameters and therefor both approaches fit the data equally well. So far the models have only been applied to data below 1.65 GeV/c. The new data will challenge the models towards higher energies and larger angular momenta. While the meson exchange model is expected to fail sooner or later due to the limited number of mesons taken into account, the quark models should provide improved description of the data because non-perturbative effects will be smaller. The study of spin propagation in this reaction is subject of a different investigation (see the corresponding contribution to this annual report).

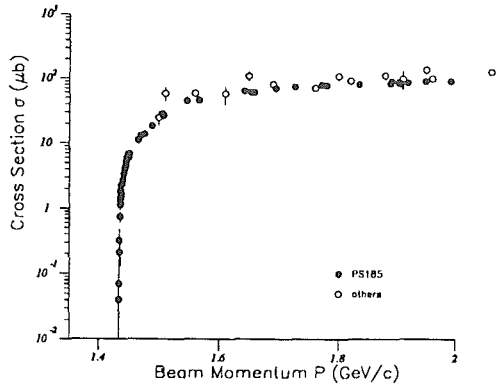

Figure1 Total cross sections for the reaction $\bar{p}p \rightarrow \bar{\Lambda}\Lambda$ from the reaction threshold at 1.435 GeV/c up to the LEAR maximum of 2.0 GeV/c. The full circles show results obtained by the PS185 collaboration. The open circles represent older data.

The PS185/2 collaboration studies the $\bar{p}p \rightarrow \bar{\Lambda}\Lambda$ reaction to resolve a possible structure [2,5] within a few MeV above the reaction threshold. Data have been taken in 1994. In total 36.8x10^{10} $\bar{p}$ were used for data taking. The readout rate was 0.87x10^{-4}/$\bar{p}$, resulting in about 33 million events on tape. Events taken at 1477 MeV/c have been analyzed and the preliminary cross section estimates are in consistency with older data. The data in the threshold region result in cross sections of the expected size, but their relative normalization is not yet fixed. The statistics will be of the order of 400 events per energy bin.

The collaboration has furthermore extended its knowledge on the reaction $\bar{p}p \rightarrow \bar{\Lambda}\Sigma^o + cc.$ with data analyzed at 1726 and 1774 MeV/c. The results for this reaction exhibit features that are similar to $\bar{p}p \rightarrow \bar{\Lambda}\Lambda$ and some that are different. The forward peaking is present although it seems to be even stronger than in $\bar{p}p \rightarrow \bar{\Lambda}\Lambda$. The Λ polarization in the $\bar{p}p \rightarrow \bar{\Lambda}\Sigma^o + cc.$ channels indicates an oscillatory structure similar to that observed in the $\bar{\Lambda}\Lambda$ final state; however, the errors on these data prevent any definitive conclusions. The singlet fraction for the $\bar{\Lambda}\Sigma^o + cc.$ shows a non-zero value. The spin-triplet dominance observed in $\bar{p}p \rightarrow \bar{\Lambda}\Lambda$ ap-

pears to not carry over into $\overline{p}p \rightarrow \overline{\Lambda}\Lambda$. To substantiate speculations about the implications of these new results more and careful theoretical work is needed.

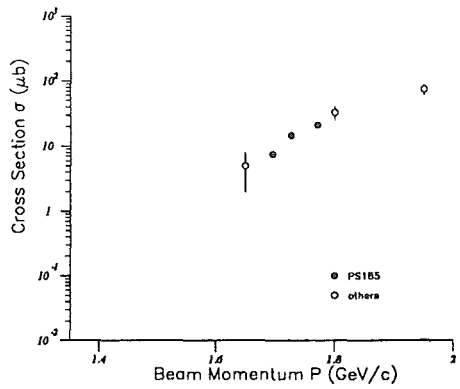

Figure2 Same as figure 1, but for the reaction $\overline{p}p \rightarrow \overline{\Lambda}\Sigma^{o} + cc.$.

[1]) Los Alamos National Lab.
[2]) CERN, Geneva
[3]) Carnegie Mellon University, Pittsburgh
[4]) Universität Erlangen
[5]) Albert Ludwigs Universität Freiburg
[6]) Rutherford Appleton Lab
[7]) University of Illinois at Urbana Champaign
[8]) The Svedberg Laboratory, Uppsala

References

[1] P.D.Barnes et al., Phys. Lett. B189(1987)249
Phys. Lett. B199(1987)147
Phys. Lett. B229(1989)432
Phys. Lett. B246(1990)273
Nucl. Phys. A526(1991)575

[2] P.D.Barnes et al., Phys. Lett. B331(1994)203

[3] J. Haidenbauer et al., Phys. Lett. B291(1992)223
J. Haidenbauer et al., Phys. Rev. C45(1992)931

[4] M.A. Alberg et al., Phys. Atom. Nucl. 57(1994)1608

[5] J.Carbonell et al., Phys. Lett. B306(1993)407

Measurement of spintransfer and depolarization in the reaction $\bar{p}p \rightarrow \bar{\Lambda}\Lambda$

B.Bassalleck[1]), R.Bröders, H.Dennert[4]), H.Dutz[2]), R.A.Eisenstein[6]), W.Eyrich[4]), D.Fields[1]), H.Fischer[5]), G.B.Franklin[3]), J.Franz[5]), R.Gering[2]), R.Geyer, J.Hauffe[4]), D.Hertzog[6]), T.Johansson[7]), T.Jones[6]), K.Königsmann[5]), K.Kilian, P.Kingsberry[1]), R.A.Kraft[4]), J.Lowe[1]), C.A.Meyer[3]), W.Meyer[2]), W.Oelert, S.Pomp[7]), B.Quinn[3]), G.Reicherz[2]), K.Röhrich, E.Rössle[5]), K.Sachs, H.Schmitt[5]), T.Sefzick, F.Stinzing[4]), E.Traneus[7]), D.Wolfe[1])

Quantum Chromo Dynamics (QCD) as the most fundamental description of strong interactions is part of the standard model. The interaction between quarks or antiquarks is mediated by the colour field, quantized as gluons. The strength of this interaction grows with the distance of the interacting particles. This leads to the asymptotic freedom of the involved particles at very high energy and to the confinement into ordinary hadronic matter at low energies. Since the force increases with decreasing energy, perturbative methods fail to achieve convergence in the low and medium energy regime. To get some hints how to apply QCD on a hadronic mass scale is a major challenge in medium energy physics.

The spectroscopy of hadronic states provides constraints on models which are applicable in medium energy physics. Ordering schemes and symmetries have lead to a deeper understanding of the structure of hadronic matter. Pairs of quarks and antiquarks or three quarks combine to mesons and baryons. Recently indications for a possible gluonic state of matter have been found in the 0^{++} meson system [1]. But that this simple picture of matter does not necessarily hold has been shown in deep inelastic lepton scattering experiments [2]. Obviously not all of the nucleon's spin is carried by the charges inside that nucleon: $\Delta\Sigma = 0.3$ rather than $\frac{1}{2}$ as expected in the naïve parton model. Furthermore the nucleon might have a component of polarized $\bar{s}s$ pairs: $\Delta\Sigma = \Delta u + \Delta d + \Delta s$ and $\Delta s = -0.1 \pm 0.04$, where Δq is the contribution to the total spin from quarks and antiquarks of flavour q. Δs includes contributions from sea-quark pairs which would then be polarized opposite to the nucleons spin, while a component from polarized gluons would be aligned with the nucleon.
A natural explanation of this observation is given within the framework of chiral QCD [3]. The phenomenological analysis of the quark condensate of the non-perturbative vacuum in QCD sum rules results in a $\bar{s}s$ component, which is almost equal to that of the up and down quarks: $< \bar{s}s >= (0.8 \pm 0.1) < \bar{q}q >$. A second observation is the smallness of the masses of the 0^- mesons indicating a strong attraction in this channel. Thus, quarks pull $\bar{q}q$ pairs out of the vacuum in their vicinity. Those pairs are in the $^3P_0$ state, naturally spin aligned. Assuming a strong attraction between the quarks of the hadron and the antiquarks of the vacuum pair in the 0^- ($^1S_0$) channel, the selected vacuum pair has their spins aligned oppositely to the hadron's valence-quarks. This $^3P_0$ model does not only explain the results from lepton scattering but also provides an explanation for enhanced strangeness production observed in antiproton proton annihilations. It also explains the production of 0^{++} final state particles. Although this simple picture is diluted due to interplay with other production mechanisms and the initial and final state interactions, the study of spin-correlations between intial and final baryons in $\bar{p}p \rightarrow \bar{\Lambda}\Lambda$ will provide information on the tensor interaction in the reaction and may shed new light on the question of strangeness in the nucleon.

The quantum numbers of the Λ-hyperon are mainly determined by the quantum numbers of its s-quark, as suggested by the decomposition of its SU(6) wave function. The Λ polarization should therefore signal the polarization of the produced strange quark. Since spin-flip reactions are suppressed compared to non-spinflip transitions, the final state polarization is a measure of the inital state spin orientation. A strange quark, being knocked out from the negatively polarized sea, should maintain its polarization vector, which is in that case opposite to the inital nucleon's polarization. If the strange quark is produced in the annihilation of valence quarks or from the polarized gluon content of the nucleon, the polarization should be parallel to the inital state polarization. The depolarization parameter Dnn measures the spin transfer between initial and final state particles. It is +1 for 100% spin-transfer and -1 at 100% spin-flip.

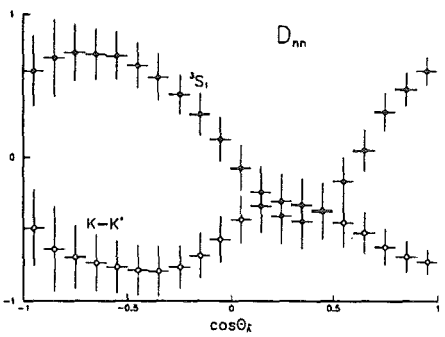

Figure 1: Depolarizations as a function of the cosine of the production angle of the $\bar{\Lambda}$ in the cms of the reaction 75 MeV above the reaction threshold. The values are from ref. [4,5] for meson exchange and quark model. The error bars are calculated simulating the PS185 experimental setup and assuming three weeks of data taking.

The PS185 collaboration has proposed to measure the depolarization and spin transfer in the reaction $\bar{p}p \rightarrow \bar{\Lambda}\Lambda$ at different momenta with a frozen spin polarized proton target [6] (see figure 2) and the hyperon decay spectrometer at LEAR [7].
The trigger will employ the charged-neutral-charged event signature using small scintillators as beam coun-

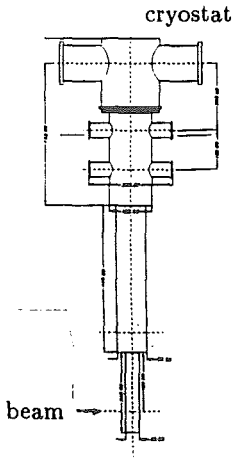

Figure 2: The He^3-He^4 dilution cryostat with the target, which is mounted in the 21 mm radius vacuum vessel at the bottom of the cryostat. The incoming beam is indicated by the arrow. This target is being built for use at COSY, but can be employed at LEAR for this dedicated experiment.

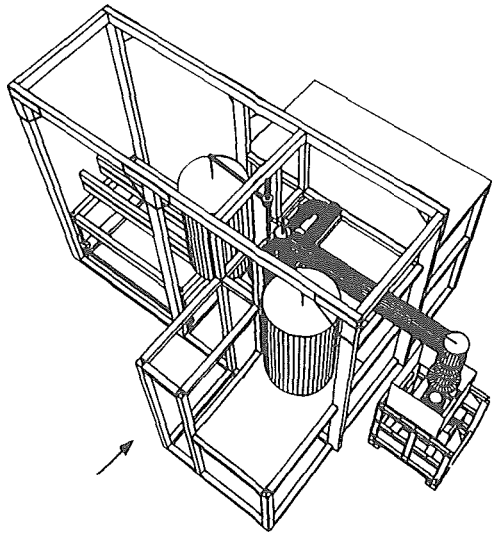

Figure 3: A view onto the proposed target setup from above the beamline. The decay spectrometer is not shown for clarity. The incoming beam is indicated by the arrow. One large liquid helium dewar is located close to the target, while a second one to supply the superconducting polarization magnet can be moved onm rails away from the target and the beam.

ters and larger scintillation counters between target and downstream tracking detectors. The acceptance of the detector with the new target was studied and found to be roughly a factor of two smaller compared to a setup with a CH_2-sandwich target. This is mainly due to the distance between the interaction region and the first trigger counters. The other features of the experiment remain almost unchanged. The result of a simulation with the new target and the trigger is shown in figure 1. The large and complex target arrangement (figure 3) requires to move the experiment to another external beamline at LEAR. There the beam has to be shared with PS197. The new beam properties were studied. It was found neccessary to shift the last quadrupol dublet of the beamline further downstream to achieve the required beam size of 1 mm diameter and emitance of 5 mrad. Beam-halo due to the beam splitting can be up to 15% of the central intinsity.
The experiment has been approved and is scheduled to take data during three month in automn and winter 1996.

1) University of New Mexico, Albuquerque
2) Universität Bonn
3) Carnegie Mellon University, Pittsburgh
4) Universität Erlangen
5) Albert Ludwigs Universität Freiburg
6) University of Illinois at Urbana Champaign
7) The Svedberg Laboratory, Uppsala

References

[1] C. Amsler and F.E. Close, Phys. Lett. B356(1995)123
[2] L. Maiani, Phys. Lett. B353(1995)325
[3] J. Ellis et al., Phys. Lett. B353(1995)319
M. Alberg et al., CERN-TH 95-47, 1995
[4] J. Haidenbauer et al., Phys. Lett. B291(1992)223
J. Haidenbauer et al., Phys. Rev. C45(1992)931
[5] M.A. Alberg et al., Phys. Atom. Nucl. 57(1994)1608
[6] W.Meyer et al., Nucl.Instr.Meth A244(1986)574
H.Dutz et al., Verhandl. DPG(VI) 26(1992)37
[7] Letter of Intent I192, CERN-SPSLC/92-53
Proposal P287, CERN-SPSLC/95-13

K^+-meson production in pBe interactions at $T_p = 2.9$ GeV

M. Büscher, R. Eßer, A. Franzen, L. v. Horn, D. Kopyto, H. Ohm, H. Seyfarth, K. Sistemich, H. Müller[a], B. Prietzschk[a], B. Rimarzig[a], C. Schneider[a], C. Schneidereit[a], A. Akindinov[b], M. Chumakov[b], V. Demechin[b], V. Ergakov[b], A. Gerasimov[b], V. Goryachev[b], V. Kiselev[b], V. Kostromin[b], A.A. Sibirtsev[b,c], V. Sopov[b], V. Tchernyshev[b], V. Kruglov[c], A. Petrus[c], V. Koptev[d], and S. Mikirtychants[d]

We have investigated the production of K^+, π^+ mesons and protons in p^9Be interactions at projectile energies T_p = 2.9 GeV at the Institute of Theoretical and Experimental Physics (ITEP), Moscow. The experimental setup which is sketched in Fig. 1 is described in detail in[1,2,3]. The primary proton beam of the ITEP synchrotron was used to produce secondary particles in an internal Be target. The ejectiles leaving the target under angles $\vartheta = 17°$ were separated in the N530 beam channel which consists of two dipole and six quadrupole magnets for momentum analysis. In our experiment an ejectile momentum p = 545 MeV/c was chosen. The momentum and angular acceptance of the separator are $\Delta p/p \approx 2\%$ and $\Delta\Omega = 0.6$ msr, respectively. Furthermore, two electrostatic elements allow to separate pure K^+, π^+ and p beams and, thus, an efficiency calibration of the detection system is easily possible[1,2,3].

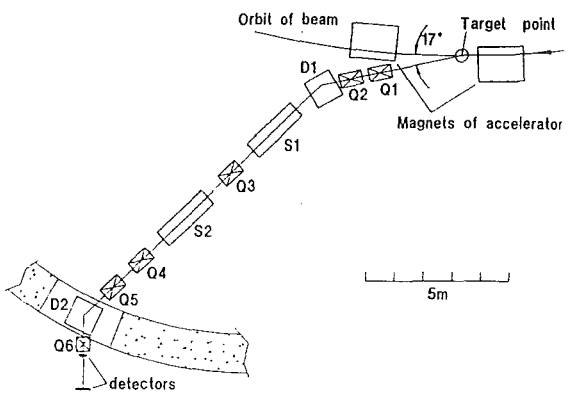

Fig. 1: The N530 beam line for secondary particles with dipoles D1 and D2, quadrupoles Q1 to Q6 and electrostatic separators S1 and S2.

The measured detection efficiencies for K^+, π^+ and p are (34 ± 5)%, (55 ± 2)% and (91 ± 1)%, respectively. In addition to the high K^+-detection efficiency the fraction of π^+ and p misidentified as K^+ is less than $3\cdot10^{-7}$ [1,2,3]. Therefore, our detection system allows the simultaneous measurement of K^+, π^+ and p at the exit of the separator where the K^+ rate is much lower than the π^+ and p rates.

During ~ 24 hours of beam time 11 K^+, ~ $1.6\cdot10^5$ π^+ and ~ $2\cdot10^5$ p were identified. Correcting for the detection efficiencies and for K^+- and π^+-decay in flight (only ~ 0.5% of all K^+ survive) yields a production cross-section ratio of

$$d^2\sigma/d\Omega dp\ (K^+) : d^2\sigma/d\Omega dp\ (\pi^+) : d^2\sigma/d\Omega dp\ (p) = (1 \pm 0.34) : (85 \pm 1) : (31 \pm 1). \quad (1)$$

All quoted errors are of statistical nature.

The cross sections for the production of π^+ mesons have already been studied in a wide range of projectile beams as well as ejectile momenta and angles (see [3] and references therein). Therefore, it is possible to extract from the existing data the invariant production cross section $E\ d^3\sigma/d^3p\ (\pi^+)$ for the kinematical conditions of our experiment. We obtain[3] a value of

$$E\ d^3\sigma/d^3p\ (pBe \rightarrow \pi^+X) = 200 \pm 44\ \text{mb GeV}^{-2}\ c^3sr^{-1}.$$

From the measured ratios (1) we then obtain

$$E\ d^3\sigma/d^3p\ (pBe \rightarrow K^+X) = 3.1 \pm 1.2\ \text{mb GeV}^{-2}\ c^3sr^{-1}.$$

In order to compare our measured K^+-production cross section with other experimental data and theoretical predictions we calculated from the invariant double differential cross section the total K^+-production cross section σ_{tot} in a phase-space approach using the formula

$$E\frac{d^3\sigma}{d^3p}(pA \rightarrow K^+X) = \frac{\pi}{4}\cdot\frac{\sigma_{tot}(pA \rightarrow K^+X)}{\Phi}\cdot\frac{\lambda(s_{\Lambda p}, m_\Lambda^2, m_p^2)}{s_{\Lambda p}} \quad (2)$$

Here, λ is the kinematical function

$$\lambda^2(x,y,z) = [x - (\sqrt{y} + \sqrt{z})^2]\,[x - (\sqrt{y} - \sqrt{z})^2]$$

and ϕ the phase-space volume

$$\Phi = \left(\frac{\pi}{2}\right)^2 \int_{s_{min}}^{s_{max}} \frac{\lambda(s_{\Lambda p}, m_\Lambda^2, m_p^2)}{s_{\Lambda p}} \cdot \frac{\lambda(s, s_{\Lambda p}, m_K^2)}{s} ds_{\Lambda p}$$

with $s_{min} = (m_p + m_\Lambda)^2$, $s_{max} = (\sqrt{s} - m_K)^2$.

m_Λ, m_p are the p and Λ masses and $s_{\Lambda p}$ the total energy of the Λp subsystem. The justification of this phase-space approach is shown in[3] by an application to existing experimental data[4]. Using (2) we obtain a total K^+-production cross section for $T_p = 2.9$ GeV:

$$\sigma_{pA}\ (pBe \rightarrow K^+X) = 3.7 \pm 1.5\ \text{mb}. \quad (3)$$

Table 1 shows our cross section (3) in comparison with existing data[4,5]. In[4,5] also double differential cross sections were measured and we also use approach (2) for the extraction of the total K^+-production cross sections.

Table 1: Values for the total K^+-production cross sections σ_{pA} from our work and from[4,5]. The elementary K^+-production cross sections σ_{pp} were taken from Refs. 6,7.

T_p [GeV]	Target	σ_{pA} [mb]	σ_{pp} [μb]	Ref.
2.9	Be	3.7±1.5	140	--
2.1	NaF	0.85±0.10	22	4
2.1	Pb	5±1	22	4
2.5	C	0.39±0.05	71	5

Also shown in the table are the elementary K^+-production cross sections for the beam energies in the various measurements[6,7]. They can be used to eliminate the energy dependence of the elementary cross section by calculating the ratios σ_{pA}/σ_{pp}. These ratios are shown in Fig. 2 as a function of the target mass A. Also shown in the figure are lines of constant ratios $\sigma_{pA}/\sigma_{pp} = A^{\alpha}$ for various slope parameters α. It can be shown[3] that one expects values for α in the range 0.7 ... 0.8 for K^+ production in reactions where the K^+ meson is produced in collisions with a single nucleon N in a one-step reaction $pN \rightarrow K^+\Lambda N$[8,9]. From our measured cross section, however, we extract a value of $\alpha = 1.48 \pm 0.19$. This substantially larger value suggests a collective behaviour of the Be nucleus in K^+ production even far above the nucleon-nucleon threshold ($T_{NN} = 1.58$ GeV) like e.g. K^+ production in two-step processes[8,9], $pN_1 \rightarrow \pi NN$, $\pi N_2 \rightarrow K^+\Lambda$, via the formation of an intermediate π meson.

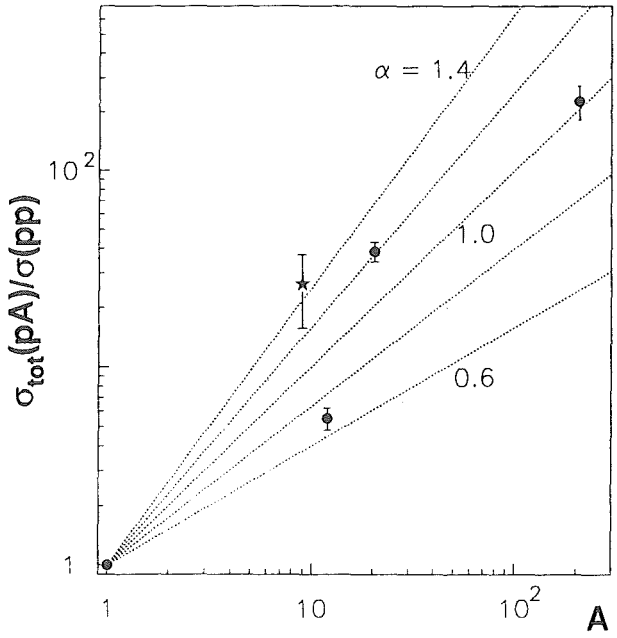

Fig. 2: A dependence of the K^+-production cross sections σ_{pA}. The star indicates our value, the dots the cross sections from Refs. 4,5. In order to eliminate the energy dependence of the elementary cross section σ_{pp} the ratio σ_{pA}/σ_{pp} is shown. The dashed lines show the parametrization $\sigma_{pA} = A^{\alpha}\sigma_{pp}$ for various values of α.

Summarizing, our study may indicate the importance of multi-nucleon mechanisms for K^+ production in pA reactions at energies above the nucleon-nucleon threshold. This finding is also important in view of the planned studies on subthreshold K^+ production at ANKE where one wants to illuminate the role of the one- and two-step mechanisms[10].

References:

1. R. Eßer et al., Ann. Rep., KFA-IKP 1994, p. 52
2. A. Franzen et al., Ann. Rep., KFA-IKP 1994, p. 54
3. M. Büscher et al., submitted to Z. Phys. A
4. S.Schnetzer et al., Phys. Rev. C40, 640 (1989)
5. M. Debowski, Ph.D. Thesis, Cracow 1995
6. V. Flaminio et al., Compilation of cross sections, CERN-HERA 84-01 (1984), Geneva
7. A. Sibirtsev et al., submitted to Phys. Lett.
8. M. Büscher et al., Ann. Rep. KFA-IKP 1993, p. 33
9. A. Sibirtsev et al., Z. Phys. A347 (1994) 191
10. M. Büscher et al., Proc. Int. Conf. on Mesons and Nuclei at Intermediate Energies, May 3-7, 1994, Dubna, Russia, World Scientific Publishing ISBN 981-02-1787-0, p. 446

a Institut für Kern- und Hadronenphysik, Forschungszentrum Rossendorf, Postfach 510119, D-01314 Dresden, Germany

b Institute of Theoretical and Experimental Physics, Cheremushkinskaya 25, 117259 Moscow, Russia

c Laboratory of Nuclear Problems, Joint Institute of Nuclear Research, 141980 Dubna, Russia

d High Energy Physics Department, Petersburg Nuclear Physics Institute, 188350 Gatchina, Russia

Spectroscopy of X-rays from Antiprotonic Hydrogen and Helium Isotopes

D. Anagnostopoulos[1], M. Augsburger[2], G. Borchert[3,5], D. Chatellard[2], P. El-Khoury[4], J.-P. Egger[2], H. Gorke[5], D. Gotta[5], P. Hauser[6], P. Indelicato[4], K. Kirch[6], S. Lenz[5], K. Rashid[7], O.W.B. Schult[5], Th. Siems[5], L.M. Simons[6]

The aim of LEAR experiment PS207 is to study at threshold the antiproton-proton and antiproton-nuclear spin-spin and spin-orbit interaction in light nuclei by means of the observation of the characteristic X-radiation from the deexcitation of the antiprotonic atom [1,2]. We report on results of the initial measurement, where, for the first time, antiprotonic X-rays could be observed with a crystal spectrometer and for the first time strong interaction effects could be observed in antiprotonic deuterium.

The response function of the crystal spectrometer has been measured with narrow antiprotonic X-ray lines, which are not affected by strong interactions and where no electrons are left in the atom to avoid screening corrections. The transitions $\bar{p}^4$He(5-4) and $\bar{p}^{20}$Ne(13-12) fulfil these requirements (fig. 1a,b). The energy resolutions obtained are 230±30 meV at 1.799 keV and 360±40 meV at 2.444 keV. (The theoretical limits are 170±10 meV and 320±20 meV as calculated from crystal diffraction theory and a Monte-Carlo ray-tracing code including the geometrical broadening).

The Lα transitions from $\bar{p}$H and $\bar{p}$D show a significant broadening as compared to the calibration transitions from $\bar{p}^4$He and $\bar{p}^{20}$Ne (fig. 1c,d). The hadronic shift for the $\bar{p}$H Lα transition is compatible with zero, but due to the low statistics the experimental error for the shift is large (≈60 meV) and also a strong interaction broadening cannot be extracted.

For $\bar{p}$D, the best fit is obtained with a single Voigt profile (fig.2: solid line, χ^2_{red} = 0.86 per degree of freedom). χ^2 is minimal for a Gaussian contribution close to the experimental resolution as obtained from $\bar{p}^{20}$Ne transition. We obtain for the spin-averaged shift and broadening

$$\bar{\varepsilon}_{2p} = -110 \pm 20 \pm 70 \text{ meV}$$
$$\bar{\Gamma}_{2p} = 570 \pm 60 \pm 60 \text{ meV}$$

indicating a very strong absorption and (from the minus sign) a repulsion of the 2p level. The first error is due to statisctics, the second one due to systematical uncertainties. For the shift, the

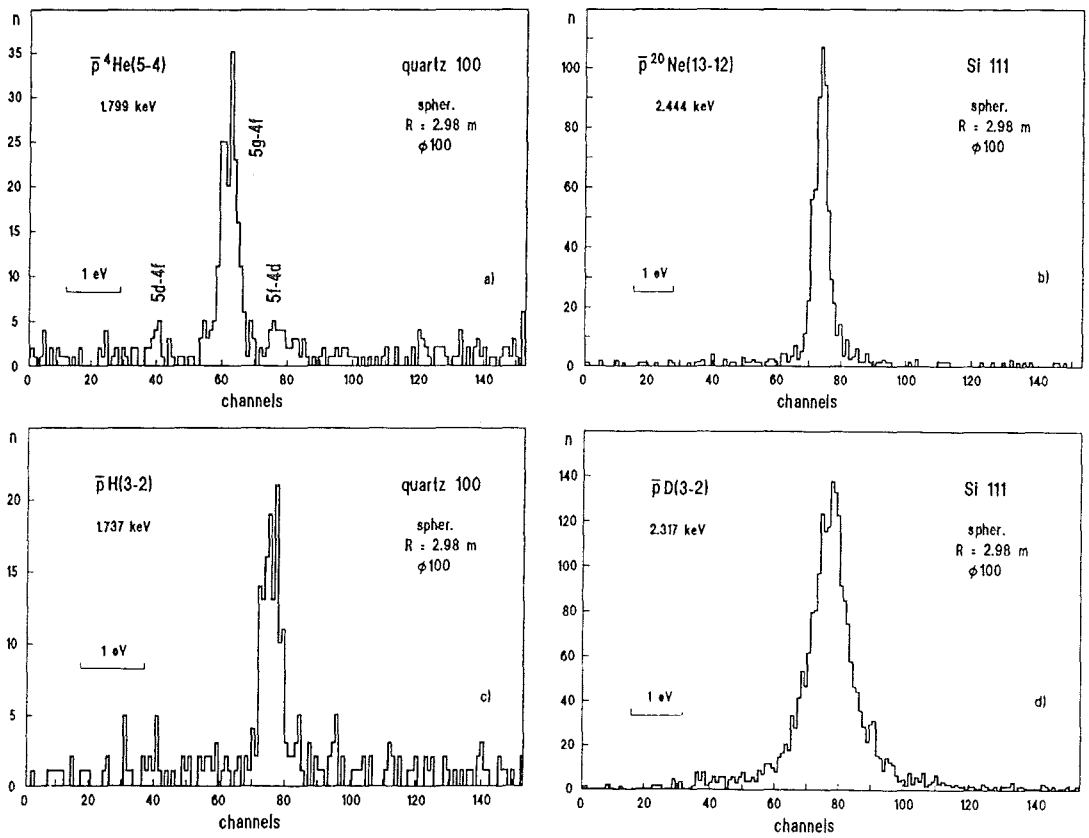

Fig. 1: Antiprotonic X-rays measured with the Bragg crystal spectrometer.
a), b) Measurement of the spectrometer response function with narrow antiprotonic transitions.
c), d) Lα transitions from antiprotonic hydrogen and deuterium.

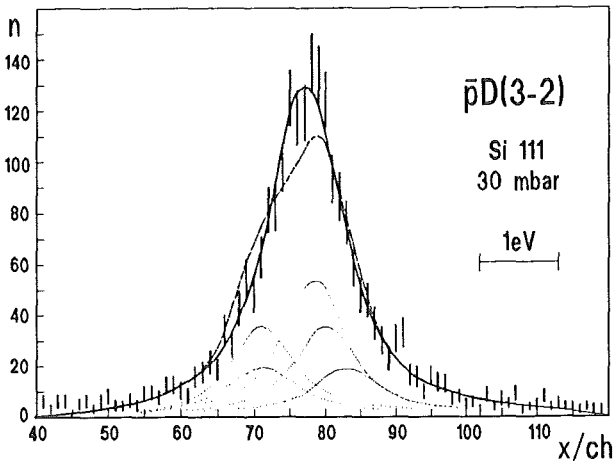

Fig. 2: Lα line shape of antiprotonic deuterium.

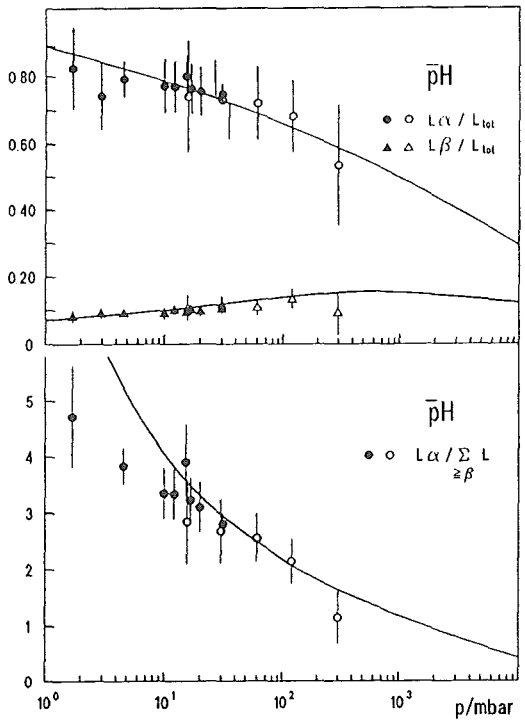

Fig. 3: Pressure dependence of the Balmer series of antiprotonic hydrogen. The solid lines are predictions of the cascade model of Borie and Leon [7] with the parameters as obtained from a fit to the line intensities by Heitlinger et al. [8]. (full symbols: this exp.; open symbols: previous results from PS175 [8])

systematical error stems from the energy calibration with sulphur fluorescence X-rays. In the case of the level width, the error reflects various assumptions for the shape of the spectrometer response function.

The predictions for the strong interaction broadening vary from 70 - 500 meV, i.e. 2-15 times the spin-averaged width of protonium [8]. Fixing the electromagnetic splitting as predicted by Barmo et al. [6], modified with the relative shifts as given by Wycech et al. [3] and with the hadronic width being a free parameter, only a much worse χ^2_{red} of 1.55 is achieved (fig.2-dashed line: sum of the hyperfine components (dotted lines)). In this case, the spin-averaged level width reduces to (280±50±120) meV, but the description of the line shape becomes very poor. In conclusion, the present measurement shows no evidence for a line splitting of the order of the hadronic width. Further progress could be achieved by using asymmetrically cut crystals, which should allow to increase the resolution by a factor of about two.

The yields of inner transitions are useful information on the atomic cascade. For $\bar{p}^4$He, the parallel transitions 5f-4d and 5d-4f could be resolved from the circular transition 5g-4f (fig. 1a). The relative intensities are 12±3% and 5±2% as compared to the circular transition (100%).

The pressure dependence of the L series of antiprotonic hydrogen was measured from 1.3 to 30 mbar showing that Stark mixing and Coulomb deexcitation are very important even at very low pressures. A sensitive quantity for the description of the cascade is the ratio of the Balmer α transition to all other Balmer transitions (fig. 3). At pressures below 10 mbar, the prediction of the Borie-Leon-Bethe cascade model [7] disagrees with the data, a deviation which is not seen from the yields of the Lα or Lβ transitions.

[1] Dep. of Physics, Univ. of Ioannina, Greece

[2] Institut de Physique de l'Université de Neuchâtel, Switzerland

[3] CERN, Geneva, Switzerland

[4] Institut du Radium, Université Pierre et Marie Curie, Paris, France

[5] IKP, Forschungszentrum Jülich, Germany

[6] PSI, Villigen, Switzerland

[7] Quad-I-Azam University, Islamabad, Pakistan

[1] D. Anagnostopoulos et al., CERN/PSCC/90-9/P124, 1990; G. Borchert et al., SPSLC/93-17/P124 Add. 3, 1993 (PS207)

[2] Ann. report, IKP, 1994, p.101

[3] S. Wycech, A. M. Green, and J. A. Niskanen, Phys. Lett. B152(1985)308

[4] G. P. Latta and P. C. Tandy, Phys. Rev. C42(1990)R1207

[5] G. Q. Liu, J.-M. Richard, and S. Wycech, Phys. Lett. B260(1991)15

[6] S. Barmo, H. Pilkuhn, and G. Schlaile, Z. Phys. A301(1981)283

[7] E. Borie and M. Leon, Phys. Rev. A21(1980)1460

[8] K. Heitlinger et al., Z.Phys. A342(1992)359

Feasibility Study to Determine The Pion to Myon Mass Ratio

D. Anagnostopoulos[1], M. Augsburger[2], G. Borchert, D. Chatellard[2], M. Daum[3], J.-P. Egger[2], R. Frosch[3], H. Gorke, D. Gotta, P. Hauser[3], P. Indelicato[4], P. El-Khoury[4], K. Kirch[3], S. Lenz, O.W.B.Schult, Th.Siems, L.M. Simons[3]

The feasibility study has been continued using the 5-4 transitions from pionic nitrogen and myonic oxygen as well as fluorescence X-rays from copper, scandium, and xenon [1].

The measurement was performed at the newly set up πE5 channel of the Paul-Scherrer-Institut (PSI). The pion beam was injected into the cyclotron trap and stopped to 1-2% in a cylindrical target container of 50 mm diameter filled with nitrogen, oxygen, or xenon. The scandium and copper fluorescence targets were installed without breaking the vacuum by retracting the target container and placing at the center of the trap metal plates of suitable size. For Bragg reflection, a spherically mounted Si (110) crystal of 10 cm diameter was used in second and forth order reflection [2]. The X-rays were recorded with a Charge-Coupled-Device of $2\times17\times26$ mm^2 sensitive area having a pixel size of 22.5 μm $\times$ 22.5 μm.

The injection modus was chosen to maximize the rate of the πN(5-4) transition in order to perform a systematic investigation of the stability of the spectrometer. About 100 events per hour from pionic nitrogen were recorded at a target pressure of 1 bar with a beam current of 1 mA of the ring accelerator. The stability of the angular setting was checked with fluorescence X-rays, where within a few hours the statistical accuracy of about 1 ppm for the position of the line can be achieved.

	E / eV	Θ_B
μ^{16}O(5g-4f)	4023.212	53°22'2.5"
Cu Kα_1	8047.838(6)[a]	53°21'13.8"
π^{14}N(5g-4f)	4055.362	52°45'38.8"
π^{14}N(5f-4d)	4057.665	
Sc Kα_1	4090.6(1)[b]	52°6'58.4"
Xe Lα_1	4110.09(2)[c]	51°46'5.1"

Table1: X-ray energies and Bragg angles. The present uncertainties for the fluorescence X-ray energies are given in paranthesis ([a]:[3], [b]:[4], [c]: [5]). The transition energies are calculated with the mass values of m_π=139.56995 MeV/c^2 for pions [6] and m_μ=105.658387 MeV/c^2 for myons [7].

In Fig. 1, the X-ray spectra from one cycle are shown. Several cycles of πN, Xe Lα_1, and Cu and Sc Kα_1 prove the reproducibility of the angular settings (Fig.2).

From the circular transition πN(5g-4f), the inner transition πN(5f-4d) is resolved providing new information on the atomic cascade (fig. 1). The intensity ratio of the parallel transition to the circular one was measured to be (7.1±0.5)%.

An energy calibration of the πN (5-4) transition at the ppm level, however, is impossible at present due to the lack of a detailed modelling of the X-ray line shapes. Even in the case of the copper Kα_1 transition, where a comprehensive study has been performed using a flat crystal set-up and an accurate parametrization of the satellite transitions was achieved [3], transferring the results to curved crystal measurements needs some clarification. Additional uncertainties stem from the use of two different orders of reflection because of the different penetration into the crystal material and the different indices of refraction. For xenon, a noticable intensity for an Lα_1 satellite has not been reported [5], but has been observed in our experiment. As can be seen from the πN spectrum (fig.1), there is no geometrical broadening or defocussing, which could cause tails for the X-ray lines. In the case of scandium, no recent value of the Kα_1 transition energy is available (see tab. 1). A remeasurement of the xenon and scandium X-rays is planned at NIST, Washington beginning of 1996 [8]. Having available parametrizations for the xenon and scandium line shapes, it should be possible to fix the πN (5-4) transition energy to 5-10 ppm. This allows to resolve the ambiguity of 15 ppm from the K electron contamination of a recent measurement of the pion mass with X-rays from pionic magnesium [9].

With the present set-up, the rate for the μO(5-4) transition is a few per cent only of the rate of pionic nitrogen transition. The accuracy of the energy and, therefore, the mass determination is restricted to about 20 ppm from the statistics as obtained from the myonic spectrum. The mass value obtained is still consistent with both solutions A and B from [9].

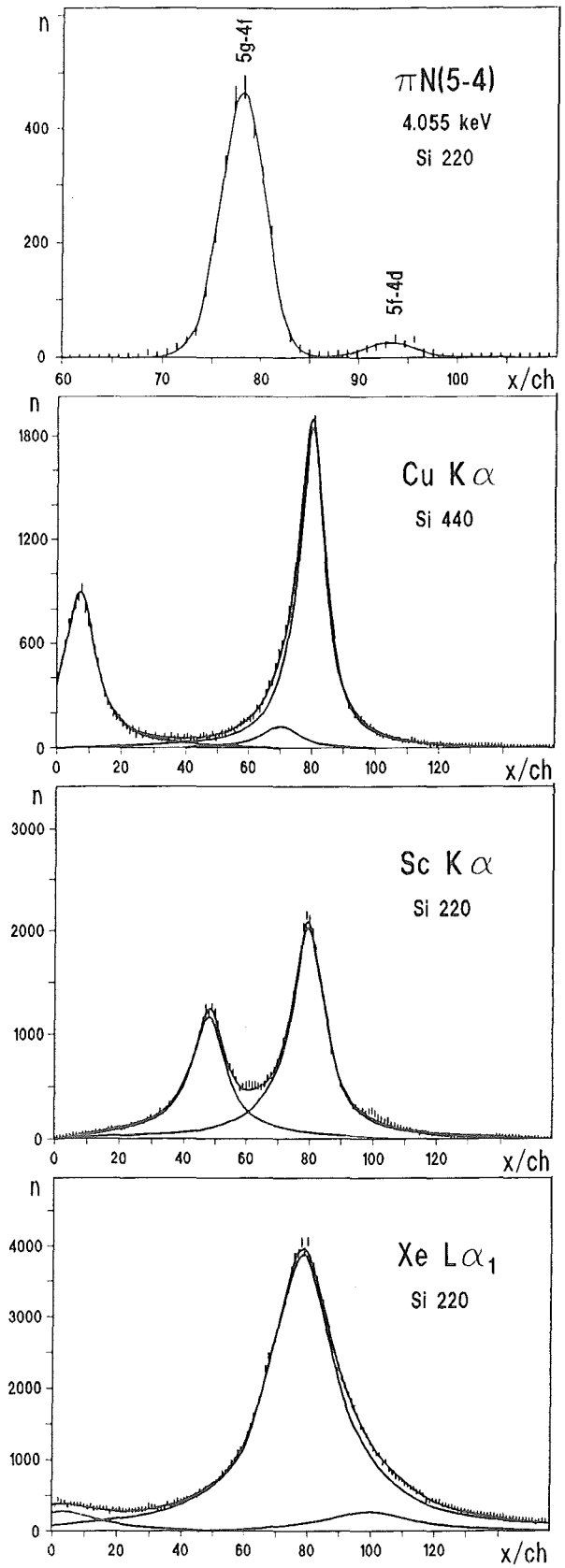

Fig. 1: Position spectra of the πN (5-4) transition and the fluorescence X-rays from Cu, Sc, and Xe from one cycle of the stability measurement. Note the expanded x axis of the πN spectrum.

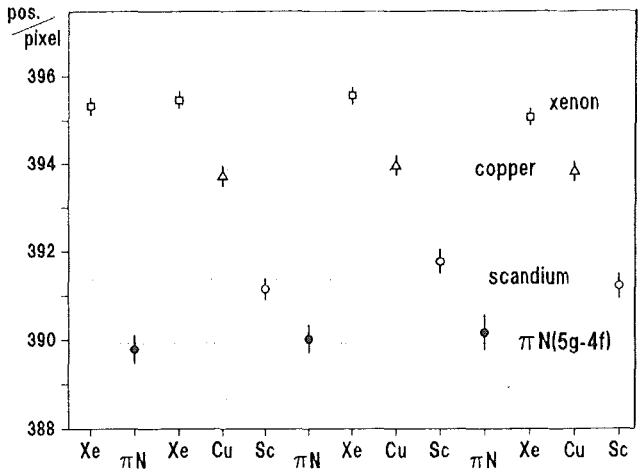

Fig.2: Stability of the spectrometer set-up for several cycles πN(5-4), Cu $K\alpha_1$, Sc $K\alpha_1$, and Xe $L\alpha_1$. In second order reflection, one pixel (of 22.5μm) corresponds to 8 ppm accuracy for the determination of the pion mass.

From the results of the feasibility study we conclude, that we are able to achieve with fluorescence X-rays an accuracy at the 5-10 ppm level in the pion mass determination. As can be seen from fig. 2, the stability of the apparatus, however, approaches 1-2 ppm, which then also can be reached for the pion to myon mass ratio if the more accurate energy calibration with the myonic transition becomes possible. With the new cyclotron trap, higher rates for the myonic transitions will be achieved and then the direct comparison can be performed of the pionic and myonic transitions.

[1] Department of Physics, University of Ioannina, Greece

[2] Institut de Physique de l'Université de Neuchâtel, Switzerland

[3] Paul-Scherrer-Institut (PSI), Villigen, Switzerland

[4] Institut du Radium, Université Pierre et Marie Curie, Paris, France

[1] Annual report, IKP 1994, p. 103

[2] The Bragg crystal was manufactured in collaboration with Carl-Zeiss-Company in D-73446 Oberkochen

[3] J.Härtwig et al., J.Appl.Cryst.26(1993)539

[4] J.Bearden, Rev. Mod. Phys. 39(1967)125

[5] T.Mooney et al.,Phys.Rev.A45(1992)1531

[6] P. Goudsmit, priv. comm.

[7] S. Rinker, MUON, upgrade 1986

[8] R. Deslattes, priv. comm.

[9] B. Jeckelmann et al., Phys. Lett. B 335(1994)326

Eta-Production Experiment PROMICE/WASA *

K. Kilian, W. Oelert, V. Renken
for PROMICE/WASA collaboration

During the past years the CELSIUS accelerator at The Svedberg Laboratory in Uppsala (Sweden) runs with increasing success. The PROMICE/WASA experiment (PROduction Of Mesons In CElsius / Wide Angle Shower Apparatus) aims in the first step to investigate fundamental reaction mechanisms in the Pion- and Eta-meson production. Very accurate measurements in proton-proton collisions with $p+p+\pi^0$ [1] and $p+p+\eta$ [2] in the exit channel close to production threshold were finished in 1995.

After test measurements with a proton beam on a deuteron target and different improvements in the detector setup the good suitibility also for these kind of reactions became obvious.

The present setup consists of an internal cluster jet target surrounded by a central detector measuring neutral and charged tracks followed by a forward detector system, which is only charge sensitive. The window counters are followed by two straw chamber planes for accurate track definition. Three layers of thin, spiral and sector shaped plastic scintillator for dE/dx measurement and fast multiplicity determination are located before four planes of segmented scintillator calorimeter and the veto hodoscope. Temporarily, a small silicon detector for luminosity monitoring and normalization purposes was fixed at approximatly 160 degrees in φ-angle outside the scattering chamber.

In October 1994 nearly three weeks beamtime were dedicated for studies of the reaction $p+d\rightarrow{}^3He+\eta$ and on parallel $p+d\rightarrow p+d+\eta$.

In principle there are two independent ways of event reconstruction, either to measure the ^3He or the η-meson by its decay products. Due to high statistics the identification of the desired reaction is mainly done by missing mass analysis of the ^{3}Helium recoil nucleus alone. A preliminary but typical missing mass distribution for $p+d\rightarrow{}^3He+X$ is shown in figure 1 with a clear and narrow η-peak. With low statistics it is possible to do a full event reconstruction by measuring the ^{3}Helium and the two γ's from the eta decay. Up to now the emphasis is put to the method with high statistics and the others are so far used for comparison, cross check and confirmation of the our results. The analysis is still in progress, but first angular distributions are extracted.

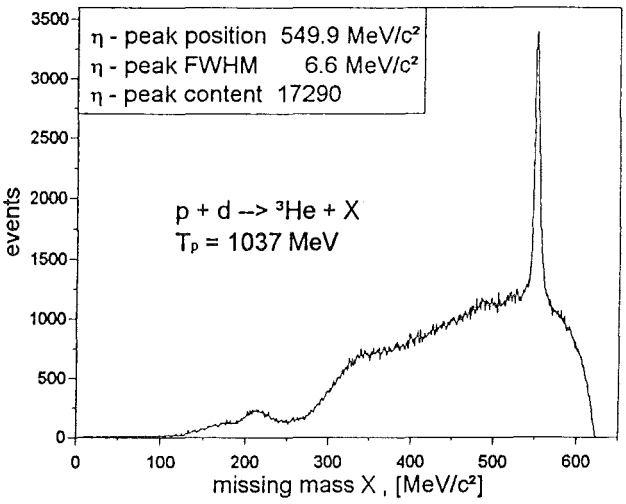

Figure 1: Missing mass distribution for $p+d\rightarrow{}^3He+X$ at T_p=1037 MeV. (complete statistics)

The normalization is done with proton deuteron elastic scattering. Knowing the integrated luminosity and the effective detector acceptance (i.e. geometrical, subdetector failures and nuclear reaction losses) one can estimate the total cross section. Taking into account the accuracy of about 20% our data shows a good agreement with existing data at threshold and at higher energy. The very preliminary results for σ_{tot} and an overview of measured energies and the detected η's are:

Energy [MeV]	total Number of $^3He+\eta$ events	$^3He+\eta$ events to obtain σ_{tot}	σ_{tot} [nb]
930	11600	1880	469
965	18200	5600	662
1037	17290	5300	717
1100	8300	8300	663

After futher improvements in the Monte Carlo simulations for the background processes we'll obtain final angular distributions and values for the total cross section.

*This programme is supported by DAAD (HSP II/AUFE)

References:

[1] A. Bondar et al., Phys.Lett. B356 (1995) 8
[2] H. Calen et al., to appear in Phys.Lett.B

Exclusive Study of the Roper Resonance Excitation

SPES 4π Collaboration
R. Dahl[1], C. Ellegaard[1], C. Gaarde[1], M. Kalargis[1], J.S. Larsen[1], M. Skousen[1], J. Golovanov[2], V. Ladygin[2], N.M. Piskunov[2], J.M. Sitnik[2], E.A. Strokovsky[2], G.D. Alkhasov[3], I.V. Khanzadeyev[3], V.A. Mylnikov[3], A.N. Prokofjev[3], V.A. Samsonov[3], I.V. Tkach[3], V.V. Vikhrov[3], A.A. Vorobyov[3], A.A. Zdanov[3], H.P. Morsch[4], M. Boivin[5], J.L. Boyard[5], T. Hennino[5], R.A. Kunne[5], F. Plouin[5], P. Radvanji[5], E. Tomasi[5], L. Bimbot[6], L. Fahri[6], J.C. Jourdain[6], B. Ramstein[6], L. Rosier[6], M. Roy-Stephan[6], W. Augustyniak[7], P. Zupranski[7], M. Jones[8], C. Perdrisat[8]

To investigate in more detail the excitation of the P_{11}(1440 MeV) resonance in exclusive hadron scattering experiments, a detection system around the target point of the SPES 4 spectrometer at SATURNE was designed [1]. In such experiments we can hope to be able to separate different reaction graphs which contribute to inelastic hadron scattering [2], excitation of projectile and target as well as double excitation of target and projectile. Further, it will be possible to investigate the interference between the different processes.

The new detection system consists of a large gap C-type magnet, „Tethys", a sideway and a forward spectrometer, both consisting of large size multiwire proportional chambers and scintillation hodoscopes. A general view of the system is shown in Fig. 1.

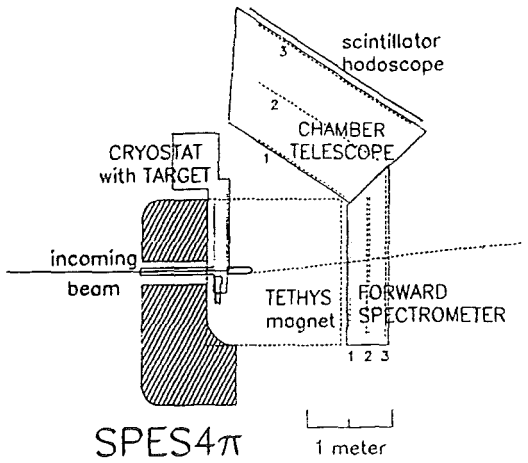

Figure 1: Design of the SPES 4π detection system

The sideway detection system with two wire chambers of sizes of 50 cm x 120 cm and 90 cm x 220 cm were constructed at Copenhagen and Orsay, respectively. They were assembled in spring of this year and first tests have been performed in summer. As in the new experiments the beam passes into the SPES 4 spectrometer it was necessary to test the optimal beam conditions. Further, difficulties in the chamber read-out system PECOS 4 were encountered which could be resolved by small changes of the mechanical stability and improvements in the connections. Final tests of the lateral system were performed in fall. In December a first production run could be scheduled in which coherent pion-production in the (^{3}He,t) charge exchange reaction on carbon was measured under the following conditions: triton angle 1 degree, average momenta p/z of 3.47 and 3.67 GeV/c in SPES 4 and fields of 4 and 6 kGauß in Tethys.

Parallel to the set-up of the lateral arm, the design of the forward spectrometer, in particular the beam hole was tested by measurement of the beam halo size. The responsibility for the construction of the full forward detection system is taken by the Gatchina group, prototypes of the multiwire chambers were constructed and tested at St. Petersburg which work satisfactorily. Tests of the scintillations wall were scheduled in fall. It is planned to have the entire detection system assembled by summer next year followed by tests and a first experimennt before the end of the year. It is forseen to do experiments with α-particle and polarized deuteron beams on liquid hydrogen targets. Further, it would be interesting to complement our inclusive α-scattering measurements [3] on targets of deuterium and carbon by exclusive experiments using the new set-up.

[1] Copenhagen (NBI)
[2] Dubna (JINR)
[3] Gatchina (PNPI)
[4] KFA Jülich (IKP)
[5] Saclay (LNS)
[6] Orsay (IPN)
[7] Warsaw (Soltan Institute)
[8] Williamsburg (W&M)

References:

[1] T. Hennino, R. Kunne et al., Nouvelles de Saturne 17 (1993) 35
[2] H.P. Morsch et al., Phys. Rev. Lett. 69 (1992) 1336
[3] V. Jaeckle et al., Ann. Rep. Jülich 1994

A Combined HETC FLUKA Intranuclear Cascade Event Generator

P. Cloth, D. Filges, G. Sterzenbach

for the ZEUS Collaboration

Monte Carlo simulations of hadron cascades in detectors of high energy physics require nuclear event generators which can perform hadron-nucleus collisions in all ranges of incident momentum and internuclear cascade particle momenta. Especially in hermetic calorimeter type detectors, like the HERA ZEUS detector, the showers comprise particles of all momenta.

Two event simulation models are available that gain good results, as compared to experimental data, in their regimes of momentum or energy:

(a) The Bertini INC model, mainly used in the HETC code; and

(b) The EVENTQ quark model, used in FLUKA87.

Table 1 gives an overview of the appropriate energy/momentum ranges of the two. Both codes are strongly energy und momentum conserving. An intranuclear cascade coupling of the two codes seemed to be desirable and was introduced under the name FLUBERT [1,2].

Table 1: Energy/Momentum Ranges

BERTINI INC:	
20 MeV to 3.5 GeV	for nucleons
20 MeV to 2.5 GeV	for pions
⇒ upper momentum limit	
4.34 GeV/c	for nucleons
2.64 GeV/c	for pions
EVENTQ:	
5.0 GeV/c to 1000 GeV/c	for all hadrons

The gap between Bertini and EVENTQ is closed by simply using the Bertini model in this energy region, in spite of the fact that the model is no longer valid.

The FLUBERT Parent Codes

The Bertini INC model is an intranuclear particle transport Monte Carlo model considering the nucleons to have Fermi gas momentum distributions in three zones of different nucleon density. Elastic and inelastic nucleon-nucleon and pion-nucleon collisions are performed using tabulated cross sections [3,4].

The EVENTQ model performs nuclear collisions in three phases. For the socalled "soft cascade" part of the hadron nucleus collision and for the excitation of the residual nucleus, fractions of the incident energy are set aside using inelasticity functions for the projectile-nucleus system. The third phase, the high energy phase, is called the "Dual Parton Multi-Chain Fragmentation Model", which considers two types of collisions with nucleons inside the nucleus: diffractive collisions and non-diffractive collisions [5].

In each of the interacting hadrons the valence quarks are separated into two coloured systems (quarks, diquarks), which share the particle momentum. These systems then are combined to form two colour-neutral chains, which finally hadronize into a multi-particle final state. In addition to this non-diffractive component of particle production, the single diffractive component of particle production, is included. In single diffractive events the chain generation takes place between an exchange meson and one of the interacting hadrons. There is no particle transport by EVENTQ inside the nucleus. The number of intranuclear collisions is also pre-estimated [6].

In the medium energy range the Bertini INC model simulates inelastic collisions between the projectile and a nucleon inside the target nucleus via formation and decay of D33 resonances. Therefore, only single and double pion production can occur.

FLUBERT Implementation

FLUBERT is part of the MC4 code, a particle shower simulation code integrated in the HERMES system [7].

Comparison of FLUBERT to FLUKA

After checking the performance of the FLUBERT code, it was decided to compare the results with the ones of the parent code, FLUKA. First, the resulting total cross sections were compared. Figures 1 and 2 show the results for protons of kinetic energies from 1 to 1000 GeV on iron and depleted uranium, respectively. One may notice, that the cross section values in the case of FLUKA are taken from a table, whereas in the FLUBERT code the total cross section is the resulting effect of all the nucleons of the nucleus. There is good agreement in the case of iron, apart from some deviation near the code coupling energy. The uranium cross section is also reasonable and differs by around 10%.

Next to the total cross section, the productions of nucleons and pions as secondary particles were compared in Figs. 3 and 4. The agreement is relatively good below 10 GeV, but the nucleons differ by approximately a factor of two for higher energies. For pions the agreement is good over the whole energy range.

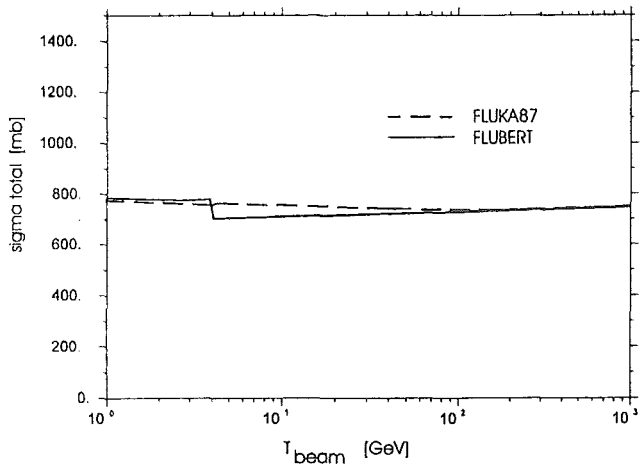

Fig. 1: Total cross section of protons on ^{56}Fe

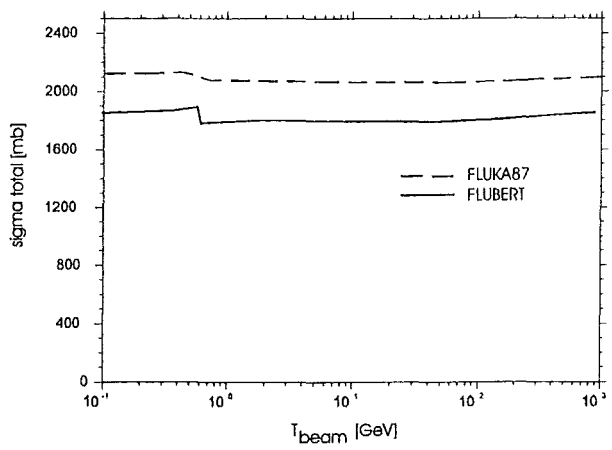

Fig. 2: Total cross section of protons on ^{238}U

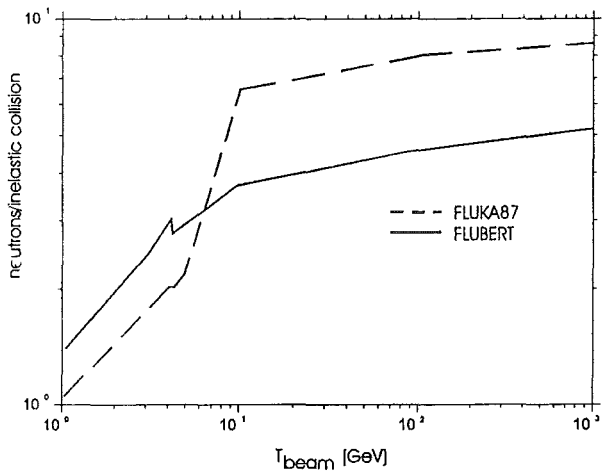

Fig. 3: Nucleon production of protons on ^{238}U

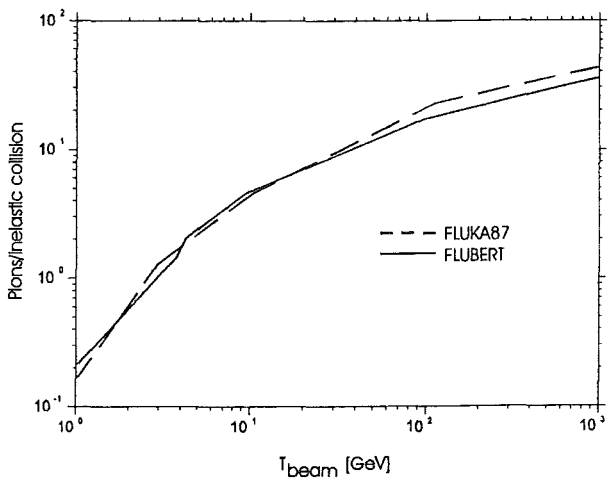

Fig. 4: Pion production of protons on ^{238}U

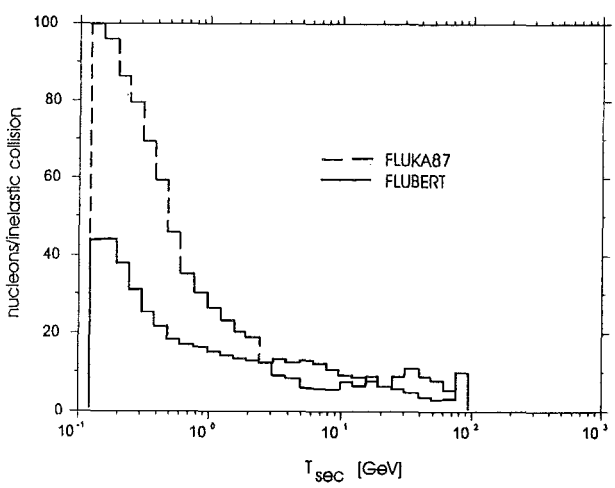

Fig. 5: Secondary nucleon spectrum of protons of 100 GeV on ^{238}U

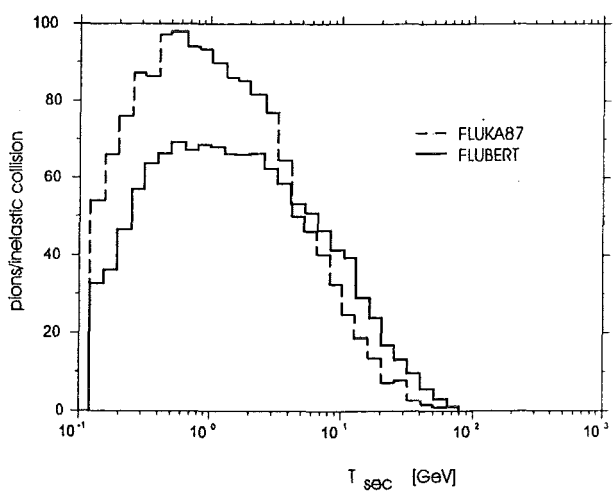

Fig. 6: Secondary pion spectrum of protons of 100 GeV on ^{238}U

Finally we give as example the nucleon production as a function of the secondary energy at an incident energy of protons of 100 GeV on depleted uranium (Fig. 5). There is a tendency of FLUBERT to produce less secondary nucleons at the low energy end of the spectrum as compared to FLUKA, and to generate a more pronounced peak near the incident energy. The differences occur, although the FLUBERT runs were made with the same ratio of diffractive and non-diffractive collisions, as in FLUKA. The stochastic generation of the intranuclear cascade in FLUBERT, in contrast to the collective treatment of collisions in EVENTQ, howover, leads to these deviating results. In the case of pions, the spectra differ less than for the nucleon production (Fig. 6).

The FLUBERT code, as a successful combination of the advantages of the codes Bertini INC and EVENTQ, provides intranuclear cascade simulation in the wide energy range from 20 MeV to 1000 GeV with strong energy and momentum conservation. The differences from FLUKA87 could be overcome by adjustment of some free parameters, e.g., the diffractive/non-diffractive collision ratio. It was, however, decided to make the adjustment to available experimental results.

References

[1] P. Cloth, D. Filges, H.J. Möhring, and G. Sterzenbach, Proceedings of the MC91 Workshop on Detector and Event Simulation in High Energy Physics, Amsterdam, The Netherlands (April 1991)

[2] P. Cloth, D. Filges, G. Sterzenbach, Proceedings of the MC93 International Conference on Monte Carlo, Simulation in High Energy and Nuclear Physics, Tallahassee, Florida, USA, 22-26 February 1993

[3] H.W. Bertini, Phys. Rev. C6 (1973) 631

[4] T.W. Armstrong and K. Chandler, Nucl. Sci. Eng. 49 (1972) 110

[5] D.A. Aarnio et al., Report CERN, Tis-RP/168

[6] K. Hänßgen and J. Ranft, Nucl. Sci. Eng. 98 (1984) 537

[7] P. Cloth, V. Drüke, D. Filges, K. Kilian, A. Röser, and G. Sterzenbach, "Monte Carlo Simulations of Medium Energy Detectors at COSY Jülich", Proceedings of the MC93 International Conference on Monte Carlo, Simulation in High Energy and Nuclear Physics, Tallahassee, Florida, USA, 22-26 February 1993

2. NUCLEAR SPECTROSCOPY

Excited Superdeformed Band in the Double Magic Nucleus ^{144}Gd

S. Utzelmann[1], R.M. Lieder[1], W. Gast[1], A. Georgiev[1], S. Lunardi[2], C.M. Petrache[2], D. Bazzacco[2], N.H. Medina[2], M.A. Rizzuto[2], C. Rossi-Alvarez[2], L-H. Zhu[3], G. de Anglis[3], G. Maron[3], D.R. Napoli[3], R. Wyss[3]

The discovery of multiple superdeformed bands within a single nucleus has allowed the detailed study of the microscopic nuclear structure in the second well. It exists a wealth of data on excited superdeformed bands in all mass regions where superdeformation at high spins has been discovered. The interpretation is given in terms of single particle excitations in the Nilsson orbitals available at such high deformation. Only very recently a superdeformed band has been identified in the nucleus ^{144}Gd [1] with proton and neutron numbers corresponding to pronounced shell gaps at superdeformed shapes ($Z = 64$, $N = 80$). The superdeformed band shows a backbending at $\hbar\omega = 0.45$ MeV which was interpreted as a crossing between bands based on configurations with zero and two protons int the $N = 6i_{13/2}$ orbital. The bandcrossing is well reproduced by cranked shell-model calculations based on a Wood-Saxon potential with pairing and deformation treated selfconsistently. The same calculations predict also as a second band crossing at $\hbar\omega \approx 0.8$ MeV related to the occupation of the $N = 7j_{15/2}$ orbital. Another point of interest to investigate in ^{144}Gd is the low intensity reported for the superdeformed band. Furthermore excited superdeformed bands should be searched for.

Excited states in ^{144}Gd were populated using the reaction ^{100}Mo + ^{48}Ti at beam energies of 215 and 209 MeV. The target consisted of three self-supporting foils of 350$\mu g/cm^2$ ^{100}Mo each. The beam was provided by the Tandem XTU accelerator of the Legnaro National Laboratories and γ-rays have been detected using the GASP array consisting of 40 anti-Compoton spectrometers and an inner ball of 80 BGO detectors. Events were collected when at least three Ge detectors and seven inner ball elements fired in coincidence. After unfolding the data a total of 5 Giga and 1 Giga coincidence events with fold higher than three were available for off-line analysis at the two beam energies of 215 and 209 MeV respectively. The data has been sorted into various γ-γ-γ cubes and matrices with proper conditions on the fold and sum energy of the BGO ball.

A search for new superdeformed bands has been carried out through channel by channel analysis in order to identify the probably irregular sequences of transitions and also with automatic search programs for detecting regular sequences of γ-ray transitions. Seven superdeformed bands have been observed in the present data set, three of them were already assigned to the nuclei ^{144}Gd [1], ^{143}Eu [3] and ^{142}Sm [2] respectively. The four new bands have been assigned to ^{144}Gd on the basis of their coincidence relationships with intense characteristic transitions of the normal deformed level scheme of this nucleus [6]. The superdeformed bands recently observed in ^{145}Gd [5] and ^{144}Eu [4] could not be seen.

Coincidence γ-ray spectra for the five superdeformed bands assigned to ^{144}Gd are shown in fig. 1. The spectra were obtained by setting double gates on all clean transitions in each band. At a beam energy of 215 MeV the superdeformed yrast band is populated with higher intensity than in the previous experiment at 221 MeV, being now ≈ 1.2 % of the total ^{144}Gd population. This result indicates that, by choosing the right beam energy, the intensity of the superdeformed yrast band in ^{144}Gd is comparable to that of the other superdeformed yrast bands in the A = 150 mass region. The superdeformed yrast band has been extended by one transition below the bandcrossing region and by five transitions at higher frequencies, s. fig. 1. The ordering of the three close-lying transitions around 890 keV could be definitely established with the high statistics of the present experiment.

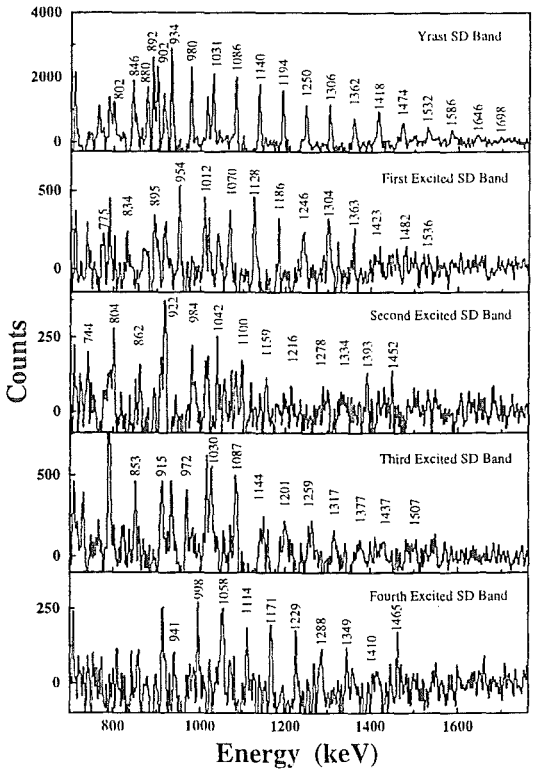

Figure 1: Doubly-gated coincidence spectra showing the five superdeformed bands assigned to the nucleus ^{144}Gd. The spectra are obtained from sums of all possible combinations of two-fold gates on clean transitions.

The configuration of the superdeformed yrast band of ^{144}Gd has been already discussed in [1], where calculations are reported which nicely reproduce the observed bandcrossing at $\hbar\omega = 0.45$ MeV. The alignment of two N = 6 protons causes the experimentally observed sharp crossing and drives the nucleus from a deformation of

β_2 = 0.46 to a larger deformation of β_2 = 0.51. The superdeformed yrast band has been extended up to a rotational frequency $\hbar\omega \approx 0.8$ MeV where the next bandcrossing, related to the occupation of the N = 7 neutrons should occur [1]. The $\mathcal{J}^{(2)}$ moment of inertia, plotted in fig. 2, does not show any rise at this frequency. The crossing frequency is very sensitive to changes in deformation at superdeformed shapes and to uncertainties in the position of single-particle levels. The expected N = 7 crossing could be shifted to higher frequencies by a slight change of the β_2 deformation.

The dynamic moments of inertia of the four excited superdeformed bands of ^{144}Gd are also plotted in fig. 2. In the A = 140 - 150 region the dynamic moments of inertia of superdeformed bands are extremely sensitive to the underlying microscopic structure of the bands, i.e. to the number of occupied intruder orbitals from higher oscillator shells. The alignment of a pair of N = 6 quasiprotons induces a rise of the dynamic moment of inertia $\mathcal{J}^{(2)}$ at low frequencies denoted as a crossing between the 6^0 and 6^2 configurations [1], however if the N = 6 proton orbital is occupied only by one quasiproton, then this orbital is blocked and no crossing occurs. This results in a constant $\mathcal{J}^{(2)}$. It is therefore clear from the figure that the excited superdeformed bands are not build on coinfigurations with two N = 6 protons as in the case of the yrast superdeformed band. The moments of inertia of the excited superdeformed bands stay in fact constant over the full observed frequency range, their values being slightly lower than that of the superdeformed yrast band above the crossing. Similar flat dynamic moments of inertia have been observed also in superdeformed bands of the isotones ^{142}Sm, ^{143}Eu and ^{145}Tb where they are fairly well understood through the occupation of the N = 6 intruder orbital by a single proton. From such comparison one can therefore reasonably assume that also the excited superdeformed bands discovered in ^{144}Gd involve one proton in the N = 6 orbital, the other unpaired proton being in one of the orbitals lying abore the Z = 64 gap.

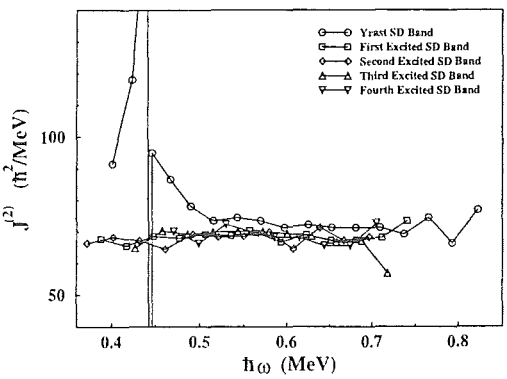

Figure 2: Dynamic moments of inertia for the five superdeformed bands identified in 144Gd.

Fig. 3 shows single-particle routhians diagrams for protons calculated at the deformations β_2 = 0.51 which is obtained by total routian surface calculations for the second minimum of ^{144}Gd. For $\hbar\omega$ > 0.5 MeV the orbitals available for a proton excitation above Z = 64 have the [404] $9/2^+$ and [411] $3/2^+$ configurations. Due to their high K values these two Nilsson orbitals exhibit nearly vanishing signature splitting for the observed frequency range. Their occupation would give rise to two couples of signature partner superdeformed bands. In fact the transition energies of bands 2 and 3, as well as those of bands 4 and 5, satisfy the characteristic relation for signature partner bands, i.e. the energies of the transitions of one band are arithmetic averages of the energies of the near-lying transitions of the other band. We suggest therefore $6^1 \otimes$ [404]$9/2^+$ and $6^1 \otimes$ [411] $3/2^+$ ($\alpha = \pm 1/2$) configurations for the first and second couple of excited superdeformed bands in ^{144}Gd respectively.

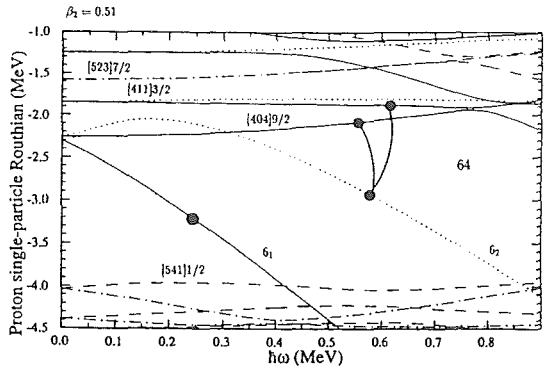

Figure 3: Single particle routhian diagram for protons, calculated at β_2 = 0.51, β_4 = 0.05 and $\gamma = 2^0$, which is a representative deformation for the superdeformed bands in ^{144}Gd. Some of the levels are labelled with their Nillson-model configurations.

While all the observed excited superdeformed bands in 144Gd can be explained through proton excitations across the Z = 64 gap, no superdeformed bands corresponding to neutron excitations across the N = 80 gap have been observed. This fact points to the high stability of the N = 80 shell closure at superdeformed shapes with respect to the Z = 64 one.

[1] IKP, KFA Jülich
[2] Dip. di Fisica and INFN, Sezione di Padova, Italy
[3] INFN, Laboratori Nazionali di Legnaro, Italy
[4] Royal Inst. of Technology, Physics Departement Frescati, Stockholm, Sweden)

References:

[1] S. Lunardi et al., Phys. Rev. Lett. **72** (1994) 1427
[2] G. Hackmann et al., Phys. Rev. Lett. **C47** (1993) R433
[3] A. Atac et al., Phys. Rev. Lett. **70** (1993) 1069
[4] S. Mullins et al., Phys. Rev. Lett. **C50** (1994) R2261
[5] T. Rzaca-Urban et al., Phys. Rev.Lett. **B356** (1995) 456
[6] T. Rzaca-Urban et al., Phys. Rev.Lett. **A579** (1994) 319

Lifetime Measurement in ^{144}Gd

H.J. Jensen, W. Gast, A. Georgiev, H.M. Jäger, R.M. Lieder, S. Utzelmann, M. Gierlik[1], T. Morek[1], K. Przestrzelska[1], T. Rzaca-Urban[1], A. Dewald[2], R. Kühn[2], C. Meier[2], C. Ender[3], T. Härtlein[3]

Evidence for the coexistence of superdeformed, triaxially deformed collective $\Delta I = 2$, and weakly deformed oblate $\Delta I = 1$ structures has been recently reported for ^{144}Gd [1,2], which at low spins has an approximately spherical shape. Such a complicated coexistence of very different excitation modes was predicted already in 1985 by J. Dudek et al. [3] to be a general feature for nuclei in this mass region. Ever since the first superdeformed band was observed in this mass region, most effort was concentrated on the search for, and the interpretation of these "exotic,, shapes. The observation and the interpretation of the coexistence and the transition between different shapes at lower spins, plays nevertheless an important role for the applied mean field description. The present work was therefore concentrated on the latter aspect.

In the previous work on ^{144}Gd by T. Rzaca-Urban et al. [2], the multipolarities of the strongest γ-transitions placed in the level scheme were obtained in a directional correlation (DCO) analysis of the coincidence data. DCO ratios of the transitions forming the $\Delta I = 1$ sequence were found to have values consistent with a quadrupole/dipole mixing ratio δ changing from ≈ -1.0 to ≈ -0.2 as a function of spin. This was interpreted as an indication of a negative quadrupole moment (or an oblate nuclear shape) for the dipole band in ^{144}Gd, similarly to the dipole bands in the $^{198\text{-}201}$Pb nuclei (see, e.g., [4,5]).

In the case of an oblate shape of ^{144}Gd, the $\Omega = 1/2$ orbital of the neutron $h_{11/2}$ subshell lies in the vicinity of the neutron Fermi surface. For the proton $h_{11/2}$ subshell, depending on deformation, the Fermi surface lies in the lower part of the subshell, close to the $\Omega = 11/2$ state. Hence, the $h_{11/2}$ neutron holes easily align their angular momenta along the rotation axis, whereas the $h_{11/2}$ protons remain deformation aligned. The situation is thus similar to Pb, where the observed oblate rotational dipole bands involve rotation-aligned $i_{13/2}$ quasineutrons, coupled, e.g., to the deformation-aligned $h_{9/2}$ and $i_{13/2}$ protons [4,5]. For the dipole band in ^{144}Gd it is, from a simple Fermi-aligned coupling scheme, expected that the lowest band member of the $\nu h_{11/2}^{-2} \otimes (\pi h_{11/2}^{2})_{K=10+}$ configuration has a spin of ≈ $14\hbar$. Indeed, starting at $I = 14\hbar$, a very strong sequence of dipole transitions can be seen. The observed sequence is not regular, i.e., the transition energies do not follow the I(I+1) law. This behaviour reflects the fact that the oblate minimum is rather shallow, as found in TRS calculations.

In the Pb region it was found that oblate dipole bands have large B(M1) and small B(E2) values, as measured for ^{198}Pb [6]. The proof that the dipole bands in ^{144}Gd have similar features requires lifetime measurements. Therefore lifetime measurements of excited states in ^{144}Gd were carried out using the Köln RDM-plunger together with the 2x3 CLUSTER detector setup in Heidelberg. This setup of two rings of three CLUSTER detectors symmetrically arranged around the beam- entrance and exit, provides a good geometry for lifetime measurements, with 6, 9, 6, 6, 9 and 6 detectors at detector-angles relative to the beam-axis of θ = 151°, ~ 136°, 122°, 58°, ~ 44° and 29° respectively. The nucleus was populated in the ^{100}Mo(^{48}Ti,4n)^{144}Gd reaction at a beam energy of 205 MeV, giving a recoil velocity of v/c ≈ 2.6 %. The target consisted of a self-supporting foil of ^{100}Mo enriched to 97.4 % with a thickness of 1.02 mg/cm^2. A gold foil with a thickness of 11.5 mg/cm^2 was used, in the plunger, as a stopper for the recoiling nuclei. Three- and higher fold γ-ray coincidences were measured at 12 target-stopper distances between 0μm and 400 μm. More than 10^8 events were collected at each distance.

Examples of γ-ray spectra recorded for a detector at θ = 151° and 29° relative to the beam axis are shown in, respectively, the left and right column of figure 1. Spectra are shown for target-stopper distances of 0, 45, 100, 250 and 400 μm. A dependence of the intensity of the stopped

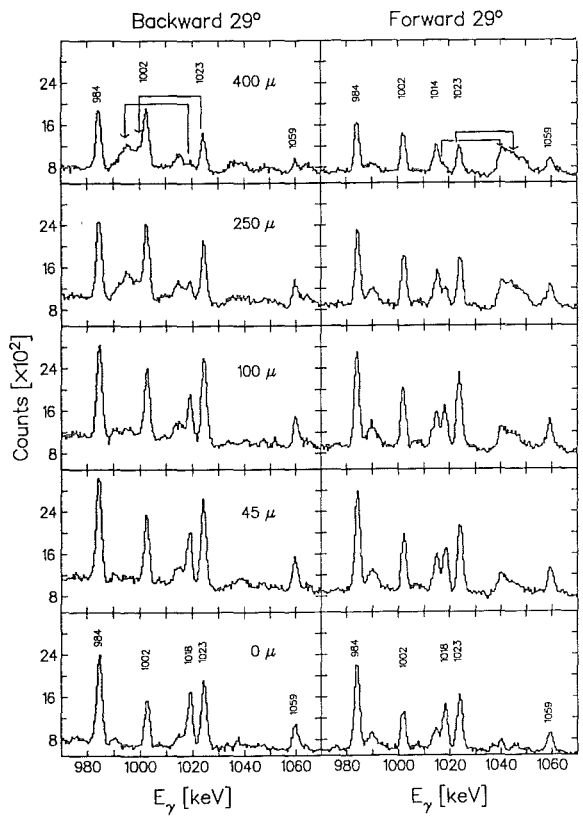

Figure 1: Examples of γ-ray spectra recorded for one detector at θ = 151° and 29° relative to the beam axis. Spectra are given for target-stopper distances of 0, 45, 100, 25 and 400 μm.

and shifted components on the target-stopper distance are clearly seen for the 1017.8 keV $12^+ \rightarrow 10^+$ transition in ^{144}Gd, and for the 1023 keV transition, which has been placed in the level schemes for both ^{144}Eu and ^{143}Gd. The 1002 keV transition, belonging to the level scheme of ^{144}Gd is an example of a transition depopulating a long-lived state, which therefore has no shifted component!

The analysis is still in progress, but shifted and stopped components for transitions in both the dipole and quadrupole bands in ^{144}Gd have been observed. From the preliminary analysis it seems feasible to obtain lifetimes also for levels in several of the neighbouring nuclei.

[1] Institute of Experimental Physics, University of Warsaw, Poland
[2] Institut für Kernphysik, Universität zu Köln
[3] Max-Planck-Institut für Kernphysik, Heidelberg,

References:

[1] S. Lunardi et al., Phys. Rev. Lett. 72 (1994) 1427.
[2] T. Rzaca-Urban et al., Nucl. Phys. 579 (1994) 319.
[3] J. Dudek and W. Nazarewicz, Phys. Rev. C31 (1985) 298.
[4] R.M. Clark et al., Nucl. Phys. A562 (1993) 121.
[5] G. Baldsiefen et al., Nucl. Phys. A574 (1994) 521.
[6] T.F. Wang et al., Phys. Rev. Lett. (1992) 1737.

Double Band Crossing in the Superdeformed Nucleus ^{145}Gd

T. Rzaca-Urban[1], R.M. Lieder, S. Utzelmann, W. Gast, A. Georgiev[2], H.M. Jäger, D. Bazzacco[3], S. Lunardi[3], R. Menegazzo[3], C. Rossi-Alvarez[3], G. de Angelis[4], D.R. Napoli[4], G. Vedovato[4], and R. Wyss[5]

The experimental investigations of the Z=64 isotopes $^{144,146\text{-}150}$Gd [1,2] proved the existence of several superdeformed bands in each of these nuclei. Many of the superdeformed bands observed in $^{146\text{-}148}$Gd and the yrast superdeformed band in ^{149}Gd are considered to have a $\nu 7^1 \pi 6^2$ configuration (one neutron is in the $j_{15/2}$ orbital and two protons in the $i_{13/2}$ orbital). In ^{146,147,148}Gd [2,3] band crossings in superdeformed bands are known which result from the intersection of the $i_{13/2}$ ν[642]5/2 and $i_{11/2}$ ν[651]1/2 neutron orbitals. The superdeformed band in ^{144}Gd [1] shows a sharp band crossing at a rotational frequency of $\hbar\omega$ = 0.45 MeV, which is interpreted as a proton crossing between the $\pi 6^0$ and $\pi 6^2$ configurations [1]. The observation of band crossings at superdeformed shapes is crucial for the understanding of residual interactions, e.g., pairing correlations, for configuration assignments as well as for determining the location of the high-j Nilsson orbitals.In order to fully understand the band crossings in the superdeformed bands of the Gd nuclei and why a proton crossing occurs only in the lightest Gd isotope, experimental information on the missing nucleus ^{145}Gd is needed.

High-spin states in ^{145}Gd were populated in the ^{114}Cd(^{36}S,5n) reaction at a beam energy of 182 MeV. The beam was delivered by the Tandem XTU accelerator of the Legnaro National Laboratory and the γ-rays were measured with the GASP array which consists of 40 large escape-suppressed Ge detectors and an inner ball of 80 bismuth germanate (BGO) scintillators acting as a γ-ray multiplicity and sum-energy filter. The target consisted of a self-supporting foil of ^{114}Cd enriched to 99.2 % with a thickness of 1.07 mg/cm^2. Events were collected when $\geq$3 escape-suppressed Ge detectors and > 8 BGO scintillators detected a γ-ray in coincidence. In total 2.3 Giga events have been collected. The nucleus ^{145}Gd was produced the strongest in the reaction with ≈ 35 % of the total cross section for compound nucleus formation through the 5n channel. It was enhanced in the sorting procedure by requiring that a large number of BGO detectors of the inner ball fired.

In order to search for superdeformed bands a γ-γ matrix has been produced requiring a BGO fold $\geq$ 24. Discrete superdeformed transitions have been searched for in the matrix through gating channel by channel. In this way three superdeformed bands have been identified. In order to increase the selectivity a γ-γ-γ cube has been produced requiring a BGO fold $\geq$ 15. After unpacking, $1.3 \cdot 10^9$ three-fold events were available for analysis in a fully symmetrized cube. Specra of the three superdeformed bands, as obtained by setting double gates on the strongest transitions of the superdeformed bands, are shown in fig. 1). All the bands can firmly be assigned to ^{145}Gd [4] since the strong transitions of 794.9, 924.6 and 1552.6 keV (labelled by stars in fig. 1) between normal deformed states in ^{145}Gd [5] can clearly be seen, whereas γ-transitions belonging to the neighbouring nuclei disappear. The strongest band is considered to be the yrast superdeformed band, consisting of 17 members. The weaker SD bands are assigned as first excited superdeformed band consisting of 16 transitions and second excited superdeformed band consisting of 10 transitions. The intensities of the superdeformed bands in ^{145}Gd relative to that of the 721.5 keV transition, deexciting the 11/2$^-$ isomer [5] are ≈ 1.1 % for the yrast superdeformed band, ≈ 0.6 % for the first excited superdeformed band and ≈ 0.2 % for the second excited superdeformed band.

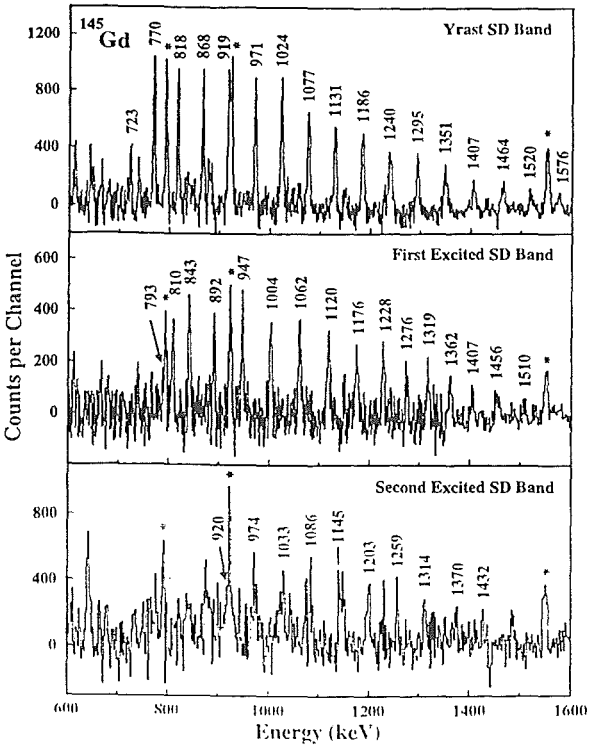

Figure 1: The superdeformed bands observed in ^{145}Gd. Strong transitions between low-spin states in ^{145}Gd are denoted by stars.

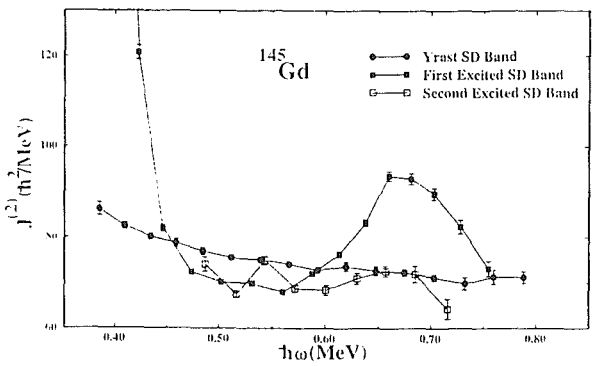

Figure 2: The dynamic moments of inertia as function of the rotational frequency for the superdeformed bands in ^{145}Gd.

The dynamic moments of inertia of the superdeformed bands in ^{145}Gd are plotted as function of the rotational frequency in fig. 2. It can be seen that the yrast superdeformed band starts with a dynamic moment of inertia of 86 $\hbar^2$/MeV which decreases smoothly to a value of $\approx$ 71 $\hbar^2$/MeV similarly to the values observed in the neighbouring nuclei $^{144,146\text{-}148}$Gd [1,2] outside the respective band crossing regions. The first excited superdeformed band, however, shows two subsequent band crossings at rotational frequencies of $\approx$ 0.4 and 0.68 MeV, respectively. This is the first time that such a double band crossing has been observed in a superdeformed band. It should be pointed out that the pronounced low-frequency crossing is similar to that observed at a rotational frequency of 0.45 MeV in ^{144}Gd whereas the second band crossing has similar features as the one found in ^{146}Gd at 0.65 MeV. The second excited superdeformed band has only been established in the frequency range of 0.46 to 0.72 MeV and it is considered to be the signature partner of the first excited superdeformed band since outside the band-crossing region the transition energies of the second excited superdeformed band lie approximately in the middle of those of the first excited superdeformed band. In the observed frequency range the second excited superdeformed band does not show a band crossing.

The interpretation of the superdeformed bands in ^{145}Gd is based on calculations in the framework of the cranked Woods-Saxon-Strutinsky approach [6]. As results of the calculations, plots of the excitation energy vs. spin and the dynamic moment of inertia vs. rotational frequency are shown in fig.3 for relevant configurations in ^{145}Gd. The dynamic moment of inertia $J^{(2)}$ is shown in fig. 3(b) for the individual proton and neutron components as well as for configurations consisting of these components. Outside the crossing region, unambiguous configuration assignments can be made and the following picture of the structure at superdeformed shapes emerges. At low frequencies the lowest $(\pi,\alpha) = (+,\pm 1/2)$ and $(-,-1/2)$ states, respectively, are assigned to the $\nu[642]5/2\nu 7^{o}\pi 6^{o}$ and $\nu[514]9/2\nu 7^{o}\pi 6^{o}$ configurations (cf. fig. 3(a)). At higher frequencies the $\nu[514]9/2\nu 7^{o}$ configuration is crossed by the $\nu 7^{1}$ orbital. Below spin I=30 the $i_{13/2}$ protons are not occupied and the calculated deformation is only $\beta_2 \approx 0.48$. The alignment of the $i_{13/2}$ proton pair above I=30 drives the nucleus to a larger deformation, and produces a pronounced rise in the dynamic moment of inertia $J^{(2)}$ (cf. fig. 3(b)). The proton crossing is strongly deformation dependent [6,7]. This is shown schematically in fig. 3(b), where calculations of the dynamic moment of inertia $J^{(2)}$ for the $\pi 6^2$ band crossing at fixed deformations of $\beta_2 = 0.508$ and 0.523 are plotted. For the former deformation the $\pi 6^2$ band crossing is sharper than for the latter one. At I $\approx$ 40 the negative-parity $\nu 7^{1}\pi 6^{2}$ configuration becomes yrast and crosses the positive-parity $\nu[642]5/2\nu 7^{o}\pi 6^{2}$ configuration (cf. fig. 3(a)).

The experimental yrast superdeformed band was observed only above a rotational frequency of 0.38 MeV showing a smooth decrease of the dynamic moment of inertia with increasing frequency (cf. fig. 2). This behavior can qualitatively be understood in terms of the occupation of the N=7 neutron orbital as well as the proton alignment. In the calculations, the yrast superdeformed band has a

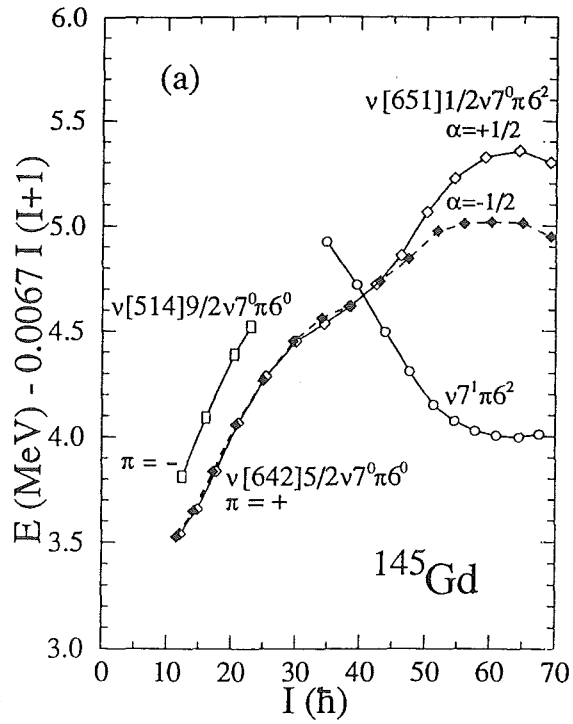

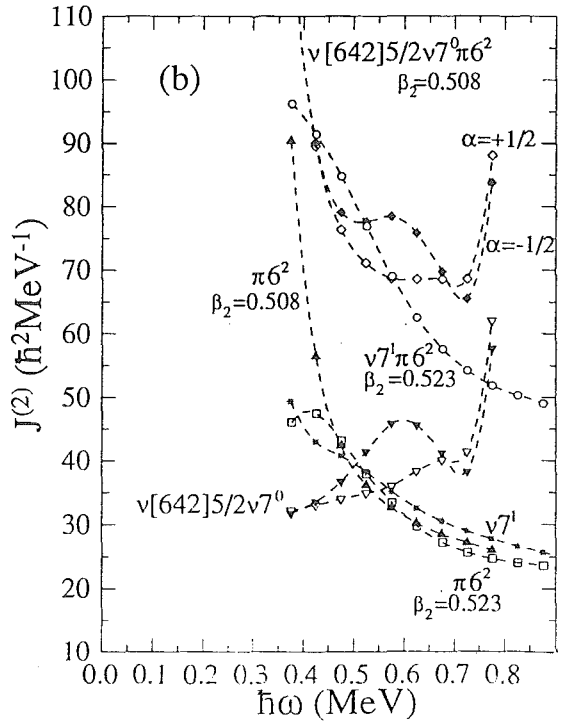

Figure 3: Calculated excitation energies, after subtraction of the rigid-rotor energies, as function of spin (a) and dynamic moments of inertia as function of the rotational frequency (b) for superdeformed bands in ^{145}Gd. The excitation energies are extracted from the minima of the TRS calculations, whereas the dynamic moments of inertia are calculated at fixed deformations. The dynamic moments of inertia of individual proton and neutron components as well as those of the configurations assigned to the yrast and excited superdeformed bands are shown.

deformation of $\beta_2 = 0.523$, due to the deformation-driving effect of the $j_{15/2}$ neutron orbital, and the crossing between the $\nu 7^1 \pi 6^0$ and $\nu 7^1 \pi 6^2$ configurations occurs at $\hbar\omega \approx 0.40$ MeV. The configuration of the yrast superdeformed band in ^{145}Gd involves the same high-j orbitals as the yrast superdeformed band in ^{146}Gd but does not show the crossing at 0.65 MeV which was interpreted as the intersection of the [642]5/2 and [651]1/2 quasineutron orbitals [3]. In the yrast superdeformed band of ^{145}Gd the [642]5/2 orbital is not occupied and hence this crossing is absent.

The first excited superdeformed band in ^{145}Gd shows a double band crossing at rotational frequencies of ≈ 0.4 and 0.68 MeV, respectively. It can be rather firmly established that the first crossing is due to the alignment of a pair of N=6 protons, observed also in the neighbouring nucleus ^{144}Gd [1]. The calculated deformation after this crossing is $\beta_2 \approx 0.508$ and there is little difference between the signature partners. The second observed intersection is due to the crossing of the ν[642]5/2 and ν[651]1/2 orbitals. The calculated moments of inertia reproduce fairly well the observed trends (cf. figs. 2 and 3(b)). The crossing of the two N=6 neutron orbitals result in a clear hump in the calculated dynamic moment of inertia $J^{(2)}$. It strongly supports the assignment of $\alpha = -1/2$ to the first excited superdeformed band. The second excited superdeformed band has been identified as the signature partner ($\alpha = +1/2$) of the first excited superdeformed band. The crossing at the rotational frequency of 0.68 MeV between the two N=6 neutron orbitals is neither observed in the data nor predicted by the calculation (cf. figs. 2 and 3(b)), supporting the suggested assignment. This crossing occurs much later in the $\alpha = +1/2$ branch. The predicted $i_{13/2}$ proton crossing at ≈ 0.4 MeV is not observed, since the band was only established above 0.46 MeV.

[1] Institute of Experimental Physics, University of Warsaw, Poland

[2] INRNE, Bulgarian Academy of Sciences, Sofia, Bulgaria

[3] Dipartimento di Fisica and Istituto Nazionale di Fisica Nucleare, Sezione di Padova, I-35131 Padova, Italy

[4] Istituto Nazionale di Fisica Nucleare, Laboratori Nazionali di Legnaro, I-35020 Legnaro, Italy

[5] Royal Institute of Technology, Department of Physics Frescati, Frescati. 24, S-10405 Stockholm, Sweden

References:

[1] S. Lunardi et al., Phys. Rev. Lett. 72 (1994) 1427

[2] X.-L. Han and C.-L. Wu, Atomic Data and Nucl. Data Tables 52 (1992) 43

[3] G. Hebbinghaus et al., Phys. Lett. B240 (1990) 311

[4] T. Rzaca-Urban et al., Phys. Lett. B356 (1995) 456

[5] D. Bazzacco et al., Z. Phys. A310 (1983) 65

[6] W. Nazarewicz, R. Wyss and A. Johnson, Nucl. Phys. A503 (1989) 285

[7] R.M. Lieder et al., Polonica Physica Acta B26 (1995) 249

Complete Valence Particle Yrast Lines in N=84 Nuclei above Gadolinium

C.T. Zhang, P. Kleinheinz, M. Piiparinen[a], R. Broda*, R. Collatz, P.J. Daly[b], K.H. Maier[c], R. Menegazzo, G. Sletten[a], J. Styczen* and J. Blomqvist[d]

In Recent in-beam γ-ray studies we have investigated high-spin states in the N=84 nuclei from $^{151}_{67}$Ho to $^{154}_{70}$Yb and have identified all yrast states formed within the two configurations $\pi h^n_{11/2}\nu f^2_{7/2}$ and $\pi h^n_{11/2}\nu f_{7/2}h_{9/2}$ (n=Z-64) from the ground states up to their maximum aligned spins in ^{151}Ho, ^{152}Er, and ^{153}Tm, and up to 24 in ^{154}Yb. The observed level energies are shown to be in excellent agreement with shell model predictions in which single particle energies and empirical two-body matrix elements were taken from experiment, thus exploiting recent results for the key two-body multiplets located in the three A=148 two-valenceparticle nuclei.

The yrast lines in N=82 nuclei above Gd are dominated by the gradual alignment of valence protons in the $h_{11/2}$ shell, and in the yrast states at N=83 the valence neutron in $f_{7/2}$ couples to these proton excitations. At N=84, the two valence neutrons in $f_{7/2}$ provide up to 6 units of angular momentum below 2 MeV excitation, and the 6→0 triple E2 transition sequence forms the lowest portion of the yrast cascade in the even-Z nuclei, while in the odd-Z species it connects the $(\pi h_{11/2}\nu f^2_{7/2})23/2^-$ state to the $11/2^-$ ground state. The next high-j neutron orbital is $h_{9/2}$; together with the $f_{7/2}$ neutron it forms a low-lying 8^+ state which is also strongly populated in the yrast cascade. Above, the yrast line continues with $\pi h^2_{11/2}$ coupled to 10, followed again by the 2^+ to 8^+ couplings of the two valence neutrons, giving $I^\pi=12^+$ to 18^+ in the even-Z and $31/2^-$ to $43/2^-$ in the odd-Z species.

The N=84 nuclei were produced in heavy ion induced fusion-evaporation reactions, and their high spin level schemes were established in γ-ray measurements with the Nordball detector array which consists of 20 Compton-suppressed Ge-detectors. The ^{151}Ho yrast states were observed up to 10 MeV excitation with spins assigned up to 49/2 at 6.2 MeV [1]. Of interest here is the odd-parity level sequence from the $11/2^-$ ground state up to $43/2^-$ at 4.812 MeV, the maximum aligned $\pi h^3_{11/2}\nu f_{7/2}h_{9/2}$ state. The ^{152}Er high spin states were recently investigated [2] in reactions with higher angular momentum input than in our experiment. We agree with the previous assignments up to 18^+ at 5.081 MeV, but assign E1 multipolarity to an intense 330 keV γ-ray deexciting the 7.450 MeV I=24 level, which gives even parity for that state and for the next three levels shown below it in Fig. 1. In ^{153}Tm, levels up to 9.2 MeV and spin 57/2 were established, with the odd-parity sequence up to $51/2^-$ at 6.900 MeV firmly characterised [3]. The highest state observed in ^{154}Yb is an I=(24) level at 7.610 MeV; firm spin-parities are established up to 18^+, confirming earlier [4] tentative assignments.

The pertinent yrast states for the four nuclei are compiled in Fig. 1 where they are compared with excitation energies calculated from the shell model for the $\pi h^n_{11/2}\nu f^2_{7/2}$ and $\pi h^n_{11/2}\nu f_{7/2}h_{9/2}$ configurations. The lines connecting the experimental levels represent the yrast line formed by the joint two configurations. We note that two levels with the same I^π are detected only in cases where theory predicts two close neighbours, and E2 decay occurs when M1 deexcitation is energetically excluded or predicted to have low energy.

To calculate the couplings of the valence particles distributed in the three orbitals of the configurations one needs in total 36 diagonal two-body interactions which are compiled in Ref. [4] and one single particle energy separation, i.e. $\nu h_{9/2}$ to $\nu f_{7/2}$, taken as 1397 keV, as observed in the one-neutron nucleus ^{147}Gd.

The level energies for the N=84 nuclei were calculated separately for each configuration, by fractional parentage decomposition into the two-body substructures, and matrix diagonalization.

The overall agreement of theory and experiment is excellent, with average deviations of less than 0.12 MeV, as indicated for each nucleus in Fig. 1. In light of these results, and keeping in mind that no other levels of the same parity are expected in these ranges of the yrast lines, the configuration assignments based on theory can be considered firm. It is worth mentioning that Gamow-Teller decay of the respective N=83 9^+ and $27/2^-$ parents independently establishes $\pi h^n_{11/2}\nu f_{7/2}h_{9/2}$ character for the 8^+ yrast states in ^{152}Er and ^{154}Yb, and for the $25/2^-$ state in ^{151}Ho.

We have normalized the calculated and experimental level energies in Fig. 1 at the ground states. The shell model also predicts the ground state binding energies [6] provided that the masses of the ^{146}Gd core and its five one- and two-valenceparticle neighbours are known. In calculating the binding energies for the N=84 isotones with up to eight valence particles by decomposition into two-body structures the individual input masses are multiplied with large integer factors, up to as much as 36, which severely limits the accuracy of the results. Nevertheless, the six present input masses specified in table 1 give very satisfactory agreement with experiment for the resulting N=84 binding energies as is shown in the last column.

An important aspect of the present investigation is the overall very good agreement of theory and experiment for

Table 1. The six input masses, and the six N=84 masses compared with values calculated from the shell model, given in keV.

Input masses		N=84 isotones		
Nucleus	Mass excess	Nucleus	Mass excess	S.M.−Exp.
$^{147}Gd^a_{82}$	−76097(5)	$^{149}Tb^{a,b}$	−71463(5)	+20(62)
$^{147}Gd^a_{83}$	−75367(4)	$^{150}Dy^a$	−69321(5)	+219(130)
$^{148}Gd^a_{84}$	−76279(3)	$^{151}Ho^{a,b}$	−63635(12)	+171(230)
$^{147}Tb^{a,b}_{82}$	−70704(12)	$^{152}Er^c$	−60490(30)	+133(360)
$^{148}Tb^{b,c}_{83}$	−70437(30)	$^{153}Tm^{a,b}$	−54000(22)	+67(530)
$^{148}Dy^c_{82}$	−67849(30)	$^{154}Yb^d$	−50070(100)	+20(740)

a G. Audi et al., Nucl. Phys. A565, 1 (1993)
b Masses refer to $11/2^-$ or 9^+ ß-decay isomer
c H. Keller et al., Z. Phys. A352, 1 (1995), and $Q_{EC}(^{148}Dy)$ and $Q_\alpha(^{152}Er)$ from Audi[a)]
d Recommended ^{154}Yb mass from Audi[a)], Table C, p. 17

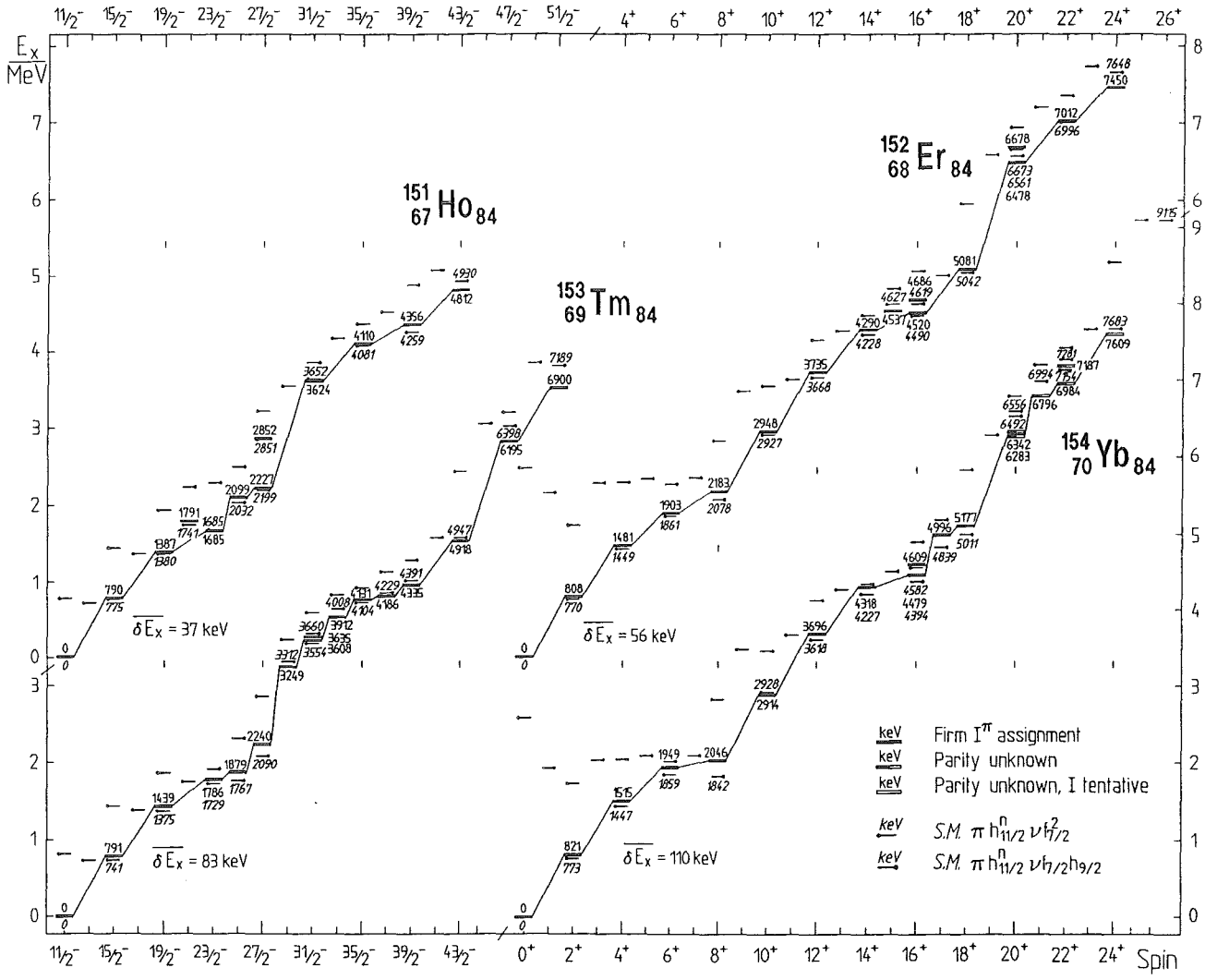

Fig. 1. The observed yrast states of odd-parity in ^{151}Ho and ^{153}Tm, and of even-parity in ^{152}Er and ^{154}Yb. The data are compared with the results from shell model calculations of the $\pi h^n_{11/2} \nu f^2_{7/2}$ and $\pi h^n_{11/2} \nu f_{7/2} h_{9/2}$ configurations. The configuration is indicated for each calculated state, and for each spin the calculated position for the lowest unobserved level is also shown. The mean absolute deviation δE of theory from experiment in keV is shown for each nucleus.

nuclei with up to eight valence particles covering a wide range of excitation energy and spins, including the nuclear ground states. To our knowledge theoretical results of similar accuracy have so far not been reported for shell model yrast states in heavy nuclei. This success can be attributed to the exclusive use in our analysis of experimental two-body matrixelements, since current nuclear theory can predict these quantities only within an accuracy near a factor two. Although the experimental input data may not represent the pure configurations, the amixtures often reamin essentially unaffected in high-spin states, and the present treatment in general compensates these energy shifts to second order. We note, however, that complete identification of the required two-body excitations often needs dedicated and unconventional experiments, and at present similar analyses in other regions may be hampered by a lack of input data.

It is obvious that our calculated results are parameter-free since the theory exploits exclusively the symmetries of angular momentum coupled multiparticle configurations while all dynamic input quantities are extracted from experiment. The excellent agreement obtained demonstrates the high predictive power of such shell model analysis for heavy nuclei.

[a] NBI Roeskilde, Denmark
[b] Purdue Univ., W.-Lafayette, USA
[c] HMI Berlin
[d] Royal Inst. of Technology, Stockholm
* permanent. adress: INP Cracow, Poland

References:

1. C.T. Zhang et al., Z. Phys. A348, 65 (1994)
2. A. Kuhnert et al., Phys. Rev. C46, 484 (1992)
3. C.T. Zhang et al., Z. Phys. A348, 249 (1994)
4. C.T. Zhang et al., Z. Phys. A345, 327 (1993)
5. M. Lach et al., Z. Phys. A341, 25 (1991); a recent study of ^{148}Tb 9^+ GT-decay identified the ^{148}Gd $\nu f_{7/2} \nu h_{9/2}$ 7^+ state at 2.869 MeV (cf. R. Collatz et al., IKP KFA Jülich, Ann. Rep. 1990, p. 25)
6. J. Blomqvist et al., Z. Phys. A312, 27 (1983)

Investigation of the Decay of high-K Isomers in ^{180}Os with the CLUSTER Cube

R.M. Lieder, W. Gast, A. Georgiev, H.M. Jäger, H.J. Jensen, S. Utzelmann, T. Morek[1], R. Kaczarowski[2], E. Ruchowska[2], C. Ender[3], T. Härtlein[3], D. Schwalm[3], G. Sletten[4]

The existence of two high-K isomers in ^{180}Os has previously been established [1]. They have spins of $I \geq 20$ and ≥ 16 and half lives of $T_{1/2} = 12\pm4$ and 41 ± 10 ns, respectively. However, their decay is poorly known since they are populated only to ≈ 1 % of the ground state and the deexcitation proceeds over many parallel branches. A sensitive way to study the deexcitation of isomers is the recoil-shadow technique, in which the γ-ray detectors are shielded from the target so that the prompt γ-radiation is suppressed to a large extent. The recoiling nuclei are collected on a catcher placed in the center of the detector system. The γ-radiation from the decay of the isomeric states, emitted from stopped recoils, can then be studied with a large peak-to-background ratio. In such experiments the flight time must be shorter than the half life of the isomer. The prompt background leaking through the shield can be further reduced if the beam is pulsed by accepting only γ-radiation emitted between beam bursts. In a first attempt to study the deexcitation of the high-K isomers in ^{180}Os utilizing six detectors of the OSIRIS array only $6\cdot10^5$ γ-γ coincidence events have been collected [1]. The statistics was insufficient to establish the levels populated in the decay of the isomers. Therefore, the experiment has been repeated with the CLUSTER cube setup at the MPI Heidelberg since due to its large detection efficiency for photo events of ≈ 16 % in the recoil-shadow geometry an improvement of the statistics by a factor of 2000 is expected. Due to the large efficiency γ-γ-γ coincidence events can be measured with a probability which is only a factor of ≈ 2 smaller than that for γ-γ coincidence events. This allows to suppress γ-radiation related to low-multiplicity events, like, e.g., Coulomb excitation.

The experimental arrangement for recoil-shadow investigations of isomers with the CLUSTER cube is shown in fig. 1. In this geometry six CLUSTER cryostats containing seven large Ge detectors each are arranged in a close geometry to achieve a maximum solid angle. The distance of the Ge detectors from the catcher is ≈ 10 cm. To shield the detectors from the target and from the recoiling nuclei produced in the reaction two cylinder-symmetric W shields are arranged around the beam tube. Essentially only γ-radiation emitted from the catcher can be detected. In this way the Doppler broadening of the γ-lines for deexcitation of the isomers in flight can be avoided which would be large due to the small distances of the Ge detectors from the catcher. In this way about 25 % of the Ge detectors are shielded from the target, however, they contribute to the detection efficiency due to add-back of Compton-scattered γ-radiation. If the target was arranged outside the CLUSTER cube then the distance would become prohibitively large for the study of short-lived isomers.

The high-K isomers in the nucleus ^{180}Os have been excited through the ^{150}Nd(^{34}S,4n) reaction using a beam energy of 153.5 MeV. The beam was provided by the tandem accelerator Emperor of the MPI Heidelberg. The target was a self-supporting metal foil with a thickness of 1.23 mg/cm^2. The catcher was a Au foil with a thickness of 7.0 mg/cm^2. A hole with a diameter of 5 mm in the center of the Au foil allowed to reduce the beam hitting the catcher to reduce Coulomb excitation. The beam energy is well below the Coulomb barrier for ^{34}S on ^{197}Au of 170 MeV.

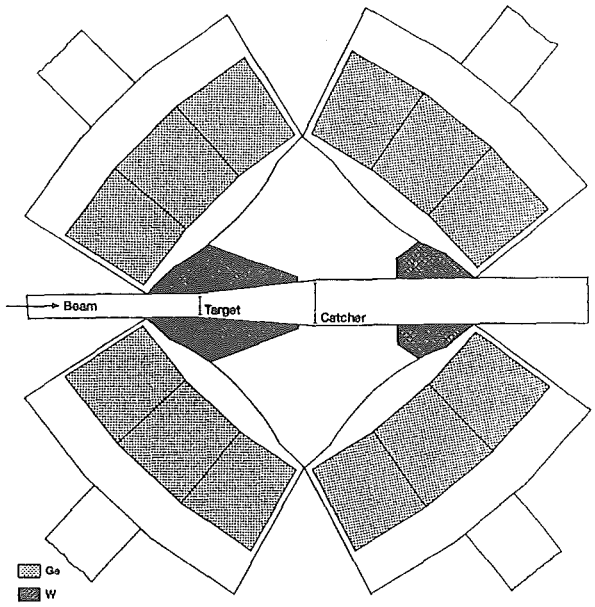

Figure 1: Cross section of the recoil-shadow arrangement for the CLUSTER cube.

Calculations of the angular distribution of the projectiles and the recoils due to scattering in the target showed that only 6 % of the recoils escape through the hole in the catcher but that it is large enough to let 50 % of the projectiles pass. The used target-catcher distance of 10 cm corresponds to a flight time of 18.3 ns since the velocity of the recoils is v/c = 1.82 %. In the experiment we collected $\approx 3.5\cdot10^8$ γ-γ-γ coincidence events.

A preliminary analysis showed that the yrast band can be observed up to the $24^+ \rightarrow 22^+$ transition. This indicates that one of the isomers should have a spin $I \geq 24$. A detailed analysis of the data is in progress.

[1] Institute of Experimental Physics, University of Warsaw, Poland
[2] Soltan Institute for Nuclear Studies, Swierk, Poland
[3] Max-Planck-Institut für Kernphysik, Heidelberg, Germany.
[4] Niels Bohr Institute Copenhagen, Denmark

Reference:

[1] Ts. Venkova et al., Z. Phys. A344 (1993) 417

Study of Incomplete Fusion Reactions using Charged Particle - Gamma Ray Coincidence Techniques*

W. Gast, A. Georgiev, S. Utzelmann, H. Jäger, R.M. Lieder, B. Bochev[1], P. Mishev[1], K. Janakiev[1], T. Grigorov[1], V. Tomov[1], K.H. Maier[2]

A well established experimental technique in γ-ray spectroscopy is to study the decay of highly excited nuclei produced in heavy ion (HI) induced complete fusion reactions. In such reactions relatively cold residual nuclei with high angular momentum are obtained since the evaporated charged particles and neutrons carry away only little angular momentum. Complete fusion is achieved most efficient at projectile energies slightly above the Coulomb barrier. For increasing projectile energies the cross section for complete fusion is limited by the critical angular momentum at which the fission process starts. In addition the complexity of nuclear reactions in general increases at higher beam energies. Before fission occurs one observes processes like projectile fragmentation, sequential decay, deep inelastic scattering, etc., which prevent or at least complicate γ-ray spectroscopic studies. Therefore one usually restricts this type of spectroscopy to complete fusion reactions. However, this of course also imposes restrictions to the kind of nuclei which can be populated and to their modes of excitation.

The project presented here aimes at an extension of the experimental techniques applied in γ-ray spectroscopy with HI induced reactions by employing the incomplete fusion (massive transfer) reaction mechanism. The incomplete fusion reaction mechanism is considered as a quite peripheral binary process in which the projectile transfers a part of its mass to the target nucleus while the rest bypasses at approximately beam velocity. The transfered part fuses with the target nucleus giving a compound nucleus with very high angular momentum, which decays in the same way as the the compound nuclei resulting from complete fusion reactions. To extract the incomplete fusion reaction channel from the complexity of competing processes the charged particle-γ coincidence technique is applied. This type of coincidence measurement actually represents one of the main features of the new experimental technique as it allows gamma spectroscopic studies for predefined excitation energy and angular momentum windows of the compound nuclei by putting the appropriate kinematic conditions on the coincident ejectiles of the reaction. In a first test experiment the cross sections for incomplete fusion and competing reaction channels as well as the associated excitation energies and angular momentum distributions of the resulting residual nuclei for the interaction of 350 MeV ^{40}Ar with ^{108}Pd were studied employing the charged particle-γ coincidence technique. The experiment was carried out at the heavy ion accelerator VICKSI of HMI-Berlin. The experimental setup consisted of the OSIRIS γ spectrometer [1] with an incorporated charged particle identification telescope (PIT) [2] and a modified sum energy and multiplicity filter detector with a reduced number of 32 instead of 40 elements. For the energy calibration of the PIT we used the Coulomb scattered beam projectiles from the reaction ^{197}Au(^{40}Ar,^{40}Ar')^{197}Au at 350 MeV. The PIT was setup in a Δ_1-Δ_2-E configuration with thicknesses of the silicon detectors of Δ_1=50μ, Δ_2=200μ, and E=3000μ, respectively. The Δ_1 detector was segmented into 16 rings and 2 sectors and the Δ_2 and E detectors into 4 rings and 8 sectors, respectively, giving a total number of 96 individual detector elements. The analog signal processing electronics provided 96 medium resolution channels for the PIT, 32 for the sum energy and multiplicity filter detector, 12 high resolution channels for the Ge-detectors, and a corresponding total number of 140 fast constant fraction timing channels. Together with two 64 bit pattern units all energy channels and the analog multiplicity signal were mapped onto the 28 individually gated input parameters of the MEMPHIS data acquisition system [3] This parameter reduction was achieved by employing a dedicated, compact and fast ECL trigger logic system and a home made analog multiplexing circuitry [4]. Particle-γ-γ coincidences were recorded only for those events, where the particle trajectories fulfilled sensible coincidence requirements between Δ and E segments of the PIT predifined by fast hardware look-up tables. In this way a tremendous reduction of real background and background due to chance coincidences was achieved although the first Δ-detector had to process an integral rate of $9 \cdot 10^5$ events/s during the experiment. The particle-γ-γ coincidence rate finally recorded at a singles rate of the Ge-detectors of 3000 events/s was approx. 100 counts/s. Although the total reverse current of the first Δ-detector of the PIT increased from 2μA to 6μA during the experiment no degradation of the performance parameters of the telescope could be observed after 5 days of beam time. The two or more γ-ray energies of the high resolution Ge-detectors, the γ-ray sum energy and multiplicity, the Δ and E energies and the hit pattern of the particle telescope elements were recorded in list-mode on magnetic tape for each particle-γ-γ coincidence event. A preliminary inspection of the data shows that the reaction channels associated with the emission of charged particles are accompanied with an at least as high γ-ray multiplicity as one usually observes in experiments with complete fusion reactions. This might be a first indication that the new experimental technique applied in our experiment indeed is able to extract the interesting incomplete fusion reaction channel from the large amount of competing reactions. The analysis of the data is still in progress. The results are expected at least to allow a redesign of the detector configuration which is optimized for this type of experiments.

[1] Institute for Nuclear Research and Nuclear Energy INRNE, Sofia, Bulgaria.
[2] Hahn-Meitner-Institut Berlin, Germany.

References:

[1] R. M. Lieder et al., NIM 220 (1984) 363
[2] B. Bochev et al., KFA Jülich, Ann. Rep. (1988) 172
[3] K.H. Watzlawik et al., KFA Jülich, Ann. Rep. (1985) 154
[4] B. Bochev et al., KFA Jülich, Ann.Rep. (1988) 174, 172

* Supported by the BMBF Bonn, Germany, Project 212.1 and in part by the BulgarianNational Found for Scientific Investigations, Contract PH525.

Application Specific Digital Signal Processor

A. Georgiev, W. Gast, K. Göcking[1], Th. Rose[1]

An Application Specific Integrated Circuit (ASIC) for digital processing of signals from high-resolution semiconductor detectors has been reported previously [1]. The ASIC has been designed to incorporate the basic Moving Window Deconvolution (MWD) algorithm [2], and in this way to ease the application of the method in high-resolution, high-throughput spectroscopy. In addition, the circuit provides an oversampling (decimation) of up to 256 clock cycles, which reduces the output data rate by the same factor. This allows more time for the following Digital Signal Processor (DSP) to perform additional analysis of the detector information.

A set of 30 chips has been produced and tested. The functional behaviour of the circuit corresponded to the design ideas. The overall performance of the ASIC met all and even surpassed some design goals. For example the total power consumption has been found to be below 460 mW,which is a factor of two less than the expected value. The measured fault-free clock rate of 38MHz is about 40% higher than the design value. Due to the well distributed power and ground pins (16 pins in total) the ASIC produces very low switching noise. The ground bounce at 20MHz clock rate was found to be below 0.3 mV.

These positive results encourage us to design a second generation of the MWD-ASIC. The performance has been increased in two aspects: improved functionality with respect to the extraction of additional information from the detector signals, and improved low-frequency noise stability.

The first aspect has been motivated from the development of the segmented CLUSTER detector [3]. For these detectors pulse-shape analysis for position determination is required. However, the oversampling of the output data rate would reduce the accuracy of that analysis. Therefore in the new design an adaptive oversampling has been implemented. The method is illustrated in fig. 1. The

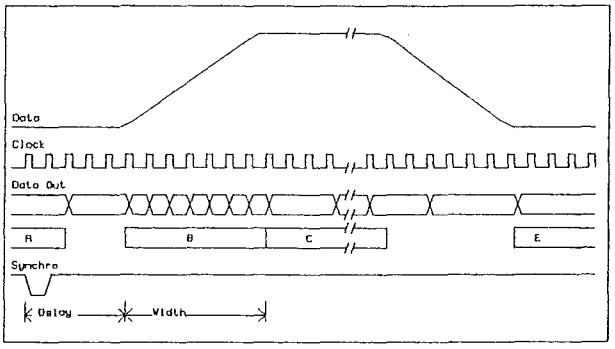

Figure 1: Illustration of the Adaptive Oversampling Method.

detector signal, already processed by the MWD stages of the ASIC, is shown in fig. 1a. The top-flat part of the pulse (interval C) carries the information about the energy of the event. The flat surroundings of the pulse (intervals A and E) correspond to the background level. These intervals can be oversampled without any loss of information. However, the leading edge information (interval B) has to be sent to the following DSP with the original sampling rate. The output of the circuit with mixed oversampled and full-rate data is shown in fig. 1b. The delay (relative to the synchronization input pulse) and the duration of the full-rate interval can be set-up as configuration parameters.

The second modification of the ASIC has been done with respect to the low-frequency stability. We observed during the tests that several MWD stages placed in cascade became unstable if a low-frequency signal with relatively high amplitude was applied to the input of the circuit. This effect is related to the accumulation of DC offset in the MWD stages. The block diagram of the modified MWD stage is shown in fig. 2. The units with the double line have been added to the original design. They provide a

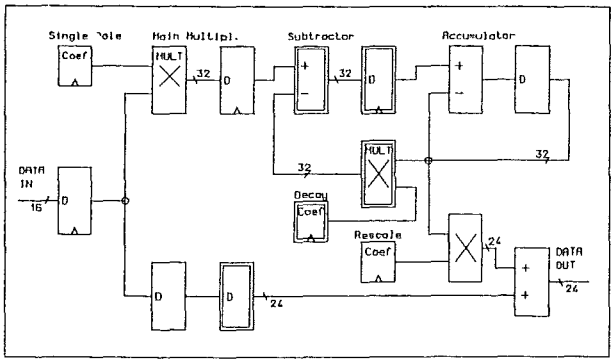

Figure 2: Block diagram of the MWD stage with a discharge of the accumulator.

discharge of the accumulator in the stage and thus ensure stable conditions for the following stages. The discharge rate is a configuration parameter controlled by the user. The samples of the second generation MWD-ASIC will be delivered and tested in the beginning of 1996.

[1] Fachhochschule Münster, Germany

References:

[1] A. Georgiev at al. KFA, IKP Ann. Rep. 1994, (1995) 124.

[2] A. Georgiev and W. Gast, IEEE Trans. Nucl. Sci. 40 (1993) 770.

[3] Physics with a Germanium-Mini-Ball, Workshop MPI Heidelberg, May 1995.

II. Theoretical Nuclear Physics

3. MEDIUM AND HIGH ENERGY PHYSICS

Photon-photon physics in ultrarelativistic hadron-hadron collisions

A. Alscher[1], G. Baur[2], O. Conradt[1], K. Hencken[3], H. Meier[1], and D. Trautmann[1]

1) Institute fürTheoretische Physik, Universität Basel
2) KFA Jülich
3) Institute for Nuclear Theory, University of Washington, Seattle, USA

Two-photon physics has been mainly studied at e^+e^- colliders in the past. In peripheral hadron-hadron collisions, with practically no strong interaction between the collision partners, photon-photon collisions occur. This opens up new interesting physics possibilities, also in new energy domains, which have hitherto not been accessible.

Effective γ-γ-luminosities are calculated for various realistic hadron collider scenarios [1]. It is concluded that feasible high luminosity Ca-Ca collisions at the Large Hadron Collider are an interesting option for γ-γ physics up to about 100 GeV γ-γ CM energy. The experimental possibilities of two-photon physics at RHIC are considered in Ref. 2, the case for LHC is given e.g. in Ref. 3.

Lepton pair production via the two photon mechanism is proportional to $(Ze)^2e^2$, in amplitude. The same final state can be reached via the bremsstrahlung pair creation mechanism, with an amplitude proportional to $(Ze)^3e$. Nevertheless, it was shown quantitatively [4] that the two-photon graph is strongly dominant. The reason is that the two virtual photons can come very close to real, i.e. the corresponding photon propagators can become very large. This is not possible for the bremsstrahlung mechanism.

It was shown theoretically that multiple e^+e^- pairs will be produced with large cross-section in relativistic heavy ion collisions, for recent references see Refs. 5 and 6. Smaller values of the impact parameter are important for multiple pair production. Using the accurate results of Ref. 6, reliable N-pair probabilities and cross-sections are calculated, see Ref. 7.

The measurement of $\mu^+\mu^-$ pairs can be used as a luminosity monitor at the LHC. Muon spectra are calculated in p-p collisions at LHC energies [8]. In addition to the elastic-elastic case, also elastic-inelastic processes are considered, following the procedure of Refs. 1 and 9. We consider especially the p-Δ transition.

It is of special importance to study the background contributions due to strong interactions in the nuclear stratosphere. They can depend sensitively on the actual nuclear density distribution, or on the impact parameter dependent distribution of partons (quarks, gluons, Pomerons, ...). We want to study the model dependence of such background calculations by assuming various (more or less) realistic nuclear densities. For a given N-N (or more general, parton-parton) cross-section σ_{NN} we calculate the impact parameter dependent background probability in a double pancake model as

$$P(b) = \sigma_{NN} \int d_2b_1\, f_1(b_1) f_2 b\,(\vec{b}_1 - \vec{b}) \equiv \sigma_{NN} \cdot F(b) \qquad (1)$$

where the impact parameter dependent nucleon (or parton, in a suitable generalization) distribution is given by

$$f(b) = \int_{-\infty}^{\infty} dz \rho(\vec{b}, z) \qquad (2)$$

The nuclear density is given by $\rho(r)$. We consider the square well, Gaussian (less realistic) and Fermit (more realistic) distributions and the sensitivity on the parameters, especially the diffuseness.

References:

[1] K. Hencken, D. Trautmann, G. Baur, Z. Phys. **C68** (1995) 473
[2] Spencer Klein, Two Photon Physics at RHIC, LBL-37295, preprint May 1995
[3] S. Sadovsky, Talk at Hadron '95 Conference, Manchester, to be published in the proceedings
[4] H. Meier, Diplomarbeit, Universität Basel 1994, unpublished
[5] K. Hencken, D. Trautmann, G. Baur, Phys. Rev. **A51** (1995) 998
[6] K. Hencken, D. Trautmann, G. Baur, Phys. Rev. **A51** (1995) 1874
[7] A. Alscher, Diplomarbeit, Universität Basel, in preparation
[8] O. Conradt, Diplomarbeit, Universität Basel, in preparation
[9] K. Hencken, D. Trautmann, G. Baur, to be submitted to Phys. Rev. C

Pion threshold production

C. Hanhart, J. Haidenbauer, A. Reuber, C. Schütz and J. Speth

The pion production is the dominant inelastic process in the nucleon nucleon interaction. It is therefore essential to understand this fundamental mechanism. When in 1990 the Indiana University Cyclotron Facility began to operate, very high precision data at very low energies became available for the reaction $pp \to pp\pi^0$. Early theoretical studies followed closely the conventional approach to s-wave meson production which goes back to the work of Koltun and Reitan from 1966 [1]. In this model two production mechanisms are considered: (i) direct production of a pion, depicted in Fig. 1a, (ii) production of a pion which first scatters off the other nucleon before emission, as shown in Fig. 1b. It became clear that such a model grossly underestimates the empirical cross section. On the other hand, the predicted energy dependence, which in this model is determined essentially by phase-space factors and the pp final-state interaction, was found to be in agreement with the IUCF data.

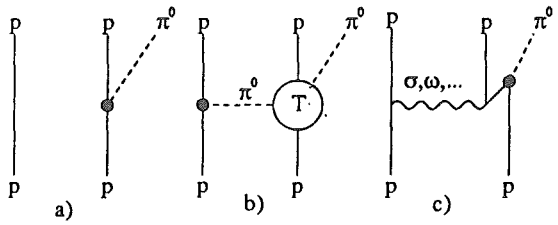

Figure 1: Mechanisms for the π-production (a) direct production, (b) pion rescattering, (c) heavy meson exchange

A first quantitative description of the $pp \to pp\pi^0$ cross section was achieved by Lee and Riska [3]. These authors considered in addition effects from meson-exchange currents due to the exchange of heavy (i. e. short ranged) mesons, as shown in Fig. 1c. The resulting contributions (in particular that of the σ meson) enhance the cross section near threshold by a factor of 3-5 [3, 4] and thus eliminate most of the underprediction found in earlier investigations. As a consequence it was argued in ref. [3] that the reaction $pp \to pp\pi^0$ could provide direct information on the short range part of the NN force.

However, in a very recent investigation by Hernández and Oset [5] an alternative explanation for the missing strength in the π^0 production close to threshold is presented. The off-shell properties of the πN amplitude are taken into account explicitly when evaluating the rescattering diagram. Since the off-shell πN isoscalar amplitude is, in general, much larger than its on-shell value, which was used in former computations, the contribution from rescattering is now considerably enhanced and the resulting $pp \to pp\pi^0$ cross section can even be brought into agreement with the experimental data. Thus their result suggests that the reaction $pp \to pp\pi^0$ might be a tool to pin down the off-shell behavior of the πN interaction.

We re-examine critically [6] some of the published results. In these publications several approximations to the pion production vertex and the kinematics have been tacitly taken over from the very first investigation by Koltun and Reitan [1] and we want to shed some light on their validity. We also review the importance of contributions from pion rescattering. We believe that this is necessary because in the work of Hernández and Oset phenomenological prescriptions for the off-shell extrapolation of the πN amplitude are applied. We use a realistic meson-theoretical model for the πN interaction which was recently developed in Jülich.

We consider only the lowest partial waves in the outgoing channel; the pp pair is taken to be in the $^1S_0$ and the pion in an s-wave relative to the nucleon pair. From angular momentum and parity conservation it then follows that the initial pp state has to be $^3P_0$. Distortions in the initial and final NN states are taken into account. The distorted waves are expressed in terms of the (half-off-shell) T-matrices in the standard way and the occurring loop integrals are then computed numerically.

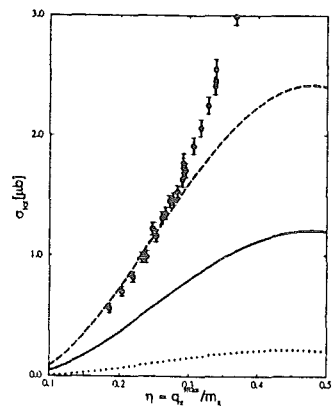

Figure 2: Our results for $pp \to pp\pi^0$. Solid line: full calculation, dashed line: the latter scaled by a factor of 2, dotted curve: direct production. The data points are taken from ref. [2].

Our results are shown in figure 2. It turns out that the more correct treatment of the direct production vertex not only reduces the magnitude of the direct production amplitude, but it also modifies the energy dependence. The rescattering contribution evaluated with our microscopic πN model is somewhat smaller than the one obtained in ref. [5]. Consequently our model calculation fails to describe the magnitude of the total cross section of the π^0 production and it also predicts a different energy dependence.

In the same framework we can also calculate the reaction $pp \to d\pi^+$. Here we actually overestimate the

experimental result for the total cross section as is depicted in figure 3. Niskanen has shown that the energy dependence can be described by inclusion of the Δ isobar [7]. But still he fails to describe the magnitude.

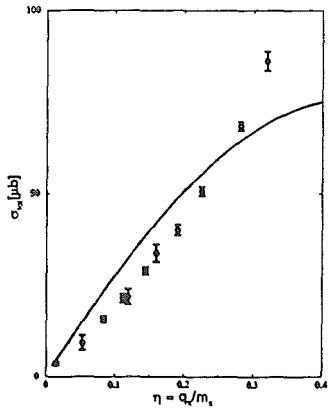

Figure 3: Our results for $pp \longrightarrow d\pi^+$.

Evidently pion threshold production is still not well understood. Presently we study the influence of the Δ-isobar. Further we started to investigate the contribution from the heavy meson exchanges. The latter have the attractive feature to give a large contribution to the neutral pion production whereas they have a negligible influence on $pp \longrightarrow d\pi^+$.

References:

[1] D. Koltun and A. Reitan, Phys. Rev. **141**, 1413 (1966).

[2] H.O. Meyer et al., Nucl. Phys. **A539**, 633 (1992).

[3] T.-S. Lee and D. Riska, Phys. Rev. Lett. **70**, 2237 (1993).

[4] C.J. Horowitz, H.O. Meyer and D.K. Griegel, Phys. Rev. **C49**, 1337 (1994).

[5] E. Hernández and E. Oset, Phys. Lett. **B350**, 158 (1995).

[6] C. Hanhart, J. Haidenbauer, A. Reuber, C. Schütz and J. Speth, Phys. Lett. **B358**(1995)21-26.

[7] J. Niskanen, Phys.Rev.C, to be published.

Short-range part of the NN interaction: ω exchange versus quark-gluon exchange

D. Hadjimichef*, J. Haidenbauer, K. Holinde, G. Krein*, and J. Speth

For a long time hadron-hadron interactions, in particular the NN interaction, have been studied in terms of meson exchange models employing baryon and meson degrees of freedom. Such models have achieved a good description of the empirical data. A common undesirable feature in all meson exchange models is the necessity of a (semi)phenomenological parametrization of the short range part of the interaction. However, since the advent of quantum chromodynamics (QCD) as the most promising candidate for the fundamental theory of the strong interactions, there is the hope that the short range part of the hadron-hadron interaction can be derived from first principles. However, because of complications due to the nonperturbative nature of the QCD interactions at low energies, the use of models is a practical necessity for making progress in this direction.

There is a great variety of quark models that can describe with reasonable success single-hadron properties. Therefore, there arises the natural question of to what extent the same model which gives a good hadron structure is able to describe the hadron-hadron interaction. In this respect, in the recent past several studies of the NN interaction have employed the nonrelativistic quark model, *a la* Isgur and Karl, which is one of the most successful quark models for hadron structure. The main ingredient of such calculations is the one-gluon exchange interaction. Although the initial results are encouraging as far as the very short range part is concerned (which is reflected in the successful description of NN scattering S-wave phase shifts) there are severe difficulties for the intermediate-range part. For example, the repulsion as well as the spin-orbit force generated by the present treatment of one-gluon-exchange is definitely too weak in high partial waves corresponding to distances between 1 and 2 fm [1]. More recently, the Tübigen group [2], working in the context of the "Resonating Group Method" (RGM), has made some progress on the spin-orbit problem in the NN system by including, in addition of the one-gluon-exchange interaction, a scalar-isoscalar meson coupled to quarks in a chirally symmetric way.

In the present project we started to investigate in detail the NN interaction as well as scattering observables in terms of different quark models. Our aim is to obtain detailed understanding of the effects of the various pieces contributing to the NN process such as size and form of the baryon wave function, quark-gluon and quark-meson couplings, ranges and cutoffs, etc.

Effective NN potentials can be derived from microscopic quark models in a elegant way by means of a field-theretic approach to composite particles recently transcribed from atomic physics to hadron physics [3]. The effective potentials are constructed as a power series in the hadron bound-state wave function. As an example, we present the contribution of the spin-spin part of the one-gluon exchange to the effective NN interaction to lowest order in the nucleon wave function. We take for the bound-state wave function of the nucleon a gaussian form, such that the r.m.s. radius of the nucleon is b. The effective NN potential is of the form:

$$V_{NN} = v_0 + \sigma^1 \cdot \sigma^2 \, v_\sigma + \tau^1 \cdot \tau^2 \, v_\tau + \sigma^1 \cdot \sigma^2 \, \tau^1 \cdot \tau^2 \, v_{\sigma\tau} \quad (1)$$

where each of the components $v_i, i = 0, \sigma, \cdots$ can be written as:

$$v_i = \kappa_{ss} \sum_{j=1}^{3} \lambda_{ij} f_j \quad (2)$$

where $\kappa_{ss} = 8\pi\alpha_s/3m_q^2(2\pi)^3$, the λ's are given in the Table 1 below, and the $f's$ are radial functions of the initial and final c.m. momenta $\mathbf{p}$ and $\mathbf{p}'$ given by:

$$f_1 = \left(\frac{3}{4}\right)^{3/2} e^{-b^2(\mathbf{p}^2+\mathbf{p}'^2)/6}$$
$$f_2 = e^{-b^2(\mathbf{p}-\mathbf{p}')^2/3} \quad (3)$$
$$f_3 = \left(\frac{12}{11}\right)^{3/2} e^{-b^2(7\mathbf{p}^2+13\mathbf{p}'-12\mathbf{p}\cdot\mathbf{p}')/33} + (\mathbf{p} \leftrightarrow \mathbf{p}').$$

Table 1. The coefficients λ of Eq. (2).

	1	2	3
0	1/12	3/4	1/4
σ	1/36	−1/36	−1/36
τ	1/108	1/12	−1/36
$\sigma\tau$	1/324	−25/324	5/324

When solving the Lippman-Schwinger equation for this potential one obtains phase-shifts numerically similar to the ones obtained with the RGM, and on-shell ($\mathbf{p}^2 = \mathbf{p}'^2$) it is identical to the potential of Barnes et al. [4] derived in the context of the "quar-Born diagram" method. Higher order (in the wave function) corrections give rise to many-body (> 2-body) forces and also to orthogonality corrections [3].

Due to the fact that the nucleon bound-state wave function is of gaussian form the effective potential falls off very fast at large distances. This has the consequence that higher partial waves receive very little contribution from quark-gluon exchange. In the conventional meson-exchange models a good description of higher partial waves is ensured by the long-ranged Yukawa tail of ω exchange and perhaps quark-gluon exchange models should keep the long-range tail of ω-exchange with a reduced strength as compared to the Bonn potential value [1].
We illustrate the effect of the rapid gaussian falloff of the potential by calculating the $^1F_3$ phase-shift for three values of the r.m.s. radius of the nucleon $b = 0.3, 0.5, 0.6$ fm, and compare with the corresponding one of ω-exchange for two values of coupling constant $g_\omega^2/4\pi = 20, 10$. The quark mass is taken to be $m_q = 313$ MeV and κ_{ss} is adjusted to fit the $N - \Delta$ mass splitting. This is shown in Figure 1 below.

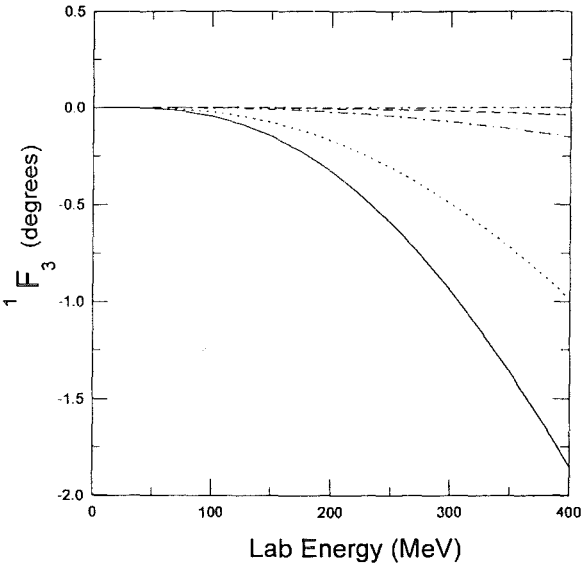

Fig. 1: $^1F_3$ phase shift as a function of the laboratory energy: solid $g_\omega^2/4\pi = 20$, dot $g_\omega^2/4\pi = 10$, dash-double-dot $b = 0.3$ fm, dash $b = 0.5$ fm, dash-dot $b = 0.6$ fm

From this figure it is evident the very small contribution from the quark potential. Notice that doubling the radius of the nucleon does not make a big effect and the result is far from the ω exchange contribution with a $g_\omega^2/4\pi = 10$.

Work is in progress in which the form of the nucleon wave function is changed to a more flat distribution than a gaussian one. Of course, the potential cannot then be expressed in an analytical form as in Eqs. (1-2) and a Monte Carlo integrator has to be used to integrate over the quark coordinates.

References:

[1] K. Holinde, Nucl. Phys. A543 (1992) 143c.

[2] A. Valcarce, A. Buchmann, F. Fernandez, and A. Faßler, Phys. Rev. C **51**, 1480 (1995).

[3] D. Hadjimichef, G. Krein, S. Szpigel, and J.S. da Veiga, to appear in Phys. Lett. B.

[4] T. Barnes, S. Capstick, M. Kovarik, and E.S. Swanson, Phys. Rev. C **48**, 538 (1993).

* Instituto de F´sica Teórica, Universidade Estadual Paulista, Rua Pamplona, 145, 01405-900 Sao Paulo, SP, Brazil

Structure of nonlocalities in meson exchange NN interactions and their role in the NN and $3N$ system

J. Haidenbauer and K. Holinde

In this work we want to discuss the structure of the nonlocalities present in meson-exchange models of the nucleon-nucleon (NN) interaction and their role for the resulting triton binding energy. We will do this mainly for the Bonn-B potential [1], which is based on the Blankenbecler-Sugar (BbS) [2] reduction scheme. Therefore, the starting point is the 4-dimensional Bethe-Salpeter equation (BS) [3]

$$T = K + \int d^4k \; KGT \; . \tag{1}$$

with an (energy-dependent) kernel consisting of all irreducible Feynman diagrams. In order to simplify this equation various reduction schemes introduce modified propagators g which lead to a 3-dimensional equation. Surely, such a procedure modifies the scattering amplitude, which however can be restored by adding suitable correction terms to the original BS-kernel K, i.e. we have

$$\begin{aligned} T &= V + VgT \\ V &= K + K(G-g)K + \ldots \end{aligned} \tag{2}$$

In case of the BbS-reduction, energy components of (relative) four-momenta are restricted to be zero (whereas they are integrated over in the original BS-equation). This leads to the 3-dimensional equation

$$T(\vec{k}',\vec{k};E) = V(\vec{k}',\vec{k};E) + \int d^3k'' \times$$
$$V(\vec{k}',\vec{k}'';E)\frac{M}{E_{k''}}\frac{1}{E^2-E_{k''}^2}T(\vec{k}'',\vec{k};E) \; , \tag{3}$$

which after a suitable transformation of amplitudes

$$\tilde{V}(\vec{k}',\vec{k};E) \equiv \sqrt{\frac{M}{E_{k'}}}V(\vec{k}',\vec{k};E)\sqrt{\frac{M}{E_k}} \tag{4}$$

and the same for T acquires the usual Schrödinger form, with $E_k = \sqrt{M^2+\vec{k}^2}$ and M the nucleon mass.

From the above it is immediately clear that the nonlocality structure of the original Bethe-Salpeter kernel is modified by such reductions; in addition, the modifications should depend on the kind of reduction chosen. Certainly, in order to remove such ambiguities, systematic corrections have to be done by going beyond the OBE-approximation, as indicated in Eqs. (1) and (2).

In the following we would like to divide the nonlocalities into standard ones which are essentially scheme-independent, and those called non-standard which depend on the reduction scheme. In the first group we have e.g. the M/E factors, which always arise in order to guarantee relativistic unitarity. They disappear when we do a nonrelativistic approximation neglecting 3-momenta versus the nucleon mass. More important is the nonlocal structure of the πNN vertex. Choosing the $i\gamma^5$-coupling in the Hamiltonian, we obtain for the nucleon matrix element

$$\begin{aligned} \overline{u}(\vec{k}')\gamma^5 u(\vec{k}) &= \sqrt{\frac{(E_{k'}+M)(E_k+M)}{4M^2}} \times \\ &\vec{\sigma}\cdot\left(\frac{\vec{k}'}{E_{k'}+M} - \frac{\vec{k}}{E_k+M}\right) \end{aligned} \tag{5}$$

which only after an on-shell approximation $E_{k'} = E_k$ boils down to the well-known local expression $\frac{1}{2M}\vec{\sigma}\cdot(\vec{k}'-\vec{k})$. Similar standard nonlocalities due to the structure of the Dirac spinors occur at the other ρNN, ωNN,... vertices.

Non-standard nonlocalities arise in potential terms which depend on the energy components of four-momenta. The best example is the meson propagator, which in the original Feynman amplitude can be written as

$$\frac{1}{(k_0'-k_0)^2-(\vec{k}'-\vec{k})^2-m^2} \; , \tag{6}$$

with energy components completely unrelated to corresponding 3-momenta. The BbS-reduction yields the well known local expression whereas in another reduction scheme advocated by Franz Gross [4] a nonlocal correction term appears. Another example is the ρNN tensor coupling involving $\sigma^{\mu\nu}(k'-k)_\nu$ which after a BbS reduction goes into $\sigma^{\mu i}(\vec{k}'-\vec{k})_i$ whereas the Gross-scheme implies an additional nonlocal term $\sigma^{\mu 0}(E_{k'}-E_k)$.

These examples show that there are numerous nonlocalities with prescribed structure which can (and should) be kept in momentum space representations. Clearly, the aforementioned nonrelativistic and on-shell approximations are a priori not justified even for extremely low-energy NN scattering since the 3-momenta are integrated over in the scattering equation. The question then arises how important are such nonlocalities for the evaluation of observables. We first want to look at the actual role of these nonlocalities in NN scattering. Fig. 1 shows the $^3S_1$ phase shift and ϵ_1 mixing parameter, which have strong impact on the triton binding. Obviously the removal of the nonlocal structure at the πNN vertex together with the neglection of M/E factors in the Bonn-B potential provides a drastic change. Of course, by readjusting suitable parameters a description with roughly the same quality can be again obtained within this local approximation. Thus, if the interaction is considered to be purely phenomenological, this approximation does not seem to matter at all, at least in the NN system. However, the parameters in meson exchange NN interactions (coupling constants and cutoff masses) are physical and will be ultimately fixed from QCD. Therefore it indeed mat-

ters already at this stage whether an approximation is done which forces you to change parameters.

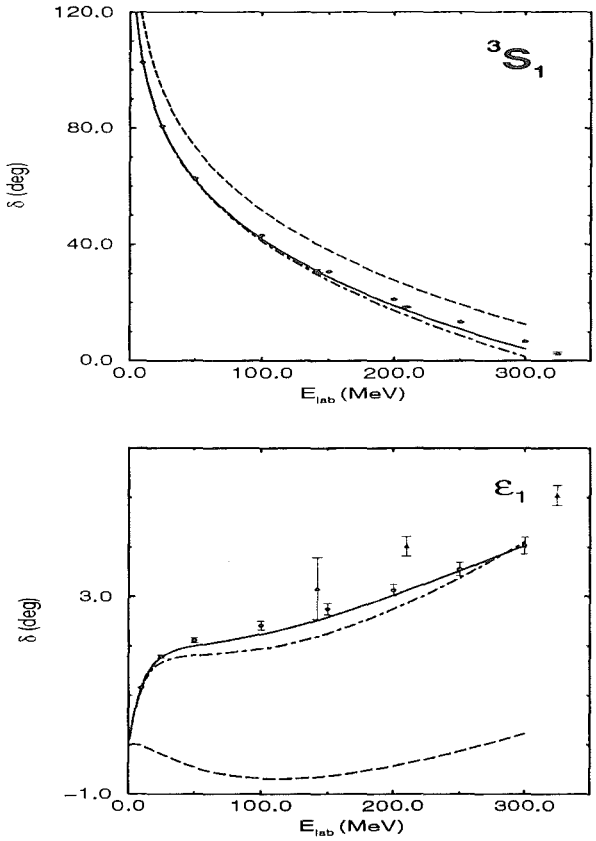

Figure 1: $^3S_1$ NN phase shift and ϵ_1 mixing parameter. The solid curve denotes the predictions of the Bonn-B potential. For the dashed curve, the local approximation (5) has been applied at the πNN vertex, together with the suppression of all m/E factors. With the same approximation a readjustment of parameters leads to the dash-dot curves.

Even after a refit of the S-wave phase shifts, the ϵ_1 mixing parameter and the deuteron observables like binding energy, etc. consequences of the local approximation remain in the deuteron D-wave as shown in Fig. 2. Compared to the original Bonn-B wave function a sizeable increase occurs which ranges out well above 2 fm leading to a increase in the D-state probability from 4.99 % (for Bonn-B) to 5.4 % and a corresponding decrease in the triton binding of 0.35 MeV. Further nonlocalities occur; their combined effect on the triton binding seems to be small since Gibson et al. [5] found a total increase of 0.30 MeV obtained by comparing the original Bonn-B potential result with a strictly local but phase-equivalent version obtained by inversion methods.
However one should realize that part of these effects are scheme-dependent (i.e. are generated by non-standard nonlocalities), and thus might change when systematic corrections beyond the OBE-approximation will be applied. Indeed, if in the original Bonn-B potential the tensor coupling of ρ exchange is modified according to the Gross prescription [4] as outlined before the resulting different nonlocal structure leads, after a suitable refit of NN observables, to a sizable modification of the deuteron

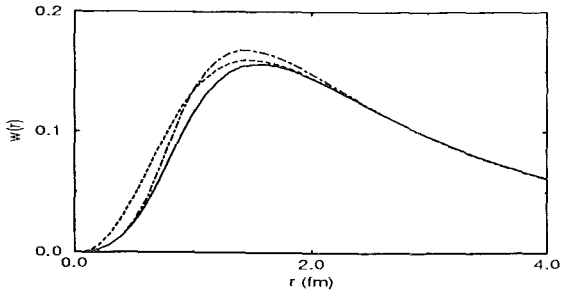

Figure 2: Deuteron D-wave. The solid curve denotes the result of the Bonn-B potential. The dash-dot curve corresponds to those of Fig. 1. For the short-dashed curve, the ρ-meson tensor vertex coupling is evaluated according to the Gross reduction scheme [4] (see text), again with a suitable readjustment of parameters.

D-wave shown in Fig. 2, with a new value for p_D of 5.47 % and a reduction of the triton binding by 0.15 MeV [6].

References:

[1] R. Machleidt, Adv. Nucl. Phys. **19**, 189 (1989).

[2] R. Blankenbecler and R. Sugar, Phys. Rev. **142**, 1051 (1966).

[3] H. A. Bethe and E. E. Salpeter, Phys. Rev. **84**, 1232 (1951).

[4] F. Gross, Phys. Rev. **186**, 1448 (1969).

[5] B. F. Gibson, H. Kohlhoff, and H. V. v. Geramb, Phys. Rev. C **51**, R465 (1995).

[6] J. Haidenbauer and K. Holinde, Phys. Rev. C, in press.

A fully relativistic phenomenological model of πN scattering

M. Hoffmann, J. Haidenbauer, and J. Speth

Our investigations of kaon production in πN scattering indicate that the initial πN interaction plays an important role [1]. At the onset of kaon production the energy of the πN system is around $E_{kin} \approx 765$ MeV. At such relativly high energies πN dynamics is already very complicated so that a rather sophisticated microscopic model would be required. However, since we are primarily interested in studying the kaon production processes $\pi N \rightarrow K\Lambda$, $K\Sigma$ we want to keep the interaction model in the initial πN state as simple as possible. Therefore we decided to resort to a phenomenological description by means of separable interaction potentials.

Most separable models of the πN interaction available in the literature, e.g. the one of McLeod and Afnan [2], treat the nucleon nonrelativistically. Such a treatment is not consistent with the fully relativistic framework in which our study of kaon production is carried out. Moreover, it is questionable whether a nonrelativistic treatment is still justified around the kaon production threshold. For these reasons we constructed a separable model of the πN interaction with fully relativistic kinematics.

We use the same type of parametrization as McLeod and Afnan [2] but treat the nucleon as well as the pion relativistically. To insure unitarity we include the inelasticity in our propagator,

$$G(E) = \int_0^\infty dk k^2 \frac{|k><k|}{\hat{\eta}(k)(E - W(k))}, \qquad (1)$$

where $W(k) = \sqrt{m_N^2 + k^2} + \sqrt{m_\pi^2 + k^2}$, and E is the total energy of the system.

In a given partial wave inelasticity and phase shifts are related to the T-matrix in the following way:

$$T_\alpha(k) = -\frac{\hat{\eta}_\alpha(k)}{\rho(k)} e^{i\hat{\delta}_\alpha(k)} sin\hat{\delta}_\alpha(k), \qquad (2)$$

where k denotes the center of mass momentum and $\rho(k)$ the density.

For $\hat{\eta}_\alpha(k)$ we choose the form

$$\hat{\eta}_\alpha(k) = 0.5 + \sum_{i=1}^{N} \frac{B_\alpha(i-1) - B_\alpha(i)}{1 + exp\{[k - k_\alpha]/C_\alpha(i)\}}, \qquad (3)$$

with

$$B_\alpha(0) = 1, \lim_{k->0} \hat{\eta}_\alpha(k) = 1, \text{and} \lim_{k->\infty} \hat{\eta}_\alpha(k) = 0.5. \qquad (4)$$

For most partial waves we use a rank-one separable potential

$$V_\alpha(k, k') = g_\alpha(k) \lambda_\alpha g_\alpha(k'), \qquad (5)$$

with

$$g_\alpha(k) = \frac{k^l}{\omega(k)^{1/2}} \left[\frac{C_1}{(k^2 + \beta_1^2)^{n_1}} + \frac{C_2 k^{n_2}}{(k^2 + \beta_2^2)^{n_3}} \right] \qquad (6)$$

and $\lambda_\alpha = \pm 1$. Only in the P_{11} partial wave we use a rank-two separable potential [1].

After fitting the free parameters we get a good description of the experimental phase shifts and inelasticities up to $E_{kin} = 1600$ MeV. We show as an example phase shifts and inelasticities for the S_{31} partial wave. Further partial waves are presented in [1].

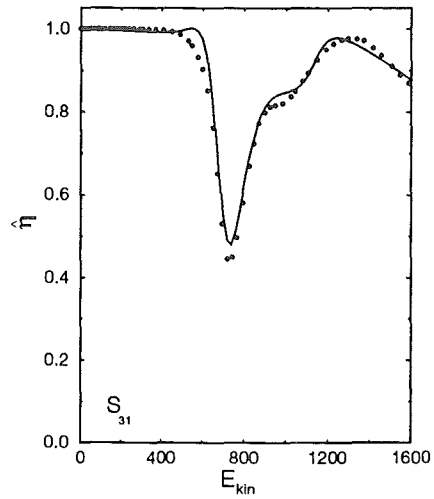

Figure 1: Inelasticity in the S_{31} partial wave as a function of the kinetic energy of the pion. Experimental data is taken from [3].

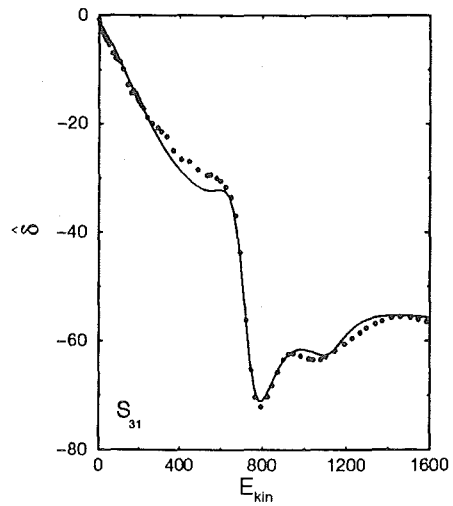

Figure 2: Phase shift in the S_{31} partial wave as a function of the kinetic energy of the pion. Experimental data is taken from [3].

References:

[1] M. Hoffmann, J. Haidenbauer, and J. Speth, in preparation.

[2] R.J. McLeod and I.R. Afnan, Phys. Rev. **C32**, 222 (1985).

[3] G. Höhler, phase shift analysis KA84, private communication.

The nucleon form factors and the transition from meson to quark dynamics

Z.Dziembowski[1], H.Holtmann, A.Szczurek[2] and J.Speth

In this communication a calculation of the Q^2-dependence of the electromagnetic (EM) form factors of nucleons dressed by pions is presented. From the Heisenberg uncertainty principle it is expected that the pion cloud of the nucleon, with excitations of the delta, would play a dominant role in the long-distance structure of the nucleon. The low Q^2 data are described within the framework of the vector meson dominance (VMD) approach which depicts the photon-nucleon interaction in terms of an intermediary coupling of the photon to vector meson resonance states. On the other hand , at high Q^2, the photon is considered to interact directly with the valence quarks, and perturbative quantum chromodynamics (PQCD) is believed to give the correct asymptotic Q^2 dependence. A variant of the semi-phenomenological formula proposed by Gari and Krümpelmann [1] is used to interpolate between the meson dynamics at low Q^2 and quark-gluon dynamics at large Q^2. As a result a suggestive description of the observed deviations from dipole fit and the correct scaling is obtained. The moderate Q^2 region ($\approx$1-20 GeV^2) is identified as the region where the transition from photon-meson coupling to photon-quark coupling takes place.

The calculation is an extension of work in Refs. [2, 3] to a full calculation of the Dirac $F_1^N = (G_E^N + \tau G_M^N)/(1+\tau)$ and Pauli $F_2^N = (G_M^N - G_E^N)/(1+\tau)$ form factors; $\tau = Q^2/4m_N^2$. This is performed within the light-cone formalism: it allows one to perform a relatively simple calculation of matrix elements in which composite baryons and pions recoil with large momentum. Although there has been much work on mesonic effects for the EM properties of nucleons in the cloudy bag model [4], virtually all previous calculations have been done in the no-recoil (static) approximation, so that they are relevant only in the domain of very small Q^2.

The calculation presented here is based on the meson cloud model developed here in Jülich [5], in which a 'bare' nucleon is surrounded by a mesonic cloud. This model was successful in the explantion of the Gottfried Sum-Rule and in the understanding of an recent Drell-Yan result of the NA51-Kollaboration. Once, using this model, the wave functions of the πN and $\pi\Delta$ Fock states are obtained, the G_E^N and G_M^N form factors of the nucleon can be expressed in terms of the EM form factors for the core and π. In earlier work only point-like pions were considered. In the present calculation the pion structure is found to be rather important. In addition, some simple symmetry arguments applied to the bare delta and $N \to \Delta$ transition form factors allow the form factor of the physical nucleon to be expressed in terms of the form factors of the bare nucleon only.

The electromagnetic properties of the bare nucleons are the input to our calculation. We begin with the extraction of the magnetic moments of the bare (b) proton and neutron by fitting them to the experimental nucleon magnetic moments. We find from this procedure $\mu_p^b = 2.65\,\mu_N$, and $\mu_n^b = -1.53\,\mu_N$.

In the next step the electric radii of the proton and neutron are expressed in terms of the bare magnetic moments, which are listed above, and electric radius of the bare nucleons. In order to fit the experimentally measured radii [6] $\langle r^2\rangle_E^p = 0.743 \pm 0.022$ fm^2 and $\langle r^2\rangle_E^n = -0.120 \pm 0.004$ fm^2 the bare electric radii have to be $\langle \mathcal{R}^2\rangle_E^p = 0.664 \pm 0.027$ fm^2, and $\langle \mathcal{R}^2\rangle_E^n = -0.060 \pm 0.009$ fm^2. We find there to be a 50% contribution to $\langle \mathcal{R}r^2\rangle_E^n$ due to the pionic cloud , with the dominant source in the πN component. Now we have all the ingredients needed to determine the bare magnetic radii. Fitting the experimentally measured magnetic radii $\langle r^2\rangle_M^p = 0.736 \pm 0.022$ fm^2 and $\langle r^2\rangle_M^n = 0.767 \pm 0.077$ fm^2 using the bare electric radii found above yields $\langle \mathcal{R}^2\rangle_M^p = 0.643 \pm 0.030$ fm^2, and $\langle \mathcal{R}^2\rangle_M^n = 0.623 \pm 0.141$ fm^2. Summarizing we find that the bare proton electric, proton magnetic and neutron magnetic radii are about 10% smaller than their physical counterparts. This is consistent with the result obtained in Ref. [3]. It is interesting to note that all the bare radii except the neutron electric radius are equal within experimental error bars. This universality resembles the situation for the physical radii.

In order to calculate the Q^2 dependence of EM form factors of the physical nucleons ($G_{E/M}^N$) some assumptions about EM form factors of the bare nucleons ($\mathcal{G}_{E/M}^N$) are made. To address the problem of the transition between meson dynamics at low Q^2 and quark-gluon dynamics at large Q^2, we replace the dipole parametrization used in Ref. [3] by a two-scale interpolation formula that gives the monopole form of meson physics at the low Q^2 and exhibits the characteristic pQCD fall-off in the high Q^2 region The universality of bare radii suggests the following scaling relations for the bare form factors

$$\mathcal{G}_E^p(Q^2) = \mathcal{G}_M^p(Q^2)/\mu_p^c = \mathcal{G}_M^n(Q^2)/\mu_n^c = \frac{\Lambda_1^2}{\Lambda_1^2 + \hat{Q}^2}\,\frac{\Lambda_2^2}{\Lambda_2^2 + \hat{Q}^2}, \qquad (1)$$

with $\hat{Q}^2 = Q^2 \log(\frac{\Lambda_2^2+Q^2}{\Lambda_{QCD}^2})/\log(\frac{\Lambda_2^2}{\Lambda_{QCD}^2})$. We take $\Lambda_{QCD} = 230$ MeV. The constraint $\langle \mathcal{R}^2\rangle_{univ}^c = 6\,(1/\Lambda_1^2 + 1/\Lambda_2^2)$ leaves us with only one free parameter in Eq. (1). We perform an analysis of the data for $G_M^p/\mu_p/G_D$ in [7] and the best fit gives $\Lambda_2 = 1.80$ GeV. This implies that $\Lambda_1 = 630$ MeV. This value is much smaller then the expectation from the vector dominance model where one would assume that $\Lambda_1 \approx m_\rho$. Note however that the work of Ref. [8] that uses dispersion relation technique to link the meson and quark dynamics as seen in the nucleon form factor find the same value of the meson dynamics scale.

Furuichi and Watanabe argue in [8] that the lower value of Λ_1 incorporates the effects of the uncorrelated two pion states.

To model the bare neutron form factor we note two constraints at $Q^2 = 0$, i.e. $\mathcal{G}_E^n(0) = 0$ and $(-6\,\mathcal{G}_E^n)'(0) = \langle \mathcal{R}^2 \rangle_E^n = -0.060 \pm 0.009\ \mathrm{fm}^2$. To interpolate between the low Q^2 and the PQCD at asymptotic Q^2 we propose for the bare neutron electric form factor

$$\mathcal{G}_E^n(Q^2) = \frac{-a\tau\mu_n^c}{1 - a\tau\mu_n^c} \frac{\Lambda_1^2}{\Lambda_1^2 + \hat{Q}^2} \frac{\Lambda_2^2}{\Lambda_2^2 + \hat{Q}^2}, \qquad (2)$$

with $a = 0.59$ to fit to the slope of $\mathcal{G}_E^n(Q^2)$ at $Q^2 = 0$. Shown in Fig. 1 is the EM form factor of the nucleon ploted against the dipole fit. In the figure the individual bare core contribution, and together with the addition of πN and $\pi\Delta$ components are displayed. Clearly shown in this figure are three regions. Low Q^2 region, below 0.1 GeV^2 where the scattering off the pion component brings significant contribution to the nucleon structure. The dipole-like behavior seen in this region is a result of a convolution of the monopole character of the bare form factor and the additional suppression from πN and $\pi\Delta$ body form factors. Next, there is the intermediate region, between 0.1 GeV^2 and 5 GeV^2, where the transition to quark-gluon dynamics takes place. Clearly shown is the onset of the core dominance with the Q^2 dependence expected from quark counting rules. A quite dramatic rise in the few GeV^2 region in the neutron electric form factor compared to the dipole fit is noted. Finally there is the third region, above 5 GeV^2, where a strong Q^2 fall-off compared to the dipole fit is observed. This is due to the running coupling constant that is taken into account in our model calculation by the substitution $Q^2 \to \hat{Q}^2$. In Fig. 1(a) the effect of a variation in Λ_{QCD} is shown. Neglecting the log-dependence in Eqs. (1) and (2) by the substitution $Q^2 = \hat{Q}^2$ the curve labeled $\Lambda_{QCD} = 0$ is obtained.

In conclusion, the estimated size of the nucleon core is only about 10% smaller then the physical proton radius. The deviations from the dipole fit for the nucleon form factor exhibit transitions from the meson dynamics at low Q^2 to quark-gluon dynamics. The latter seem to dominate already at $Q^2 \gtrsim$ a few GeV^2 region.

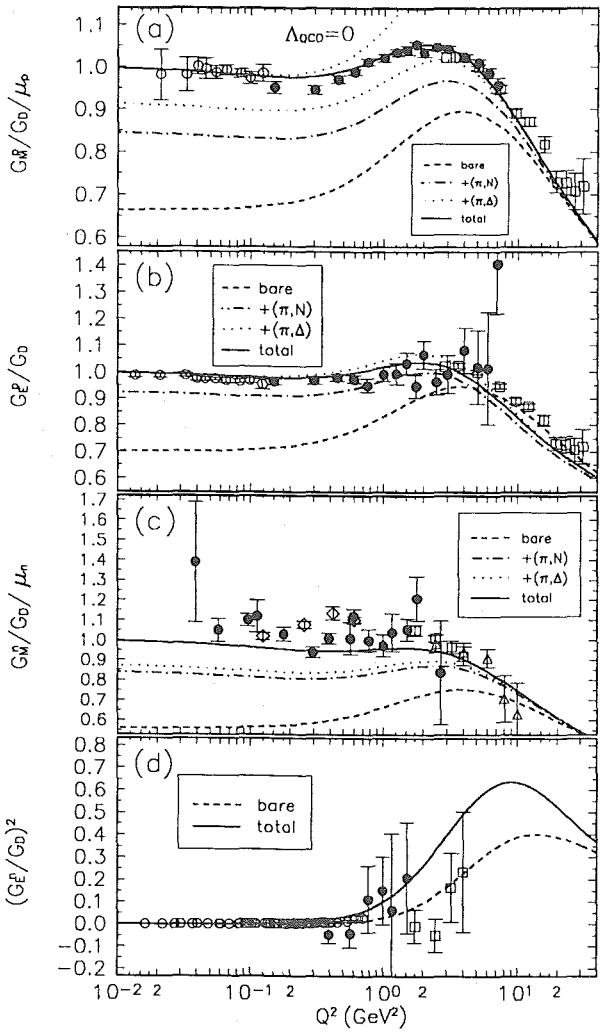

Fig. 1: The Q^2 dependence of the electromagnetic form factors obtain within our model.

[1] Department of Physics, Temple University, Philadelphia, Pennsylvania 19122, USA

[2] Institute of Nuclear Physics, ul.Radzikowskiego 152, PL-31-342 Kraków, Poland

References:

[1] M. Gari and W. Krümpelmann. *Z. Phys.* **A322** (1985) 689.

[2] Z. Dziembowski and L. Mankiewicz. *Phys. Rev.* **D36** (1987) 1556.

[3] N.N. Nikolaev, A. Szczurek, J. Speth and V.R. Zoller. *Z. Phys.* **A349** (1994) 59.

[4] S. Théberge, G.A. Miller and A.W. Thomas. *Can. J. Phys.* **60** (1982) 59.

[5] H. Holtmann, A. Szczurek and J. Speth. *Jülich preprint KFA-IKP(TH)-25* (1994) *Nucl. Phys.* **A** in print.

[6] O. Dumbrajs *et al.* *Nucl. Phys.* **B216** (1983) 277.

[7] R.C. Walker *et al.* *Phys. Lett.* **B224** (1989) 353.

[8] S. Furuichi and K. Watanabe. *Prog. Theor. Phys.* **83** (1990) 565.

Testing the meson cloud in the nucleon in Drell-Yan processes

A. Szczurek [1], M. Ericson [2], H. Holtmann and J. Speth

The deviation of the Gottfried Sum Rule from its classical value [1]

$$S_G = \int_0^1 [F_2^p(x) - F_2^n(x)]\frac{dx}{x} = \frac{1}{3} \qquad (1)$$

observed by the New Muon Collaboration (NMC) at CERN [2] has created a large interest on the possible sources of the violation. In the NMC experiment the neutron structure function which enters the sum rule is deduced from deep inelastic scattering off deuterium. This puzzling result can be understood as consequence of an internal asymmetry $\bar{d} > \bar{u}$ of the quarks in the proton (the opposite asymmetry is expected for the neutron if the proton-neutron charge symmetry holds). Since at large Q^2 the perturbative QCD evolution is flavour independent and, to leading order in $logQ^2$, generates equal number of $\bar{u}u$ and $\bar{d}d$ sea quarks nonperturbative effects must play an important role here. The effect of the asymmetry can be understood by an model, as it has been developed by our group [3], in which the physical nucleon contains an admixture of the πN and $\pi\Delta$ components in the Fock expansion [4]. The predicted effect of the asymmetry agrees [5] with that deduced from the NA51 experiment.

Another question of interest is from which region of x the $\bar{u} - \bar{d}$ asymmetry is coming from. The x-dependence of this quantity cannot be determined well from the usual inelastic electron scattering off nucleons in the deep-inelastic regime. The information gathered from these experiments has to be correllated with other information in order to adress the question raised. Reactions suited for this purpose are the Drell-Yan processes, in which a dilepton-pair is detected in hadron-hadron collisions. We looked for different easily obtained observables whether they are suited to gain information about the $\bar{u} - \bar{d}$ asymmetry [6]. The first look was on the Drell-Yan cross section itself. Because of a theoretical not known factor, which results for the extrapolation from space-like to time-like momenta of the exchanged photon, the cross section is compatibel with both $\bar{u} - \bar{d}$ symmetrical und asymmetrical quark distribution functions. Thus it is worthwhile to consider ratios of Drell-Yan cross sections to eliminate this unknown factor.

The most useful quantity found is the so-called 'Drell-Yan Asymmetry' defined by

$$A_{DY} = \frac{\sigma^{DY}(p+p) - \sigma^{DY}(p+n)}{\sigma^{DY}(p+p) + \sigma^{DY}(p+n)}. \qquad (2)$$

It can be easily shown, that this quantity can only reach negative values in the presence of the $\bar{u} - \bar{d}$ asymmetry. Moreover, it only depends weakly on the shape of the valence part of the quark distribution functions used. This can be easily seen by assuming

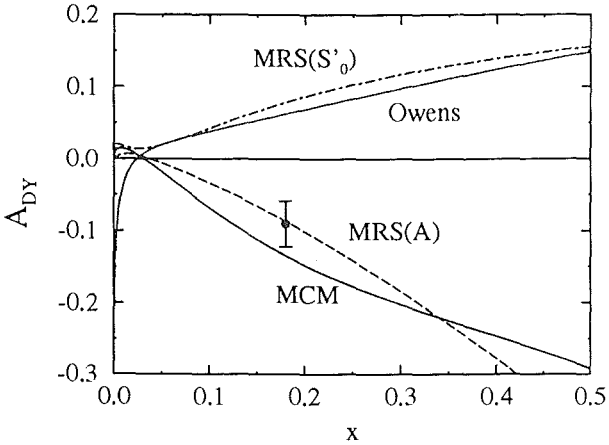

Fig. 1: The Drell-yan asymmetry for different parametrizations of quark distributions and within our model (MCM).

$u_v(x) = 2d_v(x)$ and neglecting the sea-sea terms in the asymmetry:

$$A_{DY} = \frac{-19\Delta + 6\bar{q}}{-9\Delta + 66\bar{q}} \qquad (3)$$

with $\Delta = \bar{d} - \bar{u}$, $\bar{q} = (\bar{u} + \bar{d})/2$. The NA51-Kollaborations has recently measured this asymmetry with the result [7]

$$A_{DY}(0.18) = -0.09 \pm 0.02 \pm 0.025 \qquad (4)$$

This quantity can be readily calculated within our model. It agrees well with this new data. Note however, that all parameters of our model were fixed before this data was available. As a consequence the $\bar{u} - \bar{d}$ asymmetry is concentrated at rather large-x in distinction to older parametrizations.

[1] Institute of Nuclear Physics, PL-31-342 Cracow, Poland

[2] Institut de Physique Nucleaire, Universite Claude Bernard, Lyon, F-69622 Villeurbanne cedex, France

References:

[1] K. Gottfried. *Phys. Rev. Lett.* **18** (1967) 1174.

[2] M. Arneodo *et al. Phys. Rev.* **D50** (1994) R1.

[3] H. Holtmann, A. Szczurek and J. Speth. *Jülich preprint KFA-IKP(TH)-25* (1994) *Nucl. Phys.* **A** in print.

[4] A. Szczurek, J. Speth and G.T. Garvey. *Nucl. Phys.* **A570** (1994) 765.

[5] H. Holtmann, N.N. Nikolaev, J. Speth and A. Szczurek. *Z. Phys.* **A** (1995) in print.

[6] A. Szczurek, M. Ericson, H.Holtmann and J. Speth. *Nucl. Phys.* **A** (1995) in print.

[7] A. Baldit *et al. Phys. Lett.* **B332** (1994) 244.

CORRELATED $\pi\rho$ EXCHANGE IN THE NN INTERACTION

G. Janssen, K. Holinde, and J. Speth

Quantum chromodynamics (QCD) is the underlying theory of strong interactions, with quarks and gluons as fundamental degrees of freedom. However, in the non-perturbative region of low and medium energy physics, mesons and baryons definitely keep their importance as efficient, collective degrees of freedom for a wide range of nuclear phenomena. One possibility to detect quark effects is to treat as many hadronic reactions as possible from a combined conventional viewpoint, in terms of baryons and mesons.

We demonstrate the outstanding role of meson-meson correlations in baryon-baryon interactions and describe the effect of correlated $\pi\rho$ exchange in the NN interaction, especially its implication for the (strong) πNN formfactor and the nature of the short range NN repulsion.

The importance of ρ-exchange for the dynamics of the NN system derives from the following fact: It provides a sizable intermediate range tensor force, which has opposite sign to the tensor force generated by one-pion exchange. Thus there is a strong cancellation, over a relatively broad range of energies and distances, between π and ρ exchange in the tensor channel. A similar cancellation occurs between K and K* exchange, e.g. in the hyperon-nucleon interaction. Therefore, in the NN (and in the baryon-baryon system in general) it is strongly suggested to always group π and ρ (as well as K and K*) together in order to reach sufficient convergence in the expansion of the irreducible kernel (potential).

In fact this procedure has been an essential guideline when constructing the Bonn potential[1]. Unfortunately it was not followed to a sufficient degree: Whereas, in second order diagrams $\pi\pi$ as well as $\pi\rho$ exchange has been included for uncorrelated processes (with N and Δ intermediate states) this has not been done for correlated processes: correlated 2π-exchange processes have been effectively included (in terms of sharp mass σ' and ρ exchange) but correlated $\pi\rho$ processes have been left out. The reason is quite simple: The evaluation of this missing piece is technically quite complicated, much more involved (due to the spin of the ρ) compared to correlated 2π-exchange. More importantly, a dynamical model for the interaction between a π and a ρ meson was not available at that time.

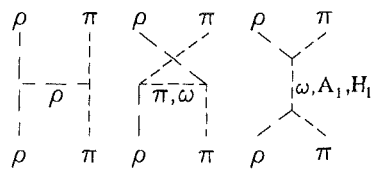

Fig. 1: Born terms included in the model of Ref.[2] for the $\pi\rho$ interaction.

We have recently constructed a corresponding potential model [2], with driving terms shown in Fig.1. Open parameters have been adjusted to empirical pole parameters of the A_1, H_1, and ω meson.

This $\pi\rho$ T-matrix is now inserted into the correlated $\pi\rho$ exchange diagram of Fig.2. The evaluation proceeds via a dispersion-theoretical treatment.

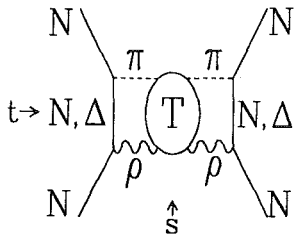

Fig. 2: Correlated $\pi\rho$ exchange.

The result can be represented as an integral over various spectral functions in the different channels $J^P(I^G) = 0^-(1^-)$ ("π"), $1^-(0^-)$ ("ω"), $1^+(1^-)$ ("A_1"), $1^+(0^-)$ ("H_1") which we have considered. Thus we have for the pionic channel:

$$V^{(0^-)}_{N,N;N,N}(t) \sim \int_{(m_\pi+m_\rho)^2}^{\infty} dt' \, \frac{\rho^{(0^-)}(t')}{t'-t} \, . \qquad (4)$$

$\rho^{(0^-)}$ is shown in Fig.3. Obviously it provides a sizable contribution, with a peak around 1.1 GeV, somewhat smaller than the mass (1.2 GeV) of the phenomenological π' introduced in our recent NN models to accommodate a soft πNN form factor [3].

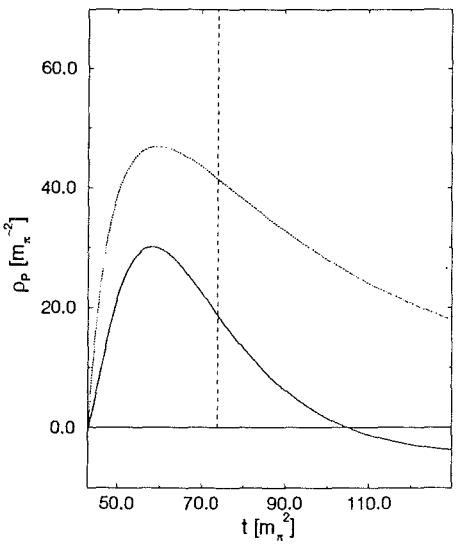

Fig. 3: The spectral function in the pionic channel $\rho^\pi_P(t)$. The dotted line shows the uncorrelated part whereas the solid line represents the correlated contribution. The vertical dashed line represents sharp mass π' exchange used in Ref.[3].

Indeed as shown in Fig.4, the resulting interaction due to correlated $\pi\rho$ exchange in the pionic channel is able to

counterbalance the substantial suppression induced in the one pion-exchange potential (OPEP) when going from a cutoff mass $\Lambda_{NN\pi}$ of 1.3 GeV, phenomenologically required in the (full) Bonn potential, to a value of 1.0 GeV. For basic theoretical reasons such a reduction is highly welcome, since various information from other sources point to a rather soft πNN form factor characterized by $\Lambda_{NN\pi} \cong 0.8$ GeV [4, 5]. This value will probably be reached if correlated $\pi\sigma$ exchange is included, too, which is also missing in the Bonn potential. (As usual, σ stands for a low mass correlated $\pi\pi$ pair in the 0^+ channel). Thus it appears that in the Bonn potential OPEP together with a hard form factor is an effective description of 'true' one-pion exchange (with a soft form factor) plus correlated $\pi\rho$ (and $\pi\sigma$) exchange in the pionic channel.

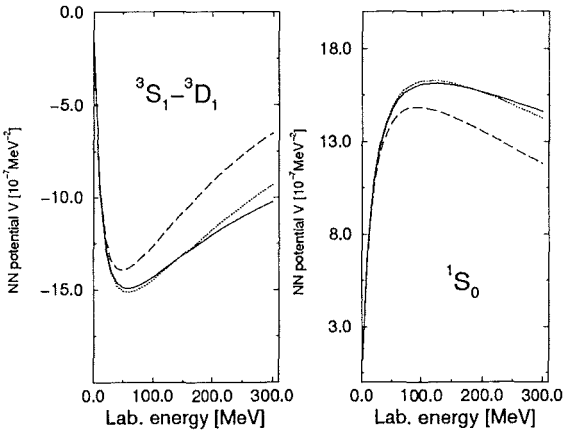

Fig. 4: On-shell NN potential V_{NN} as function of the nucleon lab energy for the $^3D_1 - {}^3S_1$ transition (lefthand side) and in the $^1S_0$ state (right-hand side). The dotted line denotes the one-pion-exchange potential as used in the Bonn potential ($g^2_{\pi NN}/4\pi = 14.4$, $\Lambda_{\pi NN} = 1.3\,GeV$). For the dashed line, $\Lambda_{\pi NN} = 1.0\,GeV$ was used. The solid line results if correlated $\pi\rho$ exchange in the pionic channel is added to the dashed line.

In the ω channel, the exchange of a correlated $\pi\rho$ pair also provides a sizable contribution to the NN interaction. Here we have included the genuine ω meson explicitly and replaced the (effective) ω exchange in the Bonn potential by the resulting correlated $\pi\rho$ potential, which can be decomposed into a pole and a non-pole piece. The former provides a microscopic model for 'true' ω exchange leading to a renormalized ωNN coupling constant at the pole, $g^2_{NN\omega}/4\pi$ = 11.0, which is about a factor of 2 smaller than the effective value of 20 used in the Bonn potential. Thus 'true' correlated $\pi\rho$ exchange, i.e. the non-pole piece, provides almost half of the empirical repulsion needed in the NN interaction. It can be roughly parametrized by sharp-mass ω'-exchange with $g^2_{NN\omega}/4\pi$ = 8.5, $f_{NN\omega}/g_{NN\omega}$ = 0.4 and $m_{\omega'}$ =1120 MeV.
The new reduced coupling constant (11.0) is still about a factor of 2 larger than provided by customary SU(3) estimates, which use $g^2_{NN\omega} = 9g^2_{NN\rho}$. Thus with $g^2_{NN\rho}/4\pi$ = 0.55 as determined by Hoehler and Pietarinen [6] we have $g^2_{NN\omega}/4\pi$ = 5. Note however, that the above relation between ω and ρ coupling constants is based, apart from ideal mixing, on the assumption of vanishing ϕNN coupling. For $g_{NN\phi}$ unequal to zero the above relation goes into

$$g_{NN\omega} = 3g_{NN\rho} - \sqrt{2}g_{NN\phi}\,. \qquad (5)$$

If we take $g_{NN\phi} = -g_{NN\rho}$, (which amounts to a rather small deviation from zero) we have $g^2_{NN\omega} \approx 20g^2_{NN\rho}$, in rough agreement with our results. Such a value for the ϕNN coupling to the nucleon and the negative sign is quite conceivable from the ϕ coupling to the nucleon via the $\Lambda\bar{\Lambda}$ continuum [7].
As a main conclusion, meson-meson correlations are important in baryon-baryon interactions and have to be included in any realistic model description.
Furthermore a model for correlated $\pi\rho$ exchange between two nucleons has been discussed, which has substantial effects: In the pionic channel it counterbalances the suppression generated by a soft πNN form factor of monopole type with a cutoff mass of about 1 GeV; in the ω-channel it provides a strong repulsive contribution, leaving little room for explicit quark-gluon effects.

References:

[1] R. Machleidt, K. Holinde, and Ch. Elster, *Phys. Rep.* **149** (1987) 1.

[2] G. Janssen, K. Holinde, and J. Speth, *Phys. Rev.*, **C49** (1994) 2763.

[3] J. Haidenbauer, K. Holinde, and A. W. Thomas, *Phys. Rev.* **C49** (1994) 2331.

[4] S.A. Coon, and M.D. Scadron, *Phys. Rev.* **D42** (1990) 2256.

[5] A.W. Thomas and K. Holinde, *Phys. Rev. Lett.* **63** (1989) 2025.

[6] G. Höhler and E. Pietarinen, *Nucl. Phys.* **B95** (1975) 210.

[7] V. Mull, private communication.

Investigation of the pion production in pion-nucleon scattering

G. Becker, K. Holinde, and J. Speth

The reaction $\pi N \to \pi\pi N$ near threshold is one of the most important sources of information about the $\pi\pi$ interaction at low energies which at present can not be measured directly. Moreover, the interpretation of the baryon spectrum requires comprehension of the πN and the $\pi\pi N$ system, because nucleon and delta resonances typically show a strong coupling to both channels.

As a first step towards a three-body unitary meson-exchange model for the πN and the $\pi\pi N$ system we developed a coupled channel model based on the formalism of Aaron, Amado and Young [1] consisting of the πN and the σN channel. The σ represents an interacting $\pi\pi$ system in the scalar isoscalar channel. To describe this $\pi\pi$ interaction we used the separable parametrization discussed in ref. [2]. The interaction in the πN channel is described by a potential containing the contributions shown in fig. 1 [(a)-(d)], while the $\pi N \to \sigma N$ transition potential is shown in fig 1 (e).

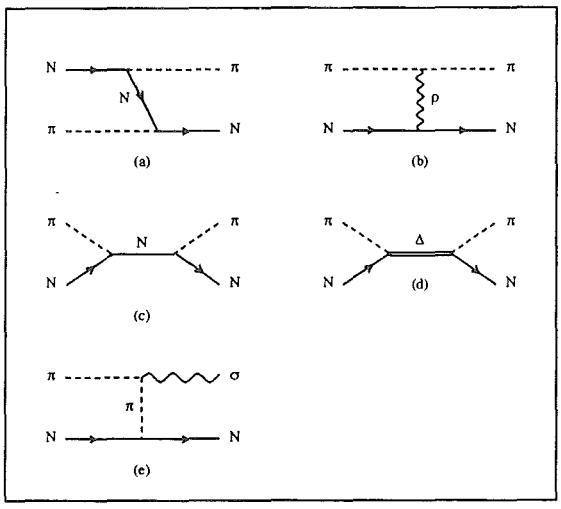

Figure 1: Contributions to the πN potential [(a)-(d)] and the $\pi N \to \sigma N$ transition potential (e).

By iteration of the potentials shown in fig. 1 we gain a good the description of the experimental πN phaseshifts up to a pion momentum of 0.5 GeV in the lab frame (fig. 3).

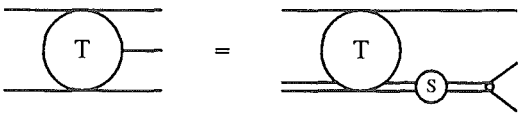

Figure 2: Diagrammatical representation of the pion production amplitude. S is the propagator of the dissociating particle including self energy contributions.

The pion production amplitudes can be derived from the transition amplitudes for two-particle final states (πN or σN) by multiplying the breakup of the σ into two pions in the σN channel and the breakup of a nucleon into a pion and a nucleon in the πN channel. This is shown diagrammatically in fig. 2.

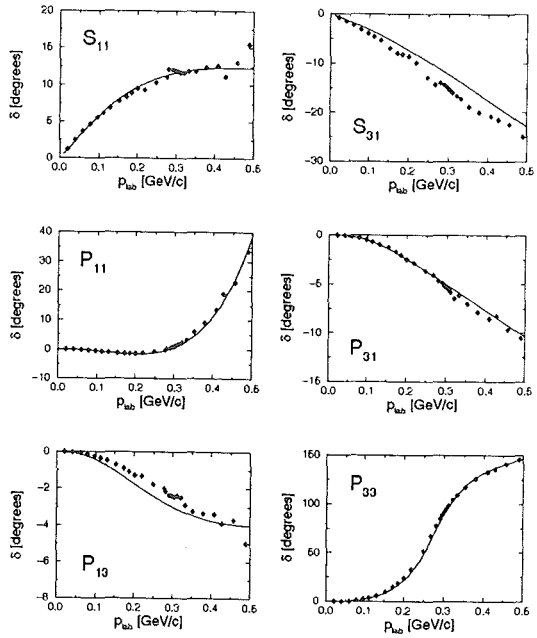

Figure 3: πN phaseshifts as a function of the pion momentum in the lab frame. Experimental data is taken from ref. [3].

The predictions of our model for the pion production amplitudes are shown in fig. 4 and fig. 5. The plotted quasi amplitude is defined by:

$$\mathbf{T}^2 = \frac{\sum_{\lambda'\lambda} \int d\rho^{(3)} \left|\langle \vec{p}_1\vec{p}_2\vec{p}_3, \lambda' \,|\, T \,|\, \vec{p}_0, \lambda \rangle\right|^2}{\int d\rho^{(3)}} \qquad (1)$$

where $d\rho^{(3)}$ is the three particle phase space element and λ and λ' are the helicities of the nucleon in the initial and final state.

For those final states that can be produced by dissociation of a σ (fig. 4), the model predicts the correct threshold production amplitudes. For pion momenta above 0.35 GeV additional contributions for example from the $\pi\Delta$ channel are necessary to explain the experimental data. In our model the channels shown in fig. 5 can only be produced by dissociation of a virtual nucleon. These contributions, introduced to insure three-particle unitarity, are not sufficient to describe the experimental data, but provide a non

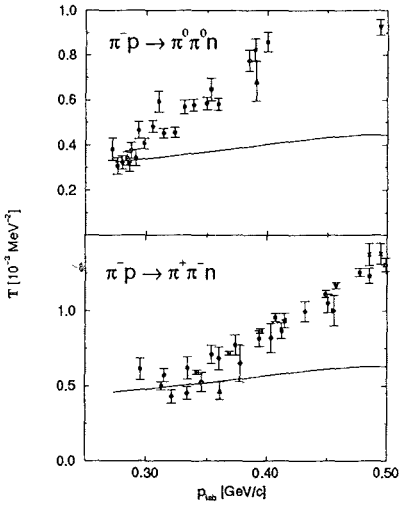

Figure 4: Quasi amplitudes for pion production as a function of the pion momentum in the lab frame: final states produced by dissociation of a sigma. Experimental data is taken from [4].

negligible contribution to the total production amplitude.

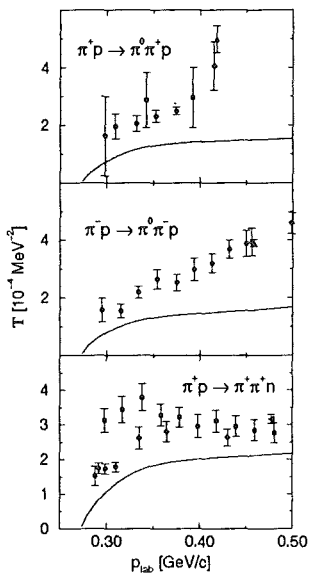

Figure 5: Quasi amplitudes for pion production as a function of the pion momentum in the lab frame: final states produced by dissociation of a nucleon. Experimental data is taken from [4].

References:

[1] R. Aaron, R.D. Amado and J.E. Young, Phys. Rev. **174**, 2047 (1969).

[2] Z. Aouissat, R. Rapp, G. Chanfray, P. Schuck, and J. Wambach, Nucl. Phys. **A581**, 471 (1995).

[3] R. Koch and E. Piertarinen, Nucl. Phys. **A336**, 331 (1980).

[4] V.V. Vereshagin, S.G Sherman, A.N.Manashov, U. Bohnert, M. Dillig, W. Eyrich, O.Jäkel and M. Moosburger, LANL preprint hep–ph/9504361 (1995).

Quadrupole deformation of deuterons and final state interaction in $^2\vec{H}(e,e'p)$ scattering on tensor polarized deuterons at CEBAF energies

A.Bianconi[1,2], S.Jeschonnek, N.N.Nikolaev[3], B.G.Zakharov[3]

The strength of final state interaction (FSI) between struck proton and spectator neutron in $^2\vec{H}(e,e'p)$ scattering depends on the alignment of the deuteron. We study the resulting FSI effects in the tensor analyzing power in detail and find substantial FSI effects starting at still low missing momentum $p_m \gtrsim 0.9 fm^{-1}$. At larger $p_m \gtrsim 1.5 fm^{-1}$, FSI completely dominates both missing momentum distribution and tensor analyzing power. We find that to a large extent FSI masks the sensitivity of the tensor analyzing power to models of the deuteron wave function. For the transversely polarized deuterons the FSI induced forward-backward (F/B) asymmetry of the missing momentum distribution is shown to have a node at precisely the same value of p_m as the PWIA (plane wave impulse approximation, i.e. neglecting FSI) missing momentum distribution. The position of this node is not affected by FSI and can be a tool to distinguish experimentally between different models for the deuteron wave function.

We are interested in scattering experiments at CEBAF energies [1], i.e. with momentum transfer over 1 GeV, where Glauber's multiple scattering theory [2] can be applied, which simplifies the evaluation of FSI effects. They are dominated by diffractive incoherent nucleon-nucleon rescattering, and scarcely affected by the details of the nuclear structure, as demonstrated, for the case of unpolarized deuteron, in [3]. Here we study scattering of unpolarized electrons on polarized deuteron, without detection of the final product polarizations. The reaction is of interest for the study of the short distance behavior of the D-wave component of the deuteron ground state. Due to the non spherical shape of the deuteron, the probability for FSI is different when the deuteron polarization axis is parallel or perpendicular to the path of the ejected proton. This is the origin of a strong FSI contribution to the tensor analyzing power of the deuteron in $(e,e'p)$ at large missing momenta. This is shown in Fig.1, for both Bonn [4] and Paris [5] model wave functions. A relevant finding is that the differences that are present at PWIA level between the two models almost disappear when FSI is included, suggesting small chances of discriminating between different models.

We present many distributions, relative to different polarization states of the target, and all the curves are heavily affected by FSI. The only quantity that is reminiscent of some PWIA features is the F/B asymmetry. Although this asymmetry is caused by FSI, its zeros (as a function of $|P_m|$) appear in the same position as the zeros of the intrinsic nuclear single particle distribution (for a given deuteron polarization). They are shown in Fig.2.

Summarizing, we show that it would be very difficult to extract information about the large momentum D-wave content of deuteron ground state from $(e,e'p)$ scattering on polarized deuteron. We suggest measurements of the F/B asymmetry as a means to study intrinsic, FSI-independent, nuclear features.

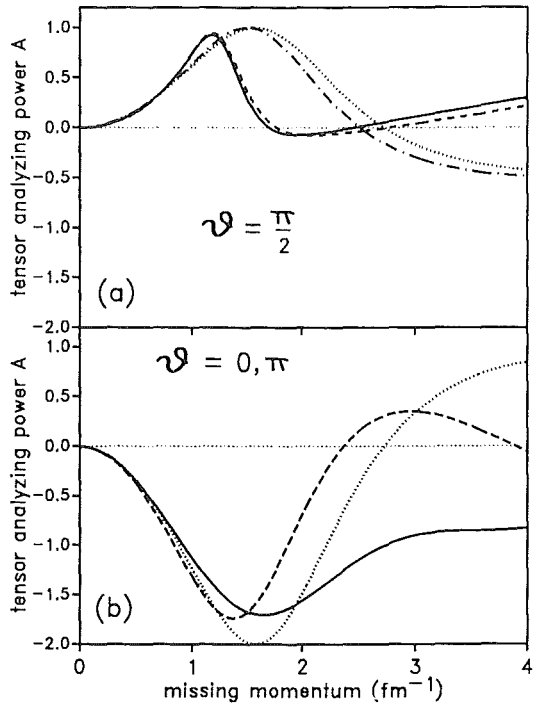

Fig. 1: The tensor analyzing power vs. the missing momentum p_m. Panel (a) shows $A^{PWIA}(p_m, \theta = 90^o)$ calculated using the Bonn wave function (dotted line) and calculated using the Paris wave function (dash-dotted line) and also $A(p_m, \theta = 90^o)$ calculated with the Bonn wave function (solid line) and with the Paris wave function (dashed line). Panel (b) shows $A^{PWIA}(p_m, \theta = 0^o) = A^{PWIA}(p_m, \theta = 180^o)$ (dotted line) and A calculated including FSI for $\theta = 0^o$ (solid line) and $\theta = 180^o$ (long-dashed line).

References:

[1] J.Mougey (spokesperson), CEBAF Proposal No. E-89-044; R.G.Milner (spokesperson), CEBAF Proposal No. E-91-007; D.F.Geesaman (spokesperson), CEBAF Proposal No. E-91-011.

[2] R.J.Glauber, in: *Lectures in Theoretical Physics*, v.1, ed. W.Brittain and L.G.Dunham. Interscience Publ., N.Y., 1959; R.J.Glauber and G.Matthiae, *Nucl. Phys.* **B21** (1970) 135.

[3] A.Bianconi, S.Jeschonnek, N.N.Nikolaev and B.G.Zakharov, Phys. Lett. B 343 (1995) p.13.

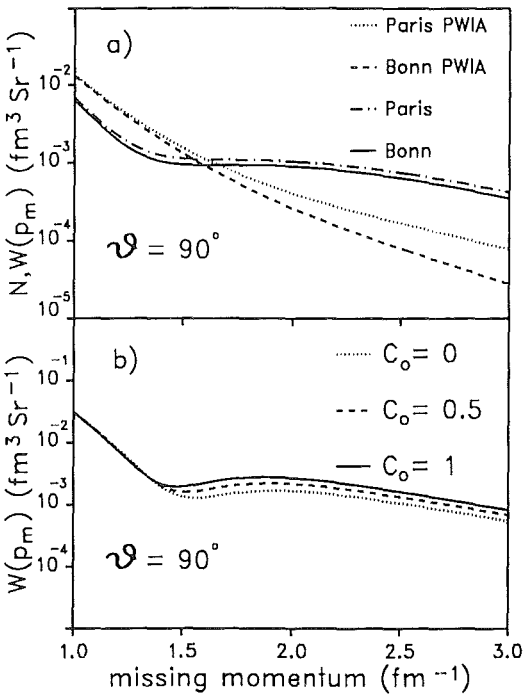

Fig. 2: (a) The forward-backward asymmetry A_{FB} vs. p_m for W_+ calculated with the Bonn wave function (solid line) and the Paris wave function (dashed line). (b) The forward-backward asymmetry A_{FB} vs. p_m for W_+ (solid line) and W_o (dotted line) calculated with the Bonn wave function.

[4] R.Machleidt, K.Holinde, and C.Elster, *Phys. Rep.* **149** (1987), 1.

[5] M.Lacombe et al., *Phys. Lett.* **B101**, 139 (1981).

[1]Istituto Nazionale di Fisica Nucleare, Sezione di Pavia, Pavia, Italy

[2]Dipartimento di Fisica Nucleare e Teorica, Università di Pavia, Italy

[3]also at: L.D.Landau Institute for Theoretical Physics, GSP-1, 117940, ul.Kosygina 2, V-334 Moscow, Russia

Do final state interaction obscure short range correlation effects in quasielastic $A(e,e'p)$ scattering?

A.Bianconi[1,2], S.Jeschonnek, N.N.Nikolaev[3], B.G.Zakharov[3]

Quasielastic $(e,e'p)$ scattering on nuclei at large missing momentum p_m is a relevant tool for the investigation of short-distance nucleon-nucleon interaction (initial state two-nucleon correlations (ISC)) in the nuclear medium and constitutes an important part of the CEBAF experimental program [1]. The measured p_m distribution is distorted by final state interaction (FSI) of the struck proton in the target nucleus debris. In the CEBAF range of energies, the radius b_o of the FSI is very close to the radius r_c of ISC. This makes FSI an important background in the production of protons with large p_m, which may obscure the relationship between the observed p_m distribution and the ISC.

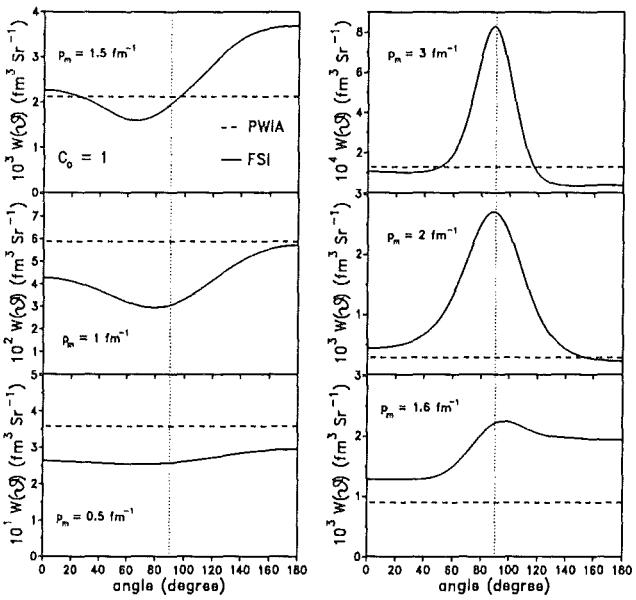

Fig. 1: The angular dependence of the missing momentum distribution $W(\vec{p}_m)$ for different missing momenta p_m (full line). For comparison, the corresponding value of the single particle momentum distribution $N(p_m)$ is also plotted (dotted line).

We have calculated the effect of FSI in $^4He(e,e'p)$ scattering, employing a model Jastrow-like wave function with a mean-field term and central nucleon-nucleon correlations[2],

$$\Psi(1,2,3,4) = \Psi_o(1,2,3,4)$$
$$\times[1 - C(1-2)][1 - C(1-3)]\ldots[1 - C(3-4)],$$

with $C(1-2)$ of the form $C_o F(r_{1,2}/r_c)$. We concentrate on the region of 4-momentum transfer squared $Q^2 \gtrsim$(1-2)GeV^2. In this kinematical regime, FSI can be described by Glauber's multiple scattering theory [3], which simplifies the evaluation of FSI effects. Multiple correlation and rescattering terms have been taken into account at all orders.

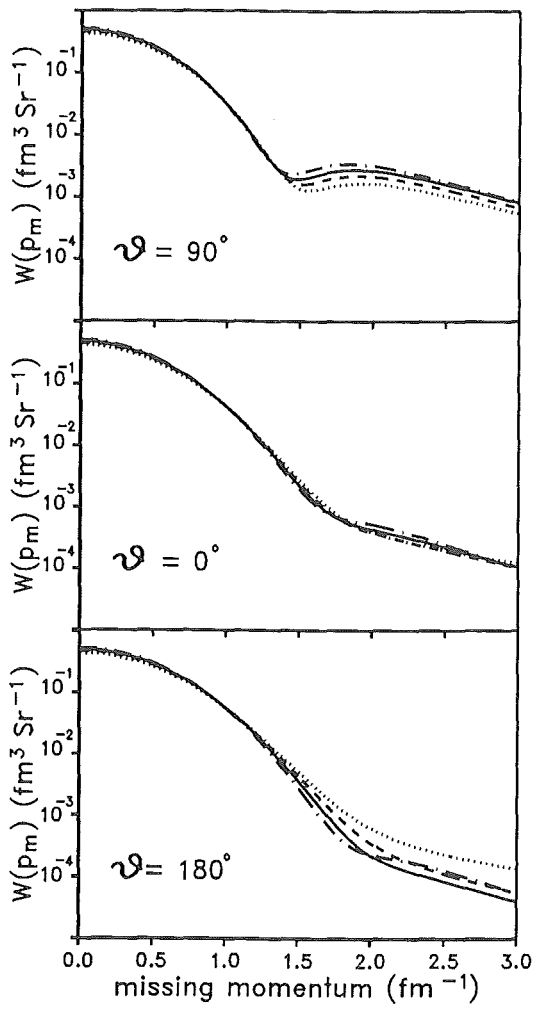

Fig. 2: In each panel the missing momentum distribution $W(\vec{p}_m)$ for correlation radius $r_c = 0.5fm$ is plotted for hard core correlations, $C_o = 1$, (solid line), soft core correlations, $C_o = 0.5$, (dashed line) and no correlations at all, $C_o = 0$ (dotted line). The dot-dashed curve is calculated for $C_o = 1$, $r_c = 0.6fm$. The upper panel shows the results for $\theta = 90^o$, $\theta = 0^o$ is shown in the middle panel and $\theta = 180^o$ is shown in the lower panel. The other parameter is $R_o = 1.29fm$.

We show how FSI lead to an anisotropic p_m distribution, with the dominance of FSI effects in transverse kinematics and significant FSI corrections to ISC effects in parallel kinematics. In the latter case, the most striking effect is a marked forward/backward asymmetry. We show that the forward/backward averaged distribution is much less sensitive to FSI ef-

fects. We find a strong effect of quantum-mechanical interference of correlations and FSI which is different from the quasi-classical expectation, showing an enhancement of FSI-dominated distributions when a hard-core repulsion is introduced. In addition the effect of correlations on the integrated transparency is found to be small. The multiple rescattering and correlation series is shown to converge very slowly. This is an important finding in itself, suggesting the inadequacy of few-nucleon clustering as an approach to (e,e'p) scattering.

In Fig. 1 we show the angular distribution $W(\vec{p}_m)$ for six different values of the missing momentum p_m in the range $0.5 - 3fm^{-1}$. One can notice how the FSI generated asymmetry and anisotropy arise in the critical range $1 - 2fm^{-1}$.

To illustrate this general insensitivity of FSI effect with respect to the nuclear wave function details in Fig. 2 we show distributions corresponding to different choices for the parameters of the initial state C_o, r_c.

Summarizing the main results, we have presented a detailed study of FSI effects in $^4He(e,e'p)X$, with special stress on the comparison with short distance initial state effects. Our findings show the inadequacy of many of the current ideas on the field (semiclassical intuition, relevance of short range correlations in the tails of the distributions and in integrated nuclear transparency, few-body clustering approximations). Our results suggest that the experimental separation of the FSI and ISC effects is more difficult than previously thought.

References:

[1] J.Mougey (spokesperson), CEBAF Proposal No. E-89-044; R.G.Milner (spokesperson), CEBAF Proposal No. E-91-007; D.F.Geesaman (spokesperson), CEBAF Proposal No. E-91-011.

[2] A.Bianconi, S.Jeschonnek, N.N.Nikolaev and B.G.Zakharov, Phys. Lett. B338 (1994) 123.

[3] R.J.Glauber, in: *Lectures in Theoretical Physics*, v.1, ed. W.Brittain and L.G.Dunham. Interscience Publ., N.Y., 1959; R.J.Glauber and G.Matthiae, *Nucl. Phys.* **B21** (1970) 135.

[1]Istituto Nazionale di Fisica Nucleare, Sezione di Pavia, Pavia, Italy

[2]Dipartimento di Fisica Nucleare e Teorica, Università di Pavia, Italy

[3]also at: L.D.Landau Institute for Theoretical Physics, GSP-1, 117940, ul.Kosygina 2, V-334 Moscow, Russia

Universal pattern in (e,e'p) at large missing momenta: Quasi-deuteron or diffractive final state interactions?

A.Bianconi[1,2], S.Jeschonnek, N.N.Nikolaev[3], B.G.Zakharov[3]

In $(e, e'p)$ scattering on nuclei at large missing momentum p_m, the PWIA (plane wave impulse approximation, which neglects any rescattering in the final state) distribution at large missing momenta p_m is dominated by the universal short range behavior of the nuclear ground state. However, the measured p_m distribution is distorted by final state interaction (FSI) of the struck proton in the target nucleus debris. In particular at large missing momenta $p_m \gg p_{Fermi}$ the distortion is strong enough to create universal patterns that are independent of the details of the nuclear wave function. Here we show a comparison of large p_m distributions calculated in different models for the wave function of both ^4He and deuteron. Universal features are evident.

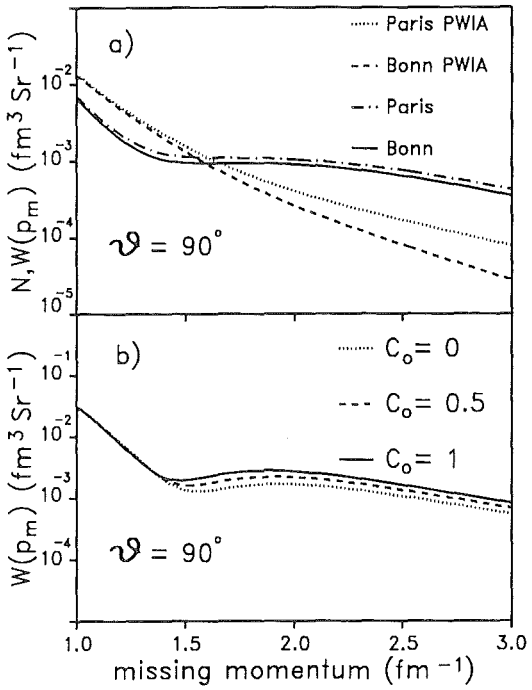

Fig. 1: a) The PWIA missing momentum distribution $N(p_m)$ in the $D(e, e'p)$ reaction calculated with the Bonn wave function (dashed line) and with the Paris wave function (dotted line) and the full missing momentum distribution $W(\vec{p}_m)$ including FSI in the $D(e, e'p)$ reaction at $\theta = 90^o$ calculated with the Bonn wave function (solid line) and the Paris wave function (dash-dotted line). b) The full missing momentum distribution $W(\vec{p}_m)$ including FSI in the $^4He(e, e'p)$ reaction for hard core correlations $C_o = 1$ (solid line), soft core correlations $C_o = 0.5$ (dashed line), and pure mean field, $C_o = 0$ (dotted line).

We have calculated the effect of FSI in $(e, e'p)$ scattering, on: (I) ^4He, with a pure mean-field wave function $\Psi_o(1, 2, 3, 4)$; (II) again ^4He, with a model Jastrow-like wave function with a mean-field term and central nucleon-nucleon correlations,

$$\Psi(1, 2, 3, 4) = \Psi_o(1, 2, 3, 4)$$

$$[1 - C(1 - 2)][1 - C(1 - 3)] \ldots [1 - C(3 - 4)],$$

with $C(1 - 2)$ of the form $C_o F(r_{1,2}/r_c)$; (III) Deuteron, with a realistic Bonn model [1] wave func-

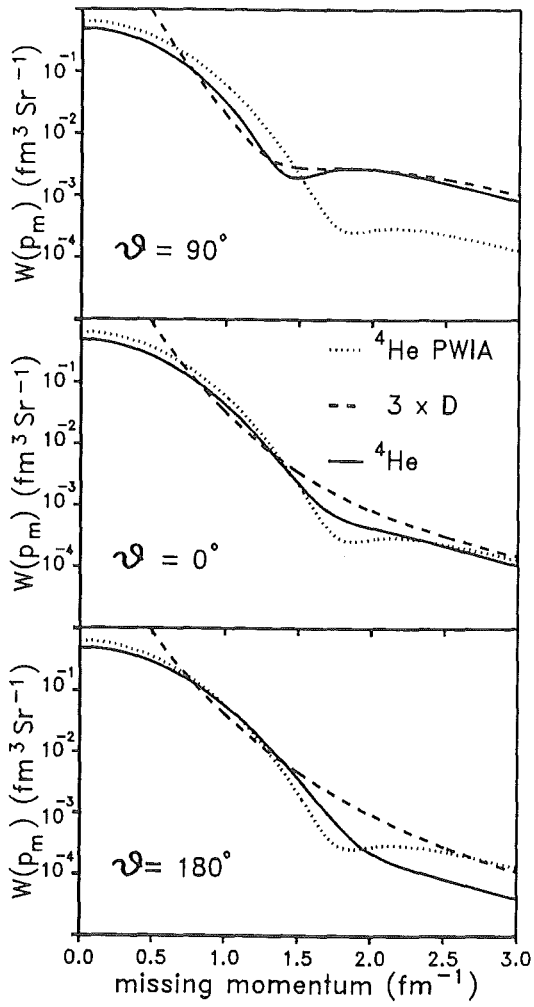

Fig. 2: The full missing momentum distribution $W(\vec{p}_m)$ for the $^4He(e, e'p)$ reaction (solid line) and for the $D(e, e'p)$ reaction (dashed line) multiplied with a factor of 3 to account for the higher number of FSI scatterers in ^4He. For comparison, the PWIA missing momentum distribution $N(p_m)$ for ^4He is also shown (dotted line). On top, we show transverse kinematics, $\theta = 90^o$, and in the middle and the lower panel we show parallel and antiparallel kinematics, $\theta = 0^o$ and $\theta = 180^o$.

tion including both S and D waves, (IV) again Deuteron, with Paris model [2] wave function. We concentrate on the region of 4-momentum transfer squared $Q^2 \gtrsim$(1-2)GeV^2. In this kinematical regime, FSI can be described by Glauber's multiple scattering theory [3], which simplifies the evaluation of FSI effects. They are dominated by diffractive incoherent nucleon-nucleon rescattering, and scarcely affected by the details of the nuclear structure.

In Fig. 1 we show the distribution $W(\vec{p}_m)$ for Deuteron within both Bonn and Paris models. The relevant differences in the PWIA distributions disappear when FSI are included. Similar negligible differences among the curves relative to ^4He with or without correlations are evident in the same figure (for details and more extensive calculations on the above ^4He and deuteron models, see ref.[4,5,6]).

In Fig. 2 we compare the distributions for ^4He and deuteron (times a factor 3 to take into account the number of nucleons that can take part in the final state interaction with the struck proton). We show both parallel and perpendicular kinematics. Two points should be noted: (a) the large p_m tails look almost the same; (b) in perpendicular kinematics the large p_m tail is one order of magnitude larger than in parallel kinematics. This last point demonstrates that the showed universality does not originate in similar details of the initial nuclear state (only FSI are able to produce anisotropies in the distributions).

Summarizing, we show the inadequacy of the idea that the similarity of large momentum distributions in $(e, e'p)$ is a signal of universal patterns in the nuclear wave function at short distances.

References:

[1] R.Machleidt, K.Holinde, and C.Elster, *Phys. Rep.* **149** (1987), 1.

[2] M.Lacombe et al., *Phys. Lett.* **B101**, 139 (1981).

[3] R.J.Glauber, in: *Lectures in Theoretical Physics*, v.1, ed. W.Brittain and L.G.Dunham. Interscience Publ., N.Y., 1959; R.J.Glauber and G.Matthiae, *Nucl. Phys.* **B21** (1970) 135.

[4] A.Bianconi, S.Jeschonnek, N.N.Nikolaev, and B.G.Zakharov, Phys. Lett. B338 (1994) 123.

[5] A.Bianconi, S.Jeschonnek, N.N.Nikolaev, and B.G.Zakharov, Phys. Lett. B 343 (1995) p.13.

[6] A.Bianconi, S.Jeschonnek, N.N.Nikolaev, and B.G.Zakharov, preprint KFA-IKP(TH)-1995-13, submitted to Nucl. Phys.**A**.

[1]Istituto Nazionale di Fisica Nucleare, Sezione di Pavia, Pavia, Italy

[2]Dipartimento di Fisica Nucleare e Teorica, Università di Pavia, Italy

[3]also at: L.D.Landau Institute for Theoretical Physics, GSP-1, 117940, ul.Kosygina 2, V-334 Moscow, Russia

Hypernuclei with meson-exchange hyperon-nucleon interactions

Zhong-yu Ma*, J.Speth, S.Krewald, Bao-qiu Chen* and A.Reuber

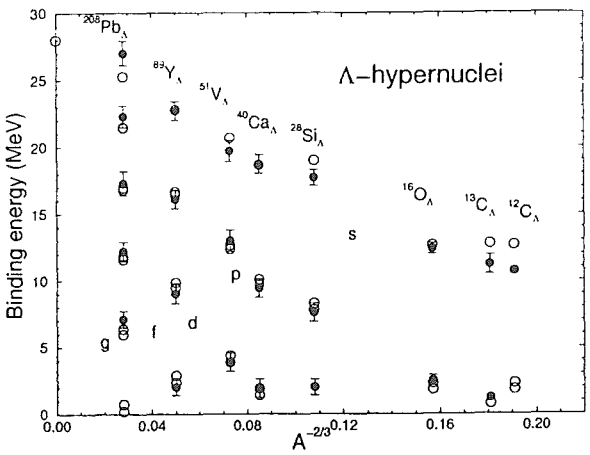

Fig. 1: Single particle levels of Lambda-hypernuclei. Open circles: relativistic mean field model. Solid disks: experimental data

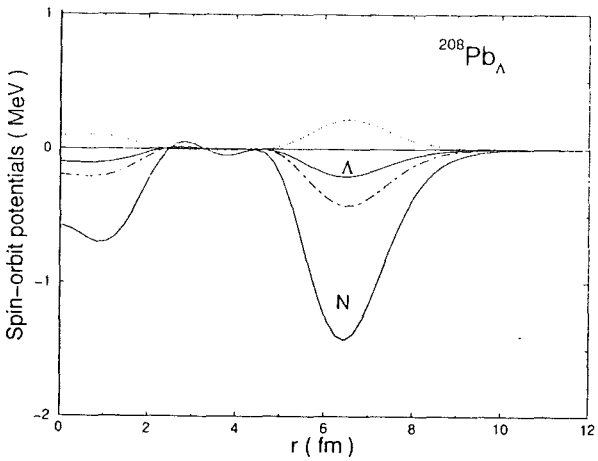

Fig. 2: Spin-orbit potentials of protons and Λ in ^{208}Pb. Dotted: contribution due to tensor couplings. Dash-Dotted: contributions due to scalar and vector potentials.

The interaction between a hyperon and a nucleon contains an attractive part which is produced by exchanging a scalar meson and a repulsive one due to the exchange of a vector meson . The coupling of the ω-meson to the hyperon can be constrained by SU(3)-symmetry, the coupling of the σ-meson to the hyperon is treated as a free parameter in most studies of hypernuclei, however. [1, 2]. It is known that the scalar σ-meson is a fictitious hadron which provides a simple representation of the underlying exchange of two correlated pions and kaons. Recently, the Juelich group has explicitly evaluated the correlated two-pion as well as two-kaon contribution to the baryon-baryon interaction, starting from the Juelich meson-exchange model for pion-pion scattering which describes the pion-pion scattering data up to 1.3 GeV. The results obtained in the hyperon-nucleon channels can be parameterized by means of an exchange of an effective zero-width σ-meson with a suitable coupling constant and a mass of $m_\sigma = 550MeV$. The ratio of the Lambda-sigma coupling strength to the nucleon-sigma coupling strength is found to be 0.502 which is 24 percent less than the value of .621 employed by Mares and Jennings. The two-kaon correlations play an important role, without two-kaon correlations, the ratio is pushed down to 0.36. With these strong constraints for the sigma- as well as rho- exchange, the application of the effective interaction to studies of hypernuclei provides an interesting test of the short range part derived from omega-exchange. Although the omega-nucleon tensor coupling is small and usually neglected, the same is not true for the omega-hyperon coupling. It has a large influence on the spin-orbit interaction of hyperons.

The single particle states of Λ-hypernuclei are calculated self-consistently in the relativistic mean-field approach. The results are shown in Fig.1.

A good agreement with the experimental data from light to heavy hypernuclei is obtained. Very small spin-orbit splittings for the Λ, in comparison with that for nucleons, are observed. The weak spin-orbit splitting for the Λ is the result of the weak scalar and vector couplings, as well as the attractive tensor coupling of the vector meson. The Λ-nucleon interaction in the relativistic mean field theory can be analized by recasting the Dirac equation into a Schroedinger-type equation with equivalent potentials. The spin-orbit potentials are shown in Fig.2. The spin-orbit part of the Λis only 15 percent of that for the nucleons, although the central part of the effective potential for the Λ is about 40 percent of that for the nucleons.

For sigma-hypernuclei, the $\sigma - \Sigma - \Sigma$ coupling strength is relatively weak, and does not provide enough attraction to balance the repulsion produced by the ω-meson. Therefore the Σ-hyperon is no longer bound in a nuclear state, but only in an atomic orbit due to the Coulomb attraction. A weaker effective ω-coupling might lead to a bound Σ–hypernucleus. Further microscopic investigations of this point are therefore required.

References:

[1] R.Brockmann et al., Nucl.Phys.**A355**,365(1981)
[2] J.Mares et al., Phys.Rev.C**49**,2472(1994)
[3] A.Reuber et al.,preprint

* China Institute of Atomic Energy, Beijing 102413, P.R.China

To fix up the free parameters in a model designed by us to describe D(p,n) reactions [1], we also calculated the cross section for pion absorption on the deuteron. This reaction $\pi^+ D \to 2p$ has already been studied in detail with rather different aproaches. Alberg et al. [2] use a field-theoretical method, while the calculations of Niskanen [3] are based on a coupled channel formalism. Alternativly, Maxwell, Weise and Brack [4, 5] employ quite a simple model where the following three processes contribute to the T-matrix: the impulse approximation, the p-wave rescattering and the s-wave rescattering (c. fig. 1)

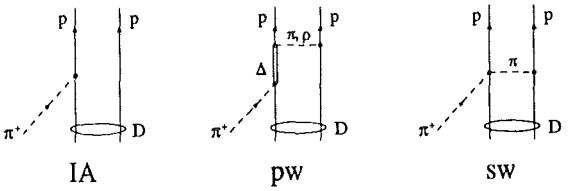

Fig. 1: Contributions to $\pi^+ D \to 2p$: Impulse approximation (IA), p-wave rescattering (pw) and swave-rescattering (sw).

We adopt the main features of the model of Maxwell et al. but use a ρ-exchange instead of correlated $2\pi(1^-)$ in the p-wave rescattering term. At the vertices, formfactors of the type

$$f_\pi(q) = f_\pi \left(\frac{\Lambda_\pi^2 - m_\pi^2}{\Lambda_\pi^2 - q^2} \right), \quad f_\rho(q) = f_\rho \left(\frac{\Lambda_\rho^2 - m_\rho^2}{\Lambda_\rho^2 - q^2} \right)$$

are employed. The Cutoffs $\Lambda_\pi, \Lambda_\rho$ are treated as free parameters, while for the coupling constants we choose $f_{\pi NN}^2/4\pi = 0.081$, $f_{\rho NN}^2/4\pi = 4.67$ and $f_{\pi N\Delta} = 2 f_{\pi NN}$, $f_{\rho N\Delta} = 2 f_{\rho NN}$.
The cross section is calculated in the LAB-frame where the incoming pion can be represented by a plane wave. The deuteron and the 2p wavefunctions are taken from the Paris potential [6].

Results

In fig. 2 the total cross section $\sigma_{\pi^+ D \to 2p}$ is shown as a function of the πD center of mass momentum q_{CM}. The solid curve has been calculated with $\Lambda_\pi = 1.0$ GeV and the dashed one with $\Lambda_\pi = 1.1$ GeV. For Λ_ρ, we always use a value of 2.0 GeV. The crosses in fig. 2 illustrate the theoretical results of Maxwell et al. [4] which are reproduced very well for $\Lambda_\pi = 1.0$ GeV. Near threshold, the s-wave rescattering is the dominant contribution, while at higher pion momenta the p-wave rescattering mechanism is most important and responsible for the typical resonance structure of the cross section. The experimental data are from ref. [7, 8].

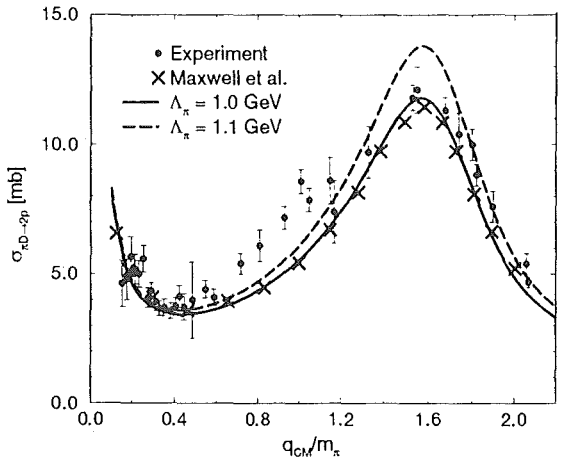

Fig. 2: Total cross section for pion absorption on the deuteron with $\Lambda_\rho = 2.0$ GeV and two values for Λ_π. The crosses show the results of Maxwell et al. [4].

Fig. 3 illustrates the differential cross section $d\sigma/d\Omega$ as a function of $\cos(\theta_{CM})$, where θ_{CM} is the angle between pion momentum and relative momentum of the two outgoing protons in the πD center of mass frame. Again, our calculations are in good agreement with the empirical values when choosing $\Lambda_\pi = 1.0$ GeV, $\Lambda_\rho = 2.0$ GeV. The shape of the curve is sensitive to the relation between the spin-longitudinal and spin-transversal contribution to the tensor part of the p-wave rescattering potential. This fact allows to fix both cutoff parameters Λ_π and Λ_ρ simultaneously, which is not possible by fitting the total cross section alone.

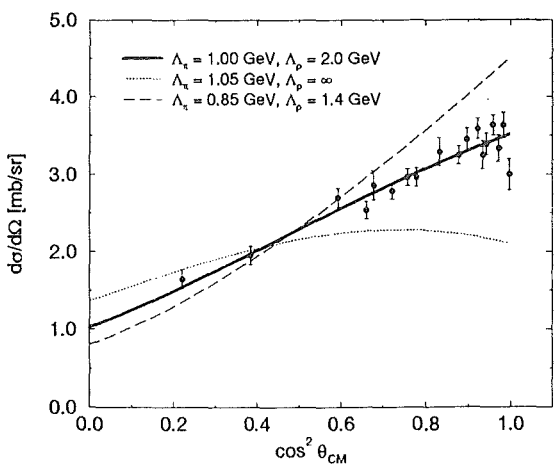

Fig. 3: Differential cross section for pion absorption on the deuteron at $q_{CM}/m_\pi = 1.53$ with different values for Λ_π and Λ_ρ. Experimental data from ref. [9].

References:

[1] C. A. Mosbacher, Mesonaustauschströme in (p,n)-Reaktionen am Deuterium (Diplomarbeit, Forschungszentrum Jülich, 1995).

[2] M. A. Alberg, E. M. Henley, G. A. Miller, and J. F. Walker, Nucl. Phys. **A306**, 447 (1979).

[3] J. A. Niskanen, Nucl. Phys. **A298**, 417 (1978).

[4] O. V. Maxwell, W. Weise, and M. Brack, Nucl. Phys. **A348**, 388 (1980).

[5] M. Brack, D. O. Riska, and W. Weise, Nucl. Phys. **A287**, 425 (1977).

[6] M. Lacombe *et al.*, Phys. Rev. C **21**, 861 (1980).

[7] C. Richard-Serre *et al.*, Nucl. Phys. **B20**, 413 (1970).

[8] B. M. Preedom *et al.*, Phys. Rev. **C17**, 1402 (1978).

[9] D. Aebischer *et al.*, Nucl. Phys. **B108**, 214 (1976).

Meson exchange currents in (p,n) reactions on a deuteron target

C. A. Mosbacher and F. Osterfeld

Meson exchange currents have been used with great succes in a variety of theoretical calculations, including radiative np capture, nuclear magnetic moments and inelastic electron scattering [1, 2]. But only little is known about their importance in hadronic charge exchange reactions like (p,n). To investigate the influence of two-body effects especially in the so-called "dip-region" between the quasi-elastic peak and the Δ-peak, we developped a model for D(p,n)-reactions with goes beyond impulse approximation by including contributions of meson exchange currents in the target [3].

1. Theory

Fig. 1 shows the diagrams which contribute to D(p,n) in impulse approximation, and fig. 2 shows those meson exchange diagrams which are included in our model so far. In the experiment [4], the incoming proton has a kinetic energy of 789 MeV, so the

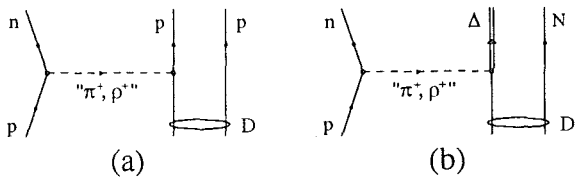

Fig. 1: Diagrams contributing to D(p,n) in the impulse approximation: (a) quasi-elastic scattering, (b) direct delta production.

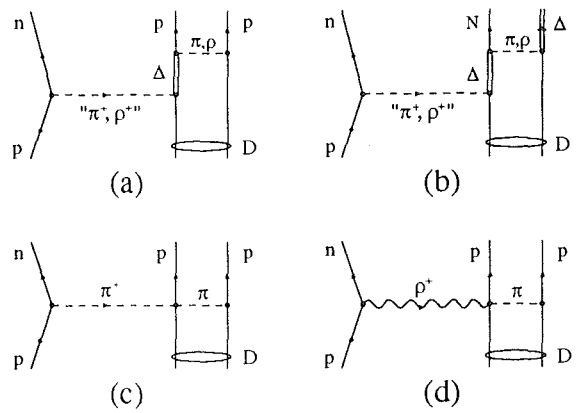

Fig. 2: Meson exchange diagrams contributing to D(p,n): (a) p-wave rescattering, (b) delta production after rescattering, (c) s-wave rescattering, (d) Kroll-Rudermann diagram.

deuteron is broken up in the reaction and the production of an additional pion via the Δ-resonance is easily possible. Only the energy and the scattering angles of the outgoing neutron are measured, therefore we calculate the inclusive double differential cross section $d^2\sigma/dE_n d\Omega_n$ as a function of the energy transfer ω onto the target. In the LAB-frame and with two outgoing protons on the target side, this cross-section can be written

$$\frac{d^2\sigma_{2p}}{dE_n\, d\Omega_n} = \frac{M^2}{(2\pi)^5}\frac{p_n}{p_p}\frac{1}{2} \times \int d^3p\, \frac{1}{6}\sum_{Spin} |T_{fi}|^2\ (2\pi)\,\delta(E-\omega-2M), \tag{1}$$

where $\vec{p}$,E are the relative momentum and the total energy of the two protons, respectively. In the case that there is a Δ-resonance in the final state, which is supposed to decay freely into a nucleon and a pion, an additional integration over the invariant mass s_Δ has to be performed. This yields

$$\frac{d^2\sigma_{NN\pi}}{dE_n d\Omega_n} = \int \frac{ds_\Delta}{\pi}\,\frac{d\sigma_{N\Delta}}{dE_n d\Omega_n}\,\frac{\Gamma_\Delta/4m_\Delta}{(m_\Delta-\sqrt{s_\Delta})^2+\Gamma_\Delta^2/4}, \tag{2}$$

where $d\sigma_{N\Delta}/\,dE_n d\Omega_n$ is given by an expression analogous to equation (1).

For the calculation of the T-Matrix, appropriate transition operators are needed, as well as the wavefunctions for the incoming and outgoing particles. The transition operators describing the diagrams in impulse approximation can be deduced from effective NN-NN and NN-$N\Delta$ transition matrices, respectively, which are e. g. given in ref. [5]. The operators describing diagrams with meson exchange currents on the target-side contain in addition rescattering potentials. In our model, the rescattered particle is either a pion or a ρ-meson, and the corresponding rescattering potentials follow directly from well known interaction lagrangians [6, 7]. Coupling constants and cutoff parameters have been fixed with the help of the $\pi^+ D \to 2p$ reaction.

For the wavefunctions of the proton projectile and the measured neutron we use distorted waves in eikonal approximation [8]. The deuteron wavefunction can be deduced from the Paris NN-interaction. The Paris potential is also applied to calculate the 2p-wavefunction by solving the Schrödinger equation numerically [9]. This includes final states interactions of the outgoing protons. If the final state is a $N\Delta$-system, however, correlations cannot be treated in the same way because of the appearance of the Δ-propagator. For simplicity, we apply plane waves instead and neglect any $N\Delta$-interaction.

2. Results

In fig. 3 the results of our calculations are compared with the experimental data for different scattering angles θ_n. The quasi-elastic peak is reproduced very

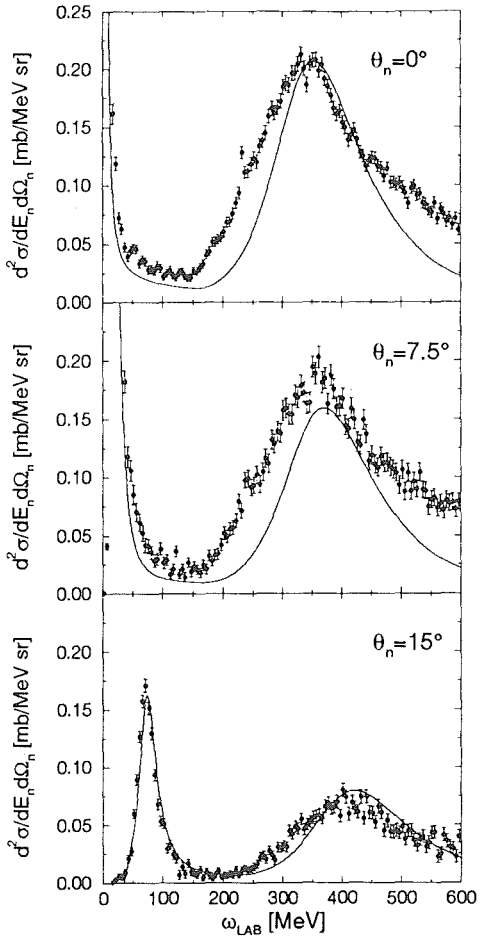

Fig. 3: Differential cross section for D(p,n) in the LAB–frame as a function of the energy transfer ω for scattering angles $\theta_n = 0^o$, 7.5^o and 15°. Experimental data from ref. [4]

well and clearly dominated by the diagram of fig. 1(a). This process also contributes in the dip–region (around $\omega \approx 100$ MeV for $\theta_n = 0^o$), but about half of the calculated cross–section there is due to the meson exchange currents, especially diagram fig. 2(a). Nevertheless, our model still underestimates the data in the dip–region. A more detailed analysis shows that the cross section is missing in the spin–transversal channel. Probably some additional meson exchange currents like those shown in fig. 4 must be taken into account in order to explain the discrepancies.

As far as the Δ–peak is concerned, the magnitude of the calculated cross–section is correct, but the position of the peak seems to be shifted to higher energies when compared with the data. This might be due to the neglection of $N\Delta$–interactions. Indeed we found a shift of the peak by replacing the plane wave for the $N\Delta$–system and accounting for a very simple $N\Delta$–potential like $V(r) = -V_0 \exp(-r^2/r_0^2)$ with $V_0 = 45$ MeV and $r_0 = 1.4$ fm (c. fig. 5). We would like to emphasize that we did not modify the Δ–propagator, which means that our treatment of the $N\Delta$–interaction is not consistent so far. On the lower edge of the Δ–resonance, there may also be a significant contribution from coherent pion–production which is not included in our model. Both $N\Delta$–interaction and coherent pion–production could be calculated within the Δ–hole–model [10] and are subject of further investigation.

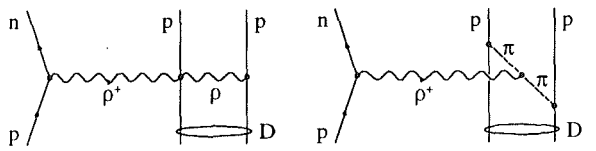

Fig. 4: Other possible meson exchange diagrams, contributing to the spin–transversal channel in D(p,n).

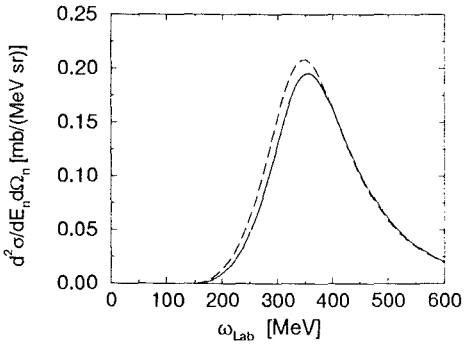

Fig. 5: Contribution of the Δ–production diagram (fig. 1(a), $\theta_n = 0^o$) without $N\Delta$–interaction (full line) and with a simple gaussian $N\Delta$–potential (dashed line).

References:

[1] M. Chemtob, in *Mesons in Nuclei*, edited by M. Rho and D. Wilkinson (North–Holland, Amsterdam, 1979), Vol. 2, p. 495.

[2] D. O. Riska, Phys. Rep. **181**, 207 (1989).

[3] C. A. Mosbacher, Mesonaustauschströme in (p,n)–Reaktionen am Deuterium (Diplomarbeit, Forschungszentrum Jülich, 1995).

[4] D. Prout *et al.*, private communication.

[5] T. Udagawa, P. Oltmanns, F. Osterfeld, and S. W. Hong, Phys. Rev. C **49**, 3162 (1994).

[6] R. Machleidt, K. Holinde, and C. Elster, Phys. Rep. **149**, 1 (1987).

[7] D. S. Koltun and A. S. Reitan, Phys. Rev. **141**, 1413 (1966).

[8] B. K. Jain and A. B. Santra, Phys. Rep. **230**, 1 (1993).

[9] M. Lacombe *et al.*, Phys. Rev. C **21**, 861 (1980).

[10] F. Lenz, Ann. Phys. **95**, 348 (1975).

Calculation of the NNϕ Vertex in a Hadronic Framework

V. Mull, K. Holinde, and J. Speth

The $NN\phi$-Vertex is of particular interest for our understanding of low-energy strong interaction, non-perturbative QCD and the structure of the nucleon. The ϕ meson is believed to be an almost pure $\bar{s}s$ state whereas the nucleon consists, at least in a naive constituent quark model, of u and d quarks only. Therefore, the ϕ meson cannot couple directly to the nucleon, at least in this scenario, in line with the phenomenological OZI-rule [1]. On the other hand, it has been known for quite some time that ϕ production is enhanced beyond expectation from the OZI-rule in various hadronic reactions [2].

Such an enhancement could point to the existence of resonant gluonic intermediate states (glueballs) or a sizable $\bar{s}s$ component in the nucleon, see Ref. [2]. However, one should be aware that OZI-forbidden transitions can go via two-step processes in which each individual transition is OZI-allowed [3]. In this way the ϕ-meson can couple via non-glueball, i.e. hadronic intermediate states to the nucleon.

In a recent work we have shown that the sizable cross section for the annihilation reaction $\bar{p}p \longrightarrow \phi\phi$ [4] can be explained in a hadronic framework by two-step processes with $\bar{\Lambda}\Lambda, \bar{\Sigma}\Sigma$ intermediate states [5].

Now we want to address the question what is the effective coupling constant of the ϕ meson to the nucleon. The coupling of a vector meson to the nucleon is described by a field theoretical Lagrangian. The general form of this Lagrangian looks like

$$\begin{aligned} \mathcal{L}_{BBV} &= g_v\, \bar{\Psi}_\alpha\, \gamma^\mu\, \Psi_\beta\, \Phi^j_\mu \qquad (1) \\ &+ \frac{f_v}{4M_N}\, \bar{\Psi}_\alpha\, \sigma^{\mu\nu}\, \Psi_\beta\, (\partial_\mu \Phi^j_\nu - \partial_\nu \Phi^j_\mu) \end{aligned}$$

In addition, form factors are generally included to take into account the effects from meson clouds and the inner structure of the particles.

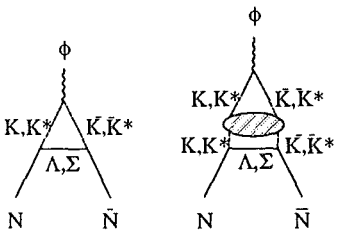

Fig. 1: The hadronic model for the $NN\phi$ Vertex function consists of Born terms (left-hand side) and interaction diagrams (righthand side).

We performed a calculation of the $NN\phi$ vertex function in a hadronic picture, considering $\overline{K}K, \overline{K^*}K - \overline{K}K^*$ and $\overline{K^*}K^*$ intermediate states, cf. fig. 1. The interaction T-matrix is calculated in a coupled channels framework with π, ρ, ω, ϕ exchange diagrams [6].

The time-like vertex functions $\Gamma^{L=0}$ and $\Gamma^{L=2}$ can be calculated from the diagrams shown in fig. 1 in a straightforward way. (L being the angular momentum in the $\overline{N}N$ system!) In analogy to the coupling constants g and f, two t-dependent coupling functions $G(t)$ and $F(t)$ can be defined, which describe the structure of the $NN\phi$ vertex, cf. eq.1. These coupling functions have to be thought of as the product of coupling constant and form factor. They are given by the following relations:

$$\begin{aligned} G(t') &= \frac{\sqrt{6}\, t'^{\frac{3}{4}}}{16\, q_0^2}((2M_N + \frac{t'^{\frac{1}{2}}}{2})\, \Gamma^{L=2}(t') \\ &+ \sqrt{2}(\frac{t'^{\frac{1}{2}}}{2} - M_N)\, \Gamma^{L=0}(t')) \qquad (2) \\ F(t') &= \frac{\sqrt{6}\, M_N t'^{\frac{1}{4}}}{8\, q_0^2}(-(M_N + t'^{\frac{1}{2}})\, \Gamma^{L=2}(t') \\ &+ \sqrt{2}(\frac{t'^{\frac{1}{2}}}{2} - M_N)\, \Gamma^{L=0}(t')) \qquad (3) \end{aligned}$$

The results for the imaginary part of the time-like coupling functions (spectral functions) are shown in fig. 2. There, the contributions of various intermediate states either with Born terms only or with the full interaction taken into account are plotted. The spectral functions resulting from the $\overline{K}K$ and $\overline{K^*}K - \overline{K}K^*$ states have a negative sign, whereas the $\overline{K^*}K^*$ channel gives a positive contribution to the spectral function.

The space-like coupling functions are then obtained using a dispersion integral of the following form:

$$G(t) = \frac{1}{\pi} \int_{2m_K}^{\infty} \frac{Im\, G(t')}{t - t'}\, dt' \qquad (4)$$

$$F(t) = \frac{1}{\pi} \int_{2m_K}^{\infty} \frac{Im\, F(t')}{t - t'}\, dt' \qquad (5)$$

Assuming a monopole structure for the form factor, as it is commonly used for instance in the Bonn NN potential[7], values for the coupling constants and the

Table 1: Values for the coupling constants and the cutoff parameter of the form factor as fitted to the coupling function $G(t)$ and $F(t)$. Here a monopole structure is assumed for the form factor. The results are shown for various intermediate states in the vertex.

	g	$g^2/4\pi$	Λ_g[MeV]	f	$f^2/4\pi$	Λ_f[MeV]
			Born Terms only			
$\overline{K}K$	-0.18	0.003	1700	-0.08	0.001	1350
$\overline{K^*}K - \overline{K}K^*$	-0.34	0.009	2025	-0.17	0.002	1900
$\overline{K^*}K^*$	0.19	0.003	2200	0.29	0.007	2200
all mes.	-0.33	0.009	1750	0.09	0.001	3300
			with Interaction			
$\overline{K}K$	-0.32	0.008	1650	-0.15	0.008	1350
$\overline{K^*}K - \overline{K}K^*$	-0.39	0.012	2000	-0.20	0.003	1900
$\overline{K^*}K^*$	0.25	0.005	2200	0.40	0.013	2200
all mes.	-0.47	0.018	1650	0.14	0.001	3350

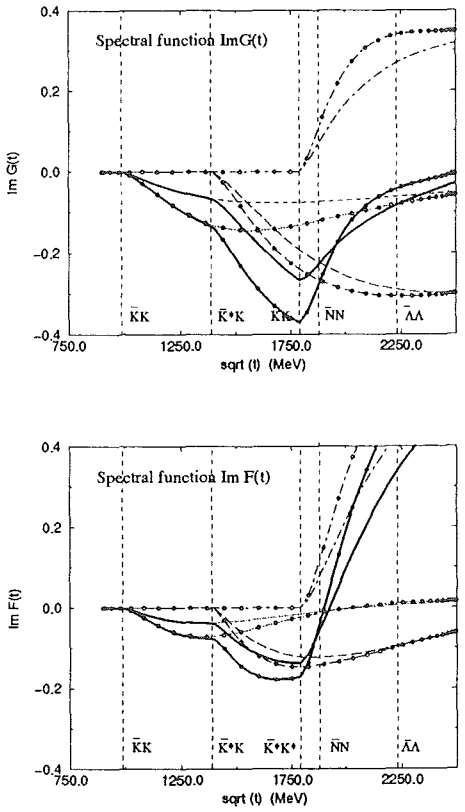

Fig. 2: Spectral functions $Im\,G(t)$ (upper part) and $Im\,F(t)$ (lower part) for the annihilation reaction $\overline{N}N \rightarrow \phi$ in the pseudo-physical region. The solid lines denote the results with all meson combinations $\overline{K}K$, $\overline{K^*}K - \overline{K}K^*$, $\overline{K^*}K^*$ included. The dotted lines include only the $\overline{K}K$ channel, the dashed ones the $\overline{K^*}K - \overline{K}K^*$ channel and the dash-dotted ones the $\overline{K^*}K^*$ channel. The lines with circles are the results with meson-meson interaction, whereas the plain curves include the Born terms only. The vertical dashed lines indicate the various thresholds.

cutoff parameters can be calculated through a two-parameter fit to the calculated coupling function. The results are shown in table 1.

$$G(t) \stackrel{!}{=} g\,\frac{\Lambda_g^2 - m_\phi^2}{\Lambda_g^2 - t} \tag{6}$$

$$F(t) \stackrel{!}{=} f\,\frac{\Lambda_f^2 - m_\phi^2}{\Lambda_f^2 - t} \tag{7}$$

The resulting coupling strength of the ϕ meson to the nucleon with all meson combinations and the interaction included for the vector coupling ($g^2/4\pi \approx 0.01$) is rather small compared to the coupling constant of the ω and ρ meson ($g_\omega^2/4\pi \approx 20$, $g_\rho^2/4\pi \approx 0.8$)[7].
First, this is due to the fact, that the individual contributions from the different intermediate states are small. Additionally, the contributions from the $\overline{K}K$ and $\overline{K^*}K - \overline{K}K^*$ channels to the spectral function are negative, whereas the one from the $\overline{K^*}K^*$ channel is positive. Therefore, the cancellation between these contributions results in a small coupling constant g. The form factor is a rather soft one with a cutoff mass $\Lambda_g = 1650 MeV$.
For the tensor like coupling f the resulting coupling constant $f^2/4\pi \approx 0.001$ is even smaller. In this case, there is an almost complete cancellation between the contributions of the various intermediate channels. The form factor for the tensor coupling f is very hard ($\Lambda_f = 3350 MeV$).
In addition to these mesonic intermediate state, the ϕ meson might couple to the nucleon also via baryonic intermediate states ($\overline{\Lambda}\Lambda$, $\overline{\Sigma}\Sigma$). We plan to investigate the possible impact of $\overline{\Lambda}\Lambda$ and $\overline{\Sigma}\Sigma$ intermediate states on the $NN\phi$ vertex and in particular on coupling constants and form factors in the near future.

References:

[1] S. Okubo, *Phys. Lett.* **5** (1963) 165, G. Zweig, CERN Reports TH-401, TH-412(1964), unpublished, J. Iizuka, *Progr. Theor. Part. Sci.* 37-38(1966)21.

[2] J. Ellis, E. Gabathuler, and M. Karliner, *Phys. Lett.* **B 217** (1989) 173.

[3] see e.g. H.J. Lipkin, *Nucl. Phys.* **B 244** (1984) 147; *ibid.* **B 291** (1987) 729.

[4] O. Steinkamp, PhD.-thesis, University of Bonn.

[5] V. Mull, K. Holinde, and J. Speth, *Phys. Lett.* **B 334** (1994) 295.

[6] V. Mull and K. Holinde, in preparation.

[7] R. Machleidt, K. Holinde, Ch. Elster, *Phys. Rep.* **149** (1987) 1.

Annihilation of the $\overline{N}N$ System into more than two Pions

V. Mull, E.A. Veit*, M. Betz*

The $\overline{N}N$ system and its physics are well suited for exploring the capabilities and limits of the traditional hadronic picture of strong interactions. Annihilation phenomena are supposedly governed by short distance physics. "Quark effects" are often expected to show up in this system, which are phenomena that cannot be explained in the traditional hadronic picture in an elegant and efficient way. But to unambigously prove or disprove the breakdown of the hadronic picture, a consistent hadronic model of the $\overline{N}N$ interactions has to be constructed. The elastic part of the $\overline{N}N$ interaction can be obtained from a corresponding NN model via a G-parity transformation. Recently, V. Mull and K. Holinde from the IKP/KFA Jüich presented a model for the annihilation part describing annihilation into two-meson channels microscopically [1-3]. All possible two-meson combinations of $\pi, \eta, \rho, \omega, a_0, f_0, a_1, f_1, a_2, f_2$ as well as K and K^* were taken into account. Unfortunately, these channels contribute less than 30% to the total annihilation cross section. The rest has to be attributed to channels with higher-mass mesons, three or more uncorrelated mesons or exotic contributions. These processes were described by a phenomenological parametrization in the $\overline{N}N$ interaction model.

E.A. Veit, M. Betz and coworkers from the IF-UFRGS in Porto Alegre, Brasil constructed recently a hadronic model for the annihilation of the $\overline{N}N$ system into n pions ($n = 2, 3, 4, 5, \ldots$) taking into account nucleon exchange[4,5]. Starting from a fieldtheoretical Lagrangian they obtained a transition amplitude by summing over all possible Feynman diagrams. Annihilation cross sections were calculated using Monte Carlo integration method for the phase space integration. In a first step, they could not include any interactions in the initial or final state. Unfortunately, they were not able to describe experimental data within their model because of this deficiency. From calculations in the two-meson sector it is well known that the inclusion of initial state interaction effects is necessary to obtain the right magnitude for cross sections due to the strong absorptive part of the $\overline{N}N$ potential.

With this project the investigation of the annihilation of the $\overline{N}N$ system into more than two pions was continued with the goal of the inclusion of initial state interaction effects. This calculation of the annihilation process into more than two pions with inclusion of inital state interaction effects is done for the first time.

The $\overline{N}N$ interaction model of the Jülich group and the $\overline{N}N \rightarrow n\pi$ transition model constructed in Porto Alegre had to be combined.

This was done in the following steps:

- The $\overline{N}N \rightarrow \overline{N}N$ amplitude is given in a partial wave expanded form. Since a partial wave expansion for the final state with several particles is not possible, we decided to work in a spin-momentum representation. The transformation from the JLS representation to the momentum-spin representation required for the calculation of the $\overline{N}N \rightarrow n\pi$ transition amplitude has been calculated.
- The calculation of the $\overline{N}N \rightarrow n\pi$ transition potential is extended also for off-shell states.
- The full $\overline{N}N \rightarrow n\pi$ amplitude is calculated using the distorted wave born approximation (DWBA) method. A three-dimensional integral over the intermediate $\overline{N}N$ state momentum has to be computed.
- Cross sections can be calculated From the $\overline{N}N \rightarrow n\pi$ amplitude using the Monte-Carlo integration method for the phase space integration.

Final results for the cross sections can be expected for the very near future. Of particular interest are the results for the ratios of different charge combinations within the same number of pions produced.

We plan to extend this work in the future in the following way:

- to include additionally further baryons to exchange in the transition process $\overline{N}N \rightarrow n\pi$
- to consider also the production of different types of mesons (i.e. $\rho, \omega, K, K^*, \ldots$).

One of us (V.M.) would like to thank all members of the IF-UFRGS, but especially professor Victoria Herscovitz, for their generous hospitality and friendship during his visit in Porto Alegre, Brazil.

References:

[1] V. Mull and K. Holinde, *Phys. Rev.* **C51** (1995)2360.

[2] T. Hippchen, J. Haidenbauer, K. Holinde, and V. Mull, *Phys. Rev.* **C44** (1991)1323.
V. Mull, T. Hippchen, J. Haidenbauer, and K. Holinde, *Phys. Rev.* **C44** (1991)1337.

[3] V. Mull, Ph.D. thesis, Universität Bonn, 1993; Berichte des Forschungszentrums Jülich Nr. 2844, 1993.

[4] E.A. Veit, J. Moraes, M.H. Steffani and T. Kodama, PANIC/93-Particles and Nuclei Intern. Conf., Perugia, Proceed. (1993) 462.

[5] J.Moraes, Ms. Thesis, Instituto de F´sica, UFRGS, september 1995.

* Instituto da Fisica, Universidade Federal do Rio Grande do Sul (UFRGS), Porto Alegre, RS, Brasil

The influence of negative-energy states on proton-proton bremsstrahlung

F. de Jong*,†, K. Nakayama*

Until very recently only the positive energy contributions of the nucleon single and rescattering diagrams were included in calculations of the proton-proton bremsstrahlung (ppγ) reaction, since these diagrams give the most dominant contribution to the transition amplitude. With much progress made in the study of hadronic interactions combined with new ppγ data, a number of authors have started investigating higher order effects in this reaction. For example, the diagrams which contain a $\Delta N\gamma$ vertex turned out to increase the cross-section up to 30 %, due to a very effective interference with the nucleonic current [1]. Also, vector-meson decay processes have been investigated [2, 3, 4].

In this work, we consider the contributions from nucleon negative-energy states to the single and rescattering diagrams. These are of order k in the photon momentum in ppγ reactions. Eden and Gari [3] calculated the single-scattering contributions and found a sizable effect at certain energies and kinematics and argued that this effect can be used to determine the pseudo-vector content of the pino-nucleon coupling. For a dependable calculation however, one has to use a T-matrix which includes negative energy states in a dynamic way and include all possible diagrams. One of the few available nucleon-nucleon(NN) interactions that include nucleon negative-energy states is that based on the spectator-type three dimensional reduction [5] of the Bethe-Salpeter equation. It provides an excellent fit to the phase-shifts up to pion threshold. It is thus very well suited for use in a ppγ calculation which requires a detailed reproduction of the phase-shifts. Since Grosss *et al.* [5] include formfactors depending on the nucleon momentum on NN-meson vertices, the Ward-Takahashi identity requires that the electric part of the $NN\gamma$ vertex is changed to retain gauge invariance.

Our main findings are presented in Fig 1, which gives the cross-section for one of the kinematics of the TRIUMF experiment. The result with only positive energy states (of course the T-matrix still contains negative energy intermediate states) is given by the dashed line. For practical purposes it is equivalent to the result calculated with the Bonn potential (solid line). Adding to our result the single-scattering negative energy diagrams we find the dotted curve. As seen in the figure it provides a dramatic increase in the cross-section. However, upon including the negative energy rescattering diagrams (dash-dotted line), the effect vanishes totally: the sum of all negative energy diagrams is negligible in comparison with the positive energy contributions. Although we could not explicitly find a cause for this behaviour, we think the most probable reason is gauge invariance. When we do not allow for the change in the $NN\gamma$ vertices induced by the NN-meson formfactors, and thus have a model which is not gauge-invariant, the cancellation is less perfect although still there. In conclusion, the approximation of the nucleonic current by its positive energy contribtutions appears to be justified.

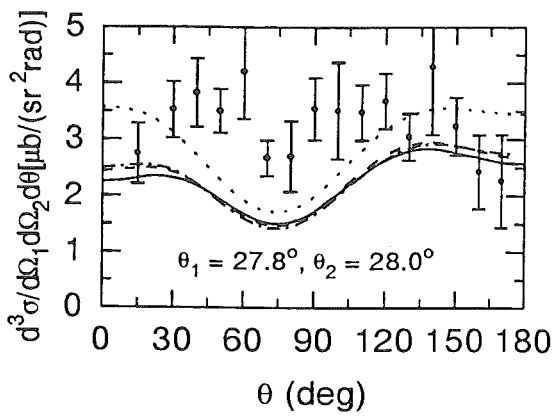

Fig. 1: Results for a selected kinematical setup from the TRIUMF experiment. The solid line are the Bonn results, the dashed line using only positive energy diagrams. The dotted line is obtained after adding the negative energy single scattering diagrams while the dash-dotted line is the result with all diagrams included.

References:

[*] Also Department of Physics and Astronomy, University of Georgia, Athens, GA 30602.

[†] Also Kernfysisch Versneller Instituut, 9747 AA Groningen, the Netherlands.

[1] F. de Jong, K. Nakayama, and T.-S. H. Lee, *Phys. Rev.* **C 50** (1995) 2334.

[2] M. Jetter and H. W. Fearing, *Phys. Rev.* **C 51** (1995) 1666.

[3] J. A. Eden and M. F. Gari, preprint: RUB-MEP-93/94 (1995).

[4] F. de Jong and K. Nakayama, *Phys. Rev.* **C 52** (1995) 2377.

[5] F. Gross, J.W. van Orden, and K. Holinde, *Phys. Rev.* **C 45** (1992) 2094.

Pion photo-production with a final state interaction based on a meson-exchange model.

K. Nakayama*, Ch. Schuetz, J. Speth, S. Krewald, and W. Pfeil**

Pion photo-production off nucleons has been studied for many years since the pioneering work by Chew, Goldberger, Low, and Nambu. In the past few years there has been a considerable effort in investigating effects of the final state interaction(FSI) [1, 2] in this process. Among other things, it is crucial that we understand theoretically the role of the FSI in order to extract the resonance parameters of the nucleon, since the background contribution cannot be separated experimentally from the resonance contribution. In particular, the investigation of the so-called off-shell behavior of the πN interaction is intimately related to this problem. In this work we calculate

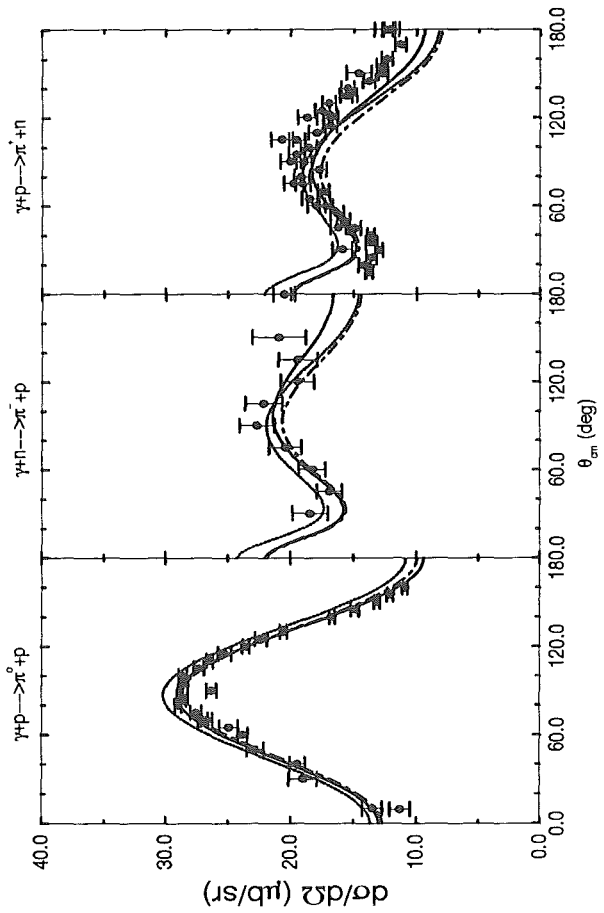

Fig. 1: Differential cross sections at a photon incident energy of $T_{lab} = 340MeV$. The solid lines are the full results; the dash-dotted lines are the results with the a_1-meson switched off; the dotted lines are when both the a_1-meson and the Δ-exchange (cross) diagram are switched off.

the pion photo-production process using the πN interaction developed by Schuetz et al. [3] which are based on a meson-exchange model of the hadronic interactions. The model treats the correlation of two pions explicitly in contrast to the usual one-boson approximation for the correlated two pions. The electromagnetic part of the reaction is calculated using an effective chiral Lagrangian which includes also the a_1-meson as a chiral partner of the ρ-meson [4]. The complete photo-production amplitude is unitary and gauge invariant. The model has three parameters: the N$\Delta\gamma$ coupling constants $g_1 = 1.032GeV^{-1}$ and $g_2 = -0.02GeV^{-2}$, and the overall monopole form-factor with a cutoff parameter $\Lambda = 450MeV$. They are adjusted to reproduce the pion photo-production data.

Fig.1 shows the effects of the a_1-meson as well as the Δ-exchange (cross) diagram on the differential cross sections at a photon incident energy of $T_{lab} = 340MeV$. Here the separable interaction of ref.[1] is used with slightly readjusted parameters g_1, g_2 and Λ from those given in ref.[1]. We see that the a_1-meson enhances the cross sections at backward angles while the Δ-exchange diagram reduces the cross section at forward angles for charged pions. Both contribute to improve the agreement with the data. Fig.2 shows the full results using

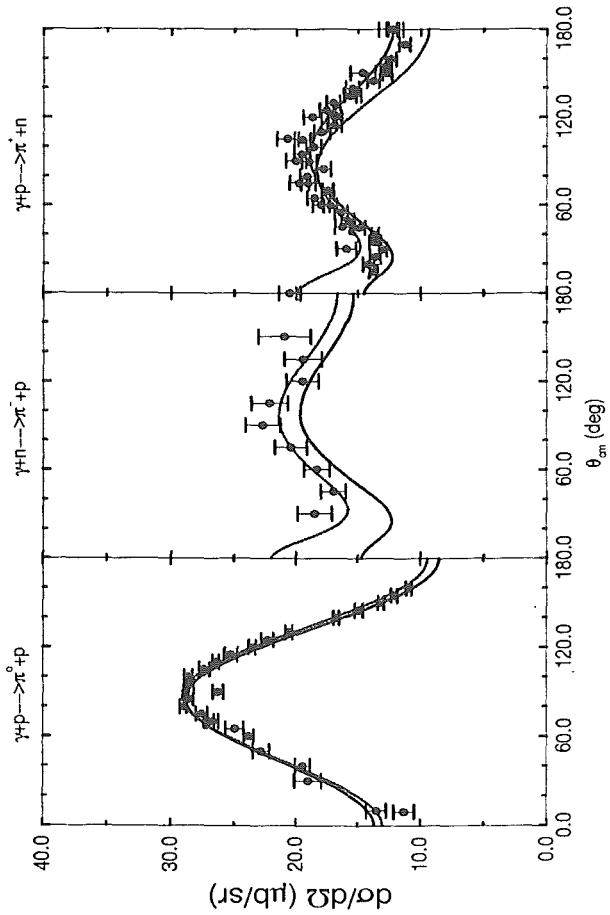

Fig. 2: Differential cross sections at a photon incident energy of $T_{lab} = 340MeV$. The solid lines are the results using the πN interaction of ref.[3], while the dotted lines are the results of ref.[1] using a phenomenological separable interaction.

the meson-exchange interaction (model 1) of ref.[3].We

see that the data are described well although the π^- production cross section is somewhat underestimated. The predictions of ref.[1] are also shown for a comparison. Pion photo-production processes are extremely sensitive to the hadronic formfactors. Our cutoff parameter of $\Lambda = 450MeV$ is small as compared to the value of $\Lambda = 650MeV$ obtained by Nozawa et al.[1] who use a purely phenomenological separable interaction. Also, our the value of the N$\Delta\gamma$ coupling, $g_1 = 1.032GeV^{-1}$, is about a factor two smaller than that found in ref.[1]. These are a direct consequence of the much stronger off-shell πN interaction used in the present work than that in ref.[1]. Also, recently, Surya and Gross [2] have described the pion photo-production data using an one-boson-exchange interaction with a formfactor which corresponds roughly to a monopole formfactor with a cut-off parameter of about $\Lambda = 300MeV$. The pion photo-production reaction seems, therefore, an interesting tool for studying the quark-gluon degrees of freedom in nuclear physics. We should also mention that our calculation cannot describe the the total cross section for the neutral pion production at energies near the threshold. In order to reproduce the data one needs a much smaller cutoff parameter ($\Lambda = 200MeV$) than that quoted above. These findings may be an indication that the off-shell behavior of the πN interaction we used is inadequate. However, before this can be concluded, we need to formulate and calculate the electromagnetic and hadronic parts of the photo-production amplitude consistently from each other.

References:

[1] S. Nozawa et al.,Nucl. Phys. **A513**(1990)459.

[2] Y. Surya and F. Gross, preprint: CEBAF-TH95-04.

[3] Ch. Schuetz et al., Phys. Rev. **C49**(1994)2671.

[4] J. Wess and B. Zumino, Phys. Rev. **163**(1967)1727.

* also, Department of Physics and Astronomy, University of Georgia, Athens GA 30602.

** Institut fuer Kernphysik, University of Bonn, Bonn.

Color dipole phenomenology of diffractive electroproduction of light vector mesons at HERA

J. Nemchik[1], N.N. Nikolaev[2], E. Predazzi[3] and B.G. Zakharov[2]

To leading $\log\frac{1}{x}$, scattering of high energy photons (hadrons) can be viewed as interaction with the target of color dipoles with the frozen size $\vec{r}$ and fraction z of the momentum of the photon (hadron). Diagonalization of the S-matrix in the $(\vec{r}, z)$ representation allows to write down the photoabsorption cross section in the factored form,

$$\sigma_{\gamma^* p}(x, Q^2) = \langle\gamma^*|\sigma(x,r)|\gamma^*\rangle \quad (1)$$

$$= \int_0^1 dz \int d^2\vec{r}\,|\Psi_{\gamma^*}(\vec{r}, z)|^2\sigma(x,r)\,, \quad (2)$$

where $\Psi_{\gamma^*}(\vec{r}, z)$ is the probability amplitude to find the color dipole of size r in the photon [1], and $\sigma(x, r)$ is a x (energy) dependent cross section for interaction of the color dipole $\vec{r}$ with the target nucleon. Much progress in understanding the small x physics came from the color dipole approach proposed in [1, 2] and recently extended to the BFKL pomeron by Nikolaev, Zakharov and Zoller [3, 4], and Mueller and Patel [5] in a somewhat different form.

The implementation of asymptotic freedom in the gBFKL equation is unambiguous and is not related to the issue of the next-to-leading $\log\frac{1}{x}$ correctiuons. It provides the perfect continuity between the gBFKL and the GLDAP evolutions in their common applicability domain [4]. Furthermore, in this double-leading-log domain

$$\sigma(x, r) = \frac{\pi^2}{3} r^2 \alpha_S(r) G(x, \frac{B}{r^2})\,, \quad (3)$$

where $G(x, Q^2)$ is the gluon structure function of the proton and $B \approx 10$ [6]. Eq. (3) establishes the connection between the color dipole approach and the more familiar language of the GLDAP parton densities

Diffractive electroproduction $\gamma^* p \to Vp$, $V = \rho^0, \omega^0, \phi^0, J/\Psi, \Upsilon\, \rho(2S), \omega(2S), \phi(2S), \Psi', \Upsilon'$, offers a unique possibility of studying the gBFKL pomeron. The color dipole factorization formula for the forward production amplitude reads [8, 7]

$$\mathrm{Im}\mathcal{M} = \langle V|\sigma(\nu, r)|\gamma^*\rangle \quad (4)$$

$$= \int_0^1 dz \int d^2\vec{r}\,\sigma(x_{eff}, r)\Psi_V^*(\vec{r}, z)\Psi_{\gamma^*}(\vec{r}, z)\,. \quad (5)$$

Taking the constituent quark wave function $\Psi_V(\vec{r}, z)$ for the probability amplitude to find the color dipole of size r in the vector meson, provides an extremely economic and viable phenomenology of vector meson production. To leading $\log\frac{1}{x}$, the effect of higher Fock states in the photon and vector meson is reabsorbed in the energy dependence of the dipole cross section, which enters at $x_{eff} = (Q^2 + m_V^2)/2m_p\nu$.

For the shrinking of the transverse size of the photon [1], $V(1S)$ leptoproduction probes $\sigma(x_{eff}, r_S)$ at the scanning radius [8, 7] $r_S \approx A_S/\sqrt{m_V^2 + Q^2}$ and

$$\mathrm{Im}\mathcal{M}_T \propto r_S^2\sigma(x_{eff}, r_S) \quad (6)$$

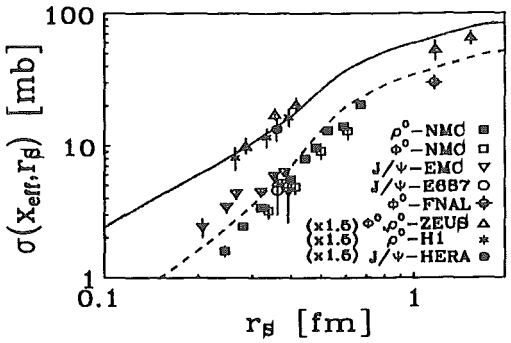

Figure 1: The dipole cross section $\sigma(\nu, r_S)$ as a function of the color dipole size r_S deduced [14] from the fixed-target ($\nu \sim$ 100-300 GeV) and (scaled up by the factor 1.5) HERA ($\nu \sim 10^4$ GeV) data on vector meson production. The solid and dashed curves are the predictions from the color dipole BFKL dynamics [7].

$$\propto \frac{1}{Q^2 + m_V^2}\sigma(x_{eff}, r_S) \propto \frac{1}{(Q^2 + m_V^2)^2}\,, \quad (7)$$

$$\mathrm{Im}\mathcal{M}_L \approx \frac{\sqrt{Q^2}}{m_V}\mathcal{M}_T \propto \frac{\sqrt{Q^2}}{m_V} r_S^2\sigma(x_{eff}, r_S) \quad (8)$$

$$\propto \frac{\sqrt{Q^2}}{m_V}\frac{1}{(Q^2 + m_V^2)^2}\,. \quad (9)$$

All the ρ^0 production data confirm [9, 10, 11] the prediction [8] of $\sigma_L/\sigma_T \sim Q^2/m_V^2$. For the large $A_S \approx 6$ and large r_S, the onset of the pQCD regime is very slow [7] and the pQCD formulas [12, 13] are entirely inapplicable at the presently studied $Q^2 \lesssim 20\,\mathrm{GeV}^2$. Only at $r_S \ll R_c$ one can use (3) with the result $M_{T,L} \propto G(x_{eff}, q^2)$, where $q^2 = \tau(Q^2 + m_V^2)$ with the very small scale $\tau_{T,L}(J/\Psi) \approx 0.2$, $\tau_L(\rho^0) \approx 0.15$ and $\tau_T(\rho^0) \approx$0.07-0.1 [7], much smaller than $\tau = 0.25$ in [12] and $\tau = 1$ in [13].

In the typical kinematics, the longitudinal polarization of the virtual photon $\varepsilon_L \approx 1$. In the fit $\sigma(\gamma^* \to V) = \sigma_T + \varepsilon_L\sigma_L \propto (Q^2 + m_V^2)^{-n}$, for the typical $W = 100\,GeV$ at HERA the gBFKL dynamics predicts $n \approx 2.4$ for the semiperturbative $0 \lesssim Q^2 \lesssim 10$ GeV^2, which rises to $n \approx 3.2$ for the perturbative $15 \lesssim Q^2 \lesssim 100\,\mathrm{GeV}^2$ [14]. At fixed W, the Q^2 dependence is strongly affected by the x_{eff} dependence of $\sigma(x_{eff}, r_S)$.

Inverting Eqs. (7),(9) one can evaluate $\sigma(x_{eff}, r_S)$ vs. r_S from the vector meson production data with the results shown in Fig. 2 [14]. The so found $\sigma(x_{eff}, r_S)$ decreases by one order of magnitude from $r_S \approx 1.2$ fm in ϕ^0 real photoproduction, down to $r_S \approx 0.24$ fm in the electroproduction of ρ^0 at $Q^2 = 23\,\mathrm{GeV}^2$ and of J/Ψ at $Q^2 = 13\,\mathrm{GeV}^2$. The prediction [4, 7] of faster growth $\sigma(\nu, r)$ at smaller

dipole size r is confirmed, although the error bars are still large and the vector meson production data can not compete yet with the higher accuracy data on the proton structure function. Eqs. (7),(9) show the flavor symmetry is restored when different reactions are compared at identical values of r_S and/or $Q^2 + m_V^2$ rather than the same Q^2. Indeed, at the overlapping r_S, there is a consistency between the $\sigma(x_{eff}, r_S)$ determined from the ρ^0, ϕ^0 and J/Ψ production data. The curves show the gBFKL cross section [7] used in predictions of $F_2(x, Q^2)$ shown in Fig. 1. The agreement between the theoretical dipole cross section and the one extracted from the data on vector meson production proves we have a good unified description of all the DIS data. We mention also the successful prediction [8] within the same formalism of color transparency effects in ρ^0 production on nuclei [9].

Extremely interesting predictions for $V(2S)$ production are available [15, 7, 14]. For the node in the $2S$ radial wave function, the $V(2S)/V(1S)$ cross section ratio is strongly suppressed at $Q^2 = 0$. The suppression $\Psi'/(J/\Psi) \sim 0.15$ predicted within the color dipole scheme has been confirmed experimentally [16]. The $\rho'(2S)/\rho^0$ and $\phi'(2S)/\phi^0$ ratios are predicted to rise steeply with Q^2, there is an evidence for this rise from the E665 experiment [17]. The color dipole gBFKL dynamics predicts a nontrivial variation with Q^2 of the energy dependence of the $V(2S)/V(1S)$ ratio and the weaker t-dependence of the $V(2S)$ differential cross section as compared to the $V(1S)$ production, which changes to the stronger t-dependence at larger Q^2 [14], which can be observed at HERA.

References:

[1] N.N. Nikolaev and B.G. Zakharov, *Z. Phys.* **C49** (1991) 607.

[2] N.N. Nikolaev and B.G. Zakharov, *Z. Phys.* **C53** (1992) 331.

[3] N.N.Nikolaev and B.G.Zakharov, *JETP* **78** (1994) 598; *Z. Phys.* **C64** (1994) 631.

[4] N.N.Nikolaev, B.G.Zakharov and V.R.Zoller, *JETP Letters* **59** (1994) 8; *JETP* **78** (1994) 866; *Phys. Lett.* **B328** (1994) 486.

[5] A.E.Mueller and H.Patel, *Nucl. Phys.* **B425** (1994) 471.

[6] N.N.Nikolaev and B.G.Zakharov, *Phys. Lett.* **B332** (1994) 184.

[7] J.Nemchik, N.N.Nikolaev and B.G.Zakharov, *Phys. Lett.* **B341** (1994) 228.

[8] B.Z.Kopeliovich, J.Nemchik, N.N.Nikolaev and B.G.Zakharov, *Phys. Lett.* **B309** (1993) 179; **B324** (1994) 469.

[9] E665 Collab., M.R.Adams et al., *Phys. Rev. Lett.* **74** (1995) 1525

[10] NMC Collab., M.Arneodo, et al., *Nucl.Phys.* **B 429** (1994) 503

[11] ZEUS Collab., M.Derrick et al., *Phys. Lett.* **B356** (1995) 601

[12] M.G.Ryskin, *Z. Phys.* **C57** (1993) 89.

[13] S.J.Brodsky et al., *Phys. Rev.* **D50** (1994) 3134.

[14] J.Nemchik, N.N.Nikolaev, E.Predazzi and B.G.Zakharov, **DFTT /95**

[15] J.Nemchik, N.N.Nikolaev and B.G.Zakharov, *Phys.Lett.* **B339** (1994) 194.

[16] NMC Collab., P.Amaudruz, et al., *Nuc. Phys.* **B 371** (1992) 3; E687 Collab., P.Frabetti et al., Europhys. Conf. on HEP, Brussels, 1995.

[17] E665 Collab., C.Salgado, Workshop on CT at CEBAF, May 1995.

[1] Institute for Experimental Physics, Slovak Academy of Sciences, 04353 Kosice, Slovak Republik

[2] Also at: L.D.Landau Institute for Theoretical Physics, 117334 Moscow, Russia

[3] Department of Theoretical Physics, University of Torino and INFN, Sezione di Torino, I-10125 Torino, Italy

Breaking of the Ingelman-Schlein-Regge factorization for diffractive deep inelastic scattering

M.Genovese[1], N.N. Nikolaev[2] and B.G. Zakharov[2]

Large rapidity gap (LRG) events and/or diffraction dissociation (DD) of photons $\gamma^* + p \to X + p'$ into states X of mass M can be reinterpreted as DIS on pomerons radiated by the target proton. The diffractive structure function $F_D(x_{\mathbb{P}}, \beta, Q^2)$ is defined by

$$(M^2+Q^2)\frac{d\sigma_D(\gamma^* \to X)}{dt\, dM^2}\bigg|_{t=0} = \frac{\sigma_{tot}(pp)}{16\pi}\frac{4\pi^2\alpha_{em}}{Q^2}F_D(x_{\mathbb{P}}, \beta, Q^2)\,. \quad (1)$$

Here $\beta = Q^2/(Q^2+M^2)$ and $x_{\mathbb{P}} = (Q^2+M^2)/(Q^2+W^2) = x/\beta$ are interpreted as the Bjorken variable for DIS on the pomeron and the fraction of the momentum of the proton carried away by the pomeron, respectively. Following [1], it has become customary to endow the pomeron with the usual attributes of a hadron such as the partonic structure function $F_{2\mathbb{P}}(\beta, Q^2)$ and the flux of pomerons $\phi_{\mathbb{P}}(x_{\mathbb{P}})/x_{\mathbb{P}}$ in the proton:

$$F_D(x_{\mathbb{P}}, \beta, Q^2) = \phi_{\mathbb{P}}(x_{\mathbb{P}})F_{2\mathbb{P}}(\beta, Q^2) \quad (2)$$

The Ingelman-Schlein factorization (2) has never been derived from QCD. It involves a series of strong and questionable assumptions on $d\sigma^D$: i) the $x_{\mathbb{P}}$ dependence is reabsorbed entirely in the Q^2, β and flavor independent pomeron flux function $\phi_{\mathbb{P}}(x_{\mathbb{P}})$, ii) the β, Q^2 and flavor dependence of $d\sigma_D$ are contained entirely in the structure function of the pomeron, iii) the ratio $R^D = F_L^D(x_{\mathbb{P}}, \beta, Q^2)/F_T^D(x_{\mathbb{P}}, \beta, Q^2)$ does not depend on $x_{\mathbb{P}}$. None of properties i) to iii) is borne out by the rigorous QCD theory of diffraction [2, 3, 4]. Furthermore, the non-factorizable Nikolaev-Zakharov colour dipole approach to DD [2, 5] is well known to provide, without adjustable parameters, the best *quantitative* description of LRG data [6].

Here we summarize the recent results on factorization breaking in DD into open heavy flavor, $X = c\bar{c}, b\bar{b}$, and DD of longitudinal photons. The crucial point is that in DD into $q\bar{q}$ pairs the relevant dipole size and pQCD factorization scale q^2 depend on Q^2 and/or β, entailing the inextricable β, Q^2 and flavor dependent "flux of pomerons"

$$\phi_{\mathbb{P}}(x_{\mathbb{P}}, \beta, Q^2) \propto \alpha_S^2(q^2)G^2(x_{\mathbb{P}}, q^2)\,, \quad (3)$$

where for the T and L photons the pQCD scale q^2 equals

$$q_T^2 \sim m_f^2(1+\frac{Q^2}{M^2}) = \frac{m_f^2}{1-\beta}\,, \quad q_L^2 \sim \frac{1}{4}Q^2\,. \quad (4)$$

For the T photons, barring the weak β dependence of $\phi_{\mathbb{P}}(x_{\mathbb{P}}, \beta, Q^2)$, the satisfactory parameterization of the "valence structure function" of the pomeron is $F_{\mathbb{P}}^{(q\bar{q})}(\beta, Q^2) \sim \beta(1-\beta)$, although in the extreme limit of $\beta \to 1$ one finds $F_{\mathbb{P}}^{(q\bar{q})}(\beta, Q^2) \propto (1-\beta)^2$. For the L photons,

$$F_L^D(x_{\mathbb{P}}, \beta, Q^2) \propto \frac{1}{Q^2}(1-2\beta)^2\beta\,. \quad (5)$$

The specific prediction from the color dipole gBFKL dynamics is a restoration of the Regge factorization at $\beta \ll 1$, where the dimensionful, $[GeV]^{-2}$, nonperturbative triple-pomeron coupling was shown to not depend on Q^2 [3, 7]. For instance, $R = \sigma_L/\sigma_T \approx 0.2$ is predicted for both the conventional DIS at $x \ll 1$ and LRG at $\beta \ll 1$.

The convenient parameterization of the "flux functions" is

$$\phi_{\mathbb{P}}(x_{\mathbb{P}}) = \left(\frac{x_0}{x_{\mathbb{P}}}\right)^{[a+d\log(Q^2/10)+f\log^2(Q^2/10)]} \cdot \left[\frac{x_{\mathbb{P}}+c}{x_0+c}\right]^{[b+e\log(Q^2/10)]}\,, \quad (6)$$

where Q^2 is in GeV^2 and the normalization is $\phi_{\mathbb{P}}(x_0 = 0.03) = 1$. The typical parameters are (for the T photons we show only the β-averaged fluxes) : i) $\beta \sim 1$, DD of the L photons into all the flavors: $a = 0.456, b = 0.678, c = 0.012, d = 0.112, e = 0.078, f = 0.01$, ii) $\beta \sim 1$, DD of the T photons into light flavors: $a = 0.569$, $b = 0.489$, $c = 0.153 \cdot 10^{-3}$, $d = e = f = 0$, iii) $\beta \sim 1$, DD of the T photons into open charm: $a = 0.723$, $b = 0.394$, $c = 2.38 \cdot 10^{-3}$, $d = e = f = 0$, iv) $\beta \ll 1$, DD of the T and L photons into all the flavors: $a = 0.741$, $b = 0.586$, $c = 0.8 \cdot 10^{-3}$, $d = e = f = 0$. The dramatic difference of all these fluxes will for sure be observed with the next generation data from HERA. For instance, the charm content of DD is predicted to rise by one order in magnitude from $x_{\mathbb{P}} = 0.01$ to $x_{\mathbb{P}} = 10^{-4}$.

Evidently, the fact that the valence light and heavy $q\bar{q}$, glue and the sea $q\bar{q}$ components of $F^D(x_{\mathbb{P}}, \beta, Q^2)$ have the different $x_{\mathbb{P}}$ dependence, invalidates the GLDAP description of the Q^2 dependence of $F^D(x_{\mathbb{P}}, \beta, Q^2)$. Even at fixed $x_{\mathbb{P}}$ the GLDAP evolution considerations are illegitimate for the rise of the pQCD factorization scale q_T^2 towards large β. Recall that the Q^2 evolution derives from the radiation of gluons, which is obviously suppressed unless $Q^2 \gg q^2$. Therefore, the onset of the Q^2 evolution of $F^D(x_{\mathbb{P}}, \beta, Q^2)$ depends on β and starts later at large β which further invalidates the conventional GLDAP description of the Q^2 dependence. Furthermore, the open charm excitation leads to a substantial rise $F^D(x_{\mathbb{P}}, \beta, Q^2)$ at fixed β when Q^2 passes the threshold value $Q^2 = 4\beta m_c^2/(1-\beta)$ [2]. To summarize, the GLDAP interpretation of the observed Q^2 dependence of $F^D(x_{\mathbb{P}}, \beta, Q^2)$ at large β [6] invoking the gluon distribution which is strongly peaked at $\beta = 1$, is misleading at best. Only at $\beta \ll 1$, to the leading $\log\frac{1}{\beta}$, one recovers the approximate double-leading-log GLDAP evolution at fixed $x_{\mathbb{P}}$, even here the Q^2 and $x_{\mathbb{P}}$ dependence do not factor, though [3]. With much reservations for the large menagery of different pomeron fluxes, one can introduce the valence gluon-gluon, valence $q\bar{q}$ and the sea $q\bar{q}$ components

of the multicomponent pomeron [2, 5]. Imposing the momentum sum rule does not make any sense, the obvious reasons are the explicit $x_{\mathbb{P}}$ dependence of the weight of different components and the breaking of the GLDAP evolution. The normalizations of the different components were calculated in [2, 3, 5] with the result that at moderately small $x_{\mathbb{P}}$ gluons and (anti)quarks in the pomeron carry comparable momentum. This prediction has been confirmed recently in the ZEUS study of jet production in LRG events [8].

The t integration of the DD cross section requires the knowledge of the diffraction slope B_D. It has been argued that at large β one expects $B_D \sim 10\,\mathrm{GeV}^{-2}$, while at small β rather B_D ~5-6 GeV^{-2} [2, 5], for the discussion of double diffraction dissociation see [9]. The t and $x_{\mathbb{P}}$ integrated DD cross section defines the diffractive component of the proton structure function

$$F_{2p}^D(x,Q^2) = \frac{\sigma_{tot}(pp)}{16\pi B_D}\int_x^{x_0}\frac{dx_{\mathbb{P}}}{x_{\mathbb{P}}}F_D(x_{\mathbb{P}},\frac{x}{x_{\mathbb{P}}},Q^2)\,. \qquad (7)$$

Experimentally, $F_{2p}^D(x,Q^2) \approx 0.1F_{2p}(x,Q^2)$ in agreement with the prediction [2]. The large rate of diffraction has the far reaching implications for the parton model of DIS. Only the bare photoabsorption cross section is a linear functional of parton densities, the observed, unitarized, cross section contains the shadowing corrections which are the nonlinear functional of the parton densities. The theory of the unitarization is still in its formative stage, to the leading approximation

$$F_{2p}(x,Q^2) = F_{2p}^{bare}(x,Q^2) - \chi F_{2p}^D(x,Q^2)\,, \quad (8)$$

where $\chi \sim$ 1-2 [3, 10]. The shadowing correction could be as large as 10-20% and it persists at all Q^2. How the unitarity must be imposed remains an open issue, there is an uncertainty in the value of χ. The theoretical curves shown in Fig. 1 are for F_{2p}^{bare}, the unitarity corrections (not shown here) will bring the predicted F_{2p} to a still better agreement with the experiment. Only the bare structure function is GLDAP/gBFKL evolving. As we have commented above, at small β and fixed $x_{\mathbb{P}}$ the diffractive structure function and the shadowing correction thereof, obey the approximate double-leading-log GLDAP evolution. For this reason, it would be very difficult to see a signal of shadowing corrections from the scaling violation analysis [3].

In DIS on the free protons the direct measurement of the shadowing correction is impossible. To this end, we recall that DD, unitarity corrections and nuclear shadowing are of the similar origin [11] and it would be very interesting to look for departures from the GLDAP evolution in nuclear structure functions which has not been done before. Running HERA in the electron-nucleus collider mode can contribute much to our understanding of small x. LRG scattering which is ~10% effect in DIS on the free proton, is predicted to become ~50% effect in DIS on heavy nuclei [12, 13]. This prediction has already been confirmed by the E665 μXe scattering data [14]. Unusual effects of DD in leptoproduction on nuclei were discussed in detail in [13], they typically can be summarized as a weakening of the multiple production of hadrons from nuclei in the shadowing region of small x as compared to the non-shadowing region of large x. This is quite a paradoxical prediction because one usually associates the shadowing with the hadronlike behavior of the photon in contrast to the pointlike behavior of the photon in the non-shadowing region of large x.

References:

[1] G.Ingelman and P.Schlein, *Phys. Lett.* **B152** (1985) 256.

[2] N.N. Nikolaev and B.G. Zakharov, *Z. Phys.* **C53** (1992) 331.

[3] N.N.Nikolaev and B.G.Zakharov, *JETP* **78** (1994) 598; *Z. Phys.* **C64** (1994) 631.

[4] N.N.Nikolaev and B.G.Zakharov, *Phys. Lett.* **B332** (1994) 177.

[5] M.Genovese, N.N.Nikolaev and B.G.Zakharov, *JETP* **108** (1995) 625.

[6] ZEUS Collab., M.Derrick et al., *Z. Phys.* **C68** (1995) 569. H1 Collab., T.Ahmed et al., *Phys. Lett.* **B348** (1995) 681.

[7] M.Genovese, N.N.Nikolaev and B.G.Zakharov, - *JETP* **81** (1995) 633.

[8] ZEUS Collab., M.Derrick et al., *Phys. Lett.* **B356** (1995) 129.

[9] H.Holtmann et al., *Z. Phys.* **C69** (1996) 297.

[10] V.Barone et al., *Phys. Lett.* **B326** (1994) 161.

[11] N.N. Nikolaev and B.G. Zakharov, *Z. Phys.* **C49** (1991) 607.

[12] N.N.Nikolaev, DESY Mini-School, May 1994.

[13] N.N.Nikolaev, V.R.Zoller and B.G.Zakharov, *Z. Phys.* **A351** (1995) 435.

[14] E665 Collab., M.R.Adams et al., *Z. Phys.* **C65** (1995) 225.

[1] Department of Theoretical Physics, University of Torino and INFN, Sezione di Torino, I-10125 Torino, Italy

[2] Also at: L.D.Landau Institute for Theoretical Physics, 117334 Moscow, Russia

Chirally Constraining the $\pi\pi$ Interaction in Nuclear Matter

R. Rapp, J. W. Durso and J. Wambach*

The role of correlated two-pion exchange in the interaction of two nucleons is well-established [1], with the bulk of the intermediate range attraction due to the scalar-isoscalar (σ-meson) channel. This same mechanism is presumably responsible for most of the attraction between nucleons in nuclei, despite the possibly strong influence of the nuclear medium on the $\pi\pi$ correlations [2], especially in the σ-channel [3].
In a recent study Aouissat *et al.* [4], hereafter referred to as I, demonstrated the unattractive possibility of $\pi\pi$ pair condensation at nuclear densities of 1.2-1.3ρ_0 ($\rho_0 = 0.16$ fm^{-1}, normal nuclear matter density) for two phenomenological models [5, 6] which fit $\pi\pi$ s-wave phases over a broad energy range. It was also found in I that the tendency towards $\pi\pi$ pair condensation appeared to be dramatically suppressed if the $\pi\pi$ amplitude were forced to satisfy constraints required by chiral symmetry, *i.e.* that the amplitude must satisfy the so-called soft-pion theorems [7]. Implicit in these constraints is that the $\pi\pi$ s-wave scattering lengths be proportional to the pion mass as the pion mass approaches zero.
The difficulty in imposing the constraint on the scattering lengths is that the $\pi\pi$ amplitudes used in the in-medium calculations are generated from an interaction kernel which is unitarized by means of a scattering equation (*e.g.*, the Blankenbecler-Sugar (BbS) equation [8]). In that case, any symmetries of the interaction kernel are usually destroyed by iteration in the scattering equation. Let us illustrate this point with the common example of t-channel exchange of ρ meson (in the Jülich model, *e.g.*, this process dominates the low-energy s-wave $\pi\pi$ interaction [6]); the corresponding Born amplitude is given by

$$M_{\rho,B}^{I=0,2} = (2,-1)g_{\pi\pi\rho}^2 \left(\frac{s-u}{t-m_\rho^2} + \frac{s-t}{u-m_\rho^2}\right) \quad (1)$$

where in the BbS framework the Mandelstam variables are to be chosen 'on-energy-shell', leading to

$$\begin{aligned} s &= E^2 \\ t &= -q^2 - q'^2 + 2qq'\cos\theta \quad (2) \\ u &= -q^2 - q'^2 - 2qq'\cos\theta\ . \quad (3) \end{aligned}$$

The occurence of q^2 and q'^2 standing separately implies that already in second order of the iteration in the BbS-equation,

$$M_\rho^{I,(n=2)}(E;q,q') = \int_0^\infty \frac{k^2dk}{(2\pi)^2} V^I(E;q,k) \times G_{\pi\pi}(E,k)V^I(E;k,q') \quad (4)$$

(V denoting the pseudopotential generated from the Born amplitude eq. (1)), the amplitude contains terms of $\mathcal{O}(1)$ for $q, q', m_\pi, E \to 0$. Thus the s-wave scattering lengths, given by

$$a^I = -\lim_{q\to 0} \frac{M^I(E=2m_\pi;q,q)}{32\pi\omega_q}\ , \quad (5)$$

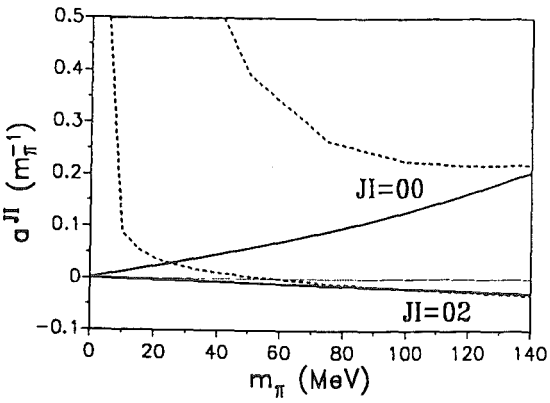

Figure 1: S-Wave scattering lengths in the chiral limit; dashed lines: Lohse/Pearce Jülich model; full lines: chirally improved Jülich model.

diverge as $1/m_\pi$ in the chiral limit $m_\pi \to 0$ (see Fig. 1). In I this problem was solved by using a once-subtracted form of the 2-pion propagator in the BbS-equation, resulting in the replacement

$$\begin{aligned} G_{\pi\pi}(E,k) &= \frac{1}{\omega_k(E^2-4\omega_k^2+i\eta)} \longrightarrow \\ \tilde{G}_{\pi\pi}(E,k) &= \frac{1}{\omega_k(E^2-4\omega_k^2+i\eta)}\frac{E^2}{4\omega_k^2}\ . \quad (6) \end{aligned}$$

The appearance of E^2 in the numerator of $\tilde{G}_{\pi\pi}(E,k)$ as an *external* variable in the integral equation ensures that the amplitude generated by solving the BbS-equation will be $\mathcal{O}(m_\pi^2)$ for $q, q' = 0$ and $E = 2m_\pi \to 0$. The difficulty with this solution is that the suppression of the rescattering terms at small momenta forces one to use large coupling constants and unrealistically high values of cutoffs, and to rely on heavy meson-exchange (*e.g.*, the $f_2(1270)$), in meson exchange models such as the Jülich model [6] in order to achieve a good fit to $\pi\pi$ phase shifts, so that one loses contact with the underlying low-energy physics of the $\pi\pi$ interaction.
Here we wish to construct interaction kernels which will yield amplitudes that obeyy the scattering length constraint without having to resort to the subtraction scheme of I, and thereby avoid its unattractive features. One simple way to accomplish this is through a slight modification of the off-shell continuation of the Mandelstam variables, *e.g.* [9]

$$\begin{aligned} s &= E^2 \\ t &= 2m_\pi^2 - 2\omega_q\omega_{q'} + 2qq'\cos\theta \\ u &= 2m_\pi^2 - 2\omega_q\omega_{q'} - 2qq'\cos\theta \quad (7) \end{aligned}$$

which amounts to placing the pions on the mass shell ($\omega_q \equiv \sqrt{\mathbf{q}^2+m_\pi^2}$) in t and u, but taking s as an external variable in the scattering equation. In this way

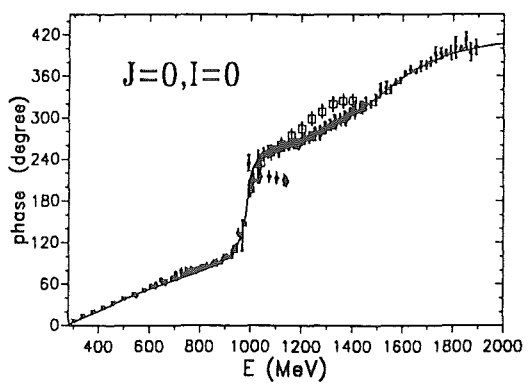

Figure 2: Fit to the experimental $\pi\pi$ phase shifts in the σ-channel within the chirally improved Jülich model.

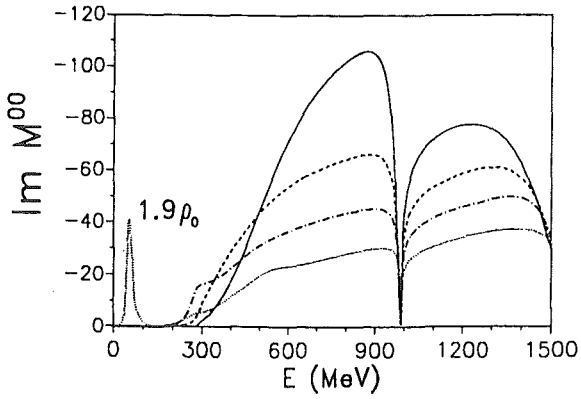

Figure 3: In-medium results for the imaginary part of the invariant M^{00} $\pi\pi$ amplitude calculated in the chirally improved Jülich model; solid curve: vacuum result, dashed: $\rho = 0.5\rho_0$, dashed-dotted: $\rho = \rho_0$, dotted: $\rho = 1.9\rho_0$.

each term in the Born amplitudes contains either an external factor (*e.g.*, E^2 or m_π^2) or a factor which is a product of terms $(\omega_q\omega_{q'})$ which survive the integration and are $\mathcal{O}(m_\pi^2)$ as $q, q' \to 0$. Consequently, the s-wave scattering lengths calculated in terms of the fully iterated $M_{\pi\pi}$-amplitude now vanish in the chiral limit (Fig. 1).

Chiral symmetry also imposes further soft-pion theorems on the low-energy $\pi\pi$ scattering. To satisfy these (at least at the tree level), additional $\pi\pi$ contact interactions have to be taken into account in the underlying lagrangian. After supplementing the corresponding Born amplitudes with form factors they are suitable for iteration in the BbS-scattering equation.

With this chirally improved version of the Jülich $\pi\pi$ model we performed a refit to the $\pi\pi$ vacuum scattering data, the result of which is illustrated in Fig. 2 for the case of the scalar-isoscalar channel (a similar quality is reached in all other partial waves for $J \leq 2$).

Applying this model to the calculation of the in-medium $\pi\pi$ amplitude in the σ-channel we find that the condensation mechanism is indeed significantly inhibited (compare Fig. 3): as a result of the chiral constraints (especially the repulsion induced by the contact terms) the critical density for the pair instability ($\rho_c^{\pi\pi} \simeq 2\rho_0$) is alomost twice as high as in the original non-chirally symmetric version of the Jülich model [6], which gives $\rho_c^{\pi\pi} \simeq 1.2\rho_0$ [4].

References:

[1] R. Machleidt, K. Holinde and Ch. Elster, Phys. Reports 149 (1987) 1.

[2] T.O. Ericson and W. Weise, Pions and Nuclei (Clarendon, Oxford, 1988).

[3] P. Schuck, G. Chanfray and W. Nörenberg, Z. Phys. A 330 (1988) 119; G. Chanfray, Z. Aouissat, P. Schuck and W. Nörenberg, Phys. Lett. **B256** (1991) 325.

[4] Z. Aouissat, R. Rapp, G. Chanfray, P. Schuck, J. Wambach, Nucl. Phys. A 581 (1995) 471.

[5] J.A. Johnstone and T-S.H. Lee, Phys. Rev. **C34** (1986) 243.

[6] D. Lohse, J.W. Durso, K. Holinde and J. Speth, Nucl. Phys. **A516** (1990) 513; B.C. Pearce, K. Holinde and J. Speth, Nucl. Phys. **A541** (1992) 663.

[7] S. Weinberg, Phys. Rev. Lett. 17 (1966) 616; Phys. Rev. 166 (1968) 1568

[8] R. Blankenbecler and R. Sugar, Phys. Rev. 142 (1966) 1051

[9] R. Rapp, J. W. Durso and J. Wambach, Nucl. Phys. **A**, in press.

* also at: Department of Physics, University of Illinois at Urbana-Champaign, Urbana, IL 61801-3080, U.S.A.

Medium Modifications of the Rho Meson at CERN/SpS Energies

R. Rapp*, G. Chanfray and J. Wambach*

In central heavy-ion reactions at ultrarelativistic energies hot and dense hadronic matter is formed at the early stages of the collision. From such experiments one hopes to infer properties of mesons and baryons in the vicinity of the chiral phase transition. Because of its electromagnetic origin, lepton pair emission is an ideal probe. Once produced, the dilepton will decouple from the strongly interacting particles and thus carry undistorted information of the dynamical properties of the hot nuclear system. For this reason the recent low-mass dilepton spectra measured by the CERES collaboration in p+Be, p+Au and S+Au [1] collisions at 450 GeV/u and 200 GeV/u, respectively, have produced considerable interest. While the proton data are well described by known decays from a hadronic fireball an excess of dielectrons with invariant masses of 0.2 GeV/c^2 to 1 GeV/c^2 has been observed in the S+Au case and has been attributed to $\pi^+\pi^-$ annihilation from the pionic component of the hadron gas [1]. When this process is included in the description of the data the excess of strength between the $2m_\pi$-vacuum threshold and the rho peak is still unexplained. This led the authors of ref. [2] to the conclusion that one is seeing a signal of partial restoration of chiral symmetry through a decrease of vector meson masses (here especially the rho meson) near the phase boundary. Since the rho meson strongly couples to the $\pi^+\pi^-$ channel this effect may also be explained more conventionally, however, namely by modifications of the pion propagation in the presence of nucleons and isobars [3, 4, 6, 5, 7].

To study the dilepton emission from $\pi^+\pi^-$ annihilation we invoke the vector-dominance model (VDM) in which the electromagnetic current is related to the third isospin component of the rho meson field by the field current identity $J^\mu = (m_\rho^2/g)\rho_3^\mu$ where m_ρ and g denote the rho meson mass and the universal VDM coupling constant, respectively. In terms of the retarded (thermal) rho-meson propagator

$$D_\rho^{\mu\nu}(q;T) = -i\int d^4x e^{-iqx}\sum_i \frac{e^{-\beta E_i}}{Z} \times\langle i|[\rho_3^\mu(x),\rho_3^\nu(0)]|i\rangle\Theta(x_0) \quad (1)$$

($\beta = 1/T$) the dilepton emission rate per unit volume, $R{=}dN_{l^+l^-}/d^4x$, is given by

$$\frac{dN_{l^+l^-}}{d^4x d^4q} = \frac{\alpha^2}{3\pi^2 M^2} H(q;T) \quad (2)$$

where $q = p_+ + p_- = (q_0,\vec{q})$ denotes the total momentum for (massless) dileptons and $M^2 \equiv q_\mu^2 > 0$ is the invariant mass. Restricting ourselves to back-to-back kinematics, i.e. $\vec{q} = \vec{0}$, the hadronic piece is given by

$$H(q_0,\vec{q}=0;T) = -f^\rho(q_0,T)\frac{3(m_\rho^{(0)})^4}{\pi g^2} \times \mathrm{Im}D_\rho(q_0;T) \quad (3)$$

where

$$D_\rho(q_0;T) = [q_0^2 - (m_\rho^{(0)})^2 - \Sigma_\rho(q_0;T)]^{-1} \quad (4)$$

involving the scalar part of the rho self energy Σ_ρ.

To investigate medium modifications of the ρ propagator we first need a realistic model for the ρ meson in free space. As is well known [8] an appropriate description is provided by a bare pole graph renormalized by $\pi\pi$ rescattering. The free parameters g, $m_\rho^{(0)}$ and Λ_ρ (entering the hadronic form factor) are fitted to the experimental p-wave $\pi\pi$ phase shifts and the pion electromagnetic form factor [10].

A proper calculation of the in-medium ρ propagator must include constraints from gauge invariance. A detailed derivation for the self energy in homogeneous matter is given in refs. [5, 6]. The result can be expressed in terms of the spin-isospin longitudinal and transverse response functions $\Pi_L(k_0,k)$ and $\Pi_T(k_0,k)$, at a given density and temperature. Making use of derivations in ref. [6] the imaginary part of the self energy for a ρ meson at rest then takes the form

$$\mathrm{Im}\Sigma_\rho(q_0,\vec{0}) = \int_0^\infty k^2\, dk\, v(k)^2 \int_0^{q_0}\frac{dk_0}{\pi} \times\mathrm{Im}D_\pi(q_0-k_0,k)\mathrm{Im}\{\alpha(q_0,k_0,k)D_\pi(k_0,k) + \frac{1}{2k^2}\Pi_L(k_0,k) + \frac{1}{k^2}\Pi_T(k_0,k)\}, \quad (5)$$

where D_π denotes the in-medium 1-pion propagator and the function α is given by

$$\alpha(q_0,k_0,k) = [1 + \tilde{\Pi}_R^0(q_0-k_0,k) + \tilde{\Pi}_R^0(k_0,k) + \frac{1}{2}\tilde{\Pi}_R^0(k_0,k)\tilde{\Pi}_R^0(q_0-k_0,k)]$$
$$\tilde{\Pi}_R^0(k_0,k) = \frac{1}{k^2}\mathrm{Re}\Sigma_\pi(k_0,k)\,. \quad (6)$$

The real part of Σ_ρ is obtained via a dispersion integral:

$$Re\Sigma_\rho(q_0) = -\mathcal{P}\int_0^\infty \frac{dE'^2}{\pi}\frac{\mathrm{Im}\Sigma_\rho(E')}{q_0^2 - E'^2}\frac{q_0^2}{E'^2}\,. \quad (7)$$

The factor q_0^2/E'^2 results from a subtraction at $q_0{=}0$, which is necessary to ensure gauge invariance [6]; the imaginary part is unaffected by this subtraction since $Im\Sigma_\rho(q_0=0)=0$.

For the 1-pion selfenergy Σ_π we employ the standard model of p-wave particle-hole excitations extended to finite temperature [7]. Here the pions are dressed by NN^{-1}, ΔN^{-1} as well as $N\Delta^{-1}$ and $\Delta\Delta^{-1}$ excitations, the latter appearing as a consequence of a thermally excited Δ abundance in the gas. One has

$$\Sigma_\pi(k_0,k) = -k^2\sum_\alpha \chi_\alpha(k_0,k)\,, \quad (8)$$

where the summation is performed over all excitation channels $\alpha=ab^{-1}$, $a,b=N,\Delta$. The thermal susceptibilities χ_α contain short-range correlations taken into account by Landau-Migdal parameters $g'_{\alpha\beta}$ which we fix at $g'_{\alpha\beta}=0.8$ for $\alpha\beta=aa^{-1}bb^{-1}$ and $g'_{\alpha\beta}=0.5$ for all others. Finally, to account for a finite pion density, we supplement eq. (16) with a 2-pion Bose factor, $[1+f^\pi(k_0)+f^\pi(q_0-k_0)]$, which can be derived rigorously within a Matsubara formalism [9].

A realistic description of the dilepton yield has to account for the time evolution of a central S-Au collision. Therefore we make use of the transport results of Li *et al.* [2] by fitting their time dependence of the temperature with

$$T(t)=(T^i-T^\infty)e^{-t/\tau}+T^\infty \qquad (9)$$

(T^i=170 MeV, T^∞=115 MeV and τ=10 fm/c). By furthermore adjusting the initial baryon density of $\rho^{ini}=3.5\rho_0$ with a common baryon chemical potential ($\mu_B=0.448$ GeV) for the 12 lowest lying resonances, the time evolution of the baryon abundances is then determined assuming chemical equilibrium [10].

For a direct comparison with experiment two further points have to be considered. The first is related to the fact that the rate is only evaluated in back-to-back kinematics ($\vec{q}$=0). Minimally this can be corrected for by using [11]

$$\frac{dN_{l^+l^-}}{d^4xd^4q}(q_0,\vec{q})=\left(\frac{dN_{l^+l^-}}{d^4xd^4q}\right)_{\vec{q}=0}F(M,q,T)$$

$$F(M,q,T)=\frac{e^{-(\sqrt{\vec{q}^2+M^2}-M)/T}}{\sqrt{1+\vec{q}^2/M^2}}\,, \qquad (10)$$

which is exact for free pions. The second, more severe point is the finite momentum acceptance of the detector. In the CERES S+Au experiment only dielectrons with opening angles $\Theta_{ee}>35$ mrad and transverse momenta $p_t>0.2$GeV are detected. To include this we statistically model e^+e^- ρ decays at given temperature and invariant mass and apply the acceptance cuts to each of the two lepton tracks [12] resulting in an acceptance function $A(M,T)$. The final dilepton yield can now be calculated by integrating over momentum and the time evolution of the fireball up to the freeze-out time t_f to obtain

$$\frac{dN_{e^+e^-}}{d^3xdM}=\int_0^{t_f}dt\,C(M,T(t))\left(\frac{dN_{e^+e^-}(t)}{d^4xd^4q}\right)_{\vec{q}=0} \qquad (11)$$

where $C(M,T(t))$ contains the acceptance function as well as the finite q correction to the back-to-back rate. We take t_f=10 fm/c, but our results are affected less than 10% when choosing t_f=15fm/c. Finally we fix the overall normalization in the measured rapidity window to the total yield from vacuum ρ decay obtained by Li *et al.* [2]. Fig. 1 shows our final results supplemented with contributions from free Dalitz decay of π^0's, η's and ω's (dashed-dotted line), which we extracted from ref. [1]. We also implemented the contributions from free ω decay ($\omega\to e^+e^-$) according to ref. [2], which, due to the small ω width, are

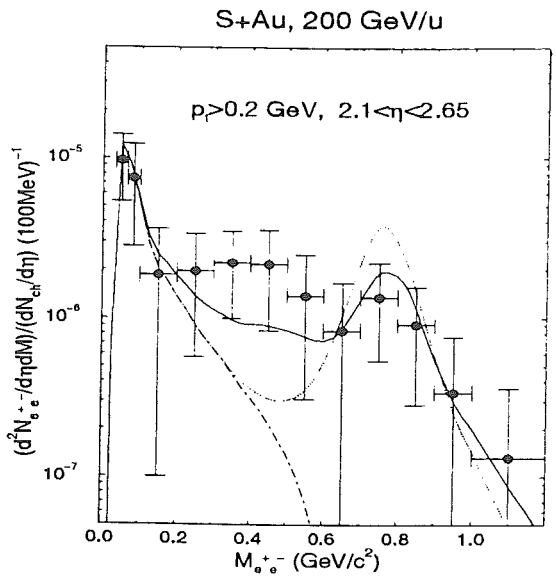

Figure 1: Dielectron yield from free Dalitz decay (dashed-dotted line), free Dalitz + free ω + free ρ (dotted line) and free Dalitz + free ω + in-medium ρ decay (full line); the dots are the CERES data.

expected to undergo only minor medium modifications [2]. The inclusion of the medium modifications of the ρ meson leads to an increase of the e^+e^- yield of about a factor of 3 for invariant masses around M~0.5 GeV/c^2 (full line compared to the dotted line in fig. 1), which, to a large extent, accounts for the experimentally observed enhancement.

References:

[1] J. P. Wurm for the CERES Collaboration, in *Proc. Quark Matter '95*, Nucl. Phys. **A590**, 103c (1995).

[2] G. Q. Li, C. M. Ko and G. E. Brown, Phys. Rev. Lett. **75** 4007 (1995); Phys. Rev. C, sub. .

[3] C.L. Korpa and S. Pratt, Phys. Rev. Lett. **64**, 1502 (1990).

[4] M. Asakawa, C. M. Ko, P. Lévai and X. J. Qiu, Phys. Rev. **C46**, R1159 (1992).

[5] M. Herrmann, B. Friman and W. Nörenberg, Nucl. Phys. **A545**, 267c (1992); Nucl. Phys. **A560**, 411 (1993).

[6] G. Chanfray and P. Schuck, Nucl. Phys. **A545**, 271c (1992); Nucl. Phys. **A555**, 329 (1993).

[7] R. Rapp and J. Wambach, Nucl. Phys. **A573**, 626 (1994).

[8] J. A. Johnstone and T.-S. H. Lee, Phys. Rev. **C34**, 243 (1986).

[9] R. Rapp and J. Wambach, Phys. Lett. **B351**, 50 (1995).

[10] G. Chanfray, R. Rapp and J. Wambach, Phys. Rev. Lett. **76**, 368 (1996).

[11] C. Song, V. Koch, S. H. Lee and C. M. Ko, to be published.

[12] V. Koch, private discussion.

* Also at: Department of Physics, University of Illinois at Urbana-Champaign, 1110 West Green St., Urbana, IL 61801-3080, USA

CORRELATED $\pi\pi$ AND $\bar{K}K$ EXCHANGE IN THE BARYON-BARYON INTERACTION

A. Reuber, K. Holinde, H.-C. Kim* and J. Speth

Quantum chromodynamics (QCD) is the underlying theory of strong interactions, with quarks and gluons as fundamental degrees of freedom. However, in the non-perturbative region of low and medium energy physics, mesons and baryons definitely keep their importance as efficient, collective degrees of freedom for a wide range of nuclear phenomena.

We determine correlated $\pi\pi$ as well as $K\bar{K}$- exchange between two baryons, which should replace the sharp mass σ' and ρ exchange used before in the Bonn nucleon-nucleon (NN) [1] and Jülich hyperon-nucleon [2] interaction models.

First, we want to describe briefly our dynamical model [3, 4] for correlated two-pion and two-kaon exchange in the baryon-baryon interaction (Fig.1), both in the scalar-isoscalar (σ) and vector-isovector (ρ) channel. The contribution of correlated $\pi\pi$ and $K\bar{K}$ exchange is derived from the amplitudes for the transition of a baryon-antibaryon state ($B\bar{B}'$) to a $\pi\pi$ or $K\bar{K}$ state in the pseudophysical region by applying dispersion theory and unitarity. For the $B\bar{B}' \to \pi\pi, K\bar{K}$ amplitudes a microscopic model is constructed, which is based on the hadron exchange picture.

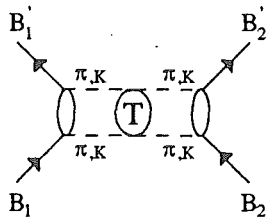

Fig. 1: Correlated $\pi\pi$ and $K\bar{K}$ exchange

The Born terms include contributions from baryon exchange as well as ρ-pole diagrams (Fig.2). The correlations between the two pseudoscalar mesons are taken into account by means of a coupled-channel ($\pi\pi$, $K\bar{K}$) model [5, 6] generated from s- and t-channel meson exchange Born terms (Fig.3). This model describes the empirical $\pi\pi$ phase shifts over a large energy range, from threshold up to 1.3 GeV. The parameters of the $B\bar{B}' \to \pi\pi, K\bar{K}$ model, which are related to each other by the assumption of SU(3) symmetry, are determined by the adjustment to the quasiempirical $N\bar{N} \to \pi\pi$ amplitudes in the pseudophysical region, $t \geq 4m_\pi^2$ [7] obtained by analytic continuation of empirical πN and $\pi\pi$ data.

Schematically the baryon-baryon potential due to correlated $\pi\pi$ and $K\bar{K}$ exchanges can be represented as

$$V^{(0^+,1^-)}_{B_1',B_2';B_1,B_2}(t) \sim \int_{4m_\pi^2}^{\infty} dt' \, \frac{\rho^{(0^+,1^-)}_{B_1',B_2';B_1,B_2}(t')}{t'-t} \qquad (1)$$

in terms of spectral functions, which characterize both the strength and the range of the interaction. Clearly, for sharp mass exchanges, the spectral function becomes a delta-function at the appropriate mass.

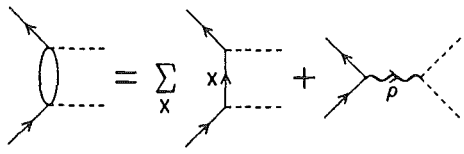

Fig. 2: Microscopic model for the $B\bar{B}' \to \pi\pi, K\bar{K}$ Born amplitudes. The solid lines denote (anti-)baryons, the dashed lines the pseudoscalar mesons $\pi\pi$ or $K\bar{K}$. The sum extends over all $J^P = \frac{1}{2}^+$ and $J^P = \frac{3}{2}^+$ baryons allowed by the conservation of strangeness and isospin.

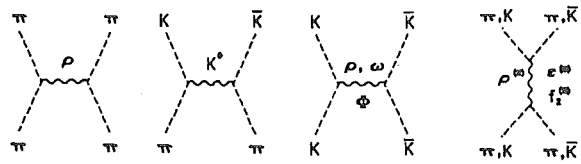

Fig. 3: Born amplitudes included in the model of Refs.[5, 6] for the $\pi\pi - K\bar{K}$ interaction.

Fig.4 shows the resulting spectral functions in the scalar-isoscalar channel for the $NN \to NN$ and $\Sigma N \to \Sigma N$ reaction compared to sharp mass σ exchange used in the Bonn NN and Jülich YN ($Y = \Lambda, \Sigma$) models. Obviously the ΣN spectral function is considerably smaller than the result for the NN case. Note also that correlated $K\bar{K}$ exchange processes play a minor role in the NN system but are very important for the interactions involving hyperons. Compared to sharp-mass σ' exchange of the Bonn potential the present dynamical treatment provides stronger attraction. The difference is especially large in high partial waves since σ' exchange does not contain the long-ranged part of the correlated processes.

For the following discussion it is convenient to parametrize our results in terms of effective coupling strengths. In the simple one-boson-exchange picture the intermediate range attraction is provided by σ exchange; the underlying baryon-baryon potential has the following structure

$$V^{(\sigma)}_{B_1',B_2';B_1,B_2}(t) \sim g^\sigma_{B_1'B_1} g^\sigma_{B_2'B_2} \frac{1}{m_\sigma^2 - t} \, . \qquad (2)$$

The correlated potential is given by Eq. (1), which can be parametrized in terms of t-dependent strength functions $G^{(0^+)}_{B_1',B_2';B_1,B_2}(t)$.

$$V^{(0^+)}_{B_1',B_2';B_1,B_2}(t) \sim G^{(0^+)}_{B_1',B_2';B_1,B_2}(t) \frac{1}{m_\sigma^2 - t} \qquad (3)$$

Note that in the OBE frame the three reactions $NN \to NN$, $\Sigma N \to \Sigma N$, $\Sigma\Sigma \to \Sigma\Sigma$ are determined by two parameters (coupling constants) g^σ_{NN} and $g^\sigma_{\Sigma\Sigma}$ whereas

*Institut für Theoretische Physik II, Ruhr-Universität Bochum, 44780 Bochum, Germany

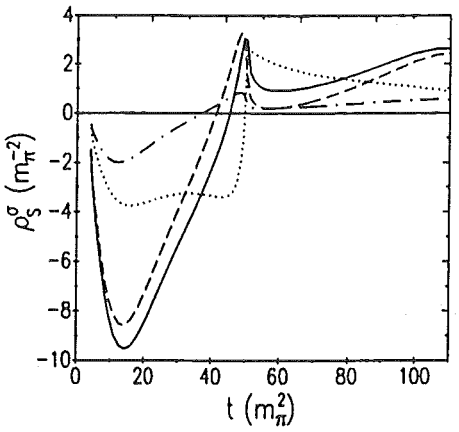

Fig. 4: Spectral function $\rho_S^\sigma(t)$ in the NN (solid) and $N\Sigma$ (dotted) channel derived with the full model (cf. Fig.1). If the contributions of the $B\bar{B}' \to K\bar{K}$ Born amplitudes are neglected the dashed (NN) and the dash-dotted lines ($N\Sigma$) are obtained.

Table 1: Values of the strength function $G^{(0^+)}(t=0)$ for BB' channels with increasing strangeness.

	NN	ΛN	ΣN	$\Lambda\Lambda$	$\Sigma\Sigma$	$N\Xi$
$G^{(0^+)}(t=0)$	1	0.49	0.41	0.26	0.30	0.19

the correlated exchanges are characterized by three independent strength functions, which means of course that vertex coupling constants cannot be well defined.

In the physical region the strength of the contributions is to a large extent governed by the value of G at t=0. The values for the various channels (with normalization 1 in the NN channel) are shown in Table 1.

Thus as a main result the strengths of correlated $\pi\pi$ and $K\bar{K}$ exchange decrease with increasing strangeness (becoming more negative). Furthermore they do not fulfill SU(3) relations.

The situation is similar but more complicated in the vector-isovector (ρ) channel. Now we have in the OBE at each vertex a vector (g) and a tensor (f) coupling. Thus the NN interaction is determined by two coupling constants, $g_{\rho NN}$ and $f_{\rho NN}$ whereas the correlated result requires three strength functions $G^{vv}_{NN,NN}(t)$, $G^{tt}_{NN,NN}(t)$, $G^{vt}_{NN,NN}(t)$. Fig.5 shows our results in comparison to the corresponding coupling constants including formfactors used in the Bonn potential. Again our results are considerably larger. The reason is the form factor with $\Lambda_{NN\rho}$ = 1.4 GeV used in the Bonn potential, which reduces the strength at t=0 by as much as 50 %.

For the general baryon-baryon case, the resulting strength functions can be likewise determined. Again they deviate from what is expected in the naive SU(3) picture for genuine ρ exchange, due to a sizable admixture of baryon exchange processes to the (SU(3) symmetric) ρ-pole contributions.

As a main conclusion, meson-meson correlations are important in baryon-baryon interactions and have to be included in any realistic model description. An explicit dynamical model for correlated $\pi\pi$ (plus $K\bar{K}$) exchange

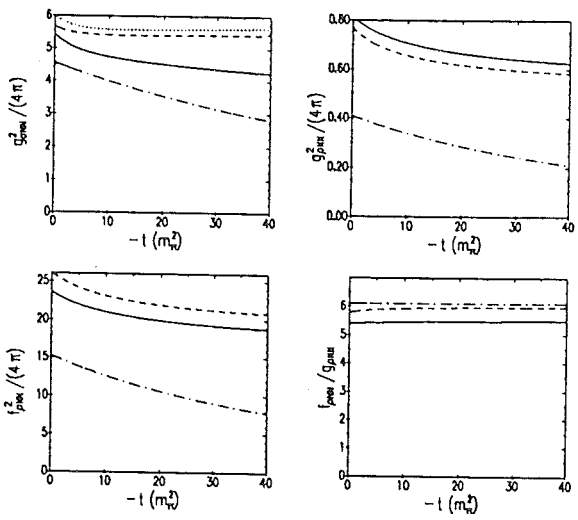

Fig. 5: Effective strength of the NN interaction due to correlated $\pi\pi$ and $K\bar{K}$ exchange in the σ and ρ channel as a function of the 4-momentum transfer $t < 0$. Shown are $g^2_{\sigma NN} \equiv G^\sigma_{NN}$, $g^2_{\rho NN} \equiv {}^{vv}G^\rho_{NN}$, $f^2_{\rho NN} \equiv {}^{tt}G^\rho_{NN}$ and $f_{\rho NN}/g_{\rho NN} \equiv [{}^{tt}G^\rho_{NN}/{}^{vv}G^\rho_{NN}]^{\frac{1}{2}}$. The solid (dotted) line is derived from the microscopic model for correlated $\pi\pi$ and $K\bar{K}$ exchange using $t'_{max} = 120m_\pi^2$ ($50m_\pi^2$) as cutoff in the dispersion integral. The dashed line follows from the quasiempirical $N\bar{N} \to \pi\pi$ amplitudes [7] with $t'_{max} = 50m_\pi^2$. The effective strength of σ' and ρ exchange in the Bonn potential[1] is denoted by the dash-dotted line.

leads to results characteristically different from the simplified treatment in terms of sharp-mass σ' and ρ exchange; for example, the effective strengths do not fulfil SU(3) relations. In the scalar-isoscalar channel the predicted attraction decreases with increasing strangeness (becoming more negative) of the BB system.

References:

[1] R. Machleidt, K. Holinde, and Ch. Elster, *Phys. Rep.* **149** (1987) 1.

[2] B. Holzenkamp, K. Holinde, and J. Speth, *Nucl. Phys.* **A500** (1989) 485. A. Reuber, K. Holinde, and J. Speth, *Nucl. Phys.* **A570** (1994) 543.

[3] H.-C. Kim, J. W. Durso, and K. Holinde, *Phys. Rev.* **C49** (1994) 2355.

[4] A. Reuber, (1995), Berichte des Forschungszentrums Jülich, Nr. 3117. A. Reuber, K. Holinde, H.-C. Kim, and J. Speth, submitted to *Nucl. Phys.* **A**.

[5] D. Lohse, J.W. Durso, K. Holinde, and J. Speth, *Nucl. Phys.* **A516** (1990) 513.

[6] C. Schütz, K. Holinde, J. Speth, B.C. Pearce, and J.W. Durso, *Phys. Rev.* **C51** (1990) 1374.

[7] G. Höhler, F. Kaiser, R. Koch, and E. Pietarinen, "Handbook of Pion-Nucleon Scattering", *Phys. Data 12-1*, Fachinformationszentrum, Karlsruhe (1979).; O. Dumbrajs et al., *Nucl. Phys.* **B216** (1983) 277.

Coherent Pion-Electroproduction in the Reaction $^{12}C(e,e'\pi^+)^{12}B(g.s)$

G. van de Sand, B. Körfgen, F. Osterfeld

Recently, new information on the Δ-propagation in nuclei has been obtained from intermediate energy $(p,n\pi^+)$ and $(^3He,t\pi^+)$ exclusive charge exchange reactions [1, 2]. The exclusive cross section data of these reactions show a substantial downward energy shift of the Δ-resonance in nuclei, as compared to the proton target. As in pionabsorption, which involves a purely spin-longitudinal excitation-mechanism, the shift in charge exchange reactions is due to a coherent pion wave in the spin-longitudinal channel [3, 4]. The shift is caused by the attractive π-exchange interaction between Δ-particle nucleon-hole states in the nucleus.

In this report we investigate the reaction $^{12}C(e,e'\pi^+)^{12}B(g.s)$ in order to study the coherent pion-wave in nuclei [5]. In comparison to hadronic reactions the $(e,e'\pi^+)$-reaction offers various advantages: First, the virtual photon has a large mean free path in the nucleus, thus this reaction is volume sensitive. Second, energy and momentum transfer to the nucleus can be varied independently. Third, in contrast to pion-photoproduction, the pion-electroproduction [6] involves the structure function F_5, which provides a spin-longitudinal coupling. Therefore the excitation of a coherent pion-wave in forward direction is possible. The transverse component of the pion-electroproduction can be separated from the longitudinal one by a Rosenbluth-plot. By measuring the energy of the electron and the pion in the final channel, it is possible to trigger on the reaction $^{12}C(e,e'\pi^+)^{12}B(g.s)$. The energy of the pion is determined by the energy of the virtual photon and the energy difference of 13.37 MeV between the ^{12}C and ^{12}B ground states.

The mechanism for the excitation of the coherent pion wave in the nucleus is shown in fig. 1. The mechanism involves two steps:

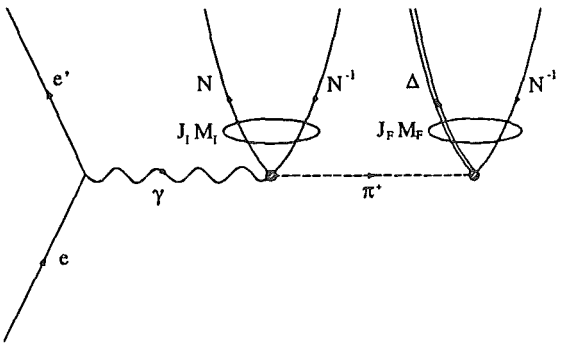

Fig. 1: The two-step excitation process

In the first step a virtual pion is produced the strength of which is proportional to the spin-longitudinal component L_{0+} of the pion-electroproduction amplitude.Simultaneously a $p_{3/2}$ proton of ^{12}C is converted into a $p_{1/2}$ neutron exciting the $^{12}B(g.s.)$. Values for the L_{0+}-amplitude were calculated by dispersion relations [7]. After its creation, the pion can either leave the nucleus (born term, fig. 2 a) or it can excite in a second step a Δ-hole-pair, (fig . 2 b). This Δ-hole-pair propagates then through the nucleus (coherent term, see fig. 2 b).

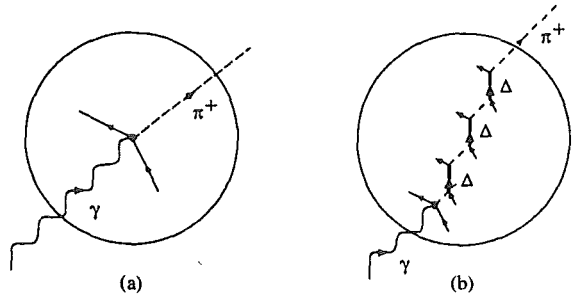

Fig. 2: Bornterm (a), coherent pion-wave (b)

The final pion-production cross section is given by the interference of the born amplitude und the coherent amplitude. It turns out, that both terms are important. The interference is strongly energy dependent. In fig. 3 the angular disribution of the co-

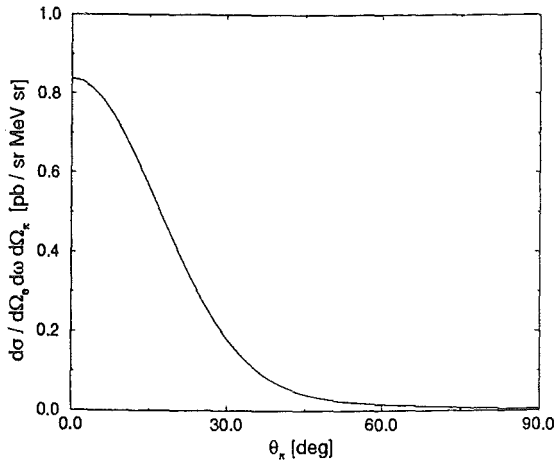

Fig. 3: Angular distribution for the reaction $^{12}C(e,e'\pi^+)^{12}B$ with $\omega = 320$ MeV, $\varepsilon_i = 730$ MeV and $\theta_e = 37°$.

herent pion cross section is shown. It is strongly forward peaked. The scattering angle θ_π is measured relatively to the direction of the photon three momentum $\vec{q}$. The peak in forward direction is a result of the spin-longitudinal excitation and de-excitation of the pion-wave in the nucleus. The nucleus acts as a filter and emits the pions in forward direction.
In fig. 4 the energy spectrum of the coherent pions is shown. It can be seen that there is a distinct resonance structure in the pion cross section at small excitation energies (solid curve). The peak is shifted

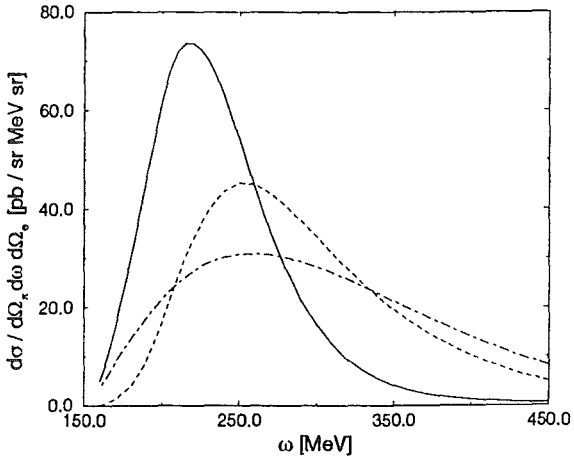

Fig. 4: Energy spectra for the $^{12}C(e,e'\pi^+)^{12}B(g.s)$-reaction with $\theta_e = 15°$: Born cross section (dashed-dotted), cross section due to the coherent term (dashed), final coherent cross section (solid).

downward in energy relative to the born cross section and the coherent cross section. For low energies born term and coherent term interfere constructively while for higher energies they interfere destructively. This interference pattern is caused by the pion-propagator which introduces a phase in the coherent term. For low energies the phase vanishes and born term and coherent term interfere constructively. At higher energies the phase is complex leading to destructive interference. In this way the nucleus can act as an energy filter: only pions with small frequencies can pass through the nucleus, while those with higher frequencies are suppressed.
The peak position in the pion-spectrum is very sensitive to the Δ-hole residual interaction which induces the pion multiple scattering in the nucleus. In fig. 5 we show calculated energy spectra with and without inclusion of the residual interaction. It can be seen that the spectrum calculated with inclusion of the residual interaction is shifted down in energy by 50 MeV relative to that without inclusion of the residual interaction. The magnitude of the shift depends on the four-momentum transfer in the (e,e')-reaction. The higher the momentum transfer, the smaller the

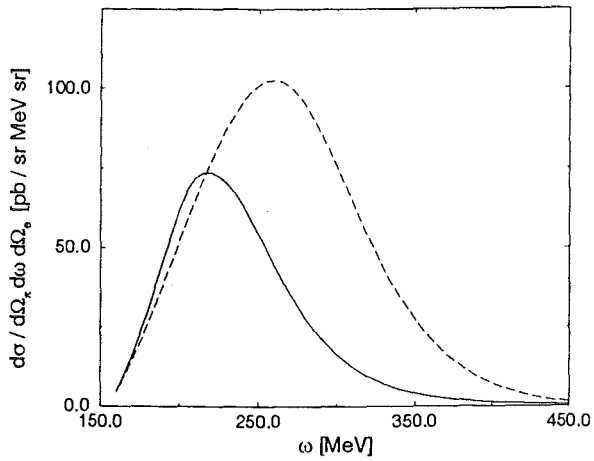

Fig. 5: The cross sections with (solid) and without (dashed) inclusion of the residual interaction at $\theta_e = 15°$.

shift.
We remark that this reaction can also be used to determine the magnitude of the L_{0+}-Amplitude. This amplitude is difficult to measure in pion-electroproduction on the nucleon because in this case the cross section is dominated by the M_{1+}-amplitude which excites the Δ-resonance.

References:

[1] F. Osterfeld, B. Körfgen, P. Oltmanns and T. Udagawa, Phys. Scr. **48**, 95 (1993)
[2] P. Oltmanns, F. Osterfeld and T. Udagawa Phys. Lett. B **B 299**, 194 (1993)
[3] B. Körfgen, F. Osterfeld and T. Udagawa, Phys. Rev. C **50**, 1637 (1994).
[4] T. Udagawa, P. Oltmanns, F. Osterfeld und S.W. Hong, Phys. Rev. C **49**, 3162 (1994)
[5] Gerd van de Sand, Diplomarbeit, Uni Bonn
[6] E. Amaldi, S. Fubini and G. Furlan, *Pion-Electroproduction*, Springer Verlag, (1979).
[7] G. von Gehlen, Nucl. Phys. **B 20**, 102 (1970).

C. Schütz and K. Holinde

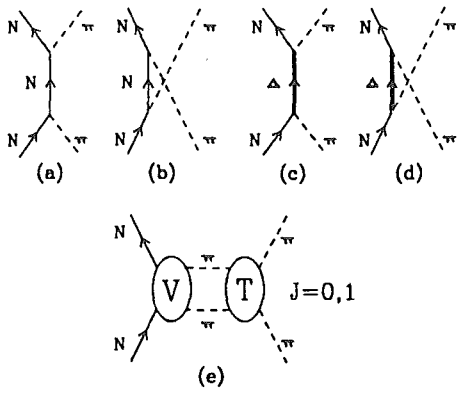

Figure 1: Contributions to our πN interaction model.

In this work we focus our interest on the first resonant partial waves of πN interaction. Within our πN interaction model [1] we are able to disentangle meson–cloud effects arising from the underlying meson–baryon dynamics (like e.g. the crossed pole diagrams and the correlated 2π exchange in Fig.) from genuine three–quark resonance contributions which correspond to the direct pole diagrams in our model. Therefore we can investigate whether there is any need for a three–quark core to describe the resonant partial waves and if so, we are able to calculate within our model the contributions from the non–resonant background.

In Chew–Low theory it was shown that it is possible to generate the Δ resonance from the crossed nucleon pole of Fig. (b). Therefore it is not surprising that we also find within the model described above that this process plays an important role for the understanding of the P_{33} partial wave of πN scattering. It dominates the non–pole part of the interaction in this partial wave. However, to generate a resonant behavior without inclusion of a direct Δ pole (cf. Fig (c)), one needs an extremely hard πNN form factor which is not consistent with the description of the other partial waves and therefore unrealistic.

How large is the effect of the non–resonant background ? To answer this question, we have plotted in Fig. 3 (a) a simplified model which does not include any non–resonant background and which is based on the same bare $N\Delta\pi$ coupling as our full model. As one can already see from the phase shift, the background plays a crucial role for the quantitative understanding of the Δ width. From the imaginary part of the T matrix plotted in part (b) of this figure one can conclude that the non–pole interaction accounts for about 40% of the Δ width.

One of the most interesting partial waves in πN scattering is the P_{11} partial wave. It is a challenge for models of πN interaction to describe quantitatively the repulsion at low energies followed by the attraction leading to the Roper resonance at higher energies. Within the model presented here, the rise of the P_{11} phase shift in the elastic region of the interaction can be reproduced without any contribution from a genuine N^* particle, cf. Fig. 4. The non–pole part of the interaction in this partial wave is dominated by correlated 2π–exchange in the ρ channel. If this strong attraction is counterbalanced by the direct nucleon pole contribution we are able to obtain the quantitative description of the data shown above.

However, to really learn about the nature of the $N^*(1440)$ resonance, we have to extend the energy range of our model. For energies above 1.3 GeV, the pion–nucleon interaction gets inelastic due to coupling to the $\pi\pi N$ channel. Here the dominant contributions are coupling to the $\pi\Delta$ and the σN channel, where σ denotes an isoscalar $\pi\pi$ S–wave state.

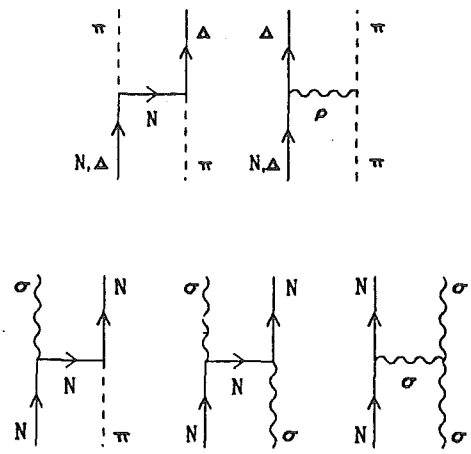

Figure 2: Additional contributions to our interaction model.

Therefore we have extended our model of elastic πN interaction to a coupled–channel model involving the reaction channels πN, $\pi\Delta$ and σN. The additional contributions to the interaction which we have taken into account are summarized in Fig. . Self–energy contributions of the Δ as well as the σ are taken into account. The coupling constants occuring in the transition πN — $\pi\Delta$ and the direct $\pi\Delta$ interaction have been obtained from the $SU(2) \times SU(2)$ quark model [2]. The (effective) σNN coupling is taken from Ref. [3].

As one can see from the dash–dotted lines in Fig. 4, already the coupled channel model involving the πN and the $\pi\Delta$ channels can generate a resonant behavior in the P_{11} partial wave at the correct energy to explain the $N^*(1440)$ dynamically. However, coupling exclusively to the $\pi\Delta$ channel accounts only for a small part of the inelasticity. The description of

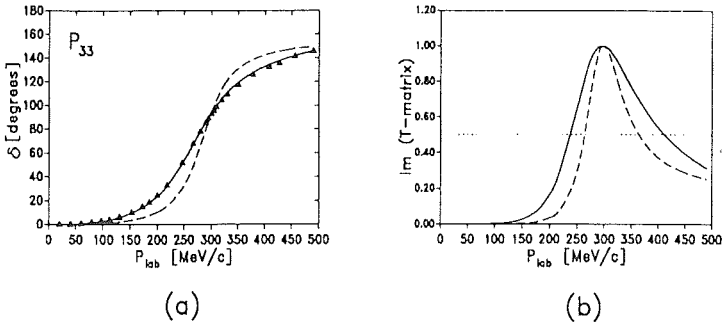

Figure 3: (a) πN scattering phase shift in the P_{33} partial wave, (b) imaginary part of the T matrix in this partial wave. The solid line denotes the result of our full model whereas the dashed line is the prediction if we do not include the non–pole part of the interaction.

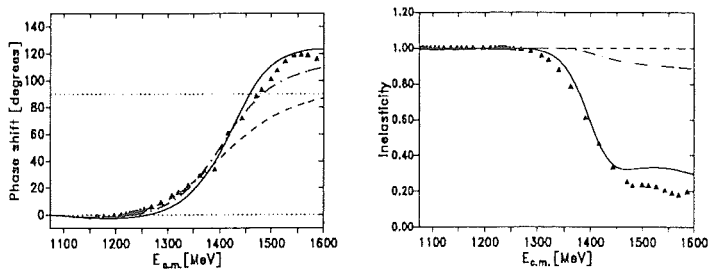

Figure 4: Phase shift and inelasticity in the P_{11} partial wave of πN scattering compared to the KA84 phase shift solution [4]. The dashed line denotes the extrapolation of our elastic model, the dash–dotted line takes into account coupling to the reaction channel $\pi\Delta$, and the solid line is the result of our full $\pi N/\pi\Delta/\sigma N$ coupled–channel model.

the inelasticity can be improved considerably if additional coupling to the reaction channel σN is taken into account. The strong inelasticity indicates that there is a considerable direct σN interaction which is modelled by the effective σ exchange in our calculation. In our full $\pi N/\pi\Delta/\sigma N$ interaction model the $N^*(1440)$ resonance thus can be understood purely in terms of the meson–baryon dynamics. There is no need to include a direct pole diagram corresponding to a three–quark contribution to the $N^*(1440)$.

[1] C. Schütz, J.W. Durso, K. Holinde, and J.Speth, Phys. Rev. C **49**, 2671 (1994).

[2] G.E. Brown and W. Weise, Phys. Rep. **C22** (1975) 281.

[3] J.W. Durso, A.D. Jackson, and B.J. Verwest, Nucl. Phys. **A 345** (1980) 471.

[4] G. Höhler, private communication.

πNN form factor determined from a microscopic model for πN scattering

C. Schütz and K. Holinde

The strong πNN vertex plays an outstanding role everywhere in nuclear physics. Therefore a precise knowledge of the corresponding form factor is essential in order to reach a combined and consistent understanding of nuclear phenomena.

The πNN form factor can be extracted quite directly from an off-shell model of πN scattering, according to a method used recently by Saito and Afnan [1]. Whereas their work is based on a purely phenomenological, separable πN interaction model, the work presented here starts from a microscopic meson exchange model for πN scattering which has been developed by our group in Jülich [2]. It contains, apart from nucleon- (N) and delta-isobar (Δ) s-channel pole terms, non-pole pieces consisting of crossed N and Δ exchange and correlated $\pi\pi$ exchange in the $0+$ (σ) and $1-$ (ρ) channels. Iterating this interaction model, a satisfactory description of all πN scattering phase shifts below pion production is achieved. It is important to note that the non-pole pieces which determine the πNN form factor (see below) act with a unified set of parameters in all partial waves and are therefore strongly constrained by the simultaneous description of all S and P waves.

In order to derive the renormalized πNN form factor we start from the 'dressed' vertex function $v^{\pi NN}$

$$v^{\pi NN} \equiv v_0^{\pi NN} + T_{\pi N}^{non-pole} G_{\pi N}\, v_0^{\pi NN} \quad ,$$

where $v_0^{\pi NN}$ denotes the bare $N \rightarrow \pi N$ vertex, $G_{\pi N}$ is the πN propagator, and the non-pole amplitude $T_{\pi N}^{non-pole}$ is generated by iterating the non-pole part of the potential.

The physical form factor $F^{\pi NN}(p, Z)$ is then obtained from $v^{\pi NN}(p, Z)$ by dividing out the momentum dependence already inherent in the bare πNN vertex. Here the assumptions made for the πNN coupling scheme play a crucial role. If the form factor determined from the πN T-matrix is to be applied in combination with pseudoscalar (pseudovector) πNN coupling afterwards, one has to choose the consistent momentum dependence of the vertex in extracting the form factor from the dressed πNN vertex. The form factor is a function of both Z and p and it is normalized to unity at the physical nucleon pole, i.e. at $Z = m_N$.

In the following we use two different πN models 1, 2 (for details, see Ref. [2]), which are based on the same dynamical input, but differ in the parameterization of the (bare) form factors in both the pole and non-pole contributions. Results for the dressed πNN form factor at $Z = m_N$ are shown in the figure below. Interestingly, the results for model 1 and 2 are somewhat different although the non-pole amplitude is generated from identical dynamics and is constrained by all πN partial waves. Obviously the remaining freedom in parameterizing the (bare) form factors in the pole terms and those in the non-pole contributions can induce some variations in the dressed form factors.

The results obtained based on the assumption of pseudovector πNN vertex structure are much softer than those obtained for pseudoscalar πNN coupling. The latter result for model 1 of Ref. [2] can be well parameterized by a monopole parameterization, $F(p) = (\Lambda^2 - m_\pi^2)/(\Lambda^2 + p^2)$, with cutoff mass 0.7 GeV. Quite remarkably, this result is in good agreement with independent information [3], also from QCD lattice calculations [4], about that form factor.

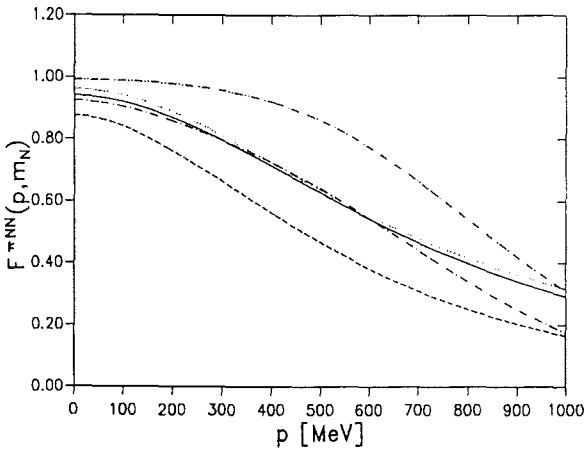

πNN form factor for alternative πNN coupling schemes as function of the pion momentum in the πN c.m. system. The dashed (dash-dotted) line denotes our prediction resulting from model 1 (2) of Ref. [2] based on the assumption of pseudovector πNN coupling, whereas the solid line (model 1) and the dash-double dotted line (model 2) are the corresponding results if pseudoscalar πNN coupling is assumed. The dotted line is a monopole form factor with the cutoff mass Λ = 700 MeV.

References:

[1] T.-Y. Saito and I.R. Afnan, Phys. Rev. C **50** (1994), 2756.

[2] C. Schütz, J.W. Durso, K. Holinde, and J. Speth, Phys. Rev. C **49** (1994), 2671.

[3] S.A. Coon and M.D. Scadron, Phys. Rev. C **42** (1990), 2256.

[4] K.F. Liu, S.J. Dong, T. Draper, and W. Wilcox, Phys. Rev. Lett. **74** (1995), 2172.

ωNN Vertex Function and the γππ Anomaly

J.Speth and R.Tegen

We consider the electromagnetically gauged Lagrangian of the σmodel

$$L^{EM} = L_\sigma - \frac{1}{4}F_{\mu\nu}F^{\mu\nu} - j_\mu A^\mu \qquad (1)$$

with $j^\mu = j_N^\mu + j_{\pi\pi}^\mu + j_{\pi\pi\pi}^\mu$, where

$$j_N^\mu(x) = \overline{\psi}(x)e_N\gamma^\mu\psi(x)$$

$$j_{\pi\pi}^\mu(x) = e\varepsilon_{3ab}\phi_a(x)i\overleftrightarrow{\partial}^\mu\phi_b(x)$$

and an "anomalous" contribution related to the Wess-Zumino anomaly term,

$$j_{\pi\pi\pi}^\mu(x) = -ieH\varepsilon^{\mu\nu\sigma\tau}\varepsilon_{abc}\partial_\nu\phi_a(x)\partial_\sigma\phi_b(x)\partial_\tau\phi_c(x) \qquad (2)$$

With this L^{EM} we calculate diagram Fig.1's contribution to the nucleon electromagnetic form factors $F_{1,2}(q^2)$ or, equivalently, the Sachs form factors $G_{E,M}(q^2)$. Note that the $\pi^+\pi^-\pi^0$ intermediate state couples only to the isoscalar component of the photon. Under the additional assumption of vector meson dominance (VMD) this process would be dominated by the isoscalar vector mesons (ω(782), φ(1020), J/ψ(3097), ...). Without any vector mesons the chiral anomaly (2) comes only in one variety (the "contact" term); then [1] $H = H^c = (24\pi^2 f_\pi^3)^{-1}$ in eq.(2). If one includes, however, the vector mesons in (1), then the constant H in eq.(2) obtains structure due to the now possible processes $\gamma \to \begin{pmatrix} \omega \\ \phi \\ J/\psi \\ \Upsilon \end{pmatrix} \to \pi\rho \to \pi^+\pi^-\pi^0$. The ω decays into $\pi^+\pi^-\pi^0$ with a branching ratio of ~ 90%; the corresponding branching ratio for the φ (J/ψ) is ~ 3% (1%).

The contribution of Fig.1 to $F_{1,2}^{(I=0)}(q^2)$ can then be decomposed into their vector meson content $F_{1,2}^{(V)}(q^2)$ (V= ω, φ, J/ψ , Υ , ...)

$$eF_{1,2}^{(I=0)}(q^2) = \sum_{V=\omega,\phi,\ldots} \frac{\frac{em_V^2}{g_V}}{m_V^2 - q^2 - im_V\Gamma_V(q^2)} F_{1,2}^{(V)}(q^2) \qquad (3)$$

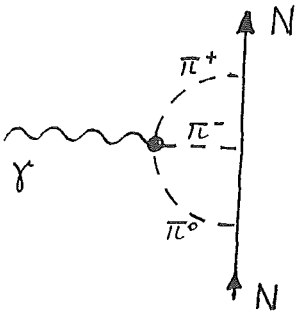

Fig.1 : Coupling of a virtual photon to the nucleon via the isoscalar $\pi^+\pi^-\pi^0$ state. The solid dot represents a contact interaction as well as the two-step process via the πρ intermediate state.

The two-meson-loop calculation of Fig.1 uses Feynman's parametrization of products of propagators as well as a Wick rotation to Euclidean 4-space [2]. Our result can be parametrized in a simple way ($\eta = -q^2/4m_N^2 \geq 0$):

$$G_E^{(I=0)c}(q^2) \equiv F_1^{(I=0)c}(q^2) - \eta F_2^{(I=0)c}(q^2) \approx -\frac{\eta}{\eta_0}e^{-\eta a}$$

$$G_M^{(I=0)c}(q^2) \equiv F_1^{(I=0)c}(q^2) + F_2^{(I=0)c}(q^2) \approx \frac{\mu_c}{\mu_N}e^{-\eta a'}$$

with $\eta_0 \approx 0.6$, $a \approx a' \approx 13$, $\mu_c/\mu_N \approx -0.04$ for typical Euclidean cut offs around 1 GeV. The two-step process $\gamma \to \pi\rho \to 3\pi$ yields $G_{E,M}^{(I=0)\pi\rho}(q^2) \cong -3G_{E,M}^{(I=0)c}(q^2)$

so that the total

$$G_E^{(I=0)total}(q^2) \approx 2\frac{\eta}{\eta_0}e^{-\eta a}, \quad G_M^{(I=0)total}(q^2) \approx 2\left|\frac{\mu_c}{\mu_N}\right|e^{-\eta a} \qquad (4)$$

If added to the usual quark model contribution one sees that the ω meson stabilizes the nucleon, a well-known effect observed also in Skyrme-type models [3] ; here this effect is manifest in a shrinking of the nucleon radius due to the presence of the ω (3π) cloud. We recall here the presence of $\log(m_\pi)$ and m_π^{-1} terms in the isovector radii $\langle r_{1,2}^2\rangle^{I=1}$ due to the presence of the ρ (2π) cloud, which tend to 'destabilize' the nucleon, in the sense that these radii become infinite in the chiral limit. The isoscalar radii (including the anomaly) contain only terms $O(m_\pi^2 \log m_\pi)$ and $O(m_\pi^2)$ which are finite in the chiral limit ; there is, therefore, no connection between isoscalar radii and the pion Compton wave length [2].

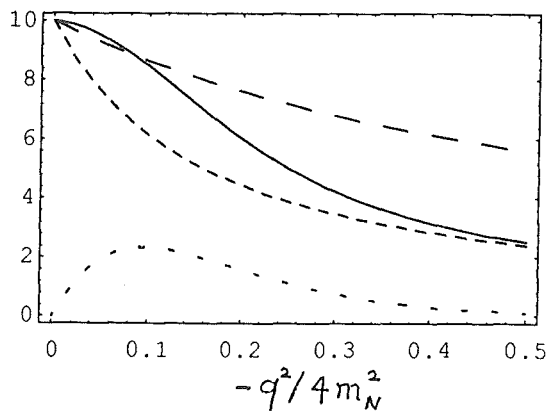

Fig.2: ωNN vertex function. Dotted curve: anomaly contribution; short-dashed curve: quark contribution with Λ_Q =750MeV; solid curve: sum of anomaly and quark contributions; long-dashed curve: monopole fit with Λ_{eff} = 1.5 GeV.

The contribution of heavier isoscalar vector mesons (φ(1020), J/ψ(3097), ...) in (3) is suppressed because the time-like pole they induce via (3) moves further and further away from the space-like region considered here; we will neglect them here for the purpose of our qualitative discussion. Then

$$G_E^{\omega\to3\pi}(q^2) = g_\omega(1+4\eta\frac{m_N^2}{m_\omega^2})\,2\frac{\eta}{\eta_0}\,e^{-\eta a}$$

$$G_M^{\omega\to3\pi}(q^2) = g_\omega(1+4\eta\frac{m_N^2}{m_\omega^2})\,2\frac{|\mu_c|}{\mu_N}\,e^{-\eta a} \qquad (5a)$$

or, equivalently,

$$F_1^{\omega\to3\pi}(q^2) = 2g_\omega(1+4\eta\frac{m_N^2}{m_\omega^2})\frac{\eta}{1+\eta}\,e^{-\eta a}(\frac{1}{\eta_0}+\frac{|\mu_c|}{\mu_N})$$

$$F_2^{\omega\to3\pi}(q^2) = 2g_\omega(1+4\eta\frac{m_N^2}{m_\omega^2})(\frac{|\mu_c|}{\mu_N}-\frac{\eta}{\eta_0})\,e^{-\eta a}\frac{1}{1+\eta} \qquad (5b)$$

so that $g_{\omega NN}^T \equiv F_2^{\omega\to3\pi}(0) \cong 2g_\omega\left|\mu_c/\mu_N\right| = 1.3$ for g_ω =16 [4]. If one assumes for the quark model ωNN vertex function a monopole form

$$F_{(1,2)}^{\omega\to q\bar{q}}(q^2) = \frac{g_{\omega NN}^{(V,T)q\bar{q}}}{1-\frac{q^2}{\Lambda_Q^2}} \qquad (6)$$

with $g^{V,q\bar{q}}_{\omega NN} = 3g^{V,q\bar{q}}_{\rho NN} = 10$, $g^{T,q\bar{q}}_{\omega NN} = 0$, then the total ωNN vertex function is $F_1^{\omega}(q^2) = F_1^{\omega\to 3\pi}(q^2) + F_1^{\omega\to q\bar{q}}(q^2)$ and the associated radius reads $\langle r_1^2 \rangle^{\omega} = \frac{6}{\Lambda_Q^2} + \frac{\langle r^2 \rangle^{anomaly}}{g^{V,q\bar{q}}_{\omega NN}}$, $\langle r^2 \rangle^{anomaly} \cong -3.5 fm^2$

where the minus sign is due to (4). If we assume again that the total vertex function displays an equivalent monopole form (6), but now with $\left(g^{V,eff}_{\omega NN}, \Lambda_{eff}\right)$ we find $\Lambda_{eff} = \Lambda_Q / \sqrt{1 + \frac{\Lambda_Q^2 \langle r^2 \rangle^{anomaly}}{6 g^{V,q\bar{q}}_{\omega NN}}} > \Lambda_Q$.

For Λ_Q (700-800) MeV one easily obtains $\Lambda_{eff} \sim 1.5\ \Lambda_Q$ = GeV with the given values for $< r^2 >^{anomaly}$ and $g^{V,q\bar{q}}_{\omega NN}$, see Fig.2. Note that the relevant range is $0 \le \eta \le 0.1$, corresponding to $0 \le -q^2 \le (600 MeV/c)^2$.

This trend could explain why in NN scattering a large cut off $\Lambda_\omega \sim 1.5$ GeV is necessary for a quantitative fit to the phase shifts. Our result confirms the findings in [5] which model the ωNN coupling in NN scattering via correlated πρ exchange, leaving much less room for explicit quark-gluon effects than previously assumed.

References:

[1] T.D.Cohen, Phys.Lett. B233 (1989) 467, and references therein.

[2] J.Speth and R.Tegen, in preparation for publication.

[3] I.Zahed and G.E.Brown, Phys.Rep. 142 (1986) 1

[4] J.W.Durso, Phys.Lett. B184 (1987) 348

[5] G.Janssen, K.Holinde, J.Speth , Phys.Rev.Lett. 73 (1994) 1332 and (1995):"correlated πρ exchange in the NN interaction". Preprint IKP-KFA-TH ...

*On sabbatical leave from: Physics Department, University of the Witwatersrand, Johannesburg 2050, South Africa

Threshold effects and Parity violation for Neutron Resonances

Erich Vogt

Motivated by the search for contributions to the understanding of parity violation in narrow, p-wave, neutron resonances a number of threshold effects have been explored for neutron size resonances in heavy nuclei.

Among a number of experimental investigations of parity violation (PV) in p-wave neutron resonances, the recent Los Alamos experiment[1] for ^{232}Th+n has aroused considerable interest. The data provide the analyzing power for the scattering of polarized neutrons. For the eight individual resonances for which the analyzing power differs significantly from zero it was found that the average polarization asymmetries were not only large (up to 10 %) but also all of the same sign.

A number of recent theoretical investigations have tried to understand the large asymmetries and their common sign. Among the most attractive of these investigations is that of Bouman et al[2] which assigned the asymmetry to the mixing into the p-wave reduced-width amplitudes, by PV forces, of s-wave reduced width amplitudes from the near by 4s & 5s size resonances. In the vicinity of ^{232}Th the 4p size resonance dominates for the p-wave reduced width amplitudes. Therefore the perturbation theory analysis of the PV effect reduces, in this analysis, to the mixing caused by a single-particle PV force ($V_{PV} = \in \bar{\sigma} \cdot \vec{p}c$) of the bound 4s state and unbound 5s state into the 4p resonant state.

Subsequent reviews[3] of this model-which, inter alia, produces the common and correct sign of the individual measured asymmetries - have suggested that the PV force required to explain the magnitude of the asymmetries appears to be too large by perhaps an order of magnitude. Here we explore whether or not the reaction dynamics cannot augment the asymmetry and lessen the contribution required from the PV matrix element.

In the perturbation theory approximation of the single-particle model[2] the average polarization asymmetry, $\bar{P}m$ is directly proportional to a sum over the s-wave single-particle states s of the following quantity

$$P\int_{-\infty}^{+\infty} \sum_s \frac{S_s(E)}{E - E_m} < s|V_{PV}|4p > \qquad (1)$$

where m is the individual p-wave neutron resonance, $S_s(E)$ is the contribution from the state s (=1s, 2s, 3s, ...) to the s-wave neutron strength function and $< s|V_{pv}|p >$ is the single-particle PV matrix element between the various s states and the 4p state. In Eq. (1) P stands for principal value of the improper integral. In the calculations of Bowman et al[2] the matrix element was about as large as it could be: not much help can be expected by improving the overlap between the 4p and the s-wave single-particle wave functions. We then explore what help might be expected from the integral, in Eq. (1), of the s-wave strength function.

If we use the R-matrix method for the single-particle states s, then the R-function is

$$R \equiv \Sigma_s \gamma_s^{\,2} / (E_s - E) \qquad (2)$$

where $\gamma_s^{\,2}$ is the single-particle reduced width $(\hbar^2 / ma^2$, where m is the reduced mass and a the radius). The basis of the nuclear-optical-model is, that in (2) we replace E by E+iW. This changes the R-function to

$$R \equiv \Sigma_s \gamma_s^{\,2} (Es - E - iW)$$

$$\equiv \Sigma_S (a_S^{\,\infty} + i\pi \ S_S) \qquad (3)$$

where $S_s(E)$ is the strength function of Eq. (1) and the real part of the R-function ($a_S^{\,\infty}$) is a quantity which modifies the coherent nuclear scattering length (see below). We find

$$S(E) = \frac{1}{\pi}\Sigma_s \gamma_s^{\,2} W / \left[(E_s - E)^2 + W^2\right] \qquad (4)$$

and

$$= a\infty\Sigma_S \frac{(E_S - E)\gamma_S^{\,2}}{(E_S - E)^2 + W^2} = \Sigma_S P \int_{-\infty}^{\infty} \frac{S_S(E')dE'}{E' - E} \qquad (5)$$

$$\equiv \Sigma_s a_y^{\,\infty}$$

We note that $2W = \Gamma sp$, where Γsp is he spreading width of each single-particle s-state of the strength function. We further note that it is precisely the components of $a_S^{\,\infty}$ which are needed in the PV quantity of Eq. (1).

Before exploring how $a_S^{\,\infty}$ can be augmented we subject the estimate of it, by Bowman et al, to same experimental discipline. For the 4s state they assume Γsp =1.5 MeV, so that W = 0.75 MeV, and they assume E_{4s} = -1.7 MeV (they assume that nuclear deformation pushes up the bound 4s state to just below threshold. Dropping the spreading width (because E_{4s} >> W) they conclude, effectively, that $a_{4s}^{\,\infty} \approx \gamma_s^{\,2}.(17)^{-1}$.

But a^{∞} is known experimentally from the s-wave coherent scattering length (equal to a - a^{∞}, and of great importance for condensed matter physics. The experimental value of a - a^{∞}, for ^{232}Th is 10.3 fm and if we assume a radius of 7.68 fm for we find, experimentally, a^{∞} = -2.47 fm. Adding the s-wave reduced width to the estimate we find that the estimate of Bowman et al for a^{∞} is in good agreement with experiment.

Similarly, their assumed position of the 4s state overestimates the experimentally observed value of the s-wave neutron strength function by only a factor of about two.

However now, if we want to augment a^{∞} by pushing the 4s bound state closer to zero energy we run into formidable obstacles. First, doing so destroys the agreement with the experimentally known values of the coherent scattering length and the strength functions. Second, if we move closer to zero energy the finite spreading width becomes important and removes any augmentation we might again. But, threshold effects come to the rescue.

We have found four remarkable effects which enable us to augment a^{∞}_{4s} by a sizeable amount, perhaps as much as a factor of 3 or 4, for ^{232}Th. These are:

- If one recognizes that the 4s state must satisfy bound-state, not resonant, boundary conditions then it lingers much closer to threshold;

- For the slightly bound state much of its volume is outside the nucleus so that the spreading width may be reduced to a few hundred keV.

- The diffuse-edge of the nuclear optical potential moves the single-particle state even closer to threshold and reduces its spreading width.

- The bound-state boundary conditions renormalize the contribution of a^{∞} to coherent scattering length (and similarly renormalize the reduced widths) so that agreement with data can be retained even while augmenting a^{∞} for the PV effect.

In conclusion, a remarkable conspiracy of several threshold effects suggests that PV in neutron resonances can accommodate smaller PV forces. Also, for conditims in which the s-states are slightly bound the spectral functions (for example, form (d, p) reactions) should reveal some remarkably narrow single-particle s-states whose presence may have been first revealed, indirectly, in the PV p-wave neutron experiments.

References

1) C.M. Frankle et. al., Phy. Rev. **C46,** 778 (1992)

2) J.D. Bowman, G.T. Garvey, C.R. Gould, A.C. Hayes and M.B. Johnson, Phys. Rev. Lett. **68**, 780 (1992)

3) N. Auerbach & J.D. Bowman, Phys. Rev. **C46**, 2582 (1992)

The Nucleon-Nucleon interaction within the Skyrme Model

T. Waindzoch and J. Wambach

The Skyrme model [1], as a semiclassical model of QCD in the non-perturbative regime, is quite successful in describing low-energy hadronic physics. Starting from a classical topological 'Skyrmion' solution, the calculated single-baryon properties are in qualitative agreement with measured physical values. In view of the few parameters involved this is quite remarkable. It remains as a challenging problem to obtain the nucleon-nucleon interaction within the picture of interacting Skyrmions. Due to non-linearities, the equations of motion for two Skyrmions are difficult to solve and usually one avoids this problem by constructing two-Skyrmion configurations out of the known single-soliton fields. However, the often used 'product ansatz', while valid for large separation, cannot reproduce the axially symmetric minimal energy configuration and therefore fails to give any medium-range attraction in the central component of the nucleon-nucleon interaction. A medium-range attraction was only found after performing a full lattice calculation [2, 3, 4] which implies, that one should not rely on approximations at short distances.

To gain more insight into the short-distance properties of the two-Skyrmion sector, we analyze the stability of the B=2 hedgehog on a three-dimensional spatial lattice. This special Skyrmion configuration is important because it can serve as an starting point for obtaining many different two-Skyrmion configurations at finite separation [5]. The hedgehog is a saddle point in the energy surface and is thus unstable to certain excitations. Since Skyrmions carry a conserved topological quantum number, the decay path, starting from the excited hedgehog, will connect different solitonic configurations in the same topological sector. Following various paths one should be able to construct the full interaction potential and the inertia tensor.

In terms of the collective coordinates Q_i , the paths of steepest descent are defined by the gradient flow equation [6]

$$\mathcal{M}_{ij}(R,C)\frac{\partial Q_j}{\partial \tilde{t}} = -\frac{\partial \mathcal{U}(R,C)}{\partial Q_i} \ , \qquad (1)$$

where the time $\tilde{t}$ is a pseudo-time having a dimension of $[t]^2$. At any pseudo-time $\tilde{t}$ the flow of the system is directed opposite to the gradient of the potential. This is the steepest descent direction. Vibrations are excluded on the paths and the system will approach an extremal configuration for $\tilde{t} \to \infty$. Along the paths of steepest descent one has to identify the coordinates R and C as well as the gradients of the interaction potential. A complete set of paths will be needed in order to fully determine the metric and the potential on the unstable manifold.

In order to find the unstable modes we have solved the equations of motion for the fluctuation fields around the background field of the hedgehog via relaxation employing a leapfrog method in pseudo-time. Six modes could be found (three 'electric' modes and three 'magnetic' modes) which agree semi-quantitatively with those previously found on the S^3-sphere [7]. Exciting the hedgehog with these modes, the time evolution was followed by solving the equations of motion in real time. It was found that, for the magnetic mode, the baryon number density splits in a way familiar from symmetric fission in nuclear physics. For the electric mode, on the other hand, the inner B=1 Skyrmion of the B=2 hedgehog is twisting outwards from the full configuration. Crossing critical points of numerical instability near the fission via viscous damping we see a complicated motion in space and isospace. Besides the relative motion, relevant for semiclassical quantization in terms of zero- and near-zero modes, the receding Skyrmions are excited vibrationally. This complicates the situation drastically. To avoid the excitation of vibrational modes one has to follow the paths of steepest descent. We have implemented a numerical procedure for solving the gradient-flow equations to obtain these paths. Calculations were performed for the magnetic and electric unstable modes and we have found the paths of steepest descent from the B=2 hedgehog.

The two different paths of steepest descent which we have found give the main contributions to the repulsive Skyrmion-Skyrmion interaction [8]. A plot of the static potentials, $\mathcal{U}$, as a function of R are shown in the Fig. 1. Here we have subtracted twice the lattice B=1 Skyrmion mass to define the zero of potential energy. At larger distances, the results are quite similar to those obtained in the static constrained approach [8]. Assuming that the relative isospin coordinate is frozen along the two gradient-flow curves, we can also calculate the reduced mass via the relation between the gradient of the potential and the pseudo-time velocity (1). The corresponding result is shown in the right panel of Fig. 2. For large distances, the reduced mass approaches a limiting value which is close to the correct asymptotic value of $\mathcal{M} = M_H/2$ (indicated by the horizontal line in Fig. 2). The difference between the asymptotic values for the different paths is probably due to lattice effects. At short distances, the reduced mass is increasing drastically for both paths rendering a kinetic energy which is very different from its asymptotic value.

Along both the magnetic and the electric paths the Skyrmions seem to have fixed relative isospin orien-

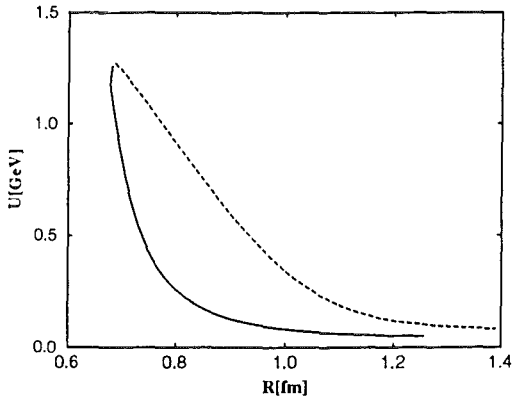

Fig. 1. The static potential, $\mathcal{U}$ along two paths of steepest descent from the B=2 hedgehog. The solid line denotes the result for the magnetic mode while the dashed line gives the result for the electric mode.

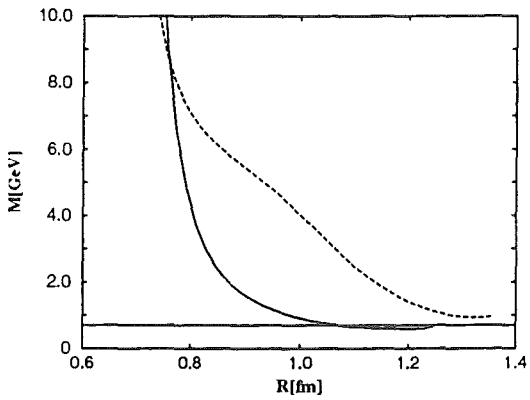

Fig. 2. The reduced mass $\mathcal{M}$ along two paths of steepest descent from the B=2 hedgehog. The solid line denotes the result for the magnetic mode while the dashed line gives the result for the electric mode.

tation. This needs to be clarified in the future. Nevertheless we believe that, with the methods discussed in this paper, we will be able to construct the full unstable manifold in the B=2 sector of the Skyrme model and hence deduce the collective Hamiltonian. A detailed analysis is in progress and will be presented elsewhere [9].

References:

[1] T. H. R. Skyrme, Nucl. Phys. **31** (1962) 556.

[2] J. J. M. Verbaarschot, T. S. Walhout, J. Wambach, and H. W. Wyld, Nucl. Phys. **A468** (1987) 520.

[3] J. J. M. Verbaarschot, Phys. Lett **B195** (1987) 450.

[4] V. B. Kopeliovich and B. E. Shtern, JETP Lett. **45** (1987) 203.

[5] N.S. Manton, Phys. Rev. Lett. **60** (1988) 1916.

[6] M. F. Atiyah and N. S. Manton, Comm. Math. Phys. **152** (1993) 391.

[7] A. Wirzba and H. Bang, Nucl. Phys. **A515** (1990) 571.

[8] T.S. Walhout and J. Wambach, Int. J. Mod. Phys. **E1** (1992) 665.

[9] T. Waindzoch and J. Wambach, work in progress

Coherent and incoherent pion photoproduction off ^{12}C in the Δ resonance region

B. Körfgen and F. Osterfeld

In this report we present our results for the coherent and incoherent π^0-photoproduction on ^{12}C. With coherent processes we mean reactions where the final nucleus is again in its ground state, like ^{12}C(γ, π^0)^{12}C(g.s.); in incoherent processes the final nucleus is in a discrete excited state, e.g. ^{12}C(γ, π^0)^{12}C(2+, T=0, 4.43 MeV). The model we used was established for the description of various pion and photon induced reactions [1, 2] and charge exchange reactions [3].

In Ref. [1] we have presented the formalism for coherent pion photoproduction and we compared our results to the data of Arends *et al.* [4]. There we have argued that the partial mismatch of our calculations with these data is due to the energy resolution of only $\approx$ 15 MeV in this experiment. Because of the poor energy resolution the data contain not only coherent pions but also incoherent pions, where the residual nucleus is left in an excited state. In order to clearify this point we calculate the incoherent pion photoproduction to discrete final states of ^{12}C.

The transition amplitude for pion photoproduction to discrete states is given by [1]

$$T = \langle J_f, M_f \mid F_{\pi N\Delta}(\vec{q}_\pi')\, G\, F^\dagger_{\gamma N\Delta}(\vec{q}_\gamma) \mid 0^+\rangle \ , \quad (1)$$

where $|0^+\rangle$ denotes the ^{12}C ground state and $\langle J_f, M_f|$ denotes the discrete excited state of the final nucleus. $F^\dagger_{\gamma N\Delta}(\vec{q}_\gamma)$ is the $\gamma N\Delta$ excitation operator and $F_{\pi N\Delta}(\vec{q}_\pi')$ is the $\pi N\Delta$ deexcitation operator. G is the Green's function propagating the ΔN-state inside the nucleus.

The $\gamma N\Delta$ excitation operator and the $\pi N\Delta$ deexcitation operator are known to have the following form [1]:

$$F^\dagger_{\gamma N\Delta}(\vec{q}_\gamma) = \frac{f_{\gamma N\Delta}}{M_\Delta}\left(\hat{\varepsilon}_{\vec{q}\lambda} \times \vec{q}_\gamma\right) \cdot \vec{S}^\dagger T_0^\dagger\, e^{i\vec{q}_\gamma\cdot\vec{r}} \ , \quad (2)$$

$$F_{\pi N\Delta}(\vec{q}_\pi') = \frac{f_{\pi N\Delta}}{M_\pi}\left(\vec{q}_\pi' \cdot \vec{S}\right)\, T_\nu\, e^{-i\vec{q}_\pi'\cdot\vec{r}} \ . \quad (3)$$

Here $\vec{S}^\dagger$ and $\vec{T}^\dagger$ are the spin- and isospin-transition operators, respectively.

The many-body Green's function is in our model given by [1, 2]:

$$G = \frac{1}{\omega + i\Gamma_\Delta/2 - H_B - T_\Delta - U_\Delta - V_{\Delta N,\Delta N}} \quad (4)$$

H_B is the Hamiltonian of nucleus B, $\Gamma_\Delta(\omega)$ is the energy dependent free decay width of the Δ, T_Δ and U_Δ are the kinetic energy operator and the Δ-nucleus one-body potential, respectively, and $V_{\Delta N,\Delta N}$ is the ΔN^{-1} residual interaction. For the target ground state wave function a pure shell model configuration was assumed. The single particle wave functions were generated from a Woods-Saxon potential with the geometrical parameters $a_0 = a_{so}$=0.53 fm,

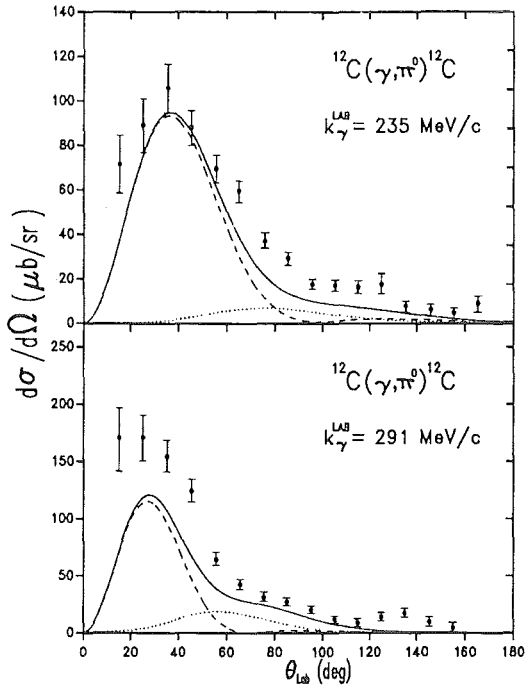

Fig. 1: Differential cross section for coherent pion photoproduction at incident photon momenta of k^L = 235 MeV/c and k^L = 291 MeV/c in comparison with the data [4]. The dashed curves are the contributions of the coherent processes and the dotted curves show the contributions of processes where the residual nucleus is in the excited state (2+, T=0) at 4.43 MeV. The full curves show the sum of coherent and incoherent processes.

and $r_0 = r_{so} = r_C$=1.20 fm and the spin-orbit strength V_{so} =5.53 MeV. The strength parameters for the proton and neutron potentials were fixed as V_p=65.7 MeV and V_n=66.0 MeV, respectively. The Δ-nucleus potential is taken as a complex Woods-Saxon potential, $U_\Delta = V_\Delta + iW_\Delta$, with radius parameter $R = 1.1A^{1/3}$ fm and diffuseness a = 0.53 fm. The depths for the real and imaginary potential are V_Δ = −35 MeV and W_Δ = −40 MeV, respectively. Note that V_Δ is assumed to be the sum of the Δ-nucleus single particle potential (depth=-65 MeV) and of the real part of the Δ-spreading potential (strength=+30 MeV). W_Δ represents the imaginary part of the spreading potential. The spreading potential accounts in a phenomenological way for the Pauli-blocking effects and the increase of the Δ width in nuclei due to decay channels such as $\Delta N \to NN$. The residual interaction, $V_{\Delta N,\Delta N}$, is treated within the $\pi + \rho + g'_{\Delta\Delta}$ model. In the ρ-exchange we keep only the tensor interaction and drop the central part assuming that the latter can be effectively included

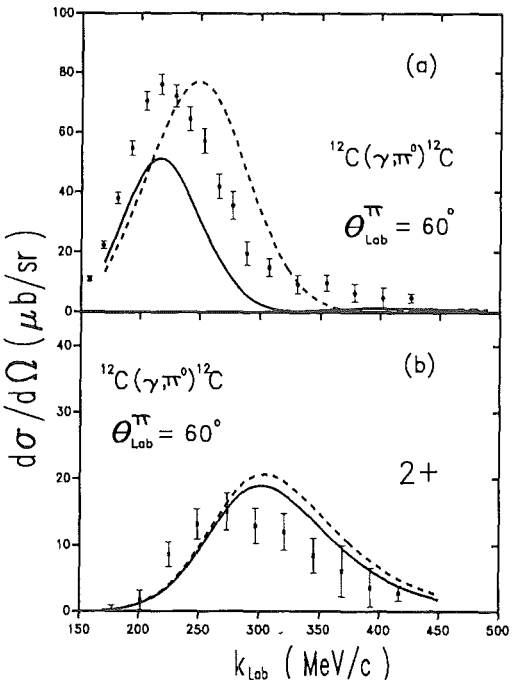

Fig. 2: Pion photoproduction cross section as function of the momentum of the ingoing real photon. The outgoing π^0 is detected under $\theta = 60°$ with respect to the incoming beam. The data are taken from Ref. [5]. The solid and dashed curves represent cross section calculations with and without inclusion of the residual interaction, respectively. In (a) we have plotted the results for coherent pionproduction, i.e. the nucleus is after the reaction again in its ground state. In (b) we show the results for incoherent pionproduction, where the residual nucleus is in the (2+, T=0) excited state of ^{12}C at 4.43 MeV.

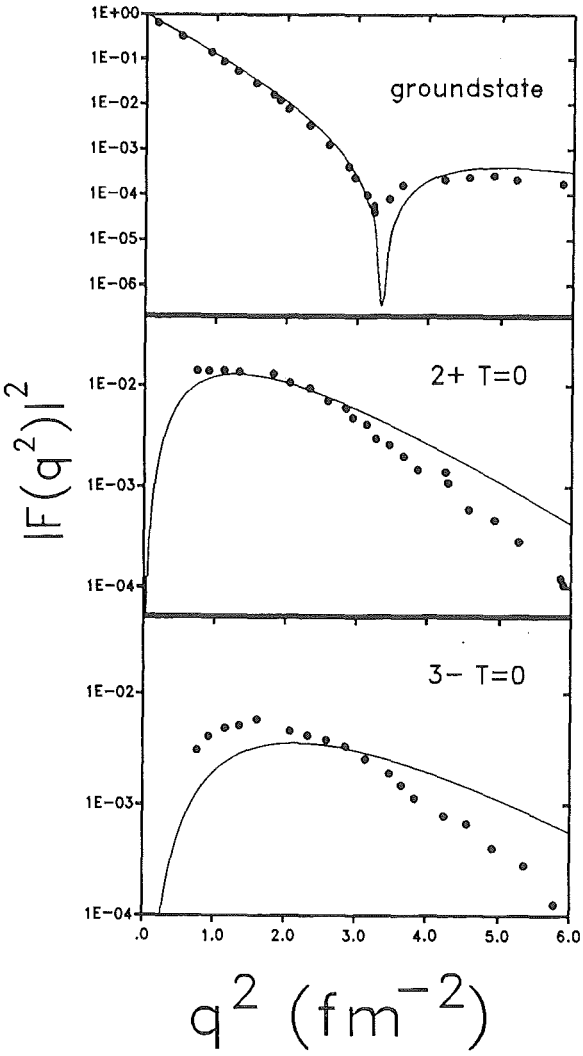

Fig. 3: Formfactors of the ground state, the (2+, T=0) excited state at 4.43 MeV and the (3-, T=0) excited state at 9.6 MeV of ^{12}C. The data are taken from Ref. [6]. The full curves show our results for the formfactors.

in the short-range interaction[2].

In Fig. 1 we compare the calculated differential cross section for the reaction $^{12}C(\gamma,\pi^0)^{12}C$ at two different incident photon momenta with the data [4]. The full curves represent the sum of coherent processes and the most important incoherent processes, where the nucleus is either excited to the state (2+, T=0) or the state (3-, T=0). The dashed curves show the contribution of the coherent processes alone, while the dotted curves show the contribution of the reaction $^{12}C(\gamma,\pi^0)^{12}C(2+, T=0)$. One can recognize that the contributions of the incoherent processes help to fill up the cross section at higher pion angles and improve the agreement with the data, as we have claimed before. Nethertheless we underestimate the magnitude of the cross sections in the peak especially at higher incident photon momenta. A similar deficiency can be observed in a comparison of our calculations with the new data of Schmitz *et al.* [5]. Recently, the reactions $^{12}C(\gamma,\pi^0)^{12}C$(g.s.) and $^{12}C(\gamma,\pi^0)^{12}C(2+, T=0, 4.43$ MeV) were measured at MAMI B with an energy resolution that allowed to separate the coherent process and the incoherent process to the lowest excited state of ^{12}C [5]. In Fig. 2 we compare these new data with our calculations for the different reactions. The differential cross sections are given as function of the momentum of the incident photon. The outgoing pions were detected at an angle of $\theta = 60°$. The full and the dashed curves represent calculations with and without inclusion of the residual interaction $V_{\Delta N,\Delta N}$ of eq. (4). In Fig. 2 (a) one observes a large effect of the residual interaction on the coherent process. The peak position is shifted by $\approx$ 50 MeV to lower energies and the absolute magnitude is reduced. This is in agreement with our results for coherent processes in pion scattering and charge exchange reactions. The incoherent process in Fig. 2 (b) shows no effect of the residual interaction, i.e. of the multiple scattering. The different nuclear formfactors for the ground state and the discrete final states, as shown in Fig. 3, lead to

different radial overlap integrals and thus to a different momentum dependence. As a consequence the coupling of the Δ's to the collective pion wave inside the nucleus is suppressed in the incoherent processes.

References:

[1] B. Körfgen, F. Osterfeld and T. Udagawa, Phys. Rev. C **50**, 1637 (1994).

[2] F. Osterfeld, B. Körfgen, P. Oltmanns, and T. Udagawa, Nucl. Phys. **A577**, 237c (1994).

[3] T. Udagawa, P. Oltmanns, F. Osterfeld, and S.-W. Hong, Phys. Rev. C **49**, 3162 (1994).

[4] J. Arends, N. Floss, A. Hegerath, B. Mecking, G. Nöldeke and R. Stenz, Z. Phys. **A311**, 367 (1983).

[5] M. Schmitz, Insitut für Kernphysik, Universität Mainz, private communication

[6] Hall Crannell, Phys. Rev. **148**, 1107 (1966).

Short-range part of the NN interaction: ω exchange versus quark-gluon exchange

D. Hadjimichef*, J. Haidenbauer, K. Holinde, G. Krein*, and J. Speth

For a long time hadron-hadron interactions, in particular the NN interaction, have been studied in terms of meson exchange models employing baryon and meson degrees of freedom. Such models have achieved a good description of the empirical data. A common undesirable feature in all meson exchange models is the necessity of a (semi)phenomenological parametrization of the short range part of the interaction. However, since the advent of quantum chromodynamics (QCD) as the most promising candidate for the fundamental theory of the strong interactions, there is the hope that the short range part of the hadron-hadron interaction can be derived from first principles. However, because of complications due to the nonperturbative nature of the QCD interactions at low energies, the use of models is a practical necessity for making progress in this direction.

There is a great variety of quark models that can describe with reasonable success single-hadron properties. Therefore, there arises the natural question of to what extent a model which gives a good hadron structure is, at the same time, able to describe the hadron-hadron interaction. In this respect, in the recent past several studies of the NN interaction have employed the nonrelativistic quark model, *a la* Isgur and Karl, which is one of the most successful quark models for hadron structure. The main ingredient of such calculations is the one-gluon exchange interaction. Although the initial results are encouraging as far as the very short range part is concerned (which is reflected in the successful description of NN scattering S-wave phase shifts) there are severe difficulties for the intermediate-range part. For example, the repulsion as well as the spin-orbit force generated by the present treatment of one-gluon-exchange is definitely too weak in high partial waves corresponding to distances between 1 and 2 fm [1]. More recently, the Tübingen group [2], working in the context of the "Resonating Group Method" (RGM), has made some progress on the spin-orbit problem in the NN system by including, in addition of the one-gluon-exchange interaction, a scalar-isoscalar meson coupled to quarks in a chirally symmetric way.

In the present project we started to investigate in detail the NN interaction as well as scattering observables in terms of different quark models. Our aim is to obtain detailed understanding of the effects of the various pieces contributing to the NN process such as size and form of the baryon wave function, quark-gluon and quark-meson couplings, ranges and cutoffs, etc.

Effective NN potentials can be derived from microscopic quark models in a elegant way by means of a field-theoretic approach to composite particles recently transcribed from atomic physics to hadron physics [3]. The effective potentials are constructed as a power series in the hadron bound-state wave function. As an example, we present the contribution of the spin-spin part of the one-gluon exchange to the effective NN interaction to lowest order in the nucleon wave function. We take for the bound-state wave function of the nucleon a gaussian form, such that the r.m.s. radius of the nucleon is b. The effective NN potential is of the form

$$V_{NN} = v_0 + \sigma^1\cdot\sigma^2\, v_\sigma + \tau^1\cdot\tau^2\, v_\tau + \sigma^1\cdot\sigma^2\,\tau^1\cdot\tau^2\, v_{\sigma\tau} \quad (1)$$

where each of the components $v_i, i = 0, \sigma, \cdots$ can be written as

$$v_i = \kappa_{ss} \sum_{j=1}^{3} \lambda_{ij} f_j \quad (2)$$

where $\kappa_{ss} = 8\pi\alpha_s/3m_q^2(2\pi)^3$, the λ's are given in the Table 1 below, and the $f's$ are radial functions of the initial and final c.m. momenta $\mathbf{p}$ and $\mathbf{p}'$:

$$\begin{aligned} f_1 &= \left(\frac{3}{4}\right)^{3/2} e^{-b^2(\mathbf{p}^2+\mathbf{p}'^2)/6} \\ f_2 &= e^{-b^2(\mathbf{p}-\mathbf{p}')^2/3} \\ f_3 &= \left(\frac{12}{11}\right)^{3/2} e^{-b^2(7\mathbf{p}^2+13\mathbf{p}'-12\mathbf{p}\cdot\mathbf{p}')/33} + (\mathbf{p} \leftrightarrow \mathbf{p}'). \end{aligned} \quad (3)$$

Table 1. The coefficients λ of Eq. (2).

	1	2	3
0	1/12	3/4	1/4
σ	1/36	−1/36	−1/36
τ	1/108	1/12	−1/36
$\sigma\tau$	1/324	−25/324	5/324

When solving the Lippman-Schwinger equation for this potential one obtains phase shifts numerically similar to the ones obtained with the RGM, and on-shell ($\mathbf{p}^2 = \mathbf{p}'^2$) it is identical to the potential of Barnes et al. [4] derived in the context of the "quark-Born diagram" method. Higher order (in the wave function) corrections give rise to many-body (> 2-body) forces and also to orthogonality corrections [3].

Due to the fact that the nucleon bound-state wave function is of gaussian form the effective potential falls off very fast at large distances. This has the consequence that higher partial waves receive very little contribution from quark-gluon exchange. In the conventional meson-exchange models a good description of higher partial waves is ensured by the long-ranged Yukawa tail of ω exchange and perhaps quark-gluon exchange models should keep the long-range tail of ω-exchange with a reduced strength as compared to the Bonn potential value [1].

We illustrate the effect of the rapid gaussian falloff of the potential by calculating the $^1F_3$ phase-shift for three values of the r.m.s. radius of the nucleon $b = 0.3, 0.5, 0.6$ fm, and compare with the corresponding one of ω-exchange for two values of coupling constant $g_\omega^2/4\pi = 20, 10$. The quark mass is taken to be $m_q = 313$ MeV and κ_{ss} is adjusted to fit the $N - \Delta$ mass splitting. This is shown in Figure 1 below.

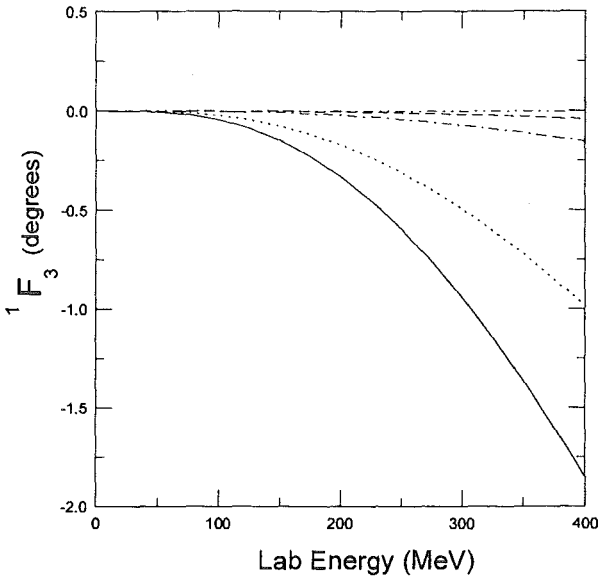

Figure 1: $^1F_3$ phase shift as a function of the laboratory energy: solid $g_\omega^2/4\pi = 20$, dot $g_\omega^2/4\pi = 10$, dash-double-dot $b = 0.3$ fm, dash $b = 0.5$ fm, dash-dot $b = 0.6$ fm

From this figure the very small contribution from the quark potential is evident. Notice that doubling the radius of the nucleon does not make a big effect and the result is far from the ω exchange contribution with a $g_\omega^2/4\pi = 10$.

Work is in progress in which the form of the nucleon wave function is changed to a more flat distribution than a gaussian one. Of course, then the potential cannot be expressed in an analytical form as in Eqs. (1-2) and a Monte Carlo integrator has to be used to integrate over the quark coordinates.

References:

[1] K. Holinde, Nucl. Phys. A543 (1992) 143c.

[2] A. Valcarce, A. Buchmann, F. Fernandez, and A. Fäßler, Phys. Rev. C **51**, 1480 (1995).

[3] D. Hadjimichef, G. Krein, S. Szpigel, and J.S. da Veiga, to appear in Phys. Lett. B.

[4] T. Barnes, S. Capstick, M. Kovarik, and E.S. Swanson, Phys. Rev. C **48**, 538 (1993).

* Instituto de Física Teórica, Universidade Estadual Paulista, Rua Pamplona, 145, 01405-900 São Paulo, SP, Brazil

4. NUCLEAR STRUCTURE AND REACTION MECHANISM

Electromagnetic Excitation in Fast Hadron-Hadron Collisions and its Use for Nuclear Astrophysics

S. Baur[1], H. Rebel[2], S. Typel[3]

The electromagnetic excitation is the dominant feature in fast peripheral heavy ion collisions. It is experimentally feasible and has interesting applications in nuclear structure and astrophysics. The excitation mechanism is well understood theoretically. The Coulomb dissociation method for the determination of electromagnetic transition matrix-elements relies on the assumption that first order perturbation theories are applicable. Deviations caused by higher order effects ("post acceleration") have to be kept under control [1]. A review is being prepared, where the experimental and theoretical status is described in detail [2].

Usually it is sufficient to employ the semi-classical description of the scattering process. In general higher order effects can be studied in a coupled channel calculation [3]. A complementary theoretical approach is the direct numerical integration of the time-dependent Schrödinger equation. Simple nuclear model Hamiltonians have been studied up to now [4,5]. For transitions via non-resonant continuum states, a full coupled-channel calculation seems rather involved [6]. For certain cases, second order perturbation theory with a number of important intermediate states is sufficient [7]. Obviously, the results depend on the used nuclear model.

For certain values of the characteristic strength and adiabaticity parameters special approximations can be used. They exhibit easily the dependence of the higher order effects on the scattering angle/impact parameter, projectile and excitation energy. For very fast transitions, the sudden approximation can be used [8]. The case for finite but small values of the adiabaticity parameter was developed in [9], by using closure. Purely classical considerations of the "post acceleration" [5,8] are not a useful guide. Higher order effects in the Coulomb dissociation of ^{8}B [10] (the inverse reaction is relevant for the solar neutrino problem) are studied in [11]. The first and second order contributions of different multipolarity show distinct dependences on the experimental conditions. The angular distribution of the fragments is sensitive to interference effects. At GSI energies, we show that higher order effects are rather small.

Similar investigation are performed in Ref. 12. Higher order effects are treated using the methods of Ref. 5. A quenching of 1st order E2 effects by higher order E1 couplings was found there. This is not easily accomodated in the theoretical approach of Ref. 9.

Of special interest is the E1 bound state transition in ^{11}Be [13]. A depletion of the $\frac{1}{2}^-$ state could occur due to higher order transitions into the continuum. We calculate the transition probability in first order and sudden approximation, using the dipole approximation and simple model wave functions. The ranges of the two approximations overlap and the reduction of the excitation cross section due to higher order effects can be obtained in a simple interpolation procedure [14].

1) IKP, KFA
2) Forschungszentrum Karlsruhe, Institut für Kernphysik
3) Universität München, Sektion Physik

References

[1] G. Baur, C. A. Bertulani, and H. Rebel, Nucl. Phys. **A458**(1986) 188
[2] G. Baur, and H. Rebel, Annual Review of Nuclear and Particle Science, to be published.
[3] K. Alder and A. Winther, Electromagnetic Excitation (North-Holland, Amsterdam, 1975)
[4] C. A. Bertulani and G. F. Bertsch, Nucl. Phys. **A556**(1993) 136; Phys. Rev. **C49**(1994) 2839
[5] H. Esbensen, G. F. Bertsch, and C. A. Bertulani, Nucl. Phys. **A581**(1995) 107
[6] L. F. Canto, R. Donangelo, A. Romanelli, and H. Schulz, Phys. Lett. **B318**(1993) 415
[7] S. Typel and G. Baur, Phys. Rev. **C49**(1994) 379
[8] G. Baur, C. A. Bertulani, and D. M. Kalassa, Nucl. Phys. **A550**(1992) 527
[9] S. Typel and G. Baur, Nucl. Phys. **A573**(1994) 486
[10] T. Motobayashi et al., Phys. Rev. Lett. **73**(1994) 2680
[11] S. Typel and G. Baur, Phys. Rev. **C 50**(1994) 2104
[12] H. Esbensen, and G. F. Bertsch, preprint
[13] R. Anne et al., Z. Phys. **A352**(1995) 397
[14] S. Typel and G. Baur, Phys. Lett. **B356**(1995) 186

Low Energy charged Particle Interactions studied with Transfer Reactions

S. Baur[1], S. Cherubini[2], D. Miljanic[3], V.N. Kondratyev[2], M. Lattuada[2], C. Spitaleri[2], M. Zadro[3]

Transfer reaction of the type (b+x)+A→(A+x)+b→C+b, where C denotes some final channel of the (A+x)-subsystem, can be used to investigate charged particle interactions at low relative energies, see e.g. Ref. 1. This is also useful for nuclear astrophysics [2] Recent experimental studies of resonances in the (A+x)-subsystem relevant for nuclear astrophysics are e.g. given in Refs. 3,4.

Also the continuum of the (A+x)-system can be investigated by this method. The d+^{6}Li→α+α reaction was recently studied in the ^{6}Li+^{6}Li scattering in this way. This is published in Ref. 5.

The key astrophysical reaction $^{12}C(\alpha,\gamma)^{16}O$ was recently studied at the Heidelberg Tandem with the $^{12}C(^7Li,t\gamma)^{16}O$ reaction [6,7]. An upper limit of the astrophysical S-factor was obtained. In the course of such an analysis, the following question arises: What is the connection of the transfer reaction to a state just below threshold to the astrophysical S-factor S_λ just above threshold? E.g. in the $^{12}C(\alpha,\gamma)^{16}O$ reaction the relevant multipolarities are E1 and E2. In ^{16}O there are 1^- and 2^+ states at 7.12 MeV und 6.92 MeV just below the $\alpha+^{12}C$ threshold. They are also experimentally measured in the (^{7}Li,t) transfer reaction, the cross-section is denoted by $\left(\frac{d\sigma}{d\Omega}\right)_{bound,\lambda}$.

The transition from bound state transfer to unbound (continuum) states was studied theoretically in Ref. 8. In a simple model for Coulomb penetration effects, the following relation can be found:

$$\frac{d^2\sigma}{d\Omega dE_x} = \sum_\lambda \frac{4m_x^2c^4r_c^2}{3(\hbar c)^4\pi^2(2J+1)}\, e^{-\sqrt{\frac{8r_{int}}{a_{Bohr}}}} \cdot S_\lambda \frac{\left(\frac{d\sigma}{d\Omega}\right)_{bound,\lambda}}{\theta_\alpha^2}$$

E_x is the excitation energy in the (A+x)-system, I its spin m_x is the mass of the transferred particle x. The reduced width and the channel radius are denoted by θ_α^2 and r_c, they are found e.g. in a DWBA analysis [10]. The radius, where the strong nuclear attraction in the A+x-system sets in, is denoted by r_{int}, the Bohr radius is given by $a_{Bohr} = \frac{\hbar^2}{mZ_xZ_Ae^2}$. In a more sophisticated analyis, one can do (full finite range) DWBA calculations. This can remove the dependence on the rather loosely defined parameter r_{int}.

1) IKP, KFA
2) Università di Catania and INFN-Laboratorio Nozionale del Sud, Catania, Italy
3) Ruder Boskovic Institute, Zagreb, Croatia

References

[1] G. Baur, F. Rösel, D. Trautmann, and R. Shyam, Phys. Rep. **111**(1984)333
[2] G. Baur, Phys. Lett. **B178**(1986)135
[3] S. Schmidt et al. Nucl. Phys. **A591**(1995)227
[4] J.G. Ross et al. Phys. Rev. **C52**(1995)1681
[5] S. Cherubini, V.N. Kondratyev, M. Lattuada, C. Spitaleri, D. Miljanic, M. Zadro and G. Baur, Astrophysical Journal, to be published in January 1996
[6] Jahresbericht 1994, Max-Planck-Institut für Kernphysik Heidelberg, page 1
[7] G. Heusler et al., private communication and
G. Heusler, Diplomarbeit Universität Heidelberg, 1995
[8] G. Baur, D. Trautmann, Z. Phys. **267**(1974)103
[9] G. Baur, unpublished
[10] F. Pühlhofer et al., Nucl. Phys. **A147**(1970)258

Colour Van der Waals effects in Pb-Pb scattering?

K. Hencken[1)], H. Mühry[1)], I. Sick[1)], D. Trautmann[1)], G. Baur[2)]

In order to study the contribution of a possible colour Van der Waals potential to ^{208}Pb-^{208}Pb elastic scattering we discuss the influence of small additional potentials to the pure Coulomb interaction. The study shows, that - besides relativistic effects, vacuum polarisation and nuclear polarisability - the formation of quasimolecules during the scattering process gives the dominant contribution. Perfect agreement with the data would require a colour Van der Waals contribution, but the uncertainty in the quasimolecular effect is considerable. For further details see Ref. 1.

What is the influence of the swarm of (loosely bound) electrons, which is not taken into account in the actual measurement? In a simple model, where one electron is bound to one of the nuclei, the following microscopic processes occur:

$$A+(A+e)_i \rightarrow A+(A+e)_f \qquad (1)$$

In the semiclassical approximation [2], the amplitude of this process can be written as

$$f_{s.cl.}^{i\rightarrow f}(\theta) = f(\theta)a_{i\rightarrow f}^{dir}(\theta) + f(\pi-\theta)a_{i\rightarrow f}^{trans}(\pi-\theta) \qquad (2)$$

where f(θ) denotes the Rutherford amplitude, the semiclassical amplitude for the electronic excitation i→f is denoted by $a_{i\rightarrow f}^{dir}(\theta)$ („elastic" $(i = f)$ and „inelastic" $(i \neq f)$ transfer).

The second term corresponds to a transfer of the electron from one nucleus to the other, the nuclear scattering angle is now given by π-θ, and the amplitude by $a_{i\rightarrow f}^{trans}(\pi-\theta)$. The cross-section, where the electron transition i→f is also measured, is given by

$$\frac{d\sigma^{i\rightarrow f}}{d\Omega} = \left|f_{s.cl.}^{i\rightarrow f}(\theta)\right|^2 \qquad (3)$$

The actually measured cross-section disregards the electronic states, this cross section is given by

$$\frac{d\sigma^{\exp}}{d\Omega}(\theta) = \sum_f \left(\frac{d\sigma^{i\rightarrow f}}{d\Omega}(\theta) + \frac{d\sigma^{i\rightarrow f}}{d\Omega}(\pi-\theta)\right) \qquad (4)$$

In terms of the amplitudes, e.g. 2, this can be written as

$$\frac{d\sigma^{\exp}}{d\Omega}(\theta) = |f(\theta)|^2 + |f(\pi-\theta)|^2$$
$$+2\,\mathrm{Re}\left\{f(\theta)f(\pi-\theta)^*\left[a_{i\rightarrow f}^{dir}(\theta)a_{i\rightarrow f}^{tr}(\pi-\theta)^* + a_{i\rightarrow f}^{tr}(\theta)a_{i\rightarrow f}^{dir}(\pi-\theta)^*\right]\right\} \qquad (5)$$

Here the unitarity condition $\sum_f\left(\left|a_{i\rightarrow f}^{dir}(\theta)\right|^2 + \left|a_{i\rightarrow f}^{tr}(\theta)\right|^2\right) = 1$ has been used. If the quantity in square brackets were equal to 1, the usual Mott scattering cross-section would be obtained. It can be shown that this quantity is less than one, i.e. there is a damping of the Mott interference pattern. This was found experimentally in Ref. 3 where it was attributed to „fluctuations" of the atomic excitation. The actual value of the quantity in the square brackets seems to be hard to calculate in a realistic situation. It is equal to one when

$a_{i\rightarrow f}^{dir}(\theta) = a_{i\rightarrow f}^{tr}(\pi-\theta)^*$, for all values of θ and f. Since the electron cloud is very far away from the nuclear interaction region, this condition will be rather well fulfilled.

1) Universität Basel, Institut für Physik
2) KFA, IKP

References

[1] K. Hencken, H. Mühry, I. Sick, D. Trautmann, and G. Baur. Nucl. Phys. **A591**(1995) 548
[2] K.W. Ford and J.A. Wheeler, Annals of Physics **7**(1995)259
[3] A.C.C. Villari et al. Phys. Rev. Lett. **71**(1993)2551

A Brueckner-Hartree-Fock-Bogoliubov model for proton and neutron rich nuclei

F.Gruemmer, Bao-qiu Chen*, Zhong-yu Ma*, and S.Krewald

Proton and neutron rich nuclei will be intensively investigated experimentally by radioactive beam facilities and provide us with new data about exotic nuclei which may challenge our microscopic theories of bulk properites of nuclear matter. At present, relativistic mean field theories manage to predict bulk properties of matter with relatively few free parameters [1]. As one moves away from closed shell nuclei, however, one has to realize that the exchanges of the pion and the rho-meson can no longer be ignored [2]. In the virtually parameter-free Dirac Brueckner-Hartree-Fock approaches, one includes all mesons, and is able to reproduce the bulk properties of nuclear matter, but one has problems with finite nuclei [3]. A possible shortcoming of both non-relativistic and relativistic many-body theories concerns the sigma-meson. The sigma-meson does not exist as a free particle, but should be interpreted as a parameterization of the correlated two-pion exchange. In nuclear matter, the exchange of a correlated pion pair is modified e.g. by Pauli-blocking of the intermediate nucleon states. When representing the correlated two-pion exchange by an effective sigma-meson, one ignores the Pauli-blocking effects.

We now propose to explore possible effects of the medium modification of the correlated two-pion exchange by simply treating both the coupling strength and the mass of the exchanged sigma meson as free parameters which can deviate in nuclear matter from the constants required for free two-nucleon scattering. We apply the medium-modified interaction not only to doubly-closed shell nuclei, but to whole isotope chains in order to allow for more systematics. As one moves away from closed shell nuclei, deformation effects and pairing effects have to be taken care of. We do this by performing Hartree-Fock Bogoliubov calculations with a G-matrix interaction, starting from a modified bare interaction.

In a first step, we have concentrated on the oxygen and neon isotope chains. In Fig.1, the binding energies of the neon isotopes obtained in our approach are compared with a spherical relativistic mean field calculation based on the interaction of Sharma et al. We find that the present model produces results of a quality comparable to the relativistic mean field model, even though less free parameters are used (the coupling strength and the mass of the sigma were reduced by approximately 5 percent). The deformation effect is clearly visible for ^{20}Ne and ^{22}Ne.

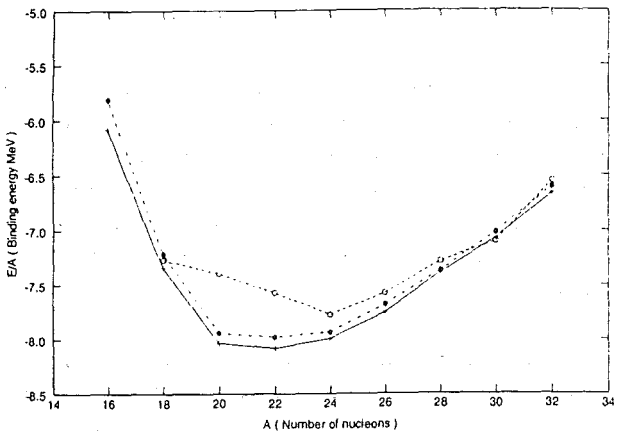

Fig. 1: Binding energy per particle for Neon isotopes. Dashed-Dotted: our model; Dashed: relativistic mean field model; Solid : experimental data

References:

[1] B.D.Serot et al., Adv.Nucl.Phys.**16**,1(1986)

[2] M.M.Sharma et al., Phys.Lett.B**312**,377(1993)

[3] R.Fritz et al., Phys.Rev.C**42**,1981(1990)

* China Institute of Atomic Energy, Beijing 102413, P.R.China

Radiative capture of neutrons to bound states of higher angular momentum

D.M. Kalassa and G. Baur

The cross-sections for the radiative capture of a neutron by a ground state of angular momentum l_f and spin $I_f = l_f + 1/2$ given in [1] are determined by the radial integrals

$$R_{li1l_f} \cong \int_0^\infty dr\, r^3\, g_f(r)\; g_{li}(r) \tag{1}$$

The radial eigenfunctions g_f, g_i have to be computed numericaly for realistic nuclear models. Analytic relations are available in some cases (e.g. square well potential). The behaviour of the wave function inside the nucleus is of little importance for low-energy photo-nuclear reactions, this allows us to derive simple but accurate approximations. We try to find them by extending the external integral to the interaction region provide the integrand in eq. (1) does not diverge and the exponential factor does not vary much there. For the capture of *p*- and *f*-wave neutrons by ^{12}C leading to the excited *d*-wave state with 1.09 MeV binding-energy we use the following radial wave functions

$$g_{li} = j_{li}(kr) \qquad l_i \geq 0 \tag{2}$$

$$g_{lf} = N_2 \sqrt{2\beta^3}\, h_2(i\beta r) \tag{3}$$

in agreement with recent developements of the effective range treatment of the electromagnetic reactions of loosely bound nuclei [2, 3] and we find the neutron capture cross-section in the electric dipole approximation:

$$\sigma^{(n,\gamma)} \cong N_2^2 \frac{8\pi}{3} \alpha Z_{eff}^2 \lambda\!\!\!^{-}_{\mu}{}^2 \frac{k(3k^4+6k^2\beta^2+5\beta^4)}{\beta^3(k^2+\beta^2)} \tag{4}$$

where $\beta = \sqrt{\left(\frac{2\mu B}{\hbar^2}\right)}$, μ is the reduced mass of the $(^{12}C, n)$-system, B is the binding energy, $Z_{eff} = \mu(Z_1 / M_1 - Z_2 / M_2)$ is the effective charge of the clusters, $\lambda\!\!\!^{-}_{\mu}$ is the Compton-length of a quasi-particle with the reduced mass μ. N_2 is a dimensionless normalisation factor, which can be shown to be independent of the shape of the nuclear potential for zero binding-energy, it yields for loosely bound d-wave states [3]

$$N_2^2 \cong \frac{x^3 e^{2x}}{(1+x)(15+15x+6x^2+x^3)} \tag{5}$$

where

$$x = \beta R \tag{6}$$

with the interaction range

$$R \cong \left(A_1^{1/3} + A_2^{1/3}\right) 1.2fm \tag{7}$$

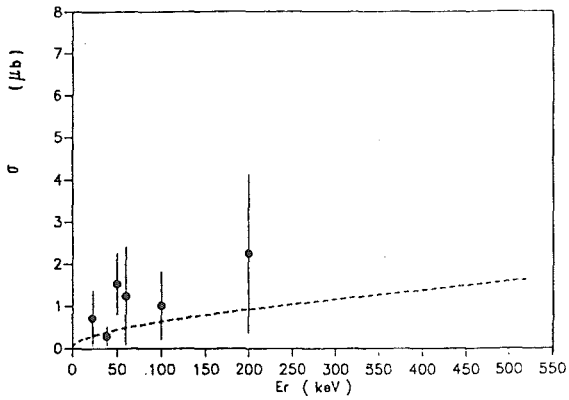

Fig.1 gives the neutron capture cross-section versus the relative energy of the clusters in the effective range approximation, the experimental data are from ref [4]. This method can be extended to bound states of higher angular momenta, however it will require an empirical normalisation of the cross-sections, for p-waves see e.g. [2]. In conclusion we find that the effective range approximation yields the qualitative behaviour and in many cases the magnitude of the electromagnetic cross-sections at low energy. It is a good starting point in making theoretical predictions and in the analysis of nuclear reaction data at low energies. It allows us to study higher order effects of the interaction in the Coulomb dissociation. Corrections should be found to improve the accuracy.

References:

[1] D. M. Kalassa, G. Baur, J. Phys. **G20** (1994)

[2] D. M. Kalassa, G. Baur, analytical cross-sections for the photodissoziation of loosely bound nuclei, J. Phys. **G22**(1996)115-121

[3] D. M. Kalassa, PhD-Thesis, University of Bonn (1996)

[4] A. Mengoni, T. Otsuka, M. Ishihara, Phys. Rev. **C52** (1995) R2334

Properties of neutron and proton rich nuclei in the vicinity of ^{100}Sn in relativistic mean field theory

Bao-qiu Chen*, Zhong-yu Ma*, S.Krewald, and F.Gruemmer

The discovery of the new nucleus ^{100}Sn, which was produced by GSI and GANIL in 1994 respectively, is a significant event in the study of exotic nuclei. On the theoretical side, in the past ten years the relativistic mean field theory (RMF) has turned out to be a very successful tool for describing the properties of both nuclear matter and finite nuclei. It would be interesting to extend the RMF theory used in stable nuclei to describe the properties of nuclei far from the β stability line and near the neutron and proton drip line. We therefore calculate the ground state properties of proton and neutron rich nuclei in the vicinity of the ^{100}Sn systematically using the relativistic mean field theory.

Recently, Toki et al. used the RMF theory with various interactions to investigate the ground state properties of nuclei far from the β stability line. However, the effective interactions such as NL1 and NL2 used in the RMF produce large neutron radii and neutron skin thicknesses of nuclei with large neutron excesses. The reason is that these interactions provide a very high asymmetry energy of about 44 MeV. In order to solve this problem, M.M.Sharma et al. [1] present a realistic interaction called NL-SH in the RMF theory , which in addition to the sigma and omega meson contains the isospin-dependent rho-meson exchange. The parameters are obtained by adjusting the ground state properties of a few spherical nuclei and the binding energies, deformations of Xe isotopes on both sides of the stability line. The binding energies obtained by the RMF theory with the NL-SH interaction for even Sn isotopes are listed in the second column of the table 1. The experimental data [2] and the binding energies calculated by the HFB with Skp interaction [3] are also given in the thirth and fourth columns of the table 1,respectively. It can be seen from table 1 that our results calculated in the RMF are in a good agreement with the data. It is surprising that the binding energies of even Sn isotopes predicted by the RMF with the NL-SH interaction are close to those of the HFB with the Skp interaction,which reproduce the experimental binding energies of some spherical nuclei and Sn isotopes($100<A<176$). The binding energies for ^{134}Sn predicted by the RMF and HFB are almost the same and agree with the data. A discussion of the neutron excess and proton-rich nuclei can be found in ref. [4] Our conclusion is that the relativistic mean field theory, when employing an interaction that reproduces the experimental asymmetry energy, is a useful tool to describe nuclear gross properties within an isotope chain that reaches the drip lines.

Nuclei	RMF E/A (MeV)	Exp. E/A(MeV)	HFB E/A(MeV)
^{100}Sn	-8.3303	-8.2448*	-8.3245
^{102}Sn	-8.3676	-8.3226*	-8.3125
^{104}Sn	-8.4083	-8.3832	-8.3757
^{106}Sn	-8.4522	-8.4327	-8.4244
^{108}Sn	-8.4986	-8.4685	-8.4596
^{110}Sn	-8.5053	-8.4960	-8.4846
^{112}Sn	-8.5150	-8.5136	-8.5010
^{114}Sn	-8.5271	-8.5225	-8.5103
^{116}Sn	-8.5083	-8.5231	-8.5133
^{118}Sn	-8.4806	-8.5165	-8.5099
^{120}Sn	-8.4721	-8.5045	-8.5007
^{122}Sn	-8.4559	-8.4879	-8.4871
^{124}Sn	-8.4419	-8.4674	-8.4684
^{126}Sn	-8.4297	-8.4436	-8.4455
^{128}Sn	-8.4198	-8.5505	-8.4198
^{130}Sn	-8.4116	-8.3877	-8.3875
^{132}Sn	-8.4052	-8.3557	-8.3534
^{134}Sn	-8.2909	-8.2811*	-8.2832

Table 1: The binding energies of even Sn isotopes. Second column: relativistic mean field theory; third column: experimental data and estimates(*); fourth column : Hartree-Fock-Bogoliubov calculation.

* China Institute of Atomic Energy, Beijing 102413, P.R.China

References:

[1] M.M.Sharma et al.,Phys.Lett**B312**(1993)377

[2] G.Audi et al., Nucl.Phys.**A565**(1993)1

[3] J.Dobaczewski et al., Nucl.Phys.**A422**(1984)103

[4] B.Chen et al., J.Phys.**G21**(1995)1759

Effects of Strong Interaction on the Electromagnetic Dissociation

A. Mündel and G.Baur

1. Introduction

The Coulomb field of a fast moving heavy ion is an intense source of quasi real photons [1]. With raising projectile energy this photon spectrum becomes harder and there exist a variety of applications in nuclear– as well as astrophysics, like the excitation of giant resonances or the Coulomb dissociation of the ions [2, 3]. The advantage of using heavy ion collisions to study this processes is the large equivalent photon number and the resulting large cross section. Therefore the Coulomb dissociation is an interesting tool to study the astrophysical S–factor for reactions like $^7Be(p,\gamma)^8B$ [2].
In this work we give a brief introduction to the equivalent photon method to calculate the cross sections. Since this simple approach via the equivalent photon number does not take into account excitations due to the strong interaction. Therefore it is interesting to study these effects. It is the purpose of this work to investigate these nuclear contributions.

2. Equivalent photon method in the presence of strong absorption

In the following we consider a situation where a projectile (particle 1) with charge Z_1 excites a target (particle 2) with charge Z_2 from the ground state $|0\rangle$ to the excited state $|l,m\rangle$ in a peripherical collision via the exchange of one quasi real photon of energy $E_\gamma = \hbar\omega$. The velocity $\vec{\beta} = \frac{\vec{v}}{c}$ of the projectile is in z direction and we use $\gamma = \left(1-\beta^2\right)^{-\frac{1}{2}}$. The scattering angle of the projectile is denoted by θ.
In the eikonal approximation [7] the inelastic scattering amplitude $f(\theta)$ is given by [4]:

$$f(\theta) = \frac{ik}{2\pi\hbar v}\int d^3r\, d^3r'\, e^{i\vec{q}\cdot\vec{r}}\, e^{i\chi(b)} \langle\Phi_f(\vec{r}')|V_{int}(\vec{r},\vec{r}')|\Phi_i(\vec{r}')\rangle, \quad (1)$$

where $\vec{q}$ denotes the momentum transfer. We define $\vec{r}$ to be the separation of the centers of mass of the two nuclei, and $\vec{r}'$ to be the intrinsic coordinate of the target nucleus.
The Glauber phase $\chi(b)$ is the sum of a Coulomb and a nuclear part. If we assume the 'sharp cut–off' model for the nuclear part

$$e^{i\chi_N(b)} = \begin{cases} 0 & \text{if } b \le R = R_1 + R_2 \\ 1 & \text{if } b > R \end{cases}, \quad (2)$$

where $R_i = 1.2\ fm\ A^{1/3}$, $(i = 1,2)$, the Coulomb part is simply given by

$$\chi_C(b) = 2\,\eta\, ln(kb). \quad (3)$$

Here $\eta = \frac{2Z_1Z_2e^2}{\hbar v}$ is the Sommerfeld parameter and k is the wavenumber of the incoming projectile.
Using standard methods [1, 4, 5] and defining the reduced electromagnetic transition probabilities $B(\pi l, I_i \rightarrow I_f)$ and the photo-nuclear absorption cross section for a given multipolarity $\sigma_\gamma^{\pi l}(\omega)$ as in ref. [1] we can write the cross section in the form:

$$\frac{d\sigma}{d\Omega} = \sum_{\pi l}\int \frac{d\omega}{\omega}\,\sigma_\gamma^{\pi l}(\omega)\,\frac{dn^{\pi l}}{d\Omega}. \quad (4)$$

Under these assumptions the equivalent photon number per unit solid angle for a given multipolarity $\frac{dn^{\pi l}}{d\Omega}$ is given by:

$$\frac{dn_C^{\pi l}}{d\Omega} = Z_1^2\alpha\left(\frac{\omega k}{\gamma v}\right)^2 \frac{l[(2l+1)!!]^2}{(2\pi)^3(l+1)} \sum_m \left|G_{\pi lm}\left(\frac{1}{\beta}\right)\right|^2 \left|\Omega_m^C(q_T)\right|^2. \quad (5)$$

$G_{\pi lm}$ are the Alder–Winther function as defined in ref. [6]. In eq. (5) is the transverse momentum transfer q_T the only scattering angle dependent quantity. Defining the variables $x = \frac{b}{R}$, $\xi = \frac{\omega R}{\gamma v}$, and $\Theta_{diff} = \frac{1}{kR}$, Ω_m^C can be written as:

$$\Omega_m^C(\theta) = R^2\int_1^\infty x\, dx J_m\left(\frac{\theta x}{\theta_{diff}}\right) K_m(\xi x)\, e^{2i\eta ln\left(\frac{x}{\theta_{diff}}\right)}. \quad (6)$$

In the case of the classic trajectory of the projectile $(\eta \rightarrow \infty)$, eq. (6) can be integrated analytically [4]:

$$\Omega_m^{sc}(\theta) = R^2\sqrt{-i}\,\frac{y^2}{2\eta}\, e^{i\tilde{\phi}}\, K_m(\xi y)\ , \quad (7)$$

where the variables $y = 2\eta\frac{\theta_{diff}}{\theta}$ and $\tilde{\phi} = \frac{1}{2}\pi(m+\frac{1}{2}) + 2\eta\left(ln\left(\frac{2\eta}{\theta}\right) - 1\right)$ were introduced.

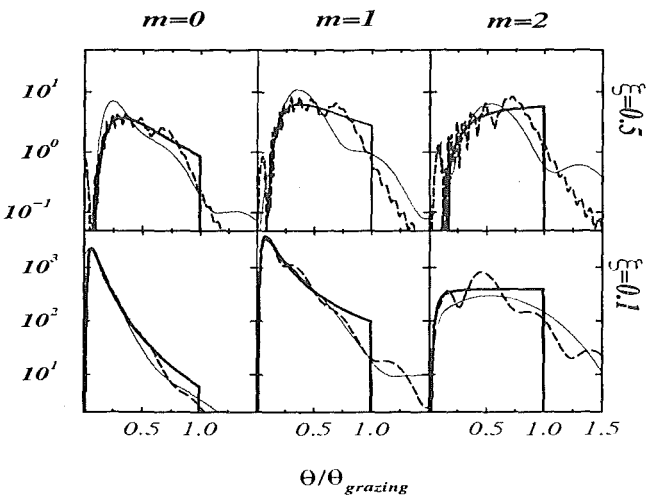

Fig. 1: $|2\eta\frac{\Omega_m}{R^2}|^2$ in arbitrary units $(m = 0,1,2)$. The upper row shows the results for $\xi = 0.5$, $\eta = 20$ (dashed) and $\eta = 2$ (thin), while the lower row shows the results for $\xi = 0.1$, $\eta = 3$ (dashed) and $\eta = 1.2$ (thin). In both cases the thick line is the semi classical solution.

Both expressions for Ω_m mainly depend on two parameters, the interaction strength η and the adiabatic parameter ξ, which is the ratio of transition time to collision time.

Introducing the grazing angle for the classical trajectory $\theta_{gr} = 2\eta\theta_{diff}$ one can compare $|2\eta\frac{\Omega_m}{R^2}|^2$ as a function of $\frac{\theta}{\theta_{gr}}$ for fixed ξ but different η as shown in the 'universal plots' in fig. (1). The thick solid line shows the semi classical limit according to eq. (7) while the dashed and thin lines are the solutions of eq (6) for different values of η. At $\frac{\theta}{\theta_{gr}} = 1$ the semi classical limit drops to zero while the full solutions extend to slightly higher angles. At small angles the full solution shows diffraction effects. Where $\Omega_m^{sc} \neq 0$ the full solution for sufficiently large η is a fast oscillating function around the semi classical limit (dashed line). Only for small η (dashed line) the full solution differs namely from the semi classical limit.

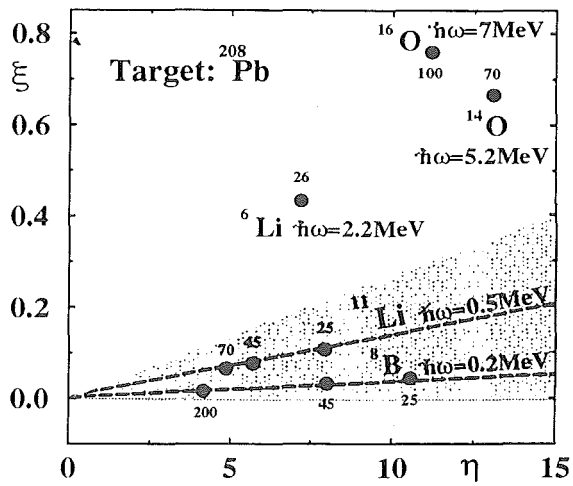

Fig. 2: Some experiments characterized in a ξ–η–plot. Each dot is labeled with the corresponding projectile nucleus, the incident energy per nucleon (small number) and the excitation energy ($\hbar\omega$).

In many relevant cases the semi classical solution for the inelastic scattering amplitude (eq. 1) provides already a good description of the experimental situation. Fig. (2) classifies some existing experiments in a ξ–η–plot where the experiments well described by the semi classical solution are at large η and small ξ (Shadowed region. Notice that the limits of this region are not well defined).

To complete the discussion of the sharp cut-off model we want to give the expression for the total cross section, which is obtained by integrating eq. (4) over the solid angle and using the closure relation for the Bessel functions. We find:

$$\sigma_{tot} = 2\pi \left(\frac{Ze}{\hbar c}\right)^2 \left(\frac{\omega}{\gamma v}\right)^2 \sum_{\pi lm} \left(\frac{\omega}{c}\right)^{2(l-1)} R^2 \int_1^\infty x\, dx\, K_m(\xi x). \quad (8)$$

This expression is independent of η.

3. Excitation by nuclear interaction

Even though the sharp cut–off model for the nuclear phase shift simplifies the calculation, it neglects effects like nuclear interaction in grazing collisions and modifications of the Coulomb potential V_C due to the penetration of the charge distributions. The second effect is generally small and mathematically very difficult to treat. In this work we will neglect this effect and concentrate on an estimation of the nuclear effects.

In the following the interaction between the two particles is given by $V_{int} = V_C + V_N$, with [5]:

$$\langle \Phi_f(\vec{r}')|V_N(\vec{r},\vec{r}')|\Phi_i(\vec{r}')\rangle = \langle t_{NN}(E)\rangle\ \rho_1(\vec{r}-\vec{r}')\ \langle l,m|\rho_2(\vec{r}')|0\rangle . \quad (9)$$

Here ρ_i, $(i = 1,2)$ denotes the charge density of the i'th nucleus. For the energy dependent t_{NN}–matrix see ref. [5]. To determine the transition density matrix elements $\langle l,m|\rho_2(\vec{r}')|0\rangle$ we assume the hydro-dynamical model of Bohr and Tassie [8]. In this model the matrix element is proportional to the derivative of the charge distribution ρ_2. Under these assumptions the inelastic scattering amplitude (eq. 1) can be written as:

$$f(\theta) = \sum_{\pi lm} \frac{i^{m+1}k}{\hbar v}\, e^{-im\alpha}\, M(\pi l, m) \int_{R_{min}}^\infty b\, db\, e^{i(\chi_C(b)+\chi_N(b))} J_m(q_T b)\ \{\Gamma_C^{\pi lm} + \Gamma_N^{\pi lm}\} . \quad (10)$$

If we neglect the corrections of the Coulomb part due to the penetration of the two particle, $\Gamma_C^{\pi lm}$ is given by:

$$\Gamma_C^{\pi lm} = \frac{Z_1 e}{\gamma}\, \kappa^l \sqrt{2l+1}\, G_{\pi lm}\left(\frac{1}{\beta}\right) K_m\left(\frac{\omega b}{\gamma v}\right) . \quad (11)$$

In addition we always find $\Gamma_N^{Mlm} = 0$.

The simplest model, to take into account nuclear effects, is to make the nuclei transparent for $b \geq R$ instead of $b > R$ (eq. 2), and assume a homogeneous charge distribution $\rho_i(0)$ for both nuclei. In this case we find $R_{min} = R$ in eq.(10) and:

$$\Gamma_N^{Elm} = \frac{\rho_1(0)}{R^l} \langle t_{NN}(E)\rangle\ Y_{lm}\left(\frac{\pi}{2},0\right) \delta(b-R). \quad (12)$$

A more realistic model is to extend the region of nuclear interaction to a small ring from $b = R - \frac{\Delta}{2}$ up to $b = R + \frac{\Delta}{2}$. In this model the integration in eq. (10) starts at $R_{min} = R - \frac{\Delta}{2}$ and we find:

$$\Gamma_N^{Elm} \approx \frac{2}{\Delta}\frac{\rho_1(0)}{R^l} \langle t_{NN}(E)\rangle\ Y_{lm}\left(\frac{\pi}{2},0\right)\ \Theta\left(R+\frac{\Delta}{2}-b\right) . \quad (13)$$

The influence of such a nuclear contribution on the cross section in the case of ^{17}O on $208Pb$ at an incident energy of $84MeV/nucleus$ and an excitation

energy of shown in fig. (3). The dashed line shows $\frac{dn^{E1}}{d\Omega}$ for the pure Coulomb contribution, the dotted line the pure nuclear contribution with $\Delta = 0.1R$, while the solid line gives the interference of both. We see that the nuclear contribution has only a minor effect on the excitation cross section.

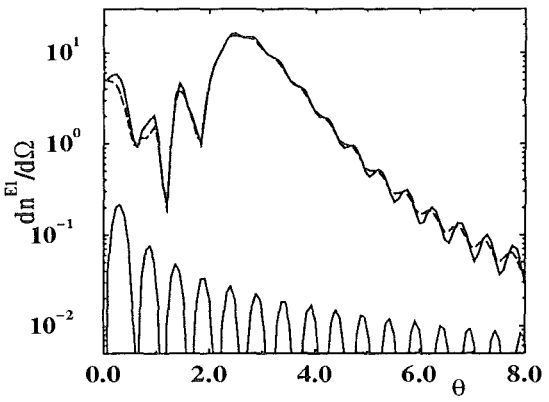

Fig. 3: Influence of the nuclear part on $\frac{dn^{E1}}{d\Omega}$. The dashed line shows the Coulomb part, the dotted line the nuclear part and the solid line gives the interference of both parts.

The previous models still starts from quite simple pictures of the nucleus, but it has the advantage of the simple expressions for Γ_N^{Elm} (eqn. 12 and 13), which can give a first estimate of the nuclear effects. More realistic models will have to start from more sophisticated models for the nucleus and the nuclear potential. We are currently working on the inclusion of such nuclear contributions.

References:

[1] C.A. Bertulani and G. Baur, *Phys. Rep.* **163** (1988) 299.

[2] G. Baur and H. Rebel, *J. Phys. G* **20** (1994) 1.

[3] S. Typel and G. Baur, *Phys. Rev.* **C 50** (1994) 2104.

[4] C.A. Bertulani and A.M. Nathan *Nucl. Phys.* **A 554** (1993) 158.

[5] A.N.F. Aleixo and C.A. Berulani *Nucl. Phys.* **A 528** (1991) 436.

[6] A. Winther and K. Alder, *Nucl. Phys.* **A 319** (1979) 518.

[7] R.J. Glauber, *Lectures in theoretical Physics I* (Interscience Publishers, Inc., New York 1959).

[8] L.J. Tassie, *Austral. J. Phys.* 9(1956)407.

5. GENERAL PHYSICS

On Thermodynamic Systems in Static External Fields

V. Klemt

In most textbook derivations of the basic laws of thermodynamics it is tacitly assumed that the systems are homogeneous in space. In the presence of external fields this is of course not true in general. To include time-independent conservative external fields, mainly two modifications have to be made:

a) The basic thermodynamic relations have to be written in terms of intensive instead of extensive quantities,

b) external-field contributions have to be added to the thermodynamic potentials.

For simplicity we begin with the one-dimensional case where all quantities depend on only one spatial coordinate x. If we denote all extensive quantities with capital and the respective intensive ones (as eg. $s = S/V$ for the entropy per unit volume) with lower-case letters, we are lead from

$$\mathrm{d}U = T\mathrm{d}S - p\mathrm{d}V + \mu\mathrm{d}N \tag{1}$$

to

$$\mathrm{d}u = T\mathrm{d}s + \mu\mathrm{d}n. \tag{2}$$

In the presence of an external potential $\phi(x)$ the total energy density is $e = u + n\phi$ and the respective total differential reads

$$\mathrm{d}e = T\mathrm{d}s + (\mu + \phi)\mathrm{d}n + n\phi'\mathrm{d}x, \tag{3}$$

where $-\phi' \equiv -\mathrm{d}\phi/\mathrm{d}x = k$ is the force per particle exerted by the external field.

Here the quantities $\mathrm{d}e$, $\mathrm{d}s$ and $\mathrm{d}n$ have to be interpreted as substantial differentials, insofar as an infinitesimal spatial displacement of the considered volume element is implied.

If we now consider a system in a fixed cylindrical volume V of length a (in x-direction) and cross section A (which we shall choose to be unity, so that $\mathrm{d}x$ is identical with the volume element), then all the extensive quantities can be written as spatial integrals over $\mathrm{d}x$. For the total entropy we get:

$$S(a) = \int_0^a s(e, n, x)\,\mathrm{d}x. \tag{4}$$

Now e and n are the total spatial derivatives of the respective extensive quantities

$$e(x) \equiv E'(x) = \frac{\mathrm{d}E(x)}{\mathrm{d}x} \quad \text{and} \tag{5}$$

$$n(x) \equiv N'(x) = \frac{\mathrm{d}N(x)}{\mathrm{d}x}. \tag{6}$$

The quantities $E(x)$ and $N(x)$ are to be understood as those parts of the total energy and particle number that are enclosed in the volume interval (0,x), so that $E(0) = N(0) = 0$, $E(a) = E$ and $N(a) = N$.

The total entropy can thus be written

$$S = \int_0^a s(E', N', x)\,\mathrm{d}x, \tag{7}$$

where, now in terms of the variables N' and E', the total differential of the specific entropy reads:

$$\mathrm{d}s = \frac{1}{T}\{\mathrm{d}E' - (\mu + \phi)\mathrm{d}N' - N'\phi'\mathrm{d}x\}. \tag{8}$$

Expression (7) shows a close analogy to the action integral of classical mechanics,

$$S = \int_{t_0}^{t_1} L(q_i, \dot{q}_i, t)\,\mathrm{d}t. \tag{9}$$

In fact, the integral (7), representing the total entropy, has, for an isolated closed system, to be stationary,

$$\delta S(E, N) = \int_0^a \delta s(E', N', x)\,\mathrm{d}x, \tag{10}$$

with respect to variations of integration paths described by the coordinates $E(x)$ and $N(x)$, whereby the boundary values (total energy and particle number) have to be kept fixed. The quantities E' and N' play exactly the role of the generalized velocities.

As a result we get two EULER-LAGRANGE equations:

$$\frac{\mathrm{d}}{\mathrm{d}x}\frac{\partial}{\partial N'}s(E', N', x) = 0, \tag{11}$$

$$\frac{\mathrm{d}}{\mathrm{d}x}\frac{\partial}{\partial E'}s(E', N', x) = 0. \tag{12}$$

The differential expression (8) gives explicitly

$$\frac{\mathrm{d}}{\mathrm{d}x}\frac{\mu + \phi}{T} = 0, \tag{13}$$

$$\frac{\mathrm{d}}{\mathrm{d}x}\frac{1}{T} = 0. \tag{14}$$

The latter equation is the fundamental

$$T = \text{const.}, \tag{15}$$

which, inserted into the former, gives

$$\mu + \phi = \text{const.} \tag{16}$$

In the state of thermal equilibrium, the quantity $\overline{\mu} = \mu + \phi$, which plays the role of the chemical potential in the presence of an external field, is constant over the whole volume. The relations (15) and (16) are of course well known [1], but it is interesting to see how they result simultaneously from a single variational equation (10).

The DUHEM-GIBBS relation

$$n\mathrm{d}\mu = -s\mathrm{d}T + p \tag{17}$$

generalizes to $(n = N'(x))$

$$\mathrm{d}(\mu + \phi) = -\frac{s}{n}\mathrm{d}T + \frac{1}{n}\mathrm{d}p + \phi'\mathrm{d}x, \tag{18}$$

which, because of the constancy of the temperature, leads to a differential equation for the pressure in dependence of the coordinate x:

$$\frac{\mathrm{d}(\mu+\phi)}{\mathrm{d}x} \equiv \frac{1}{n}\frac{\mathrm{d}p}{\mathrm{d}x} + \phi'(x) = 0. \tag{19}$$

In the case of an ideal BOLTZMANN gas in the homogeneous gravitational field we have

$$p = nT \quad \text{and} \quad \phi(x) = mgx. \tag{20}$$

This gives

$$\frac{\mathrm{d}p}{\mathrm{d}x} = -\frac{mgp}{T} \tag{21}$$

or

$$p = p_0\, e^{-mgx/T}, \tag{22}$$

the barometric formula.

The question of course arises, whether this variational concept allows generalization to truly three-dimensional conservative fields $\phi(\mathbf{r})$.
In fact, we can introduce curvilinear orthogonal coordinates ξ, η, ζ in a way that thin layers between equipotential surfaces are defined by $\zeta = c = \text{const.}$ and $\zeta = c + \delta c = \text{const.}$ Within such a layer we have exactly the same situation as in homogeneous systems without external field, since the total energy per particle differs from the internal one only by the constant value $\phi(\zeta = c)$. In particular, everywhere within the layer we have the same temperature, pressure, chemical potential, particle as well as energy and entropy density. In the entropy integral we can therefore simply intergrate over the coordinates ξ and η to get

$$S = \int_{\zeta_{\min}}^{\zeta_{\max}} s(E', N', \zeta)\, f(\zeta)\, \mathrm{d}\zeta \tag{23}$$

with

$$f(\zeta) = \int J(\xi, \eta, \zeta)\, \mathrm{d}\xi \mathrm{d}\eta \mathrm{d}\zeta, \tag{24}$$

where $J(\xi, \eta, \zeta)$ is the Jacobian of the transformation from the cartesian to the curvilinear coordinates.
Now, since it is obvious that $f(\zeta)s(E', n', \zeta) = \mathrm{d}S/\mathrm{d}\zeta$, and E' and N' can be taken to be the respective substantial derivatives with respect to ζ, we end up with an equation that has exactly the form (10). Though, of course, in general the equipotential layers are neither uniform in thickness (measured in cartesion coordinates!) nor equal in their in $\xi\eta$-extension, all the reasoning of eq. (11) and the following remains unchanged. Temperature and chemical potential $\overline{\mu} = \mu + \phi$ are constant over the whole volume and the pressure follows an equation like eq. (19) with ζ substituted for x.

Reference:

[1] Landau, Lifshitz, Vol. V, Statistical Physics, Pergamon 1959, §25.

III. Accelerator Division

6. COOLER SYNCHROTRON COSY

Machine Development at COSY in 1995

R. Maier, U. Bechstedt, J. Dietrich, S. Martin, D. Prasuhn,
A. Schnase, H. Schneider, H. Stockhorst, R. Tölle

In 1995, the machine development at COSY was dominated by several topics which led to an enhanced knowledge of the machine properties as well as in an increase of the beam quality at internal and external target stations:

- improvement of ramping functions
- characterization of beam properties and proof of lattice flexibility with the EDDA and COSY 11 experiment
- shifting transition energy upwards during acceleration
- acceleration of an electron-cooled beam
- increase of resonant and stochastic extraction efficiency

Improvement of ramping functions

During operation of COSY it was found that the procedure for modifying the final momentum does not allow a fast change of the vital machine settings. The control functions for the dynamic devices, e.q. dipoles, rf-system and quadrupoles were re-examined and now incorporate the knowledge gained during machine and development runs. In general, the final momentum and the flat-top time are given. The dipole current ramp is then calculated from the momentum domain. It includes also corrections for eddy-currents in the COSY beam pipe. In a second step the saturation of the iron cores of the dipoles is compensated by driving the dipoles with a higher current. The compensation function was derived by increasing the final momentum step by step together with closed orbit measurements. The driving voltage for the dipole power converter is then computed from the corrected current ramp. A similar procedure is applied to the different quadrupole families. Finally, the frequency ramp is determined. It is now possible to modify a given ramping function in a specific time region more easily. This is of great importance, e.g. for setting up extraction, chromaticity measurements and special optic modifications required by a physical experiment.

Internal experiments

There is a very intimate relation between internal experiments and the accelerator as they affect each other in a direct way. EDDA [1] is an internal experiment at TP2 that has been set up to measure excitation functions with high precision. A new insight into hadron-hadron interaction is expected if minute anomalies were found. The basic design is a thin horizontally oriented fiber target that intercepts the beam combined with a cylindrical detector system surrounding the thin walled beam pipe. Due to its construction the EDDA experiment is not only a tool for medium energy physics but also an excellent probe for investigating and verifying beam properties of COSY with high precision.

This experiment has special requirements on the beam to achieve optimal measurement conditions. It concerns the lateral stability and the orientation of the phase space ellipses. It is the latter point where the flexibility of the target telescopes proved invaluable. Figure 1 shows relevant parameters of an early run. Four parameters versus time are combined in this picture.

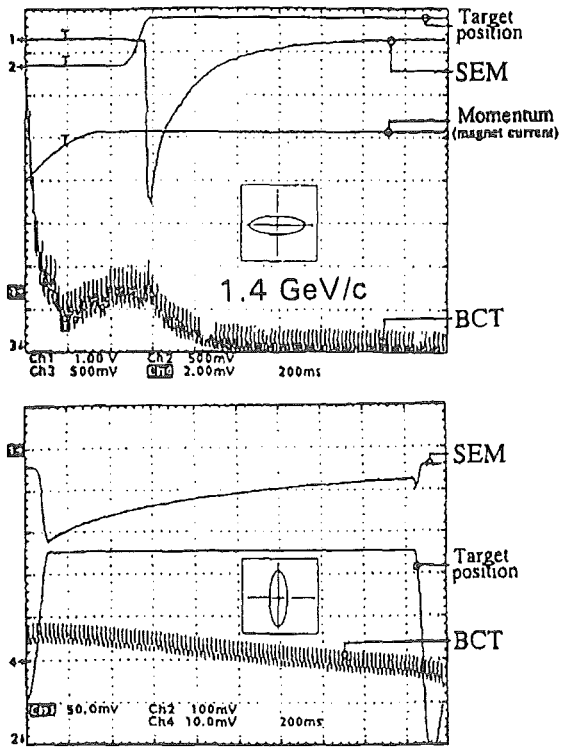

Fig. 1: Beam current on the internal target measured with SEM

One horizontal division corresponds to 200 ms. The vertical scale shows the parameters under measurement converted to a voltage with an arbitrary scaling and offset. Curve 2 gives the vertical position of the fiber target. It rests underneath the beam and is moved into the beam at a fixed time. Curve 1 shows the secondary electron current (SEM) which steeply rises the moment the fiber dives into the beam. The current then gradually fades away proportional to the diminishing beam as particles get scattered outside the ring's acceptance. The circulating particles are monitored with a beam current transformer (BCT) as shown in the lowest curve. The curve labeled Momentum is derived from the magnetic dipole fields. As depicted the target was moved into the beam shortly after the flat top of the beam momentum had been reached with 1.4 MeV/c. A beam life time of 160 ms can be deduced from the curves. Although this value was fine for the first data taking, the rush of data

was hard to handle by the computers. Therefore, the experimenters required a much longer life time.
The key to this goal is found in the small ellipse shown in this picture. This ellipse represents a cross section through the beam at the target position. The large horizontal extent was less optimal for the horizontally stretched 5 μm carbon fiber. By changing the settings of the straight section the ellipse was rotated by 90 degree shown in the picture underneath yielding a significantly better behavior. The time scales are identical.
It is important to note that this change was virtually transparent to the rest of the ring's ion optics. More important, the beam life time could be extended by more than a factor of five to 870 ms. This dramatic increase in beam life time meant a real breakthrough for the experiment, relieving the data acquisition from the high peak count rate it had to deal with before. With a somewhat thinner PE-fiber beam life times of 4 s have been reached meanwhile.
Meanwhile proton-proton elastic scattering excitation functions in the kinetic energy range 0.5 to 2.5 GeV have been successfully measured [1]. The data were taken while ramping up to flat top energy. The quality of the data proves the machine's parameter stability even while ramping. Examples are shown in figures 2 to 4. Figure 2 depicts the momentum ramp of the machine together with the horizontal beam position measured at the EDDA target location by the EDDA detector [2]. It is clearly visible from the figure that the beam moves outwards during ramping up and stays constant when reaching the flat-top momentum of 3.4 GeV/c. As a sensitivity test the beam was then horizontally moved in flat-top by two steerers located closely to the EDDA-experiment station. This bump, starting at 2.8 s and finishing at approximately 4 s, could be clearly measured.

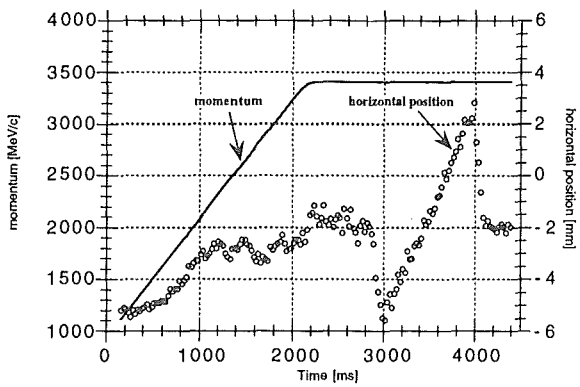

Fig. 2: Momentum ramp and horizontal beam position at the EDDA experiment station

Observe that the vertical beam position, figure 3, is not affected by these beam manipulations. The small dip in the vertical position is due to moving the EDDA fiber target into the beam. From the measured raw data also the horizontal beam width could be deduced, figure 4. It shows that the beam will be heated after the target has been moved in. It seems that the beam attains an equilibrium due to the adiabatic shrinking of the transverse phase space during acceleration.

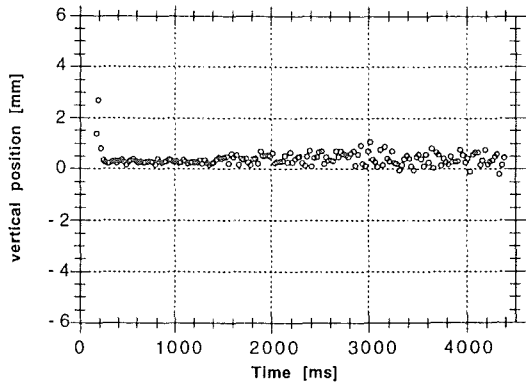

Fig. 3: Vertical beam position at the EDDA experiment

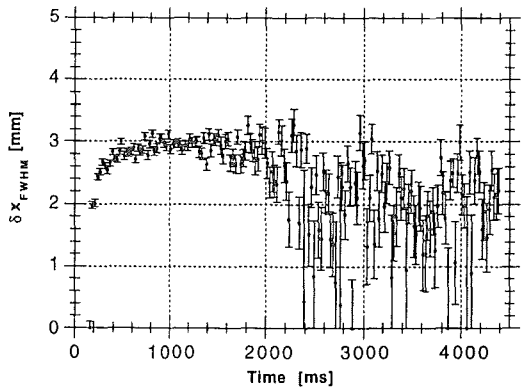

Fig. 4: Horizontal beam width during acceleration

In the middle of 1995 first experiments of COSY 11 have been started. This experimental facility [3] has been designed to study production, internal structure, and decay of mesons as well as meson-nucleon and meson-meson interactions. For this reason a cluster target is placed in front of a C-type dipole magnet in which a modification of the vacuum chamber became necessary so as to contain an extraction window for the reaction ejectiles. Back-leg windings are used to compensate eddy currents in the thick walls of this large vacuum chamber during ramping up the energy. Proton-proton and proton-deuteron scattering meson production will be measured and the reaction ejectiles will be determined via a set of drift chambers and scintillation counters. The interaction should be studied close to the production threshold with the emphasis on the meson mass range around 1 GeV/c^2. First measurements have been done successfully for the production of η mesons and the mesonic $\pi^+\pi^-$ system. In later runs the optic of the ring was changed to optimize the overlap of beam and target which requires a low beta-function and almost zero dispersion at the target station of COSY-11. A special ramping program based on optical calculations was developed to meet these requirements. At injection and during acceleration the optical settings were as usual. At flat-top the beam was then debunched. Thereafter the horizontal tune was increased to ensure a low beta-function and almost zero dispersion at the target station TP3. By this the counting ratio with and without target could be enhanced from 10/1 to 30/1.

In many synchrotrons it is unavoidable to cross transition energy [4] during acceleration. In the vicinity of this energy, completely determined by lattice functions, the circulating bunched beam may become highly unstable, especially at high beam currents and tiny bunches. In previous machine experiments the flexibility of the COSY-lattice was proven which allows a shift of the transition point upwards during acceleration. In flat-top the rf-voltage was then adiabatically turned off, and after debunching the transition energy was reduced to its nominal value giving the desired dispersion in the straight sections. After that the beam could be rebunched nearly without losses. The downwards shift of transition energy was clearly visible in a 180^0 rf-phase jump as shown in figure 5. The upper two traces show the radio frequency and the circulating bunch after reaching flat top energy. The lower two traces show radio frequency and bunch after recapturing. It should be noted that this manipulations can be done without changing the machine's working point.

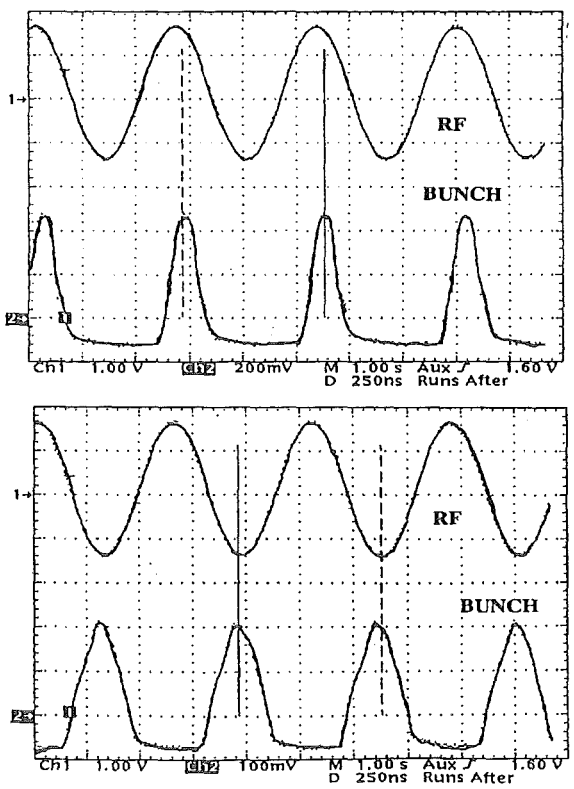

Fig. 5: Transition energy shift in flat-top

External beams

The circulating proton beam can be extracted by the conventional resonant extraction mechanism as well as with the method of stochastic extraction. In several machine runs the extraction mechanisms were studied at 800 MeV/c, 1.8 GeV/c and 3.2 GeV/c. A new digital noise generator developed at COSY was used for stochastic extraction. At present an extraction efficiency of nearly 30% is realized. Spill times of more than 30 s were obtained. Detailed information on extraction experiments are found in this report.

Stochastic cooling

The stochastic cooling is using a two band RF-system (1 - 1.8 GHz; 1.8 - 3 GHz). The gap width of the ultra cold pickup electrodes as well as of the kicker electrodes can be adjusted according to the beam size to get maximum sensitivity. All active components of the RF signal path are available meanwhile. A programmable delay is used that will allow to cool over an energy range from 0.8 to 2.5 GeV. Prototypes of critical components inside the cooling tank have already been tested and optimized. One horizontal and vertical pick-up tank of band I (1 - 1.8 GHz) are now installed in COSY for test measurements. The electrode bars are cryogenically cooled down to about 30 K to achieve a good signal-to-noise ratio even for low particle numbers in COSY. A detailed description is given in this report.

Electron cooling

At the end of 1995 further electron cooling experiments were carried out. In these sessions a cooled proton beam could be accelerated for the first time at COSY. For detailed informations see also this report.

Beam statistics

In figure 6 the beam statistics are summarized. In total 5256 hours were scheduled for 1995. From this the machine was running 4683 hours. User experiments were served for 2645 hours in total. The monthly beam statistics represent scheduled time (dark column), operational time (white column) and user time (shaded column).

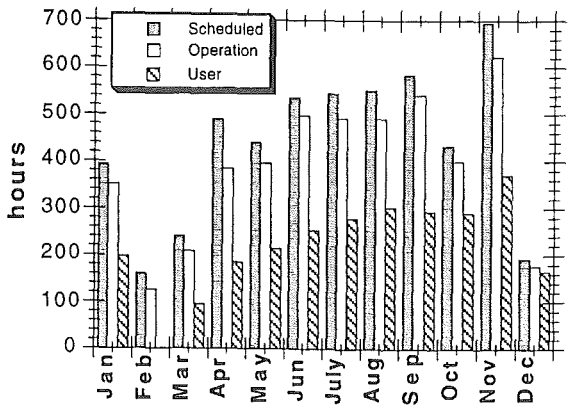

Fig. 6: Beam statistics in 1995

References

[1]. J. Bisplinghoff et al., AIP Conf. Proc. 221, Am. Inst. of Phys. 1990 p. 312, Physica Scripta **48** 1993 p. 92, Annual Report 1994, Institut für Kernphysik Jül-Spez 3035, p. 23

[2] H. Rohdjess for the EDDA collaboration, to be published

[3] D. Gronzka et al., Proceedings of the Int. Conference "Physics with GeV-Particle Beams", Forschungszentrum Jülich, Aug. 22-25, 1995, World Scientific Publishing Co. Pte. Ltd.

[4] K. Johnsen, "Transition", CERN ACCELERATOR SCHOOL, CERN 85-19, p. 178

Acceleration of a Cooled Proton Beam in COSY

R. Maier, D. Prasuhn, H.J. Stein, J.-D. Witt

Introduction

Electron cooling at injection has been successfully demonstrated in 1993 [1]. Acceleration of the cooled beam, however, always failed at that time. After a longer period of standstill, a few days of accelerator time have been dedicated to starting the investigation of the causes of the acceleration problem. There are three basic effects of the electron cooler device which may stronger or weaker disturb the circulating beam in the ring.

i) The closed orbit distortion due to the vertical magnetic field component of the cooler toroids.
ii) The tune shift of the proton beam due to the longitudinal field in the solenoids and toroids.
iii) The tune shift and a possibly broad tune spread of the proton beam due to the electric field inside and outside of the electron beam.

Correction of the closed orbit distortion

The principle of the correction scheme has been described in an earlier report [2]. Since the electron cooler magnets are mounted in the form of an upright U, it is the vertical field component in the toroids which causes antisymmetric deflections in the horizontal plane. With the arrangement of two correction steerers on each side of the cooler the proton beam can be aligned with the cooler magnet axis without influencing any initial orbit. If the initial orbit and the toroid trajectory are known, the horizontal steerer deflection angles can be determined with a transport calculation taking into account the ion-optical elements in between the various orbit defining beam position monitors. Fig. 1 shows the downstream half of the cooler telescope with the two quadrupole triplets, the two orbit defining BPMs 21 and 22, the two correction steerers h-col and h-25, the collector toroid, and the orbit trajectories before and after activation of the electron cooler magnets. Given the proton beam momentum, the deflection angle and the apparent beam origin in the toroid have been calculated on the basis of the measured transverse toroid field, Fig. 2 [3]. The steerer angles are then determined by the two actually measured beam positions, the defined zero position of the proton beam inside the cooler, and the quadrupole settings. At our injection energy of 37.8 MeV, corresponding to $p = 269$ MeV/c or $B\rho = 0.897$ Tm, there are no further active elements in the considered part of the beam line.

Compensation of tune shifts

The cooler magnets, here the solenoidal fields with their stray fields at the ends, act as focussing magnetic lenses equally in both directions. The corresponding tune shift [4] is in first order given by:

$$\Delta Q = (\beta/4\pi)\,(B_{sol} / 2B\rho)^2 L_{sol}$$

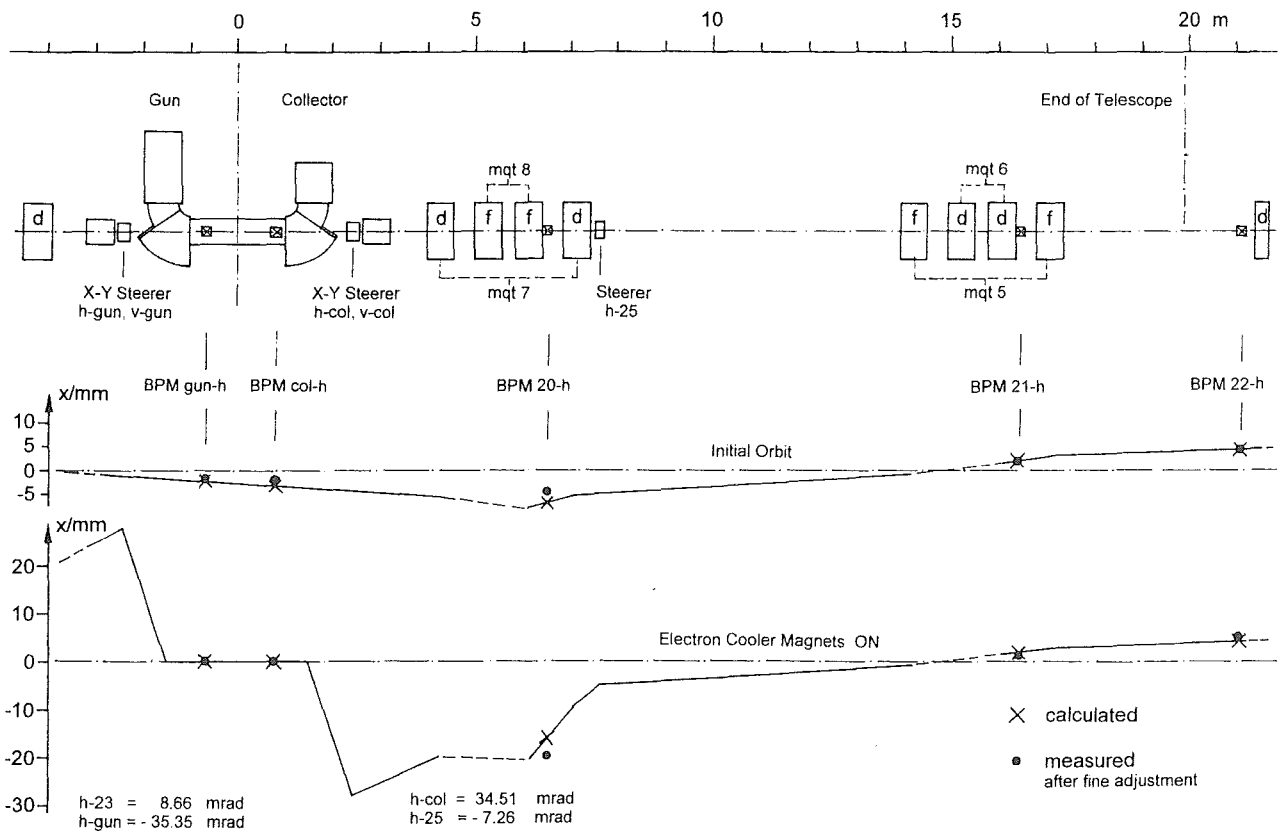

Fig. 1: Electron cooler magnets and downstream half of the cooler telescope with orbit (schematic) before and after activation of the electron cooler magnets, $B_{nom} = 0.08$ T. For the upstream side data from the symmetrically arranged BPMs 17 and 18 is used to determine the steerer angles there.

β the beta function at the site of the cooler, [m],
B_{sol} the solenoid field strength, [T],
$B\rho$ the proton beam momentum, [Tm],
L_{sol} the B^2 effective length of the solenoids, [m].

This positive tune shift is proportional to the β function and inverse proportional to the square of the beam momentum.. For the cooler solenoids and toroids at B_{sol} = 0.08 T, an effective L_{sol} = 3 m, and $B\rho$ = 0.897, a β = 10 m yields ΔQ = 0.005. The shorter compensating solenoids which we have introduced for phase space decoupling [5] contribute with ΔQ = 0.015 due to their accordingly higher B field. Also vertical edge focussing at the orbit steerers h-gun and h-col cannot be neglected. Their contribution to the tune shift is of the same amount as that of the cooler solenoids and toroids. The total value to be expected for a β = 10 m is 0.020 horizontally and 0.025 vertically. If larger β functions are involved it might be necessary to compensate disturbing tune shifts by reducing the focussing strength of appropriate quadrupoles either in the arcs or in the cooler telescope itself. Since the cooler magnets are not ramped, the tune shift vanishes during acceleration. Therefore, the quadrupole settings have to approach the non-shifted values according to the $(1/B\rho)^2$ dependence.

The electron beam introduces an additional tune shift. Here, it is the homogeneous charge distribution of the electron beam acting as a well-focussing electrostatic lens as long as the protons are travelling inside the electron beam. In this case the deflecting electric field is proportional to the radius. In thin-lens approximation this tune shift is in first order given by:

$$\Delta Q = (\beta/4\pi)\, L_e\, (E(R)/R) \,/\, (p\, \beta_r)$$

R the radius of the electron beam [m],
E(R) the electric field strength at this radius, [V/m],
p the proton beam momentum, [eV/c],
L_e the length of the electron beam, [m],
$\beta_r = v/c$, particle velocity in units of light.

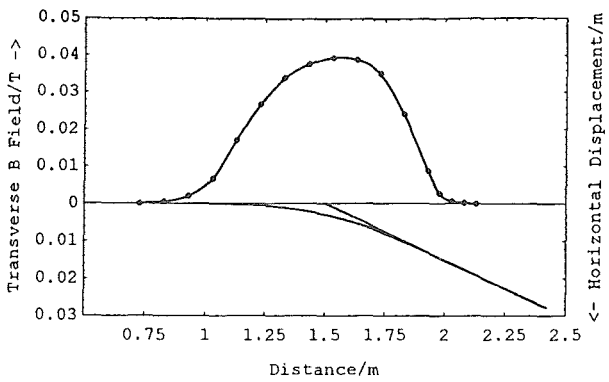

Fig. 2: Measured transverse field component of an electron cooler toroid with calculated real and effective proton trajectory for $B\rho$ = 0.897 Tm, B_{nom} = 0.08 T. The apparent beam origin is at 1.50 m, the deflection angle is 30.2 mrad. The origin of the distance scale is in the center of the cooler solenoid.

Again, the shift is proportional to the β function. For our 1 inch electron beam, its effective length of 2.5 m, a current of 0.5 A, and β = 10 m, the tune shift at injection would be 0.02. However, if the proton beam is larger than the electron beam E(r)/r is not anymore constant but falls off like $1/r^2$. There will occur a whole spectrum of tune shifts ranging from the maximum value inside the electron beam to a minimum value given by the maximum excess radius of the proton beam. Since each proton will pass any radius at a certain time, the entire tune spread and not only a well-defined shift has to be regarded in view of resonance losses. CELSIUS was the first machine where decreasing life times of a 48 MeV proton beam in the presence of a small-diameter electron beam have explicitely been observed. [6].

Experimental results

The closed orbit correction at injection worked quite satisfying. With the calculated steerer settings enough beam survived to be seen on the beam current monitor. The correctness of the steerer settings may be influenced by several factors. The calibration of the h-23 and h-25 steerers, here in %/mrad (power supply current versus deflection angle at injection momentum), is different depending on the method how it has been obtained. A calibration in the ring based on measured BPM positions and the COSY ring optics gave 2.8 %/mrad whereas a laboratory measurement yielded 3.7 %/mrad. In contrast to the laboratory situation, these steerers are mounted close to other magnets resulting in a reduced effective length which might decrease the sensitivity even more. As an estimate, a value of 4.2 %/mrad has been taken . The h-gun and h-col steerers are originally equipped with field clamps on both sides so that their laboratory calibration [2] should be reliable. The toroid data depend on the accuracy of the 1992 field measurement [3]. An in-beam calibration, only operating the solenoid and toroid magnets at a reduced field of 0.027 T failed because of large discrepancies between measured BPM positions and those predicted by the optical model of the cooler telescope. Such discrepancies were also observed for the intitial orbit, however, the displacements are much smaller here so that they might be accurate enough for the purpose of calculating the steerer settings.

After the beam was once circulating, a manual fine adjustment within a few percent of the steerer power supply currents increased the beam intensity up to 20% of the injected value which was about 2×10^{10} particles in the ring. Due to coupling of horizontal with vertical motion in the longitudinal fields one needs also steering in the vertical plane. The vertical steerers v-gun and v-col are integral part of the corresponding horizontal steerers [2]. A few tenth of a mrad at these vertical steerers were sufficient but necessary to maintain the beam intensity. The on-axis position of the proton beam in the cooler drift solenoid was checked with the two cooler BPMs. A precise horizontal positioning is possible with the outer steerers h-23 and h-25. Increasing both angles simultaneously rotates the beam, increasing one angle and decreasing the other yields parallel displacement. The vertical proton beam position was always precise enough. The correct on-axis position of the 20.64 keV electron beam had already been studied before. A careful adjustment of the gun side toroid dipole

coil, which compensates the RxB drift, automatically garantuees the almost perfect alignment of the electron beam in the drift solenoid.

Full initial intensity was then obtained by correcting the tune with the quadrupole families mqt7 and mqt8 in the cooler telescope. The measured tune shifts at injection for the cooler field of 0.08 T were $\Delta Q_h = +0.01$ and $\Delta Q_y = +0.09$, indicating β functions of about 5 and 35 m, respectively, which are in resonable accordance with MAD calculations for the COSY lattice. The MAD code was also used to calculate appropriate new current settings for mqt7 and mqt8. The changes were 33.4 to 30.2 A for mqt7 and 30.0 to 27.3 for mqt8 A, resulting in a working point of $Q_x = 3.568, Q_y = 3.674$. Acceleration of the proton beam up to 800 MeV/c was then possible when during ramping this quadrupole correction was reduced according to the $(1/2B\rho)^2$ dependence. A ramping down of the vertical steerers v-gun and v-col as expected earlier [2] was not necessary in this case.

In the run on Nov. 30, when we switched a 70 mA electron beam onto the orbit- and tune-corrected bunched proton beam, we first lost the whole beam in a fraction of a second. A few ion-optical manipulations as a 0.1% increase of the momentum via the cavity frequency, a corresponding increase of the bending magnet strength, and a bit lower mqt7, mqt8 currents - thus a defocussing action - resulted in a cooled beam. However, only 6×10^8 particles survived in the time of 2 s which was spent for cooling. (In the 1993 cooling runs with electron beams up to 0.4 A, typical intensities were 2×10^9 [1]). This cooled beam could then be accelerated - and even extracted.. The beam losses during acceleration were 60% so that 2×10^8 particles were finally found in the flat top of 8oo MeV/c. The decisive beam losses - 97% - occurred right after injection. The day before, probably with a slightly different setting of the ion-optics, we had observed almost no influence on the proton beam when we applied a non-cooling 10 keV, 70 mA electron beam. These experimental observations may be explained as fast resonance losses at critical working points in combination with various tune shifts and an unfavourable large (35 m or more?) vertical β function.

Conclusions

Up to now all electron cooling in COSY consisted of singular experiments. After the first commissioning runs in 1993 with their promising results we are now confronted with the specific problem of a mismatch of electron beam diameter and the standard ring optics of COSY as it is used for most applications. In the design phase of the COSY electron cooler β functions of about 5 m have been requested [7]. In principle, the ion-optical flexibility of the COSY ring should make possible the adjustment of the β function in a range of 7 to 15 m without disturbing other applications. Ion-optical model calculations indicate that the positive tune shift due to the electron cooler magnets helps to reduce the β function at the site of the cooler. It is proposed to set the working point at injection far enough below the 2/3 resonances, also taking into account the increasing negative space charge tune shift during cooling, and to adjust the extraction working point only after acceleration. In addition, it would be worthwhile to explore the possibility of cooling at higher proton energies. Our maximum electron beam energy is 100 keV allowing a proton energy up to 180 MeV [5]. To avoid the tune spread problem at injection one should try to switch on the electron beam only after such a pre-acceleration. Due to adiabatic shrinkage the proton beam diameter is then smaller. As a last measure one could try to increase the electron beam diameter, e.g., by increasing the magnetic field in the gun solenoid (and in the collector solenoid) which would result in the adiabatic expansion of the electron beam in the cooling solenoid [6 and 8].

Despite the encountered difficulties we have made the important progress of accelerating the uncooled beam in the frame of „standard" beam losses. Orbit correction and tune shift compensation work with presetting the relevant magnetic elements without the troublesome and time consuming step by step procedure applied earlier [1]. Electron cooling in COSY seems to be more a problem of the ring than of the cooler itself. A careful investigation of the various disturbing effects is necessary in order to reach the goal of the envisaged routine operation of the electron cooler. This will afford more and longer machine developing run times. A better knowledge of the ion-optical properties of COSY would also be helpful, not only for electron cooling.

Acknowlegment
We thank S. Martin for fruitful discussions.

References

[1] R. Maier et al., Commissioning of the COSY Electron Cooler - Phase 2, KFA-IKP Annual Report 1993, p. 171 (1994)

[2] G. Mueller et al., Design and Performance of the Proton Beam Correction Steerers for the COSY Electron Cooler, KFA-IKP Annual Report 1994, p. 215 (1995)

[3] W. Schwab et al., Magnetic Field Measurements of the COSY Electron Cooler, KFA-IKP Annual Report 1992, p.215 (1993)

[4] V.I. Kudelainen, I.N. Meshkov, R.A. Salimov, The Electron Beam Device for Heavy Particle Cooling Experiments, CERN-Report 87-08, p. 68 (1977)

[5] R. Maier , B. Seligmann, H.J. Stein, Electron Cooling in COSY Juelich, Proc. 2nd EPAC 90, Nice, p. 1580 (1990)

[6] D. Reistad et al, Measurement of Electron Cooling and „Electron Heating" at CELSIUS, Proc. Workshop on Electron Cooling and Related Topics, Montreux 1993, CERN Report 94-03, p. 183 (1994)

[7] C. Habfast et al., Der COSY Elektronenkuehler, COSY Design Note No. 52, Juelich (1986)[

[8] H. Danared, Electron Cooling with an Electron Beam of 10 meV Tranverse Temperature, Proc. Workshop on Electron Cooling and Related Topics, Montreux 1993, CERN Report 94-03, p. 322 (1994)

Experimental investigation of amplitude dependent tune

L.H.A. Leunissen, J. Dietrich, R. Tölle

Introduction

In the following the attention is concentrated on the measurement of the amplitude dependent tune with kick-excitation. The experimental procedure starts with a single bunch being kicked with various angular deflections by a pulsed deflection magnet (kicker). The subsequent beam-centroid displacement (the betatron motion) is measured by two beam position monitors (BPM's). The turn-by-turn beam positions are digitised and recorded in FIFO memories. In this way the data of 200 (with 4K FIFO-length) or of 3200 (64K FIFO-length) successive turns are recorded. It is only possible to use the kicker for horizontal displacements. The position accuracy is less then 0.4 mm. In figure 1, the forced damped oscillations around the closed orbit deviation are shown. The dots are the measured values from turn to turn.

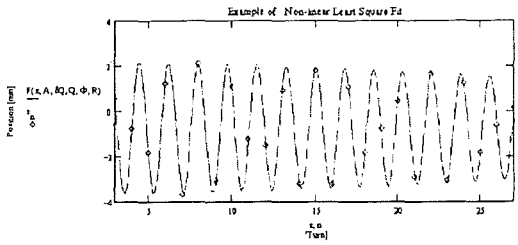

Fig. 1: Damped beam centroid in the horizontal plane and fitted curve for several turnes. The dashed line is a fit of the damped beam centroid oscillation.

The fitting curve for the damped beam centroid oscillation can be described by the following analytical expression [1,2]

$$x_n = A(\varepsilon, \beta(s))e^{-\frac{(n\pi\cdot\delta Q_x)^2}{2}} \cos(2\pi(nQ_x + \phi_x)) + R_0$$

with x_n the horizontal position at the n-the turn. The parameter A is an amplitude term which depends on the beta-function and the emmitance (in mm·mrad) of the kicked beam, Q_x is the horizontal tune, δQ_x the tune-spread, ϕ_x the phase advance and R_0 the closed orbit value. By least square fitting of the measured beam positions, accurate results for the parameters can be obtained. The measurements are done with BPM21 and BPM24 which have approximately a phase advance of $\pi/2$.

Single resonance regime

Based on the theory of betatron motion [3], the betatron amplitude of particle motion in the horizontal and vertical plane are given by,

$$\frac{d^2x}{ds^2} + K_x(s)x = \frac{\Delta B_z}{B\rho}; \qquad \frac{d^2z}{z^2} + K_z(s)z = -\frac{\Delta B_x}{B\rho}, \text{with}$$

$$\Delta B_z + i\Delta B_x = B_0 \sum_{n\geq 2} (b_n + ia_n)(x + iz)^n,$$

where b_n and a_n are respectively the normal and skew multipole components. $K_x(s)$ and $K_z(s)$ are quadrupole strength functions, $B\rho = p/e$ is the momentum rigidity and s is the longitudinal particle coordinate, which advances from 0 to $2\pi R$, the circumference, where R is the average radius. Oscillations about the closed orbit due to the linear focusing of quadrupoles are called betatron oscillations. The number of oscillation periods in one revolution are called tunes, Q_x and Q_z.

The betatron amplitude of particle motion in action angle variables are given by:
$x = \sqrt{2\beta_x J_x}\cos(\phi_x)$; $z = \sqrt{2\beta_z J_z}\cos(\phi_z)$ with J_x and J_z as invariant actions for unperturbed motion. Betatron motions are normally small, so that the kick angles due to non-linear magnets are of the order 10^{-3} or less than the corresponding kick of the quadrupoles. The Hamiltonian based on perturbation expansion of action angle variables close to a single order resonance can conveniently be represented by, see [4,5]. For a single resonance at $mQ_x = n$ in one dimension, the Hamiltonian can be expressed as [6]:

$$H = 2\pi(Q_{x,0} - \tfrac{4}{7})J_x + \tfrac{1}{2}UJ_x^2 - V_7 J_x^{\frac{7}{2}}\cos(7\phi_x)$$

for n=4 and m=7. The action $J_x \equiv \frac{1}{2}a^2$ for the horizontal plane, the coefficient U parametrizes detuning and the coefficient V_7 represents the strength of the resonance containing non-linear multipole components. After seven turns the particle is close to the point where it started. The canonical differential equations are obtained by differentiation of the Hamiltonian and are:

$$\dot{\phi}_x = 2\pi(Q_{x,0} - \tfrac{4}{7}) + UJ_x - \tfrac{7}{2}V_7 J_x^{\frac{5}{2}}\cos(7\phi_x);$$

$$\dot{J}_x = -7V_7 J_x^{\frac{7}{2}}\sin(7\phi_x).$$

The effect of the non-linearity makes the tune increase with increasing amplitude, see figure 3. There is one amplitude, a_r, for which the fractional tune is exactly 4/7. A measurement near this resonance is shown in figure 2. This is a phase-space plot in which the beam position at BPM21 and BPM24 are plotted with respect to each other. Here we see that the motion is damped in several hunderd turns.

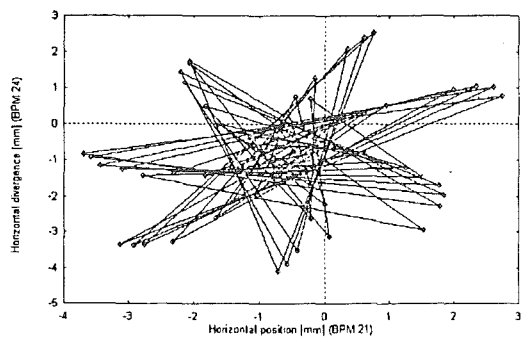

Fig. 2: Phase-space plot for BPM21 and 24 for a kick-amplitude of 21 kV at a momentum of 1250 MeV/c. The straight lines connect the measured data between two turns.

A proton launched with a small amplitude (a) advances smoothly around a circle, with ϕ_x increasing by slightly less then $6\pi/7$ per turn. The base tune ($Q_{x,0}$) is just above 0.56 and increases dependent of the amplitude according to [6]:

$Q_x(a)=Q_{x0}+\frac{1}{2}Ua^2$. Higher harmonics of the tune become more important in the Fourier expansion of the displacement as the amplitude is increased. Several measurement with different kick-amplitudes are done to determine the detuning factor for the COSY accelerator. The measured tune-shift is shown in figure 3.

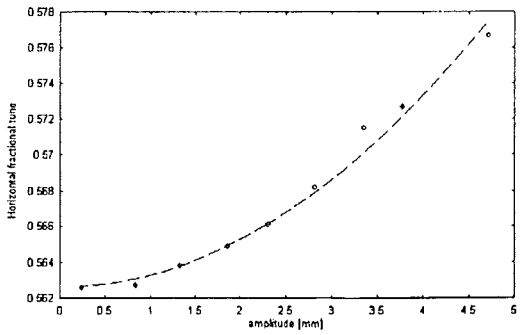

Fig. 3: Horizontal tune dependence as function of the kick amplitude at 1250 MeV/c as measured with BPM21. The dots are measured tunes and the dashed line indicates the fitted curve.

A least square fit of this curve shows that the horizontal tune changes by:

$Q_x(a)=0.5626+6.7\cdot10^{-4}a^2$. Measurements with BPM24 yield similar results (U=6.9·10^{-4}). The same measurement can be done at higher energies to determine the influence of multipole components of the dipoles and quadrupoles.

References

[1] J. Bojowald et al., Diagnostic tools for the Resonant Extraction at COSY-Juelich, DIPAC '95, Travemünde

[2] C.M.Warsop, Low Intensity and Injection Studies on the ISIS Synchrotron, EPAC '94, London

[3] E.D. Courant and H.S. Snyder, Ann. Phys. (NY) 3, 1 (1958)

[4] J. Bengtsson, Non-linear Transverse Dynamics for Storage Rings with Applications to the Low-energy Antiproton Ring (LEAR) at CERN, CERN 88-05 (1988)

[5] S.Y. Lee, Review of nonlinear Beam Dynamics Experiments, Proc. of int. Workshop, Berlin 1992, p. 249

[6] T. Satogata et al., Driven Resonance of a Trapped Particle Beam, Phys. Rev. Letters 68, 1838 (1992)

Chromaticity measurements at COSY

L.H.A. Leunissen, H. Stockhorst, R. Tölle

Introduction

In a storage ring, particles with a different momentum will experience a different focusing strength in the quadrupoles and, as a consequence have a different betatron oscillation frequency. As a result of this, the tune Q_y ($y \in \{x, z\}$) is depending on the momentum of the particles, i.e. $Q=Q(\delta)$ with $\delta=(p-p_0)/p_0$, where p_0 is the momentum of the reference particle is. The Taylor-series of the tune as function of δ is given by:

$$Q_y(\delta) = Q_y(0) + Q_y'(0)\delta + Q_y''(0)\delta^2 + \ldots \qquad (1)$$

with Q'_y the chromaticity. The normalised chromaticity ξ_y is defined as:

$$\frac{\Delta Q_y}{Q_y} = \xi_y \frac{\Delta p}{p_0}. \qquad (2)$$

In strong focusing lattices, the main contribution to the chromaticity comes from the quadrupoles, and is given by [1]:

$$Q_y' = -\frac{1}{4\pi}\oint \beta_y(s) k_{1y}(s) ds \qquad (3)$$

with $k_{1y}(s)$ the normalised quadrupole gradient (with a dimension of m^{-2}) defined as

$$K_{1y}(s) = \frac{e}{p}\frac{\partial B_z(s)}{\partial y} \qquad (4)$$

The chromaticity produced by a linear lattice is called the "natural" chromaticity. For operation of most storage rings, there are two reasons for adjusting the chromaticity to zero or to make it slightly positive. First of all, to avoid off-momentum particles to cross resonances and being lost. Secondly, to avoid "head-tail effects" in high current beam bunches [2].

To compensate for the "natural" chromaticity, sextupoles can be used. The contribution of a sextupole to the chromaticity is [1], with the positive sign for the horizontal plane and the negative sign for the vertical plane:

$$Q_{y,sext}' = \pm\frac{1}{4\pi}\oint \beta_y(s) k_{2y}(s) D(s) ds \qquad (5)$$

with D(s) the dispersion function and the normalised strength of the sextupole (with a dimension of m^{-3}) given by:

$$k_{2y}(s) = \frac{e}{p}\frac{\partial^2 B_z(s)}{\partial y^2}. \qquad (6)$$

The dispersion and beta function can be calculated with the numerical code MAD [3] for the COSY-lattice.

Measurements

For chromaticity measurements it is necessary to determine the quantities of Eq. 2. Tune measurements can be done by exciting the beam and measuring the frequency of the beam position oscillations. The momentum can be adjusted for typically a few pro mille by changing the magnetic field in the dipoles. The contribution of the dipoles is measured in this way. The momentum can also be adjusted by changing the frequency of the cavity for a few pro mille.

The measurements shown here are done with magnetic field induced momentum changes.

At an energy of 1250 MeV/c tune measurements in the horizontal and vertical plane have been done. Then the momentum was changed in steps of 0.5 pro mille and again the tune was measured. The result from this measurement is shown in figure 1.

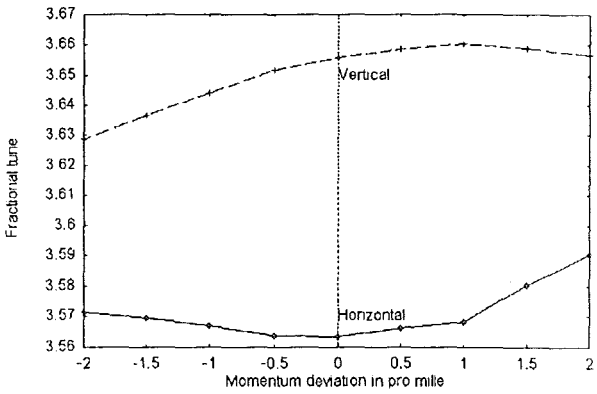

Fig. 1: Measured chromaticity at 1250 MeV/c. Horizontal tune (solid line) and vertical tune (dashed line).

The Taylor series shows that the normalised chromaticity in the horizontal plane is 1.06 and in the vertical plane 1.98. The taylor series upto second order are: $y=3.56371+0.00378x+0.00443x^2$, horizontal and $y=3.65571+0.00723x-0.00334x^2$ vertical. The same measurements can be done at different energy levels and show that the chromaticity is momentum dependent, see figure 2.

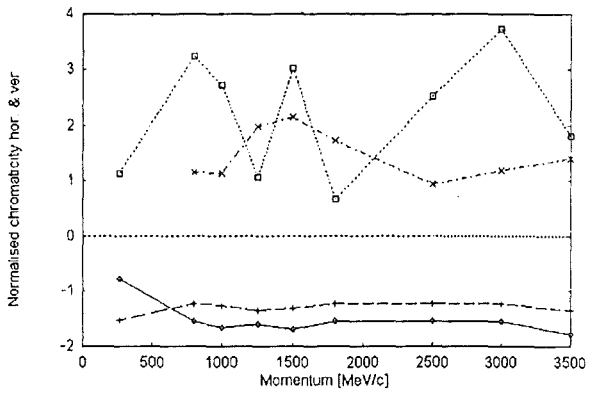

Fig. 2: Momentum dependent measured normalised chromaticity with uncorrigated closed orbit, horizontal (dotted line) and vertical (dash-dot line). Calculations with MAD show the horizontal (solid line) and vertical chromaticity (dashed line).

These measurements are done with an uncorrigated horizontal closed orbit. Measurements show that the horizontal chromaticity induced by the dipoles depends on the closed orbit distortion and the normalised chromaticity

can vary, for example at 800 MeV/c from +3 to 0. Vertically this effect is much smaller. The difference between the measured positive chromaticity and the calculated negative chromaticity is dependent on the contribution of the higher order components of the dipoles to the chromaticity.

Sextupole correction

As shown in formula 5 the "natural" chromaticity can be altered by using sextupoles. The influence of every sextupole can be calculated in advance using the following formula (7) for the horizontal and vertical plane:

$$\Delta Q'_y = k_{2y}\alpha_y \qquad (7)$$

For several sextupole families these calculations have been done and the results (α_y) are shown in table 1. These calculations are for corrections at flat top for machine settings in autumn of '95.

Sextupole	Horizontal (α_x)	Vertical (α_z)
MXL1	-0.336	0.078
MXL2	0.157	-0.348
MXL3	0.122	-0.367
MXL4	-0.408	0.080
MXL10	-0.042	0.110
MXL11	0.437	-0.224
MXL12	0.518	-0.205
MXL13	-0.043	0.131
MXL	0.567	-3.389
MXG	1.656	-1.023
MXS	-0.264	0.193

Table 1: Calculated chromaticity contributions of sextupoles. The values are normated on the sextupole strength of the individual families.

The values shown in this table have to be multiplied with the strength [m^{-3}] of the corresponding sextupole to show how much the chromaticity is changed. Measurements have also been done in this direction. The results for MXL4 are shown in figure 3. The chromaticity is measured by adjusing the magnetic field to one pro mille above and under the setting in 0.5 pro mille step-size. Five tune measurements in horizontal and vertical direction are then used to calculate the chromaticity in both transverse directions.

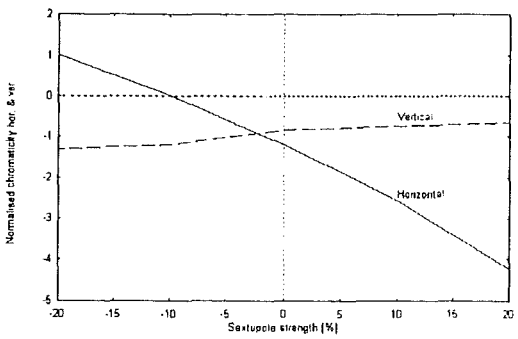

Fig. 3: Measured chromaticity as function of the sextupole strength of MXL4 at a momentum of 1250 MeV/c.

Here we see that the sextupole MXL4 changes the horizontal chromaticity from -4 to +1 before particles are lost and does not affect much the vertical chromaticity. The measured "natural" chromaticity is approximally -1.20 horizontally and -0.94 vertically, this is close to the calculated chromaticity. The same type of measurements have been done for all sextupoles. The chromaticity contributions (α_y) are shown in table 2 for all sextupole families. If we compare table 1 and 2 we see that for some sextupoles the agreement between calculation and measurement is good, while for others the difference is large.

sextupole	Horizontal (α_x)	Vertical (α_z)
MXL1	-1.108	0.127
MXL2	0.549	-0.578
MXL3	0.574	-0.348
MXL4	-1.141	0.154
MXL10	-0.063	0.192
MXL11	0.310	-0.282
MXL12	0.304	-0.220
MXL13	-0.049	0.189
MXL	0.590	-2.870
MXG	0.835	-0.633
MXS	-	-

Table 2: Measured chromaticity contributions of sextupoles. The values are normated on the sextupole strength of the individual families. For MXG the value is corrected to correspond to two sextupoles instead of one as in operation at this time.

For the calculation of the sextupole contribution, the dispersion function and the beta function were needed. The dispersion function can be measured by changing the magnetic field. The difference between measurement and calculation is minimal. The beta function is the other parameter which is used for the calculations. However, this can not be measured as easily. In the calculation of the beta function we see that this is a rapidly varying function with large amplitude variations. This may account for the poor agreement of some sextupoles with calculations. However, the sextupoles MXL3, MXL10, MXL11 MXL12, MXL13 and MXL are well described numerically.

Further investigations are in progress to determine the contributions of the individual magnets to chromaticity of the accelerator.

References

[1] S. Guiducci, Chromaticity, Proceedings CERN Accelerator School, CERN 91-04 (1991)

[2] J.-L. Laclare, Introduction to coherent instabilities, Ibid.

[3] H. Grote, F.Ch. Iselin, The MAD Program (Methodical Accelerator Design) Version 8.1, User's Reference Manuel, CERN/SL/90-13(AP) (revision 1)

First vertical beamsize measurements

L.H.A. Leunissen, D. Prasuhn, J. Bisplinghoff, R. Tölle

Introduction

The EDDA experiment is used for operation at TP2 in the COSY-ring. The experiment is designed to measure proton-proton elastic excitation function with high precision, utilising the internal beam incident on a CH_2 fiber target. Data collection is intended to proceed during synchrotron acceleration in a multi-pass technique. Elastic pp events are identified by means of kinematic coincidence. The electrons knocked out of the target are used for luminosity monitoring. An integral measurement of the secondary electron current is performed by means of PIN-diodes [1].

The EDDA fiber target can be used as a tool for beam diagnostics. As the horizontal target (for vertical beamsize measurements) is driven through the beam at flat top, the measured secondary electrons indicate whether the proton beam is colliding with the CH_2 fiber target or not. In figure 1, a typical measurement is shown. The target position in the beam (1) and the measured secondary electrons (2) are indicated in this figure. From the secondary electron curve, we can determine the vertical beamsize. For this, we take the half-width of the measured signal and see that the vertical beamsize is approximately 3.2 ±0.1 mm.

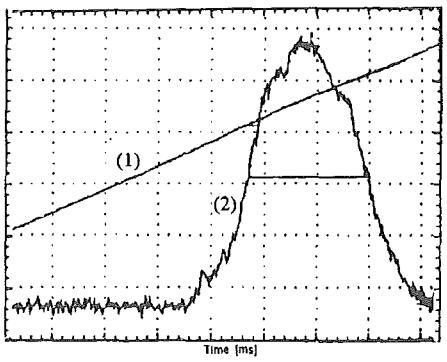

Fig. 1: Secondary electron current as function of time. Fiber target position (1), secondary electron current (2).

Sextupole induced beamsize change

For small non-linearities the accelerator behaves more or less like a linear element. A quantitative measure for this quasi-linear behaviour is the so-called smear. This quantity indicates how much the invariants of the linear machine are changed due to non-linear perturbations. As a result of this, the beamsize is changed due to the sextupoles. Calculations with the code SIXTRACK [2] show that the smear is dependent on the position of the beam in the sextupole and the strength of the sextupole, see figure 2.

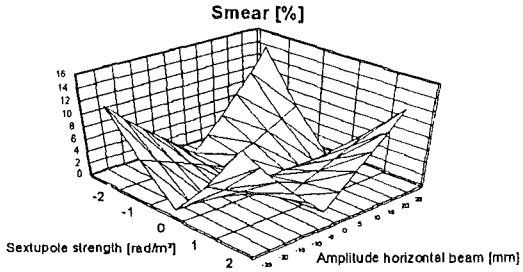

Fig. 2: Calculated smear as function of sextupole strength and horizontal position of the particle beam inside sextupole MXL1.

We see a minimum at the origin of the plot. This means that the sextupole contribution is smallest when the beam goes through the center of the sextupole and when the sextupole is turned off.

Measurements

First measurements have been done to determine the vertical width of the beam. Then a sextupole is used to change the beamsize. There were two experimental setups: first, the sextupoles were driven to their top value during acceleration. Secondly, they were driven to their top value in flat top. However, the difference between the two types of measurements is minimal. In figure 3, a measurement is shown where sextupole MXS (a family of 4 sextupoles) is used.

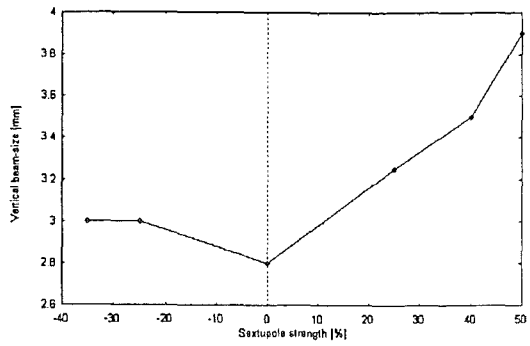

Fig. 3: Measured vertical beam-size as function of sextupole MXS.

The average beam position through the four sextupoles of MXS is approximately 5 mm. The minimum of the curve is at the point where the sextupole is off. In figure 4, we see that the minimum of the beamsize is not yet reached before the beam is lost due to the powered sextupole components. The horizontal beam position inside MXL11 is approximately 19 mm.

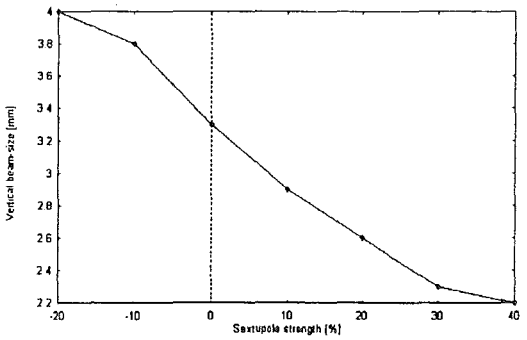

Fig. 4: Measured vertical beam-size as function of sextupole MXL11.

If we do the same measurements with MXL4, see figure 4, we see that the minimum is at 40%. Due to the dipole field component of the sextupole (typically about ± 0.4 mT), the closed orbit is shifted a few mm and as a result the beamsize becomes smaller.

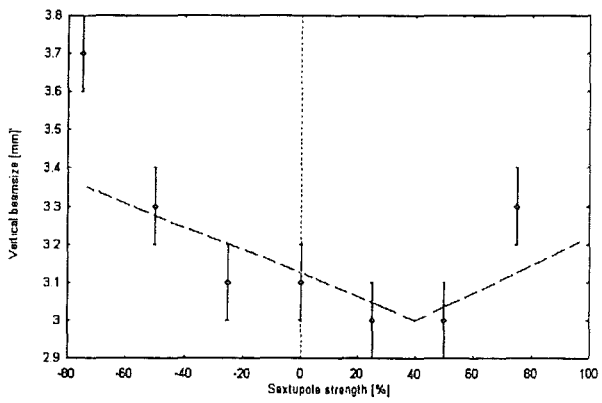

Fig. 5: Measured vertical beam-size as function of sextupole MXL4 indicated as dots with errorbars. The dashed line indicates numerical calculations with SIXTRACK.

In the same figure, the dashed line indicates the calculated beamsize. As initial conditions for the closed orbit distortion are taken: 13 mm horizontally and 2 mm vertically. This in agreement with the closed orbit measurement. The initial vertical beamsize is set to be 3 mm in the calculations.

Conclusions

The description of the beamsize is not yet accurate and it is difficult to determine the beam position inside the sextupole. Furthermore, the numerical calculations show a linear dependence of beamsize as function of sextupole strength.

The experimental setup will change for the next measurements. With the EDDA experiment it will be possible to measure the horizontal as well as the vertical beamsize. Furthermore, the closed orbit distortion can be minimised to eliminate the beam position from the measurements.

References

[1] Institut Für Kernphysik Annual Report 1993, First Events from EDDA at COSY, p.3 (1993)

[2] F. Schmidt, SIXTRACK, Version 1, Single particle tracking code treating transverse motion with synchrotron oscillations in a symplectic manner, CERN/SL/90-11(AP) (1990)

Improved Ramping-functions for COSY

A. Schnase, H. Schneider, M. Simon, H. Stockhorst

Introduction

The control-functions originally written in **smalltalk** [1] have been revisited and improved so as to include the experience gained during the last years of operation of COSY. The concept now allows a fast change of vital machine settings and also provides corrections for eddy-currents which became necessary after the internal target station COSY-11 was installed in 1995.

Improving the functions

Now the functions are calculated in a tree-structure based on the momentum-ramp that is defined by the actual experiment: The user sets the final energy and the "flat-top-time" to describe the momentum-ramp. The dipole-current is then derived from the momentum. This calculation first corrects for the eddy-currents in the COSY-beam-pipe that lowers the magnetic field. Then the saturation of the iron cores of the dipoles is compensated by driving the dipoles with a higher current. This relation for the dipoles was found by increasing the final energy step by step and measuring the closed orbit. The corrected current-ramp determines the driving-voltage for the dipole power converter. A similar procedure computes the different quadrupole-families.
The non-linear relation between momentum and frequency due to relativistic effects is represented with high resolution, e.g. with enough sample points.
With these ideas the final momentum was increased to 3.5 GeV/c on the 31-th August 95 - above the design-value of 3.3 GeV/c. We detected $2 \cdot 10^{10}$ protons. This is an improvement of accelerated particles by a factor of 10 compared to last year. The calculations now allow a change of final energy within about half an hour. Special conditions like extraction may still take longer.

Compensation of eddy-currents at experiment COSY-11

The vacuum-chamber of the experiment COSY-11 resides inside a modified COSY-dipole and produces eddy-currents due to the wall thickness of 12 mm. This influences the magnetic field that would be almost homogenous without vacuum-chamber. During a dynamic ramp the field in the beam-pipe lags due to the low-pass behaviour of the beam-pipe. Additionally, the shape of the field is modified so that a sextupole-component appears. Both effects are compensated for acceleration and deceleration. A backleg-winding corrects the magnetic field strength directly at the dipole. The sextupole mxg located nearby minimises the influence of the sextupole-component.

Calculation methods

All functions rely on sequences of real third-order polynomials

$$y = a_3 \cdot t^3 + a_2 \cdot t^2 + a_1 \cdot t + a_0 \,. \qquad (1)$$

These functions can be directly used for linear relations between functions up to third order. Functions of higher order or non-linear relations need special care. First we have found out that COSY does not reach the specified "flat-top"-momentum. An **awk** script **pcheck** corrects the slope which is entered into the cycle description:

$$\text{slope} = (p_{max} - p_{inj}) / t_r \qquad \text{with} \qquad (2)$$
$$t_r = t_{v1} / 2 + t_{lin} + t_{v2} / 2 \,. \qquad (3)$$

The time t_r is the equivalent time of a linear ramp without quadratic transitions from injection momentum p_{inj} to final momentum p_{max}. The values t_{v1} and t_{v2} describe the time in ms given to the quadratic parts of the ramp and t_{lin} is the linear ramp time. Another script **ctx** calculates the functions for the rf-system and the dipol settings. It checks, if injection momentum and start-frequency fit together (using values defined in the **tool** from R. Tölle [2]) and calls other modular scripts in a tree structure based on the momentum:

momentum.fct	→ momentum.fgen **mf2fgen**	
momentum.fgen	→ momenta.fgen **multi**	
momenta.fgen	→ freq.fgen **m2fx**	→ phas.fgen **f2p**
momenta.fgen	→ tmdbestrom.fgen **m2dx**	→ tmdbespng.fgen **mi2u**
momenta.fgen	→ mqu*strom.fgen **m2qu**	→ mqu*spng.fgen **mqu2u**
momenta.fgen	→ mqt*strom.fgen **m2qt**	→ mqt*spng.fgen **mqt2u**
momentum.fgen	→ bw08.fgen **blw**	
momentum.fgen	→ mxgstrom.fgen **mxg**	
momentum.fgen	→ volt.fgen **hf_volt**	

The script **mf2fgen** interprets a description of a ramp like

```
flat:80:269.24
trans:200:1.1502
ramp:331:1.1502
...
```

and transforms it to a coefficient-list for a function generator

```
80:269.24:0:0:0
200:269.24:0:0.0028755:0
331:384.26:1.1502:0:0
...
end
```

assuming a function generator for the momentum exists. The script **multi** takes momentum.fgen, splits the polynomials into smaller ones without loosing information or precision and writes the result to momenta.fgen. This is essential, because now one can adjust the precision of a non-linear transformation basing on the file momenta.fgen by increasing the sample rate. The script **m2fx** performs such a non-linear transformation to compute the frequency freq.fgen for the rf-system as a function of momenta.fgen.
The polynomials for the momentum

$$p = a_3 \cdot t^3 + a_2 \cdot t^2 + a_1 \cdot t + a_0 \qquad (4)$$

and its derivative

$$dp/dt = 3 \cdot a_3 \cdot t^2 + 2 \cdot a_2 \cdot t + a_1 \qquad (5)$$

define the frequency (normalised to ß)

$$ß = b_3 \cdot t^3 + b_2 \cdot t^2 + b_1 \cdot t + b_0 \qquad (6)$$

and the frequency derivative

$$dß/dt = 3 \cdot b_3 \cdot t^2 + 2 \cdot b_2 \cdot t + b_1 \,. \qquad (7)$$

The relation between p and ß

$$ß = (1 + (E_p / p \cdot c)^2)^{-1/2} \qquad (8)$$

has to be differentiated

$$ß' = (1 + (E_p / pc)^2)^{-3/2} \cdot (Ep/pc)^2 / (pc) \cdot d(pc)/dt \,. \qquad (9)$$

The proton restenergy is given by $E_p = m_p \cdot c^2 =$ 938.272310 MeV (in the **tool**). The momentum and its derivatives are taken at the begin of the interval pa = p(0), dpa = p'(0), dpa2 = p''(0) and at the end of the interval t_{int} : pe = p(t_{int}), dpe = p'(t_{int}), dpe2 = p''(t_{int}). A time-constant t_{delay} in ms can compensate eddy-currents:

$$pa = pa - t_{delay} \cdot dpa \quad dpa = dpa - t_{delay} \cdot dpa2$$
$$pe = pe - t_{delay} \cdot dpe \quad dpe = dpe - t_{delay} \cdot dpe2 \,. \quad (10)$$

Then ß(t=0), ß'(t=0), ß(t=t_{int}) and ß'(t=t_{int}) were calculated. The coefficients for the frequency polynomial match the correct values at the interval boundaries to obtain a smooth connection to the adjacent intervals

$$b_0 = ß(0) \qquad b_1 = ß'(0)$$
$$b_2 = 3 \cdot (ß(t_{int}) - b0) / t_{int}^2 - (2 \cdot b_1 + ß'(t_{int})) / t_{int}$$
$$b_3 = 2 \cdot (b_0 - ß(t_{int})) / t_{int}^3 + (b_1 + ß'(t_{int})) / t_{int}^2 \,. \quad (11)$$

The frequency is scaled with the value for $p \rightarrow \infty$: $f_u = c/l = 299792458m/s / 183.473m = 1633986.788$ Hz and the clock representation $freq_{scale} = f/Hz \cdot 2^{33} / 1.5 \cdot 10^9$.

The script **f2p** takes the frequency curve freq.fgen and computes phas.fgen for the rf-system. This compensates the transfer-functions of the analog signal paths and allows a phase-measurement between beam and acceleration gap. Alternatively the script **f2r** computes a phase curve to control the phase between beam and acceleration gap. This script implements the non-linear transformation of

$$\phi = \arcsin (k_u / (1 - ß^2)^{1.5} \cdot df/dt \quad \text{with} \quad (12)$$
$$k_u = Ep / U \cdot f_u^{-2} \text{ with U in Volts}$$

and its derivative ϕ'. It strongly depends on a frequency function with enough sample points.

The script **m2dx** defines the relation between momentum and dipole-current tmdbestrom.fgen. First the momentum and its derivatives are determined like eqn. 4, 5 and then an eddy-current-compensation like eq. 10 is applied. Measurements show that the relation in the lower quadratic region can be expressed by a stepwise linear transformation. A linear region follows. Above 2100 MeV/c this script assumes, that the magnets drive into saturation, where the magnetic field is a function of the square-root of the momentum. This relation covers a range from 600 MeV/c to 2750 MeV/c but fails for a momentum higher than 3000 MeV/c. This script was then renamed to **m2wx** and the new version **m2dx** describes the saturation curve of the dipoles as a table with non-equally spaced linear segments with different slope.

269 - 275 - 290 - 325 - 355 MeV/c: quadratic region
355 - 500 MeV/c: normalise value after quadratic region
500-2100 MeV/c: linear region
> 2100 MeV/c: saturation in 100 MeV/c steps
3700-5000 MeV/c: preventing overcurrent

This improved method covers the full momentum range from 600 MeV/c to 3500 MeV/c.
The script **mi2u** determines the voltage tmdbespng.fgen for the dipole supply. It evaluates the coefficients $a_0 \ldots a_3$ of functions and derivatives like eq. 4, 5 to generate the voltage polynomial with coefficients $b_0 \ldots b_3$. The initial current ia and its derivatives dia and dia2 result from ia = a_0, dia = a_1 and dia2 = $2 \cdot a_2$. The current and the derivatives at the end of the interval are ie, die and die2. For a current ia below saturation i_s, the initial voltage and the derivative are computed with

$$b_0 = scale_g \cdot (R \cdot ia + L_0 \cdot dia)$$
$$b_1 = scale_g \cdot (R \cdot dia + L_0 \cdot dia2) \,. \quad (13)$$

In the non-linear region ia > i_s, the inductance L depends on the current:

$$b_0 = scale_g \cdot (R \cdot ia + (lc + ll \cdot ia) \cdot dia)$$
$$b_1 = scale_g \cdot (R \cdot dia + (lc + ll \cdot ia) \cdot dia2 + ll \cdot dia^2 \,. \quad (14)$$

The same cases are recognised for the end of the interval

ie < is: $u_e = scale_g \cdot (R \cdot ie + L_0 \cdot die)$
$du_e = scale_g \cdot (R \cdot die + L_0 \cdot die2)$

ie ≥ is: $u_e = scale_g \cdot (R \cdot ie + (lc + ll \cdot ie) \cdot die)$
$du_e = scale_g \cdot (R \cdot die + (lc + ll \cdot ie) \cdot die2 + ll \cdot die^2$. (16)

Then the polynomial is matched like in eq. 11

$$b_2 = 3 \cdot (u_e - b_0) / t^2 - (2 \cdot b_1 + du_e) / t$$
$$b_3 = 2 \cdot (b_0 - u_e) / t^3 + (b_1 + du_e) / t^2 \,. \quad (17)$$

The same methods work for the quadrupoles. The script **m2qt** calculates the currents mqt*strom.fgen for the telescope-quads mqt1...8. The script **m2qu** does this for the quads mqu1...6 in the arcs and produces mqu*strom.fgen. The voltages mqt*spng.fgen and mqu*spng.fgen are calculated with **mqt2u** and **mqu2u** respectively.
The functions **blw** and **mxg** simply scale the derivative of the momentum for the backleg-winding bw08.fgen and the sextupole mxgstrom.fgen.
These ideas help to get the reciprocal function of the momentum, which is necessary for two steerers of the electron-cooler: col-y.fgen and gun-y.fgen. The script **ctc** collects the parameters and calls the routine **m2c** which satisfies, that the initial current for the steerer at injection-momentum $i(p_{inj})$ and the current at infinite momentum $i_{top} = i(p \rightarrow \infty)$ are connected with a smooth curve

$$i(p) = (i(p_{inj}) - i_{top}) \cdot (p_{inj} / p) + i_{top} \,. \quad (18)$$

The resulting functions described in this article can be viewed in the directory ~/ring/newpoco with **rampview**. Alternatively the script **lade** <filename.fgen> converts a function-generator file to a time function in ms-steps.

Function generators

After the calculations have been corrected, we looked at the function generators itself. With a time interval analyser connected to the rf-synthesizer and a digital memory circuit with MELcards [3] we measured the differences between the desired frequency ramp and the real frequency over time.

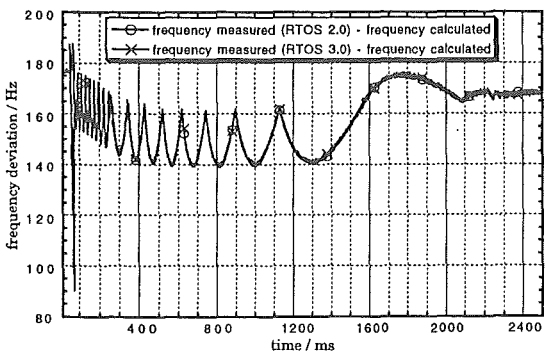

Fig. 1: Variation between expected and measured frequency

We found an interesting time structure due to interpolation (fig. 1). The "dip" in the beginning depends on the software-version in the target (fig. 2) and the "setup-string". To prove that these differences belong to the function generators and not to the synthesizer, we build a function generator based on memory-cards [3]. It seems that the deviations due to interpolation in the function generator can be tolerated for "slow" devices like magnets with their power-converters, because low-pass behaviour cancels out most of the deviations. This is not true for the rf-synthe-

sizer, because this device operates on an internal time scale faster than 1 µs. So we build a prototype of a compatible function generator based on a DSP that computes the ramps in real-time without interpolation [3].

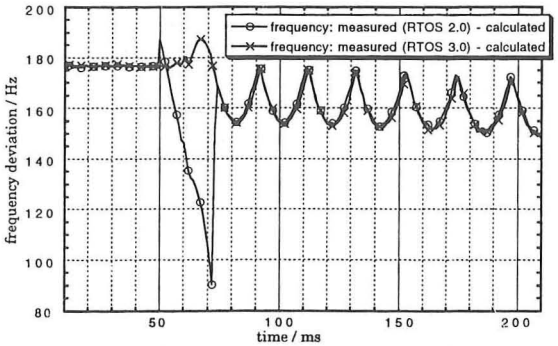

Fig. 2: Zoom of fig. 1 to show the initial "dip"

Adiabatic trapping

Measurements show that the life-time of the beam at injection energy depends on the rf-amplitude. So we tried different procedures for the amplitude as a function of time. With a constant amplitude, we find a short life-time without acceleration and a small number of particles in "flat-top". The script **hf_volt** produces a voltage curve that increases from an initial value during the first quadratic region to a final value, which is reduced after the beam has reached "flat-top". This reduction may go down to zero to switch the rf off in "flat-top". At the end of the flat-top-time, the amplitude rises again to capture the beam for deceleration. We also tried a quadratic increase of the amplitude for "real" adiabatic trapping, but it seems that the improvements compared to a linear increase during the quadratic part of the momentum ramp depends more on the optics.

New Graphical User Interface (GUI)

The next step was to give the user a graphical front-end to work with these methods. A simple TCL-front-end allowed the operators to calculate ramps for the dynamic devices. The parameters describing the ramps have to be entered in the **smalltalk**-GUI, however. This situation relies on temporary files which were only updated when the user presses specific buttons. Moreover this is difficult for the user. A new GUI for these functions has been specified and realised by co-operation of the rf-group, the magnet-group and the control-group. The result shown in figs. 3...6 is a GUI written in TCL that interfaces to modified **awk** scripts described before. It is activated by typing "**energie &**" in a shell. Figure 3 shows the actual ramping state and allows to select a window (fig. 4) which defines the main ramping parameters, and another window to select which functions have to be calculated (fig. 5) or modified. The current ramp is displayed on-line. The behaviour in flat-top can be modified for every dynamic device or every group of dynamic devices with a flat-top editor shown in fig. 6. The result is a ramp with an asymmetric jump.

Fig. 3: The starting point for calculations

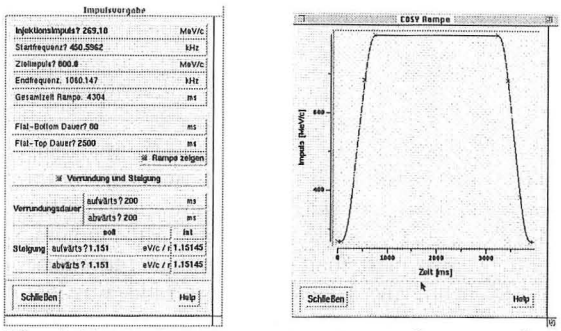

Fig. 4: Enter new ramp parameters and you get the result

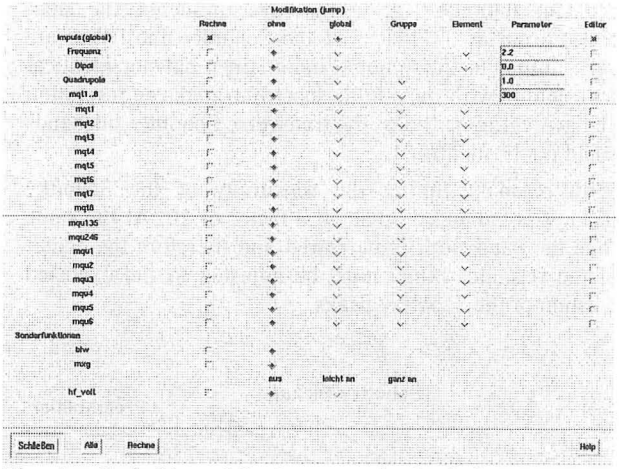

Fig. 5: Switchboard for jumps and calculations

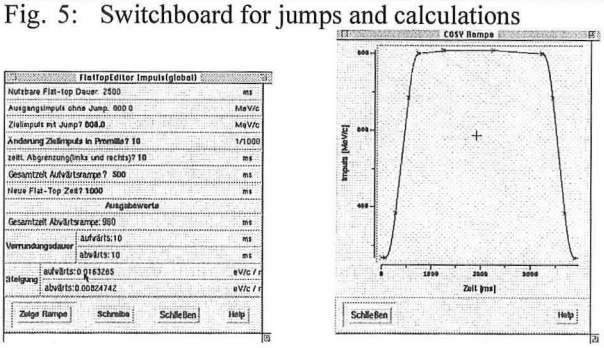

Fig. 6: Editor for jumps in flat-top and the resulting ramp

There are several parameters to play with. First the global momentum function can be modified. Every device can be calculated from the normal ramp or the modified global momentum ramp. There are groups for all quadrupoles, for the telescope quadrupoles mqt1...8, for the defocusing quads mqu1-3-5 and for the focusing quads mqu2-4-6. These modifications ease the job of measuring parameters like chromaticity or orbit and allow to specify tune shifts necessary for resonant extraction. Functions for blw, mxg (COSY-11) and rf-amplitude complete the picture.

Next steps: Modifying the working point

The working point (Q_H; Q_V) of COSY has been measured as a function of time during acceleration. The beam-loss in the first quadratic part of the momentum ramp confirm that the working point approaches a resonance. An improved calculation of quadrupole-ramps will correct this soon.

References

[1] N. Bongers et. al: "Function Generation and Automatic Resynchronisation for the Dynamic Components of COSY", IKP Annual Report 1993

[2] R. Tölle et. al: "Numerical Models for COSY", this report

[3] F.-J. Etzkorn et. al: "Status and Development of RF-Systems at COSY", this report

First Transverse Schottky-Noise Spectra with Resonant Schottky-Pickups

J. Bojowald, J. Dietrich and I. Mohos

Schottky-Noise Spectra, i. e. spectra of the beam signals measured with coasting beam and without beam excitation, could be performed until now only in the longitudinal case. In transverse measurements the monitor signals are lower by more than one magnitude (difference signals) and hence the signal to noise ratio was not sufficient enough. Even during investigations at the expected parts of the frequency spectrum (with resonant beam excitation, e. g. in tune-measurements, the sidebands occur at the places of the Schottky-lines; they are very similar to the Schottky-noise lines but not identical with them) with very high spectrum analyzer resolution and avareging methods, the transverse Schottky sidebands could not be identified.

With resonant tuning the sensitivity of the Schottky pickups is enhanced by about a factor of 20. At the same time the bandwidth is narrowed and therefore the center of the resonant range must be adjusted to the expected position of the Schottky peaks.

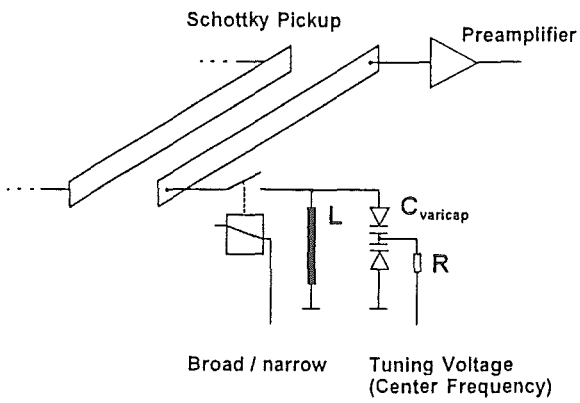

Fig. 1: Resonant tuning electronics for narrow-band measurements with the Schottky pickups; electronics for one electrode shown only.

The resonant tuning electronics is shown in fig.1. It must be installed identically for both electrodes of the pickup. The tuning is carried out by varying the capacity of the capacitance diodes with the required voltage applied. The tuning range (i. e. for the center of the resonant range) is 9 - 11 MHz, the bandwidth (3 dB) is about 100 kHz. The resonant tuning electronics can be switched off by relay contacts for use of the Schottky-pickups in BTF- or tune-measurements, where the signal to noise ratio is high due to the resonant beam excitation and the pickups can be used in broad band mode, so a frequency dependence of the pickup-transfer characteristic must not be taken into account. Since the electrodes are terminated with high impedance, in addition a further relay switch with 50 Ω-termination will be provided in order to avoid resonant high frequency modes, which e. g. may cause problems in stochastic cooling of the beam.

In case of no resonant tuning only the longitudinal lines at frequencies $f_n = n \cdot f_o$ (n = harmonic number, f_o = revolution frequency) are indicated in the transverse Schottky spectra; the transverse lines, which are to be expected as sidebands at frequencies $f_n^{\pm} = (n \pm q) \cdot f_o$ with q = fractional part of the Q-value (tune), are not visible. With resonant tuning applied even the transverse peaks are enhanced by about 20 dB over the noise level. Fig. 2 shows the region of the sidebands in the spectrum between the 23. and 24. harmonics of the revolution frequency f_o. The peaks are clearly marked and allow

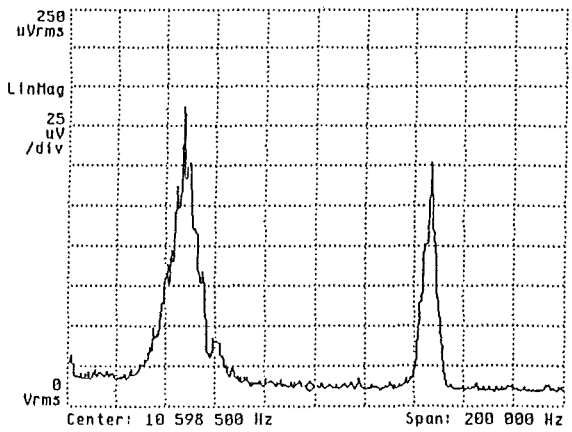

Fig. 2: Transverse Schottky spectrum measured with resonant tuning of the pickup. The region of the spectrum with the two sidebands between the 23. and 24. longitudinal harmonic lines is shown; eight spectra were averaged.

detailed analysis. For instance, the widths of the upper and lower sidebands are different by about a factor of 2, which is caused by a high chromaticity existing at the presently adjusted optics of COSY. The widths of the sidebands in the transverse Schottky spectra are given by two terms resulting from the spread Δf_o of the revolution frequency caused by the momentum distribution and from the tuneshift Δq caused by the betatron frequency distribution, which intrinsically also is due to the momentum distribution of the particles. If space charge and non-linear effects can be neglected the widths are given by [1]

$$\Delta f_n^{\pm} = (n \pm q) \cdot \Delta f_o \pm f_o \cdot \Delta q.$$

The + and −-sign, respectively, belongs to the upper and lower sideband. The width $\Delta f_o = \Delta f_n / n$ of the frequency-distribution can be taken from the width Δf_n of the n-th longitudinal line. The tuneshift Δq is related to the relative momentum distribution $\Delta p/p$ by the definition $\Delta q/Q = \Delta Q/Q = \xi \cdot \Delta p/p$, with ξ the chromaticity. The widths of the two sidebands are not equal. By comparing them, Δq can be determined and from this ξ; the Q-value and the momentum spread can be measured separately. In this case follows $\xi \approx -10$.

Reference:

[1] D. Boussard, Schottky Noise and Beam Transfer Diagnostics, CAS Oxford 1985, CERN-Rep. 87-03

Transverse Measurements with Kicker Excitation

J. Dietrich, J. Bojowald, I. Mohos

The purpose of the fast diagnostic kicker magnet is to excite the beam particles to collective transverse oscillations, which run with betatron frequency and, e.g., are used for the determination of the tune or for phase space investigations. By means of the kicker magnet the beam bunch is short-time (0.75 - 2 μs width; rise- and falltime <1μs) deflected and the resulting beam bunch position oscillations are measured using the beam position monitors (BPMs). The kicker excitation is synchronized with respect to the COSY-rf signal and can be adjusted in time by programmable delay, so a unique deflection of the total bunch can be performed (bunch- synchroneous excitation) [1]. The short-time kicker-deflection is appropriate to measure the tune also during the acceleration ramp, in contrast to the time consuming resonant excitation by the stripline unit used during steady-state conditions (e.g. in flat top) for tune measurements. The installed kicker magnet can be used for horizontal beam deflection only.

From the BPM-electrode signals the amplified and filtered Σ- and Δ-signals are deduced and digitized by flash-ADCs (20 MHz clock-rate); the results are stored in FIFO-memories [2]. In this way the data of 200 (with 4K FIFO-width) or of 3200 (with 64K) successive turns are recorded. Fig. 1 shows the display of a typical Δ-signal dataset. The oscillation is clearly seen. From the Δ- and Σ-data the beam centroid positions at each turn are extracted.

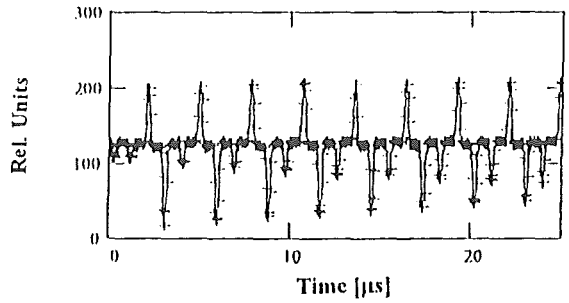

Fig. 1: Δ-signal of a BPM, sampled with 20 MHz clock-rate.

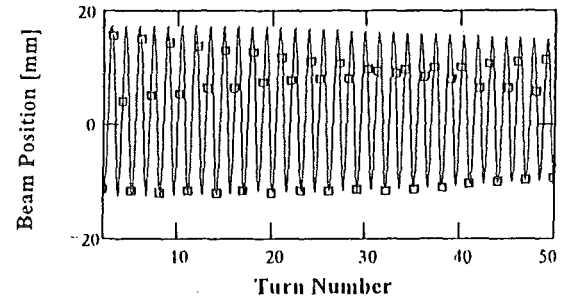

Fig. 2: Forced, damped beam centroid oscillation and fitted curve (see text)

In fig. 2 the forced damped oscillations around a small closed orbit value are shown. The open squares are the measured values from turn to turn. The solid line is a fit for a damped oscillation assuming a gaussian tune distribution [3]. The measured "damping" of the bunch centroid oscillation is caused by vanishing of the collective motion of the particles within the bunch due to their finite betatron frequency spread.

The fitting curve for the damped beam centroid oscillation can be described by the following analytical expression [3]

$$x_n = A(\epsilon, \beta(s)) \cdot e^{-\frac{(n\pi \cdot \delta Q)^2}{2}} \cdot \cos(2\pi(nQ + \varphi)) + R_o$$

with x_n = beam centroid position at the n-th turn, $A = (\varepsilon \cdot \beta(s))^{1/2}$ = amplitude term with ε = emittance of the kicked beam and $\beta(s)$ = beta function, Q = tune value, δQ = tune spread, φ = betatron phase and R_0 = closed orbit value. By least squares fitting of the measured position data to this function for each BPM, accurate results for the key-parameters involved in this expression can be obtained. Fig. 3 shows the amplitude values at each BPM position and the comparison to the square root of the β-function values obtained from MAD-calculations. Fig. 4 shows the emittance of the kicked beam deduced from the data of all BPMs and calculated using the MAD β-function values. The variance of the resulting emittance values is mainly due to the uncertainties in the calculated β-function values.

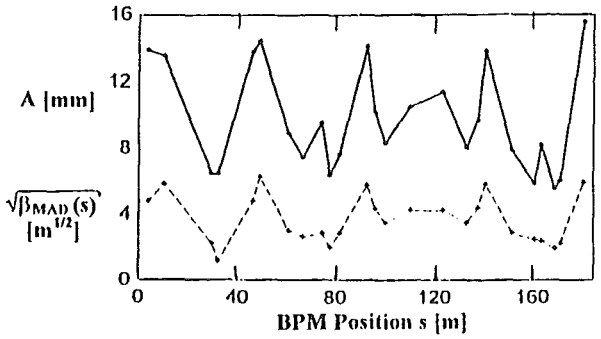

Fig. 3: Amplitude values at the BPM-positions in comparison to the square root of the β-function values from MAD calculations

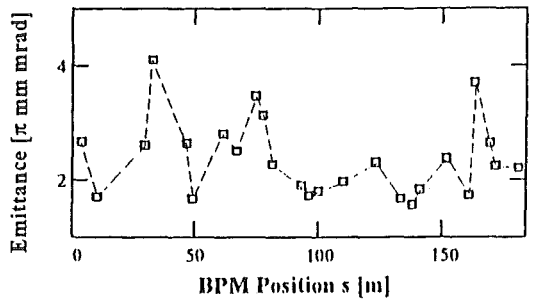

Fig. 4: Emittance of the kicked beam deduced from the amplitude term with β-function values from MAD-calculations.

References:

[1] A. Schnase and H. Schneider, private communication
[2] J. Biri et al., Beam Position Monitor Electronics at the Cooler Synchrotron COSY-Juelich, Real Time '93 Conference, Vancouver, 1993 and IEEE Trans. Nucl. Sci. 41 (1994) 221
[3] C. M. Warsop, Low Intensity and Injection Studies on the ISIS Synchrotron, EPAC'94, London, p. 1722

Development of Beam Extraction

H. Stockhorst, A. Schnase

Abstract

The circulating proton beam can be extracted by the conventional resonant extraction mechanism as well as with the method of stochastic extraction. In several machine runs the extraction mechanisms were studied at 800 MeV/c, 1.8 GeV/c and 3.2 GeV/c. A new digital noise generator developed at COSY [1] was used for stochastic extraction. At present an extraction efficiency of nearly 30% is realized. Spill times of more than 30 s were obtained. Results from 800 MeV/c machine runs will be presented.

Introduction

Conventional extraction at COSY will be made by creating a third integer resonant condition by sextupole excitation and sweeping the beam as a whole through the resonance in shifting the horizontal tune of the machine. In this extraction scheme the beam can be considered as a rigid body from which single slides, corresponding to certain momenta, are consecutively taken. Consequently, the momentum of the extracted particles will vary with time. On contrary, the idea behind ultra slow extraction (USE) [2] is to move the beam across the resonance by a diffusion process. Firstly, precisely shaped narrow band noise centred on a harmonic of the revolution frequency will be used to transform the initially Gaussian-like distributed beam into a rectangularly shaped distribution [3]. Secondly, to drive the beam towards the resonance, band limited noise, permanently covering the extraction resonance, will be slowly moved across the previously shaped beam distribution. This causes the particles to undertake a random walk within the noise bandwidth thereby filling up any void in longitudinal phase space. Particles reaching the resonance will be extracted from the circulating beam. By properly forming the extraction noise spectra, a diffusion process can be induced which significantly reduces discontinuities in the spill rate, and important as well, will make the average momentum of the extracted particles nearly constant in time with considerably abridged momentum spread. In addition, the speed at which the noise is swept across the shaped beam distribution will control the coarse spill rate of the extracted particles. In a first step experiments were carried out to gain insight into the resonant extraction. In a second step extraction induced by noise (stochastic extraction) was examined. Finally, resonant extraction supported by noise induced diffusion was tested.

Resonant extraction

At COSY conventional slow extraction extraction is done by creating a resonant condition in transverse phase space through sextupole excitation. For this, the beam is accelerated to the desired flat-top energy. After debunching an orbit bump is introduced in order to move the beam closer to the electrostatic septum. At present bumps of the order of 40 mm are used. The horizontal tune is then moved from below close to 11/3. Generally, at least three sextupole groups are necessary for resonance extraction. One group located in the cooler telescopes is used to excite the resonance the other two placed in the arcs of COSY are used for chromaticity correction in the horizontal and vertical plane. The latter condition is necessary to match the extracted beam horizontally to the extraction beam line. The beam is then extracted by sweeping the horizontal tune linearly through the resonance. An example for extraction at 800 MeV/c is shown in figure 1. Time scale is 5 s/div. In this case a spill time of nearly 30 s was achieved. The extracted beam has a symmetric distribution as is expected from the linear increase in horizontal tune. The extraction efficiency is about 30%.

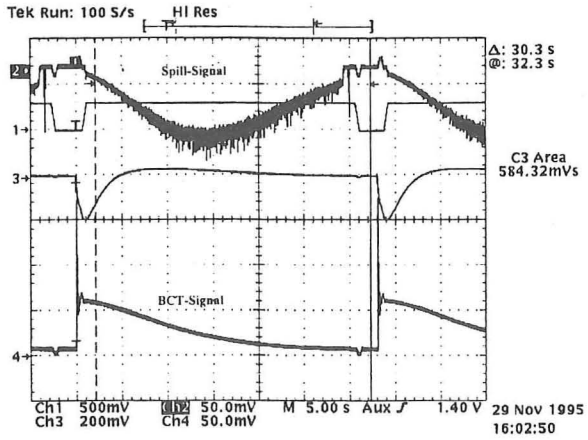

Fig. 1: Extracted beam (Spill-Signal) at 800 MeV/c and beam current transformer signal (BCT-Signal)

The beam distribution during extraction is shown in figure 2 (bright triangle). The longitudinal spectrogram shows two cycles of the machine.

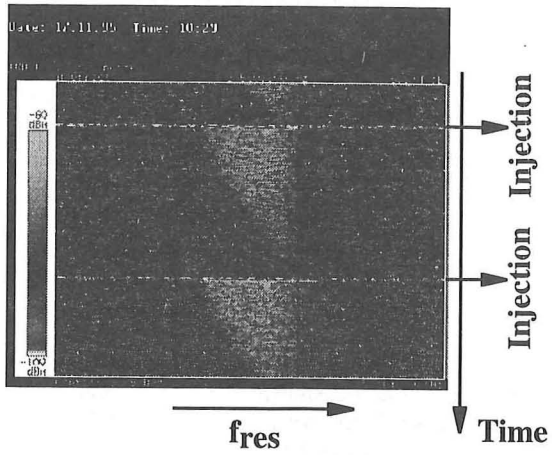

Fig. 2: Beam distribution during extraction. The linear increase of the horizontal tune during extraction creates the triangularly shaped pattern.

At flat-top extraction begins and the beam distribution is peeled off from left leading to the sharp edge on the right side of the distribution. The triangular shape results from the linear increase of the horizontal tune. As was pointed out, in this extraction scheme the beam can be considered as a rigid body from which single slides, here from left to right, corresponding to certain momenta, are consecutively extracted.

Stochastic extraction

On contrary to conventional resonance extraction using a linear tune ramp the stochastic extraction mechanism makes use of a diffusion process. A new digital rf-noise generator [1] has been used to apply band-limited white noise of constant spectral amplitude around to a harmonic of the beam. This is similar to beam shaping [3] studied in earlier machine runs. However, the bandwidth was now chosen to cover permanently the resonance. From theory [2] it is then known that the particles will diffuse into the resonance. As expected, both, the circulating beam and the spill signal decrease exponentially. A flat spill signal can be achieved if the noise power is increased during extraction as shown in figure 3. The spill time is about 18 s in this case.

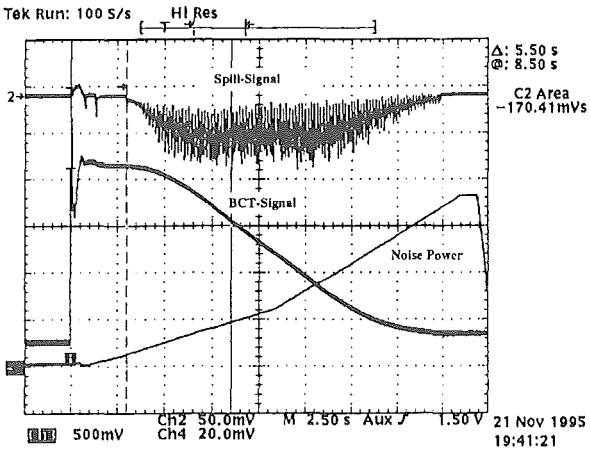

Fig. 3: During extraction the noise power is increased to flatten the spill signal.

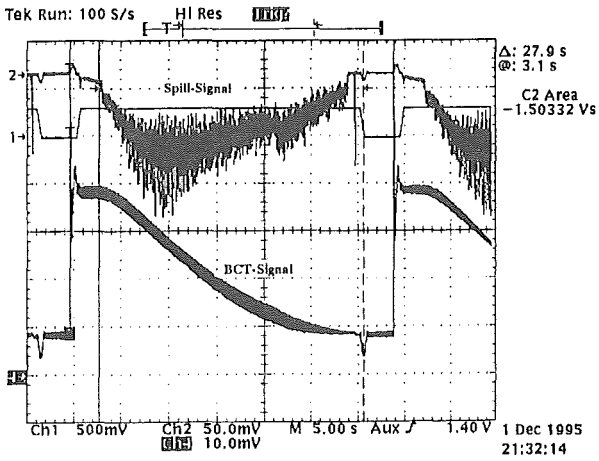

Fig. 4: BCT-Signal and spill signal from resonant extraction plus noise

The maximum extraction time is limited by power supply ripple. Moreover, it creates an unwanted modulation of the spill rate. In order to reduce the latter effect a resonant extraction was set up superimposed with band-limited noise applied around a revolution harmonic. During extraction the noise permanently covered the resonance. The result is depicted in figure 4. Figure 5 shows the FFT-magnitude of the spill signal in the frequency range up to 2 kHz with and without additional noise. Without noise the spectrum shows up lines being multiples of 50 Hz, figure 5a. Application of noise significantly suppresses these lines, figure 5b.

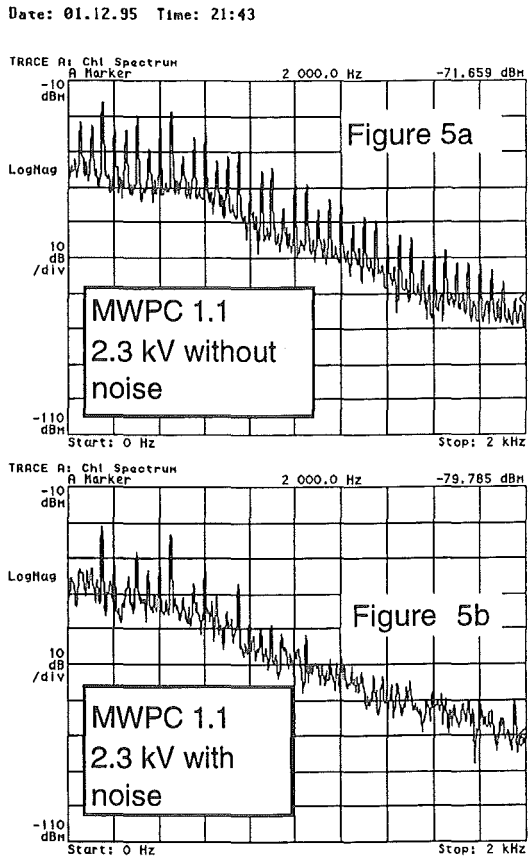

Fig. 5: FFT of the spill signal with and without additional noise applied

Conclusions

The extraction efficiency could be increased to nearly 30% with extraction times of up to 30 s. The extraction time is only limited by power supply ripple. The method of stochastic extraction was applied. This method helped to reduce the power supply ripple significantly. In further machine runs the ultra slow extraction will be brought into operation and the extraction efficiency has to be enlarged. A spill signal feedback will be studied to flatten the spill rate during conventional resonant extraction.

References

[1] G. Heinrichs et al., "A Narrow-Band Digital RF-Noise Generator", EPAC 94, London, 1994

[2] S. van der Meer, "Stochastic Extraction, A Low-Ripple Version of Resonant Extraction", CERN/PS/AA 78-6,1978

[3] H. Stockhorst et al., "Beam Shaping Using a New Digital Noise Generator", PAC 95, Dallas, Texas, 1995

Phase space boundary studies at the electrostatic septum of COSY

J. Dietrich

For the resonant extraction process at COSY, the horizontal tune is moved towards a third order resonance and the particles are shifted towards the electrostatic septum by a local closed orbit bump. By exciting one or more sextupoles, in addition a phase space boundary (separatrix) with a triangular shape characteristic of the resonance is created. The correct orientation of this separatrix at the location of the electrostatic septum is essential for getting a good extraction efficiency. For this purpose measurements of phase space conditions at the position of the electrostatic septum have been performed. The experimental procedure is described in more detail in [1]. The beam-centroid displacement (the betatron motion) after kicker excitation with different kick strength was measured turn-by-turn using two BPMs located near the electrostatic septum with a phase advance much different from $n \cdot \pi$.

Figure 1 shows transverse phase space plots (first hundred turns) at operation near the third order resonance for different kick strengths (deflection angles). Different representations of the results at the same deflection angle in figure 1 are arranged in the colums. In the lines the results for four different deflection angles are represented in the same manner. Figure 1a shows the horizontal position of the beam centroid at the beam position monitor BPM24 (just in front of the electrostatic septum) versus the position at BPM21 located 18.7 m before the electrostatic septum from turn to turn. In figure 1b the with MAD calculated phase ellipse and the beam centroid motion in the phase space at BPM24 are compared. The horizontal axis corresponds to a normalized beam position $x_{norm}= (x_n-R_o)/A(\varepsilon,\beta)$ with x_n = beam centroid position at the n-th turn, $A(\varepsilon,\beta)$ = amplitude term with ε = emittance of the kicked beam and β = beta function and R_o = closed orbit value [1], the vertical axis to the normalized angle, calculated from the normalized beam centroid positions at the two BPMs and the transfer matrix. From the normalized angle and beam centroid positions the conjugate variable of the displacement x_{norm}, namely $p_{xnorm}=\alpha x_{norm}+\beta x'_{norm}$ is calculated, whereby p_{xnorm} is a function of the α- and β-function values at the BPMs. In figure 1c the same data are plotted for the conjugate variable p_{xnorm} at the vertical axis versus the normalized beam centroid position at the horizontal axis for the first hundred turns. Figure 1d represents the same results starting with turn number 40 up to 60. The straight lines connect the measured data in turn.

With increasing angular deflection the horizontal tune changes to higher values. From figure 1 the width of the resonance curve can be estimated to about $\Delta Q = 0.01$. This explains why the results of the large deflection angle of 4.5 mrad are looking almost the same as the results with small deflection angle of 0.75 mrad. Please note that in the case of the large deflection angle the tune changes by $\Delta Q = 0.02$ and therefore shifts the particles outside of the resonance region.

A minimum value of the tune spread was observed when the tune is close to the third order resonance (plot with Q_x = 3.669). This is in contrast to the fact, that the betatron motion decoherent time is inversely proportional to the kicked amplitude [2]. In the case of a seventh order resonance an increasing tune spread by increasing kick-amplitude was found.

The measured oscillating amplitudes decrease due to Landau damping from turn to turn. If the Landau damping is numerically taken out for all four cases the so corrected amplitudes fill a circle with increasing radius as expected. In addition the studies of motion of the beam centroid after collectively perturbing the beam by a fast kicker and using the data of all BPMs, yield important information about the lattice [3]. This procedure is also useful in the nonlinear beam dynamics study. Due to the non-negligible beam size, the interpretation of the experimental results is difficult, especially if the beam center is displaced nearby the separatrix. Parts of the particles are stable here, parts are unstable. The degree to which the beam centroid motion accurately represents the motion of a single particle depends on the emittance of the beam; the smaller the emittance of the beam, the more accurate is its representation of single particle motion. Further limitations are the decoherence of the betatron motion and the crossing of uncontrollable nonlinear resonances. Work is going on including experiments with cooled beams.

References

[1] J.Dietrich et al., Transverse measurements with kicker excitation, this annual report

[2] S.Y.Lee, Nonlinear Problems in Accelerator Physics, Proc.of the Int. Workshop, Berlin (1992), p.249

[3] J.Bojowald, J.Dietrich, H.Labus, R.Maier,I.Mohos, Diagnostic tools for the resonant extraction at COSY-Jülich, DIPAC (1995),DESY M- 95 07, p. 87

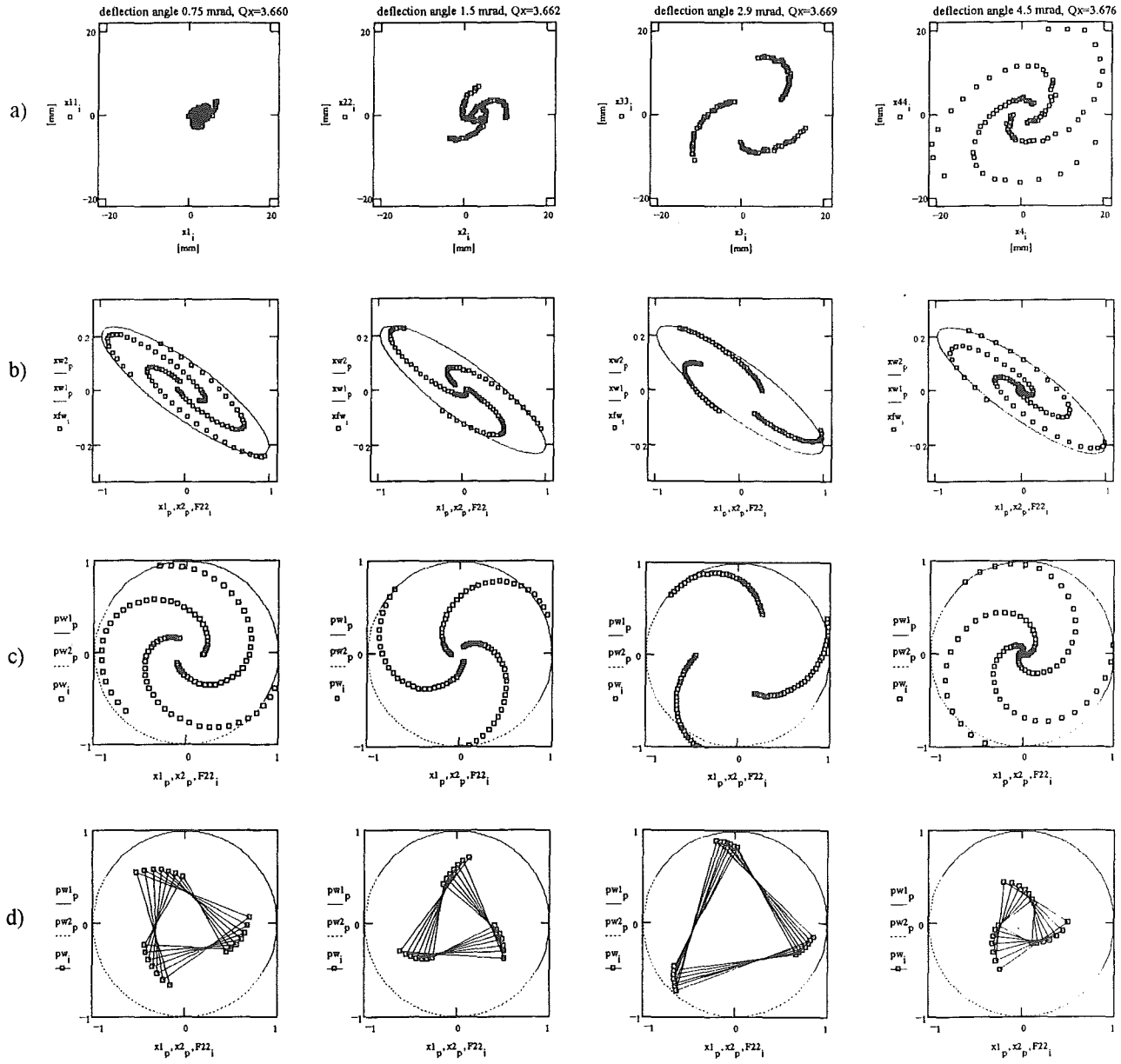

Fig. 1: Transverse phase space plots for four different kick strengths resulting in the given deflection angles. Proton momentum is 800 MeV/c (explanation in the text).

Tools for Online Evaluation of Phase Space Measurements

R. Wagner and J. Dietrich

Whenever a tracking measurement is initialized in the course of transverse phase space studies as described in preceding contributions [1], [2], resulting BPM raw data are stored in FIFOs and can be transferred to named files containing 4096 or 65536 data lines plus an end marker and 4 header lines which store

- the global description of the BPM (x or y plane, number, longitudinal position on the reference orbit, and the sensitivity S_{BPM} of the device, which is different in the cylindrical and the rectangular sections of the beam tube) and also date and time of the measurement, and

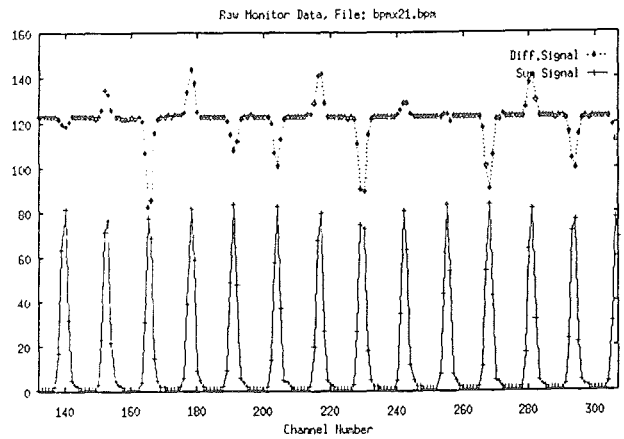

Fig. 1: BPM raw data, normal bunch form

- the settings of the sum (Σ) and difference (Δ) branch of the BPM electronics (broad and —if applicable— narrow band amplifications A in dB, filter bandwidth in kHz, and measuring cycle in ns).

For online visualization and evaluation of such measurements the experimentalist must be able to

1) view the raw data in FIFO or BPM files (7 bit integers 0 to 127 for the Σ signal and 8 bit integers 0 to 255 corresponding to −127 to +128 for the Δ signal) in a workstation window in order to see the time distribution of the bunches (Σ) and their horizontal deviations (Δ) — the latter case being shown in Fig. 1 of Ref. [1]

2) find the times when bunches pass BPMs, i.e. the channel numbers n_{peak} where Σ has maxima Σ_{peak}, and find the corresponding difference signals $\Delta_{peak} - \Delta_{zero}$, where Δ_{zero} corresponds to the equilibrium line (when no bunch passes) of the raw Δ data, and, from this, calculate true beam deviations x (e.g. in mm) using the formula

$$x = \frac{\Delta_{peak} - \Delta_{zero}}{2(\Sigma_{peak} - \Sigma_{zero})10^{(A_\Delta - A_\Sigma)/20} \cdot S_{BPM}}$$

3) combine data from 2 BPMs with a longitudinal phase difference of about $\pi/2$ and plot the tracking data x_2 of the second versus those of the first x_1 — this is roughly a phase space plot x' versus x for position 1, because roughly $x_2 \sim x_1'$ (if $\Delta\mu \sim 0.25$)

4) calculate accurate values x_1, x_1' and x_2, x_2' for any two BPM positions in the ring with any phase difference $2\pi\Delta\mu_x$ and generate phase space plots for any of the positions 1 or 2 or both.

To cope with these tasks a set of Unix shell scripts and short C programs was written and extensive use was made of GNUPLOT [3] and MAD [4].

1) To show the raw data of a tracking file in a Gnuplot window the script **sho** can be used:

```
sho <filename>          or
sho <filename> <first> <last>
```

where the latter form displays only a part of the file between two channels; without these numbers all channels (0 through 4095) are shown.

2) Displaying for example only between ~128 and ~256 channels (~8 to ~16 turns) gives a good enough resolution to examine bunch shapes which can be crucial in finding the correct positions of the Σ signal maxima. Examples are given in Fig. 1 – Fig. 3 which in the upper part include the corresponding Δ signal (cf. Fig. 1 of Ref. [1]).

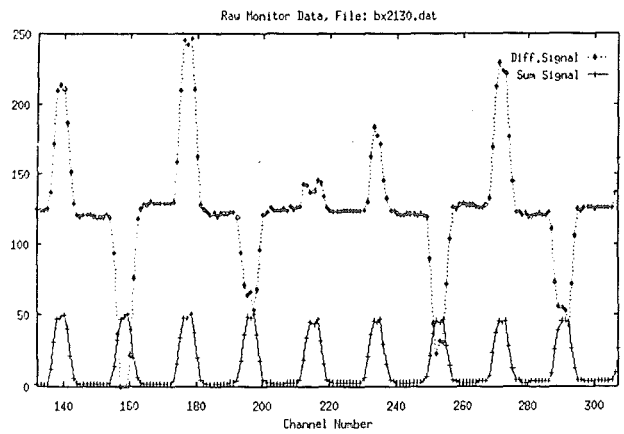

Fig. 2: BPM raw data with double peaked Σ maxima

Maxima can be found with a simple algorithm (C program) as long as peaks sit in single channels or in no more than two equal ones (Fig. 1). Problems occur with double peaked maxima (with a slight dip in the middle) or with 3 equally high channels (Fig. 2); in these cases some smoothing (summing 3 channels) is necessary while searching the maximum. However,

smoothing is not generally applicable; it may fail in cases of asymmetric bunches (Fig. 3) and yield shifted peaks whereas the simple algorithm finds the correct peak channel. Presently no automatism is included in the software; scripts with both versions of the peak finding C program are around and the need for inclusion of smoothing seems to be less frequent; experimenters decide which script to use.

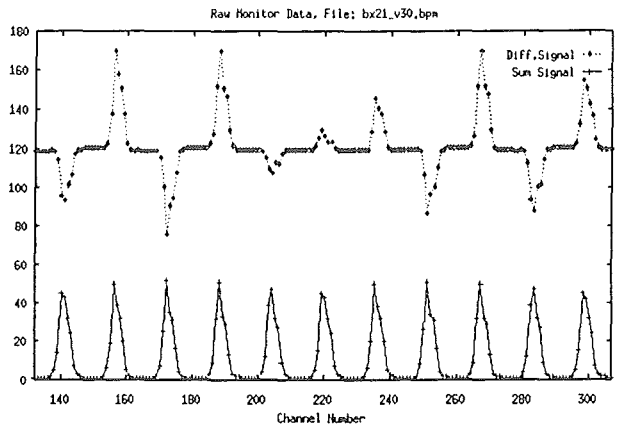

Fig. 3: Asymmetric bunch forms in raw BPM Σ data

3) Having found the peak channels, inclusion of three more C programs in the script converts the raw data to x deviations in mm and does a side by side combination of processed data files from two beam position monitors. BPMs 21 and 24 were used for the first measurements because of their location near the extraction region and the appropriate phase difference between them. So the first "x_2 vs. x_1" plots showed x_{24} versus x_{21} (cf. Ref. [2]).

With respect to envisaged application in separatrix studies the complete script was named **sepaplot**, takes no parameters except 2 filenames and defaults to plotting only the first 64 turns (in order to not overcrowd the picture); it may more generally be called as **psp** (for phase space plot). Depending on the distance of the maxima, 4K FIFOs may store about 240 to 290 turns (peak distances between 17 and 14 channels assumed). Selection of any sequence of turns is possible by using an extension of the script:

```
sepaselect <file1> <file2> <length> <last>
```

where `<length>` designs the number of turns to be shown and `<last>` the last turn to be included; `sepaselect` is also callable as `pspselect`.

4) For the accurate calculation of x_2', x_1' from x_1, x_2 the (horizontal) TWISS parameters $\beta_1, \beta_2, \alpha_1, \alpha_2$, and μ_1, μ_2 (index x omitted for convenience) are needed as to be seen in the fully symmetric formulae for x_1' and x_2', respectively:

$$\frac{1}{sin2\pi\Delta\mu_{12}}\left(\frac{x_2}{\sqrt{\beta_1\beta_2}}-\frac{x_1}{\beta_1}(cos2\pi\Delta\mu_{12}+\alpha_1 sin2\pi\Delta\mu_{12})\right)$$

and

$$\frac{1}{sin2\pi\Delta\mu_{21}}\left(\frac{x_1}{\sqrt{\beta_2\beta_1}}-\frac{x_2}{\beta_2}(cos2\pi\Delta\mu_{21}+\alpha_2 sin2\pi\Delta\mu_{21})\right)$$

with $\Delta\mu_{12} = \mu_2 - \mu_1$ and $\Delta\mu_{21} = \mu_1 - \mu_2$.

A process picture (ppic) file with the settings of the machine (quadrupole currents etc.) is needed in order to calculate β_x, α_x, and μ_x for all BPM positions around the COSY ring with a MAD run. The names of the BPM files are given in a different way, convenient for combination of any two beam monitor numbers along the reference orbit:

```
pp1,2 <ppic> <pre> <mon1> <mon2> <post>
```

where `pp1,2` stands for pp1 **or** pp2 and calls **that** script which does the phase space plot x' vs. x either for position 1 **or** 2; `<mon1>` and `<mon2>` are the monitor number parts (e.g. 21 and 24) of the two BPM filenames which otherwise are identical, i.e. the prefixes before and postfixes after the different numbers are the same for both filenames: `<pre>` and `<post>` (e.g. bpmx and _v09.bpm for the files bpmx21_v09.bpm and bpmx24_v09.bpm). In this way the monitor numbers are easily accessible for extraction of the required TWISS parameters from the MAD output file. MAD will not be restarted as long as the process picture filename (and the working directory) is not changed; so unnecessary and time consuming recalculations are avoided. The scripts, with some C code support, evaluate the formulae (after having done the raw data conversion to mm), set up convenient data files and command scripts for Gnuplot and start the plots.

References:

[1] J. Dietrich, J. Bojowald, I. Mohos, Transverse Measurements with Kicker Excitation, this Annual Report

[2] J. Dietrich, Phase Space Boundary Studies at the Electrostatic Septum of COSY, this Annual Report

[3] Thomas Williams & Colin Kelley, with many contributors, GNUPLOT — An Interactive Plotting Program; sources for most recent version obtainable from `ftp.dartmouth.edu` and other sites

[4] Hans Grote, F. Christoph Iselin, The MAD Program (Methodical Accelerator Design) Version 8.16, User's Reference Manual, CERN/SL/90-13 (AP) (Rev. 4), or on WWW: `http://hpariel.cern.ch/fci/mad/mad.html`

Intensity Calibration of Multi Wire Proportional Chambers

H. Labus, J. Dietrich, N. Dolfus

During the design period of the COSY extraction most attention was focused on a good profile measurement, and no particular effort has been made to get precise intensity information. The hope was that the experiments themselves will automatically yield intensities from their detectors. But we soon recognized that we also need an independent intensity measurement.

There are two major information concerning beam intensity, its absolute value and its time structure. Unfortunately the extracted intensity lays in a range between 10^6/s and 10^9/s i.e. 0.1 pA and 0.1 nA. Thus single particle counting is no more applicable, which else would allow absolute and fast intensity measurements simultaneously. Only ionization chambers with high sensitive current amplifiers are suitable within this range, but have too low cutoff frequencies of some ten Hz to watch large intensity oscillations from DC to some kHz. On the other hand they have the great advantage that no intensity calibration is necessary, as absolute intensity may immediately be calculated to a few percent precision with the Bethe Bloch formular if particle energy and amplifier sensitivity are known. Fortunately our MWPC's are possibly the best choice in this situation as they behave like ionization chambers with intrinsic amplification, which allows to use less sensitive but fast current amplifiers. Profile and fast intensity measurements are therefor possible with one and the same detector system, with the only disadvantage that the intrinsic gas amplifications as a function of the high voltage is not known sufficiently precise from any theoretical or empirical formulas.

To get absolute information of the extracted intensity we made a calibration of one MWPC with 38 MeV protons from our injector cyclotron. Fig. 1 shows the experimental set up:

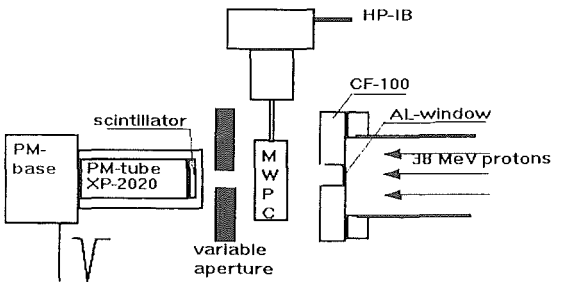

Fig.1: Experimental set up.

Protons with variable intensity and homogenous spatial distribution emerge from a 0.1 mm thick circular Al-window of 11.3 mm diameter. They traverse through the MWPC producing an approximate gauss shaped profile whose area is adjusted to 1000/s by appropriate setting of the high voltage. Then they pass through a variable aperture and finally penetrate through a 2mm thick scintillator mounted on a fast PM tube XP-2020 which produces one short pulse from every proton to count the beam intensity directly up to $< 5 \cdot 10^6$/s without significant pile up losses. The calibration at higher rates is possible by the use of the variable aperture. Suppose we measure 10^6/s with aperture fully opened that no protons can be clipped by it. We then reduce the aperture until the PM tube counts only 10^5/s. Now we increase the proton intensity until the PM's count rate is again 10^6/s knowing that the proton rate must now be 10^7/s. Finally we reduce the high voltage until the profile area is again 1000/s now at 10^7/s,- and so on. Fig. 2 shows the result:

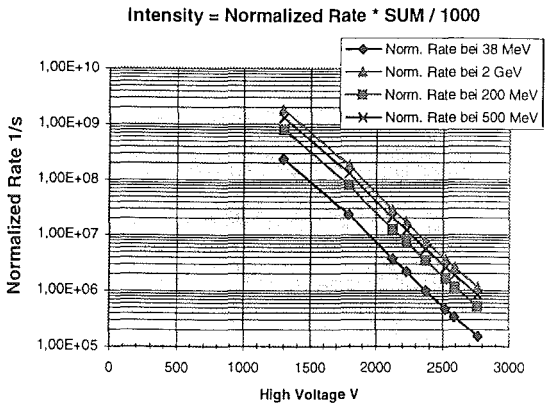

Fig. 2: Normalized intensity as a function of high voltage.

From Fig. 2 the extracted intensity is calculated by multiplying the normalized intensity with SUM/1000, where SUM is the area of the measured profile at the applied high voltage. The lower curve is the measured dependence with 38 MeV protons, the upper three curves show the dependencies for the COSY extraction energy range up to 2 GeV as calculated from the Bethe Bloch formula.

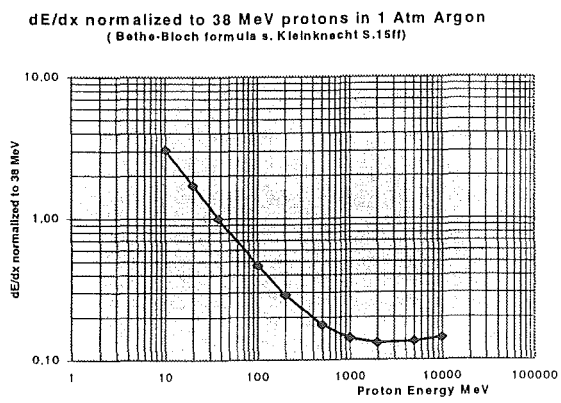

Fig. 3: Bethe Bloch formula normalized to 38 MeV protons

Due to technical limits our first measurement from Fig. 2 could not be extended to intensities above $3 \cdot 10^8$/s with 38 MeV protons. Saturation effects do obviously not occur up to this values. In further measurements we will extend the region to 10^{11}/s. To get a second independent calibration principle we also measured the proton rate with a faraday cup. To avoid long set up times for a calibration we will try to use a faraday cup which can work in normal atmosphere replacing the PM-tube in Fig. 1. It also can measure in series with the PM tube allowing quasi simultaneous intensity measurements of both devices. the principle of this cup is shown in Fig. 4.

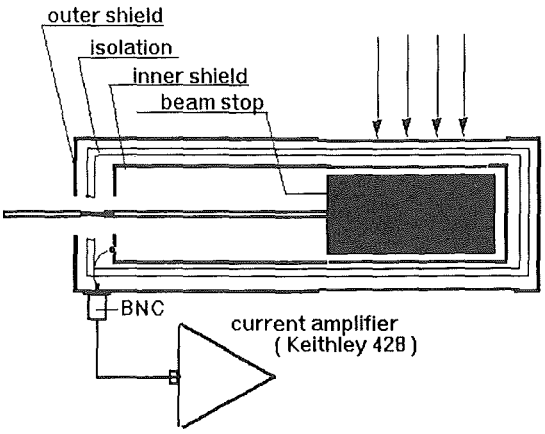

Fig. 4: Faraday cup for use in normal atmosphere.

If the beamstop is at the beam position proton charge and possible error currents are measured together. Error currents may come from ionization within the air gaps between isolation and shields in cooperation with offset voltages of the current amplifier. If the beamstop is drawn away from the beamposition the protons penetrate the cup and the error current is measured alone but twice as the error currents then are produced on both sides of the device. Fig. 5 shows the calibration when the absolute intensity was measured simultaneously with the PM-tube and the Faraday-Cup. SUM is the area of the beam profile.

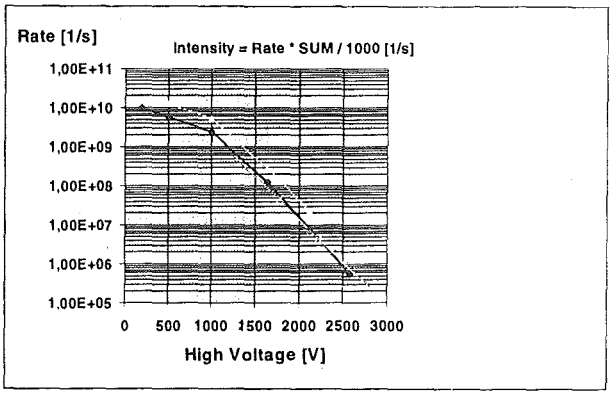

Fig. 5: Comparison of calibrations with PM-counting and Faraday-Cup measurements.

The lower curve is the PM measurement which could be extended to 10^{10} protons/s showing saturation effects above 10^9 protons/s. This measurement coincides well with a similar former PM-measurement. The upper curve shows the first calibration with the Faraday-Cup which yields a higher sensitivity roughly by a factor of two. No effect could be found until now to be responsible for this difference. Further investigations should be done.

Real time position signal from the BPM system

I. Mohos, J. Dietrich

For real-time analysis of the beam position together with other important analog informations, a new feature was added. In the Beam Position Monitor Electronics sum Σ and difference Δ signals are generated by means of a passive hybrid circuit; these are amplified and mixed to the intermediate frequency (IF) [1]. A tracking synthesizer generates the local frequency for the mixers, so the intermediate frequency doesn't depend on the beam energy even in the accelerating ramp. In the additional electronics (figure 1) for the analog position signal the band limited Σ and Δ signals with fixed frequency (10.7 MHz) will be amplified by two identical gain controlled amplifier (AD600, Analog Devices). A servo amplifier compares the amplitude of the Σ output to a reference value and simultaneously changes the gain of the Σ and Δ amplifier maintaining a constant Σ output level. The contolled gain in both channels are A = const/Σ and so the output of the Δ channel is Δ · A = const · Δ/Σ. Because of the phase relationship between Δ and Σ contains the sign of the positon, a phase-sensitive detector rectifies the Δ output signal. Properly alignment gives calibrated beam position signal with 20mV/mm sensitivity (valid only for equal gains in the Σ and Δ channels; in case of different gains the relationship between Δ and Σ gains must be used as a correction factor). In figure 2 the analog beam position signal during the machine cycle is seen in the upper trace.

The middle trace represents the ramp of one quadrupole and the lower trace is the beam current transformer signal. The sensitivity of the analog beam position signal amounts in this case 200 mV/mm due to a higher amplification of the Δ signal.

The uncorrected closed orbit at injection is 9 mm at this beam position monitor. During acceleration this closed orbit value increases to 12 mm before slowly going down. Therefore the closed orbit correction during the acceleration ramp is much more different than suggested by simple momentum scaling of the corrector strength.

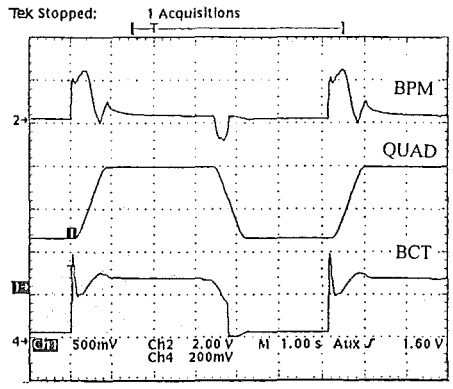

Fig. 2: Real time position signal (BPM), quadrupole ramp (QUAD) and beam current transformer signal (BCT).

References

[1] J. Biri et al., IEEE Trans. on Nucl. Sci., Vol.41, No.1 (1994)221

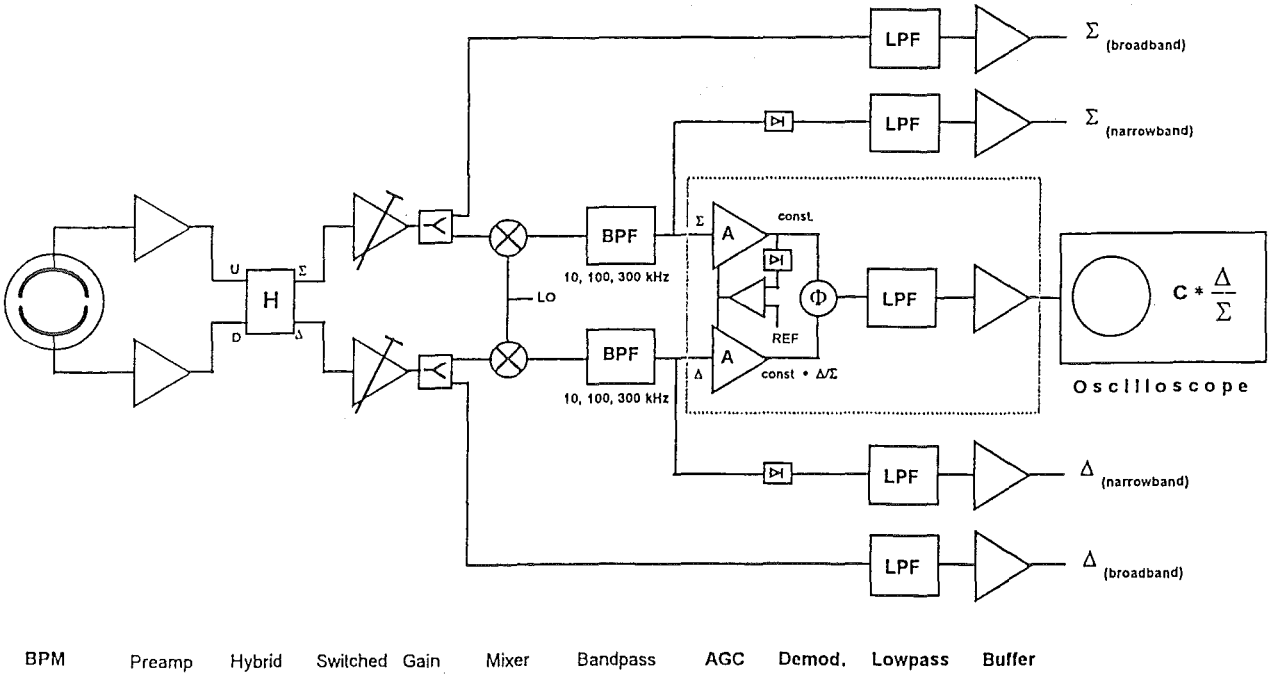

Fig.1: Beam Position Monitor (BPM) analog electronics generating the Σ and Δ signals and additionally a real time position signal (located in the dashed rectangle).

State of the COSY Stochastic-Cooling System and Interpretation of the first Schottky Signals

P. Brittner ,D. Prasuhn, G. Schug, H. Singer, W. Spieß, R. Stassen and H. Stockhorst

PU tanks

The first assembled 2-m PU tanks have been installed into the COSY ring. Rest gas pressures of around 10^{-9} hPa have been measured in the beam tubes connected to the PU tanks at working cryogenic cooling. These values are sufficiently low for most of the COSY operating modes. Vacuum bake out at 300 °C is not allowed because of the Cu-Be and Al-Mg parts. Heating the tank to 100 °C during two weeks had improved the pressure only by a little.

Two supplementary 2-m sections are being constructed and will complete the 4-m PU tanks in a next stage. The horizontal section is already cryogenically cooled and shows a rest-gas pressure of around $5*10^{-9}$ hPa.

Kicker tanks

An assembled kicker tank had been connected to a 180-l/s turbo molecular pump and a 130-l/s ion-sputter pump; two 230-l/s ion-sputter pumps were working at the tank's circumference.

Vacuum pressures of around 0,3 mPa were measured in the connected beam tubes after pumping during one week. An improvement of the outgassing rate nearly by a factor of 10 had been reached heating the interior of the tank to ca.100 °C. Therefore, COSY power amplifiers of type HLV I and II were feeding ca.100 W total into the 50-Ohm terminations of the beam-coupling electrodes. The cooling water flow both of the electrode bars and of the ferrite bars had been disconnected and the tank was thermally insulated.

Several vacuum tests have been done to localize the elements of highest outgasing rate within the tank. The team of the central workshop had modificated the electrode bar and the transmission block to improve the vacuum conductance from the internal gas stores.

RF signal processing

The low-noise preamplifiers (LNAs of type VV manufactured by Jansen Microwave, Ratingen, Germany) had been grouped to pairs matched concerning the amplification factors and the phase behaviours. The rather large reflection coefficients of the PU signal outputs (around 25 %) gave rise to instabilities of 30 % of the LNAs [1]. The oscillations have been suppressed by placing additional ferrite filled silicon polymers into the LNA cases. Nevertheless, the stability behaviour is not satisfactory.

So, the LNAs of Band II are being replaced by low-noise amplifiers of the new generation (produced by Miteq). Table 1 shows the improved noise figure and the fluctuations of group-delay times.

	VV Bd2 old	VV Bd2 new
noise figure	< 0.85 dB	< 0.5 dB
mean gain	47 dB	40 dB
ripple	< +/- 1dB	< +/- 0.2dB
group delay ripple	< +/- 200ps	< +/- 30ps
input return loss	> 10 dB	> 10 dB
output return loss	> 12 dB	> 11 dB
1dB comp. point	> -10 dBm	> 10dBm

Table 1: Comparison of two generations of LNAs

RF power amplifiers (HLVs)

Five HLVs, Band I and II each, had been operating during 300 h under conditions near to stochastic cooling. The loads of the HLVs were the power inputs of a kicker tank having only an imperfect line match.

The amplifiers were driven to about 10 W each; the cooling water was flowing. Some of the amplifier Band 2 showed a 1dB compression point 10% lower compared to the begin of the 300h CW operation. The course of that aging was found looking at the thermal conductance between the RF power transistors (FLL 50, 120) and the heat sinks. Irregularities of cooling water flow gave raise to irreversible deformation of the transistor cases and reductions of the thermal conductances even if the HLVs were switched off by case temperatures.

Motor drives

All installed motor drive controls in the ring are now connected to the COSY timing system. An interrupt controlled logical sequence process allow the integration of the movements in the COSY-cycles.

The HP Visual Engineering Environment (HP VEE) is used as graphic operator interface. All motor drives as well as the whole RF-system are controlled by two programs. The status of the system is monitored at every second. A detailed view of the drive control monitor is given in fig. 1.

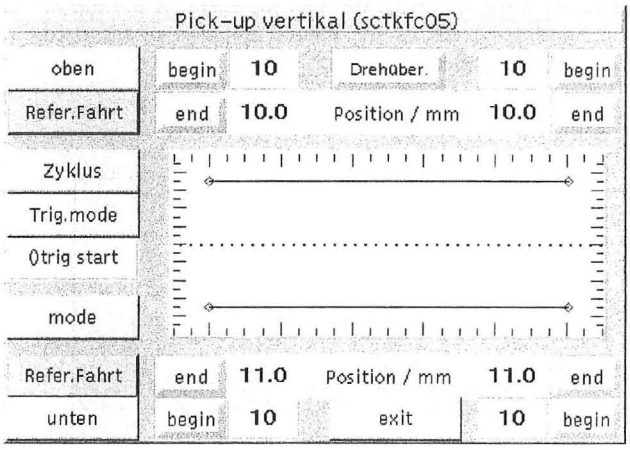

Fig. 1: full motor control using HP VEE

Signal lines across the COSY ring

The reflection coefficient of a ca. 36m long air-filled coax line is shown in Fig. 2. We used the time domain analysis to localize the single reflections. The air-filled coax line contains 4m long copper tubes constituting the outer conductor. The largest reflections in Fig. 2 are caused by the transitions between those tubes. The amplitudes of the reflections had been halved by short copper rings prolongating the inner conductor tubes at the 4m connectors. The tubes had been originally fabricated (by Spinner, Germany) to carry the thermal expansions at high RF power. Each of the higher peaks is followed by three smaller peaks which represent the three supports of the inner conductors.

The air-filled coax lines for the vertical cooling system will be reinstalled during the maintenance week before Christmas. The foreseen location of the huge bending and analyzing magnet of the ANKE experiment doesn't allow

to maintain the shortest (diagonal) path across the COSY ring. The signal delaytime of the new trace will be just yet tolerable.

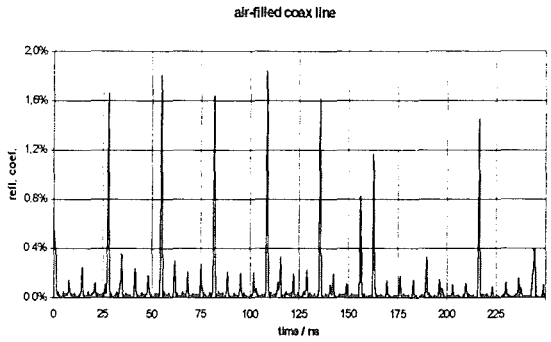

Fig. 2: time domain analysis of the air-filled coax line

Measured COSY-beam spectra

Beam measurements have been done using both PU tanks installed in the COSY ring during the last COSY11 run-times (ends of August and October). Here, long periods of constant proton energies allow accurate spectrum measurements resolved by small resolution bandwidth. The transversal and longitudinal signals measured by the band 1 system of the vertical pick-up tank are shown in Fig. 3

The small spectral elevations at the harmonics of the beam revolution frequency could be minimized by moving the upper electrode bar 1mm towards the beam. A portion of the signal is caused by the limited isolation of the used 180°-hybrid coupler.

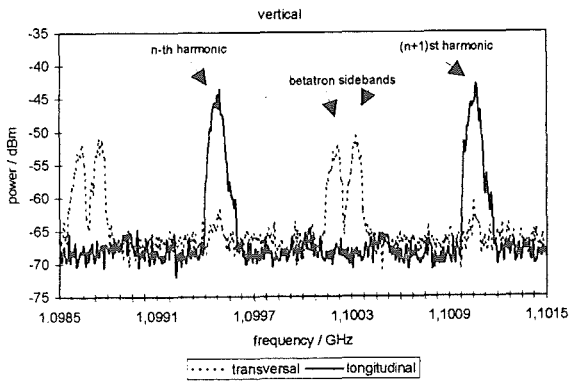

Fig. 3: vertical schottky spectrum

We now regard the beam spectrum measured using the horizontal PU tank (Fig. 4). Here, the beam center is displaced by about 7mm from the axis of the vacuum chamber as determined by the beam-diagnostic equipment. This displacement produce spectral lines near the harmonics mf_0 of the revolution frequency. The centered-electrode-pair signal in Fig. 4 contains these relative high spectral lines caused by the beam displacement. These signal lines disappear by moving the electrode bars asymmetrically to the center of the beam chamber (centered signal). But two sidebands around the revolution harmonics had been left on the displaced electrode pairs. The reason is that the beam optical settings of the COSY11 run-time leads to a dispersion at the position of the horizontal pick-up tank.

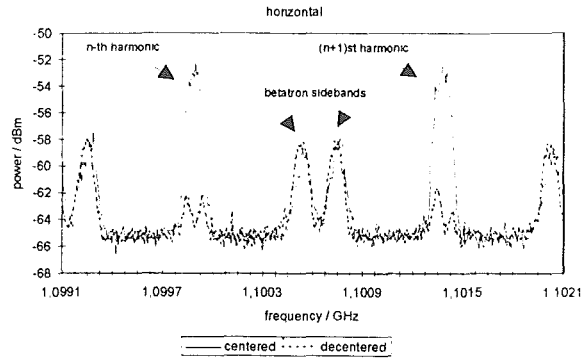

Fig. 4: horizontal schottky spectrum, electrode pairs centered to the chamber axis and decentered by 7mm

The dispersion evokes additional displacements of the particles:

$$x_D = D * \frac{\Delta p}{p_0}.$$

forming new horizontal spectral components [2]. These spectral lines are periodically around $n * f_0$ and their amplitudes tends to zero at $f = n * f_0$ (s.Fig. 4 decentered signal at the harmonics).

The horizontal and vertical fractional tunes were determined measuring the transverse sidebands. the results are in good agreement with the values given by the COSY diagnostic equipment [3].

Outlook

We plan to install the 1st Kicker tank in the middle of the next year. Then we will be able to take the first measurements of the close stochastic cooling circuit. Additionally, we are designing new tanks having an improved vacuum behavior. We intend to replace the mechanical positioning of the electromagnetic fields by an electronic phase shifting system similar to phased-array antennas.

References

[1] P.Brittner et al., First Stochastic Cooling Tank assembled in the COSY Ring, Ann. Rep.1994, p. 212

[2] Chattopadhyay S., Some Fundamental Aspects of Fluctuations and Coherence in charged-particle beams in Storage Rings, CERN 84-11

[3] J.Bojowald et al.,Longitudinal and Transverse Beam Excitations and Tune Measurements, Ann Rep. 1993, p.174

Status and Development of RF-Systems at COSY

M. Böhnke, F.-J. Etzkorn, S. Papureanu*, A. Schnase, H. Stockhorst

Corrections of rf-frequency-ramp

While operating COSY we observed that the procedure for calculating the ramping functions, especially for the frequency curve is not precise enough. The computation of the control-functions for dynamic devices, e.g. magnets and rf-system is now revised [1].

Synchronous trigger for the fast Diagnostic-Kicker

The diagnostic kicker used for beam excitation measurements has to fulfil two timing requirements. First he has to influence the beam just when the time of measurement has arrived. Then he has to kick the particle bunch reproducible when it lies inside the range of excitation. For this purpose a two-stage trigger circuit (fig. 1) has been developed which is armed with the start-pulse of the measurement and triggered with the digital zero-crossing of the revolution frequency.

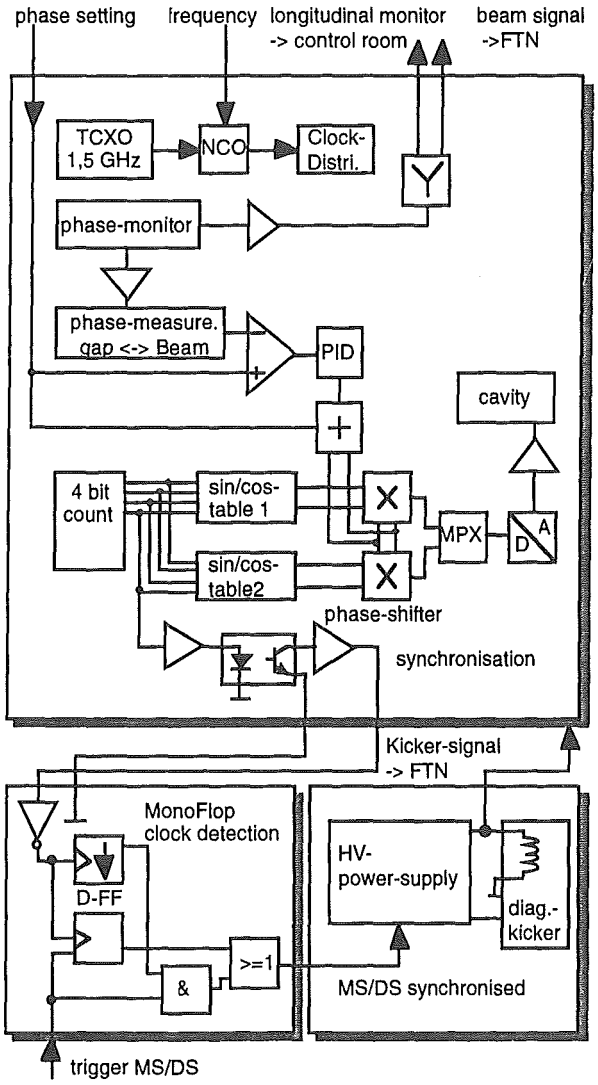

Fig. 1: Trigger circuit for the Diagnostic kicker

Development of the (h=1)-acceleration station

To guarantee a proper functionality of the (h=1)-system, components that have shown to be critical in operation are replaced by improved versions. This concerns especially the distribution amplifiers. They serve to distribute different rf-signals form the acceleration gap and the power tetrodes to subsequent systems. Their internal power supplies have shown problems at temperatures >50°C in the rf-rack, so that a new version of these amplifiers has been developed and successfully installed.

The resonator of COSY is tuned according to the revolution frequency of the protons. The recent method was to use a combination of a linear tuning function of the frequency together with an analog controller for fine-tuning. The pre-tuning (steering) of the frequency is now done with an optimised measured curve stored in EPROMs (fig. 2).

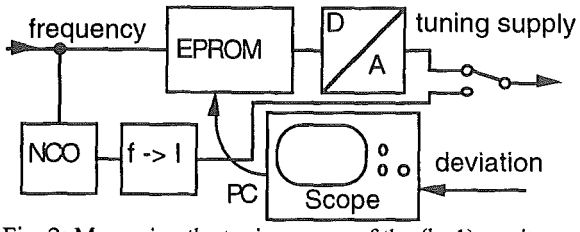

Fig. 2: Measuring the tuning-curve of the (h=1)-cavity

This removes the burden from the analog controller for fine-tuning as shown in fig. 3.

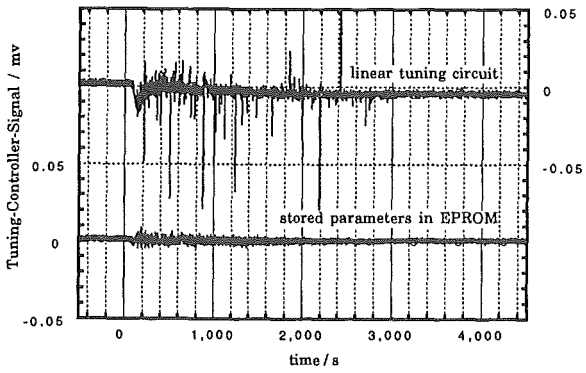

Fig. 3: Tuning signal during a ramp to 3.3 GeV/c

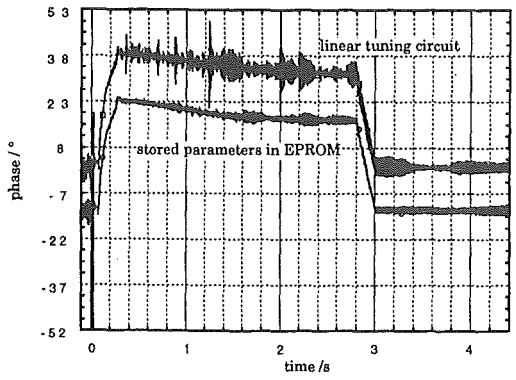

Fig. 4: Phase measurement beam <-> gap

The deviation of the center frequency is smaller and the phase relation between proton-beam and acceleration voltage is stabilised. The phase-noise of the tuned resonator is reduced and the chance that the beam will be excited to unwanted oscillations is smaller. This is a prerequisite for an improved measurement of the phase relation between

proton beam and acceleration voltage. This signal (fig. 4) is now shown on-line on an oscilloscope in the control-room. The implementation of a full digital phase control is on the way.

Regarding stochastic cooling it will be necessary to short-circuit the acceleration gap after reaching the final energy. The vacuum-relays from KiloVac which are convenient for high voltages at rf-frequencies and the coil drivers are installed and tested. The control of the timing and the logic to prevent unwanted operation of the contacts is in progress (fig. 5).

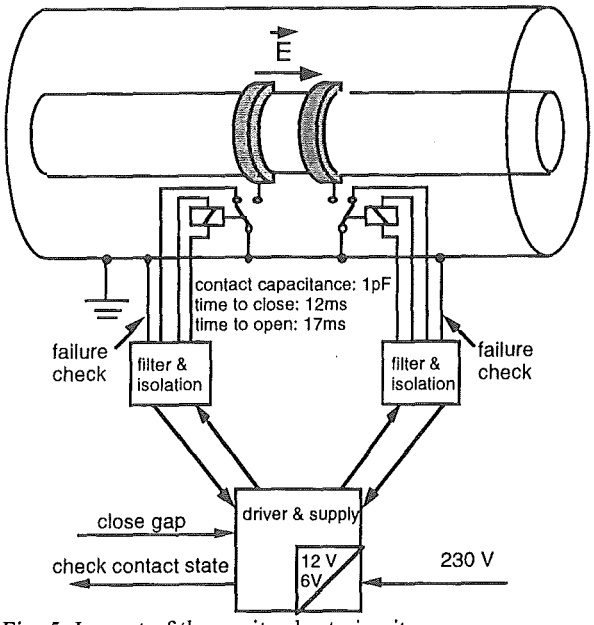

Fig. 5: Layout of the cavity short-circuit

Modifications of the USE-System

Both kicker-elements for the ultra-slow-extraction are now installed. They operate independent of each other in a broad-band or a small-band-mode. Additional control lines and special manufactured matching and termination elements allow a remotely controlled change of configuration. The low-level electronics have been completed with an individual trigger signal derived from the timing-receiver of the (h=1) rf-system. The former lab-version of the narrow-band digital noise-generator which is applied for a patent is now rebuild to a two-channel operational version which is permanently installed. For service requirements and improvement studies, an additional lab-version of the noise generator exists that supports one channel.

The USE-system is actually brought into operation. It has already shown its fitness for extraction during the beam time for the experiment GEM at Big Karl [2]; [3]. The calculation routines for different noise spectra are extended from rectangular shape to trapezoidal and gaussian spectra. Now bandwidths from 1, 2...10, 20...100, 200...500 kHz with rectangular and 1, 2...10 kHz with trapezoidal and gaussian shape are available. The HP-UX-machine "snoopy" runs about 20 minutes per 1 kHz bandwidth to calculate a spectrum with 5.96 Hz resolution and 2^{21} data-points per DSP.

The USE-system can also bunch the beam with the main rf-system switched off. The amplitude (0...200 V) is high enough to allow BPM-measurements. The detected level is about 30...40 dB lower. This was proven during the flat-top of a ramp, e.g. the rf was switched off, the beam de-bunches and then the USE-system rebunches the beam. This experiment has shown that the cavity tuning current does not steer the beam. Another point is that the USE-system allows to excite the beam at several harmonics of the revolution frequency with an amplitude curve starting at zero.

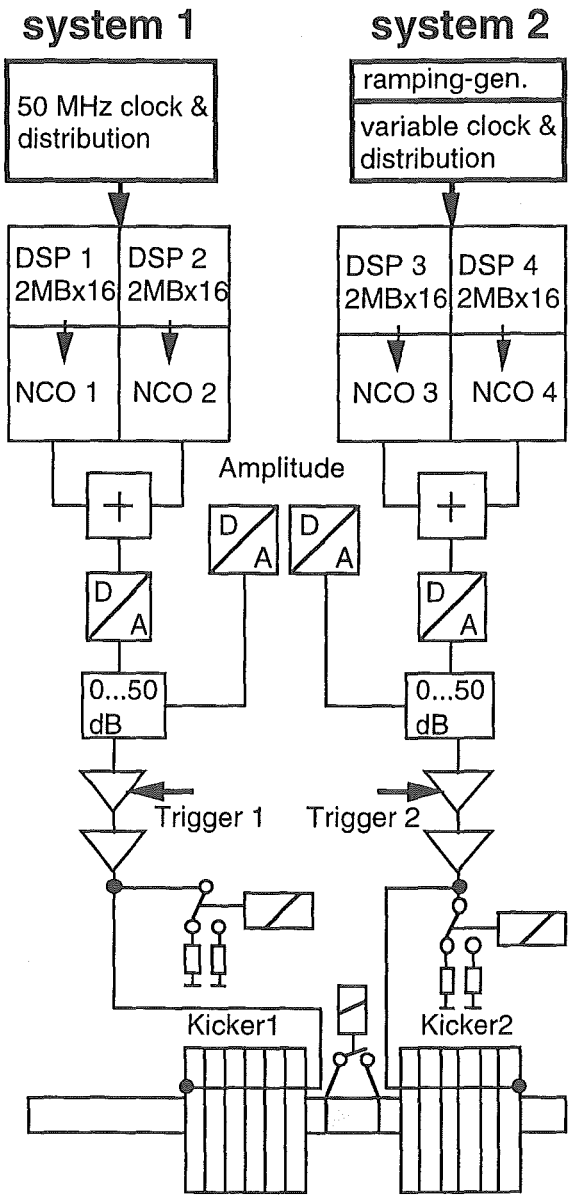

Fig. 6: Simplified overview of the USE-system

Special DSP-function-generator

The USE-System and the planned VitroVac®-cavity for higher harmonics of the acceleration voltage need additional dynamic function generators [1]. A prototype of such a function-generator has been tested for acceleration at COSY. A signal-processor Motorola DSP 96002 calculates sequences of real polynomials of third order

$$y = a_3 \cdot t^3 + a_2 \cdot t^2 + a_1 \cdot t + a_0$$

using a small program in assembler optimised that every calculation needs exactly 32 clock-cycles. Applying a clock of 32 MHz this gives a data-rate in a µs-time-scale. The digital output of this function generator is compatible to

those previously used at COSY. The special advantage of the design shown in fig. 7 is, that its behaviour is precisely predictable. The former design approximated in steps from polynomials of third order on a ms-time-scale to polynomials of second order and at last to stepwise linear functions on the µs-time-scale. The program of the DSP is stored in an EPROM, so that it is operational after power-on and reset. A special communication port of the DSP (ONCE) allows an on-line-debugging if necessary. Installed inside a VME-crate it is activated via interrupt and fetches the actual ramping function from the dedicated communication CPU - at this time an Eltec E6 that is connected to the COSY-Network. Another interrupt channel connected to the timing system will start the ramp. A third interrupt channel can be configured for special purposes, so as to stop the function generator or to allow a smooth shutdown of an interrupted machine cycle. The DSP uses its internal RAM to reach the speed of 1 MHz update rate. The internal RAM-Size limits the length of the sequence of polynomials to about 85 lines. A RAM-expansion (32k x 32bit) will be added to increase this limit. As the DSP is slower accessing external RAM, the update rate will decrease. The main advantage is that parts of the ramps can then be implemented as tables that are simple polynomials without higher coefficients.

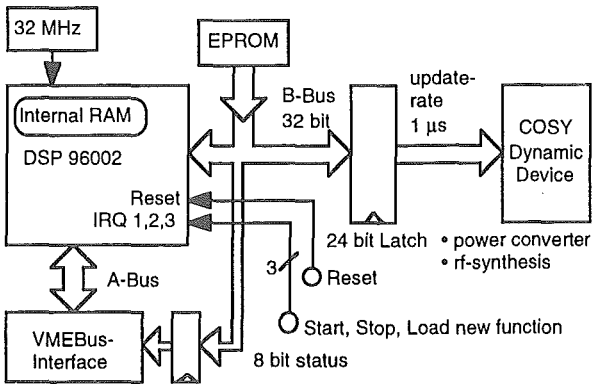

Fig. 7: Circuit of the DSP-function generator

We also tested a function generator consisting of so-called "MELcards": 2Mbit x 8 static PCMCIA-cards. A workstation converts the ramping function to a 24 bit table with up to 2097152 entries and copies it via ftp to a PC. This PC transfers the data to three battery backed up memory cards. They can then be inserted into the VME-motherboard which contains the address counters, the trigger logic and the output buffers. If this card is clocked to obtain 100 kHz data rate, it processes a ramp of about 20 seconds. The flow of information can also be inverted, so that this card captures the digital data stream produced by another function generator - an operation mode comparable to a specialised logic-analyser. The maximum data-rate of 5 MHz with 24 bit-words allowed to measure either free-running with oversampling and also clocked with the "data-valid"-signal. Both modes helped us to find some of the problems, ramping function-generators may produce.

Co-operation with Saclay (Accelerator SATURNE)

The VitroVac®-cavity (fig. 8, [4]) build in Saclay to apply the revolution frequency together with higher harmonics as a non-sinusoidal acceleration voltage is now developed further to an acceleration station which shall supplement and maybe later replace the (h=1)-cavity of COSY. At ZAT we build a 50 kW tube-amplifier which has been combined and tested with the resonator. Next tests will take place at the experimental area of Delphi at CERN, because the project TERA is also interested in this cavity. A concept for digital synthesis of higher harmonics has been realised to allow digital fourier-synthesis of rf-signals in real-time. The basic for measuring amplitude and phase of these harmonic signals is a digital phase-measurement card. This device is now tested for digital control of the (h=1)-cavity. Additionally the exchange of information between COSY and SATURNE concerning acceleration of polarised protons is very helpful.

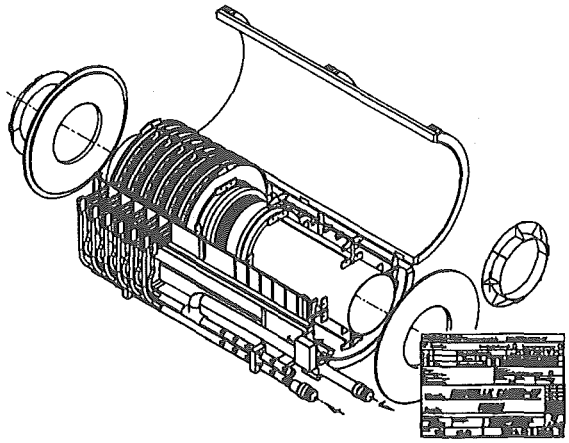

Fig. 8: Cut-away drawing of the cavity, showing inner and outer conductor, toroids, cooling and polarisation bars

Co-operation with Stockholm (Accelerator CRYRING)

The acceleration-station at CRYRING allows application of non-sinusoidal acceleration voltages [5]. The signal synthesis at CRYRING based formerly on an analog VCO. It is now replaced by a numeric oscillator that also serves as backup-solution at COSY. In this way we demonstrate how the life-time of the accelerated particle-beam depends on the quality of the acceleration voltage and therefore on the realisation of signal synthesis. The accelerator CRYRING allows to excite the particle beams with "unconventional" acceleration voltages. During our visit in august 1995 we use periodic parabolic functions. The beam experiences the derivative, in this case a saw-tooth-like waveform. For this application an arbitrary signal-generator for non-sinusoidal acceleration voltages was constructed and brought into operation.

References

[1] A. Schnase, H. Schneider, "Improved ramping functions for COSY", this report
[2] H. Stockhorst, A. Schnase, "Development of Beam Extraction", this report
[3] R. Maier et al., "Machine Development at COSY in 1995", this report
[4] P. Ausset et. al, "A High-Power Multiple-Harmonic Acceleration System for Proton- and Heavy-Ion Synchrotrons", PAC 95
[5] G. Andler et. al: "Driven Drift Tube DD-T", Manne Siegbahn Laboratory, Stockholm, Annual Report 1994

* TSR, Heidelberg

Report of the Power Supply Group

U. Bechstedt, P. Birx, H. Borsch, K. Kruck, D. Prasuhn, M. Sauer, J.Schmitz, H. Schneider

Compensation of Eddy Current Influence Caused by COSY-11 Vacuum Chamber and Modification of Main Power Supply Cyclotron

COSY-11 vacuum chamber

The change of magnetic induction (B_{dipol}) in the dipol during acceleration causes an eddy current in the vacuum chamber of refined steel to arise. This eddy current causes a magnetic induction (B_{eddy}) that influences induction internally in the chamber (B_{vacuum}).

If all chambers in the dipolgaps were built up identically, compensation for this effect could be reached by correction of set value for power supply.

In dipol 8 the COSY-11 vacuum chamber was installed with sites of 12 mm thickness during February 1995. This chamber, necessary for internal experiment, is four times thicker than the 23 others. The stronger influence of B_{vacuum} caused by this chamber can not compensate for correction of set value for the power supply, because it is only internal COSY-11 chamber.

A simple possibility of compensating this local effect in dipol 8 is to use the backlegwinding (BLW) of magnet. Detailed investigation into temporary behaviour of magnetic induction B_{vacuum} during acceleration in dependency of different chamber thickness (12 mm, 3 mm) provides foundation for compensation with a fixed current ramp (I_{blw}) for BLW.

This correction has run succesfully since the installation of COSY-11 chamber. Adjustment of set currents for quadrupol- and sextupolmagnets balances tune effects caused by COSY-11 vacuum chamber.

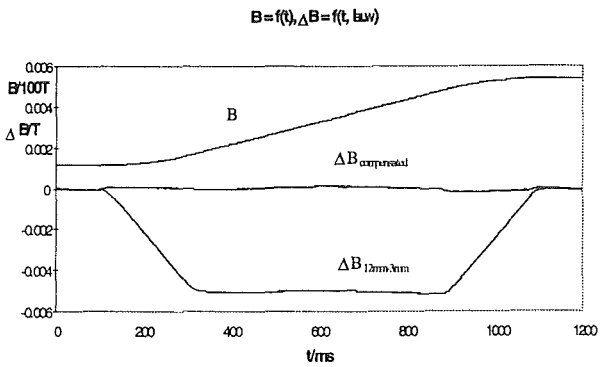

Fig. 1: $B = B_{vacuum}$,
$\Delta B_{12mm\text{-}3mm} = B_{vacuum}$ of 12 mm chamber - B_{vacuum} of 3 mm chamber
$\Delta B_{compensated}$ =Different behaviour of B_{vacuum} between 12 mm chamber and 3 mm chamber compensated by BLW

Modification of main power supply of cyclotron

The current measurement for the control loop was improved in this power supply. A high precision DCCT (DC current transformer) replaces the water-cooled shunt. The error of stability decreases from 10 ppm/per 2 h to less than 1 ppm/per 2 h.

Failure statistic of COSY Power Converter from November 1994 to Oktober 1995

Approximately 275 power supplies (PS) run on COSY (from source to external experimental places). The different PS are between 4 and 20 years old and power range is established between 100 W (correction coil) and 5 MW (ringdipol).

The separation of 275 PS are placed in three COSY domains

- Source, cyclotron and injection beamline require 98 PS .
- 136 PS supply ring components.
- The extraction beamline receives the power of 40 PS.

From November 1994 till October 1995 PS of source and ring domain ran approximately 7100 hours. The extraction beamline worked about 2600 hours during this time. Throughout this time 39 PS became imoperativ causing operating breakdowns of COSY for 43 hours.

Almost all faults were found in the power unit of PS. Defects in rectifier, transistor or thyristor were the reasons. In the dipol power supply of ring the connection of water cooling was leakage. The reason for inactivity only occasinaly connected with the fuses.

In order to keep operating breaks as short as possible 25 alternative PS have been installed for important components. If it is necessary, they are in use for less than one hour. Twice this option has been put to the purpose.

The failure and description of repair are written in the report. In some cases these reports draw the attention to properties or malfunction of particuler PS. Therefore PS can be improved in maintenance.

The list shows the failure distribution of PS in every COSY domain.

Power Converter		No	Failure
Source + Cyclotron + Injection-Beamline	Steerer	36	5
	Quadrupol	26	4
	Dipol	11	4
	Other	25	3
Ring + Electron-Cooler	Steerer	63	0
	Quadrupol	56	4
	Dipol	1	1
	Other	16	2
Extraction-Beamline + BIG-KARL	Steerer	16	4
	Quadrupol	16	10
	Dipol	7	2
	Other	1	0

New Design and Implementation of the COSY-Control Operator Interface

K. Henn, M. Schaaf, M. Simon

The experiences, gained since COSY went into operation, led to a revision of the existing concept. Because of its free availability and easy learnability and based on careful examination the programming language TCL (Tool Command Language) was chosen for the construction of the new GUIs. A high value was set on a user friendly design, which is supported by the 'look-and-feel' character of the TCL-windows technique. Figure 1 shows the schematic structure. The GUIs, organized in device groups, communicate with VME-Bus systems on TCP-connections.

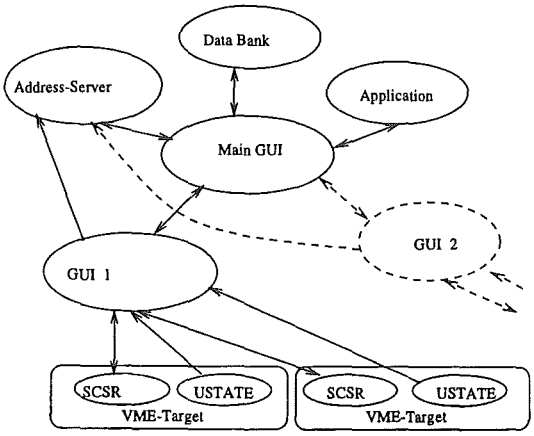

Fig. 1: Schematic Structure of the COSY User Interfaces.

After sending a command to a VME-target, the command is executed and an answer is obtained. Beside this normal communication processes can be started on the VME-targets, which informs the GUIs about status changes of the belonging devices on seperate UDP-connections. A single GUI can be started independently from each other on optional operator consoles.

An address-server, runing on a fixed host, registers the internet addresses of the hosts, on which the GUIs have been started, and the ports on which commands are accepted. By means of these informations a main-GUI can send commands to different GUIs. Furthermore the single GUIs can be started and stopped from this main-GUI. As each GUI has a default command sets for saving and restoring the complete states of the belonging devices , this design offers the possibility to rerun COSYat previous saved settings from one operator interface.

Figure 2 shows an operator interface for the COSY-injection beamline, which is already in use. The overall control panel for the power converters shows only the necessary values. More information and controling can be achieved from a single view. In a separate graphical presentation of the injection beamline singele elements can be selected and controled.

Summing up, it may be said, that the functioning of the new design has been well proved. The new GUIs have been accepted by the supervisors and the operators and the control of COSY has been improved significantly.

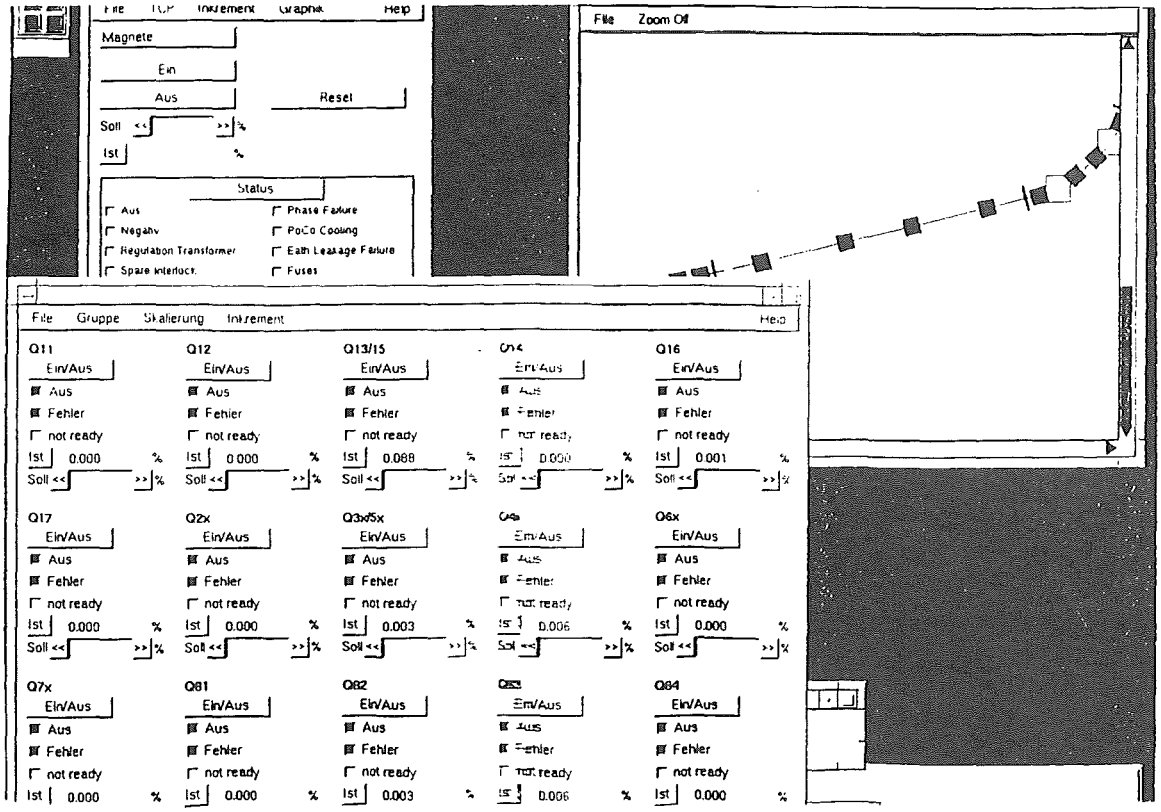

Fig. 2: Operator interface for the COSY-injection beamline.

Beam Profile and Phase Space Measurements of the Beam extracted from COSY

A. Hassan*, P. Jahn, R. Maier, B. Naumann**, D. Prasuhn, M. Rogge, R. Toelle

The method of phase space measurement by imaging with a quadrupole is now a well established method. In the first section of the extraction beam line it allows to measure the intensity distribution in the beam extracted from COSY at arbitrary distances d > 1.5 m from the quadrupole. The results of the last 3 measurements are given in Fig. 1:

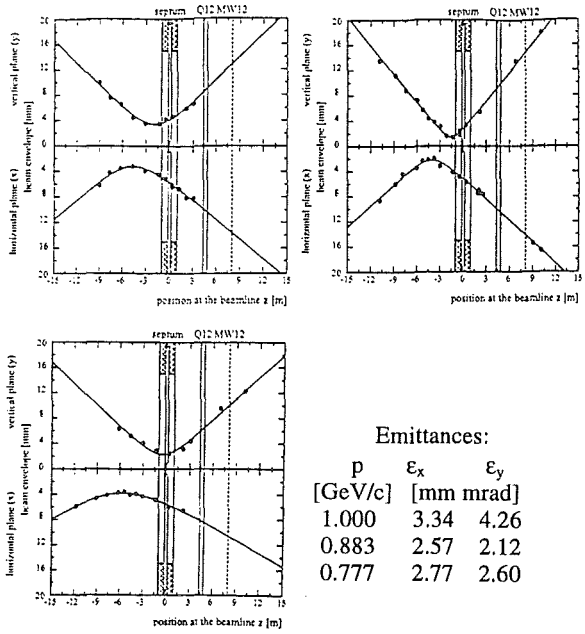

Emittances:

p [GeV/c]	ε_x [mm mrad]	ε_y
1.000	3.34	4.26
0.883	2.57	2.12
0.777	2.77	2.60

Fig. 1: The extracted beam envelope from COSY at 1.000, 0.883, and 0.777 GeV/c. Magnetic septum, quadrupole Q12 and the Multi Wire chamber MW12 are indicated.

From these curves the position of the minimum beam extension [1] z_{xwaist}, the beam radius x_{waist}, and the extension of the beam in the angle coordinate x'_{waist}, and $\varepsilon_x = x_{waist} \cdot x'_{waist}$ is derived for the horizontal plane (and for the vertical plane y respectively). Here x_{waist} is defined as: FWHM/2.

p GeV/c	z_{xwaist} m	x_{waist} mm	x'_{waist} mrad	z_{ywaist} m	y_{waist} mm	y'_{waist} mrad
1.000	-4.48	3.16	1.06	-1.86	3.43	1.24
0.883	-4.01	2.22	1.16	-1.56	1.39	1.52
0.777	-5.49	3.80	0.73	-0.45	2.27	1.15

The values for x'_{waist} and y'_{waist} can be measured directly by adjusting the focal plane of the quadrupole lens to the MW12. This agrees with the data from Fig. 1 to within 10%. These values reflect a considerable improvement in beam quality during the last year. Now the phase space of the uncooled external COSY beam approaches the values, which can be transported through the beam line to the experimental areas. All results are obtained in the thin lens approximation. meanwhile two corrections, each of them in the order of a few % in the quadrupole currents have been introduced:

- the calculations have been adapted to thick lenses
- saturation effects in the quadrupoles are included.

According to field measurements for the quadrupoles used, saturation can be described by:

$$B = a_0 \cdot I \cdot (1 + a_1 \cdot I^2 + a_2 \cdot I^4 + a_3 \cdot I^6) \quad \text{with}$$

$$a_0 = 0.03775 \qquad a_1 = -0.2 \cdot 10^{-6}$$

$$a_2 = 0.1 \cdot 10^{-11} \qquad a_3 = 1.94 \cdot 10^{-15}$$

where B is measured in [KG] and I in [A]

Some technical changes in the first part of the extraction beam line have been performed and additional calibration data have been gathered. The steerer SH10 is replaced by a stronger one with a calibration constant of 0.677 mrad/A for p = 1 GeV/c. The electrostatic septum has a (calculated) calibration constant of 8.5 mrad/KV for an electrode gap of 17 mm. (The angle of deflection is proportional to $1/(p \cdot \beta)$, where $\beta = v/c$.

The effect on the position of the beam at the entrance of the electrostatic septum was measured to be dx/dU = 0.304 mm/KV and is somewhat dependent on the working conditions of COSY.

An error in the commercial program for evaluation of the half width of the beam profile (a factor of 1.4) was found. All values given here are corrected values. The imaging method is applicable to measure the intensity distribution at some points of interest along the beam line. As an example the beam position and intensity distibution at the entrance aperture of the magnetic septum is shown in Fig. 2:

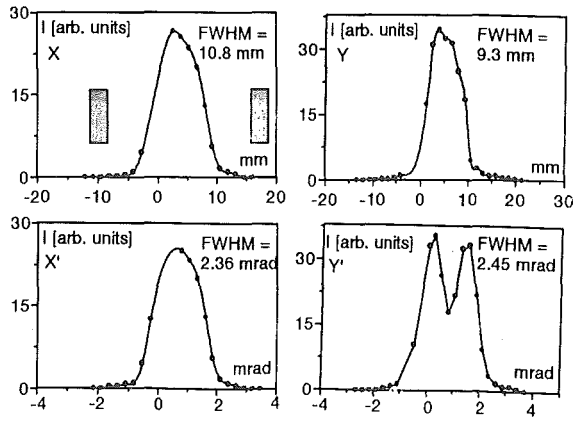

Fig. 2: Intensity distribution of the beam extracted from COSY at the entrance of the magnetic septum.The limits of the aperture were determined by changing the voltage on the electrostatic septum until the beam profile is partially cut by the aperture. Upper part: spatial distribution at 1.0 GeV/c. The horizontal aperture is indicated. Lower part: angular distribution at 1.0 GeV/c.

References

[1] IKP Annual Report 1994, p. 210

*NRC, AEA, Egypt.
**FZ Rossendorf

Beam Properties and Beam Focussing near the TOF Target

W. Eyrich*, A. Hassan**, P. Jahn, R. Klein, B. Naumann***, M. Rogge, M. Steinke****, R. Toelle

The ion optical properties and the beam transport possibilities in the last part of the TOF beam line were investigated. For the layout see Ref. [1], Fig.1, sect. IV. There is a region with a somewhat reduced aperture (R = 30 mm) between the vertically deflecting dipoles BE34 and BE35 due to the actual gap widths. Extensive calculations were done assuming a waist to waist transfer, starting at different positions upstream the aperture and producing a small beam spot at the target.In addition, the optical settings should be optimized with respect to maximum beam emittances ε_x and ε_y to pass through the aperture for a chosen waist position. The main results are: The beam extensions at the starting waist are:

$$x_{waist} = y_{waist} = R/\sqrt{2} = 21.2 \text{ mm}$$

independently from the waist position. The angle extensions are: $x'_{waist} = y'_{waist} = R/(L\sqrt{2}) = x_{waist}/L$

where L is the distance between the starting waist and the aperture. The beam emittances amount to

$$\varepsilon_x = \varepsilon_y = \varepsilon_{max} = R^2/(2L)$$

Calculations with the TRANSPORT program gave the field strengths in the last 4 quadrupoles Q35 to Q38. The results are given in Fig.1.

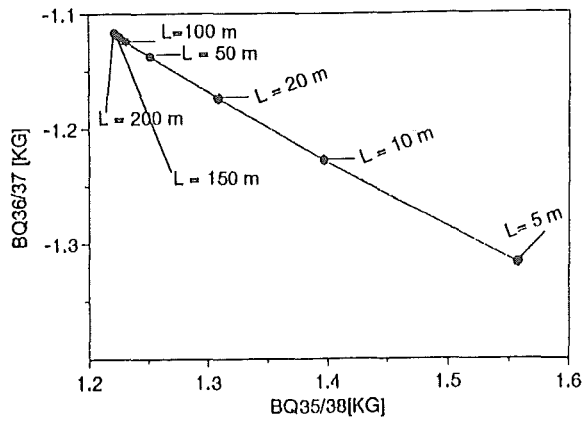

Fig.1: Field strength setting in the last 4 quadrupoles in front of TOF to get a focus (waist) on the target. Q35 and Q38 are coupled to one power supply as Q36 and Q37 to another.

Calculations assume a waist on the target 2.5 m behind the quadrupole Q38. In linear approximation the quadrupole current I is: I(Q)[A] = 26.6 · B(Q) · p [KG], where p = momentum of the protons [GeV/c] During the last TOF experiment the currents in the last quadrupoles were chosen according to these calculations for a beam spot on the target of r = 0.6 mm. Then the beam line before the waist was set experimentally to fit the starting conditions for the entrance waist. The halo normally hits the beam tube in the vertical dipoles. In order to reduce the halo near the TOF the beam was successfully limited in emittance within two upstream dipoles far away from the target. The geometrical situation near the target is shown in Fig. 2. Some properties of the beam in this region can be seen in Fig. 3.

A beam extension on target r = FWHM/2 = 0.8 mm is deduced. 87% of the beam passes through the holes of R_v = 1 mm and R_r = 1.2 mm and 93% passes through the ring detector. The center of the veto counter is shifted relative to the ring counter by 0.2 mm. The structure of the remaining halo is demonstrated in Fig. 4. A fine adjustment for minimum halo shows, that a precision of the quadrupole currents near 10^{-4} is necessary.

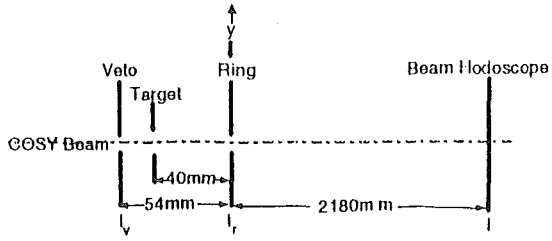

Fig. 2: Arrangement of the detectors in the target region.

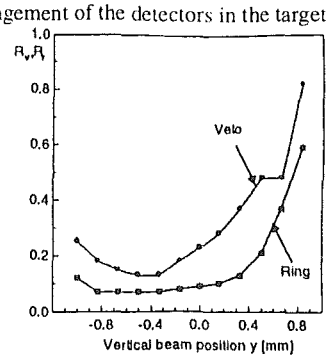

Fig. 3: Ratio of the beam intensities on the veto detector $R_v = I_v/I$ and the ring detector $R_r = I_r/I$,where I is the total intensity in the beam measured with a hodoscope. y = position of the beam,which is shifted across the detectors [2] by a vertical steerer.

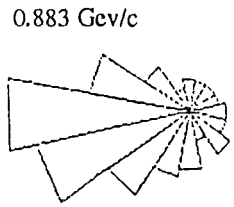

Fig. 4: Intensity distribution of the halo on the ring detector in polar presentation corresponding to the sectors of the ring detector.

The adjustment of detectors, target, viewers etc. by 2 optical telescopes to better than .5 mm has made the focussing of the beam much easier.The sensibility to steering in the quadrupoles is reduced considerably.

A viewer of Al_2O_3(Cr) was used for the adjustment of the beam. In vacuum it was applicable down to 10^6 protons/ (sec · mm^2) This material also emits light (perhaps with reduced intensity) in air.

References :

[1] P. Jahn et al., Ann. Rep. 1994, Juel-3035, p.18

[2] Hassan et al, this annual report, p.

*Uni Erlangen, ** NRC, AEA ,Egypt, *** FZ Rossendorf, ****Uni Bochum

Numerical Models for COSY

R.Tölle, A. Lehrach, L.H.A. Leunissen

Introduction

Controlling the COSY facility by the operating personnel on the one hand requires practical experience. On the other hand finding the optimal settings for the approximately 150 power supplies can be greatly facilated using numerical models. For this purpose, several numerical codes are available, for example: MAD 8.16 [1], COSY INFINITY [2], SIXTRACK [3] and TRANSPORT [4]. For the calculation of polarized particle optics POLAC [5] and DEPOL [6] can be used.

The COSY lattice is described in the MAD 8.16-syntax using the sequence feature. Starting from this basis input for other numerical codes can be generated. Furthermore, all geodetic data available are put into the lattice description file. Known errors of the magnets are taken into account as well.

MAD

With the input file and the power supply settings we can calculate several optical parameters of the COSY accelerator. For example, the tune, dispersion, chromaticity, actions of steerer magnets and so on can be predicted with an accuracy up to a few percent. Using all misalignments and magnet errors to calculate the closed orbit, all the remaining differences between the measured and calculated orbit can be assigned to a mismatch between magnetic field and RF-frequency [7]. This feature is used for fine tuning the excitation curve of the main dipoles.

COSY INFINITY and SIXTRACK

In contrast to the numerical code MAD, these programs can be used to calculate higher order effects of the beam dynamics. Whereas COSY INFINITY calculates transfer matrices which can be used for further evaluation, or an array of particles can be tracked through the lattice. Another feature is the calculation of the separatrix. In SIXTRACK two nearby particles are tracked through the six-dimensional phase space. Parameters of interest like non-linear detuning, smear [8] and dynamic aperture are determined via post-processing of the tracking data.

TRANSPORT

The injection beamline and the extraction beamlines are described using the TRANSPORT code. Calculations are possible in both directions: (i) evaluate a given setting and (ii) download an interactively optimized setting.

POLAC and DEPOL

These programs are used to calculate the strength of depolarizing resonances by Fourier analysis of spin perturbing fields. The input file of DEPOL and POLAC can be generated by MAD. Another feature of DEPOL is the determination of the degree of depolarisation after crossing a resonance.

Standard calculations for the COSY-Ring

Standard calculations are made with MAD. Up to now the actions twiss, closed orbit, survey, and B/RF-matching are available. A new feature is available for the calculation of these actions. This Tcl-script has several buttons for the different operations and is easy to use. As input, the quadrupole settings are given and the starting point in the lattice (ttstart in this case). For closed orbit calculations a measured closed orbit can be given as input, together with a magnetic field deviation.

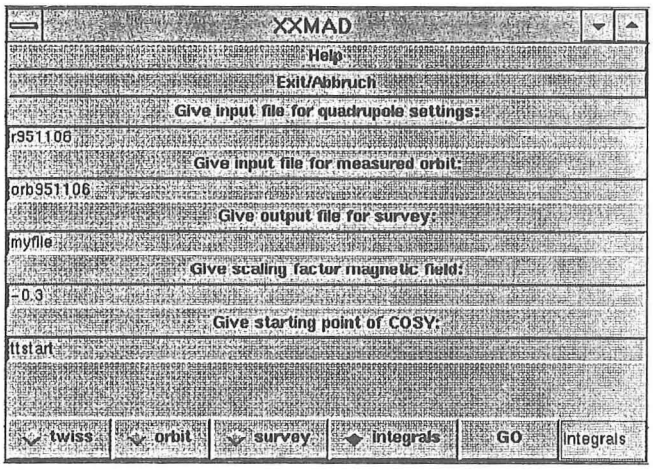

Fig. 1: Tcl-script for the calculation of optical parameters of the COSY-lattice.

Online Handbook

Operating experience is collected in several HTML-documents, which are available via an internal http-server.

References

[1] H. Grote, F. Ch. Iselin, The MAD Program (Methodical Accelerator Design) Version 8.1, User's Reference Manual, CERN/SL/90-13 (AP)(revision 1)

[2] M. Berz, COSY INFINITY User's manual, Michigan State University Cyclotron Laboratories 869 (1993)

[3] F. Schmidt, SIXTRACK, Version 1, Single particle tracking code treating transverse motion with synchrotron oscillations in a symplectic manner, CERN/SL/90-11(AP) (1990)

[4] K.L. Brown, F. Rothacker, D.L. Carey and Ch. Iselin, TRANSPORT User's guide, Technical report SLAC (1977)

[5] POLAC, programmed by T. Toyama, KEK Japan (1990)

[6] DEPOL, E.D. Courant and R.D. Ruth, The Acceleration of Polarised Protons in Circular Accelerators, Brookhaven National Laboratory (1980)

[7] L.H.A. Leunissen, U. Bechstedt, G. Krol, R. Tölle, Closed Orbit Description in COSY, this annual report

[8] L.H.A. Leunissen, D. Prasuhn, J. Bisplinghoff, R. Tölle, First vertical beamsize measurements, this Annual Report

Closed orbit description in COSY

L.H.A. Leunissen, U. Bechstedt, G. Krol, R. Tölle

For the calculation of the particle motion, we assume an ideal optical system, i.e. a system with perfectly aligned dipoles and quadrupoles. In reality however, misalignments are present. In this paper we study the effect of misalignments of the bending magnets and the quadrupoles in the accelerator. These misalignments have been measured and used for numerical calculations of the closed orbit distortion. Apart from alignment errors, magnetic field variations occur as well, which also are included in the calculations.

Horizontal closed orbit

If we consider a bending magnet or a quadrupole, each has six degrees of freedom. Namely, three translations, in the horizontal, vertical and longitudinal plane and three rotations about the different axis. After the design and building of the cooler-synchrotron at Jülich, the position of all the elements have been measured [1]. The measurements are done as followed: each of the dipoles has three reference-points in which a tripod is placed to determine the position of the dipole. The same is done for the quadrupoles, with one difference, five reference points are known here. The accuracy of the measurements is 0.05 mm. The quadrupoles in the telescopes are placed in a straight line between the arcs and their position is only known with an accuracy of 0.5 mm.

These measurements have been used to calculated the displacement of the dipoles and quadrupoles in the arcs with respect to the longitudinal axis and rotation about the vertical axis. These calculations have been used to determine the distortion of the closed orbit with the numerical code MAD [2]. The result of this calculation is shown in figure 1.

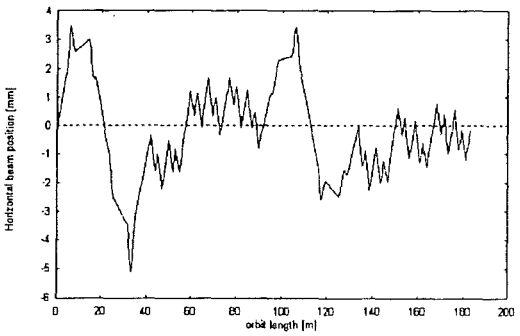

Fig. 1: Calculated horizontal closed orbit displacement due to misalignment of dipoles and quadrupoles at flat top.

However, measurements show that the misalignments of the reference trajectory is larger (about 20 mm). Furthermore, the error in the power supply settings of the quadrupoles is $8 \cdot 10^{-4}$ and for the dipoles it is $1 \cdot 10^{-4}$ at flat top, $4 \cdot 10^{-4}$ at flat bottom and $8 \cdot 10^{-4}$ during acceleration. When we take this into account, the deviation of the particle trajectory from the reference trajectory is much larger.

The calculations are not in complete agreement with the measurements done. This can be improved by using magnetic field errors from the individual dipoles with respect to each other. For this purpose, we are able to use the integrated magnetic field as function of the length of the dipole. These measurements are done at several currents, from which we will use the values of 200 A, which are close to the current used for the dipoles at injection energy. In the calculation shown in figure 2 we have used the misalignments of the dipoles and quadrupoles in the arcs, a power supply error for all quadrupoles of $8 \cdot 10^{-4}$. For the dipoles, a power supply error of $4 \cdot 10^{-4}$ is used and the magnetic field errors for all the dipoles are included. These measurements were taken at two different days at two different momenta, namely 1250 MeV/c and 2750 MeV/c. As shown, the calculations are in full agreement with the measurements.

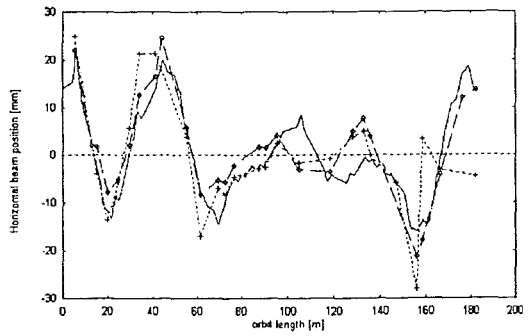

Fig. 2: Calculation of closed orbit with misalignments of dipoles and quadrupoles, a power supply error of $4 \cdot 10^{-4}$ and individual field errors of dipoles included (solid line). The other two lines indicate measurements of the closed orbit at flat top at an energy of 1250 MeV/c (dashed line) and 2750 MeV/c (dotted line).

Since we now know how we can describe the closed orbit, we can try to improve it. Several schemes have been proposed for this purpose. The closed orbit can be influenced by adjusting the independent sources.First of all, the misalignments of the dipoles and quadrupoles can be minimized. Secondly, the field errors of the independent dipoles can be altered by using correction coils that are mounted on the dipoles. These correction coils can also be used to minimize the effect of the misalignments.

It is possible to minimize the field error due to the power supplies of the dipoles. After measuring the closed orbit, we can calculate the power supply error and deduce if the current in the magnets is too high (low), the particles travel in a too small (large) closed orbit. Then the current can be adjusted to minimize the error.

The dipoles and quadrupoles are positioned within their tolerances. Calculations have shown that the improvement of the position of the individual elements in the ring would only change the displacement of the closed orbit by approximately 4 mm. More can be achieved when the individual field errors of the dipoles or the power supply error

are minimized. For this purpose small correction coils in the dipole magnets, backleg windings (BLW), can be used. Two BLW's are connected to a power supply unit and can be used for measurements. The BLW can change the main magnetic field by a few percent, depending on the current through the dipole. For example, the main magnetic field can be changed by approximately 0.03 T at 1000 A and 0.008 T at 5000 A.

This data can be fitted to give the relative field change at flat bottom (285 A), which is about $1.47 \cdot 10^{-4}$ when the current through the BLW is 1 A. BLW 8 and BLW 22 are connected to a power supply unit and are used for measurements. The closed orbit is measured at flat bottom and then the BLW is given a current of -3 A and +3 A. The orbit is measured in both cases. To determine how much the power supply error is, the measurement without the BLW is used. A power supply error of $-16 \cdot 10^{-4}$ is found to give a good description of the closed orbit in this case. The calculations show that a relative field error of $50 \cdot 10^{-4}$ is in agreement with the measured closed orbit, see figure 3.

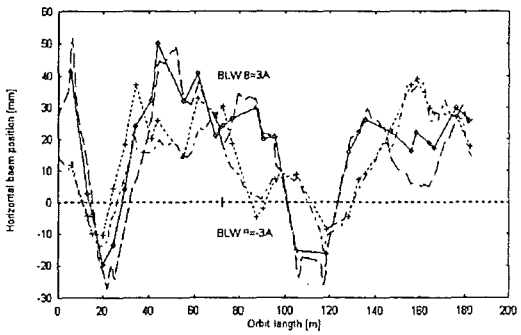

Fig. 3: Closed orbit calculations at flat bottom with BLW at 2.5 A and -2.5 A (solid and dash-dot line). Measurements with BLW 8 at 3 A and -3 A (dashed and dotted line).

The current that corresponds to the field error is 2.5 A, which is close to the setting of the power supply unit which was 3 A. The same measurements are done on flat top. Since the relative field change is smaller on flat top, the changes in the closed orbit are much smaller. The back-leg winding is set to -1.5 A and +1.5 A, which is a relative field change of $1.43 \cdot 10^{-4}$ The calculations show that the relative field error to compensate the closed orbit distortion is about $22 \cdot 10^{-4}$ which is about 2.3 A. Measurements done with BLW 22 yield similar results.

Vertical closed orbit

The position of all the elements have been measured in the vertical direction. The measurements are done as followed. On each of the dipoles, quadrupoles an sextupoles a stellage is placed to determine the vertical position on each corner of the dipole, and to determine the vertical position of the five reference points of the quadrupoles. For the sextupoles only two positions are known along the axis and the perpendicular rotation is corrected to be less than 0.1 mrad.

From these positions it is possible to determine the translation in z-direction and to calculate the rotation-angle about the x- and s-axis. The translation in the vertical plane was about 0.1 mm, the angles were small. The vertical closed orbit calculated from these misalignments is shown in figure 4.

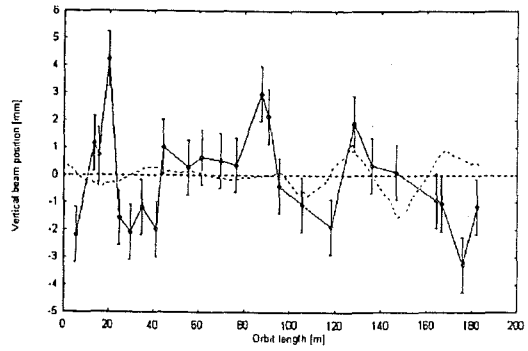

Fig. 4: Vertical closed orbit displacement due to misalignments of dipoles and quadrupoles (solid line). Measurement at 1150 MeV/c (dashed line).

We see a closed orbit distortion of about 1 mm, which is smaller than the measured closed orbit which has a amplitude of about 3 mm, as shown in figure 4. In this figure we see measurements of the closed orbit for a specific energy at flat top. The same experimental setup is used for the horizontal plane. Here, we notice only a small change in the vertical closed orbit during acceleration (approximately 1 mm). The closed orbit deviations are small in comparison with the horizontal closed orbit and as such difficult to determine

References

[1] Institut für Kernphysik Annual Report 1992, Geodetical Concept and Alignment of COSY (p. 191).

[2] H. Grote, F. Ch. Iselin, The MAD Program (Methodical Accelerator Design) Version 8.1, User's Reference Manual, CERN/SL/90-13 (AP) (revision 1)

Acceleration of polarized protons at COSY

A. Lehrach, R. Maier

Theoretical investigations of depolarizing resonances at COSY for different lattices have been done by K. Bongardt and R. Jessenberger to predict the behaviour of the polarized beam during acceleration [1,2,3,4]. To accelerate polarized protons using the actual lattice and working conditions, these calculations have been updated. Different possibilities for COSY have been studied to minimize the polarization loss at each depolarizing resonance.

Depolarizing resonances

During acceleration of a polarized beam in circular accelerators depolarizing resonances are crossed.

If the preccession frequency of the spin is equal to the frequency with which spin-perturbing magnetic fields are encountered, the beam can be depolarized.

For an ideal planar accelerator with a vertical guide field the spin vector preccesses around the vertical axis. The number of spin precessions per revolution is given by:

$$\nu_{sp} = \gamma G.$$

G = 1.7928 is the anomalous magnetic moment of the proton and γ the Lorentz factor.

In a strong-focusing synchrotron like COSY, there are two different types of strong depolarizing resonances:

a) Intrinsic resonances are caused by the horizontal fields of the focusing quadrupoles. The resonances occur at:

$$\gamma G = kP \pm \nu_y,$$

k is an integer, P the number of identical quadrupole field periods (superperiods) in the lattice and ν_y the vertical betatron tune.

b) The other type of depolarizing resonance is called imperfection resonance, which is due to the magnetic field errors and misalignments leading to vertical closed orbit distortion: $\gamma G = k$.

Weak depolarizing resonances can arise with synchrotron oscillation or nonlinear betatron oscillation due to sextupoles and skew quadrupoles:

$$\gamma G = kP \pm (a\nu_x + b\nu_y + c\nu_s),$$

a,b,c are integer ,ν_x is the horizontal betatron tune and ν_s the synchrotron tune. Only at very slow crossing speed these resonances lead to significant depolarization.

Intrinsic resonances

The number of intrinsic resonances basically depends on the superperiod of the accelerator. If the betatron phase advance in the two straight sections of COSY is equal to 2π, the resonance condition for intrinsic resonances changes to:

$$\gamma G = kP \pm (\nu_y - 2).$$

Then superperiod P=2 or 6 can be achived with the quadrupole structure at COSY. In order to control the dispersion and move γ_{tr} during acceleration only P = 2 is possible. Table I shows the calculation of the resonance strengths and depolarization with the present lattice and a usual working point (ν_x = 3.50, ν_y = 3.61) at COSY. The resonance strengths, depending on the vertical emittance, are calculated for a normalised vertical emittance of 1πmm mrad. P_{fi} is the depolarization degree for outer particles of the beam after crossing a resonance with maximum energy gain of 1.3keV/turn at COSY.

P	$K\pm\nu_y$	T [MeV]	ε_R [10^{-3}]	P_{fi} 1πmm mrad	P_{fi} 5πmm mrad
2	$6-\nu_y$	313.6	0.61	-0.54	-1
2	$0+\nu_y$	950.0	0.30	0.40	-0.68
2,6	$8-\nu_y$	1360.4	1.62	-1	-1
2	$2+\nu_y$	1996.7	0.32	0.34	-0.73

Table I: Resonance strengths of intrinsic resonances for a normalised emittance of 1πmm mrad. The depolarization is calculated for normalized emittances of 1πmm mrad and 5πmm mrad for outer particles of the beam.

In the energy range of COSY four depolarizing intrinsic resonances have to be crossed. The strength of the resonances makes it impossible to flip or conserve the polarization. A vertical tune jump is needed, which increases the crossing speed α at intrinsic resonances, in order to reduce the polarization losses [5]:

$$\alpha = \frac{\Delta\gamma G \pm \Delta\nu_T}{2\pi}.$$

$\Delta\nu_T$ is the vertical tune shift per turn. The polarization loss depends on the total width of the tune jump $\Delta\nu$ and the needed number of turns for the jump.

In his thesis, R. Jessenberger discussed the polarization loss as a function of beam emittance for a constant and gaussian distribution in the vertical phase space [4]. Using a vertical tune jump of $\Delta\nu$ = 0.04 (resp. $\Delta\nu$ = 0.02) in 10 turns at the strongest intrinsic resonance ($8-\nu_y$), the polarization loss is less than 5% (10%). The same tune jump adds less than 1% (2%) polarization loss for each of the other three resonances. Taking the synchrotron oscillation into account, the jump width has to be increased by 0.02, because the spin tune and betatron tune spread.

The resulting tune jump of $\Delta\nu$ = 0.06 (resp. $\Delta\nu$ = 0.04) is also sufficient for the actual lattice and working conditions at COSY.

Gradient errors destroy the superperiodicity and stimulate P = 1 resonances. We expect another four resonances: $-1+\nu_y$ (426.6 MeV), $7-\nu_y$ (837.0 MeV), $1+\nu_y$ (1473.3 MeV), $9-\nu_y$ (1883.7 MeV). If the gradient error ($\Delta k/k$) is in the order of magnitude of 10^{-3}, the resonance strengths are less than 10^{-5} and the polarization loss is negligibly small. However, due to internal experiments, the superperiod can be violated. Therefore, the tune jumping system should be available for gradient error resonances, as well.

Imperfection resonances

Five imperfection resonances have to be crossed in the energy range of COSY. The resonance strengths depend on the vertical closed orbit distortion (resonance strength ~ y_{RMS}). Vertical closed orbit measurements lead to a distortion of $y_{RMS} \approx 2.3$mm [6]. During acceleration the orbit only deviates within the measurement inaccuracy of 1mm. The calculation of the resonance strengths and depolarization degrees for maximal acceleration speed are shown in table II.

k	T [MeV]	ε_R [10^{-3}]	P_{fi}
2	108	1.14	-0.99
3	631	0.86	-089
4	1155	1.76	-1.00
5	1678	1.06	-0.98
6	2201	0.92	-0.93

Table II: Resonance strength ε_R and depolarization P_{fi} after crossing an imperfection resonance for $y_{RMS} \approx 2.3$mm without considering synchrotron oscillation.

A spin flip occurs at all imperfection resonaces. To achieve a total spin flip a vertical orbit distortion of $y_{RMS} \approx 3.1$mm is sufficient. Therefore, vertical correction dipoles can be used to increase the vertical orbit distortion.

The spin tune is modulated by synchrotron oscillations. This causes multiple crossing of resonances, which can not be neglect at the first resonance (k = 2). The polarization loss as a function of the resonance strength is plotted in [2] for different momentum spread at injection. A total spin flip at the k = 2 resonance is only possible at resonance strengths higher than $2.5 \cdot 10^{-3}$. The required vertical closed orbit excitation leads to particle loss, because the vertical dimension of the vacuum chamber at COSY is not large enough. A second possibility is to compensate the second harmonic of the Fourier series of the vertical closed orbit that excites the first imperfection resonance. This can be done with two vertical correction dipoles. When the resonance strength is less than $3.6 \cdot 10^{-5}$, the depolarization loss is about 1%. With several pairs of vertical correction dipoles the compensation has been simulated. The correction dipole strength for compensation was between 1mrad and 1.5mrad. This leads to a maximum closed orbit distortion between 10mm and 15mm. First particle losses at COSY arise at maximal vertical distortion of about 15mm. The compensation seems to be very critical. A good correction dipole arrangement has to be found by experimential investigation. Furthermore a high field stability of the correction correction dipoles (0.01mrad) is needed, which is in the same order of magnitude as the specification of the correction dipoles at COSY. A third possibility to overcome imperfection resonances at COSY is the so called partial snake. Partial snakes are used to flip the spin at every imperfection resonance. They effectively increase the resonance strength of imperfection resonances without changing the vertical orbit. Simulations yield, that a rotation angle of 2° along the longitudinal axis causes total spin flip at the k = 2 resonance without depolarization [7]. The main solenoid of the electron cooling system inside COSY can be used as partial snake. It can rotate the spin between 32° (108MeV) and 4.2° (2400MeV) along the longitudinal axis. Longitudinal spin rotators also excite coupling resonances, which are negligibly weak for rotation angles less than 10°.

Conclusion

Polarization conservation at intrinsic resonances is possible with a tune jumping system at COSY. The design of the tune jumping system for COSY is presented in [5]. For imperfection resonances two tools are available at COSY, the vertical correction dipoles to control the vertical orbit and the cooler solenoid used as partial snake. In practice both tools can even be used together.

These correction methods can also be used for half acceleration speed of 0.7keV/turn.

References

[1] K. Bongardt, R. Jessenberger, R. Maier, IKP Annual Report (1990) p. 146

[2] R. Jessenberger, K. Bongardt, R. Maier, IKP Annual Report (1991) p. 152

[3] R. Jessenberger, K. Bongardt, R. Maier, IKP Annual Report (1992) p. 229

[4] R. Jessenberger, Dissertation, Bericht des Forschungszentrums Jülich 2754 (1993)

[5] A. Lehrach, U. Bechstedt, N. Bongers, H. Hadamek, H. Schneider, U. Rindfleisch, 'Tune jumping system for COSY' Annual Report (1995)

[6] L.H.A. Leunissen, U. Bechstedt, G. Krol, R. Tölle, 'Closed orbit discription in COSY' Annual Report (1995)

[7] P. Nghiem, A. Tkatchenko, 'Nuclear Instruments and Methods in Physics Research A335 (1993) p.349-366

Tune jumping system for COSY

A. Lehrach, U. Bechstedt, N. Bongers, H. Hadamek, H. Schneider, U. Rindfleisch

To conserve polarization during the acceleration of a polarized beam in COSY, tune jumping was discussed in [1]. For intrinsic resonances the resonance frequency depends upon the vertical tune: $\nu_R=K\pm\nu_y$. Therefore, a vertical tune jump can be used to increase the crossing speed at an intrinsic resonance, in order to reduce the polarization loss. This can be done by changing the vertical betatron tune ν_y of the accelerator abruptly as the precession frequency of the spin comes close to the resonance. The scheme of a tune jump can be seen in figure 1.

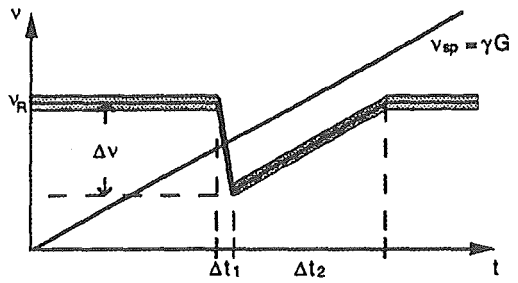

Fig 1: Scheme of a vertical tune jump., $\Delta\nu$ is the width of the jump, ν_{sp} the spin tune, Δt_1 the rise time and Δt_2 the fall time.

The width $\Delta\nu$ and rise time Δt_1 of the jump determine the polarization loss at the resonance. The fall time Δt_2 has to be long enough, so that the distance to the resonance is not reduced during crossing the resonance. The parameters for different vertical tune jumps at maximum acceleration speed (1.3keV/turn) are shown in table I.

	$\Delta\nu$	Δt_1 [μs]	Δt_2 [ms]
<5%	0.06	10	>17
<10%	0.04	13	>12

Table I: Polarization losses for different tune jumps at the strongest intrinsic resonance: $\gamma G=8-\nu_y$.

The tune jumping system for COSY has been designed, to achieve a polarization loss less than 5% at the strongest resonance. At resonances with inverse sign, like $\gamma G=2+\nu_y$ or $\gamma G=0+\nu_y$, a tune jump in the opposite direction is needed to increase the crossing speed.

Gradient field for tune jumping

A gradient field g in an accelerator produces a vertical and horizontal tune change $\Delta\nu$ depending on the betatron function β in the respective plane.

$$\Delta\nu=\frac{1}{4\pi}\beta\frac{gL}{B\rho}.$$

B is the bending field, ρ is the bending radius and L the length of the gradient field. The gradient required for a vertical tune jump can be reduced, if many long quadrupoles are placed at positions with great vertical betatron amplitudes.

Jumping quadrupoles are very expensive, because ceramic chambers and sophisticated current pulsers are needed. Moreover, inside COSY free space is rare and the lenght of the quadrupoles is limited by the maximum possible length of the ceramic chamber (about 650mm). Therefore, a system of two quadrupoles is choosen, each quadrupole with a lenght of 600mm. The vertical jump will be achieved by a jumping quadrupole placed between dipoles 3 and 4 (β_x=3.2m,β_y=21.1m). A second quadrupole will be inserted at a position with great horizontal betatron function between dipoles 2 and 3 (β_x=27.9m,β_y=9.8m), to compensate the horizontal jump. Furthermore, this jumping system also works, if the polarity of the main quadrupoles will be changed some time. The gradients for this compensated tune jump ($\Delta\nu_x$=0.00,$\Delta\nu_y$=0.06) are shown in table II.

g_J[T/m]	g_K[T/m]
0.43	-0.05

Table II: Gradients of the jumping quadrupole g_J and the compensating quadrupole g_K.

Ceramic chamber for COSY

Eddy current losses in the standard steel vacuum chamber would be too high for the required rise of the gradient fields. Two ceramic vacuum chambers are needed at the positions of the pulsed quadrupoles in the arcs of COSY. The ceramic chambers have been ordered with the usual inner dimension of the chamber in the arcs (150mm x 60mm), a length of 650mm and stainless steel flanges at the end (Meta.Ceram-Quartex, France). The averaged wall thickness is 8mm. The whole configuration is bakable to 300°C. The inner surface of the ceramic chambers will be coated with a conductive material to prevent beam induced charge build-up, which might cause beam instabilities.

Design of the pulsed quadrupoles

Several approaches have been done to find the best solution for COSY, such as laminated iron, ferrit and air quadrupoles. After this investigation air quadrupoles with only one conducting layer are choosen, because of easy construction and low inductivity. On the other hand these quadrupoles require more current. So the aperture of the quadrupoles should be choosen as small as possible. For this reason a square configuration has been preferred. The maximum diameter of the ceramic chamber is 166mm. The thickness of the heating jacket at COSY is 2x12mm. An other 2x5mm are needed to adjust the quadrupoles to the reference orbit. This leads to an aperture of 200mm for the quadrupoles. The quadrupoles are constructed and built at IKP. The layout of the quadrupoles is given in figure 2.

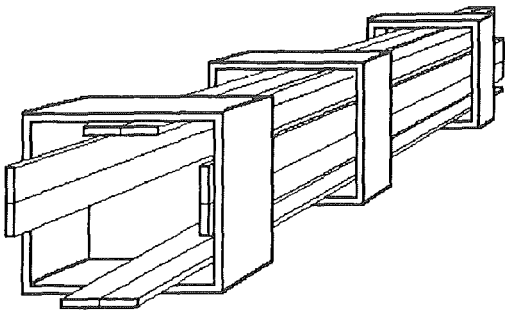

Fig. 2: Layout of the pulsed quadrupoles. Eight copper conductors are used. Between the conductors are capton stripes used as insulator. Specially pressed wood is used to fix the conductors.

Calculation of the magnetic field

Calculations are done for different width of the conductors. Narrower conductors give a higher gradient in the center of the quadrupole, whereas the quality of the field away from the center becomes low. A quadrupole with broader conductors generates a lower gradient, but the quality of the field is better. The best gradient field can be achieved with a conductor width of about 75mm, because the 12 pole component of the field is equal to zero. The gradient over the distance from the center for different width of the conductors is shown in figure 3.

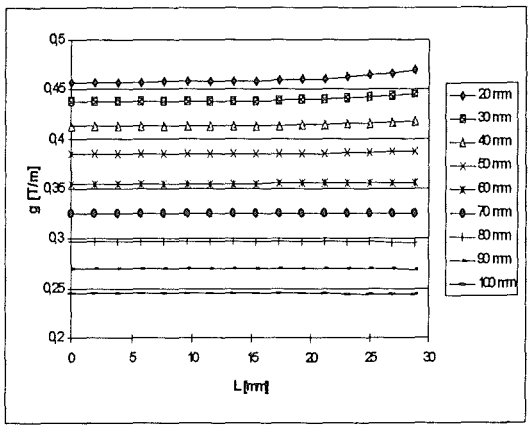

Fig. 3: Gradient versus distance from the center of the quadrupole for different width of the conductor (20-100mm). The thickness of the conductors is 5mm. The calculation are done with Poisson [2].

During the jump, the closed orbit of the beam should be on the axis of the jumping quadrupoles to reduce the emittance growth [3]. Therefore, smaller conductors can be used in order to increase the gradient. With a conductor width of 30mm the gradient is constant to less than 0.5% in a region of ±20mm. The maximum beamsize in COSY for momenta greater than 800MeV/c is less than ±7mm(FWHM) at the position of the pulsed quadrupoles.

With a current of 3057A this arrangement generates 0.43T/m. The theoretical inductivity of the conducters is about 3.6μH and the resistance 0.55mΩ. No additional cooling system for the quadrupoles is necessary.

Current bridges

The connection scheme of a one layer quadrupole, shown in figure 4, is quite simple. The currents in the two bridges flow in opposite directions. Thus the disturbing field of the bridges does not influence the integral quadrupole field.

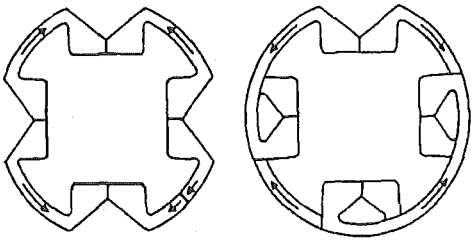

Fig. 4: Current bridges to connect the eight conductors at the entrance and the exit of the quadrupole.

The cross-section of the bridges is 5mm x 30mm and the averaged distance from the center of the quadrupole equal to 260mm. An approximative calculation assuming rectangular coils is done, to estimate the inductivity of the bridges. The resulting inductivity of the eight single bridges is about 3.0μH. This is only the lower limit, because the magnetical flux generated by one bridge also passes through the other bridges. Circular quadrupoles with similar current bridges have been built for ELSA at Bonn [4]. The measured inductivity was 80% higher than the lower limit. So the expected inductivity of the hole arrangement is about 5.4μH. The total resistance of the bridges is 0.33mΩ.

Requirements for the current pulsers

The total inductivity of the quadrupoles is about 7μH and the resistance greater than 1mΩ (16mΩ during the rise time of the pulses, due to the skin effect). The two quadrupoles will be energized with triangular current pulses. Puls-Plasmatechnik GmbH (Dortmund) will deliver two pulsers including the transfer lines beetween the pulsers and quadrupoles. The pulsers are able to generate more than eight triangular pulses with different polarities and amplitudes (up to 3060A) during one acceleration cycle. The rise time is equal to 10μsec and the fall time about 20msec (40msec for half acceleration speed).

Time schedule

The first quadrupole prototype is finished and will be tested at the beginning of 1996. The ceramic chambers will be delivered at the beginning of 1996 and inserted into COSY until May 1996. The current pulsers will be installed until July 1996.

References

[1] A. Lehrach, R. Maier, 'Acceleration of polarized protons at COSY', Annual Report (1995)

[2] M. T. Menzel, H. K. Stokes, 'User's guide for the poisson/superfish group of codes', Los Alamos (1987), LA-UR-87-115

[3] L.A. Ahrens, Proceedings. of the 8th International Symposium on High Energy Spin Physics, Minapolis (1988), p. 1068-1076

[4] H. Ebeling, 'Konzeption, Bau und Test eisenloser Quadrupole für die Resonanzextraktion aus ELSA', Diplomarbeit Bonn (1987), ISSN-0172-8741

Beam Quality and Detector Size

K. Kilian and R. Maier

One goal of scattering experiments in particle and nuclear physics is the determination of the directional correlations (scattering angles) between the beam particles and the reaction products.

The angular resolution depends on the distance D from target to the detector and spatial resolution ΔX_{Det} of the detector as well as the beam emittance $\varepsilon=\Delta X \cdot \Delta\Theta \cdot \pi$. With beamline elements one can change the beamradius ΔX up or down but then the beam divergency $\Delta\Theta$ goes correspondingly down or up such that ε remains constant as a characteristic quality criterion of the beam. It is evident that for an optimal experiment the detector resolution ΔX_{det} and the beam size on the target ΔX should be about equal $\Delta X_{Det} = \Delta X$. At the same time the angular imperfection due to the beam divergency $\Delta\Theta=\varepsilon/\pi\Delta X$ should be about the same as the angular uncertainty due to the just defined detector and target size $\Delta\Theta_{Det} = \Delta X/D$. This relates a wanted angular resolution $\Delta\Theta$ with the beam emittance and with a necessary target-detector distance D. The figure shows this dependence for fixed emittances and for fixed detector resolutions.

One sees that a good beam quality allows for small detector dimensions. Since the price of a detector goes at least proportional to its volume it becomes evident that phasespace cooled beams should allow for much cheaper and better experiments. It is also evident that both beam parameters and beamline parameters have to be identical in the horizontal and vertical plane for optimal performance.

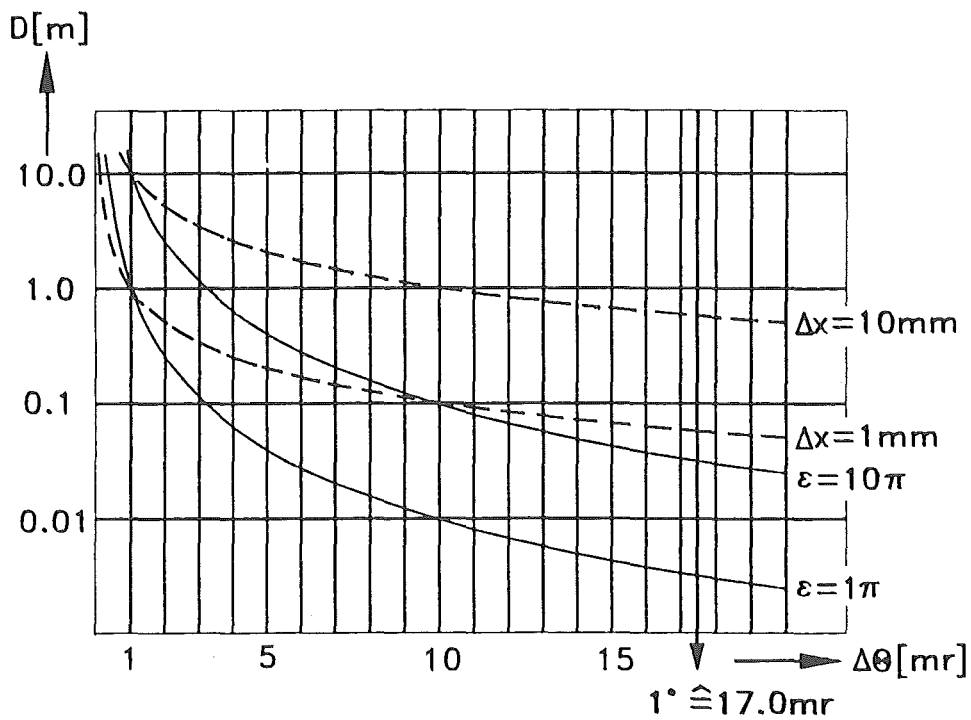

Figure: Correlation between the angular resolution and the target-detector-distance as a function of beam emittances or beam size on the target under optimal conditions

Magnets for the 0°-Spectrometer ANKE at COSY-Jülich

U. Bechstedt, M. Büscher, G. Müller, O.W.B. Schult, U. Sieling, P. Wieder

After the final decision for the erection of the 0°-Spectrometer ANKE [1] at COSY a design of the magnets was fixed and the contract for the manufacturing was placed at ANSALDO in Genua. The three dipole magnets will be delivered in mid 1996. The basic layout of COSY and the 0°-facility is given in Fig. 1

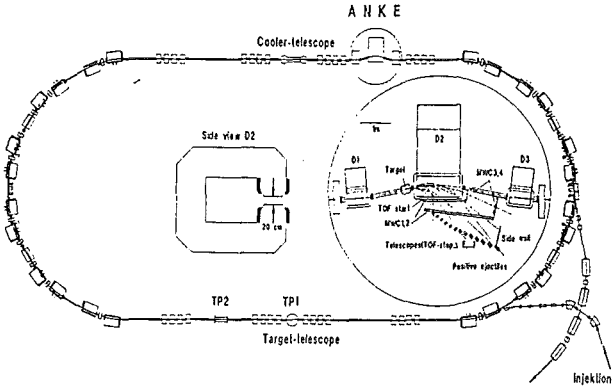

Fig. 1: Layout of COSY and the 0°-spectrometer.

The 0°-spectrometer consists of three bending magnets. The two dipoles D1 and D3 deflecting the circulating beam out of its direction and back to it are identical. For these two we use the same lamination like for the accelerator dipoles. The essential differences to the bending magnets of the accelerator are the iron length 690 mm instead of 1755 mm and the coils having 24 instead of 16 turns.

There were two motivations for the coil design. The first was to keep the magnet as short as possible because of the limited space for the installation of the spectrometer between the quadrupole triplets of the straight telescope section. This led to rectangular coils instead of quadratic ones. The second was to be able to use the available powersupply for the test of the ring dipoles giving a maximum voltage of 70 V and a maximum current of 5000 A with a maximum ramp rate of 2600 A/s. This powersupply can now be used to operate the two dipoles D1/D3 in series. The central magnet of the facility is the spectrometer magnet D2. The wish to be able to spectroscopy positively as well as negatively charged ejectiles led to the very big "yoke window" that allows for the installation of detectors for the negatively charged reaction products. The maximum-weight of this magnet was limited by the crane capacity available in the accelerator hall. Because of this saturation losses for D2 are higher than for D1/D3. The basic mechanical and magnetical data for the three dipole magnets are given in Table I. The electrical data are listed in Table II.

All the magnets are supplied with longitudinal shims to increase the width of the usable field region. The magnetic calculations were done with POISSON [2] to make the basic design and optimize the shims. The effective lengths and the currents for the maximum required field integrals are derived from 3-dimensional calculations with the PROFI code [3].

Table I: Magnetic and Mechanical data of the dipole magnets

	Bending Magnet 1/3	Bending Magnet 2	
Usable fieldregion			
horizontally	± 60	± 55	mm
vertically	± 35	±20	mm
dB/B	$\pm 2 \cdot 10^{-4}$	$\pm 2 \cdot 10^{-4}$	
B_{max}	1.6	1.6	T
Edge angle	variable, Entrance = Exit		
Sagitta	17	70	mm
Eff. length	750	1500	mm
Iron-length	690	1400	mm
Max. deflection angle	10.6	21.2	deg.
Min. bending radius	4050	4050	mm
Max. width b	1335 (incl. coils)	3000 (incl. coils)	mm
Max. length l	900 (incl. coils)	1600 (incl. coils)	mm
Max. height h	1620	2664	mm
Gap height	90	200	mm
Width of pole	430	658	mm
Entrance and exit profile	45° chamfer	45° chamfer	
Dimension of laminatic	h=810; b=1185	h=1332; b=2818	mm^2
Thickness of laminatio	1.5	1.5	mm
Weight of yoke	app. 15	app. 60	to

Table II: electrical data of the dipole magnets

	Bending Magnet 1/3	Bending Magnet 2	
Coils	2	2	
Turns/coil	24	120	
Weight/coil	244	770	kg
Insulation of conductor	0.5	0.5	mm
Ground insulation	1.5	1.5	mm
Copper profile	h=26;b=18	h=14;b=14	mm^2
Cooling bore	6	6	mm
Cooling circuits/coil	3	12	
Resistance	5.2	113.5	mΩ
Current at B = 1.6 T	2910	1375	A
Current density at B=1.6 T	6.6	8.2	A/mm^2
Range of flat top currents	582...2910	370...1375	A
DC voltage/magnet	3.0...15.1	41...156	V
DC power/magnet at B=1.6	44	215	kW
Lowest operating current	93	44	A
Max. dI/dt	2500	1221	A/s
dI/IN	$\pm 9 \cdot 10^{-6}$	$\pm 9 \cdot 10^{-6}$	
Inductivity at:			
0.13 T	~ 11	~ 424	mH
1.3 T	~ 8	~ 350	mH
1.6 T	~ 4	~ 120	mH
U_{max}/magnet (during ramp)	≤ 70	≤ 650	V
Peakpower during ramp/magnet	70 · 2910	650 · 1375	VA
Water pressure drop	3.5	6.4	bar
Temperature rise	29	33	K
Waterflow/cooling circuit	11.7	48	l/min

A plot of the fieldlines from a POISSON calculation of magnet D2 is shown in Fig. 2. Fig. 3 gives the achieved field-homogeneity of D2 at 0.13 T and 1.6 T from POISSON calculations showing that the specification is fulfilled. The normalization point is the center of the gap. The dashed line shows for comparison the measured homogeneity of one of the accelerator dipoles at 1.6 T.

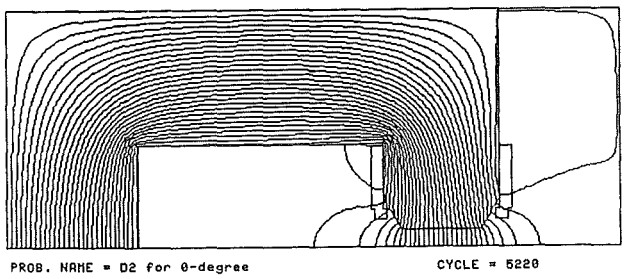

Fig. 2: Fieldline plot of dipole D2 from a POISSON calculation.

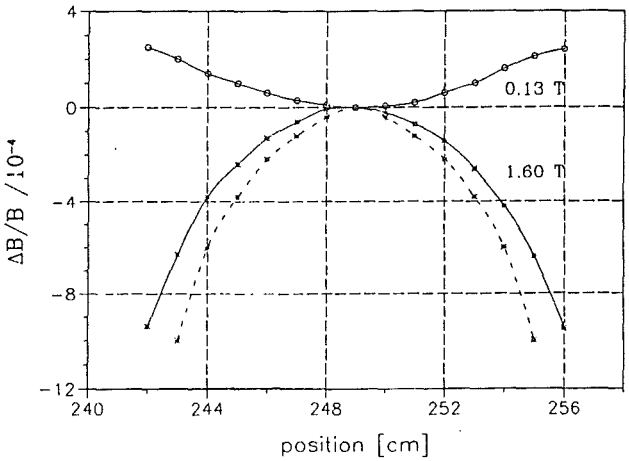

Fig. 3: Homogeneity of magnetic field in D2 in comparison to one of the accelerator magnets (dashed line).

The field integrals of the magnets as function of the excitation currents will be measured with long coils. Besides that the measurement volume of the spectrometer magnet D2 will be measured pointwise by means of three orthogonal hallplates being thermally stabilized and carefully calibrated against a NMR probe.

References:

[1] Borgs. W. et al., In Nann, H. editor, Proc. Top. Conf. in Particle Production near Threshold, Nashville, IN, USA, October 1-3, 1990, American Institute of Physics, Conf. Proceedings, No. 221, ISBN 0-88318-829-5, p. 299

[2] "POISSON/Superfish Group of Codes", Los Alamos, 1987

[3] PROFI 3-D calculation software, PROFI Engineering Systems GmbH, Darmstadt

7. ISOCHRONOUS CYCLOTRON AND ION SOURCES

The Polarized Ion-Source for COSY

P.D. Eversheim[1], R. Gebel[1], M. Altmeier[1], O. Felden[1], M. Glende[1]
W. Kretschmer[2], R. Weidmann[2], A. Glombik[2], H. Meyer[2]
H. Paetz gen. Schieck[3], S. Lemaitre[3], M. Eggert[3], G. Krause[3]

The polarized ion source for COSY that has been built by a collaboration of three groups from the universities Bonn, Erlangen, and Köln was set in operation. The negative ions for COSY are produced in a charge exchange type of ion source, which comprises three major components; the atomic beam part, the charge exchange region, and the Cs-beam part.

In the atomic beam part an intense, neutral nuclear polarized hydrogen or deuteron beam is prepared by means of two 6-pole magnets and RF-transitions. In the charge exchange region the neutral polarized atomic beam meets inside a solenoid magnet a fast neutral Cs-beam. As a consequence, the charges are exchanged according to $\vec{H}^o + Cs^o \rightarrow \vec{H} + Cs^+$. The negative ions are accelerated and subsequently pass a Wien Filter and focusing elements, in order to match the beam with respect to its envelops and spin orientation to the injection beam line of the cyclotron.

The fast neutral Cs-beam is produced in a two step process. First, Cs-atoms are ionized at a potential of about 40-50 kV and focused by a quadrupole triplet into the charge exchange region. Before the charged beam enters this region, the beam is deflected to the Faraday Cup in the deflection chamber. About 150 ms before the injection period of COSY a Cs-cell, located just behind the quadrupoles, is filled with Cs-vapor. Now the charged Cs-beam, passing through this cell is neutralized and enters the charge exchange region.

For a very first test of the complete source and beam handling system the beam was transferred to the injector cyclotron JULIC, accelerated to 45 MeV, and focused to a low energy polarimeter in the beam-line connecting JULIC and COSY. The normal and sideways (x-y) beam polarizations were measured by elastic scattering from a ^{12}C target (Fig. 1).

So far have been measured inside the source:

- $\vec{H}^o$ intensity	$> 4 \cdot 10^{16}$ atoms/s
- Cs^o intensity	> 4 pmA
- Neutralizer efficiency	> 85%
- RF-Transition efficiency	>90%
outside the source:	
- H^- intensity at source exit	~5μA
- Transmission from the source to the polarimeter	≥ 10%
- Beam polarization	>85%

[1]Institut für Strahlen- und Kernphysik, Universität Bonn
[2]Physikalisches Institut, Universität Erlangen
[3]Institut für Kernphysik, Universität Köln

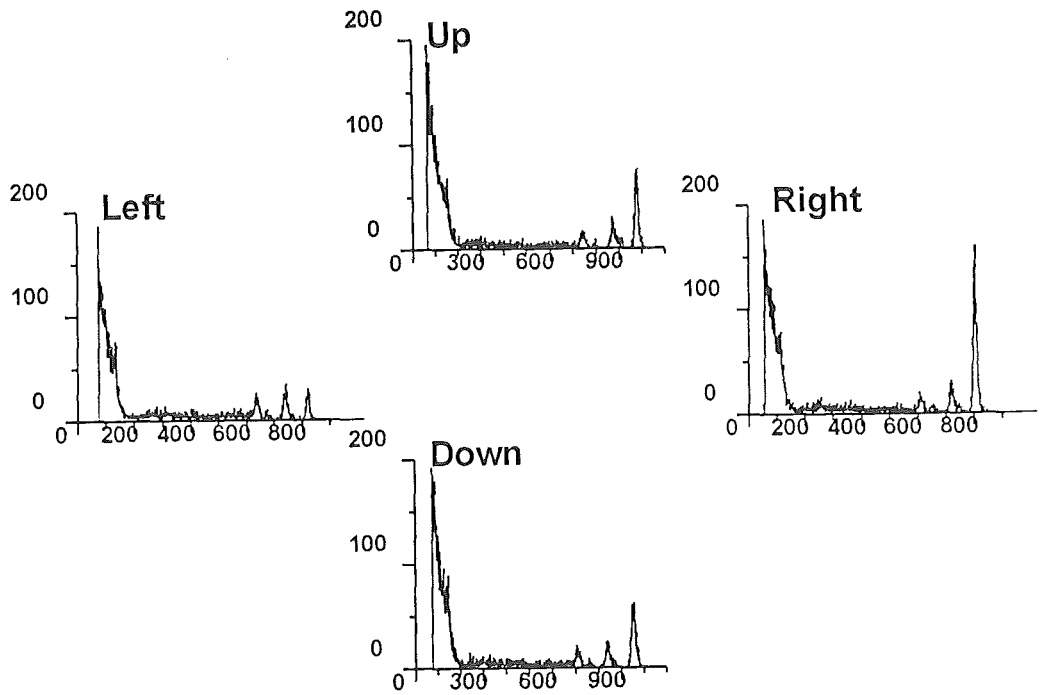

Fig. 1 Scattering of polarized protons from ^{12}C. The spectra measured by the up/down and left/right detectors show the ground- and excited-states of ^{12}C. From the ground-state asymmetry in the left/right spectra the y-polarization of >85% was calculated.

Emittance Measurement of the Extracted Cyclotron Beam

J. Dietrich, H. Lawin, I. Mohos and K. Winkler

The emittance of the cyclotron beam extracted into the injection beamline of COSY is measured by a computer controlled beam emittance-analyzer from NTG [1]. This device (EMA) works on the principle of a horizontally and vertically moveable slit/detector-system (Fig. 1). The detector-systems consist of sixty 50 μm thick tantalum stripes isolated by 280 μm thick Al_2O_3 plates. The width of both slits is 0.1 mm.

After the first measurements incorrect results caused by intolerable offset-currents for several layers of the vertical detector-system were obvious. Therefore the sandwich-target was dismounted. Some ceramic plates showed dark depositions which were the reason for low insulation-resistances down to 10 kΩ. Figure 2 gives an overall-view of the dismounted detector-system. The impurities in front of the sandwich-target can also be seen. Investigations cleared up the observed impurity as organic material. The plates could be cleaned by burning in an O_2-plasma performed in the detector laboratory of IKP. After this procedure values better than 20 MΩ were obtained for the insulation-resistances.

During dismounting and reassembling many electrical contacts of the tantalum stripes were broken. Therefore the layout was improved: Instead of the original length of 7 mm and width of 1.2 mm the new dimensions are 1.5 mm and 5 mm, respectively. The new stripes were manufactured in the central workshop of KFA. The contact to the wires was carried out by print-welding using a set-up in the detector laboratory.

The emittance analyzer is designed for measurements of positively charged ions. To measure the emittance of negatively charged ions like H^- a 25 μg/cm^2 thick carbon foil (diameter 60 mm) is placed in front of the slit for stripping.

The increase of divergence due to scattering in the foil was estimated to 0.2 mrad [2]. This means a minor contribution to the emittance. Figure 3 shows the measured density distribution in the 2-dimensional horizontal phase space and the angular profile with and without stripping foil. The agreement between estimated and measured increased beam divergence due to the stripping foil is good.

References:

[1] J. Dietrich, J. Häuser and G. Riehl, IKP Annual Report 1992, Jül-2726, p. 245 (1993)

[2] Particle Properties Data Booklet, Physics Letters, Vol.75B, No1, p. 79 (1978)

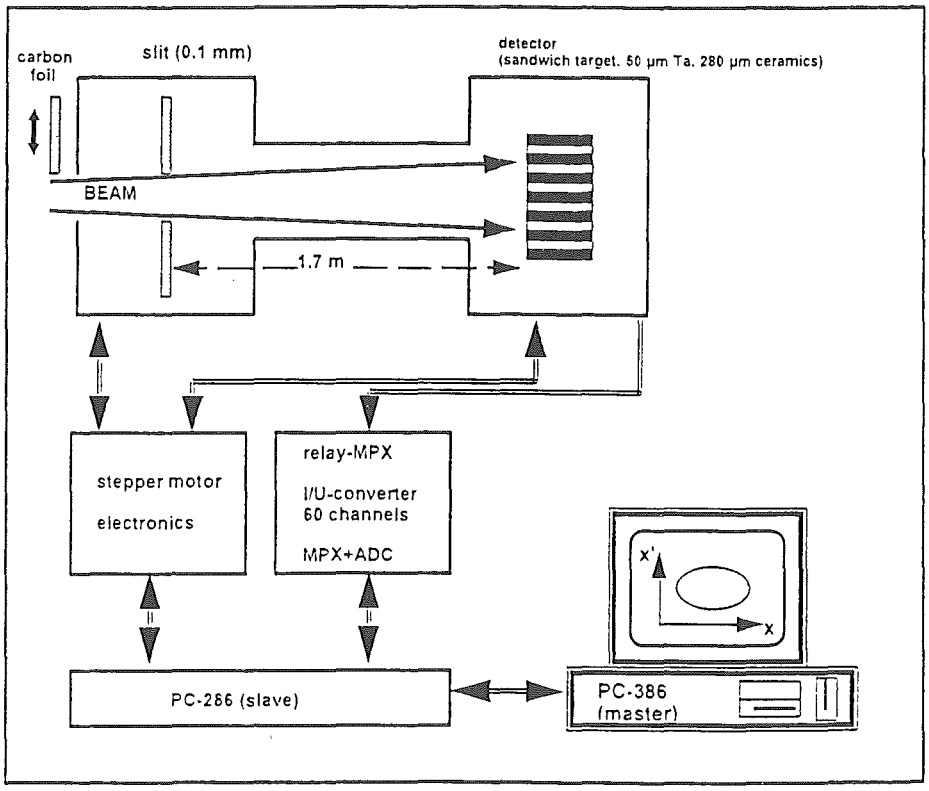

Fig. 1: Principle of the emittance analyzer-system

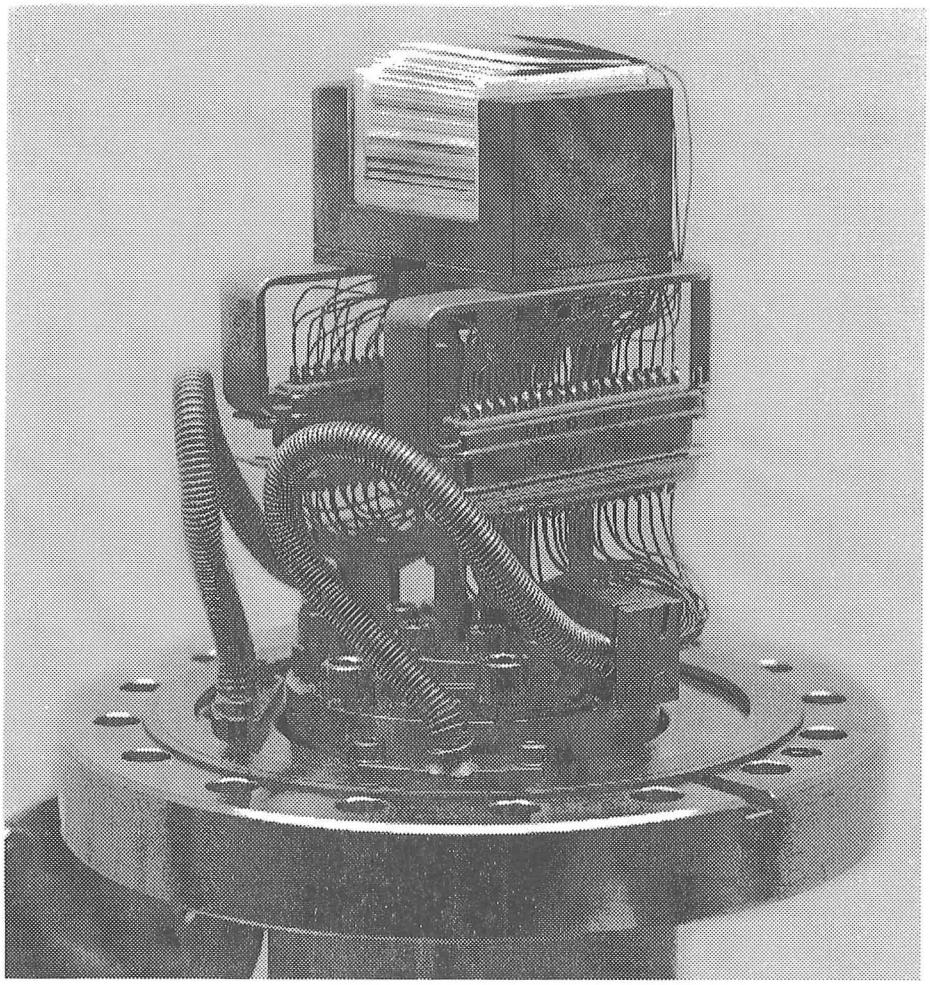

Fig2: Dismounted detector

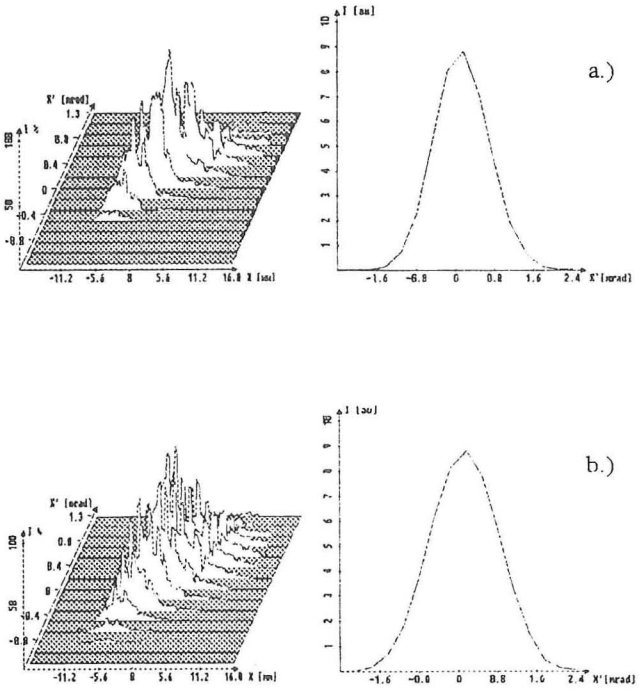

Fig.3: Density distribution in the 2-dimensional horizontal phase space and angular profile a) without and b) with stripping foil

8. SPECTROMETER BIG KARL

Magnetic Spectrometer BIG KARL

J. Engel, R. Jahn, K. Kruck, H. Machner, R. Maier, P. Schmidt, R. Tölle, V. Vau and P. v. Rossen
GEM- and MOMO-Collaboration

In several runs data were taken by both the MOMO- and the GEM-collaboration. The GEM experiment had the focus on the $pp \rightarrow d\pi^+$ reaction. For the first time the highly granular germanium wall was put into operation in an experiment together with the magnetic spectrometer. The data gained with that combination gave also complementary insight into the ion optics of the spectrometer due to the kinematic correlation between two measured particles.

The MOMO-group augmented their data on the $pd \rightarrow {}^3He\ \pi^+\pi^-$ reaction. Two major improvements helped to collect about ten thousand events. A new setting of the beam line leading to BIG KARL reduced the limiting beam halo by several orders of magnitude. Additionally, the extracted beam intensity was raised by more than one order of magnitude, while at the same time stretching the spill phase to approximately 7 seconds.

To overcome a limitation posed by radiation safety regulation the power supply gallery was arranged as a separate area closed off from the experimental area. This new structure allows now to prepare experiments in the BIG KARL area while an experiment is in progress in the neighbouring TOF site.

The setting of the spectrometer parameters has been greatly simplified by a graphical user interface that is combined with a data base.
The experimentor needs only to know the particle and its momentum respectively energy he wants to look at. Giving this information to the computer the corresponding settings for the currents are calculated and set. During the entire experiment these values are monitored and written to a data base. Any deviations that fall outside the allowed band trigger an alarm for the operator.

Graphical User Interface and Monitor System for the BIG KARL Spectrometer

Uwe Külz, J. Engel, R. Tölle, and P.v. Rossen

To ease and speed up the setting of the spectrometer and to monitor its status a graphical user interface has been developed based on VISUAL BASIC (Microsoft). This programming language belongs to the new generation of RAD tools (rapid application development) that greatly reduce the development effort by making program components available that can be integrated in the own code.

The system components of BIG KARL and their interfaces are very heterogeneous due to the legacy of components acquired over the years. This made it necessary to provide different information channels for control. Figure 1 sketches the situation.

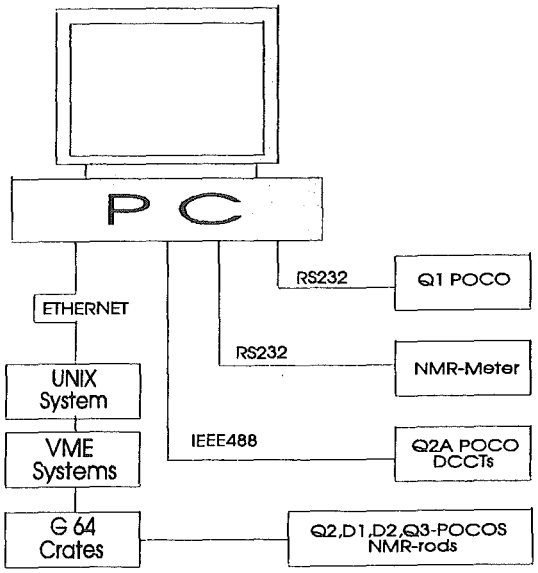

Fig. 1: Interface channels to the various components. In case of the Ether-Net the Unix-computer gets the direction from the PC, communicates with the VME-CPUs which set the registers in the G64-Crates. Q1, Q2, Q2A are the entrance quadrupoles. D1, D2 the dipoles of the spectrometer. DCCTs are Holec DC-Current Transformer.

Ether-Net, IEEE488, and RS232 are used to communicate with the various devices. One task of user interface was to hide these differences to the operator.

For a control system to be satisfactory the following goals had to be met:

- Calculate with the particle momentum or particles energy the settings for the magnetic fields.
- Set the power converters to values specified either in percent or current in amperes.
- Allow individual setting or global setting.
- Input has to be checked for plausibility and has to be confirmed before action is taken.
- Control the movable NMR-probes and read the field values.
- Calculate corrections for the dipole fields and make appropriate changes to the currents taking hysteresis effects into account.
- Monitor the set values and trigger an alarm in case of critical deviations.
- The running spectrometer should not ba affected by power loss of the computer, booting up or program crashes.
- Check with an independent program the values and polarities.
- Continuously log the values in a data base for documentation and later retrieval.

The control programs are organized as separate executables running in the cooperative multitasking Windows-environment. Communication between them is performed using the standard data exchange capabilities of the operating system.

As separate programs for setting the parameters and checking the values are used a high level of confidence is reached in the remote operation of the instrument. This is imperative as any error in the setting won't be visible immediately in the data. Therefore, a false setting could lead to a significant loss in beam time.
Redundancy is used throughout to heighten the level of reliance and to aid in trouble shooting. For instance the controllable voltage source for the setting of the quadrupole Q2A is also utilized to check and calibrate the digital voltmeter that measures the currents of the magnetic components. The expected current by setting the power converter is compared to the measured current. In case of the magnetic components not only the current is measured but also the voltage. Any significant deviation could hint a short in the windings or bad contacts. Under normal condition it allows to extract the cooling water flow and monitor it.

The highest field precision has to be reached in the dipoles. For this purpose each dipole has two NMR-probes that can be radially moved across the field range. Generally, hysteresis effects do not allow to set the fields with the desired precision of 10^{-4}. Therefore, after the current setting has been performed the NMR-probes have to be moved in to measure the actual fields. For large steps in the magnetic field about half an hour is needed for the fields to stabilize to better than 10^{-4}. The necessary correction to the dipole currents are performed semi-automatically according to the NMR-reading.

Visual Basic is a viable tool for designing control systems where speed in execution it not the primary objective. It has exhibited a shallow learning curve and did greatly speeds up the development cycle. It allows easy maintenance, addition of new components, and extension in parameters.

9. RADIATION PROTECTION

Radiation protection

H. J. Probst, K. Krafft, J. Göbbels

As in the previous years the main radiation protection activities refer to the operation of COSY. So the personnel safety system (PSA) was advanced, partly accordingly to orders of the authorities, partly for improvements of the working conditions. The measurements of the neutron and gamma dose rates in the inner hall of COSY were continued. The results of the measurements show that with few exceptions the radiation intensity allows an controlled stay of persons in the inner hall during beam in the ring. For that reason it was proposed a motion by the authorities to permit the access of persons to the inner hall also in case of beam in the ring.

Because in the meantime the planned energy of 2.5 GeV and a simultaneous filling of more than $2 \cdot 10^{10}$ protons were reached in COSY detailed measurements of the dose rate above all at the outside of the shielding of COSY were necessary. The results of the measurements are presented in the following table.

For the same beam conditions outside of the inner hall of COSY and inside, as well as outside of the injection beam line the ratios of the neutron dose and the gamme dose were determined. As expected the ratios were not constant, but nowhere at all the gamma dose was higher than the half of the neutron dose. Thereby the existing procedure, to fix two third of the permissible total dose rate as threshold for the measured neutron dose rate, is confirmed as an adequate measure. Besides that justifies the application of the same procedure in the future surveillance of the dose rate in the inner hall of COSY.

name of the position	measured pulses	bg pulses per measuring time	conversion factor (nSv/pulse)	dose (µSv)	mean dose rate (µSv/h
COSY-hall, north	377	45	0,89	0,30	0,35
"	261	51	0,89	0,19	0,22
"	337	39	0,95	0,28	0,34
"	221	43	0,89	0,16	0,19
"	255	44	0,93	0,20	0,24
material depot	303	64	0,94	0,22	0,27
"	314	44	0,91	0,25	0,29
"	540	53	0,93	0,45	0,54
IBL[1)]	128	53	0,89	0,07	0,08
"	85	43	0,95	0,04	0,05
"	76	41	0,94	0,03	0,04
IBL[1)] entrance gate	22	24	0,92	[2)]	[2)]
COSY hall, south	128	43	0,89	0,08	0,09
"	209	46	0,94	0,15	0,18
activity store	1501	39	0,95	1,39	1,67
"	1398	40	1,00	1,36	1,63
"	608	51	0,96	0,53	0,64
experimental assembly	210	43	0,90	0,15	0,18
"	303	38	0,94	0,25	0,30
power supply area	280	74	0,91	0,19	0,22
"	330	59	0,87	0,24	0,28
BIG KARL	107	95	0,94	0,01[2)]	0,01[2)]
TOF entrance gate	57	46	0,91	0,01[2)]	0,01[2)]
experimental electronic	64	67	0,94	[2)]	[2)]
"	94	53	0,90	0,04	0,04
NEMP entrance gate	85	54	0,90	0,03	0,03
Big Karl→IBL[1)]	93	56	0,89	0,03	0,04
TK37[4)], γ dose	8386	526	0,324	2,55	3,06
TK37[4)], 3m to the right	3925	53	0,96	3,72	4,46
TK37[4)]	7930	68	0,91	7,15	8,59
TK37[4)], 3m to the left	6717	163	0,87	5,70	6,84

1) IBL: injection beam line;
2) no significant difference to the bg radiation (neutron radiation of the built-in ^{262}Cf probe for the permanent default control of the actual neutron monitor);
3) in the 1. floor;
4) TK37: door between COSY hall and ring near to the injection.

Table 1: Mean neutron dose rates on different positions outside of the closed areas of COSY and mean gamma and neutron dose rates in the inner hall of COSY and the parameters needed for the calculation.

IV. Technical Developments

10. DATA ACQUISITION AND PROCESSING

COSY Experiment Data Processing

K.H. Watzlawik, M. Karnadi, R. Nellen

In collaboration with institutes inside the KFA, other research centers and external companies the activities due to the enforcement of COSY experiments have been proceeded /1,2,3,4/. The main topics in this intention are the cooperation with physicists in the buildup and the realization of experiments at COSY and other research centers as well as the preparation of the data processing infrastructure.

The development of the Control System for Scalable Experiments at COSY/4/ "Wendy" has been continued. Additional Instrumentation Systems have been implemented and advanced run control functions are realized. At experiments, the buildup of data acquisition will be supported in the installation and handling of various Instrumentation Systems and different CAMAC and FASTBUS modules including the controller, master, VME CPUs and VICbus interfacing. Therefore, the workstation data acquisition software will be provided under the operating systems ULTRIX and Digital-Unix. That system is ready to use for the experiments COSY11, GEM and ANKE.

During the reporting period, the data acquisition of the COSY11 experiment was put into operation. The workstation data acquisition software "Wendy" was applied successfully at several experiment runs with various frontend configurations. At now, the hardware configuration consists of four crates, one VME and one FASTBUS crate respectively and two CAMAC crates. Six frontend CPUs, three of type VME, two CAMAC controllers and the CHI FASTBUS master are implemented for control and data readout of Instrumentation Systems. One VME-CPU, equipped with the EXABYTE tape drive for data recording, is configured as Eventbuilder, the other two VME-CPUs are declared as Subevent Readers (SER). Two VICbus segments, each connected to one SER, provide fast data paths, one for the FASTBUS and the other one for the CAMAC crates. The event readout is synchronised by the synchronisation bus and the belonging modules, developed at GSI.
Six Instrumentation Systems, four digitizing system providing 2338 channels in summary and two auxiliary systems are controlled by the workstation data acquisition system "Wendy", running on the Alpha-Workstation. The following Instrumentation Systems are configured in the experiment environment:

- Fastbus LeCroy System (digitizing system), with 1280 channels, consisting of the modules ADC 1881, TDC 1875a, TDC 1879, TDC 1877 and CAT 1810,
- Camac DRAMS System (digitizing system), supporting 1024 channels,
- two Multipurpose Systems configured as digitizing system, one covering the LeCroy 32-fold scaler 4434 and the other one two data registers LeCroy 2371,
- Camac Scaler System covering two LeCroy 12-fold scalers model 2551 and
- one Multipurpose System configured as auxiliary system to control the 16-channel discriminator LeCroy model 4413

For the ANKE experiment, the data acquisition system/7/ has been extended with CAMAC. Currently, this system consists of the Instrumentation Systems Fastbus Multiblock, supporting the Phillips Scientific QDC type 10C2 and TDC type 10C6 modules, Camac FERA and Camac Scaler configured with LeCroy 32-fold scalers type 4434. For experiment control, the data acquisition software "Wendy" is running on the DEC-Station 5000/240.

Besides all, implementation support was performed to build up the data acquisition for the PS210 and LEX experiments at CERN.

The realization of a data processing structure for COSY experiments comprises the providing of computer networks/5/, the buildup of workstation groups and the preparation of resources for the analysis of experiment data. In software, support is granted for the operating systems OSF/1, ULTRIX, OS9, VMS and various libraries as well as extensive applications.

The existing VAX cluster /6/ is applied to several scientists for offline processing, especially the preparation of COSY experiments.

For the preparation of COSY experiments UNIX Workstations will be configured and operating systems Digital-Unix or ULTRIX will be installed as required.

To perform a reliable UNIX support for the experiment data processing, a concept of central UNIX server is prepared as a substitution of the existing VAX cluster.

To avoid problems in the error recovery, the existing Ethernet Network (IKPnet) has been improved. The ThickWire cabling, previously installed as one cable bus, was segmented into four 10BASE5 cables, all connected to one Ethernet Multiport Bridge.

Of course, the traffic at the IKPnet will be increased, caused by the new installed workstation groups, PCs, X-Terminals and printer as well as the growing amount of data analysis of COSY experiments.

The data analysis of COSY experiments requires a distributed processing with parallel access to raw and reduced data across the network from several workstations for event reconstruction and graphical presentation.

As follows by measurements of total network capacity of the IKPnet, the bandwidth of Ethernet (10Mbit/s) is sufficient for slow communications like electronic mail, remote login, file transfer and printer service. The overload, up to 90% utilization is produced by excessive access to a large quantity of data across the network from workstations with high performance of I/O and CPU power. Thereby, the amount of collisions increases drastically, the effective data rate decreases and bottlenecks are produced in the network communication. On Ethernet, power workstations are able to send data with full Ethernet bandwidth of 10Mbit/s, in

comparision to the local disk I/O is up to 6MByte/s and the I/O rate on FDDI achieves up to 7 MByte/s.
In consideration to these facts, the bandwidth of Ethernet is too small for fast communications of the required applications.
Therefore, concepts for the improvement of the existing Ethernet networks and its extention by fast networks like FDDI, ATM or FastEthernet are prepared/8/. Therein, an important topic is the realization of standardized, structured network cabling, allowing to use the same cabling for the existing and the future network technologies.

References:

/1/ K.H. Watzlawik, N. Brummund, S. Dienel, M. Drochner, W. Erven, M. Karnadi, H. Kopp, K.H. Leege, R. Nellen, W. Oehme, H. Schroeder, J. Stock, P. Wuestner, K. Zwoll, COSY Experiment Data Acquisition, IKP Annual Report 1994, ISSN 0944-2952, Berichte des Forschungszentrums Juelich; 3035, p.256

/2/ K. Zwoll, M. Drochner, W. Erven, J. Hoelzer, H. Kopp, H.W. Loevenich P. Wuestner (KFA, ZEL), K.H. Watzlawik, N. Brummund, M. Karnadi, R. Nellen, J. Stock (KFA,IKP), S. Dienel, K.H. Leege, W. Oehme (FZ Rossendorf), "Flexible Data Acquisition System for Experiments at COSY" IEEE Transactions on Nuclear Science, February 1994, Vol.41, No.1, p.37

/3/ K.H. Watzlawik, N. Brummund, M. Karnadi, R. Nellen, H. Schroeder, J. Stock (KFA,IKP), K .Zwoll, M. Drochner, P. Wuestner (KFA, ZEL), S. Dienel, K.H. Leege, W. Oehme (FZ Rossendorf) "Control System for Scalable Experiments at COSY", Proceedings of the 1995 IEEE Conference on Real-Time Computers Applications in Nuclear Particle and Plasma Physics, Michigan Sate University, May 24-28, 1995

/4/ K.H. Watzlawik, N. Brummund, M. Karnadi, R. Nellen, COSY Experiment Data Processing, IKP Annual Report 1994, ISSN 0944-2952, Berichte des Forschungszentrums Juelich; 3035, p.255

/5/ K.H. Watzlawik, N. Brummund, M. Drochner, M. Karnadi, R. Nellen, P. Wuestner, K. Zwoll, COSY Experiment Networks, IKP Annual Report 1993, ISSN 0944-2952, Berichte des Forschungszentrums Juelich; 2879, p.225

/6/ M. Karnadi, N. Brummund, R. Nellen, K.H. Watzlawik, Server Workstation System, IKP Annual Report 1992, ISSN 0366-0885, Berichte des Forschungszentrums Juelich; 2726, p.264

/7/ K.H. Watzlawik, N. Brummund, S. Dienel, M. Drochner, W. Erven, M. Karnadi, H. Kopp, K.H. Leege, H. Loevenich, R. Nellen, W. Oehme, J. Stock, P. Wuestner, K. Zwoll, First Concept of the Data Acquisition of the 0degree-Facility, IKP Annual Report 1992, ISSN 0366-0885, Berichte des Forschungszentrums Juelich; 2726, p.36

/8/ K.H. Watzlawik, "Entwurf von FDDI Networks im IKP" Internal paper, 29-Nov-1995

COSY Experiment Data Acquisition

K.H. Watzlawik, S. Dienel**, M. Drochner*, M. Karnadi, K.H. Leege**,
R. Nellen, W. Oehme**H. Schroeder, P. Wuestner*,

During the reporting period, the basic development of the Control System for Scalable Experiments at COSY "Wendy" has been concluded/1,2,3,4,5,6/. Carrying by extensive tests with various frontend configurations, that system is approved and operates successfully at several COSY11 experiment runs, at the FZ Rossendorf for detector development and is ready to use for the experiments GEM and ANKE. In future, software service for this system will be sustained and improvements, especially the implementation of new hardware components will be performed, as required.

I. Experiment Control

The structure of the control systems/2,3,4/ including all control processes, the belonging configuration and save files, the communications paths and the frontend topologies are shown in the Fig.1.
In summary, the dynamical behaviour of the control system has been improved and advanced features in the experiment control were implemented.
To allow a flexible experiment control, the functionality of the new user interface, in general represented by one OSF/Motif window was realized (Fig.2). All run control functions, especially features permitting to combine hierarchical sequences of functions were implemented (Fig.3). Accordingly, save of selected functions in a file and the restore functionality at the next run have been involved too.
The dynamical monitoring in particular the monitoring of the state and behaviour of all configured frontend hardware, as well as the monitoring of statistics have been improved. Problems in the handling and monitoring of the EXABYTE tape drive were eliminated.
The handling of additional unsolicited messages was extended in the Status Control process.
In the Synchronisation Control process, the setup of subevent readout for FASTBUS digitizing systems was extended regarding the addressing of the synchronisation module.

In software, the control system has been improved regarding restart in case of unexpected abort conditions. Currently, at start only parts of the experiment database related to the actual configuration will be mapped to shared memory sections. On exit of the last control process all active shared memory sections are deleted. The registration of activated control processes was completed. All still active control processes of one run will be finished on exit of Master Control process. Fatal errors in the frontend, e.g. crash or hangup of frontend CPUs or server processes, have been taken into consideration of control functions interlocking. At now, the control system can be activated manifold in parallel to control the same experiment environment.

The software system has been upgraded regarding the OSF/Motif version 1.2 and the features of new released C and FORTRAN compilers for the ULTRIX vers. 4.4 as well as Digital-Unix vers. 3.2 operating systems. Diverse warnings were eliminated in the software written in the C language.

A. Instrumentation Systems

The management of the Instrumentation Systems in the belonging control processes were standardized in the handling of various control functions, like control of procedure lists for setup and subevent readout, monitoring functions and the save and restore operations.
Accordingly, the OSF/Motif user interfaces were designed more uniformly and userfriendly.

A1. Fastbus Multiblock System

A new, redesigned version of the control process was put into operation. In this version, the OSF/Motif user interface is designed according to the functionality of the Fastbus LeCroy user interface. The handling of all control functions are standardized appropriately /1,3/.
The frontend setup and readout procedures were extended regarding the GSI-Synchronisation mode, used in multicrate environment.
Additionally, the building of pedestals and thresholds by the software trigger using the features of the GSI-Synchronisation module has been adapted.

A2. Fastbus LeCroy 1800 System

In addition to the supported five different module types of the serie 1800 produced by the LeCroy company, the 96 channel multihit TDC 1877 was implemented in hardware and software. Two data readout modes are involved for the TDC 1877, the single module readout, using the Sparce Data Scan in conjuction with the Sparsification features and the Multi Block Readout feature /1,3/.
For the setup an appropriate OSF/Motif user interface was developed and all nessesary control functions were implemented in the control process.
The communication to frontend has been modified regarding the new definitions of the setup and the readout procedures for all supported module types in the frontend.

A3. Camac Scaler System

In addition to the 32-fold scaler model 4434, the 12-fold scaler model 2551, both produced by the LeCroy company, has been implemented in the Camac Scaler System. For both module types the auxiliary and the digitizing mode are realized for one Instrumentation System. Inside one Instrumentation System the mixed mode operation of any or all supported module types is adapted /1,3/.

A new designed OSF/Motif user interface was implemented in the control process (Fig.4). In the main window, all scaler control operations, in particular start or stop, intialize and clear, as well as start monitoring of scaler counts are realized by PushButtons. The configured scaler system, also the appropriate scaler inside one Instrumenta-

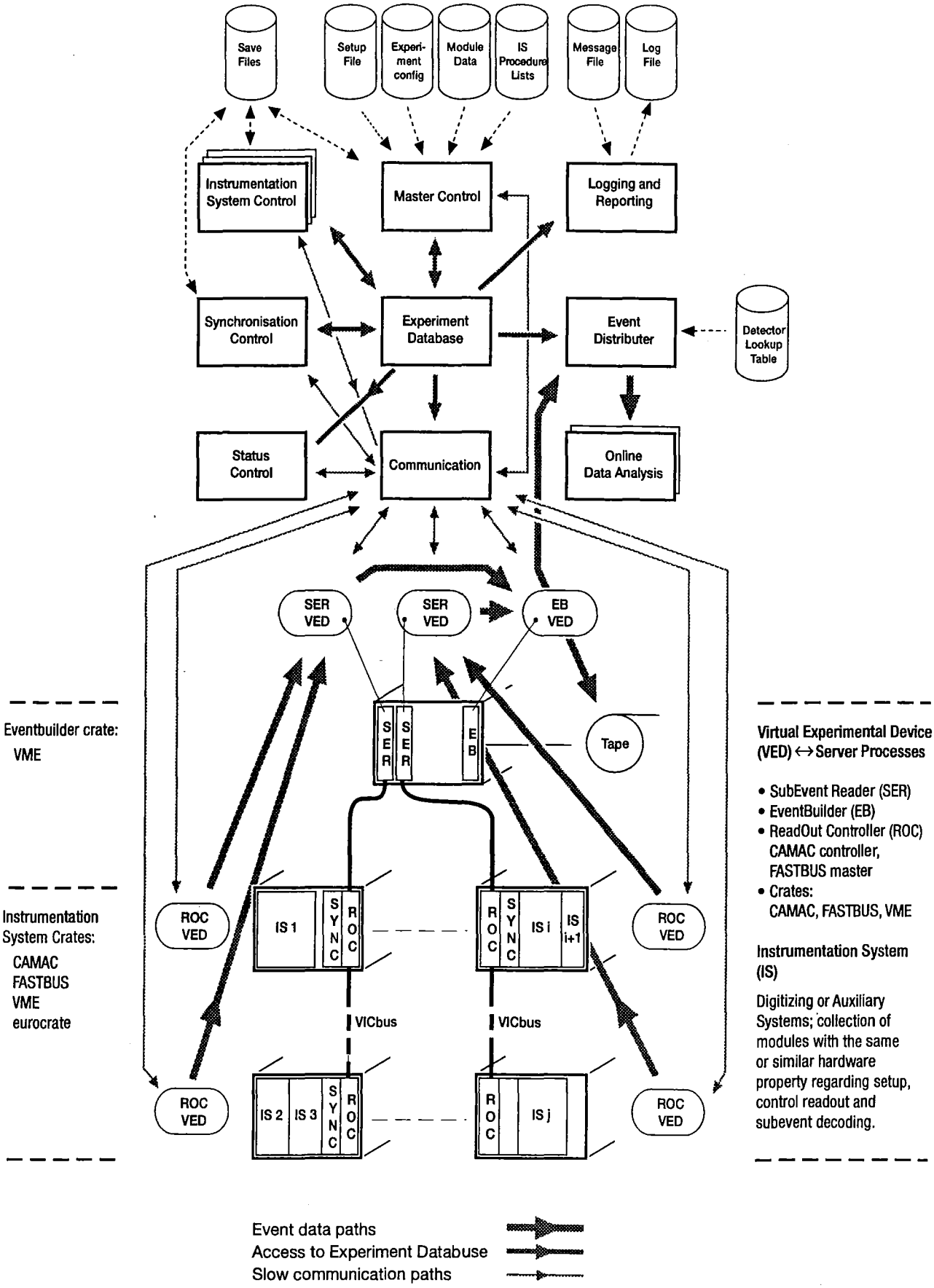

Fig. 1 Structure of the Control Sytem

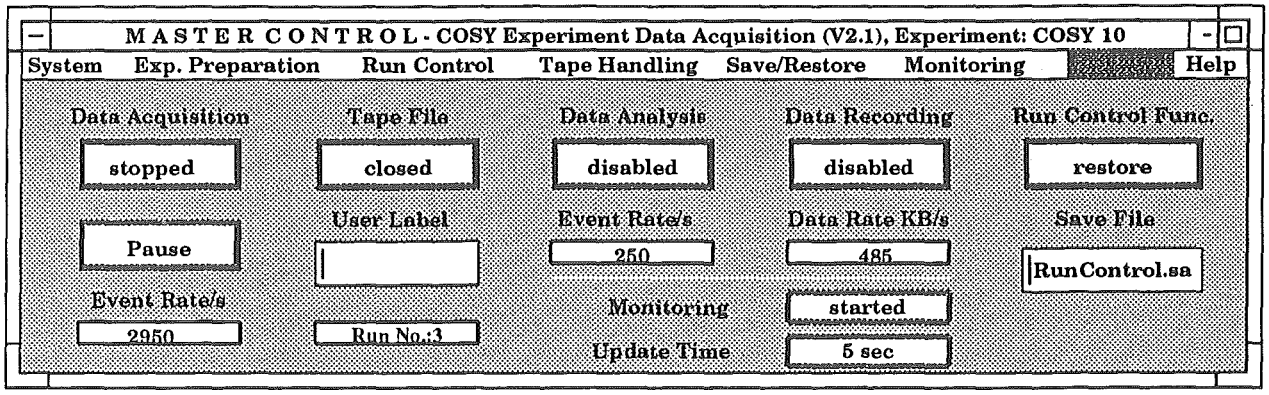

Fig. 2: Main OSF/Motif user interface of the Control System

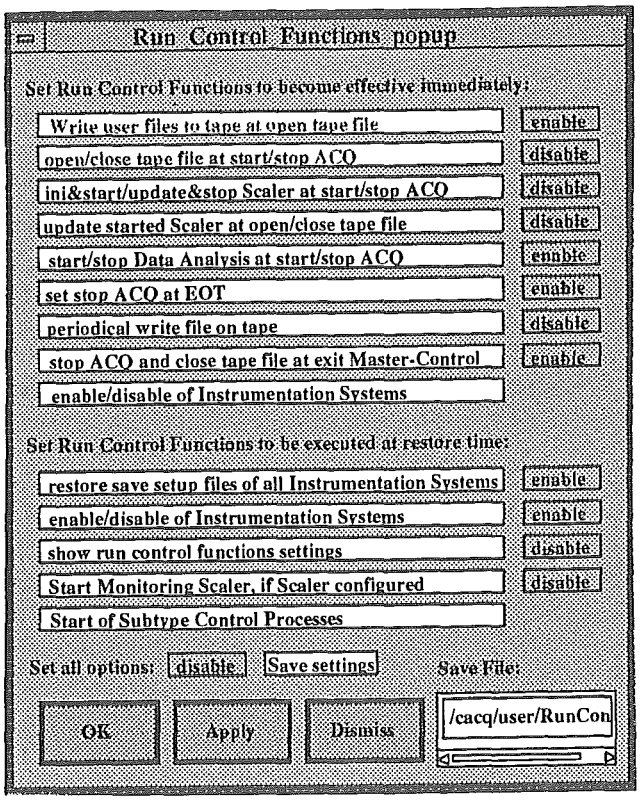

Fig. 3: Hierarchical sequences of control functions

tion System can be chosen in this window. Hence, all other setup and monitoring functionsare arranged by PullDown menus. For both modes of scaler counts monitoring, the periodical and triggered mode, exist dedicated processes with similar outfit. Optionally, this monitoring processes can also be started by master control. In the periodical monitoring of scaler the total counts of each channel and their differences between following updates are implemented too.

All operations for setup, control and data readout have been modified according to the new developed frontend procedures for this Instrumentation System subtype.

A4. Multipurpose System

The functionality of the Multipurpose control process has been improved /1,3/. For module testing, at now FASTBUS and CAMAC modules are supported. After the execution of single procedures or procedure lists, the following data will be interpreted regarding the module type, FASTBUS or CAMAC specific. A multiline editor has been implemented in the OSF/Motif user interface, allowing the definition of various procedures for each configured module was being tested. The execution of this procedures is invoked by cursor in any order as required.

II. Event Distributor

The online and offline Eventdistributors have been improved regarding the decoding of raw data in the Hardware Oriented Event Format (HOEF) and the Detector Oriented Event Format (DOEF) /1,2,3/. Currently, all supported module types in the implemented Digitizing Systems are involved in the Eventdistributors. For the Multipurpose System in digitizing mode, the LeCroy modules scaler type 4434 and 2551 as well as the data register type 2371, which are used in the COSY11 experiment, are decoded.

To achieve the standardized data values for digitizing modules with different conversion characteristics, the HOEF data values are formatted in 32 bit integer and calculated as follows:

- Fastbus LeCroy System:
  - ival = conv_val — for TDC1875 low range
  - ival = 8*conv_val — for TDC1875 high range
  - ival = conv_val-pedestal — for ADC1881
  - ival = conv_val — for all other modules
- all other Digitizing Systems:
  - ival = conv_val — for all modules

Therein, stands for:

conv_val = converted value in binary and
ival = HOEF data value in 32 bit integer.

In DOEF the data values are represented in 32 bit float format and standardized in pC for ADC data and in ns for TDC data. Additionally, for TDCs working in common stop mode, data are computed according to the Common Start Time as follows:

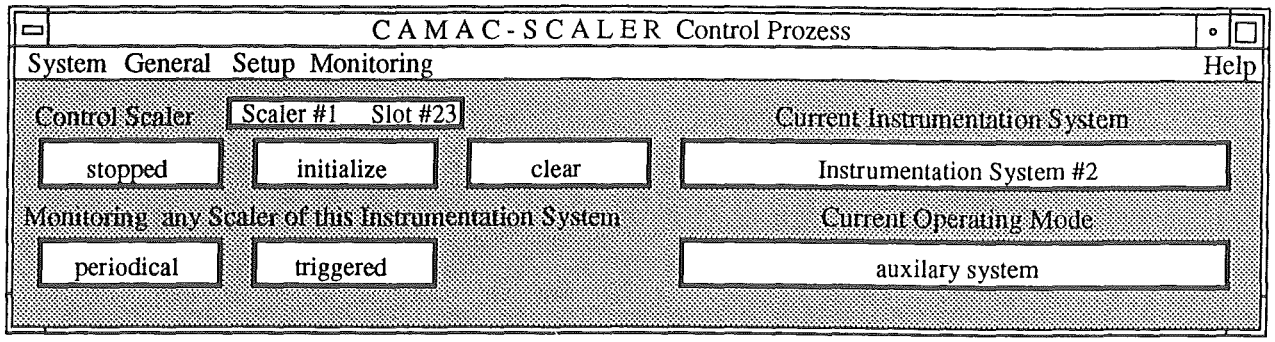

Fig. 4: Main OSF/Motif user interface of the Camac scaler system

- Camac FERA System:
  fval = ival*res/1000 for 4300B ADC
  fval = ival for other modules

- Fastbus Mutiblock System:
  fval = ival*res/1000 for QDS10C2 and TDC10C6
- Camac TDC2277 System:
  fval = ival*res/1000
- Camac Scaler System:
  fval = ival for 4434 and 2551 scalers
- Camac TDC2228 System:
  fval = ival*res/1000
- Camac DRAMS System:
  fval = ival
- Fastbus LeCroy System:
  fval = ival*res/1000 for TDC1875 common start only
  fval = ival*res/1000 for TDC1876/77 common start
  fval = T-ival*res/1000 for TDC1876/77 common stop
  fval = T-(range-ival)*res/1000 for TDC1879 common stop only
  fval = ival*res/1000 for ADC1881
  fval = ival for other modules
- Multipurpose System:
  fval = ival

Therein, stands for:

fval = DOEF data value in 32 bit float,
res = resolution of TDCs in ps and of ADCs in fC,
range= range of TDCs in ps and of QDCs in fC,
T = time delay between common start and common stop signal in ns,
0 <= T[ns] <= range[ns] of the TDC.

The resolution and the range are stored in the module data file and the time delay (T) is a part of the detector lookup table.

References:

/1/ K.H. Watzlawik, N. Brummund, S. Dienel, M. Drochner, W. Erven, M. Karnadi, H. Kopp, K.H. Leege, R. Nellen, W. Oehme, H. Schroeder, J. Stock, P. Wuestner, K. Zwoll, COSY Experiment Data Acquisition, IKP Annual Report 1994, ISSN 0944-2952, Berichte des Forschungszentrums Juelich; 3035, p.256

/2/ K.H. Watzlawik, N. Brummund, S. Dienel, M. Drochner, W. Erven, M. Karnadi, H. Kopp, K.H. Leege, H. Loevenich, R. Nellen, W. Oehme, J. Stock, P. Wuestner, K. Zwoll, COSY Experiment Data Acquisition, IKP Annual Report 1993, ISSN 0944-2952, Berichte des Forschungszentrums Juelich; 2879, p.217

/3/ K.H. Watzlawik, N. Brummund, M. Karnadi, R. Nellen, H. Schroeder, J. Stock (KFA,IKP), K. Zwoll, M. Drochner, P. Wuestner (KFA, ZEL), S. Dienel, K.H. Leege, W. Oehme (FZ Rossendorf), "Control System for Scalable Experiments at COSY", Proceedings of the 1995 IEEE Conference on Real-Time Computers Applications in Nuclear Particle and Plasma Physics, Michigan Sate University, May 24-28, 1995

/4/ K. Zwoll, M. Drochner, W. Erven, J. Hoelzer, H. Kopp, H.W. Loevenich, P.Wuestner (KFA, ZEL), K.H. Watzlawik, N. Brummund, M. Karnadi, R. Nellen, J. Stock (KFA,IKP), S. Dienel, K.H. Leege, W. Oehme (FZ Rossendorf), "Flexible Data Acquisition System for Experiments at COSY", IEEE Transactions on Nuclear Science, February 1994, Vol.41, No.1, p.37

/5/ W. Erven, J. Holzer, H. Kopp, H.W. Loevenich, W. Meiling, K. Zwoll, M. Karnadi, R. Nellen, K.H. Watzlawik, COSY Data Acquisition System for Physical Experiments, IEEE Transactions on Nuclear Science, April 1992, Vol.39, p.148

/6/ K.H. Watzlawik, N. Brummund, M. Karnadi, R. Nellen, M. Drochner, W. Erven, F.J. Kayser, H. Kopp, H. Loevenich, H. Stoff, P. Wuestner, K. Zwoll, S. Dienel, K.H. Leege, W. Oehme, A. Krivshitch, COSY Experiment Data Processing, IKP Annual Report 1992, ISSN 0366-0885, Berichte des Forschungszentrums Juelich; 2726, p.264

* KFA, Zel
**FZ Rossendorf, Germany

11. ELECTRONICS

Electronics

H. Labus, J. Bojowald, G. Brittner, E. Brökel, N. Dolfus, W. Ernst, G. Lürken and K. Winkler

In the electronics laboratory jobs were carried out for the diagnostic devices in the entire COSY-region (source beamline, cyclotron JULIC, injection beamline, synchrotron COSY and extraction beamlines) and for the nuclear experiments at COSY as well as in external accelerator laboratories. The develoments for COSY-diagnostics were performed in intensive cooperation with I. Mohos from the COSY-group. In the following the representative electronic activities are listed and briefly explained. Some of them are also described in detailed contributions of this annual report

Activities for diagnostics at COSY:
The availability of the multi-wire proportional counters (MWPCs) was improved. For online monitoring all devices are now equipped with radioactive test sources (β-radiation). Some electronic components in the high voltage supplies were replaced by those ensuring more stable operation. The computer control of the chamber-gas mixing station was nearly completed. Investigations using 38 MeV protons from JULIC were performed to calibrate the MWPCs in the COSY-extraction for absolute measurement of the extracted particle rates. For movement and positioning of MWPCs, viewers etc. in the beamlines a new pneumatic controlled mechanical system was developed, in order to make such devices considerably more cost-saving in cases of supplement or replacement.
The rf-electronics of the stripline unit was considerably enlarged: (a) for time-gated tune- and BTF-measurements, (b) for beam oscillation excitation by band limited and center frequency tunable noise, (c) for 45°-excitation of beam oscillations resulting in excitation in both planes and thus allowing to observe the walk of the two sidebands or the tune, respectively, in one spectrum and (d) for computer control by GPIB- and serial-interface.
For the Schottky-pickups a special rf-cicuitry was built up, which essentially enhances (by factor of about 20) the sensitivity of the pickups by resonant effects. The center frequency of the resonant range can be tuned by capacitance diodes. At time now the control voltage for the diodes is set manually using a variable voltage power supply; an automatic computer control by graphic user interface (VEE) is proposed.
The VEE-windows (VEE = visual engineering environment), the graphical user interfaces for the control of tune- and WCM(wall current monitor)-measurements were improved and partly extended. For BTF-measurement a new VEE-window was created.
The detector target for the measurement of the horizontal emittance had to be completely reassembled, because large offset currents indicated too low insulation impedances between the individual measuring layers (50 μm thick tantalum layers). The detector target consists of 60 such Ta-layers insulated electrically by ceramic plates. The Ta-layers are contacted and connected with current amplifiers. The electrical insulation was worsened by carbon pollution at the front surface, which was probably produced from glue material in between by the heat during beam irradiation. The ceramic plates were cleaned by plasma-etching in the detector laboratory of IKP and the Ta-layers were replaced by new ones electro-welded in KFA; at the same time the contacting mode was improved. The reassembling of the tiny and sensitive layers was carried out without any glue material.
Several NIM-modules were developed and built up (a) for computer controlled (GPIB) delay of trigger signals and (b) for the distribution of signals over far distances with special respect to avoid disturbances.
The beam pulsing system in the source beamline was extended to make possible diagnostic measurements in the cyclotron or in the injection beamline to COSY, respectively, during the beam-interval time between injections to COSY (depending on COSY cycle-time up-to some minutes).

Activities for the nuclear experiments (at COSY or external):
The control system of the low-energy crystal spectrometer for the measurement of X-rays from exotic atoms was installed and used in experiments at PSI (in Villingen, Switzerland) and afterwards at CERN. At the same time the control system, which is performed by LABVIEW running on PC-platform, was modified and extended. Now alltogether 6 positioning operations (on 2 detector arms) can be carried out and several status signals are generated and registered. For precise adjustment of the spectrometer-crystal a tilting control and a temperature monitoring was realized.
For the internal COSY-experiment ANKE (0°-facility) the development and construction of the start-detector and the associated electronics was started; 50 photomultiplier (1″) bases with high voltage devider, which have to be especially compact due to lack of space, will be developed and manufactured.
Extensive support was given for the installation and test of the analogue electronics of the external COSY-experiment GEM (performed at BIG KARL).
For several experiment groups modules were developed and constructed with signal amplifiers, signal fan-outs, impedance converters etc.; furthermore trigger-electronics for remote control of relays, switches and valves. A lot of coaxial cables, high voltage cables and special cables with particular connectors were produced.

The activities of all experiment groups of IKP were supported by repairs of electronical devices, professional discussions, purchase and storage of electronical components.

12. DETECTORS

Semiconductor Detectors

G. Fiori, A. Hamacher, S. Igel, H. Machner, H. Metz, J. Pfeiffer, D. Protic

The activity of the semiconductor laboratory was concentrated on the construction of the detector system called Germanium Wall [1] for GEM-experiments at COSY. Its first version consisted of the 1 mm thick Quirl-detector with 200 spiral elements on both sides and the E-detector with 32 radial segments. All components of the system, already constructed and separatly tested in the previous year, were mounted into the cryostat. Thorough tests concerning the vacuum, cooling to the LN_2-temperature and the leakage current of all position elements of the detectors were performed. Only several of 400 spiral elements defining the Quirl-detector had higher leakage currents than needed for expected energy resolution of about 5 keV [FWHM]. The E-detector could sustain a bias voltage of several hundred volts above the deplection voltage. Its 32 elements delivered good Cs-137 spectra. During these tests the vacuum was maintained with a turbomolocular pump instead of the ion pump mounted on the cryostat. The reason was a steady increase of the reverse current (only of the E-detector) caused by working ion pump.

Several modifications on 432 preamplifiers and their mounts were needed to improve the power supplies, cooling of components and to reduce the electrical oscillations. NIM-units containing shapers and discriminators were tested and modified for the first experiment.

The cryostat with the detectors at room temperature was then transported together with the LH_2-target to the experimental area and mounted in front of the magnetic spectrometer. After evacuating and cooling to LN_2-temperature the detectors and electronics were tested using radioactive sources and COSY-beam.

The first GEM-experiment was devoted to the $pp \rightarrow d\pi^+$ and $pp \rightarrow pp\pi^0$ reactions. An extensive report about the experiment is given in the section "Experiments at COSY". Both detectors worked properly during the experiment.

Two position sensitive ΔE detectors of the same type were finished for the "Zero degree facility" of CELSIUS in Uppsala, a collaboration with the University of Stockholm. Both contacts were made by ion implantation (boron and phosphorus) and the strips on both sides were separated through plasma-etched grooves defined by the help of the photolithography. 66 strips on p^+-contact and 18 strips on the n^+-contact surrounded by a guard-ring were connected by bonding with aluminum wires to the printed leads on Kapton-foils fixed together with the detector on a holder. In this way each strip can be joined with its own amplifier chain placed outside the vacuum chamber. The position sensitive area amounts to 66x36 mm^2 giving a pitch of 1 mm in x-direction and 2 mm in y-direction. The resolutions measured in a test-cryostat were about 6 keV [FWHM] at 661.6 keV (Cs 137).

All detectors for this collaboration are fixed to the holders using aluminum wires instead of indium. Therefore it is possible to heat them to 450 K inside the vacuum system and the limiting temperature is now determined by printed Kapton-foil.

An older E-detector with radiation damage received during the use inside the CELSIUS-ring was regenerated.

First results achieved with the stack consisting of 3 detectors (position sensitive ΔE-detectors 2.2 mm thick followed by a simple ΔE-detector 1.1 mm thick and an E-detector with a thickness of 14.5 mm) placed inside the CELSIUS-ring are interesting and will soon be published.

In collaboration with ESRF-Grenoble and KFKI-Budapest the development of germanium strip detectors was continued with regard to the best possible resolution. Three elements of 0.2x20 mm^2 separated by grooves 35 μm wide and surrounded by guard-ring were connected to the cooled first stages of the preamplifiers mounted inside the cryostat. For the 60 keV γ-rays the measured resolutions amounted to 0.62 keV [FWHM] and 0.52 keV [FWHM] for the pulser peak. The resolution of the preamplifiers without being connected to the strips was much better: 0.28 keV [FWHM]. The resulting contribution attributed to the strip alone is 0.44 keV [FWHM]. This seems to be quite high and additional investigations are needed to explain and reduce it. One reason could be that the resistance between the adjacant strips was not high enough.

Commercial silicon and germanium detectors were tested and repaired in urgent cases. A group from the University of Bonn was supported during the development and fabrication of special targets by making use of facilities for photolithography and ion-etching.

Reference:

[1] Annual Report IKP 1994, Jül-3035, p. 273

Targets

J. Pfeiffer, D. Protic

A series of different targets was produced for IKP-groups and outward laboratories. UF_4-targets on carbon foils (20 $\mu g/cm^2$) were prepared for COSY-13-experiments. One damaged carbon target of COSY injection system was replaced by a new one. A store of carbon targets for COSY injection system was periodically inspected and the poor targets were exchanged. Various materials (scintillators, foils) were coated by evaporation off different metals.

Silicon Quirl-Detectors

E. Bialkowski, A. Hamacher, K. Kilian, H. Machner, D. Protic

First measurement with the germanium Quirl-detector during the GEM-experiment at COSY confirmed the importance of such a detector type for describing the kinematics of reaction products. Similar silicon Quirl-detector could be also used at different COSY-experiments. Operating at room temperature they could be mounted almost massless using properly formed Kapton-foils with printed leads. There is only one important demand on the detector itself: the electronic resolution of a position element of the detector defined by grooves in the form of Archimedes' spirals should enable detection of minimum ionizing particles. For detectors 350 μm thick, the energy loss of such particles amounts to 100 keV. Silicon Quirl-detectors with spiral elements having an electronic resolution in order of 10 keV [FWHM] would be ideally suited for further COSY-experiments.

Position sensitive detectors of excellent quality can be ordered at several manufacturers, however, there are reasons for producing them in our semiconductor laboratory.

1. Our technology, almost identical for silicon and germanium detectors, is much simpler than the standard planar technology regularly applied by manufacturers of silicon detectors. For example, only one mask with the desired structure is needed for the photolithography on both detector contacts.
2. We do not need a guard-ring around the central hole of the detector. The sensitive volume of the spiral elements extends up to the hole, thus enabling detection of the reaction products even under small angles.
3. Commercially available position sensitive silicon detectors made by the planar technology contain always a relatively thick silicon dioxide layer which is mainly responsible for the failure due to radiation damage. In our technology we need no such silicon dioxide layer.
4. An important aspect is the so called "massless mount" which can be only realised in close interaction between experimenters and detector manufacturers.

The development of the silicon Quirl-detectors for COSY-experiments has been started last year in collaboration with INP-Cracow and ISI. A series of 500 μm thick silicon wafers (diameter of 45 mm) with a central hole was lapped and chemically etched before ion-implantation. Boron and phosphorus ions were implanted into opposite sides of the wafers. Both sides were then covered with evaporated aluminium (0.3 μm) and annealed at 700 K. The resulting p^+-n-n^+ diodes had a relatively high leakage current of about 10 μA at the depletion voltage of 100 V. Such a high leakage current does not permit the use of these diodes as detectors for charged particles (too high noise).

However, dividing a contact area of the diode into 200 spiral position elements (surrounded with a guard-ring) by realizing the Quirl-structure will lead to a leakage current of less than 50 nA per element. This relatively small current should enable an energy resolution in order of 10 keV [FWHM] for each position element.

The same Quirl-structure (200 spiral elements) performed by the very similar technique as for germanium detectors [1], using the same photomask, was realised on the p^+-contact of a silicon diode and on the n^+-contact of another. Extensive tests in two environments, air and vacuum, led to following results:

- the depletion voltage of diodes 400 μm thick, determined with the help of α-particles, amounted to ~ 100 V;
- the current flowing through the spiral position elements amounted to 10-30 nA at 100 V and about 50 nA at 300 V;
- the resistance between adjacent elements, at operating bias (100-300 V), was greater than 1 MΩ ;
- the electronic resolution, determined by means of pulser, amounted to 10.5±2.9 keV [FWHM] for the tested elements of the n^+-contact and less than 10 keV [FWHM] for p^+-contact;
- depending on the environment there was some difference in the measured values of leakage current and resistance between adjacent elements but with no serious influence on the resolution figures.

Several diodes received the Quirl-structure with 200 elements on both contacts and will soon be mounted in a holder and tested. Further developments will be concentrated on the Quirl-detector of the same size but with 128 position elements on each contact. The mask for the photolithography is under construction at ISI. Using only 4 commercial available readout ICs (32 channel 45 ns amplifier/shaper for silicon strip detectors with 32 analog outputs) connected to a Quirl-detector one would drastically reduce the demands for money and space. This will enable COSY-experiments to run with several detectors in a stack behind the target.

The existing collaboration with ISI, ZEL and INP-Cracow will be pursued.

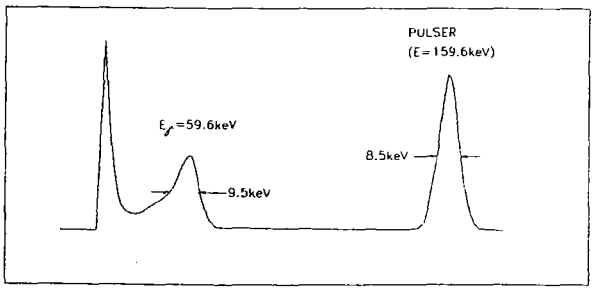

Fig. 1: γ-spectrum of ^{241}Am measured with a Quirl-element of the p^+-contact at room temperature

Reference

[1] Annual Report IKP 1993, Jül-2879, p. 242.

13. EUROPEAN SPALLATION SOURCE (ESS)

Nuclear Studies of Different Target Systems for the European Spallation Source (ESS)

D. Filges, R.D. Neef, H. Schaal

Nuclear simulation calculations to study various target concepts for the "European Spallation Source (ESS)" concerning a proton beam power of 5MW have been performed. For different target systems as rotating wheel targets,stationary targets and liquid metal targets results of beam energy - and target material investigations,induced radioactivity and afterheat production as well as usuable neutron fluxes are discussed.

1. Introduction

The simulation calculations were done using the HERMES code system [1]. This theoretical study here is directed towards assessing physics feasibility of discussed ESS target station concepts.The aim is to show the feasibility of the anticipated nuclear parameters,which will be necessary for the evaluation of the final design.

2. Beam Energy Studies

One of the first questions to us was which is the optimum proton beam energy in respect to a high thermal neutron flux in the moderators, to a long lifetime of target windows and target material, and in respect to necessary cooling power. From the experience of running spallation sources it was clear that proton beam energy should be in the energy range from 800 MeV up to 3000 MeV. In the beginning of the project we calculated a double wheel target (Fig. 1) and a double split target (Fig. 2) with three moderator positions with first moderator in front of the target, second moderator in flux trap position between target one and two, and third moderator behind second target. In Fig. 3 we can see a linear decrease of thermal neutron flux of the upstream moderator with increasing proton energy from 800 MeV up to 3000 MeV. The proton beam energy dependent thermal neutron flux in the intermediate moderator, decreases less with proton energy at a higher flux level. In contrary to neutron flux dependence in moderators described above the thermal neutron flux in the downstream moderator increases with increasing proton beam energy. Around 1500 MeV proton beam energy fluxes of up- and downstream moderators have similar values. Therefore, from neutron flux calculations there is no strong tendency to a special proton beam energy and either energy should be good.

Figure 4 shows the proton energy dependent power deposition in the first part of the split target and in the whole target. Between 800 MeV and 1600 MeV there is a strong decrease of power deposition which is much less versus higher proton energies. From this figure the proton beam for a target should not be far below 1500 MeV.

We investigated the power deposition in the target plates in an area of radius 1cm around the proton beam axis. Figure 5 shows a power deposition of 11 kW/cm^3 in the first two target plates. This power deposition is reduced by a factor of two by increasing the proton beam energy from 800 MeV to 1600 MeV. A further doubling of the proton energy gives less reductions than factor two for the power deposition.

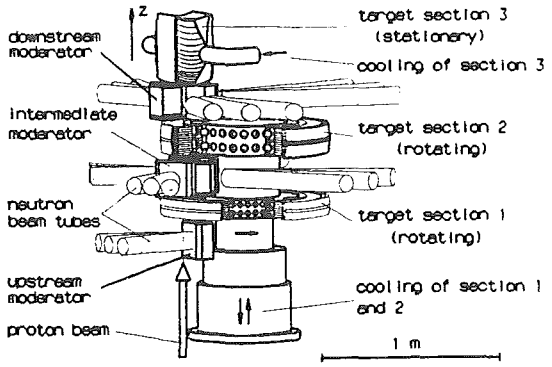

Fig. 1: Rotating double split target for vertical proton beam injection (rotation frequency 1 Hz)

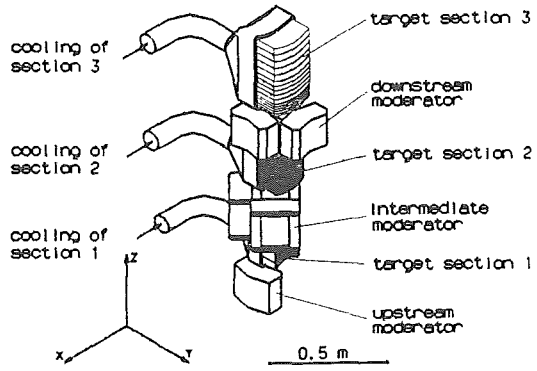

Fig. 2: Stationary double split target for vertical proton beam injection

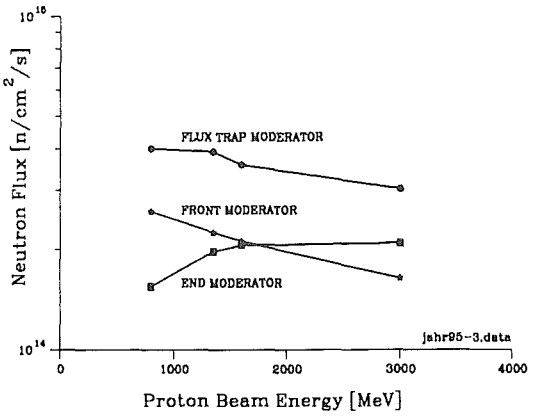

Fig. 3: Thermal neutron fluxes in moderators as a function of incident,proton energy

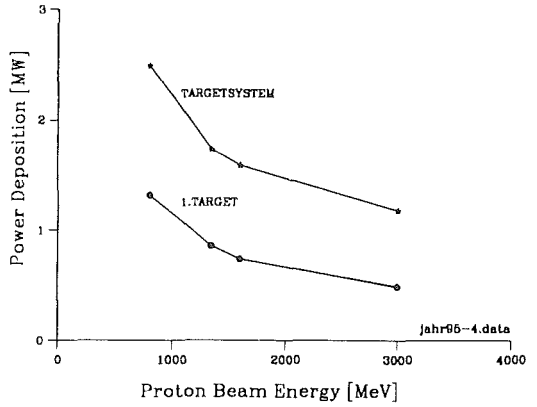

Fig. 4: Power deposition in target systems as a function of incident proton energy

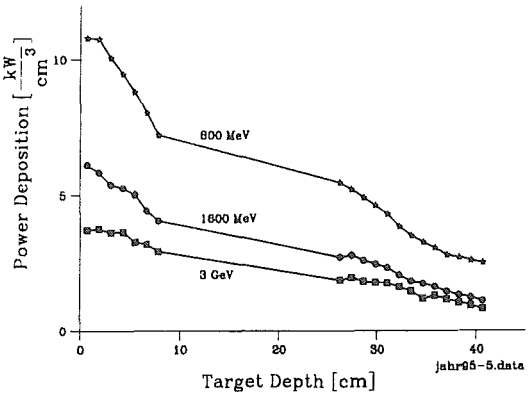

Fig. 5: Power deposition in target plates in an area of radius 1cm around beam axis

Each proton pulse of a 5 MW at 50 Hz machine contains an energy of 100 kJ which is introduced into the target. This produces a space dependent temperature jump in the target material. For a gaussian shaped circular proton beam (s = 2.5) truncated at diameter 10 cm a temperature jump of 40 K, 25 K, and 15 K for 800 MeV, 1600 MeV, and 3000 MeV is produced in the center of the first W-target plate.

The double wheel split target Fig. 1 and the stationary split target (Fig. 2) from neutronical point of view do not differ much from one another. The rotating target has the advantage that irradiation damages and heat loads of beam window and target plates are considerably lower by a factor of 50 and this means a longer lifetime by a factor of 50. The advantage of the stationary target is the lower fabrication cost. As reference target a non-split stationary target as depicted in Fig. 6 was chosen (see details in Ref. [2] (ESS reference proton beam energy is 1.334 GeV)

3. ESS Reference Energy Studies

The reference 5 MW target (see Fig. 6) is horizontal, non-split and cooled by H_2O. It consists of three stacks of slightly 1D-bent rectangular plates. The centre stack, made of tantalum as reference material, acts as the target, the

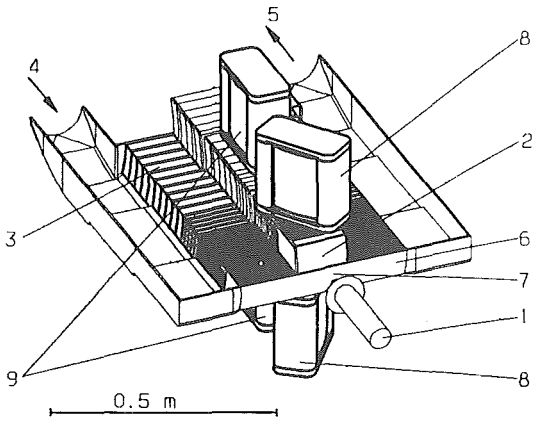

Fig. 6: Reference 5 MW ESS target with moderators (1: proton beam, 2: target plates, 3: wing reflctor plates, 4: coolant inlet, 5: coolant outlet, 6: target vessel, 7: beam window, 8: cold moderator, 9: room temperature moderator)

two other stacks on its left and right side integrated in the target are part of the reflector and are manufactured of nickel. All stacks are cooled by the same water stream in y-direction. The described target plate configuration has the front (x-y-plane) dimension of 120 x 400 mm^2 which increases to 160 x 400 mm^2 to allow for the scattering of the proton beam. The length (z-direction) of solid target material is 580 mm and, due to the cooling gaps between the plates, the overall length of the target is 690 mm. The rest of the nickel reflector, not shown in Fig. 6, encloses the target inside the volume of 900 x 800 x 1050 mm^3 (x,y,z).The ESS proton beam energy was chosen to 1.334 GeV.

To achieve the same heat flow on the surface of each target plate their thicknesses are increased in bundles of five plates from 2.6 mm up to 30 mm. The total number of plates in each stack is 55. Because of the thickness variation the water content in the cooling gaps decreases from 22% in the first cooling gap down to 8% in the last. The average water content in the target is 10%. The beam window is part of the target container and will be 2D-curved.

To simulate the transport of hadrons and to estimate particle fluxes, energy deposition and induced radioactivity the HERMES code system [1] has been used. First neutron flux estimations for the 5 MW target have been performed under the condition that all four moderators were H_2O-moderators at room temperature. For these calculations the target material was tungsten to compare the results with those of the SNQ study [3]. A detailed 3D-geometry configuration of the target has been considered. In Table 1 neutron yields per proton for the reference target with tungsten as target material are compared to various target systems of the SNQ study [3].

Targets and moderators which have been studied in the SNQ project have been compared for their average thermal neutron flux with a similar fast moderator at the ESS target. The average ESS thermal neutron flux differs by

less than 5% from that of the corresponding SNQ value, for a 5 MW beam power.

Table 1: n/p values for various targets

target	n/p 1100 MeV	n/p 1334 MeV
SNQ: U_{dep}-H_2O-Al	33.1	40.2
SNQ: Pb-H_2O-Al	21.5	26.0
SNQ: W-H_2O-Al	23.4	28.4
SNQ: W_{solid}	25.6	31.1
ESS: W*	-	31.5

Table 2: Comparison of thermal neutron fluxes in fast moderators of the SNQ and ESS for 5 MW proton beam power

target	$\Phi_{thermal}$ [n/(cm^2·proton)]	$\Phi_{thermal}$ [n/(cm^2·s)]
SNQ: U_{dep}-H_2O-Al	$2.6 \cdot 10^{-2}$	$7.5 \cdot 10^{14}$
SNQ: Pb-H_2O-Al	$1.6 \cdot 10^{-2}$	$4.5 \cdot 10^{14}$
SNQ: W-H_2O-Al	$1.8 \cdot 10^{-2}$	$5.1 \cdot 10^{14}$
SNQ: W_{solid}	$2.0 \cdot 10^{-2}$	$5.6 \cdot 10^{14}$
ESS: W*	$2.1 \cdot 10^{-2}$	$4.9 \cdot 10^{14}$

One should take into account that the flux values of Table 2 depend on the chosen target-moderator-reflector geometry and should be taken as first approximations of the expected neutron flux.

4. Target Material Studies of Tantalum,Tungsten and Mercury Targets

4.1 Usuable Neutron Fluxes

Based on the above discussed scoping calculations we compared the nuclear properties of three target material candidates, namely tantalum, tungsten, and mercury using the target geometry given in Fig. 6. For optimal positioning of the moderators it is important to know the distribution of the neutron flux density along the surface of the target. In Fig. 7 for bare reference targets (Ta- and W- with water cooling; and Hg-filled,-only with mercury-) we show the surface leakage current distributions of neutrons below energies of 20 MeV as a function of target depth. The tantalum target delivers the lowest neutron current. In the maximum of the neutron current distribution W and Hg target give same values but downstream the Hg target produces higher currents.
Figure 8 shows for lead-reflected target systems that the tantalum target delivers the lowest neutron current. A tungsten target gives a neutron current which is about 20% higher in the maximum. The highest neutron currents at the target surface are produced by the mercury target and are more than 30% higher compared to the tantalum target. Especially along the target surface the current gradient in case of Hg is lower than in case of the W target. This means that the downstream moderators receive an even higher percentage of neutrons in case of mercury.

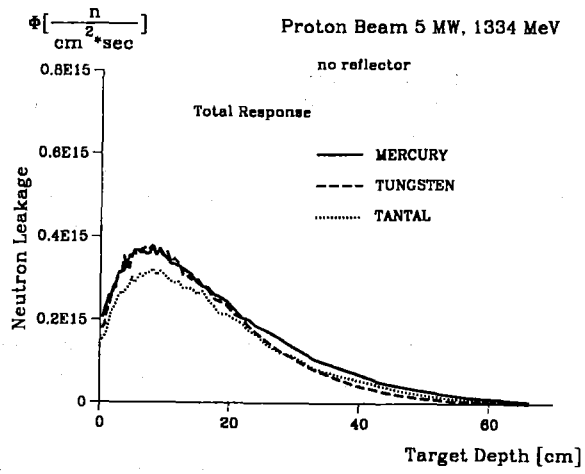

Fig. 7: Leakage distributions for neutrons below 20MeV of bare reference targets

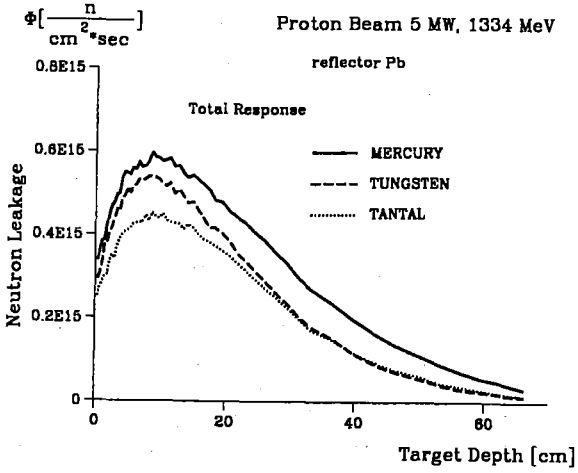

Fig. 8: Leakage distributions for neutrons below 20MeV of reflected reference targets

The following table (Tab. 3) shows a comparison of possible fast and thermal neutron fluxes averaged about the moderator volume.

Table 3: Fast and thermal neutron fluxes of Ta, W, and Hg targets

Target	Φfast [n/(cm^2 · s · 5 MW)] upstream	downstream Moderator	Φthermal [n/(cm^2 · s · 5 MW)] upstream	downstream Moderator
Tantalum	$7.25 \cdot 10^{13}$	$2.30 \cdot 10^{13}$	$3.19 \cdot 10^{14}$	$1.52 \cdot 10^{14}$
Tungsten	$6.42 \cdot 10^{13}$	$2.14 \cdot 10^{13}$	$3.52 \cdot 10^{14}$	$1.67 \cdot 10^{14}$
Mercury	$8.21 \cdot 10^{13}$	$3.52 \cdot 10^{13}$	$3.91 \cdot 10^{14}$	$2.29 \cdot 10^{14}$

4.2 Induced Radioactivity and Afterheat Production

The procedure to calculate the radioactivity and afterheat in the different materials Ta, W, and Hg proposed as ESS target materials consists of using the HERMES system[1]

to calculate the nuclide production rates caused by the spallation process and to generate the neutron source and then using MORSE[1] with the recently released cross section library MATXS11[4] to calculate the production rates caused by neutrons with energies below 15 MeV. All nuclide production rates are handed over to the nuclide generation and depletion code ORIHET[5], which calculates radioactivity and thermal power for different beam and decay times.

All calculations described here were performed for ESS beam energy 1.334 GeV and 5 MW proton beam power. The geometry used for the Monte Carlo calculations is described above. Because the reason of the study is the comparison of the different target materials Ta, W and Hg, we restricted ourselves to calculate the values of the target zones only, assuming that the activity and afterheat of the surrounding reflectors, moderators, and cooling systems are nearly the same for the different target materials. The nuclide generation and depletion was calculated for a full power beam time of 1 year and after shut down of the beam for decay times reaching from 1 day to 100 years. The results are given separately for those caused by spallation and those caused by neutrons with energies below 15 MeV.

The most interesting time with respect to problems of cooling and handling of the target is the time when the beam is shut down. The amount of radioactivity and thermal power for the three different targets is compared in Table 4. It can be seen that the activity and thermal power caused by spallation are nearly the same for all three targets, but the amounts caused by the low energy neutrons are quite different. Therefore the total amount of activity and afterheat is largest in the tantalum target, followed by the tungsten target. Here the mercury target shows the lowest values.

Table 4: Comparison of radioactivity and thermal power at shut down time for different targets for 5 MW proton beam power and 1 year full power operation

	Tantalum	Tungsten	Mercury
Radioactivity [Tbq]			
-total power	$4.55 \cdot 10^5$	$1.63 \cdot 10^5$	$1.10 \cdot 10^5$
-caused by spallation	$6.94 \cdot 10^4$	$7.73 \cdot 10^4$	$7.28 \cdot 10^4$
-caused by neutrons below 15 MeV	$3.85 \cdot 10^5$	$8.75 \cdot 10^4$	$3.67 \cdot 10^4$
Thermal power [kW]			
-total.power	56.9	15.40	9.21
-caused by spallation	8.94	8.75	7.21
-caused by neutrons below 15MeV	48.0	6.60	2.00

Next question is about the long term radioactivity and afterheat production with respect to storage and waste management. The time behaviour of the three targets is shown in Figs. 9 and 10. After 100 years the largest activity is found in the mercury target. But this value is 4 orders of magnitude smaller than the starting value.

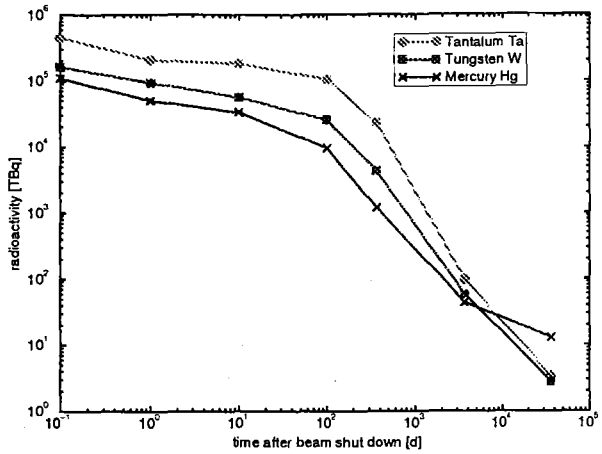

Fig. 9: Time behaviour of radioactivity in Tbq in Ta-, W-, and Hg- targets after 1 year full power operation

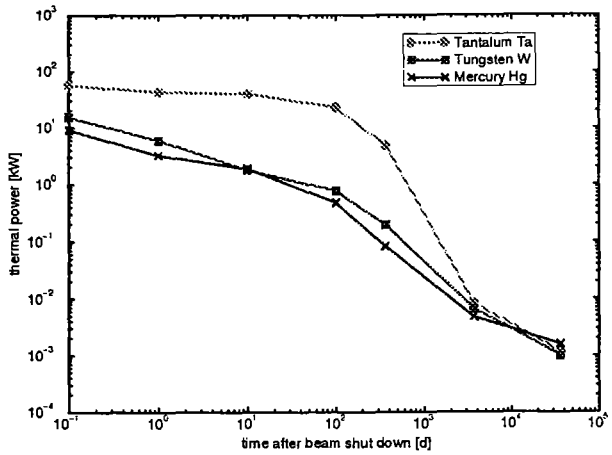

Fig. 10: Time behaviour of thermal power in kW in Ta-, W-, and Hg- targets after 1 year full power operation

It should be mentioned that the nuclide data base of the code ORIHET is incomplete. So the results of activity and thermal power caused by spallation should be increased by about 10 percent.

5. References

[1] P. Cloth et al., HERMES, A Monte Carlo program system for beam materials interaction studies, Report Jül-2203, May 1988

[2] I.S.K. Gardner, H. Lengler, G.H. Rees, (Editors), Outline Design of the European Spallation Neutron Source, Report ESS 95-30-M, September 1995

[3] SNQ-Project Proposal for a Spallation Neutron Source, KFA-Jülich, Dec. 1991

[4] R.E. MacFarlane MATXS 11, RSIC Data Library Collection, Report DLC-177, 1994

[5] J. Bell, ORIGEN, The ORNL Isotope Generation and Depletion Code, ORNL-Report 118680, 1973

The Design of FFAG - Fixed Field Alternating Gradient - Synchrotrons

S.A. Martin, P.F. Meads*, E. Zaplatin**, K. Ziegler**

The requirements are discussed for an FFAG using high intensity proton beams ($2.5 \cdot 10^{14}$ particles per pulse) suitable for an average beam power of 2.5 or 5 MW. Different scenarios has been discussed: Acceleration from 400 to 1600 Mev, or from 800 to 2500 MeV, or the two stage version accelerating from 400 to 800 MeV and from 800 to 1600 MeV in the 2nd stage. The injected beam consists of H^- delivered by a 400 (800) MeV linac. The lattices are radial type FFAG with superferic magnets. The charge exchange injection into the FFAG is optimized in terms of minimum particle losses. Dynamic apertures are calculated using the code ORBIT. A first estimate of the technical feasibility is discussed. Rough cost estimations are given.

The general properties of the FFAG for intense proton beams have been discussed in ref. [1]. The basic parameters of an FFAG have been recommended at workshops for a European Spallation Neutron Source. A example is an FFAG with an injection energy of 800 MeV, 50 Hz repetition rate and a beam power of 5 MW at the extraction energy of 2.5 GeV. Basic parameters of this machine are given in Table 1. From the average 5 MW beam power follows the $2.5 \cdot 10^{14}$ particles per bunch.

Table 1
General Specification for the 2.5 GeV FFAG

Beam Power	5	MW
Average Beam Current	2	mA
Energy at Injection	800	MeV
Energy at Extraction	2500	MeV
Average Radius at Injection	36.31	m
Average Radius at Extraction	38.00	m
Field Index k	16.95	
Repetition Rate	50	Hz
Number of requested Particles	$2.5 \cdot 10^{14}$	per puls
Br at Injection	4.88	Tm
Br at Extraction	11.03	Tm
Peak Magnet Field at Injection	2.31	T
Peak Magnet Field at Extraction	5.0	T
Cell Length	9.95	m

The 24 sector FFAG configuration is based on a super conducting magnet with a maximum field of 5.0 Tesla and a minimum field of -1.7 Tesla. The injection is at an average radius of 36.3 m, and extraction occurs at an average radius of 38 m. The requested field index k describes the radial field through $B/B_0=(R/R_0)^k$, it is related to the transition energy by $\gamma_{tr} = \sqrt{k+1}$. To work safely below transition requires k>>12. The chosen field index results in a radial distance from the injection orbit to the extraction orbit of 1.71 m. Each of the 24 cells has a length of 9.95 m, of which 7.94 m is the approximate length of the straight section. Injection will be done by charge exchange of H^- ions from an 800 MeV linac or another FFAG as it has been proposed by R.L. Kustom and G. Bauer [2].

The optical parameters are optimised to yield the maximum acceptance at the requested field index. The tunes are horizontal Q_x=4.78 and vertical Q_y=3.29. Table 2 shows further parameters.

Table 2
Lattice Parameters for the 2.5 GeV FFAG

Horizontal Tune Q_x	4.78	
Vertical Tune Q_y	3.29	
Horizontal Phase Advance per Cell	71.70	degree
Vertical Phase Advance per Cell	49.35	degree
b_{xmax}/R	0.2967	
b_{xmin}/R	0.1778	
b_{ymax}/R	0.3206	
b_{ymin}/R	0.2893	
Laslett Tune Spread DQ	0.2	
Emittance, normalised	243	π mm mr
Emittance at Injection	156	π mm mr
Beam Diameter	87	mm

The program ORBIT [3] was originally written during 1983-1985 to study FFAGs for the German SNQ program. It has been extended to allow automatic adjustment of the field index and the geometry of the magnets. The b-functions scale with the momentum and machine radius, which is a consequence of the FFAG general scaling property [4]: All orbits are photographic enlargements of a reference orbit. The integration method of Bulirsch-Stoer [5] has been implemented in the ORBIT Code. It is faster for high accuracy than the 8th order Runge-Kutta method. For the estimation of he dynamic aperture 512 sectors usually have been calculated. The horizontal and vertical planes are coupled. But the dynamic apertures are very large as shown in Figure 1.

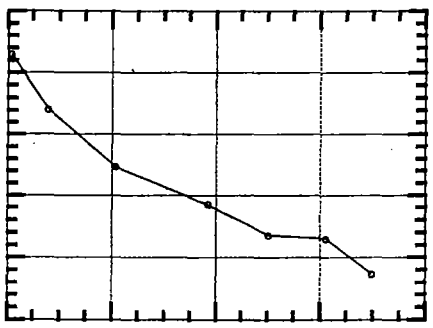

Fig. 1: Dynamic aperture for the 2.5 GeV FFAG. The tunes are Qx=4.78, Qy=3.29 at a field index of k=16.69

Vertical focusing in a radial type FFAG is done primarily by the alternating gradient created by the presence of negative gradient magnets. A pure radial machine becomes reasonably compact if strong magnetic fields of up to 5 T are used, as was shown in earlier work [6]. First design studies for the magnet have been done using the programs MAFIA [7] and PROFI [8]. Basic magnet data are given in Table 3.

Table 3
Magnet Data for the 2.5 GeV FFAG

Number of Magnets	24	
Field extraction	5	T
Field at injection	2.31	T
Flutter	64	
Bend Angle total	15	degrees
Positive Bend Angle	30	degrees
Negative Bend Angle	2·7.5	degrees
Vacuum Chamber Clearance horizontal	1.83	m
Vacuum Chamber Clearance vertical	98	mm
Magnet Size radial	2.31	m
Magnet Gap maximum	158	mm
Number of Super conducting Coils per Cell	6	
Max. Ampere Turns	2.1	MA
Maximum Thermal Loss per Magnet	20	W
Iron Weight per Magnet	243	t

The azimuthal width of the magnet at the extraction radius is 2.01 m. The magnet is scaling so the azimuthal width is proportional to the radius. The positive portion of each magnet bends the beam by 30 degrees, and each of the two reverse field sections bends the beam by -7.5 degrees in the reverse direction making the total net deflection of the beam through the magnet 15 degrees. First results of the magnetic design show that the requested field shape can be realised using one pair of coils for the positive bending magnet and one pair for each of the two negative bending gully field magnets. The multipole content of the main magnet is given by

$$B(\Delta r) = 3.417 + 1.555\,\Delta r + 0.333\,(\Delta r)2 + 0.0445\,(\Delta r)3$$

with $\Delta r = r - r_{av}$ and $r_{av} = 37.154$m .

The maximum field near the coils will not exceed 5.7 T. This is consistent with standard super conducting technology. The maximum gully field is below 2.2 T. A field shaping by the iron only has been discussed. This would require only two coils for the main magnet. A pure air coil option has been discussed by R.L. Kustom [2].

The orbit frequency is 1.107 MHz at injection and 1.208 MHz at extraction; the frequency swing is 9 %. We propose to accelerate on the first or second harmonic. The separation between two bunches would be 414 ns (centre to centre), even on the second harmonic that is enough gap for the extraction kick. The basic RF data are given in Table 4 for the acceleration on the first harmonic.

Table 4
RF-System for the 2.5 GeV FFAG

Cavity Type	Single ended, Ferrite Loaded	
Number of Cavities	16	
Frequency at Injection	1.107	MHz
Frequency at Extraction	1.208	MHz
Harmonic Number	1	
Peak Voltage per Cavity	20	kV
Ferrite Type	Philips 4M2	
Acceleration Gap radial length	1.7	m
Physical Length	1.25	m
Ferrite Area	0.25	m^2
Ferrite Volume	1.6	m^3
Ferrite max. Permeability	100	
Maximum Acceleration	260	kV / turn
Shunt Impedance	3.4	k½
RF Power Loss	59	kW

A detailed description of the RF parameters is given in a separate note [9].

A parametric cost estimation has been done to optimise the design in terms of the physical parameters and costs. This cost estimation is done in DM because the system costs for buildings, support structures, electricity, water, etc. are available at the KFA Jülich. The basic cost factors have been taken as follows. - For the magnets: iron and machining 6 DM per kg; super conducting coils 1.08 MDM per magnet; vacuum and support 450 kDM per magnet. The investment per magnet is estimated to be 3.8 MDM - For shielding and building: 300 DM per m^3 of building; 500 DM per m^3 of shielding material. - For diagnostics: 10 kDM per pick up; 12 MDM for controls. - For electricity: beam to plug efficiency 30 %; electrical installation 1 DM per W; cost factor power 0.25 DM per kWh; thermal efficiency for super conducting losses 700 W electric per W thermal. - For cooling water: installation 1 DM per W; 3 DM per wasted m^3 of water; overall temperature increase of cooling water is DT=6 degree. - For operation: 5000 h per year. Some additional costs as land, roads, depreciation etc. have not been taken into account because they do not have a strong influence on the machine design.

Table 5
Cost Investment for the 2.5 GeV FFAG

All Magnet Cost	40	MDM
Total Shielding total	18	MDM
RF total	53	MDM
Diagnostics total	21	MDM
Instrumentation	41	MDM
Building	34	MDM
Investment total	207	MDM
Operation:		
Cost of Electricity per Year	26	MDM
Cost of Water per Year	12	MDM

The main attractiveness of the described system are - the better efficiency for the wall plug to beam transformation relative to linacs, - the relaxed requirements on the injector because the adiabatic trapping at injection does not require a chopped beam for injection at 800 MeV, - the activation due to injection losses is smaller than in a linac+compressor solution, because 70 % of the beam power is gained in the FFAG, - the main field is dc (no pulsed magnets), the radial aperture is large, - the dynamic apertures are huge, - the momentum acceptance is very large, - the shimming of the dc magnets is easy.

The FFAG has the possibility to deliver a factor of 2-3 more power by going up with the repetition frequency. As a possible future option the repetition rate could be lowered to 10 Hz by stacking the beam inside the ring before extraction as has been proposed earlier [10].

References:

[1] S.A.Martin, E. Zaplatin, P.F.Meads Jr., G. Wüstefeld, K. Ziegler, "STUDY OF AN FFAG SYNCHROCYCLOTRON FOR A PULSED NEUTRON SOURCE", Proc. of the XIII Intern. Conference on Cyclotrons and their Applications, 6-10 July 1992, Vancouver

[2] G. Bauer, R.L. Kustom, private communication, Feb. 1994

[3] P.F. Meads, "A New FFAG Orbit Code", IEEE Trans. Nucl. Sci. NS-32, p. 2243 (1985); and more in "Further Studies of an Interesting 2.5 GeV FFAG for the ESS", techn note Apr 1994, also "Some Comments on the Use of FFT and the Calculation of Emittance in ORBIT", techn. note, March 1993

[4] A.A. Kolomensky and A.N. Lebedev, "THEORY OF CYCLIC ACCELERATORS", North-Holland Publishing Comp. Amsterdam, 1966, p. 332-352

[5] J. Stoer, R. Bulirsch, "Introduction to Numerical Analysis", Springer-Verlag New York, 1980

[6] P.F. Meads and G. Wüstefeld, "An FFAG Compressor and Accelerator Ring Studied for the German Spallation Neutron Source", IEEE Trans. Nucl. Sci. NS-32, p.2697(1985)

[7] T. Weiland, "MAFIA - Release 3.1", Darmstadt 1991

[8] PROFI-Engineering, Darmstadt

[9] E. Zaplatin, "FFAG RF System Study", technical note, Berlin, Nov. 1993

[10] R. L. Kustom, "The ASPUN project", in "Advanced Neutron Sources 1988", Inst. of Phys. Conf. Series No. 97, Bristol + New York(1989)

* Oakland, USA

** Hahn-Meitner-Institut, Berlin

V. SCIENTIFIC COUNCIL COSY

Prof. Dr. J. Cameron	Indiana University
Prof. Dr. D. Drechsel	University of Mainz
Prof. E.M. Henley	University of Washington
Prof. Dr. D. Husmann	University of Bonn
Dr. P. Paul (Chairman)	State University, New York
Dr. D. Reistad	University of Uppsala
Prof. Dr. Schoch	University of Bonn
Prof. Dr. H.-J. Specht	GSI Darmstadt
Prof. Dr. E.W. Vogt	TRIUMF Vancouver
Prof. Dr. Th. Walcher	University of Mainz
Prof. Dr. H. Chr. Walter	PSI Villigen
Prof. Dr. D. Welte	ICG-4, KFA Jülich

VI. ADVISORY COMMITTEES AT COSY

PAC (Program Advisory Committee)
until Dec. 31, 1995

Prof. Dr. G.E. Brown	NORDITA Copenhagen
Prof. Dr. H. Freiesleben	T.U. Dresden
Prof. Dr. K. Goeke	University of Bochum
Dr. D. Grzonka	IKP, KFA Jülich
Dr. H. Herr	CERN, Genf
Prof. Dr. B. Höistad	University of Uppsala
Prof. Dr. K. Kilian	IKP, KFA Jülich
Prof. C. Leluc-Lechanoine	University of Genf
Prof. Dr. U. Lynen	GSI Darmstadt
Dr. R. Maier	IKP, KFA Jülich
Prof. Dr. T. Mayer-Kuckuk	University of Bonn
Prof. Dr. V. Metag	University of Gießen
Dr. W. Oelert	IKP, KFA Jülich
Prof. Dr. E. Rössle (Chairman)	University of Freiburg
Prof. Dr. B. Schoch	University of Bonn
Prof. Dr. O. Schult	IKP, KFA Jülich
Prof. Dr. K. Sistemich	IKP, KFA Jülich
Prof. Dr. J. Speth	IKP, KFA Jülich
Prof. Dr. Y. Terrien	SATURNE Saclay

ENC (Exekutiv-Komitee zur Nutzung COSY)

Dr. K.W. Baurmann	WTA, KFA Jülich
Dr. D. Grzonka	IKP, KFA Jülich
Prof. Dr. D. Husmann	University of Bonn
Prof. Dr. K. Kilian	IKP, KFA Jülich
Prof. Dr. T. Mayer-Kuckuk	University of Bonn
Dr. R. Maier	IKP, KFA Jülich
DI U. Pfister	AP, KFA Jülich
Prof. Dr. E. Rössle	University of Freiburg
DK R. Scheid	FA, KFA Jülich
Prof. Dr. O. Schult	IKP, KFA Jülich
Prof. Dr. K. Sistemich	IKP, KFA Jülich
Prof. Dr. J. Speth	IKP, KFA Jülich
Prof. Dr. J. Treusch (Chairman)	VS, KFA Jülich

MAC (Machine Advirsory Committee)
since Sept. 1, 1995

Dr. N. Angert	GSI Darmstadt
Prof. Dr. D. Husmann	University of Bonn
Dr. D. Möhl	CERN, Genf
Prof. Mühlhaupt	ESRF, France
Dr. F. Willeke	DESY, Hamburg

COSY-11 Collaboration*
Spokesman: W. Oelert

S. Brauksiepe, D. Grzonka, M. Karnadi, K. Kilian, R. Nellen, W. Oelert, E. Roderburg, M. Rook, T. Sefzick, P. Turek, K.H. Watzlawik, M. Wolke:
Institut für Kernphysik, KFA Jülich, D-52425 Jülich

K.H. Diart, H. Gutschmidt, M. Jochmann, M. Köhler, P. Wüstner, K. Zwoll:
Zentralinstitut für Elektronik, KFA Jülich, D-52425 Jülich

S. Bowes, A. Hardt: Fachhochschule Aachen, Abt. Jülich, D-52425 Jülich

H. Dombrowski, W. Hamsink, A. Khoukaz, T. Lister, C. Quentmeier, R. Santo, G. Schepers:
Institut für Kernphysi, Universität Münster

L. Jarczyk, A. Kozela, P. Moskal, J. Smyrski, M. Sokolowski, A. Strzalkowski:
Institute of Physics, Jagellonian University, Cracow, Poland

J. Balewski, A. Budzanowski: Institute of Nuclear Physics, Cracow, Poland

M. Ziolkowski: CERN, PPE-Division, Geneva, Switzerland

C. Goodman: IUCF Bloomington, Indiana, USA

*supported by BMFT-Verbundforschung; International Bureau of KfK Karlsruhe; University Program of KFA Jülich; Humboldt Foundation

COSY-13 Collaboration*
Spokesman: H. Ohm

T. Hermes, W. Borgs, N. Dolfus, S. Geisler, H.R. Koch, R. Maier, H. Ohm, D. Prasuhn, U. Rindfleisch, O.W.B. Schult:
Institut für Kernphysik, KFA Jülich, D-52425 Jülich

H. Stechemesser, W. Bertram, H. Maselter:
Zentralabteilung Allgemeine Technologie, KFA Jülich, D-52425 Jülich

St. Kistryn, K. Pysz, L. Jarczyk, P. Kulessa, Z. Rudy, A. Strzalkowski:
Institute of Physics, Jagellonian University, Cracow, Poland

W. Cassing: Institut für Theoretische Physik, Universität Gießen

I. Zychor:
Soltan Institute for Nucl. Studies, PL-05400 Swierk

Y. Uozumi:
Dept. of Nuclear Engineering, Kyushu University, Fukuoka 812, Japan

*supported by International Bureau of KfK Karlsruhe; TEMPUS-Program

COSY-TOF Collaboration*
Spokesman: E. Roderburg

U. Bechstedt, P. Cloth, V. Drüke, D. Filges, R. Geyer, H. Hadamek, A. Hassan, P. Jahn, K. Kilian, R. Klein, H. Machner, H.P. Morsch, Chr. Nake, N. Paul, V. Renken, U. Rindfleisch, E. Roderburg, M. Rogge, O. Schult, T. Sefzick, G. Sterzenbach, P. Turek, D. Wallom:
Institut für Kernphysik, KFA Jülich, D-52425 Jülich

H. Nann:
IUCF Bloomington, USA

R. Gehring, P. Hermanowski, H. Koch, J. Krug, H. Matthäy, W. Meyer, G. Reichertz, C. Rohloff, M. Steinke, U. Zielinski:
Institut für Experimentalphysik, Ruhr-Universität Bochum, D-44780 Bochum

H. Dutz:
Physikalisches Institut der Universität Bonn

A. Böhm, K. Brinkmann, H. Freiesleben, B. Hübner, E. Kuhlmann, S. Lange:
T.U. Dresden, D-01062 Dresden

M. Müller-Veggian:
Fachhochschule Jülich

R. Bilger, H. Clement, T. Czarnecki, G.J. Wagner:
Physikalisches Institut, Universität Tübingen, D-72076 Tübingen

P. Michel, K. Möller, B. Naumann, L. Naumann, A. Schamlott, A. Schülke:
Institut für Subatomare Physik, FZ Rossendorf, Dresden

M. Dellert, H. Dennert, W. Eyrich, M. Fritsch, S. Gabler, J. Hauffe, J. Hays, A. Metzger, M. Moosburger, R. Sperl, F. Stinzing, S. Wirth:
Physikalisches Institut, Universität Erlangen

*supported by BMFT-Verbundforschung; University Program of KFA Jülich

COSY-MED Collaboration*
Spokesman: D. Filges

P. Cloth, V. Drüke, D. Filges, H. Kobus, R. Maier, R.D. Neef, N. Paul:
Institut für Kernphysik, KFA Jülich, D-52425 Jülich

D. Barthmann, R. Beker, H. Paganetti, H.P. Peterson, Th. Schmitz, K. Schwenke:
Institut für Medizin, KFA Jülich, D-52425 Jülich

M. Dellert, W. Eyrich, M. Fritsch, J. Hauffe, M. Moosburger, R. Sperl:
Physikalisches Institut, Universität Erlangen

J. Bienen, W. Hoffmann:
Fachbereich Physik, Bergische Universität, Gesamthochschule Wuppertal

*supported by the University Program of KFA Jülich

ZEUS Collaboration
Spokesman: R. Klanner, Deutsches Elektronen-Synchrotron (DESY), D-22603 Hamburg

P. Cloth, D. Filges, R.D. Neef:
Institut für Kernphysik, KFA Jülich, D-52425 Jülich
and 49 national and international institutions

COSY-MOMO-Collaboration*
Spokesman: R. Jahn

H. Machner, P. v. Rossen, R. Tölle:
Institut für Kernphysik, KFA Jülich, D-52425 Jülich

F. Bellemann, A. Berg, J. Bisplinghoff, G. Bohlscheid, J. Ernst, C. Henrich, F. Hinterberger, R. Jahn, R. Joosten, U. Kuhn, R. Maschuw, T. Mayer-Kuckuk, G. Mertler, T. v. Oepen, D. Rosendaal, K. Scho, F. Schwandt, D. Theis, W. Wiedmann, R. Ziegler:
Institut für Strahlen- und Kernphysik, Universität Bonn

B. Metsch, H.R. Petry:
Institut für Theoretische Kernphysik, Universität Bonn

P. v. Neumann-Cosel:
Institut für Kernphysik, Technische Hochschule Damstadt

L. Jarczyk, A. Kozela, J. Smyrski, A. Strzalkowski:
Institute for Physics, Jagellonian University, Cracow, Poland

R. Frascaria, R. Siebert,
IPN Orsay, France

R. Wurzinger
LN Saturne, Saclay, France

*supported by BMFT-Verbundforschung; University Program of KFA Jülich; International Bureau of KfK Karlsruhe

COSY-EDDA-Collaboration*
Spokesmen: J. Bisplinghoff, F. Hinterberger, W. Scobel

P. Cloth, V. Drüke, D. Filges, D. Prasuhn, P. v. Rossen:
Institut für Kernphysik, KFA Jülich, D-52425 Jülich

J. Bisplinghoff, O. Diehl, G. Dorner, H.J. Engelhardt, J. Ernst, P.D. Eversheim, R. Gebel, R. Gross-Hardt, F. Hinterberger, R. Jahn, U. Lahr, T. Mayer-Kuckuk, R. Maschuw, G. Mertler, F. Mosel, D. Rosendaal, H. Scheid, F. Schwandt, D. Theis, J. Weber, W. Wiedemann, R. Ziegler:
Institut für Strahlen- und Kernphysik, Universität Bonn

K. Ackerstaff, R. Bollmann, F. Dohrmann, S. Eisenhardt, S. Fritz, M. Gasthuber, A. Gross, R. Langkau, G. Lippert, M. Radtke, H. Rohdjess, N. Schirm, W. Scobel, K. Woller:
I. Institut für Experimentalphysik, Universität Hamburg

B. Metsch, H.R. Petry:
Institut für Theoretische Kernphysik, Universität Bonn

H. Paetz gen. Schieck: Institut für Kernphysik, Universität Köln

B. v. Przewoski: IUCF Bloomington, Indiana, USA

*supported by BMFT-Verbundforschung; University Program of KFA Jülich

COSY-GEM-Collaboration*
Spokesman: H. Machner

V. Drüke, A. Djaloeis, D. Filges, St. Igel, K. Kilian, G. Lippert, H. Machner, H.P. Morsch, C. Nake, D. Protic, E. Roderburg, P. v. Rossen:
Institut für Kernphysik, KFA Jülich, D-52425 Jülich

M. Drochner, G. Kemmerling, K. Zwoll
Zentralinstitut für Elektronik, KFA Jülich, D-52425 Jülich

J. Ernst, R. Jahn, K. Scho:
Institut für Strahlen- und Kernphysik, Universität Bonn

D. Frekers, R. Garske, K. Grewer:
Institut für Kernphysik, Universität Münster

L. Jarczyk, S. Kistryn, W. Klimala, A. Magiera, J. Smyrski, A. Strzalkowski, P. Zolnierczuk:
Jagellonian University, Cracow, Poland

A. Budzanowski, L. Freindl, S. Kliczweski, R. Siudak: Institute of Nuclear Physics, Cracow, Poland

H.S. Plendl: Physics Department, FSU, Tallahassee, Florida, USA

B.J. Lieb: Physics Department, GMU, Fairfax, Virginia, USA

L.C. Liu: LANL, T. Division, Los Alamos, USA

J. Konijn: NIKHEF-K, Amsterdam, The Netherlands

J. Rama Rao: Banaras Hindu University, Dept. of Physics, Varanasi, India

M.G. Betigeri, S.S. Kapur, R.V. Srikantya, J. Roy:
BARC Trombay, Bombay, India

T. Kutsarova: Institute of Nuclear Research and Nuclear Energy, Sofia, Bulgaria

E. Friedman: Hebrev University, Racah Institute, Jerusalem, Israel

S. Förtsch: National Accelerator Centre, Faure, South Africa

R. Tsenov, D. Kolev:
Univ. Sofia, Sofia, Bulgaria

H. Nann: IUCF, Bloomington, Indiana, USA

*supported by BMFT-Verbundforschung; University Program of KFA Jülich; International Bureau of KfK Karlsruhe

Mars Observer Collaboration
Spokesman: J. Brückner

V. Drüke, D. Filges, R.D. Neef: Institut für Kernphysik, KFA Jülich, D-52425 Jülich

J. Brückner, U. Fabian, M. Wieder, H. Wänke:
Max-Planck-Institut für Chemie, Mainz

P.A.J. Englert: San Jose State University, USA

D.M. Drake, R.C. Reedy: Los Alamos National Laboratory, Los Alamos, USA

ANKE* (0°-Facility)
Spokesman: K. Sistemich

U. Bechstedt, W. Borgs, W. Bräutigam, N. Brummund, M. Büscher, J. Dietrich, R. Eßer, A. Franzen, D. Gotta, D. Grzonka, U. Hacker, A. Hardt, M. Hartmann, L. von Horn, H.R. Koch, D. Kopyto, S. Kopyto, R. Krause, R. Maier, S. Martin, K. Meyer, P. Munhofen, W. Oelert, H. Ohm, D. Prasuhn, H.J. Probst, M. Sauer, R. Schleichert, A. Schneider, O.W.B. Schult, H. Seyfarth, K. Sistemich:
Institut für Kernphysik, KFA Jülich, D-52425 Jülich

W. Klein: Institut für Schicht- und Ionentechnik, KFA Jülich, D-52425 Jülich

H. Stechemesser: Zentralabteilung Allgemeine Technologie, KFA Jülich, D-52425 Jülich

M. Köhler, G. Müller, U. Sieling, W. Tenten, K. Zwoll:
Zentrallabor für Elektronik, KFA Jülich, D-52425 Jülich

W. Cassing: Institut für Theoretische Physik, Universität Gießen, D-35392 Gießen

H. Dombrowski, R. Santo: Institut für Kernphysik, Universität Münster, D-48149 Münster

J. Ernst: Institut für Strahlen- und Kernphysik, Universität Bonn, D-53115 Bonn

S. Dienel, T. Kirchner, N. Langenhagen, K.W. Leege, H. Müller, W. Oehme, B. Prietzschk, B. Rimarzig, Chr. Schneider, Chr. Schneidereit:
Zentralinstitut für Kernforschung, Rossendorf, D-01474 Dresden

W. Bothe: DESY, D-22603 Hamburg

U. Schwarz: FH Soest, D-59494 Soest

L. Jarczyk, B. Kamys, St. Kistryn, R. Kulessa, Z. Rudy, J. Smyrski, A. Strzalkowski, M. Wende:
Institute of Physics, Jagellonian University, Cracow, Poland

O.Yu. Denisov, O.E. Gorchakov, V. Grebenjuk, M.A. Ivanov, V.V. Ivanov, V. Karpukhin, V.I. Komarov, V.I. Komissarov, V. Kruglov, A.V. Kulikov, V.P. Nomokonov, A.Yu. Petrus, S.N. Prakhov, A.I. Puzynin, A.M. Roshdestvensky, A.I. Rudenko, M.G. Sapozhnikov, A.A. Sibirtsev, V.V. Sidorkin, V.I. Tretyak, B.Zh. Zalykhanov:
Joint Institute of Nuclear Research, Dubna, Russia

S. Belostotski, O. Grebenyuk, V. Koptev, S. Mikirtichyants, V. Nelubin:
St. Petersburg Institute of Nuclear Studies, Russian Academy of Sciences, Gatchina, Russia

V. Tchernyshev: Institute for Theoretical and Experimental Physics, Moscow, Russia

N. Amaglobeli, B. Chiladze, L. Glonti, A. Kacharava, G. Macharashvili, Z. Menteshashvili, M. Nioradze:
High Energy Physics Institute, Tbilisi State University, Tbilisi, Georgia

S. Abdulazizov, A. Kulikov, S. Trusov, V. Yazkov:
Dubna Branch of the Moscow State University, Dubna, Russia

*supported by Land Nordrhein-Westfalen, BMFT (Verbundforschung; KFA, WTZ mit Rußland), INTAS, Collaborators

PS185/2 Collaboration*:
Spokesman: K. Roehrich

R. Bröders, R. Geyer, K. Kilian, W. Oelert, K. Roehrich, K. Sachs, T. Sefzick:
Institut für Kernphysik, KFA Jülich, D-52425 Jülich

P.D. Barnes: LAMPF, Los Alamos, USA

R. Breunlich: IMEP, Wien, Austria

R.A. Eisenstein, D. Hertzog, T. Jones, R. Tayloe:
Physics Department, Loomis Lab. of Physics, University of Illinois, USA

H. Dennert, W. Eyrich, T. Fuchs, J. Hauffe, R. Kraft, M. Moosburger, S. Pomp, F. Stinzing:
Physikalisches Institut, Universität Erlangen

D. Afzali, J. Franz, J. Rauch, E. Rössle, M. Ruh, D. Ruschmeier, H. Schmitt, R. Todenhagen, T. Walter, H. Wirth:
Fakultät für Physik, Albert-Ludwigs-Univ. Freiburg

H. Fischer: Department of Physics, University of New Mexico, Albuquerque, USA

G. Franklin, R. McCrady, C.A. Meyer, B. Quinn, R. Schumacher, V. Zeps:
Physics Department, Carnegie-Mellon University, USA

M. Ziolkowski: CERN, Geneva, Switzerland

T. Johansson, E. Traneus: The Svedberg Laboratory, Uppsala, Schweden

*supported by BMFT-Verbundforschung, National Science Foundation (USA)

PS185/3 Collaboration*
Spokesman: K. Roehrich

R. Bröders, R. Geyer, K. Kilian, W. Oelert, K. Röhrich, T. Sefzick, K. Sachs:
Institut für Kernphysik, KFA Jülich, D-52425 Jülich

B. Bassalleck, D.E. Fields, P. Kingsberry, J. Lowe, D. Wolfe:
Univ. of New Mexico, Albuquerque

H. Dutz, W. Meyer, G. Reicherz, B. Schoch:
Univ. of Bonn, Institute of Physics, D-53115 Bonn

G. Franklin, C.A. Meyer, B. Quinn, R. Schumacher:
Physics Department, Carnegie-Mellon University, USA

H. Dennert, W. Eyrich, J. Hauffe, A. Metzger, M. Moosburger, F. Stinzing, St. Wirth:
Physikalisches Institut, Universität Erlangen, D-91058 Erlangen

H. Fischer, J. Franz, K. Königsmann, H. Schmitt:
Fakultät für Physik, Universität Freiburg, D-79104 Freiburg

T. Johansson, S. Pomp, E. Traneus:
The Svedberg Laboratory, Uppsala, Sweden

R.A. Eisenstein, D. Hertzog, T. Jones, R. Tayloe:
Physics Department, Loomis Lab. of Physics, University of Illinois, USA

*supported by BMFT-Verbundforschung, National Science Foundation (USA)

PS202 Collaboration*
Spokesman: M. Macri

R. Geyer, K. Kilian, W. Oelert, K. Roehrich, M. Rook:
Institut für Kernphysik, KFA Jülich, D-52425 Jülich

D. Drijard, M. Ferro-Luzzi, R. Jones, B. Mouellic, S. Ohlsson, J.-M. Perreau:
CERN, Geneva, Switzerland

W. Eyrich, M. Moosburger, S. Pomp, F. Stinzing:
Physikalisches Institut, Universität Erlangen

H. Fischer, J. Franz, E. Rössle, H. Schmitt, M. Tscheulin, H.J. Urban, H. Wirth, H. Zipze:
Fakultät für Physik, Albert-Ludwigs-Universität Freiburg

P.T. Debevec, R.A. Eisenstein, Ph. Harris, D.W. Hertzog, S.A. Hughes, P.E. Reimer, J. Ritter:
Physics Department, Loomis Lab. of Physics, University of Illinois, USA

A. Palano: Physics Department, University degli Studi di Bari, Italy

L. Bertolotto, A. Buzzo, S. Easo, K. Kirsebom, M. Lo Vetere, M. Macri, M. Marinelli, S. Passaggio, M.-G. Pia, A. Pozzo, E. Robutti, A. Santroni:
Istituto Nazionale di Fisica Nucleare, Genova, Italy

A. Johansson, T. Johansson:
The Svedberg Laboratory, Uppsala, Sweden

H. Korsmo:
Department of Physics, University of Oslo, Norwegen

*supported by BMFT-Verbundforschung; Department of Energy (USA); National Science Foundation (USA)

PS210 Collaboration*
Spokesman: W. Oelert

G. Baur, D. Grzonka, K. Kilian, W. Oelert, K. Röhrich, K. Sachs, T. Sefzick, M. Wolke:
Institut für Kernphysik, KFA Jülich, D-52425 Jülich

W. Niebur, R.S. Simon, R. Stratmann:
GSI Darmstadt

G. Schepers:
Institut für Kernphysik, Universität Münster, D-48149 Münster

W. Eyrich, J. Hauffe, M. Moosburger, F. Stinzing:
Institut für Kernphysik, Universität Erlangen, D-91058 Erlangen

G. Boero, A. Buzzo, M. LoVetere, M. Macri, S. Passaggio, A. Pozzo:
University of Genoa and INFN-Genua, Italy

*supported by BMFT-Verbundforschung; Department of Energy (USA); National Science Foundation (USA)

PROMICE/WASA Collaboration*
Spokesmen: B. Höistad and S. Kullander

M. Blom, H. Calen, S. Dahlgren, K. Fransson, L. Gustafsson, S. Häggström, B. Höistad, A. Jansson, A. Johansson, T. Johansson, S. Kullander, J. Moehn, A. Mörtsell, R. Ruber:
(*on leave of absence from Institute of Experimental Physics, Warsaw University):
Department of Radiation Sciencves, Uppsala, Sweden

K. Kilian, W. Oelert, V. Renken:
Institut für Kernphysik, KFA Jülich, D-52425 Jülich

A. Turowiecki, Z. Wilhelmi, J. Zlomanczuk:
Institute of Experimental Physics, Warsaw, Poland

Z. Zabierowski:
Institute of Nuclear Studies, Lodz, Poland

A. Kupsc, A. Nawrot, J. Stepaniak:
Institute for Nuclear Studies, PL-00681 Warsaw, Poland

A. Bondar, G. Kolachov, A. Kuzmin, T. Purlatz, B. Shwartz, V. Sidorov, A. Suchanov:
Institute of Nuclear Physics, Novosibirsk, Russia

Z. Pawlowski:
Institut of Radioelectronics, Warsaw, Poland

D. Bogoslawsky, V. Dunin, L. Komogorova, A. Kuznetsov, B. Morosov, A. Povtorejko, A. Sandukovsky, A. Sukhanov, V. Tikhomirov, A. Zernov
Joint Institute for Nuclear Research Dubna, 101000 Moscow, Russia

D. Akimov, A. Bolozdynia, I. Chuviolo, L. Kondratyuk, A. Martemyanov, M. Shepkin, A. Sibirtsev, V. Sopov, V. Tchernyshev:
Institut of Theoretical and Experimental Physics, Moscow, Russia

H. Hirabayashi, A. Yamamoto, A. Yamaoka:
National Laboratory for High Energy Physics, Tsukuba, Japan

B. Chernyshev, M. Gornov, Y. Gurov, R. Shafigulin:
Moscow Engineering Physiccs Institute, Moscow, Russia

H. Ikegami, Y. Mizuno, Y. Yuasa:
Research Center for Nuclear Physics, Osaka, Japan

C. Ekström, D. Reistad:
The Svedberg Laboratory, Uppsala, Sweden

*supported by Deutscher Akademischer Austauschdienst (DAAD)

New Muon Collaboration
Spokesman: D von Harrach

K. Roehrich:
Institut für Kernphysik, KFA Jülich, D-52425 Jülich

G. Baum, M. Siebler:
Bielefeld University, Physics Department

G.K. Mallot:
CERN, 1211 Genève 23, Switzerland

A. Brüll, H. Engelien, R. Kaiser, U. Landgraf, A. Witzmann:
Freiburg University, Physics Department

W. Brückner, U. Gaul, D. von Harrach, E.M. Kabuß, Y. Mizuno, D. Nowotny, B. Povh,
K. Rith, C. Scholz, Y. Tzamouranis, F. Zetsche:
Max Planck Institut für Kernphysik, Heidelberg

T.-A. Shibata, A. Simon:
Heidelberg Unviversity

F. Klein, G.K. Mallot, R. Rieger, R. Seitz, T. Walcher:
Mainz University, Institut für Kernphysik

R. Windmolders:
Faculté des Sciences, Universitè de Mons, Belgium

C. Broggini, L. Fluri, A. Paic, J.L. Vuilleumier,:
Universitè de Neuchatel, Switzerland

M. Ballintijn, J. Beaufays, I.G. Bird, R. van Dantzig, M. van der Heijden, M. de Jong, T.J. Ketel,
G. van Middelkoop, D. Sanders, F. Sever:
NIKHEF-K, P.O. Box 4395, Amsterdam, The Netherlands

T. Granier, A. Milsztajn, J. Oberski, M. Virchaux:
DAPNIA, Service de Physique des Particules, CE Saclay, 91191 Gif-sur-Yvette, France

C. Heusch:
University of California, Institute for Particle Physics, Santa Cruz, CA 95064, USA

M. Botje, W.J. Burger, , Q. Ingram, R. Schumacher:
Paul Scherrer Institute, Villigen, Switzerland

M. Arneodo, M.I. Ferrero, C. Mariotti, C. Peroni, A. Staiano:
Università di Torino, Istituto di Fisica, Italy

A. Arvidson, P. Björkholm, A. Drying, K. Janson-Prytz, S. Kullander, T. Lindqvist:
University of Uppsala, Department of Radiation Science, Sweden

J. Nassalski, E. Rondio, A. Sandacz, M. Szleper:
Soltan Institue for Nuclear Studies, Warsaw, Poland

B. Badelek, J. Ciborowski, L. Ropelewski:
University of Warsaw, Poland

VIII. PERSONNEL

Scientific Staff:

Prof. Dr. G. Baur (Th)
(a.o. Prof. at the Univ. of Basel)

Dr. U. Bechstedt (LI)

G. Becker (Th)
until October 31, 1995

Dr. H. Beuscher (LI)

Dr. J. Bojowald (Ec)

Dr. K. Bongardt (LI)

Prof. Dr. G. Borchert (E2)
(apl. Prof. at the Univ. of Cologne)

DI W. Bräutigam (LI)

W. Breuer (Sd)

Dr. M. Büscher (E2)

Dr. P. Cloth (Sd)

Dr. J. Dietrich (LI)

Dr. A. Djaoleis (E1)

Dr. V. Drüke (Sd)

DP R. Eßer (E2)

Dr. Dr. Filges (Sd)
(Priv. Dozent at the Univ. of Wuppertal)

DP A. Franzen (E2)

Dr. W. Gast (E1)

Dr. R. Gebel (LI)
since August 1, 1995

R. Geyer (E1)

DP H. Gorke (E2)

Dr. D. Gotta (E2)

Dr. F. Grümmer (Th)

Dr. D. Grzonka (E1)

DI U. Hacker (LI)
until September 30, 1995

Dr. J. Haidenbauer (Th)

DP C. Hanhart (Th)

DP M. Hartmann (E2)

DI K. Henn (LI)

DP T. Hermes (E2)

DP M. Hoffmann (Th)

Prof. Dr. K. Holinde (Th)
(apl. Prof. at the Univ. of Bonn)

DP H. Holtmann (Th)

DP L. von Horn (E2)

DP St. Igel (E1)
until Aug. 31, 1995

Dr. P. Jahn (E1)

Dr. G. Janssen (Th)
until July 31, 1995

DP S. Jeschonnek (Th)

Dipl. H. Junghans (E2)
since November 15, 1995

DP M. Kalassa (Th)

Prof. Dr. K. Kilian (E1)
(Prof. at the Univ. of Bonn)

Dr. P. Kleinheinz (E2)

Dr. V. Klemt (Th)

DP H. Kobus (Sd)

Dr. H. R. Koch (E2)

Dr. B. Körfgen (Th)

DP S. Kopp-Zeschonnek (Th)

Dr. D. Kopyto (E2)

Dipl. R. Krause (E2)
until June 30, 1995

O. Krehl (Th)

Prof. Dr. S. Krewald (Th)
(apl. Prof. at the Univ. of Bonn)

Dr. H. Labus (Ec)

H. R. Langohr (Sd)

Dr. H. Lawin (LI)

DP A. Lehrach (LI)
since January 1, 1995

DP S. Lenz (E2)

DP L. Leunissen (LI)
since January 1, 1995

Prof. Dr. R. M. Lieder (E1)
(Prof. at the Univ. of Bonn)

DP G. Lippert (E1)
until Aug. 31, 1995

Dr. H. Machner (E1)

Dr. R.A. Maier (LI)

Dr. S. Martin (LI)

I. Mohos (LI)

Dr. H.P. Morsch (E1)

DP Ch. Mosbacher (Th)

DP A. Mündel (Th)

Dr. V. Mull (Th)

Prof. Dr. K. Nakayama (Th)

Prof. Dr. N.N. Nikolaev (Th)

DP Ch. Nake (E1)
until June 30, 1995

Dr. R.D. Neef (Sd)

Dr. W. Oelert (E1)
(Priv. Dozent at the Univ. of Bonn)

Dr. H. Ohm (E2)

Prof. Dr. F. Osterfeld (Th)
(apl. Prof. at the Univ. of Bonn)

DI N. Paul (Sd)

Dr. D. Prasuhn (LI)

DP H.J. Probst (Rp)

DP D. Protic (Dt)

DP R. Rapp (Th)

DP B. Razen (E1)

DP V. Renken (E1)

Dr. A. Reuber (Th)
until October 15, 1995

Ch. Reul (Sd)

Dr. E. Roderburg (E1)

Dr. K. Roehrich (E1)

Dr. M. Rogge (E1)

Dr. P. von Rossen (LI)

DP K. Sachs (E1)
until March 31, 1995

DI M. Sauer (LI)
until May 31, 1995

Dr. H. Schaal (Sd)

W. Schäfer (Th)

DP R. Schleichert (E2)

Dr. A. Schnase (LI)

DP A. Schneider (E2)

DI H. Schneider (LI)

Dr. Ch. Schütz (Th)
until November 30, 1995

DI G. Schug (LI)

Prof. Dr. O. Schult (E2)
(Prof. at the Univ. of Cologne)

Dr. T. Sefzick (E1)

Dr. H. Seyfarth (E2)

DP T. Siems (E2)
(DAAD-Fellowship)

Dr. K. Sistemich (E2)
(Prof. at the Univ. of Cologne)

Prof. Dr. J. Speth (Th)
(Prof. at the Univ. of Bonn)

DI R. Stassen (LI)

Dr. H.J. Stein (E2)

N. Stein (Th)

G. Sterzenbach (Sd)

Dr. H. Stockhorst (LI)

G. van de Sand (Th)

Dr. R. Tölle (LI)

A. Trellakis (Th)
until April 30, 1995

Dr. Y. Uozumi (E2)
(Japanese Fellowship)

DP St. Utzelmann (E1)
until April 30, 1995

DI T. Vashegyi (LI)

DI V. Vau (LI)
until July 31, 1995

Dr. R. Wagner (LI)

DP Th. Waindzoch (Th)

D. Wallom (E1)
until June 3, 1995

Prof. Dr. J. Wambach (Th)
until May 31, 1995

Dr. K.-H. Watzlawik (Da)

A. Weinert (LI)

DP M. Wolke (E1)

Technical and Administrative Staff:

P. Birx (LI)
R. Bley (Ad), since April 1, 1995
H.G. Böge (LI)
M. Böhnke (LI), since February 1, 1995
W. Borgs (E2)
H. Borsch (LI)
R. Brings (LI)
G. Brittner (Ec)
P. Brittner (LI)
E. Brökel (Ec)
U. Burck (Ad), until March 31, 1995
J. But (Ws)
L. Conin (LI)
B. Dahmen (LI)
W. Derissen (Cd)
N. Dolfus (Ec)
F. Drees (LI)
G. D'Orsaneo (E2), since Jan. 2, 1995
R. Enge (LI)
J. Engel (LI)
P. Engels (LI)
W.R. Ermer (E2)
W. Ernst (Ec)
K. Esser (Ad)
H.J. Etzkorn (LI)
H.P. Faber (LI)
G. Fiori (Dt)
H.-W. Firmenich (Ws)
G. Gad (LI)
D. Gehsing (LI)
S. Geisler (Cd)
G. Göbbels (Ws)
M. Gringel (Cd)
Ch. Haberbosch (LI)
H. Hadamek (Ws)
A. Hamacher (Dt)
T. Hillenberg (Cd), until June 30, 1995
M.G. Holona (Ws)
K.D. Jach (LI)
H.M. Jäger (E1)
H.J. Jansen (Ws)
R. Janssen (Ad)
M. Karnadi (Da)
R. Klein (E1)
S. Köhn (Da), until May 31, 1995
K. Krafft (Rp)
M. Kremer (Ws)
G. Krol (LI)
K.P. Kruck (LI)
M. Küven (Ws)
K.G. Langenberg (LI)
W. Lorenz (Ad)
G. Lürken (Ec)
H. Metz (Dt)
A. Müller (LI)
M. Müskes (LI)
R. Nellen (Da)
S. Papaspyrou (Ad)
J. Pfeiffer (Dt)
H. Pütz (LI)
A. Retz (Cd)
A. Richert (LI)
U. Rindfleisch (Cd)
B. Rogozik (LI)
DI D. Rosin (LI)
N. Rotert (LI)
D. Ruhrig (LI)
Th. Sagefka (LI)
M. Schaaf (LI)
P. Schmidt (LI)
Jos. Schmitz (Ws)
Jürg. Schmitz (LI)
H. Schröder (Da), until May 14, 1995
F. Schultheiß (Ws)
R. Seidemann (E2), until Sept. 30, 1995
M. Simon (LI)
H. Singer (LI)
K. Sobotta (LI)
D.W. Spölgen (Ws)
C. Strauch (Ad)
J. Strehl (Ws)
E. Tesch (Ad)
K.P. Wieder (E2)
J. Wimmer (Sd)
K. Winkler (Ec)
DI J.-D. Witt (LI)
H.W. Zens (LI)

(E1) Institute for Experimental Nuclear Physics 1
(E2) Institute for Experimental Nuclear Physics 2
(Th) Institute for Theoretical Nuclear Physics
(LI) Large Nuclear Physics Instruments
(Ad) Administration
(Cd) Construction and Design
(Da) Data Acquisition Group
(Dt) Detector and Target Laboratory
(Ec) Electronics
(Rp) Radiation Protection
(Sd) Simulation and Detector Development
(Ws) Mechanical Workshop

Research Visitors (IKP 1)
(for one week to six months):

Dr. Z. Aouissat (Th)
until March 31, 1995
from Okt. 30 to Jan. 31, 1996
(Univ. of Grenoble, France)

Dr. J. Balewski (E1)
from Jan. 9, 1995
(Jagellonian Univ. of Krakow, Poland)

Dr. S. Barsov
29.10.-12.11.1995
(PNPI Gatchina, GUS)

Dr. St. Bass (Th)
from Febr. 21 to Febr. 28, 1995
from Aug. 3 to Aug. 8, 1995
from Sept. 1 to Dec. 31, 1995
(Univ. of Cambridge, England)

Prof. S. Belostotski (E2)
from Nov. 15 to Nov. 18, 1995
(DESY Hamburg, Germany)

DI E. Bialkowski (Dt)
from April 24, 1995 to Jan. 31, 1996
(Univ. of Crakow, Poland)

Dr. A. Bianconi (Th)
from March 19 to April 19, 1995
from Okt. 29 to Nov. 11, 1995
(Univ. of Pavia, Italy)

DP L. Blecki (E2)
from May 8 to Aug. 6, 1995
(Soltan Inst. Swierk, Poland)

Dr. B. Bochev (E1)
from April 13 to Mai 19, 1995
(Bulg. Acad. of Sciences, Sofia, Bulgaria)

Dr. M. Buballa (Th)
from July 17 to Aug. 17, 1995
(SUNY at Stony Brook, USA)

Prof. A. Budzanowski (E1)
from Nov. 11 to Nov. 25, 1995
(Kernforschungszentrum Krakau, Poland)

Dr. B. Chen (Th)
from April 10 to July 10, 1995
(Inst. of Atomic Energy, Peking, China)

M. Davies (E1)
until July 31, 1995
(Student from Coventry, England)

Prof. S. Drozdz (Th)
from May 1 to May 30, 1995
from July 27 to Aug. 27, 1995
(Univ. of Krakow, Poland)

Prof. J.W. Durso (Th)
from June 9 to Aug. 10, 1995
(Mount Holyoke College, Hadley, MA, USA)

Dr. S. Förtsch (E1)
until Aug. 31, 1995
(NAC Faure, Südafrika)

Dr. L. Freindl (E1)
from May 1 to May 15, 1995
from Aug. 7 to Sept. 5, 1995
from Nov. 5 to Dec. 4, 1995
(Kernforschungszentrum Krakau, Poland)

A. Georgiev (E1)
until Dec. 31, 1995
(Academy of Science, Sofia, Bulgaria)

Dr. S. Gevorkyan (Th)
from Okt. 16 to Oct. 21, 1995
(Erevan Phys. Inst., Amenia, Russia)

M. Gierlik (E1)
from June 1 to August 31, 1995
from Nov. 5 to Nov. 18, 1995
(Inst. of Exp. Physics, Warsaw, Poland)

Prof. Ch. Goodmann (AvH Awardee) (Th)
from April 18 to June 14, 1995
(IUCF, Bloomington, USA)

Dr. O. Grebenyuk (E2)
from Okt. 22 to Nov. 19, 1995
(PNPI Gatchina, GUS)

T. Grigorov (E1)
from Feb. 23 to April 23, 1995
(INRNE-BAS, Sofia, Bulgarien)

G. Gugulski (E1)
from Jan. 25 to Feb. 25, 1995
(Univ. of Krakow, Poland)

Prof. H. Haberzettl (Th)
until June 30, 1995
(George Washington Univ., Washington DC, USA)

Moh. A.G. Hassan (E1)
(Atom Energy Agency, Cairo, Egypt)

Moh. F. Hawash (E1)
until Sept. 30, 1995
(Atom Energy Agency, Cairo, Egypt)

A. Heczko (E1)
(Univ. of Krakow, Poland)

Prof. B.L. Ioffe (AvH-Awardee) (Th)
from March 14 to June 13, 1995
(ITEP Moskow, Russia)

Prof. L. Jarczyk (E1+E2)
from April 25 to May 25, 1995
from June 6 to June 14, 1995
from Aug. 10 to Aug. 31, 1995
from Nov. 11 to Dec. 13, 1995
(Jagellonian Univ. of Krakow, Poland)

Prof. R. R. Jayanti (E1)
from May 3 to August 3, 1995
(BHU Varanasi, India)

Dr. H. Jensen (E1)
since July 31, 1995
(EG-Stipendiat, Kopenhagen)

Prof. R. Kaczarowski (E1)
from Oct. 3 to Oct. 14, 1995
(SINS, Swierk, Poland)

Prof. S. Kamerdzhiev (Th)
until February 6, 1995
from July 17 to Aug. 10, 1995
from Nov. 15 to Dec. 27, 1995
(IPPE, Obninsk, Russia)

Prof. B. Kamys (E2)
from Nov. 11 to Dec. 13, 1995
(Univ. Cracow, Poland)

Dr. M. Kisielinski (I1)
from Dec. 8 to Dec. 15, 1995
(University of Warschau, Poland)

Dr. St. Kliczewski (E1)
from May 1 to May 31, 1995
from Aug. 6 to Sept. 5, 1995
from Oct. 9 to Dec. 31, 1995
(Kernforschungszentrum Krakow, Poland)

W. Klimala (E1)
from April 27 to May 25, 1995
from Aug. 9 to Sept. 9, 1995
from Oct. 13 to Dec. 22, 1995
(Jagellonian Univ. of Krakow, Poland)

Dr. V. Koch (Th)
from July 5 to July 11, 1995
(SUNY at Stony Brook, USA)

DP. D. Kolev (E1)
from May 13 to May 28, 1995
from Nov. 11 to Dec. 12, 1995
(University of Sofia, Bulgaria)

Prof. Dr. V. Komarov (E2)
from March 27 to April 7, 1995
from June 5 to June 15, 1995
from Nov. 6 to Nov. 17, 1995
(JINR Dubna, GUS)

Prof. Dr. V. Koptev (E2)
from Jan. 29 to Febr. 12, 1995
from April 23 to May 7, 1995
from July 2 to July 23, 1995
from Oct. 29 to Dec. 3, 1995
(PNPI Gatchina, GUS)

Dr. J. Kownacki (I1)
from Dec. 8 to Dec. 15, 1995
(University of Warschau, Poland)

Dr. A. Kozela (E1)
from Oct. 9 to Nov. 6, 1995
(Jagellonian Univ. of Krakow, Poland)

Prof. G. Krein (Th)
from July 25 to Aug. 15, 1995
(UNESP Sao Paulo, Brasil)

Dr. V. Kruglov (E2)
from Aug. 8 to Aug. 19, 1995
(JINR Dubna, GUS)

DP P. Kulessa (E2)
from Nov. 13 to Dec. 11, 1995
(Univ. Cracow, Poland)

Dr. A. Kulikov (E2)
from June 18 to June 23, 1995
from Nov. 6 to Nov. 19, 1995
(JINR Dubna, GUS)

Dr. Kurbatov (E2)
from Nov. 13 to Nov. 19, 1995
(JINR Dubna, GUS)

Dr. T. Kutsarova (E1)
from May 8 to May 29, 1995
from Nov. 8 to Dec. 23, 1995
(Bulg. Academy of Sciences, Sofia, Bulgaria)

Dr. M. Liang (E2)
from Febr. 17 to Febr. 25, 1995
(Univ. Edinburgh, GB)

Prof. J. Lieb (E1)
from May 2 to May 18, 1995
(George Mason University, Virginia, USA)

Prof. Z. Ma (DFG-fellow) (Th)
from April 10 to July 10, 1995
(Inst. of Atomic Energy, Peking, China)

Prof. M. Macfarlane (Th)
from June 1 to June 30, 1995
(IUCF, Bloomington, USA)

Dr. G. Macharashvili (E2)
from Nov. 12 to Nov. 19, 1995
(JINR Dubna, GUS)

Dr. A. Magiera (E1)
from Sept. 19 to Oct. 17, 1995
from Nov. 6 to Dec. 2, 1995
(Kernforschungszentrum Krakau, Poland)

J. Majewski (E1)
from Feb. 8 to March 7, 1995
from May 18 to June 28, 1995
from Oct. 9 to Nov. 6, 1995
from Nov. 23 to Dec. 22, 1995
(Jagellonian Univ. of Krakow, Poland)

Dr. S. Mikirtichyants (E2)
from Oct. 8 to Dec. 3, 1995
(PNPI Gatchina, GUS)

Dr. P. Mischev (E1)
from April 12 to May 28, 1995
(INRNE-BAS, Sofia, Bulgarien)

A. Misiak (E1)
from Jan. 25 to Feb. 24, 1995
from May 16 to June 28, 1995
from Oct. 9 to Nov. 6, 1995
(Jagellonian Univ. of Krakow, Poland)

Dr. T. Morek (E1)
from June 1 to July 21, 1995
from Oct. 3 to Oct. 14, 1995
(Inst. of Exp. Physics, Warsaw, Poland)

P. Moskal (E1)
from Jan 1 to Dec. 31, 1995
(Jagellonian Univ. of Krakow, Poland)

U. Mostafa (E1)
since July 7, 1995
(Atom Energy Agency, Cairo, Egypt)

Prof. Dr. H. Nann (E1)
from July 15 - 23, 1995
(Indiana University, Bloomington, IN)

Dr. V. Nelyubin (E2)
from May 29 to July 2, 1995
from Oct. 8 to Dec. 17, 1995
(JINR Dubna, GUS)

Dr. J. Nemchik (Th)
from Febr. 13 to Febr. 22, 1995
(Slovak Academy of Sciences, Kosice, Slow.)

Prof. M. Nioradze (E2)
from Nov. 12 to Nov. 19, 1995
(HEPI Tbilisi, Georgia)

Prof. S. Nishizaki (Th)
from July 18 to Aug. 20, 1995
(Iwate University, Morioka, Japan)

Dr. I. Panteleev (E2)
from Oct. 22 to Nov. 5, 1995
(PNPI Gatchina, GUS)

Dr. A. Petrus (E2)
from Nov. 13 to Nov. 19, 1995
(JINR Dubna, GUS)

Prof. H.S. Plendl (E1)
from May 18 to Sept. 20, 1995
(Florida State Univ., Tallahassee, Florida, USA)

Prof. S. Popov (E2)
from Nov. 12 to Nov. 16, 1995
(Budker Inst. Novosibirsk, GUS)

K. Przestrzelska (E1)
from June 12 to August 31, 1995
(Inst. of Exp. Physics, Warsaw, Poland)

DP K. Pysz (E2)
from Febr. 20 to March 31, 1995
(Univ. Cracow, Poland)

Prof. G.H. Rawitscher (Th)
from Nov. 11 to Nov. 22, 1995
(University of Connecticut, USA)

Dr. E. Ruchowska
from Oct. 3 to Oct. 14, 1995
(SINS, Swierk, Poland)

B.J.. Roy (E1)
since Nov. 15, 1995
(BARC, Bombay, India)

Dr. Z. Rudy (E2)
from Nov. 13 to Dec. 13, 1995
(Univ. Cracow, Poland)

Dr. T. Rzaca-Urban (E1)
from May 25 to June 18, 1995
from Oct. 20 to Oct. 29, 1995
(Inst. of Exp. Physics, Warsaw, Poland)

Prof. M. Sapozhnikov (E2)
from Nov. 12 to Nov. 19, 1995
(JINR Dubna, GUS)

Dr. A. Selikov (E2)
from July 7 to Aug. 7, 1995
from Oct. 29 to Dec. 17, 1995
(Moscow State Univ., GUS)

Dr. A. Sibirtsev (E2)
from July 17 to Aug. 11, 1995
(JINR Dubna, GUS)

Dr. R. Siudak (E1)
from May 1 to May 31, 1995
from Aug. 15 to Sept. 15, 1995
from Aug. 15o Sept. 15, 1995
from Oct. 1 to Dec. 22, 1995
(Jagellonian Univ. of Krakow, Poland)

Dr. J. Smyrski (E1)
from Jan. 30 to Feb. 10, 1995
from May 7 to May 20, 1995
from June 6 to June 14, 1995
from July 24 to Aug. 26, 1995
(Jagellonian Univ. of Krakow, Poland)

Prof. A. Strzalkowski (E1)
from May 1 to May 19, 1995
from June 5 to June 14, 1995
from Oct. 17 to Nov. 18, 1995
(Jagellonian Univ. of Krakow, Poland)

Dr. A. Szczurek (Th)
from Jan. 25 to March 24, 1995
from Oct. 8 to Nov. 6, 1995
(INP, Krakow, Poland)

Prof. V. Tchernyshev (E2)
from Nov. 13 to Dec. 10, 1995
(ITEP Moscow, GUS)

Prof. R. Tegen (Th)
from Oct. 15 to Dec. 15, 1995
(Univ. of Witwatersrand/Johannisbg, South Africa)

Dr. G. Tertychny (Th)
from Jan. 11 to March 10, 1995
from Dec. 3 to Febr. 3, 1996
(IPPE, Obninsk, Russia)

Dr. S. Trusov (E2)
from June 18 to July 14, 1995
from Nov. 7 to Dec. 12, 1995
(Moscow State Univ., GUS)

Dr. Usikov (E2)
from Nov. 13 to Nov. 19, 1995
(JINR Dubna, GUS)

Dr. A. Vasilyev (E2)
from Oct. 20 to Nov. 5, 1995
(PNPI Gatchina, GUS)

Dr. T. Venkova (E1)
from April 15 to June 5, 1995
from Nov. 20 to Dec. 19, 1995
(Bulg. Acad. of Sciences, Sofia, Bulgaria)

Prof. E. Vogt (Th)
from Sept. 18 to Dec. 20, 1995
(TRIUMF, Vancouver, USA)

Prof. C. Wilkin (E2)
from July 9 to July 15, 1995
from Nov. 14 to Nov. 21, 1995
(Univ. College London, GB)

Dr. B.G. Zakharov (DFG-fellow) (Th)
from Sept. 25 to Dec. 25, 1995
(Landau Inst. for Theor. Phys., Moscow, Russia)

Prof. B. Zalikhanov (E2)
from Nov. 6 to Nov. 19, 1995
(JINR Dubna, GUS)

Dr. V. Zoller (DFG fellow) (Th)
from March 15 to May 14, 1995
from Sept. 25 to Oct. 24, 1995
(ITEP, Moskow, Russia)

DP P. Zolnierczuk (E1)
from Jan. 1 to Dec. 15, 1995
(Jagellonian Univ. of Krakow, Poland)

Dr. I. Zychor (E2)
from March 13 to May 14, 1995
from July 9 to July 30, 1995
from Nov. 12 to Dec. 12, 1995
(Soltan Inst. Swierk, Poland)

IX. PUBLICATIONS

IKP-100195
Anagnostopoulos, D., Augsburger, M., Borchert, G., Chatellard, D., El-Khoury, P., Egger, J.P., Elble, M., Gorke, H., Gotta, D., Hauser, P., Indelicato, P., Kirch, K., Lenz, S., Rashid, K., Schult, O.W.B., Siems, Th., Simons, L.M.
High resolution X-ray spectroscopy of exotic atoms
Röntgen Centennial, Würzburg, 1995
20.50.0

IKP-100295
Anagnostopoulos, D., Borchert, G., Gotta, D., Schult, O.W.B.
High Resolution spectroscopy of electronic innershell transitions
Röntgen Centennial, Würzburg, 1995
20.50.0

IKP-100395
Aouissat, Z.; Rapp, R.; Chanfray, G., Schuck, P.; Wambach, J.
S-wave $\pi\pi$ correlations in dense nuclear matter
Nucl. Phys. A581(1995)471-492
20.80.0

IKP-100495
Aouissat, Z.; Rapp, R.; Chanfray, G.; Schuck, P.; Wambach, J.
In-medium $\pi\pi$ correlations: to condense or not to condense
Proceedings of the International Conference on Physics with GeV-Particle Beams at Jülich, Germany, 22.-25.8.1994
World Scientific, Singapore 1995, 427-430
20.80.0

IKP-100595
Ausset, P.; Charruau, G.; Etzkorn, F.J.; Fougeron, C.*; Meuth, H.*; Papureanu, S.; A. Schnase:
A High-Power Multiple-Harmonic Acceleration System for Proton- and Heavy-Ion Synchrotrons
Poster, Proc. 1995 Particle Accelerator Conference (PAC 95), Dallas (01. - 05. Mai 1995)
20.38.0

IKP-100695
Benhar, O.; Fantoni, S.; Nikolaev, N.N.; Zakharov, B.G.
Nuclear effects in diffractive electroproduction of $S\bar{S}$ mesons
Phys. Rev. Lett. 74(1995)3565
20.80.0

IKP-100795
Benhar, O.; Fantoni, S.; Nikolaev, N.N.; Speth, J.; Usmani, A.A.; Zakharov, B.G.
The longitudinal asymmetry of the (e,e'p) missing momentum distribution as a signal of color transparency
Phys. Lett. B358(1995)191
20.80.0

IKP-100895
Bianconi, A.; Jeschonnek, S., Nikolaev, N.N.; Zakharov, B.G.
Universal pattern in (e,e'p) at large missing momenta: quasi deuteron or diffractive final state interactions?
Phys. Lett. B363(1995)217
20.80.0

IKP-100995
Bianconi, A.; Jeschonnek, S.; Nikolaev, N.N.; Speth, J.; Zakharov, B.G.
Final state interactions and NN correlations: are the latter observable?
Proceedings of the Conference on Perspectives in Nuclear Physics at Intermediate Energies, Trieste, Italy, May 1995
20.80.0

IKP-101095
Bianconi, A.; Jeschonnek, S.; Nikolaev, N.N.; Zakharov, B.G.
Final State Interaction Effects in D(e,e'p) Scattering
Phys. Lett. B343(1995)13
20.80.0

IKP-101195
Bianconi, A.; Jeschonnek, S.; Nikolaev, N.N.; Zakharov, B.G.
Apparent Coulomb Reacceleration of Neutrons in Electrodissociation of the Deuteron, Phys. Rev. C51(1995)1584
20.80.0

IKP-101295
The TOF-Facility at COSY
Bilger, R., Brand, H., Brand, S., Clement, H., Dahmen, M., Cloth, P., Dutz, W., Drüke, V., Eyrich, W., Freiesleben, H., Filges, D., Geyer, R., Hermanowski, P., Jaeckle, V., Jahn, P., Kilian, K., Kirsch, M., Koch, H., Kraft, R., Krug, J., Lange, S., Kuhlmann, E., Machner, H., Matthäy, H., Meyer, W., Michel, P., Möller, K., Morsch, H.P., Nake, C., Nann, H., Naumann, B., Naumann, L., Ringe, P., Roderburg, E., Röhrich, K., Rogge, M., Schamlott, A., Schülke, A., Schult, O., Schmidt, M., Sefzick, T., Steinke, M., Stinzig, F., Renken, V., Stratmann, V., Turek, P., Wagner, G., Wirth, S.
Proceedings of the International Conference Physics with GeV-Particle Beams, Jülich, August 22-25 (1994), Eds. H. Machner and K. Sistemich, World Scientific (1995) 564
20.45.0

IKP-101395
Blessing, G.*; Bräutigam, W.; Böge, H.G.; Gad, N.; Scholten, B.; Qaim; S.M.:
Internal Irradiation System for Excitation Function Measurement via the Stacked-Foil Technique
Appl. Radiat. Isotopes Vol. 46, No 9, pp. 955-960, 95
20.35.0

IKP-101495
Bondar, A.; Calen, H.; Carius, S.; Ekström, C.; Franssonn, K.; Gustafsson, L.; Häggström, S.; Höistad, B.; Johansson, A.; Johansson, T.; Kilian, K.; Kullander, S.; Kupsc, A.; Kuzmin, A.; Morosov, B.; Mörtsell, A.; Oelert, W.; Povtorejko, A.; Reistad, D.; Ruber, R.; Sandukovsk, S.; Schuberth, U.; Shwartz, B.; Stepaniak, J.; Sukhanov, A.; Tchernyshev, V.; Wateers, M.; Wilhelmi, Z.; Zabierowski, J.; Zlomanczuk, J.
The $pp \to pp\pi^0$ Reaction Near the Kinematical Threshold
Phys. Lett. B356 (1995) 8
20.50.0

IKP-101595
Borchert, G.L.
A doubly focussing Bragg spectrometer for high resolution studies of antiprotonic X-rays
Int. Workshop Methods and Applications of curved crystal X-ray optics, Grenoble 1995
20.50.0

IKP-101695
Borchert, G.L.
High Resolution spectroscopy of antiprotonic X-rays to study the hadronic interaction
XXIV Mazurian Lakes Summer School on Nuclear Physics, Piaski, Poland, 1995
20.50.0

IKP-101795
Bräutigam, W.; Brings; R.:
Beam Stabilization by Feedback control of the Accelerating Parameters in a Cyclotron
14th Intern. Conf. on Cyclotrons and their Applications, Cape Town, SA, 8th-14th October 1995
20.30.0

IKP-101895
Brückner, W., Kallakowsky, T., Lauber, H.M., Michaels, R., Paul, S., Povh, B., Röhrich, K., Trombini, A.
The Transition Radiation Detector in the Hyperon Beam Experiment WA89 at CERN
Preprint MPI H-V14-1995, Heidelberg, May 1995
(submitted to Nucl. Instr. and Meth.)
20.50.0

IKP-101995
Büscher, M., Cassing, W., Kamys, B., Komarov, V.I., Koptev, V., Müller, H., Sibirtsev, A. and Sistemich, K.
Investigation of Nuclear-Medium Effects on Elementary-Particle Reactions with the 0° Facility at COSY-Jülich
Proceedings of the International Conference Physics with GeV-Particle Beams, Jülich, August 22-25 (1994), Eds. H. Machner and K. Sistemich, World Scientific (1995) 431
20.45.0

IKP-102095
Calén, H.; Carius, S.; Fransson, K.; Gustafsson, L.; Häggström, S.; Hoistad, B.; Johansson, A.; Johansson, T.; Kullander, S.; Moehn, J.; Mörtsell, A.; Ruber, R.; Schuberth, U.; Zlomanczuk, J.; Ekström, C.; Kilian, K.; Oelert, W.; Sefzick, T.; Waters, M.; Bondar, A.; Kuzmin, A.; Shwartz, B.; Sidorov, V.; Kupsc, A.; Stepaniak, J.; Morosov, B.; Povtorejko, A.; Sukhanov, A.; Zabierowski, J. and Wilhelmi, Z.
The pp→ppη Reaction Near the Kinematical Threshold
Phys. Lett. (1995)
TSL/ISV-95-0124, ISSN 02884-2769, Aug. 1995
20.50.0

IKP-102195
Cassing, W., Desmki, T., Jarczyk, L., Kamys, B., Rudy, Z., Strzalkowski, A., Schult, O.W.B.
Strangeness Production in Proton and Deuteron Induced Reactions at Subthreshold Energies
Proceedings of the International Conference Physics with GeV-Particle Beams, Jülich, August 22-25 (1994), Eds. H. Machner and K. Sistemich, World Scientific (1995) 431
20.45.0

IKP-102295
Chen, B.Q., Ma, Z.Y., Krewald, S., Grümmer, F.
Properties of proton and neutron rich nuclei in the vicinity of ^{100}Sn in relativistic mean field theory
Z. Phys. G21 (1995) 1759
20.80.0

IKP-102395
Chmielewski, K.; Haidenbauer, J.; Meyer, U.; Nemote, S.; Sauer, P.U.; Schellingerhout, N.W.;
Effect of the three-nucleon force based on Δ-isobar excitation in neutron-deuteron scattering
Few-Body Systems, Suppl. 8, 394(1995)
20.80.0

IKP-102495
Cloth, P.; Filges, D. and the members of the ZEUS Collaboration:
A Search for Excited Fermions in Electron-Proton Collisions at HERA
Z. Phys. C 65 (1995) 627-647
20.48.0

IKP-102595
Cloth, P.; Filges, D. and the members of the ZEUS Collaboration:
Measurement of the Proton Structure Function F_2 from the 1993 HERA Data
Z. Phys. C 65 (1995) 379-398
20.48.0

IKP-102695
Cloth, P.; Filges, D. and the members of the ZEUS Collaboration:
Jet Production in Hith Q^2 Deep-Inelastic ep Scattering at HERA
Z. Phys. C 67 (1995) 81-92/Report, DESY 95-016, February 1995
20.48.0

IKP-102795
Cloth, P.; Filges, D. and the members of the ZEUS Collaboration:
Inclusive Transverse Momentum Distributions of Charged Prticles in Diffractive and Non-Diffractive Photoproduction at HERA
Z. Phys. C 67 (1995) 227-237/Report, DESY 95-050, March 1995
20.48.0

IKP-102895
Cloth, P.; Filges, D. and the members of the ZEUS Collaboration:
Measurement of Multiplicity and Momentum Spectra in the Current Fragmentation Region of the Breit Frame at HERA
Z. Phys. C 67 (1995) 93-107/Report, DESY 95-007, January 1995
20.48.0

IKP-102995
Cloth, P.; Filges, D. and the members of the ZEUS Collaboration:
Neutral Strange Particle Production in Deep Inelastic Scattering at HERA
Z. Phys. C 68 (1995) 29-42/Report, DESY 95-084, April 1995
20.48.0

IKP-103095
Cloth, P.; Filges, D. and the members of the ZEUS Collaboration:
Study of $D^*(2010)^{\pm}$ Production in *ep* Collisions at HERA
Phys. Lett. B. 349 (1995) 225-237/Report, DESY 95-013, February 1995
20.48.0

IKP-103195
Cloth, P.; Filges, D. and the members of the ZEUS Collaboration:
Dijet Cross Sections in Photoproduction at HERA
Phys. Lett. B 348 (1995) 665-680/Report, DESY 95-033, February 1995
20.48.0

IKP-103295
Cloth, P.; Filges, D. and the members of the ZEUS Collaboration
Inclusive Jet Differential Cross Sections in Photoproduction at HERA
Phys. Lett. B 342 (1995) 417-432
20.48.0

IKP-103395
Cloth, P.; Filges, D. and the members of the ZEUS-Collaboration:
Study of the Photon Remnant in Resolved Photoproduction at HERA
Phys. Lett. B. 350 (1995) 163-177/Report, DESY 95-083, April 1995
20.48.0

IKP-103495
Cloth, P.; Filges, D. and the members of the ZEUS Collaboration:
Measurement of the Diffractive Structure Function in Deep Inelastic Scattering at HERA
Z. Phys. C 68 (1995) 569-584/Report, DESY 95-093, May 1995
20.48.0

IKP-103595
Cloth, P.; Filges, D. and the members of the ZEUS Collaboration:
Diffractive Hard Photoproduction at HERA and Evidence for the Gluon Content of the Pomeron
Phys. Lett. B 356 (1995) 129-146/Report, DESY 95-115, June 1995
20.48.0

IKP-103695
Cloth, P.; Filges, D. and the members of the ZEUS Collaboration:
Mearsurement of Elastic ρ^0 Photoproduction at HERA
Z. Phys. C 69 (1995) 39-54/Report, DESY 95-143, July 1995
20.48.0

IKP-103795
Cloth, P.; Filges, D. and the members of the ZEUS Collaboration:
Exclusive ρ^0 Production in Deep Inelastic Electron-Proton Scattering at HERA
Phys. Lett. B 356 (1995) 601-616/Report, DESY 95-133, July 1995
20.48.0

IKP-103895
Cloth, P.; Filges, D. and the members of the ZEUS Collaboration:
Observation of Hard Scattering in Photoproduction Events with a Large Rapidity Gap at HERA
Phys. Lett. B 346 (1995) 399-414
20.48.0

IKP-103995
Cloth, P.; Filges, D. and the members of the ZEUS Collaboration:
Extraction of the Gluon Density of the Proton at χ
Phys. Lett. B 345 (1995) 576-588
20.48.0

IKP-104095
Cloth, P.; Filges, D.; and the members of the ZEUS Collaboration:
Measurement of the Cross Section for the Reaction $\gamma p \rightarrow J/\psi p$ with the ZEUS Detector at HERA
Phys. Lett. B 350 (1995) 120-134/Report, DESY 95-052, March 1995
20.48.0

IKP-104195
Cloth, P.; Filges, D.; and the members of the ZEUS Collaboration:
Measurement of α_s from Jet Rates in Deep Inelastic Scattering at HERA
Phys. Lett. B 363 (1995) 201-216/Report, DESY 95-182, Oct. 1995
20.48.0

IKP-104295
Cloth, P.; Filges, D. and the members of the ZEUS Collaboration:
Inclusive Charged Particle Distributions in Deep Inelastic Scattering Events at HERA
Report, DESY 95-221, November 1995
20.48.0

IKP-104395
Cloth, P.; Filges, D.; and the members of the ZEUS Collaboration:
Measurement of Charged and Neutral Current $e^- p$ Deep Inelastic Scattering Cross Sections at High Q^2
Phys. Rev. Lett. 6, Vol. 75 (1995) 1006-1011, August 1995/
Report, DESY 95-053, March 1995
20.48.0

IKP-104495
Collatz, R., Kleinheinz, P., Zhang, C.T., Saad, A.F., Vieu, C., Dionisio, J.S., Schück, C., Wilhelm, M., von Brentano, P., Wirowski, R., Blomqvist, J.
Particle x phonon multiplets in $^{147}_{65}Tb_{82}$
Z. Phys. A351 (1995) 245-246
20.10.0

IKP-104595
Daum, M., Vinzelberg, S., Gotta, D., Ullrich, H., Backenstoss, G., Weber, P., Weyer, H.J., Furic, M., and Petkov, T.
Pion Absorption at Rest in ^{4}He
Nucl. Phys. A589 (1995) 553
20.50.0

IKP-104695
Dietrich, J.; Bojowald, J.; Labus, M.; Maier, R.; Mohos, I.:
Diagnostic Tools for the Resonant Extraction at COSY-Jülich
Proc. Europ. Workshop on Beam Diagnostic and Instr. for Particle Accelerators, DIPAC 2, Travemünde (1995), DESY M-9507
20.35.0

IKP-104795
Dietrich, J.; Bojowald, J.; Bongardt, K.; Labus, M.; Lawin, H.; Maier, R.; Mohos, I.; Wagner, R.:
Diagnostic Tools for the COSY-Jülich Synchrotron
Proc. Beam Instr. Workshop, Vancouver (1994)
AIP Conf. Proc. No. 333, ISBN 1-56396-352-3, 1995
20.35.0

IKP-104895
Drozdz, S.; Nishizaki, S.; Wambach, J.; Speth, J.
Phase-space exploration in nuclear giant resonance decay
Phys. Rev. Lett. Vol.74 (1995)7
20.80.0

IKP-104995
Filges, D.:
Target-Moderator-System: Target Concepts
Proc. of the Meetings ICANS-XIII and ESS-PM4, Vol. I, Villigen PSI, Switzerland, Oct. 11-14, 1995 and Weinfelden, Switzerland, Oct. 16-19, 1995
20.48.0

IKP-105095
Filges, D.; Neef, R.D.; Schaal, H.:
Nuclear Studies of Different Target Systems for the European Spallation Source (ESS)
Proc. of the Meetings ICANS-XIII and ESS-PM4, Vol. II, Villigen PSI, Switzerland, Oct. 11-14, 1995 and Weinfelden, Switzerland, Oct. 16-19, 1995
20.48.0

IKP-105195
Filges, D.; Nagel, P.; Neef, R.D.:
Thick Target Benchmark for Lead and Tungsten
Int. Code Comparison for Intermediate Energy Nuclear Data (AEN/NEA)
Report NSC/DOC(95)2-OECD, Feb. 1995
20.48.0

IKP-105295
Forkel-Wirth, D., Jahn, S., Otto, T., Röhrich, K., Wirth, H.
Arbeitsmarkt für Physiker: eine Bilanz aus Sicht der Betroffenen
Phys. Bl. 51,2 (1995) 85
20.50.0

IKP-105395
Gadea, A., Rubio, B., Tain, J.L., Rico, J., Bea, J., Garcia-Raffi, L.M., Kleinheinz, P., Schardt, D., Roeckl, E., Kirchner, R., Blomqvist, J.
Properties of the $^{150}_{69}Tm_{81}$ 6^- ß-decaying isomer
Z. Phys. A, in press
20.10.0

IKP-105495
Genovese, M.; Nikolaev, N.N.; Zakharov, B.G.
Direct calculation of the triple-pomeron for diffractive DIS and real photoproduction
Zh. Exp. Theor. Fiz. 108(1995)1155
20.80.0

IKP-105595
Genovese, M.; Nikolaev, N.N.; Zakharov, B.G.
Diffractive DIS from the generalized BFKL pomeron.
Predictions for HERA
Zh. Exp. Theor. Fiz. 108(1995)1141
20.80.0

IKP-105695
Gorke, H., Borchert, G., Erven, W., Gotta, D., Indelicato, P., Kendziorra, E., Krämer, J., Meidinger, N., Mohan, M., Strüder, L., von Zanthier, C., Zwoll, K.
A pn-CCD detector with high rate capability for X-ray measurements
7th European Symposium on Radiation Detectors, Elmau, 1995
20.50.0

IKP-105795
Gotta, D.
Protonium Spectroscopy
Proceedings of the Third Biennial Conference on Low Energy Antiproton Physics, Bled, Slovenia, September 12-17, 1994, Eds. G. Kernel, P. Krizan, M. Mikuz, World Scientific (1995) 525
20.50.0

IKP-105895
Gotta, D., Dörr, M., Fetscher, W., Schmidt, G., Ullrich, H., Backenstoss, G., Izycki, M., Kowald, W., Schwanner, I., Weber, P., and Weyer, H.J.
Negative Pion Absorption at Rest in ^{3}He
Phys. Rev. C51 (1995) 469
20.50.0

IKP-105995
Grzonka, D.
The experimental program at COSY-Jülich
Nucl. Phys. A585 (1995) 321c
20.50.0

IKP-106095
Hacker, U.; Röhling, R.*; Weinert, A.:
The VXIbus Industry Standard as Platform to build Scaleable Safeguards Instrumentation Systems
ESARDA 1995, 17. Ann. Symp., Proc.
Aachen, 09.-11.05.1995
20.30.0

IKP-106195
Hacker, U.; Röhling, R.*; Richter, A.; Weinert, A.;
Arlt, R.*; Lewis, W.*; Swinhoe, M.*:
VXIbus Data Collextion System - A Design Study
INMM 1995, Proc. of the 36th Annual INMM Meeting, Palm Desert/USA, Juli 1995
20.30.0

IKP-106295
Haidenbauer, J.; Holinde, K.; Kilian, K.; Sefzick, T.;
Thomas, A.W.
Weak strangeness production in nucleon-nucleon scattering
Phys. Rev. C52(1995)3496
20.80.0

IKP-106395
Hanhart, C.; Krewald, S.
Faddeev approach to the octet and decuplet baryons
Phys.Lett.B344(1995)55-60
20.80.0

IKP-106495
Hanhart, C.; Haidenbauer, J.; Reuber, A.; Schütz, C.;
Speth, J.
The reaction $\pi\pi \rightarrow pp\pi^0$ near threshold
Phys. Lett. B 359(1995)21-26
20.80.0

IKP-106595
Hanhart, C.; Haidenbauer, J.; Reuber, A.; Schütz, C.; Speth, J.;
Energy dependence of the reaction $pp \rightarrow pp\pi^0$ near threshold
Proceedings of the 6th International Symposium on Meson-Nucleon Physics and the Structure of the Nucleon, Blaubeuren 1995, edited by D. Drechsel, G. Höhler, W. Kluge and B.M.K. Nefkens, πN Newsletter 10, 167-169(1995)
20.80.0

IKP-106695
Hanhart, C.; Schütz, C.; Holinde, K.; Speth, J.
Pion-nucleon scattering and pion production
Proceedings of the „International Nuclear Physics Conference", Beijing, China, 21.-26.8.1995
World Scientific, Singapore
20.80.0

IKP-106795
Hencken, K.; Trautmann, D.; Baur, G.
Higher Order Process in Electromagnetic Production of Electron Positron Pairs in Relativistic Heavy Ion Collisions
Phys. Rev. A51(1995)998-1014
20.80.0

IKP-106895
Hencken, K.; Trautmann, D., Baur, G.
Impact-parameter Dependence of the Total Probability of the Electromagnetic Electron-Positron Pair Production in Relativistic Heavy-ion Collisons
Phys. Rev. A51(1995)1874-1882
20.80.0

IKP-106995
Hencken, K.; Trautmann, D.; Baur, G.
Photon-Photon Luminorities in Relativistic Heavy Ion Collisions at LHC Energies
Z. Phys. C68(1995)473-479
20.80.0

IKP-107095
Hencken, K.; Mühry, H.; Sick, I.; Trautmann, O.; Baur, G.
Colour van der Waals effects in Pb-Pb Scattering?
Nucl. Phys. A591(1995)548-560
20.80.0

IKP-107195
Hoffmann, M.; Durso, J.W.; Holinde, K.; Pearce B.C.; Speth, J.
The correlated 2π-exchange in K^+N interaction
Nucl. Phys. A593(1995)341
20.80.0

IKP-107295
Holinde, K.; Kim, H.-C.; Reuber, A.; Speth, J.
Correlated two-pion exchange in the hyperon-nucleon system
Nucl. Phys. A585(1995)149c
20.80.0

IKP-107395
Holinde, K.; Herscovitz, V.E., Vasconcallos, C.A.Z.; Ferreira, E.
Two-Body Reactions Involving Antiparticles
in Hadron Physic 94, Rio Grande do Sul, Brazil, 10.-14. April 1994, World Scientific (1995)
20.80.0

IKP-107495
Holinde, K.
The Bonn Potential
Few Body Systems Suppl. 8(1995)484
20.80.0

IKP-107595
Holtmann, H.; Szczurek A.; Nikolaev, N.N.; Speth, J.
Mesons and the Flavour Structure of the Nucleon
ELFE-Workshop, Cambridge, UK
Juli 1995
20.80.0

IKP-107695
Holtmann, H.; Nikolaev, N.N.; Speth, J.; Szczurek, A.
Zakharov, B.G.
On the determination of double diffraction dissociation cross section at HERA
Z. Phys. C69(1995)297
20.80.0

IKP-107795
Igel, S.; Hamacher, A., Kilian, K., Machner, H., Protic, D., Srikantiah, R.V., Kystrin, St., Budzanowski, A., Kliczewski, S.
The Germanium Wall of the GEM Detector System
Acta Physica Polonica B26 (1995) 627-631
Proc. of the Int. Conf. Physics with GeV-Particle Beams, World Scientific Publ., Singapure (1995) 556
20.45.0

IKP-107895
Janssen, G.; Pearce, B.C.; Holinde, K.; Speth, J.
On the structure of the scalar mesons $f_0(975)$ and $a_0(980)$
Phys. Rev. D52(1995)2690
20.80.0

IKP-107995
JETSET Collaboration (PS202)
Observation of $\Phi\Phi$ production in the reaction $pp \rightarrow 4K^{\pm}$ at 1.4 GeV/c incident p momentum
CERN-PPE/94-221, Phys. Lett. B345 (1995) 325
20.50.0

IKP-108095
Kalassa, D.M., Baur, G.
The effective range approach to the electromagnetic dissociation of loosely bound nuclei
Proc. of the Jülich Conf. on GeV-Beams, Eds. H. Machner and K. Sistemich, World Scientific (1995) 468
20.80.0

IKP-108195
Kamerdzhiev, S.; Speth, J.; Tertychny, G.
Splitting of the isoscalar E2 giant resonance and evidence of low-lying E0 strength in ^{40}Ca
Phys. Rev. Lett. Vol. 74 (1995) 20
20.80.0

IKP-108295
Külz; U.:
Entwicklung einer graphischen Oberfläche zur Steuerung und Kontrolle des großen Magnetspektrometers BIG KARL (Diplomarbeit)
20.30.0

IKP-108395
Kutsarova, T., Lieder, R.M., Schnare, H., Hebbinghaus, G., Balabanski, D., Gast, W., Krämer-Flecken, A., Bentley, M.A., Fallon, P., Howe, D., Mokhtar, A.R., Sharpey-Schafer, J.F., Walker, P., Chowdhury, P., Fabricius, B., Sletten, G. and Frauendorf, S.
Study of High-Spin States in $^{181,182}os$
Nucl. Phys. A587 (1995) 513-540
20.10.0

IKP-108495
Lauter, J.; Protic, D.; Förster, A., Lüth, H.:
AlGaAs/GaAs SAM-avalanche photodiode: An X-ray detector for low energy photons
Nucl. Instr. and Meth. in Phys. Res. A356 (1995) 324-329
20.20.0

IKP-108595
Lauter, J.; Bauser, E.; Förster, A.; Hardtdegen, H.; Hollfelder, M.; Lüth, H.; Protic, D.; Zehender, S.:
Epitaxial Gallium Arsenide for Nuclear Radiation Detector Applications
Nuclear Physics B (Proc. Suppl.) 44 (1995) 381-385
20.20.0

X. CONFERENCE CONTRIBUTIONS, TALKS

IKP-200195
Akindinov, A., Büscher, M., Chumakov, M., Demechin, V., Eßer, R., Franzen, A., Gerasimov, A., Goryachev, V., von Horn, L., Kiselev, Y., Koptev, V., Kopyto, D., Kostromin, V., Kruglov, V., Mikirtychants, S., Ohm, H., Pritzschk, B., Rimarzig, B., Schneider, C., Schult, O., Sibirtsev, A., Sistemich, K., Sopov, V., and Tchernyshev, V.
Measurement of the cross-section ratio $\sigma(K^+):\sigma(\pi^+):\sigma(p)$ in p-Be interactions at T_p = 2.9 GeV
Verhandlungen der DPG (VI) 30, 686 (1995) Köln
13.03.-17.03.1995
20.45.0

IKP-200295
Baur, G.; Bröders, R.; Chanel, M.; Dahmen, M.; Grzonka, D.; Kilian, K.; Lefèvre, P.; Möhl, D.; Molinari, G.; Oelert, W.; Röhrich, K.; Rook, M.; Sachs, K.; Sefzick, T.; Simon, R.S.; Steinkamp, O.
Search for Antihydrogen at LEAR/CERN
Verhandlungen der DPG (VI) 30, 684 (1995)
20.50.0, 20.80.0

IKP-200395
Baur, G.
Breakup of Neutron-Rich Nuclei
First Spiral Workshop, GANIL, Caen, France
30.-31.1.1995
20.80.0

IKP-200495
Baur, G.
Überlegungen zur „Trojan Horse"-Methode
Workshop über Nukleare Astrophysik, GSI Darmstadt, Germany
2.-3.2.1995
20.80.0

IKP-200595
Baur, G.
Indirect Methods in Nuclear Astrophysics
Seminarvortrag, University of Brüssel, Belgium
8.3.1995
20.80.0

IKP-200695
Baur, G.
Electromagnetic Dissociation, Nuclear Structure and Astrophysics
Intern. Spring Seminar on Nuclear Physics, New Perspectives in Nuclear Structure
Ravello, Italy,
22.-26.5.1995
20.80.0

IKP-200795
Baur, G.
Indirect Methods in Nuclear Astrophysics
Seminar, MPI für Kernphysik, Heidelberg, Germany
15.5.1995
University of Catania
18.5.1995

IKP 200895
Baur, G.
Coulombdissoziation: Kernstruktur und nukleare Astrophysik
Kernphysikalisches Kolloqium, LMU und TU München, Germany
15.12.1995
20.80.0

IKP-200995
Bovin, M.; Boyard, J.L.; Fuchs, P.; Hennino, T.; Jaeckle, V.; Jourdan, J.C.; Kunne, R.; Morsch, H.P.; Plouin, F.; Radvanyi, P.; Ramstein, B.; Rousteau, S.; Roy-Stephan, M.; Spang, W.; Tegner, P.E.; Zupranski, P.
Investigation of the Roper Resonance Excitation in Light Nuclei
Verhandlungen der DPG (VI) 30, 631 (1995)
20.45.0

IKP-201095
Büscher, M.
Experimente zur Mesonenproduktion in pA Stößen mit dem 0° Spektrometer an COSY-Jülich - Simulationsrechnungen und Detektorentwicklung
Seminary talk, Institut für Kernphysik, GSI Darmstadt, Germany
07.03.1995
20.45.0

IKP-201195
Büscher, M. and Franzen, A.
Simulation calculations for the side-detection system of the 0° Facility at COSY-Jülich
Verhandlungen der DPG (VI) 30, 677 (1995) Köln
13.03.-17.03.1995
20.45.0

IKP-201295
Büscher, M.
Der Physiker in staatlichen Großforschungseinrichtungen
DPG-Seminar „Der Physiker im Beruf", Bad Honnef, Germany
06.05.1995
20.45.0

IKP-201395
Büscher, M.
Planung und Status der 0°-Facility ANKE
13. CANU Arbeitstreffen, Bad Honnef, Germany
16.12.-17.12.1995
20.45.0

IKP-201495
Collatz, R., Kleinheinz, P., Zhang, C.T., Vieu, C., Dionisio, J.S., Schück, C., Wilhelm, M., von Brentano, P., Wirowski, R., and Blomqvist, J.
Particle x phonon multiplets in $^{147}_{65}Tb_{82}$
Verhandlungen der DPG (VI) 30, 781 (1995) Köln
13.03.-17.03.1995
20.10.0

IKP-201595
Diart, K.H. for the COSY-11 Collaboration
Entwicklung der Silizium-Streifen-Detektoren für das Experiment COSY-11
Verhandlungen der DPG (VI) 30, 583 (1995)
20.50.0

IKP-201695
Dietrich, J.:
Strahldiagnose zur Verbesserung der Resonanzextraktion an COSY
Winterseminar des Instituts für Angewandte Physik der J.W. Goethe-Universität, Frankfurt/Main,
Riezlern, 26.02.-04.03.95
20.30.0

IKP-201795
Dietrich, J.; Bojowald, J.; Labus, H.; Maier, R.; Mohos, I:
Diagnostic Tools for the Resonant Extraction at COSY-JUELICH
DIPAC'95, Travemünde
20.30.0

IKP-201895
Dietrich, J.:
Recent Beam Diagnostic Techniques
CYCLOTRONS'95
Süd-Afrika, Cape Town, 8-13.10.95
20.30.0

IKP-201995
Drochner, M.; Jarczyk, L.; Kemmerling, G.; Klimala, W.; Lippert, G.; Machner, H.; Zolnierczuk, P.A. for the GEM Collaboration at COSY
Event Reconstruction Analysis at GEM Experiments
Verhandlungen der DPG (VI) 30, 639 (1995)
20.45.0

IKP-202095
Ernst, J.; Drochner, M.; Igel, S.; Jarczyk, L.; Jahn, R.; Kemmerling, G.; Kilian, K.; Kliczewski, S.; Klimala, W.; Lippert, G.; Machner, H.; Mayer, R.; v. Rossen, P.; Scho, K.; Siudak, R.; Smyrski, J.; Strzalkowski, A.; Zolnierczuk, P.; Zwoll, K.
First Pion Studies at GEM
Verhandlungen der DPG (VI) 30, 744 (1995)
20.45.0

IKP-202195
Eßer, R., von Horn, L., Kopyto, D., Ohm, H., Büscher, M., Franzen, A., Chumakov, M., Gerasimov, A., Sopov, V., Tchernyshev, V., Kostromin, V., Mikirtychants, S., Koptev, V., Prietzschk, B., Rimarzig, B., Schneider, Chr. and Kruglov, V.
The detector setup for K^+-production studies at the 0° Facility of COSY Jülich: Test measurements at ITEP Moscow
Verhandlungen der DPG (VI) 30, 676 (1995) Köln
13.03.-17.03.1995
20.45.0

IKP-202295
Eyrich, W. for the PS185-Collaboration
Study of Threshold Production of $\bar{p}p \rightarrow \bar{\Lambda}\Lambda$ at PS185
Verhandlungen der DPG (VI) 30, 784 (1995)
20.50.0

IKP-202395
Filges, D.; Gloris, M.; Herpers, U.; Michel, R.; Sudbrock, F.:
Production of Residual Nuclei from Irradiation of Thin Pb-Targets with Protons up to 1.6 GeV
4th European Conf. on Accelerators in Applied Research and Technology (ECAART-4), Zürich, Switzerland, 29. August - 2. September 1995
20.48.0

IKP-202495
Filges, D.:
Teilchentransport und Simulation
Gastvorlesungen am Institut für Theoretische Physik, Techn. Univ. Graz, Austria, 20.-31.3.1995; 2.-12.5.1995; 12.-23.6.1995
20.48.0

IKP-202595
Filges, D.; Neef, R.D.:
Status and Perspectives of Theoretical Predictions for Material Damage and Gas Production of Spallation Relevant Materials,
Workshop held at Los Alamos National Laboratory, Feb. 6-10, 1995
20.48.0

IKP-202695
Filges, D.; Neef, R.D.; Schaal, H.:
Comparison of the Target Materials Mercury, Tungsten and Tantalum for ESS Specifications
Fourth General ESS-Meeting, Weinfelden/Switzerland, Oct. 16-19, 1995
20.48.0

IKP-202795
Filges, D.; Neef, R.D.; Schaal, H.:
Nuclear Simulations for the ESS Tantalum Reference Target Concept
Third General ESS-Meeting, Baden/Austria, March 21-26, 1995
20.48.0

IKP-202895
Freindl, L.; Igel, S.; Kilian, K.; Kliczewski, S.; Lippert, G.; Machner, H. for the GEM-Collaboration
The Scintillation Detectors at BIG KARL
Verhandlungen der DPG (VI) 30, 676 (1995)
20.45.0

IKP-202995
Gast, W.
Investigation of Configuration-Dependent Shape Changes in ^{180}Os
Workshop on Experiments wwith EUROBALL CLUSTER Detectors in 1995/96, Bad Honnef, 19.1.1995
20.10.0

IKP-203095
Gast, W.
Digitale Signalverarbeitung in der hochauflösenden Spektroskopie
Seminarvortrag im ISKP der Universität Bonn, 12.6.1995
20.10.0

IKP-203195
Gast, W.
Digital Signal Processing in High Resolution Spectroscopy
XII Int. School on Nucl. Phys., Neutron Physics and Nuclear Energy, Varna, Bulgarien, 30.9.1995
20.10.0

IKP-203295
Georgiev, A.; Gast, W.; Goecking, K.; Rose, T.; Wolters, H.
An ASIC for Detector Signal Processing
Verhandlungen der DPG (VI) 30, 735 (1995)
20.10.0

IKP-203395
Geyer, R. for the COSY-TOF collaboration
Results of the First Measurement of the Time of Flight Spectrometer TOF at COSY
Verhandlungen der DPG (VI) 30, 744 (1995)
20.50.0

IKP-203495
Gotta, D.
Status report on LEAR experiment PS207
BVRA, PSI Villigen
20.06.1995
20.50.0

IKP-203595
Gotta, D.
Protonium X-ray spectroscopy
Third Bienniel Workshop on Nucleon-Antinucleon Physics
11.-16.9.1995, ITEP, Moscow, Russia
20.50.0

IKP-203695
Gotta, D.
Status report on LEAR experiment PS207
SPSLC, CERN Geneva
21.11.1995
20.50.0

IKP-203795
Haidenbauer, J.
Weak strangeness production in nucleon-nucleon scattering
DPG, Frühjahrstagung, Köln, Germany,
15.3.1995
20.80.0

IKP-203895
Haidenbauer, J.; Holinde, K.; Schütz, C.; Speth, J.
πNN form factors determined from πN scattering and its role in NN scattering
15th European Conference on Few-Body Problems in Physics
Peniscola, Spanien,
5.-9.6.1995
20.80.0

IKP-203995
Haidenbauer, J.
The reaction $pp \rightarrow pp\pi^0$ near threshold
6th International Symposium on Meson-Nucleon Physics and the Structure of the Nucleon,
Blaubeuren/Tübingen, Germany
10.-14.7.1955
20.80.0

IKP-204095
Haidenbauer, J.
Meson production in nucleon-nucleon collisions near threshold
Seminar, Physics-Institute, University Sao Paolo, Brazil
24.10.1995
Seminar, Linear Acclerator Laboratory, University Sao Paolo, Brazil
7.11.1995
Seminar, University Florianopolis, Brazil
14.11.1995
Seminar, University Niteroi, Brazil
21.11.1995
20.80.0

IKP-204195
Haidenbauer, J.
Hyperon production in antinucleon-nucleon reactions
PS 185 Collaboration Meeting, Bad Honnef
29.11.1995
20.80.0

IKP-204295
Hanhart, C.
Consistent Description of Octed and Decuplet Baryons in the NJL-model
DPG-Frühjahrstagung, Köln, Germany
14.3.1995
20.80.0

IKP-204395
Hanhart, C.
The reaction $pp \rightarrow pp\pi^0$ at threshold
TRIUMF, Vancouver, USA
17.7.1995
Indiana University, Bloomington, USA
3.10.1995
20.80.0

IKP-204495
Hanhart, C.
π-Threshold production
University of Ohio, USA
9.11.1995
State University of New York, Stony Brook, USA
22.11.1995
Brooklyn College, New York, USA
20.80.0

IKP-204595
Heinrichs, G.:
Digitale Rauschsynthese für USE an COSY
Beschleunigerseminar, Uni Bonn, 11.07.1995
20.38.0

IKP-204695
Hencken, K.; Trautmann, D.; Baur, G.
Photon-Photon Physics with Heavy Ions at LHC
Photon '95 Sheffield University
8.-13.4.1995
20.80.0

IKP-204795
Hoffmann, M.
Role of correlated 2π-exchange in the K^+N-interaction
SUNY at Stony Brook, New York, USA
5.1.1995
W. K. Kellog Radiation Lab. California, USA
10.7.1995
Los Alamos National Lab., New Mexico, USA
20.7.1995
20.80.0

IKP-204895
Holinde, K.
Towards a Consistent Description of $N\bar{N}$ Scattering and Annihilation
Seminar, Univ. of Valencia, Spain
2.6.1995
20.80.0

IKP-204995
Holinde, K.
The Bonn Potential
Invited Talk, 15th European Conference Few-Body Problems in Physics, Peniscola, Spain
9.6.1995
20.80.0

IKP-205095
Holinde, K.
Recent Developments in the Hyperon-Nucleon Interaction
Seminar, Univ. of Barcelona, Spain
12.9.1995
20.80.0

IKP-205195
Holinde, K.
Meson Meson Correlations in Baryon-Baryon and Antibaryon-Baryon Interactions
Invited seminar, International School of Nuclear Physics, 17th course; „Quarks in hadrons and nuclei", Erice, Italy, 25.9.1995
20.80.0

IKP-205295
Holtmann, H.; Szczurek, A.; Nikolaev, N.N.; Speth, J.
Non-perturbative mesonic structure of nucleons as seen in elastic and deep-inelastic scattering off nucleons
DPG-Frühjahrstagung, Köln, Germany
14.3.1995
20.80.0

IKP-205395
Holtmann, H.
Mesonen im Nukleon und die $\bar{u} - \bar{d}$ Asymmetrie
Studientage des Graduiertenkolleges „Die Erforschung der subnuklearen Struktur der Materie"
Brodenbach, Germany
November 1995
20.80.0

IKP-205495
Holtmann, H.
Mesons in the Nucleon and their Consequences in elastic and deep-inelastic scattering
Invited Talk, Heidelberg, Germany
December 1995
20.80.0

IKP-205595
Igel, S.; Hamacher, A.; Kilian, K.; Machner, H.; Protic, D.
The Germanium Wall of the GEM-Detector System
Verhandlungen der DPG (VI) 30, 732 (1995)
20.45.0

IKP-205695
Jeschonnek, S.
Final State Interaction Effects in Quasielastic Electron Scattering
DPG-Frühjahrstagung, Köln, Germany
14.3.1995
20.80.0

IKP-205795
Jeschonnek, S.
Final State Interaction Effects in Quasielastic Electron Scattering from Light Nuclei
University of Pisa, Italy
20.6.1995
University of Perugia, Italy
22.6.1995
Istituto Nazionale di Fisica Nucleare, Rome, Italy
26.6.1995
University of Lecce, Italy
28.6.1995
20.80.0

IKP-205895
Jeschonnek, S.
Final State Interaction Effects in Quasielastic Electron Scattering at CEBAF energies
Seminar NIKHEF, Amsterdam, The Netherlands
16.11.1995
20.80.0

IKP-205995
Kalassa, D.M.; Baur, G.
Time evolution of the ^{8}Be final state wave function after a Coulomb dissociation.
DPG-Frühjahrstagung, Köln, Germany
13.-17.3.1995
20.80.0

IKP-206095
Kalassa, D.M.
The effective range approach to the electromagnetic dissociation of loosely bound nuclei.
Int. Students Workshop on Electromagnetic Interactions, Bosen/Saar, Germany
3.-8.9.1995
20.80.0

IKP-206195
Kilian, K.
Zweistufen-Prozesse im Teilchenbild
Arbeitstreffen „Kernphysik", Schleching, 1.-9.3.1995
20.50.0

IKP-206295
Kilian, K.
COSY Physics
Int. Workshop on Polarized Beams and Polarized Gas Targets
Köln, 6.-9.6.1995
20.50.0

IKP-206395
Kilian, K.
Physik an COSY
6th Int. Symp., Tübingen, 10.-14.7.1995
20.50.0

IKP-206495
Kilian, K.
COSY-Physics: Baryon Resonances and Meson Production at Threshold
ELFE Summer School, Cambridge, 22.-28.7.1995
20.50.0

IKP-206595
Kilian, K.
Status and Future Plans for COSY
7th Int. Conf. Baryons '95, Santa Fe, New Mexico, 3.-7.10.1995
20.50.0

IKP-206695
Kilian, K.; Oelert, W.; Renken, V.; Sefzick, T.; Waters, M.
Eta Production in Proton Deuteron Collision
Verhandlungen der DPG (VI) 30, 595 (1995)
20.50.0

IKP-206795
Kleinheinz, P.
The Gamow-Teller 1^+ interaction in Yrast states of N=84 nuclei
IFIC Valencia
02.03.1995
20.10.0

IKP-206895
Kleinheinz, P., Zhang, C.T., Collatz, R., Saad, A.F., Menegazzo, R., Broda, R., Maier, K.H., Grawe, H., Schramm, M., Schubart, R., Lach, M., Heese, J., Eberth, J., Krolas, W., Hofmann, S., Folger, H., and Blomqvist, J.
Shell-model yrast states in the many-particle nucleus $^{157}_{52}Hf_{85}$
Verhandlungen der DPG (VI) 30, 782 (1995) Köln
13.03.-17.03.1995
20.10.0

IKP-206995
Kobus, H.; Cloth, P.; Drüke, V.; Filges, D.; Maier, R.; Paganetti, H.:
Comparison of Different Monte Carlo Programs for Use in Proton Dosimetry
Eighth Symposium on Neutron Dosimetry, Paris/France, 13.-17. November 1995
20.48.0

IKP-207095
Kobus, H.:
Teilchentransportsimulation zur Entwicklung der Protonentherapie
Seminar Institut für Theoretische Physik, Techn. Univ. Graz, Austria, 15.12.1995
20.48.0

IKP-207195
Krewald, S.
Endzustandswechselwirkung in der (e,e'n) Reaktion
Seminar, Universität Basel, Schweiz
9.2.1995
20.80.0

IKP-207295
Krewald, S.
Neutrino and Electron Induced Reactions in Nuclei
Invited Talk, APS Meeting, Washington, USA
17.-21.4.1995
Seminar, Universität Grenoble, France
19.10.1995
20.80.0

IKP-207395
Lehrach, A.:
Simulationen für die Beschleunigung polarisierter Protonen in COSY
Beschleunigerseminar, Uni Bonn, 13.06.1995
20.38.0

IKP-207495
Lehrach, A.:
Vorbereitungen für einen polarisierten Strahl
13-CANU Arbeitstreffen, 18. und 19.12.1995
Physikzentrum Bad Honnef
20.30.0

IKP-207595
Leunissen, P.:
Simulationen für die Beschleunigung polarisierter Protonen in COSY
Beschleunigerseminar, Uni Bonn, 30.05.1995
20.38.0

IKP-207695
Lieder, R.M.
Study of K-isomers in ^{180,181}02
Workshop on Experiments with EUROBALL CLUSTER Detectors in 1995/96, Bad Honnef, 19.1.1995
20.10.0

IKP-207795
Lieder, R.M.
The EUROBALL Project and New Results on Superdeformation in ^{145}Gd
Seminarvortrag im Institute of Experimental Physics, Univ. of Warsaw, Polen, 2.2.1995
20.10.0

IKP-207895
Lieder, R.M.
Triaxial Shapes in Os Nuclei at high Spin
Gruppenvortrag auf der Frühjahrstagung der DPG, Fachausschauß Physik der Hadronen und Kerne, Köln, 14.3.1995
20.10.0

IKP-207995
Lieder, R.M.; Gast, W.; Hebbinghaus, G.; Krämer-Flecken, A.; Rzaca-Urban, T.; Schnare, H.; Urban, W.; Balabanski, D.; Hristov, D.H.; Wyss, R.
Band Termination in ^{186}Os
Verhandlungen der DPG (VI) 30, 658 (1995)
20.10.0

IKP-208095
Lieder, R.M.
Complex Decays of K-isomers
MINIBALL Workshop, Heidelberg, 24.5.1995
20.10.0

IKP-208195
Machner, H.
The GEM Detector: Status and first Experiments
Seminar Bhabha Atomic Research Centre, Bombay, India, 3.1.1995
20.45.0

IKP-208295
Machner, H.
Study of the $p+p \rightarrow \pi^+ + d$ Reactions Close to Threshold
Int. Conf. on Meson-Nucleon Physics, Blaubeuren, 13.7.1995
20.45.0

IKP-208395
Machner, H.
COSY Jülich and first Experiments with the GEM-Detector System
Koll. talk, St. Petersburg Inst. of Nucl. Phys., Gatchina, Russia, 8.9.1995
20.45.0

IKP-208495
Machner, H.
With COSY Accelerator and first Pion Production Studies with the GEM Detector System
3rd Int. Conf. on Nucleon-Antinucleon Physics, Moscow, Russia, 16.9.19955
20.45.0

IKP-208595
Machner, H.
Status of the $p+p \rightarrow \pi^+ + d$ Reaction Close to Threshold
CANU Jahrestreffen Bad Honnef, 18.12.1995
20.45.0

IKP-208695
Machner, H.
Production of π^0's in Ion-Ion Interactions Close to the Absolute Threshold
Dae Symposium on Nuclear Physics, Utkal University, Bhubaneswar, India, 20.12.1995
20.45.0

IKP-208795
Maier, R.:
Physik der Kühlerringe
FZ- Rossendorf, 21. März 1995
20.30.0

IKP-208895
Maier, R.:
Die Beschleunigeranlage COSY
GSI Darmstadt, 18. Mai 1995
20.30.0

IKP-208995
Maier, R.; Bechstedt, U.; Dietrich, J.; Martin, S.; Prasuhn, D.; Schnase, A.; Schneider, H.; Stockhorst, H.; Tölle, R.:
Commissioning of the Cooler Synchrotron COSY
CYCLOTRONS'95
Süd-Afrika, Cape Town, 8-13.10.95
20.30.0

IKP-209095
Maier, R.:
Scherpunkte in Betrieb und Entwicklung von COSY
13-CANU Arbeitstreffen, 18. und 19.12.1995
Physikzentrum Bad Honnef
20.30.0

IKP-209195
Mohos, I.:
Strahlpositionsmonitore für ELSA
Beschleungierseminar, Uni Bonn, 23.05.1995
20.35.0

IKP-209295
Morsch, H.P.
Study of the Roper Resonance Excitation in α-Scattering
Invited Talk, 11. Nordic Meeting onn Intermediate and High Energy Physics, Gräftavallen, Sweden, 4.-8.1.1995
20.45.0

IKP-209395
Morsch, H.P.
Summary of the Nordic Meeting on Intermediate Ennergy Nuclear Physics
Café LNS, 10.3.1995
20.45.0

IKP-209495
Morsch, H.P.
Astro-Nuclear Problems
Café LNS, 24.3.1995
20.445.0

IKP-209595
Morsch, H.P.
Excitation of the Roper (1440 MeV) Resonance
Innvited Talk, 10. Journée Thématique, IPN Orsay, 21.6.1995
20.45.0

IKP-209695
Morsch, H.P.
The Problem of the Baryon Compressibility
Invited Contribution, Internal Conference „Baryon '95", Santa Fe, 2.-7.10.1995
20.45.0

IKP-209795
Mull, V.
Role of Meson-Meson Correlations in the $\bar{N}N \rightarrow p\pi$ Annihiltion Process
DPG-Tagung, Köln, Germany
17.3.1995
20.80.0

IKP-209895
Mull, V.
A Combined Description of $\bar{N}N$ Scattering and Annihilation with a Hadronic Model
Seminar, Instituto da Fisica, Universidade Federal do Rio Grande do Sul, UFRGS, Porto Alegre, RS, Brazil
11.10.1995
Seminar, Instituto da Fisica, Universidade Federal de Santa Catarina, UFSC, Florianapolis, SC, Brazil
26.10.1995
Seminar, Instituto da Fisica, Universidade Federal Fluminense, UFF Rio de Janeiro - Niterói, RJ, Brazil
14.11.1995
20.80.0

IKP-209995
Nikolaev, N.N.; Zakharov, B.G.
Color Transparency
Invited Talk at the INPC Conference, Beijing, China
21.-26.8.1995
20.80.0

IKP-210095
Nikolaev, N.N.
Invited Talk at the Blois Workshop on Diffractive and Elastic Scattering, Blois
June 1995
20.80.0

IKP-210195
Nikolaev, N.N.
Invited Talk at the International Conference on Perspectives of Intermediate Energy Nuclear Physics, Trieste, Italy
May 1995
20.80.0

IKP-210295
Oelert, W.
Production of Strangeness in Proton-Proton and Antiproton-Proton Sccattering
University of Witwatersrand, Johannesburg, 26.5.1995
20.50.0

IKP-210395
Oelert, W.
LEAR Experiment PS210: Search for Antihydrogen
PS/AR Scientific Meeting at CERN, 11.9.1995
20.50.0

IKP-210495
Ohm, H., Hermes, Th., Borgs, W., Schult, O., Pysz, K., Kistryn, St., Jarczyk, L., Rudy, Z., Kulessa, P. and Cassing, W.
Production and fission decay of heavy Λ hypernuclei at COSY Jülich
Verhandlungen der DPG (VI) 30, 686 (1995) Köln
13.03.-17.03.1995
20.45.0

IKP-210595
Ohm, H.
Der Physiker in staatlichen Großforschungseinrichtungen,
DPG-Seminar "Der Physiker im Beruf", Bad Honnef, Germany
24.11. - 26.11.1995
20.45.0

IKP-210695
Ohm, H.
Produktion und Zerfall schwerer Hyperkerne
CANU-Arbeitstreffen, Bad Honnef, Germany
18.12. - 19. 12. 1995
20.45.0

IKP-210795
Osterfeld, F.
Delta-Anregungen in Kernen und ihre Zerfallseigenschaften
Universität Basel, Switzerland
19.1.1995
Expertentreffen für Kernphysik 1995, Schleching, Germany
Universität Göttingen, Germany
5.5.1995
Universität Tübingen, Germany
11.5.1995
20.80.0

IKP-210895
Osterfeld, F.
The Collective Pionic Model in Nuclei
DPG-Frühjahrstagung, Köln, Germany
13.-17.3.1995
20.80.0

IKP-210995
Osterfeld, F.
Nucleon Resonances in the Nuclear Medium
Invited talk, Groningen Giant Resonance Conference, Groningen, Netherlands
28.6.-1.7.1995
20.80.0

IKP-211095
Patt, J. for the COSY-TOF Collaboration
Signal Velocity and Pulse Height Distributions in the COSY-TOF Scintillator Hodoscopes
Verhandlungen der DPG (VI) 30, 677 (1995)
20.50.0

IKP-211195
Prasuhn, D.:
Interne und externe Experimente aus maschinenphysikalischer Sicht
Beschleunigerseminar, Uni Bonn, 17.01.1995
20.35.0

IKP-211295
Probst; H.J.:
Strahlenschutzbereiche
Strahlenschutzlehrgang für Naturwissenschaftler
FH-Aachen, Jülich, 13.03. - 17.03.1995 und 09.10 - 13.10.1995

IKP-211395
Probst; H.J.:
Strahlenschutzsicherheit
Strahlenschutzlehrgang für Naturwissenschaftler
FH-Aachen, Jülich, 13.03. - 17.03.1995 und 09.10 - 13.10.1995

IKP-211495
Probst; H.J.:
Strahlenschutzbereiche
Strahlenschutzlehrgang für Diplomingenieure
FH-Aachen, Jülich, 20.03. - 24.03.1995 und 23.10 - 27.10.1995

IKP-211595
Probst; H.J.:
Strahlenschutzsicherheit
Strahlenschutzlehrgang für Diplomingenieure
FH-Aachen, Jülich, 20.03. - 24.03.1995 und 23.10 - 27.10.1995

IKP-211695
Probst; H.J.:
Gerätetechnischer Strahlenschutz und Sicherheitsmaßnahmen
Spezialkurs für Beschleungerstrahlenschutz
RWTH Aachen, Haus der Technik, Essen
04.09-07.09.1995

IKP-211795
Probst; H.J.:
Betriebsinterne Überwachung und Kontrollen, Wartung, Aufzeichnungen und Meldepflichten
Spezialkurs für Beschleungerstrahlenschutz
RWTH Aachen, Haus der Technik, Essen
04.09-07.09.1995

IKP-211895
Probst; H.J.:
Arbeitsabläufe und Strahlenschutzplanung
Spezialkurs für Beschleungerstrahlenschutz
RWTH Aachen, Haus der Technik, Essen
04.09.-07.09.1995

IKP-211995
Probst; H.J.:
Strahlenschutzsicherheit
Sonderkurs im Strahlenschutz
FH Aachen, Jülich
15.11-17.11.95

IKP-212095
Rapp, R.
Phenomenological $\pi\pi$ Interactions in Cold Nuclear Matter
DPG-Frühjahrstagung, Köln, Germany
13.3.1995
20.80.0

IKP-212195
Rapp, R.
Equation of State of an Interacting Ho^+ Pion Gas
Seminar, Lyon, France
15.6.1995
20.80.0

IKP-212295
Rapp, R.
Medium Modifications of the ρ Meson at CERN/SpS Energies
Summer School on Developments in Particle Physics and Nuclear Theory, Dubna, Russia
2.9.1995
20.80.0

IKP-212395
Roehrich, K.
Strangeness Production in Antiproton Proton Annihilations in Flight
Hadron 95-Konferenz, Manchester, England, 9.7.-13.7.1995
20.50.0

IKP-212495
Sachs, K. for the PS185 collaboration
Optimized Event Reconstruction in the PS185 Decay Spectrometer
Verhandlungen der DPG (VI) 30, 784 (1995)
20.50.0

IKP-212595
Schmidt, K. for the COSY-TOF-Collaboration
Development and Test of a Scintillator Calorimeter for the COSY Time of Flight Spectrometer TOF
Verhandlungen der DPG (VI) 30, 629 (1995)
20.45.0

IKP-212695
Schmitz, Th.; Becker, R.; Drüke, V.; Eyrich, W.; Filges, D.; Hoffmann, W.; Kobus, H.; Maier, R.; Paganetti, H.:
Modelling of the Energy Deposition in Tissue Equivalent Phantoms for Incident Protons between 100 MeV and 250 MeV: Experimental Setup and First Results
Eighth Symposium on Neutron Dosimetry, Paris/France, 13.-17. November 1995
20.48.0

IKP-212795
Schnase, A.; Ausset, P.*; Etzkorn, F.J.; Fougeron, C.*; Maier, R.; Papureanu, S.; Stockhorst, H.:
(Kooperation mit dem Laboratoire National Saturne, CEA CE Saclay)
Preparing Acceleration Studies with a Multiple-Harmonic Cavity
DPG-Frühjahrstagung "Physik der Hadronen und Kerne"
Köln, 16.03.95
20.38.0

IKP-212895
Schnase, A.:
Ultralangsame Extraktion an COSY
Beschleunigerseminar, Uni Bonn, 24.01.1995
20.38.0

IKP-212995
Schnase, A.:
Frequenztreue des COSY HF-Systems
COSY-Beschleunigungsseminar, Jülich, 01.03.1995
20.35.0

IKP-213095
Schneider, A., Eßer, R. and Ohm, H.
Cerenkov counters for a K^+-detector system
Verhandlungen der DPG (VI) 30, 733 (1995) Köln
13.03.-17.03.1995
20.45.0

IKP-213195
Schütz, C.
πN Scattering and the Nature of the Roper Resonance
11th Nordic Meeting on Intermediate and High Energy Nuclear Physics,
Gräftavallen, Schweden
4.-8.1.1995
20.80.0

IKP-213295
Schütz, C.
Pion-Nucleon Scattering and the Nature of Nucleon Resonances
DPG-Frühjahrstagung, Köln, Germany
13.3.-17.3.1995
20.80.0

IKP-213395
Schütz, C.
Pion-Nucleon Scattering and the πNN and πNΔ form factors
International School of Nuclear Physics „Quarks in Hadrons and Nuclei
Erice, Sicily
19.-27.9.1995
20.80.0

IKP-213495
Schult, O.W.B.
The Physics Research Program at COSY-Juelich
RCNP Osaka, Japan
December 1995
20.45.0

IKP-213595
Sistemich, K.
The Status of COSY
Conference on Perspecitieves in Nuclear Physics at Intermediate Energies
08.05.-12.05.1995
20.45.0

IKP-213695
Speth, J.
Nonperturbative Mesonic Structure of Nucleons as seen in Elastic and Deep-Inelastic Scattering of Electrons
Gerry Garvey Fest,
19. - 20.1.1995
20.80.0

IKP-213795
Speth, J.
Zurück in die Zukunft - Mesonen in der Kern- und Teilchenphysik
Kolloquium, Univ. Hannover, Germany
7.2.1995
Ernst Werner Festkolloquium, Regensburg, Germany
8.5.1995
20.80.0

IKP-213895
Speth, J.
Meson-Meson and Meson-Nucleon Systems
6. International Symposium on Meson-Nucleon Physics and the Structure of the Nucleon, Blaubeuren/Tübingen, Germany
10.-14.7.1995
20.80.0

IKP-213995
Speth, J.
Meson Meson Scattering and the Nature of the Scalar Mesons
Institute of Atomic Energy, Peking, China
INPC-Conference, Peking, China
21.-26.8.1995
20.80.0

IKP-214095
Speth, J.
The Structure of Mesons and Nucleons
Kolloquium, Indiana University, Bloomington, USA
19.10.1995
Kolloqium, PSI Zürich, Switzerland,
24.11.1995
20.80.0

IKP-214195
Speth, J.
The Hyperon-Nucleon Interaction in the Meson Exchange
Invited Talk, CEBAF, Newport News, USA
30.10.1995
20.80.0

IKP-214295
Speth, J.
Mit COSY an der Forschungsfront der Hadronen-Physik
KFA Kolloquium
10.11.1995
CANU-Treffen, Bad Honnef, Germany
18.12.1995

IKP-214395
Stockhorst, H.:
Trackingsimulation mit dem longitudischen Code TIBETANC für höherharmonische Beschleunigungsspannungen
Beschleunigerseminar, Uni Bonn, 10.01.1995
20.35.0

IKP-214495
Stockhorst, H.; Heinrichs, G.; Schnase, A.; Papureanu, S.; Bechstedt, U.; Maier, R.; Tölle, R.:
Beam Shaping using a new digital noise Generator
Particle Accelerator Conference 1995
Dallas, Texas, 01.-05.05.1995
20.30.0

IKP-214595
Tölle, R.; Bechstedt, U.; Dietrich, J.; Hacker, U.; Maier, R.; Martin, S.; Prasuhn, D.; Stockhorst, H.:
Operational Experience at COSY Jülich
Spring Meeting of Nuclear Physics Sections, DPG-Tagung, Köln,
13.03.-17.03.1995
20.35.0

IKP-214695
Tölle, R.:
Strahlparameter an den Experimentierplätzen
Beschleunigerseminar, Uni Bonn, 20.06.1995
20.35.0

IKP-214795
Utzelmann, S.
Recoil Distance Lifetime Measurements of Oblate Bands in ^{144}Gd
Workshop on Experiments with EUROBALL CLUSTERS Detectors in 1995/96, Bad Honnef, 18.1.1995
20.10.0

IKP-214895
Utzelmann, S.; Lieder, R.M.; Gast, W.; Georgiev, A.; Lunardi, S.; Bazzacco, D.; Rossi-Alvarez, C.; Pavan, P.; de Angelis, G.; de Acuna, D.; de Poli, M.; Maron, G.; Rico, J.; Stuch, O.; Weil, D.; Satula, W.; Wyss, R.
The Superdeformed Band in ^{144}Gd and Candidates for Linking Transitions
Verhandlungen der DPG (VI) 30, 682 (1995)
20.10.0

IKP-214995
Utzelmann, S.
Superdeformed Bands in ^{144,145}Gd and High-Spin Structure of ^{180}Os
XII Int. School on Nucl. Phys., Neutron Physics and Nuclear Energy, Varna, Bulgarien, 30.9.1995
20.10.0

IKP-215095
Venkova, Ts.; Utzelmann, S.; Lieder, R.M.; Georgiev, A.; Hoernes, P.; Kaczarowski, R.; Rzaca-Urban, T.; Bazzacco, D.; Menegazzo, R.
Band Structures in ^{180}Os
Verhandlungen der DPG (VI) 30, 658 (1995)
20.10.0

IKP-215195
Wirth, H. for the PS202-Collaboration
Search for Resonances in the Reaction $\bar{p}p \rightarrow \Phi\Phi$ at the JETSET Experiment
Verhandlungen der DPG (VI) 30, 784 (1995)
20.50.0

IKP-215295
Wolke, M.
Schwellennahme Mesonenproduktion am internen COSY-Strahl
13. CANU-Arbeitstreffen „After 5000 Hours of User Beam", Physikzentrum Bad Honnef, Dezember 1995
20.50.0

IKP-215395
Wüstner, P. for the COSY-11-Collaboration
Datenaufnahmesystem für das Experiment COSY-11
Verhandlungen der DPG (VI) 30, 639 (1995)
20.50.0

IKP-215495
Zhang, C.T., Kleinheinz, P., Piiparinen, M., Blomqvist, J., Collatz, R., Broda, R., Grawe, H., Lönnroth, T., Maier, K.H., Schubart, R., und Sletten, G.
Complete Shell Model Yrast Lines and Seniority Inversion in N=84 Nuclei above Gadolinium
Verhandlungen der DPG (VI) 30, 713 (1995) Köln
13.03.-17.03.1995
20.10.0

XI. PATENTS

IKP-300195
Gast, W.; Lieder, R.; Georgiev, A.
Abtast-Analog-zu-Digital-Umsetzer mit Grob-Feinbereichs-Architektur („subrangig" Prinzip" und interpolierender Residuums-Kodierung
US: 5,442,575 (15.8.95)
20.10.0

XII. INTERNAL REPORTS

IKP-500195
Becker, G.
Die Pionproduktion in Pion-Nukleon-Streuung
Diplomarbeit, Dezember 1995
20.80.0

IKP-500295
Dahmen, M.
Das Flugzeitspektrometer an COSY: Ein Detektor zur exklusiven Messung von Mehrteilchenreaktionen
ISSN 0944-2952, KFA Jülich, Institut für Kernphysik, Jül-3140, Nov. 1995
20.50.0

IKP-500395
Holtmann, H.
Mesonen im Nukleon und ihre Auswirkungen in elastischer und tief-elastischer Streuung
Dissertation, Jül-3166, Dezember 1995
20.80.0

IKP-500495
Janssen, G.
Meson-Meson-Prozesse in der starken Wechselwirkung
Dissertation, Jül-3065, Mai 1995
20.80.0

IKP-500595
Jeschonnek, S.
Die Endzustandswechselwirkung in der quasielastischen Elektronenstreuung
Dissertation, Jül-3175, Dezember 1995
20.80.0

IKP-500695
Kalassa, M.
Effekte höherer Ordnungen in der elektromagnetischen Dissoziation leicht gebundener Kerne
Dissertation, Jül-3168, Dezember 1995
20.80.0

IKP-500795
Köhler, et al.
Die Silizium-Pad-Detektoren im Experiment COSY-11
Technical Report, Jül-3071, June 1995, ISSN 0944-2952
20.50.0

IKP-500895
Lempke, M.:
Schnelle Temperaturerfassung für den universellen Einsatz an gleichstromerregten Wicklungen
Diplomarbeit, Jül-3061 (ISSN 0944-2952, Mai 1995)
20.30.0

IKP-500995
Maier, R.:
Strahloptische Gesichtspunkte bei der Auslegung hochbrillanter Speicherringe
Jül-Bericht 3120, ISSN 0944-2952, November 1995
20.30.0

IKP-501095
Mosbacher, C.
Mesonaustauschströme in (p,n)-Reaktionen am Deuterium
Diplomarbeit, Oktober 1995
20.80.0

IKP-501195
Oelert, W. for the PS210-Collaboration
Production of Antihydrogen in Flight at LEAR
KFA-IKP(I)-1995-2
20.50.0

IKP-501295
Reuber, A.
Der Austausch korrelierter Pionen und Kaonen in der Baryon-Baryon Wechselwirkung
Dissertation, Jül-3117(ISSN 0944-2952), September 1995
20.80.0

IKP-501395
Roderburg, E. for the COSY-11 Collaboration
COSY-11; An Internal Experimental Facility for Threshold Measurements
KFA-IKP(I)-1995-1

IKP-501495
Schmidt, K.
Ein Szintillationskalorimeter für das COSY-Flugzeitspektrometer
ISSN 0944-2952, KFA Jülich, Institut für Kernphysik, Jül-3142, Nov. 1995
20.50.0

IKP-501595
Schütz, C.
Pion-Nukleon-Wechselwirkung und die Struktur von Nukleon-Resonanzen
Dissertation, Jül-3130, Oktober 1995
20.80.0

IKP-501695
Spross, T.
Methoden zur Qualitätsprüfung von Plastikszintillatoren und Lichtleitern
ISSN 0944-2952, KFA Jülich, Institut für Kernphysik, Jül-3141, Nov. 1995
20.50.0

IKP-501795
Trellakis, A.
Quantensignaturen von Chaos in nuklearen Riesenresonanzen
Diplomarbeit, Juni 1995
20.80.0

XIII. INTERNAL TALKS

IKP-600195
Bange, A.:
Aufbau einer 3D-Magnetfeldmeßeinrichtung
COSY-Beschleunigerseminar, Jülich, 29.11.1995
20.35.0

IKP-600295
Becker, G.
Die Pionproduktion in Pion-Nukleon-Streuung
Diplom-Kolloquium, Jülich, 30.11.1995
20.80.0

IKP-600395
Dietrich, J.:
Strahlanregung mit Diagnosekicker an COSY
COSY-Beschleunigerseminar, Jülich, 29.03.1995
20.30.0

IKP-600495
Lainck, H.:
Einfluß der Vakuumkammer auf das Magnetfeld der Quadrupole
COSY-Beschleunigerseminar, Jülich, 29.11.1995
20.30.0

IKP-600595
Lempke, M.:
Schnelle Temperaturerfassung bei Magneten mit hoher Stromdichte mit einem DSP-System
COSY-Beschleunigerseminar, Jülich, 19.04.1995
20.30.0

IKP-600695
Leunissen, P.:
Closed Orbit: Rechnungen und Messungen an COSY
COSY-Beschleunigerseminar, Jülich, 27.09.1995
20.30.0

IKP-600795
P. Leunissen
Chromatizitätsmessungen (u.a. mit Sextupolen) an COSY
COSY-Beschleunigerseminar, Jülich, 11.10.1995
20.30.0

IKP-600895
Lippert, G.
Übersicht über die Pion-Nukleon-Streuung
IKP1-Seminar, Jülich, 13.12.1995
20.45.0

IKP-600995
Maier, R.:
Introduction to the COSY Facility
Polarized Ion Source Workshop der Universität Köln, Jülich, 08. Juni 1995
20.30.0

IKP-601095
Mosbacher, Ch.
Mesonenaustauschströme bei (p,n)-Reaktionen am Deuterium
Diplom-Kolloquium, Jülich, 5.9.1995
20.80.0

IKP-601195
Patt, J.
Eigenschaften der langen Szintillatorstreifen am Flugzeitspektrometer TOF
IKP1-Diplomkolloquium, Jülich, 25.10.1995
20.45.0

IKP-601295
Schmidt, K.
Ein Szintillationskalorimeter für das COSY-Flugzeitspektrometer
IKP1-Diplomkolloquium, Jülich, 25.10.1995
20.45.0

IKP-601395
Schnase, A.:
Cooler-Synchrotron COSY-Jülich- ein Beschleuniger für die Mittelenergiephysik
Vortrag im Rahmen eines Strahlenschutzlehrganges, Jülich, 13.06.1995
20.30.0

IKP-601495
Schneider, H.:
Magnetrampen und Messungen
COSY-Beschleunigerseminar, Jülich, 22.02.1995
20.30.0

IKP-601595
Tölle, R.:
Tool: Applikationsprogramme an COSY
COSY-Beschleunigerseminar, Jülich, 27.09.1995
20.30.0

IKP-601695
Trellakis, A.
Signatures of Chaos in Nuclear Giant Resonances
Diplom-Kolloquium, Jülich, 31.5.1995
20.80.0

IKP-601795
Watzlawik, K.H.:
Server and Network Concepts for online and offline data analysis
ANKE Collaboration Meeting, IKP, Jülich, November 14-16,1995
20.45.0

FORSCHUNGSZENTRUM JÜLICH GmbH

KFA

Jül-3200
February 1996
ISSN 0944-2952